

# Third ARO Workshop on Smart Structures

Sponsored by:

**U.S. Army Research Office  
Research Triangle Park, North Carolina**

DISTRIBUTION STATEMENT A  
Approved for public release  
Distribution Unlimited

Hosted by:

**Center for Intelligent Material Systems and Structures  
Virginia Polytechnic Institute and State University**



Virginia Tech



19971203 045

DTIC QUALITY INSPECTED 2

**August 27-29, 1997**

Donaldson Brown Hotel and Conference Center ■ Blacksburg, Virginia

## REPORT DOCUMENTATION PAGE

*Form Approved*  
OMB NO. 0704-0188

Public reporting burden for this collection of information is estimated to average 1 hour per response, including the time for reviewing instructions, searching existing data sources, gathering and maintaining the data needed, and completing and reviewing the collection of information. Send comment regarding this burden estimates or any other aspect of this collection of information, including suggestions for reducing this burden, to Washington Headquarters Services, Directorate for Information Operations and Reports, 1215 Jefferson Davis Highway, Suite 1204, Arlington, VA 22202-4302, and to the Office of Management and Budget, Paperwork Reduction Project (0704-0188), Washington, DC 20503.

**PROGRAM**

**THIRD ARO WORKSHOP ON SMART STRUCTURES**

**VIRGINIA POLYTECHNIC INSTITUTE AND STATE UNIVERSITY  
BLACKSBURG, VIRGINIA**

**AUGUST 27-29, 1997**

**The views, opinions, and/or findings contained in this report are those of the author(s)  
and should not be construed as an official Department of the Army  
position, policy, or decision, unless so designated by other documentation.**

## **PROGRAM**

### **THIRD ARO WORKSHOP ON SMART STRUCTURES\* VIRGINIA POLYTECHNIC INSTITUTE AND STATE UNIVERSITY**

**TUESDAY, AUGUST 26, 1997**

7:00-9:00 PM WELCOME RECEPTION AND REGISTRATION, Old Guard Room, DBHCC

**WEDNESDAY, AUGUST 27, 1997**

7:30 AM Light breakfast available in Owens Hall Banquet Room (included in registration fee)

8:00 AM Welcome/Overview; G. Anderson, U.S. Army Research Office; Chair: D. Inman, H. Cudney, Virginia Tech

#### **SESSION 1: HELICOPTER APPLICATIONS - I**

Session Chair: D. Merkley, U.S. Army Labs

8:15 AM "Design, Fabrication and Hover Testing of a Mach-Scaled Rotor Model with Piezo-Bimorph Actuated Trailing-Edge Flaps," N. A. Koratkar and I. Chopra, University of Maryland

8:35 AM "Modeling of Smart Composite Box Beams with Nonlinear Induced Strain," A. Chattopadhyay, H. Gu and Q. Liu, Arizona State University

8:55 AM "Characterization of Semi-Active Magneto-Rheological Helicopter Lag Mode Dampers," G. M. Kamath, N. M. Wereley and M. R. Jolly, University of Maryland, Lord Corp.

9:15 AM "ARL Active Twist Rotor Research," W. K. Wilkie, K. C. Park, W. K. Belvin, M. L. Wilbur and P. H. Mirick, ARL/Vehicle Technology Center, University of Colorado, NASA LaRC

9:35 AM "Development of an Active Trailing Edge Flap for a Rotor Using Piezostacks," T. Lee and I. Chopra, University of Maryland

9:55-10:10 AM BREAK

*\*All sessions held in Owens Hall Banquet Room (across the street from the rear entrance to the Donaldson Brown Hotel and Conference Center). The Poster Session and Reception on Thursday evening will be held in the Commonwealth Room of the Donaldson Brown Hotel and Conference Center.*

## **SESSION 2: DAMPING TREATMENTS**

Session Chair: W. Snowden, DOD

10:10 AM "Characteristics of Enhanced Active Constrained Layer Damping Treatments with Edge Elements," W. H. Liao and K. W. Wang, Penn State

10:30 AM "Segmented Active Constrained Layer Damping Treatments for Structural Vibration Damping," G. Kawiecki and P. F. Cento, University of Tennessee

10:50 AM "Vibration Control of Laminated Plates with Active Constrained Layer Damping," C. Kim, T. Chen and A. Baz, NASA-Goddard, University of Maryland

11:10 AM "Damping Using a Solid-State Tunable Piezoceramic Vibration Absorber," G. A. Lesieurte and C. L. Davis, Penn State

11:30 AM "On the Structural Damping Characteristics of Active-Passive Piezoelectric Shunt Networks," M. S. Tsai and K. W. Wang, Penn State

11:50 AM-1:30 PM GROUP LUNCH BUFFET (included in registration fee), Owens Hall Banquet Room (adjacent to sessions)

## **SESSION 3: MR/ER DEVICES**

Session Chair: J. Heeg, NASA

1:30 PM "Nondimensional Analysis of Semi-Active Electrorheological and Magnetorheological Dampers," L. Pang and N. N. Wereley, University of Maryland

1:50 PM "Damping Properties of Magneto-Rheological Fluids," M. Ahmadian, X. Song and B. Reichert, Virginia Tech

2:10 PM "Helicopter Blade Response and Aeromechanical Stability with Magnetorheological and Fluid Based Lag Dampers," S. Marathe, F. Gandhi and K. W. Wang, Penn State

2:30 PM "Qualitative Analysis of the Bulk Ferromagnetic Hysteresis Model," R. Venkataraman and P. S. Krishnaprasad, University of Maryland

2:50 PM "Active Nonlinear Vibration Absorber," S. S. Oueini and A. H. Nayfeh, Virginia Tech

3:10-3:30 PM BREAK

## **SESSION 4: ACOUSTICS**

Session Chair: G. Gibbs, NASA

3:30 PM "Control System Design for Adaptive Structures," R. L. Clark and D. S. Bernstein, Duke, University of Michigan

3:50 PM "Active Control of Enclosed Sound Fields," B. Balachandran, C. W. Ahn and A. Sampath, University of Maryland, Scientific Systems, Inc.

4:10 PM "A Generalized Theory for Distributed Active-Passive Beam Structures for Vibration and Sound Radiation Control," P. Cambou, F. Charette and C. R. Fuller, Virginia Tech

4:30 PM "Control of Low Frequency Structurally Radiated Noise with an Array of Weak Radiating Cells," B. W. Ross and R. A. Burdisso, Virginia Tech

4:50 PM "ARMARKOV/Toeplitz Models: A New Paradigm for Model Identification and Adaptive Cancellation," J. C. Akers, R. Venugopal and D. S. Bernstein, University of Michigan

6:00-7:30 PM WINE AND CHEESE RECEPTION AND LAB TOURS\*\*  
(Reception and tours begin at CIMSS lab, 381 New Engineering Building)

## THURSDAY, AUGUST 28, 1997

7:50 AM Light breakfast available in Owens Hall Banquet Room (included in registration fee)

### SESSION 5: HELICOPTER APPLICATIONS - II

Session Chair: P. Mirick, U.S. Army Labs

8:20 AM "Development of a Smart Moving-Blade-Tip and an Active-Twist Rotor Blade Driven by a Piezo-Induced Bending-Torsion Coupled Beam," A. P. F. Bernhard and I. Chopra, University of Maryland

8:40 AM "Design, Manufacture, and Hover Testing of an Integral Twist-Actuated Rotor Blade," J. P. Rodgers and N. Hagood, MIT

9:00 AM "Development of Neural Network Controller for Smart Structure Activated Rotor Blades," M. G. Spencer, R. M. Sanner and I. Chopra, University of Maryland

9:20 AM "Application of LARIS Principle to Directly-Deformable Aerodynamics Surfaces," V. Giurgiutiu and C. A. Rogers, University of South Carolina

9:40 AM "Wind Tunnel Testing of a Small-Scale Rotor with On-Blade Elevons," M. Fulton and R. Ormiston, NASA-Ames, U.S. Army Aeroflightdynamics Directorate

10:00-10:20 AM BREAK

### SESSION 6: NOVEL SYSTEMS

Session Chair: M. Mattice, U.S. Army Armament Research and Development Center

10:20 AM "An Initial Study of the Dynamic Characteristics of Honeycomb Structures with a Negative Poisson's Ratio," F. Scarpa and G. Tomlinson, University of Sheffield, England

10:40 AM "Finite Element Modeling of Magnetic Constrained Layer Damping," M. Ruzzene, J. Oh and A. Baz, University of Maryland

11:00 AM "Vibrations of Piezoelectric Crystal and Ceramic Plates with Functionally Graded Material Properties," P. C. Y. Lee, Princeton

11:20 AM "Nonlinear Modeling and Characterization of Repolarizing Piezoelectric Materials," K. Ghandi and N. Hagood, MIT

11:40 AM "Evaluating the Response of Piezoelectric Materials: Analytical and Experimental," G. Carman and D. Wang, University of California - Los Angeles

12:00-1:20 PM GROUP LUNCH BUFFET (included in registration fee), Owens Hall Banquet Room (adjacent to sessions)

#### **SESSION 7: CONTROL DESIGN**

Session Chair: R. Ormiston, U.S. Army Aeroflight Dynamics Directorate

1:20 PM "Electromechanical Tuning of Self-Sensing Piezoelectric Transducers," E. Brusa, S. Carabelli, F. Carraro and A. Tonoli, Politecnico di Torino, Italy

1:40 PM "Controllable Resonance in Structures and Fluids and the Rectification of Oscillatory Motion," R. Brockett, Harvard University

2:00 PM "Actuator Limited Multivariable Controllers for Smart Structural Systems," S. Sana, M. Jadi and V. S. Rao, University of Missouri - Rolla

2:20 PM "Power Flow Analysis of an Electrostrictive Actuator Driven by a PWM Amplifier," D. K. Lindner and G. A. Zvonar, Virginia Tech

2:40-3:00 PM BREAK

#### **SESSION 8: SENSORS**

Session Chair: Y. Senda-Sanabri, USAEWES

3:00 PM "Deflection Response for Series Configurations of Piezoceramic Unimorph C-Block Actuators," A. Moskalik, D. Brei, S. J. Palko and R. Barrett, University of Michigan, Auburn University

3:20 PM "Fiber Optic Sensors for Soldiers' Smart Uniform," M. El-Sherif, Drexel University

3:40 PM "Optical Fiber Sensors Used in Smart Structural Systems," K. A. Murphy, M. F. Gunther, R. O. Claus, P. G. Murphy, M. E. Jones and M. B. Miller, Virginia Tech, F&S, Inc.

4:00 PM "Distributed Modal Sensors," H. Sumali and H. Cudney, Virginia Tech

4:20 PM "Wireless MEMS Sensors for Measuring Deflection, Acceleration and Ice Detection on Scale Model Rotor Blades," V. K. Varadan and V. V. Varadan, Penn State

4:40 PM "Structurally Embedded Multifunction Fiber Optic Sensors," X. D. Jin, J. S. Sirkis and J. K. Chung, University of Maryland, Chosun University, Korea

6:00-8:00 PM POSTER SESSION AND RECEPTION\*\*\* (Heavy Hors D'oeuvres)  
Commonwealth Room, Donaldson Brown Hotel and Conference Center

**FRIDAY, AUGUST 29, 1997**

7:30 AM Light breakfast available in Owens Hall Banquet Room (included in registration fee)

**SESSION 9: HYSTERESIS MODELS**

Session Chair: W. K. Wilkie, U.S. Army Labs

8:00 AM "Smart Material Structures with Viscoelastic Components and Hysteresis," H. T. Banks, North Carolina State University

8:20 AM "Compensation for Hysteresis Using KP Integral Operators," W. S. Galinaitis and R. C. Rogers, Virginia Tech

8:40 AM "Micro-Mechanics and Control of Hysteresis in Shape Memory Alloys," D. Lagoudas, Z. Bo, A. Kurdila and G. Webb, Texas A&M University

9:00 AM "SMA-Induced Deformations of General Unsymmetric Composite Laminates," M. Dano and M. W. Hyer, Virginia Tech

9:20 AM "Comparative Evaluation of Shape Memory Alloy Constitutive Models with Test Data," J. Epps and I. Chopra, University of Maryland

9:40 AM "Viscoelastic Effects in the Dynamics of Thick Beams," A. R. Johnson and A. Tessler, NASA LaRC

10:00-10:20 AM BREAK

**SESSION 10: DAMAGE ASSESSMENT**

Session Chair: A. Johnson, U.S. Army Vehicle Structures Directorate

10:20 AM "Damage Detection Methodology for Composite Rotorcraft Flexbeams," K. A. Lakshmanan and D. J. Pines, University of Maryland

10:40 AM "Rotor Blade Damage and Deterioration Detection Through the Wavelet Transform Method," X. Deng, C. A. Rogers, V. Giurgiutiu and M. A. Sutton, University of South Carolina

11:00 AM "Fault Detection in Main Rotor Blades," J. Kiddy and D. Pines, University of Maryland

11:20 AM "Three-Dimensional Boundary Elements for Flawed Piezoelectric Materials," L. R. Hill and T. N. Farris, Purdue University

11:40 AM "Finite Dynamic Deformations of Laminated Structures Containing PZT Laminas," R. C. Batra and X. Q. Liang, Virginia Tech

12:00-1:00 PM GROUP LUNCH BUFFET (included in registration fee), Owens Hall Banquet Room (adjacent to sessions)

**SESSION 11: MEMS**

Session Chair: E. Kathe, U.S. Army Benet Laboratory

1:00 PM "Artificial Robotic Fingers Driven by Piezoelectric Actuators," M. Tanaka, Z. Jiang and S. Chonan, Tohoku University, Japan

1:20 PM "Feedback Control with Shape Memory Alloy Actuators," C. Dickinson and J. Wen, RPI

1:40 PM "MEMS and MOMS Sensors and Actuators - Design, Fabrication and Networking," M. B. Miller, F&S, Inc.

2:00 PM "Soft Lithography and Smart Materials," G. M. Whitesides, Harvard University

2:20 PM "Smart Trim Panels Using MEMS Sensors for Interior Noise Suppression," V. V. Varadan, V. K. Varadan and X. L. Bao, Penn State

2:40-3:00 PM BREAK

**SESSION 12: PROGRAM OVERVIEWS**

Session Chair: Gary Anderson, U.S. Army Research Office

3:00 PM "Active Controls/Smart Structures S&T Strategy for Army Aviation," D. Hoad and R. Ormiston, ARL, ATCOM

3:30 PM "Smart Weapon Systems," M. Mattice, U.S. Army Armament Research and Development Center

3:45 PM "Innovative Smart Technologies for Actively Controlled Jet-Smooth Quiet Rotocraft," I. Chopra, University of Maryland

4:00 PM "Overview of Research in the Active Materials and Structures Lab," N. W. Hagood, Massachusetts Institute of Technology

4:15 PM "Smart Materials Systems through Mesoscale Patterning," I. A. Aksay, S. M. Gruner, P. C. Y. Lee, R. K. Prud'homme, S. Torquato, W. H. Shih and G. M. Whitesides, Princeton University, Drexel University, Harvard University

4:30 PM ADJOURN

**\*\*Virginia Tech Laboratory Tours (optional)**

Composites Fabrication Lab (Mike Hyer)

Nonlinear Dynamics Lab (Ali Nayfeh)

Fiber and Electro-Optics Research Center (FEORC) (Rick Claus)

Applied Control Systems Laboratory (Will Saunders)

Center for Intelligent Material Systems and Structures (CIMSS) (Dan Inman and Harley Cudney)

Rapid Prototyping Laboratory (Jan Helge Bohn)

Vibration and Acoustics Laboratories (VAL) (Chris Fuller)

Modal Analysis Laboratory (MAL) (Larry Mitchell)

Advanced Vehicle Dynamics Laboratory (Mehdi Ahmadian)

**\*\*\*Poster Session Program**

"Active Control for 2-D Dynamic Smart Beam," D. Cai and D. Y. Gao, Virginia Tech

"Progressive Failure Analysis of Shape Memory Alloy Hybrid Composite Beams Under Low-Velocity Impact," H. Jia and F. Lalande, Virginia Tech

"Boring Bar Chatter Control," J. Pratt and A. Nayfeh, Virginia Tech

"Natural Frequencies of Multi-Layer Composite Plate with Shape Memory Alloy," W. Ostachowicz, M. Krawczuk and A. Zak, Polish Academy of Sciences, Poland

"Temperature Effects in PZT-Based Control Design," M. I. Friswell and D. J. Inman, University of Wales, Virginia Tech

"Active Control of Vibration Transmission Through Struts," I. Pelinescu and B. Balachandran, University of Maryland

"Microfabricated Conformal Wall Shear Stress Sensor for Aircraft," V. J. Varadan and V. V. Varadan, Penn State

"Self-Assembled Nanoparticle-Based Multi-Layer Thin-Films and Devices," Y. Liu, J. R. Heflin, W. Zhou and R. O. Claus, Virginia Tech

"Effects of Implementation of Smart Materials Technology and Optimal Control of Dynamic Response of Cantilevers Exposed to Blast Loadings," S. S. Na and L. Librescu, Virginia Tech

"A Comparison of H<sub>2</sub> Optimized Design and Cross-Over Point Design for Acceleration Feedback Control," M. de Noyer and S. Hanagud, Georgia Tech

"Control of Deformable Mirrors Using Piezoelectric Actuators," R. K. Kapania, Virginia Tech

"Application of Neural Networks to Crack Detection in Cantilever Beams," G. Kawiecki, University of Tennessee

"Piezo-Generated Elastic Waves for Structural Damage Detection," G. Kawiecki, University of Tennessee

"Viscoelastic Analysis of Composite Structures," R. K. Kapania

"Adaptive Tuning of Piezo-Actuated Delayed Resonator Absorbers," M. Renzulli, R. Ghosh-Roy and N. Olgac, University of Connecticut

"Analysis and Testing of an Electrorheological Bypass Damper," J. E. Lindler and N. M. Wereley, University of Maryland

"Dynamic Response of Sandwich Beam with Viscoelastic Layer," G. Wang and N. M. Wereley, University of Maryland

"Damping Identification in Helicopter Rotor Systems," C. B. Smith, J. Perez and N. M. Wereley, University of Maryland

"Switchmode Amplifiers for Smart Materials," T. Schelling, D. K. Lindner and G. A. Zvonar, Virginia Power Technologies, Inc. and Virginia Tech

**CONTENTS**

---

**1**

---

**2**

---

**3**

---

**4**

---

**5**

---

**6**

---

**7**

---

**8**

---

**9**

---

**10**

---

**11**

---

**12**

---

# **Design, Fabrication and Hover testing of a Mach-Scaled Rotor Model with Piezo-Bimorph actuated Trailing-Edge Flaps**

Nikhil A. Koratkar \* and Inderjit Chopra \*\*

Alfred Gessow Rotorcraft Center  
Department of Aerospace Engineering  
University of Maryland at College Park, MD 20742

This research deals with the development of a Mach scaled rotor model with piezoceramic bimorph actuated trailing-edge flaps. The purpose of the flap in this research is to provide an active vibration control device that cancels the vibration at its source (in the rotating frame), by directly altering the airloads on the blades. The flap is actuated using piezoceramic benders mounted into the spar of the blade (Figure 1). A rod-cusp mechanism is used to amplify the actuator tip displacement. The piezo-induced response is formulated by coupling an unsteady aerodynamic model for the flap hinge moment with a structural finite element beam model for the piezoceramic bender. Both frequency domain, incompressible unsteady aerodynamics (Theodorsen theory) as well as time domain, compressible, unsteady aerodynamic models (indicial theory) were investigated. The analysis also accounted for the centrifugal, inertial and frictional loads acting on the coupled actuator-flap system in the rotating environment.

Two operational 1/8<sup>th</sup> (Froude) scale rotor models with piezo-bimorph actuated trailing-edge flaps were fabricated. The analytical model was validated by carrying out a series of bench tests, vacuum chamber tests and hover tests. Flap deflections of  $\pm 6$  degrees (4/rev excitation) were achieved in hover at the Froude scaled operating speed of 900 RPM (figure 2,3). The oscillatory thrust, pitching moment, rolling moment and torque were measured using a rotating frame balance. 10% flap authority for the rotor thrust was achieved at 4 degrees collective for a 4/rev excitation (figure 4).

The analytical model was used to design a Mach scaled rotor model with piezo-bimorph actuated trailing-edge flaps. The analysis indicates that two side-by-side, tapered, 8-layered bimorphs excited using a bias voltage (2:1 amplification) can generate flap deflections of  $\pm 6$  degrees at the Mach scaled operating speed of 2100 RPM (Figure 5). Presently, a Mach scaled rotor model is under fabrication. Static tests on individual components such as spars, root inserts, ribs, 8-layered tapered bimorphs are in progress. The full paper will cover design, fabrication and hover testing of the rotor model at several operating speeds and excitation frequencies.

---

\* Graduate school fellow

\*\* Minta Martin Professor and Director

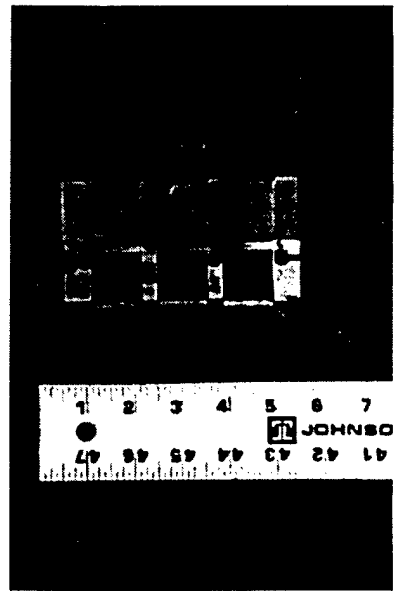


**Figure 1 : Smart rotor with piezo-bimorph actuated trailing-edge flaps**

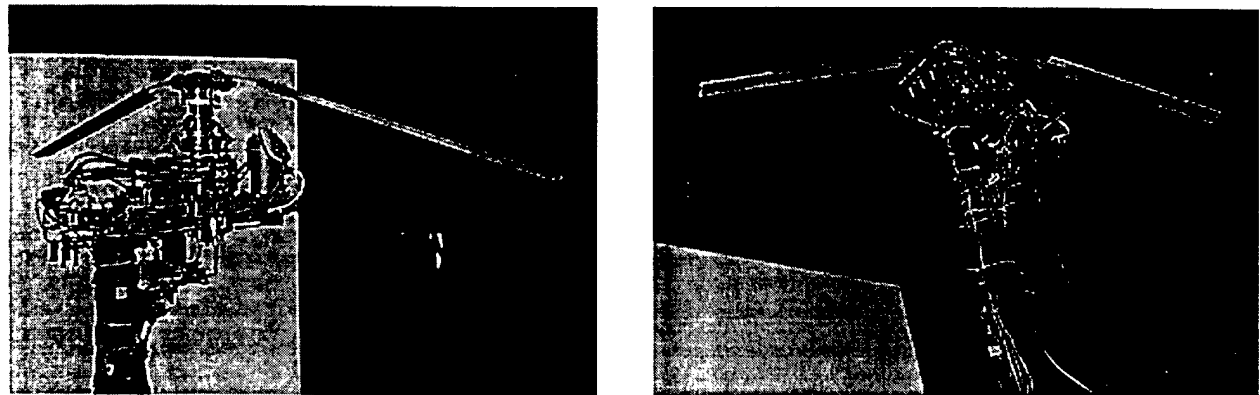


**Figure 2 : Hover testing (Froude scaled rotor models)**

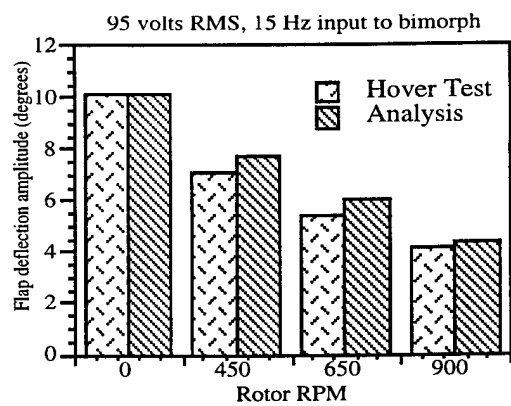


**Figure 3 : Hover test (RPM Sweep) - for Froude scaled model**

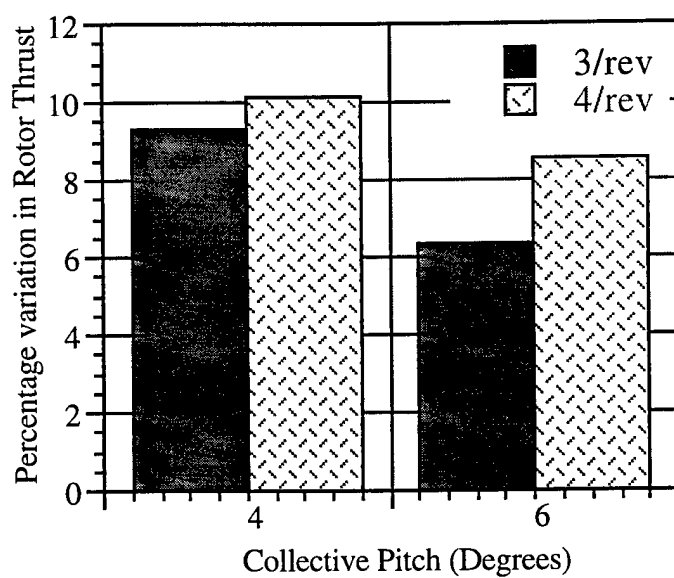


**Figure 4 : Flap Authority - for the Froude scaled model**

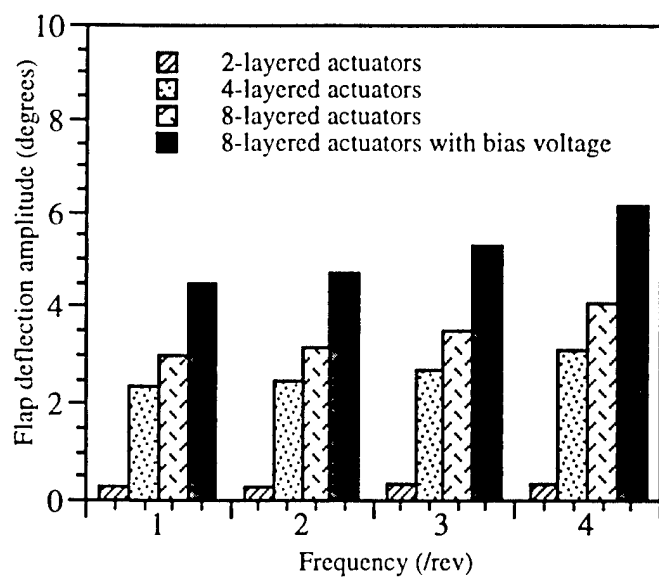
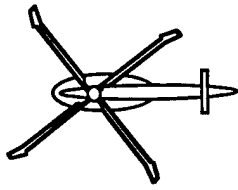


**Figure 5 : Predicted response for Mach-scaled configuration**

**UM**

**ALFRED GESEOW  
ROTORCRAFT CENTER**



**UNIVERSITY OF MARYLAND AT COLLEGE PARK**

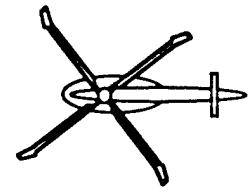
**DEVELOPMENT OF A MACH SCALED  
ROTOR MODEL WITH PIEZO-BIMORPH  
ACTUATED TRAILING-EDGE FLAPS**

**NIKHIL A. KORATKAR**

**GRADUATE FELLOW**

**INDERJIT CHOPRA**

**PROFESSOR AND DIRECTOR**



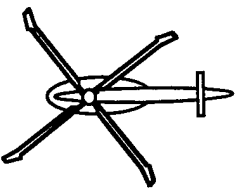
UM

# Major Challenges in Rotorcraft

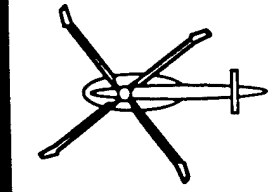


- Vibration Suppression
- Noise Reduction
- Enhancement of Handling Qualities

# Outline of Presentation



- Introduction : Smart Rotor
- Piezo-Bimorph actuation
- Analytical model for coupled bimorph-flap dynamic response
- Proof of Concept : Froude Scale
- Design and Fabrication of a Mach scaled model



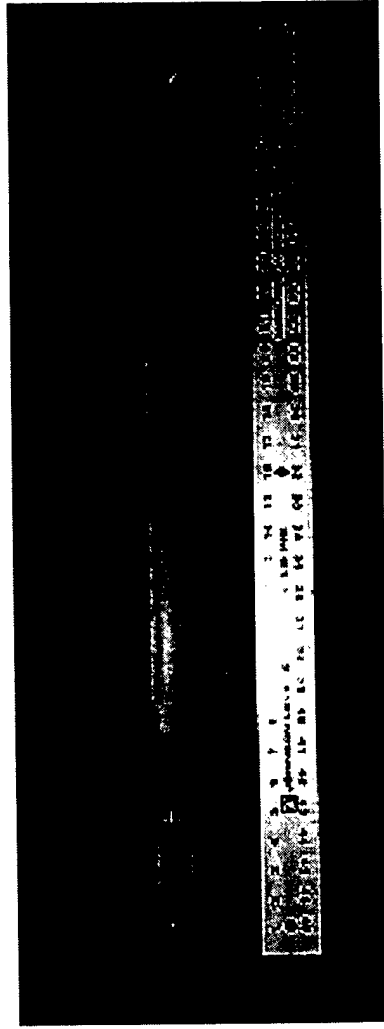
UM

# SMART ROTOR (Active Trailing-Edge Flaps)

- Helicopter Vibration

For an N-Bladed Rotor,

- $N/\text{rev}$  and  $N \pm 1/\text{rev}$  blade loads
- Transmitted to fuselage via hub as  $N/\text{rev}$  forcing

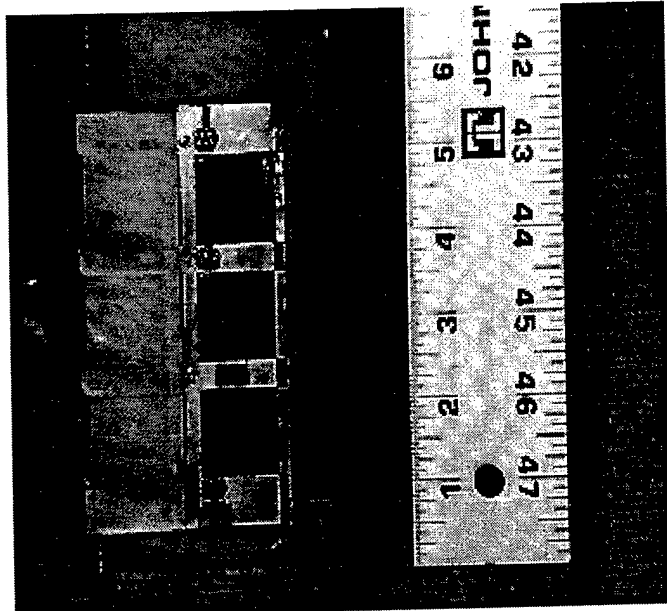
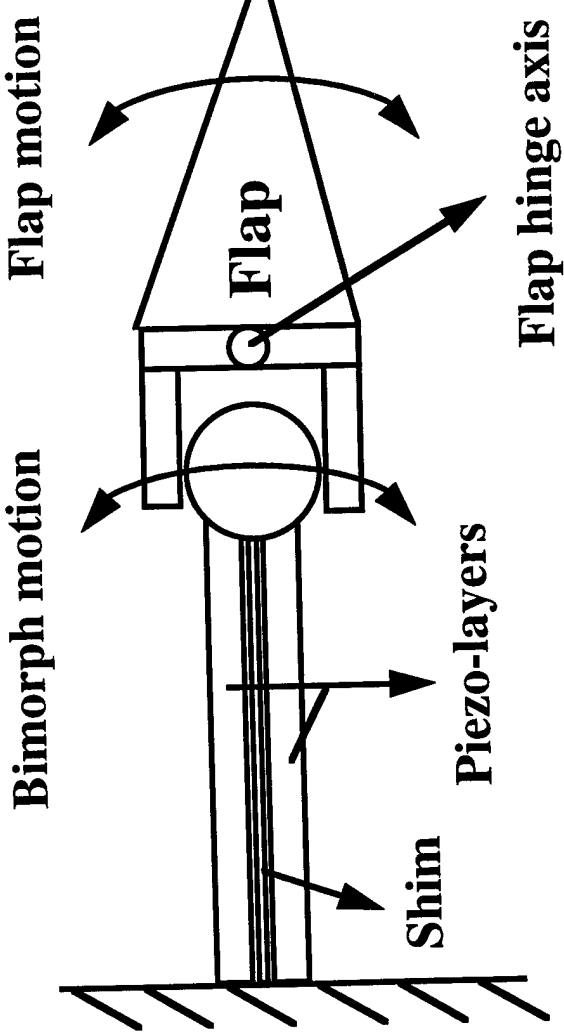
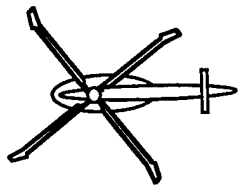


## SMART ROTOR BLADE MODEL

- Active Vibration Control : Flap motion causes new unsteady aerodynamic forces. Correctly phased this activation can reduce the vibratory hub loads (**Individual Blade Control**).

UM

# Piezo-Bimorph Actuation

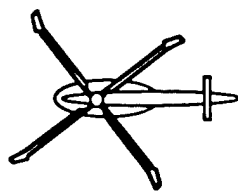


## Rod-Cusp Amplification Mechanism

## Smart Rotor with Piezo-Bimorph actuation

UM

## Analytical model for coupled Bimorph-Flap dynamic response



INPUT : Voltage excitation  
to the actuator

### UNSTEADY AERODYNAMICS

- Time domain Leishman-Hariharan formulation (Indicial Concepts)

- Frequency domain Theodorsen Theory

### FEM MODEL

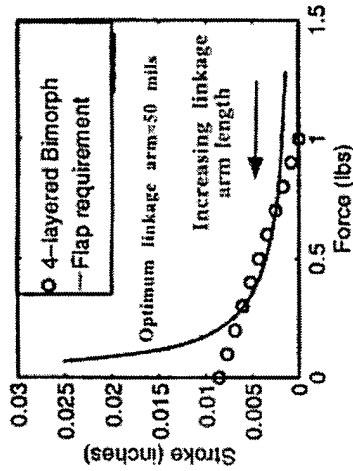
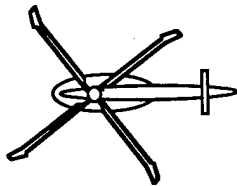
- Bimorph is modeled as an elastic beam
- PZT induced strain is included in the strain energy expression
- Flap Hinge Moment is modeled as a tip force acting on the bimorph

### Dynamic Analysis

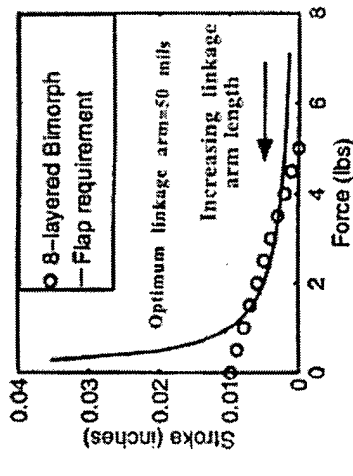
OUTPUT :  
Amplitude and phasing  
of Flap motion

# UM

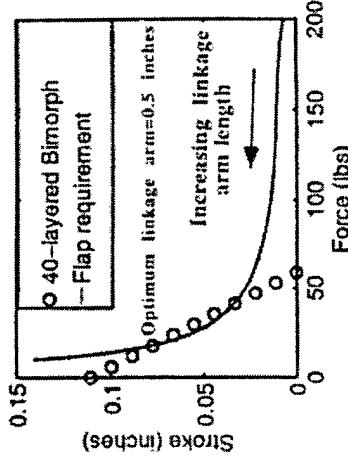
# Feasibility Study (Piezo-Bimorph Actuation)



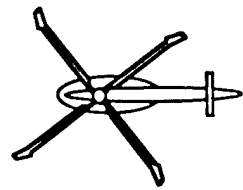
a) Froude scale



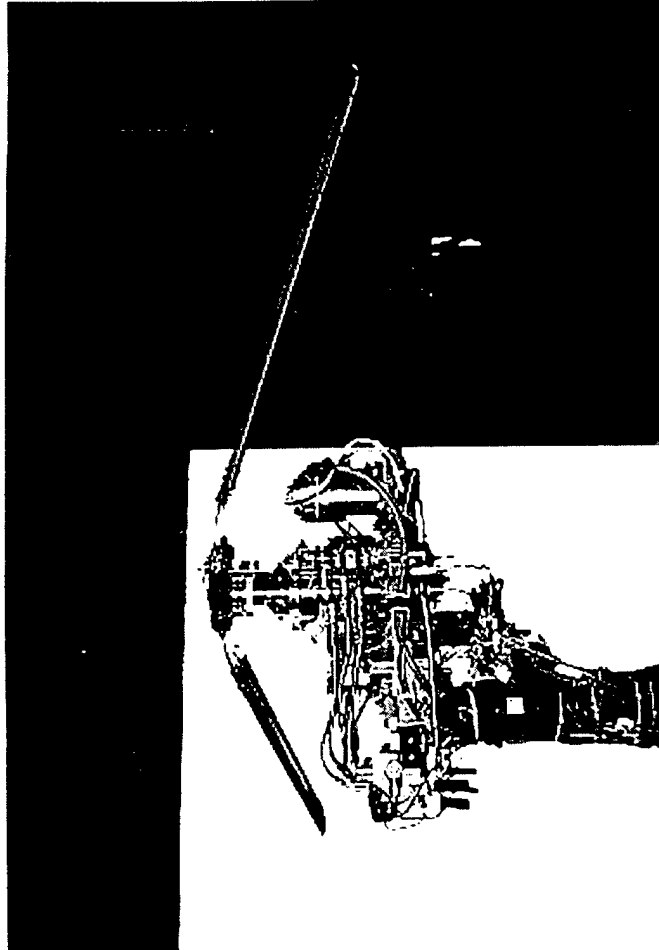
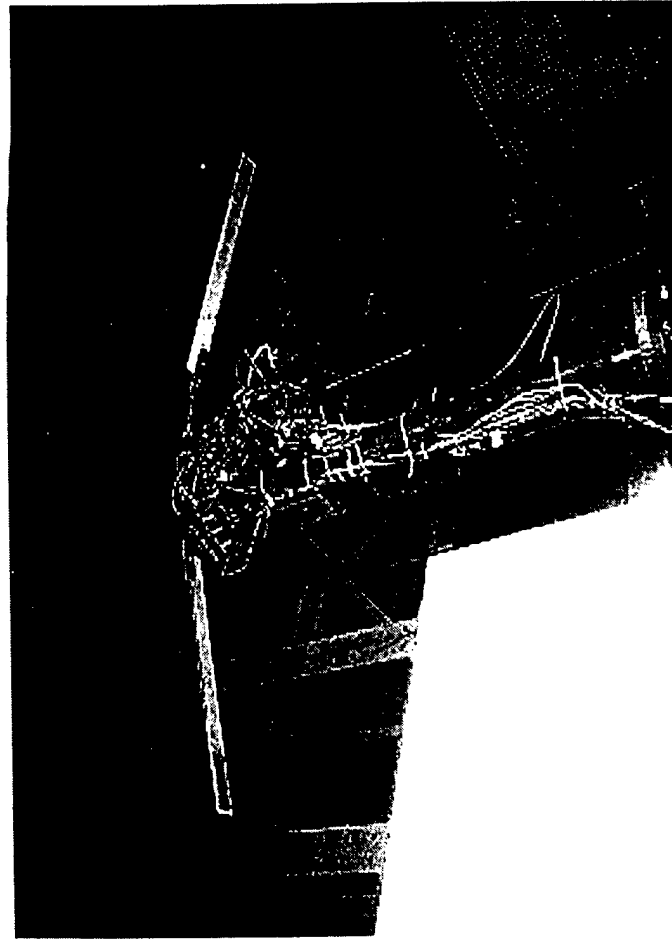
b) Mach scale



c) Full scale : S-76 rotor



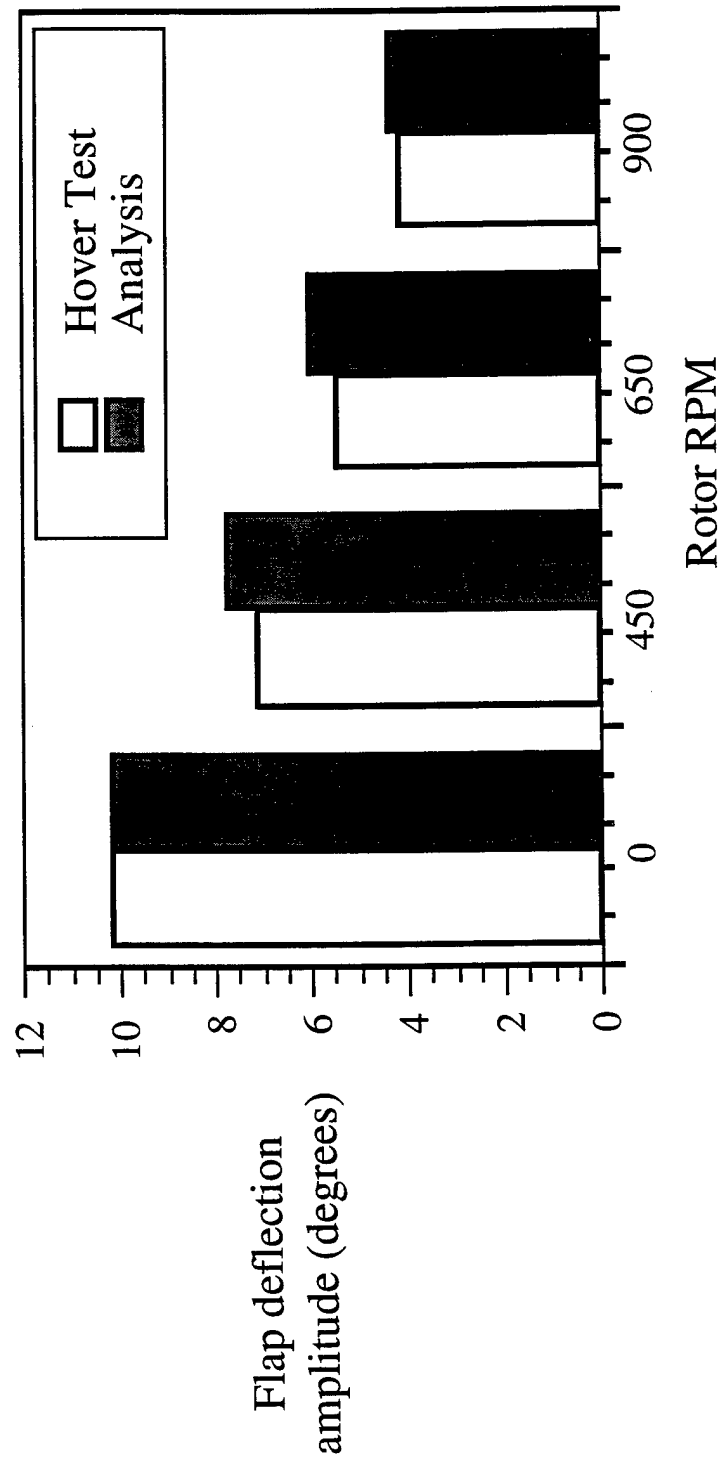
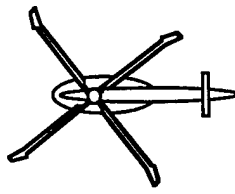
# Experimental Validation - Froude scale UH-60 Hover Testing



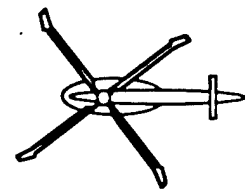
Hover stand test facility

UM

# Hover Test : RPM Sweep (Froude scaled operating speed=900 RPM)

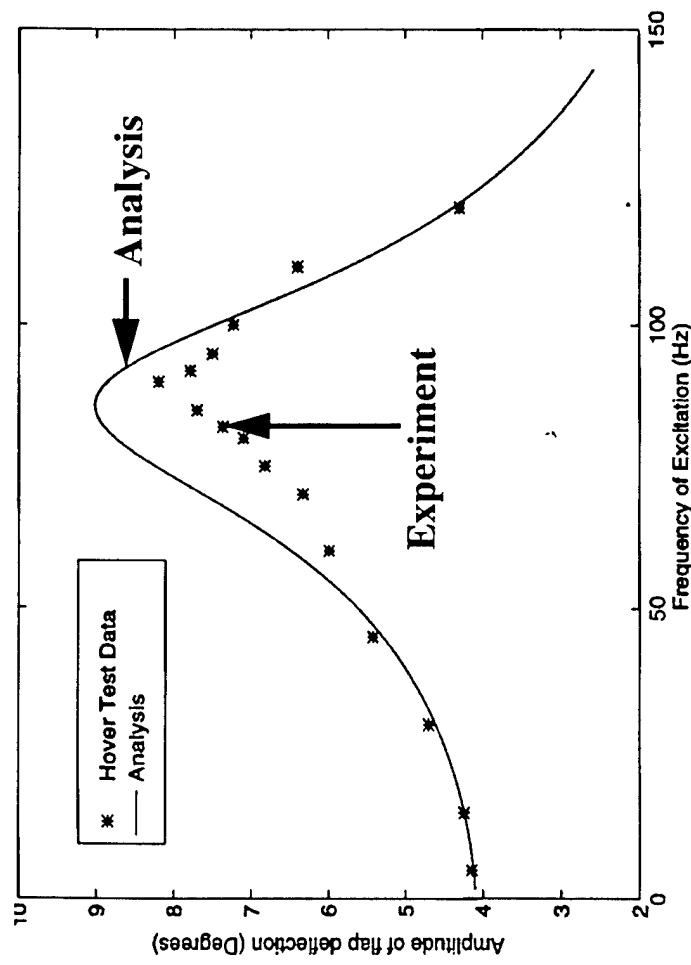


95 Volts RMS, 15 Hz input excitation to Bimorph  
Linkage arm length = 54 mils, Blade collective pitch = 0 degree



# UM Hover Test : Frequency Sweep at 900 RPM

Flap amplitude (degrees)

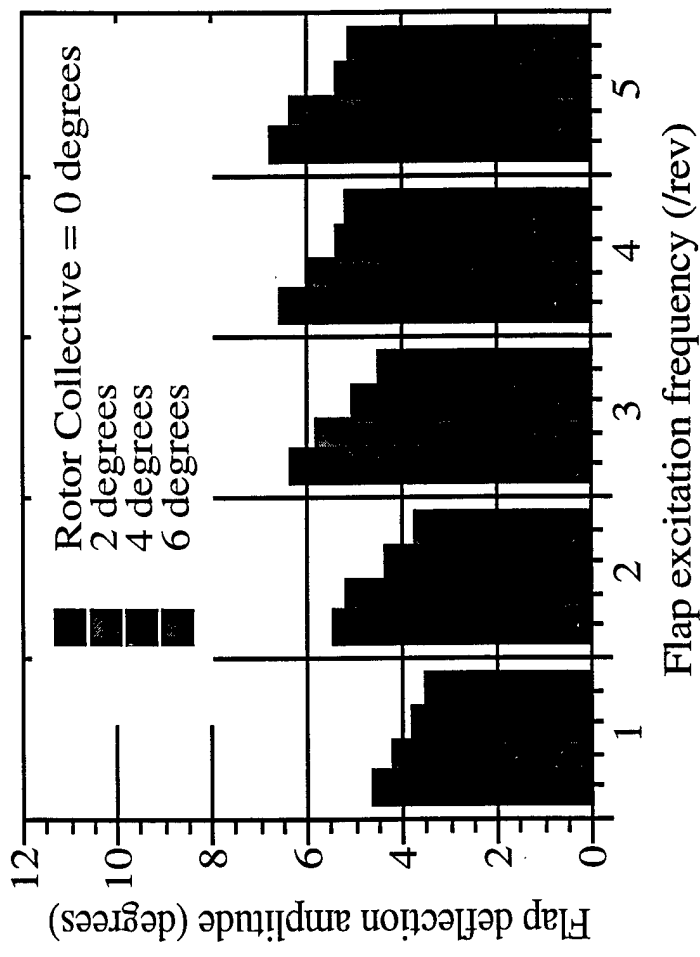
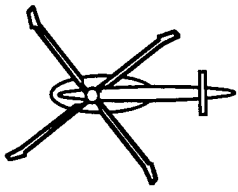


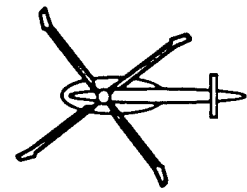
95 Volts RMS input excitation to Bimorph

Linkage arm length = 54 mils, Blade collective pitch= 0 degrees

# UM

## Effect of rotor collective pitch (Rotor speed=900 RPM)



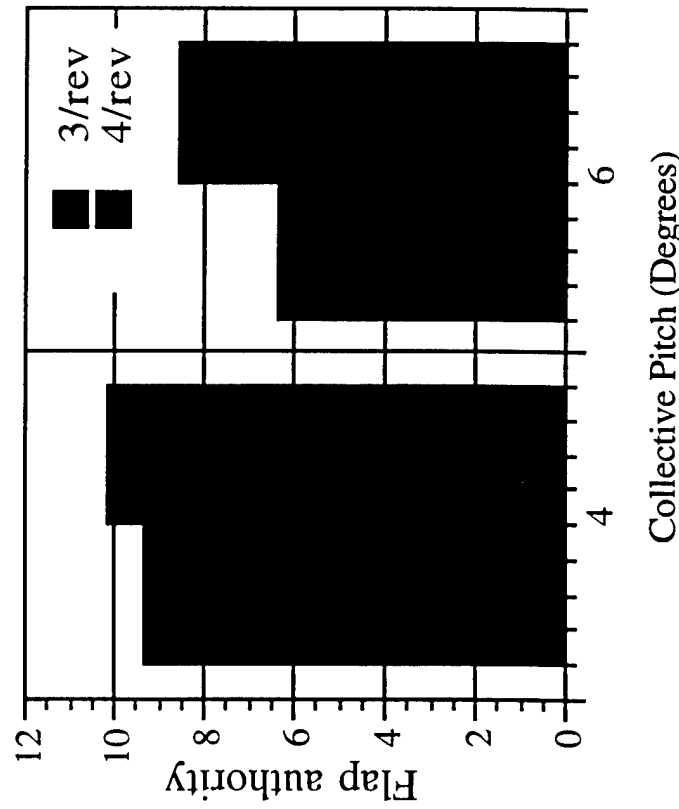
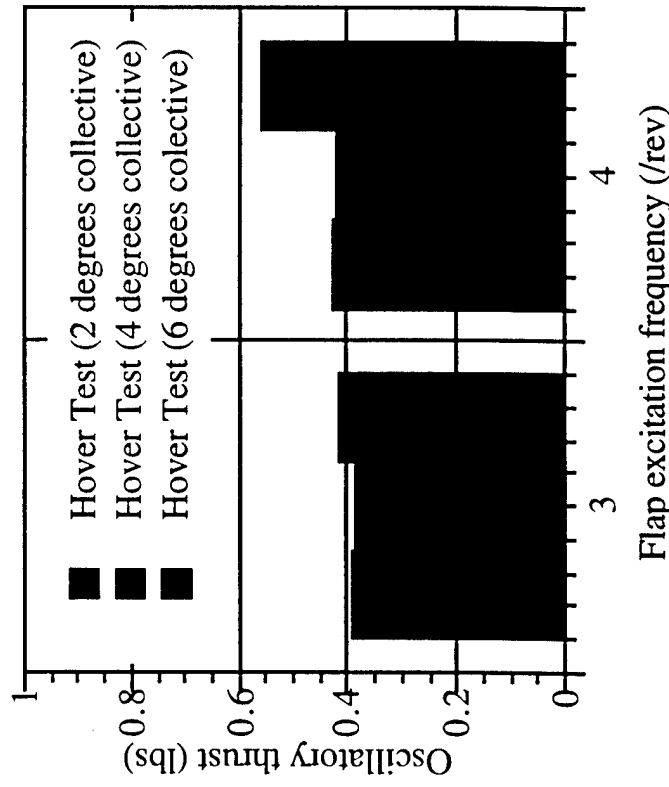


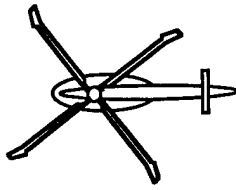
UM

## Oscillatory Rotor Thrust

Flap authority=Oscillatory thrust/Steady rotor thrust

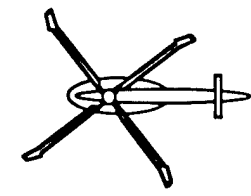
- 10% flap authority achieved at 4 deg collective and 4/rev flap excitation





# Mach Scaled Rotor Model

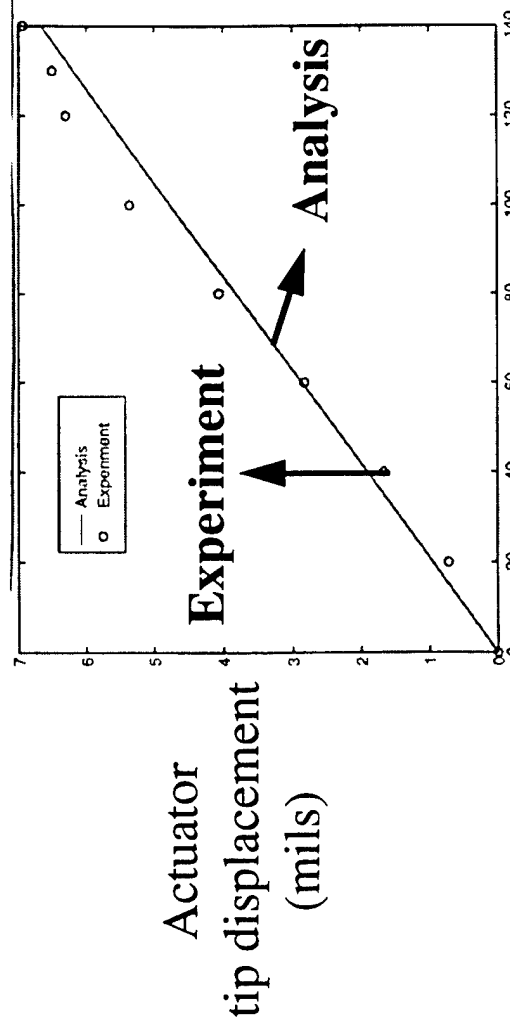
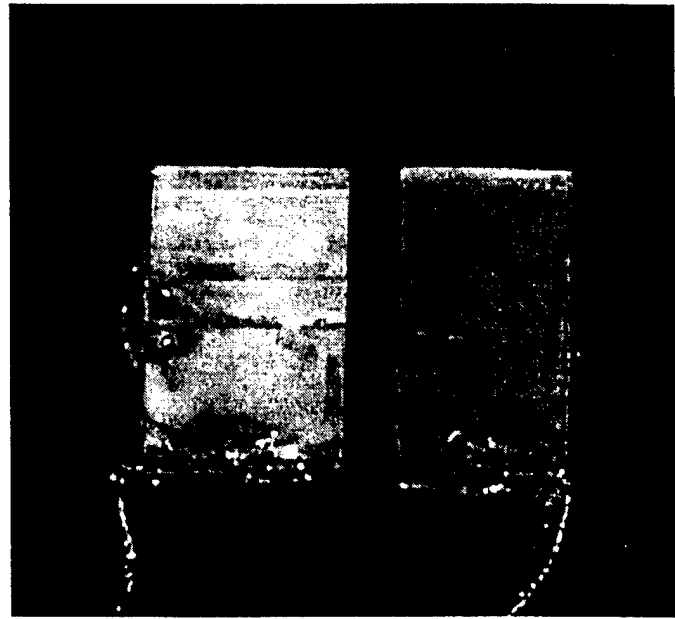
- Mach scale is more representative of full scale (Tip Mach number is simulated).
- Mach scaled operating speed = 2150 RPM (For S-76 Rotor)
- Smart rotor design issues,
  - Flap sizing : 20% chord, 5% span flap
  - Actuator design : 8-layered, tapered bimorph
  - Blade structural design : Sustain CF and Aerodynamic loads
  - Weight Penalty : Should be as low as possible



UM

## Actuator Design

- 8-layered, Tapered bimorphs were designed and Fabricated.



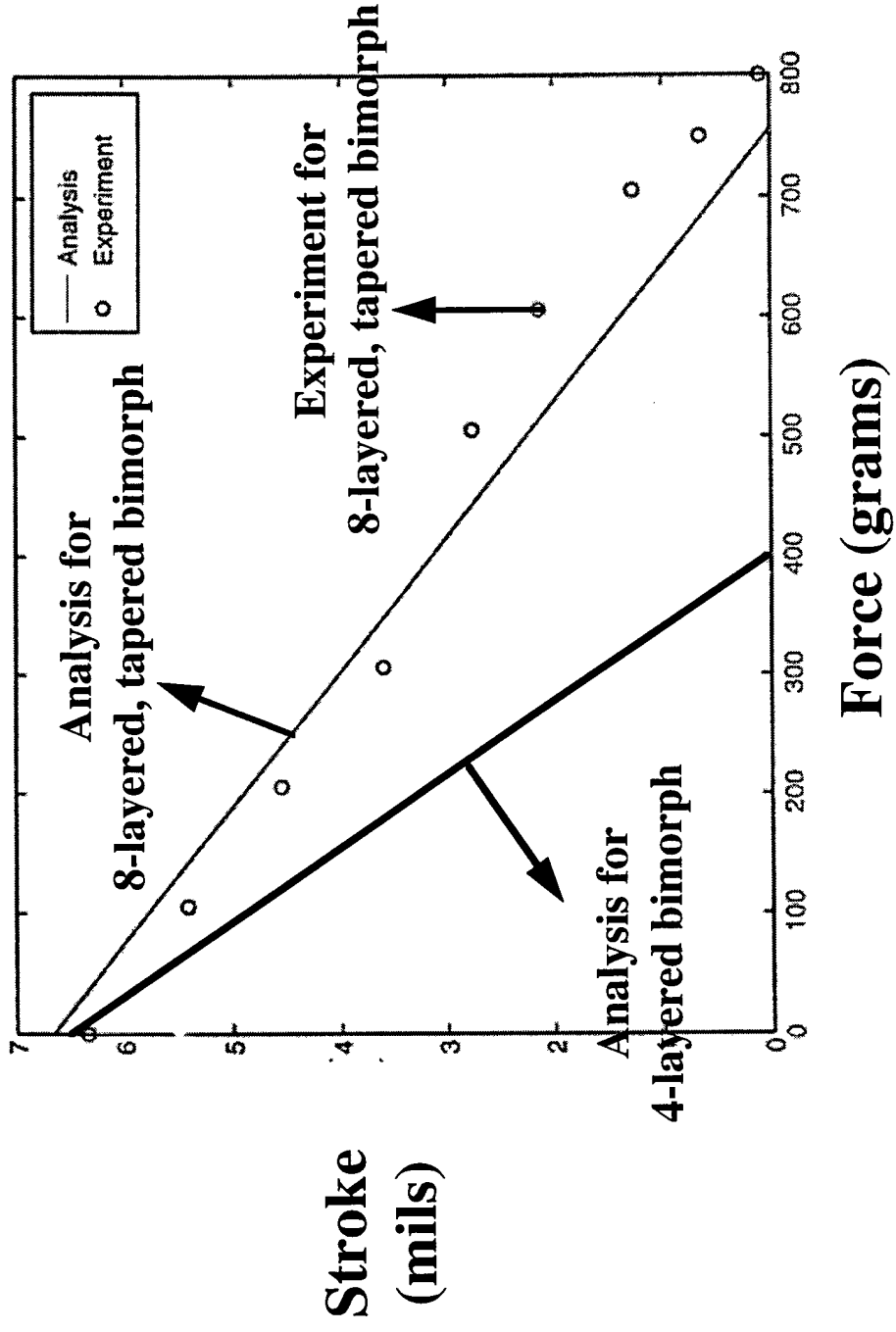
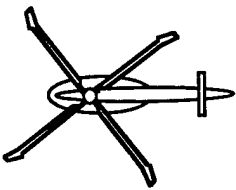
Input to Bimorph (volts)

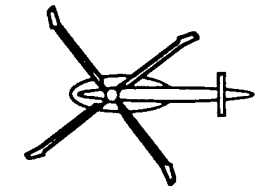
8-layered, tapered Bimorph

Actuator Free Displacement  
(1 inch cantilever)

UM

# Force-stroke characteristics (135 volts input, 1 inch cantilever)

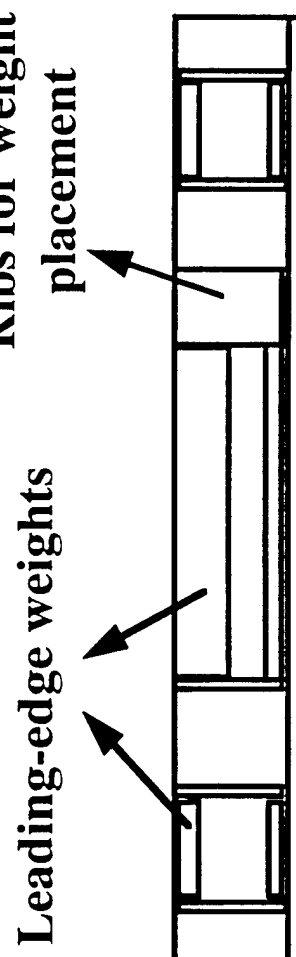




UM

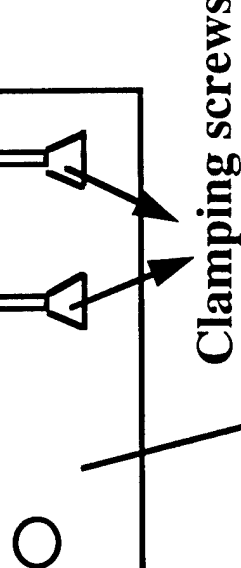
# Rotor Blade Fabrication

Composite Spar  
designed to sustain 3700 lbs  
of tensile load



Leading-edge weights  
Ribs for weight placement

Anchor Plate  
Assembly



Clamping screws

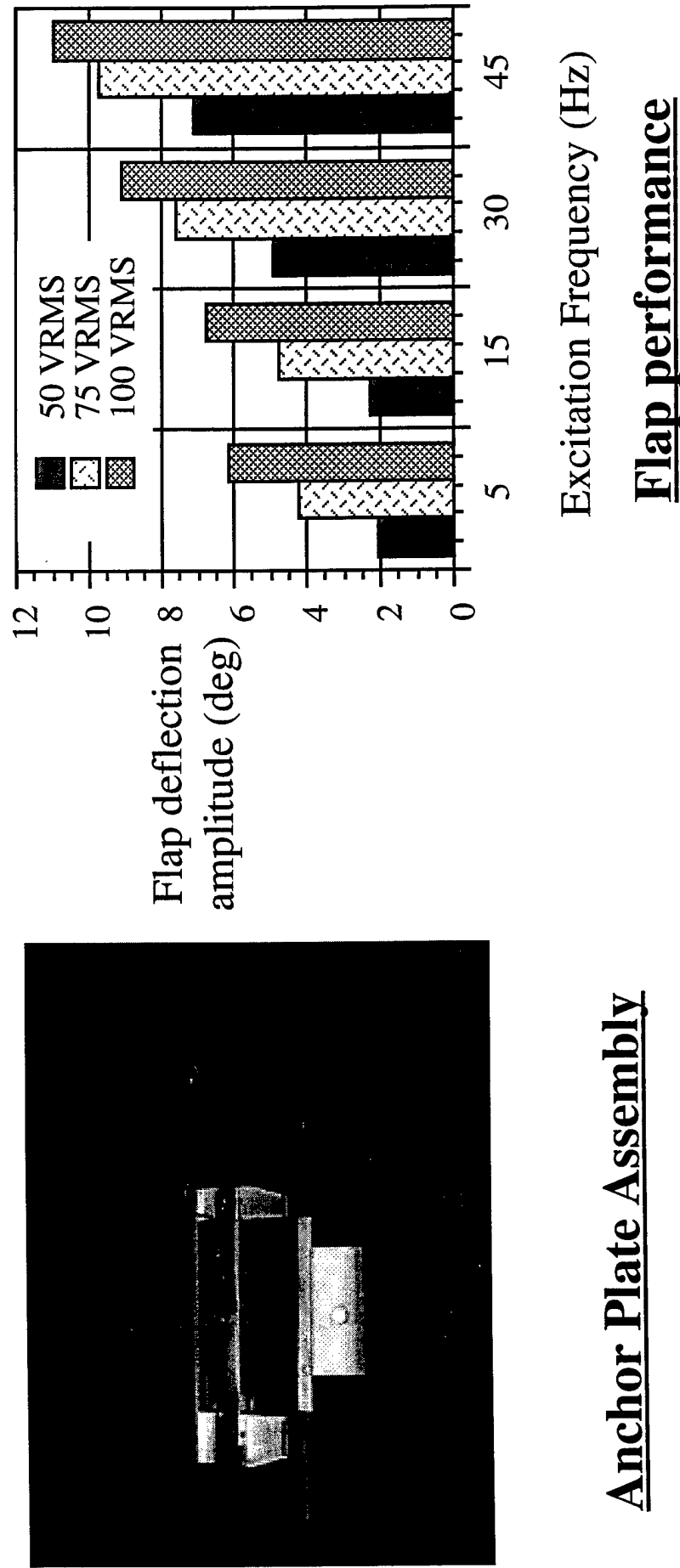
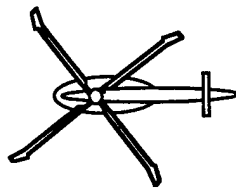
8-layered piezo-bimorph

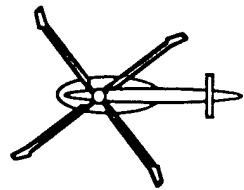
Flap

Aluminum Root  
Insert (NACA 0012 profile)

UM

# Non-rotating, bench tests

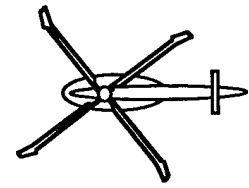




UM

## Concluding Remarks

- Piezo-Bimorph actuation is feasible for Froude scale
  - Flap deflection of 6 degrees (4/rev) excitation achieved at the Froude scaled operating speed of 900 RPM.
  - 10 % flap authority was achieved at 4 degrees collective
- Actuation scheme is feasible for Mach scale as well as well as for full scale.
- Weight penalty < 20 %



## Future Work

- Testing of the Mach scaled rotor model
  - Vacuum Chamber Testing
  - Hover Stand Testing
  - Wind Tunnel Testing
- Validation of test data with analysis

# **Modeling of Smart Composites Box Beams with Nonlinear Induced Strain**

Aditi Chattopadhyay<sup>†</sup>, Haozhong Gu<sup>\*</sup> and Qiang Liu<sup>\*\*</sup>

Department of Mechanical and Aerospace Engineering  
Arizona State University

## **Abstract**

Recently, smart composite structures have received considerable attention due to the potential for designing adaptive structures which are both light in weight and possess adaptive control capabilities. Due to the high strength-to-weight ratio offered by composites, structural weight is much less of an issue than it is for isotropic materials. Therefore it is no longer necessary to use thin-walled sections to model the load-carrying sections. Thus, it is essential to develop a general framework for the comprehensive analysis of such smart composite structures of arbitrary wall thickness.

A new smart composite box beam-model is developed to investigate vibration control of helicopter rotor blades built around the active box beam. The mechanical behavior of the composite box beam with surface bonded and embedded piezoelectric actuators and sensors is studied in detail. A previously developed higher order theory-based composite box beam approach is extended to model rectangular smart box beams with arbitrary wall thicknesses. The theory, which is based on a refined displacement field, is a three-dimensional model which approximates the elasticity solution so that the beam cross-sectional properties are not reduced to one-dimensional beam parameters. Both inplane and out-of-plane warpings are included automatically in the formulation. The developed model satisfies the stress free boundary conditions at the inner and outer surfaces of the beam. Continuities in displacements are also ensured at the interface between the composite laminate and the embedded piezoelectric actuators. The analytical model is implemented using the finite element technique. The developed beam model is then used to model the load carrying member of helicopter rotor blades with moderately thick-walled sections. Since the relationships between the induced strain due to actuation and the applied electric field are nonlinear in nature, formulations presented in the current research include these nonlinear induced strain effects.

Static analysis of the smart box-beam under varying degree of actuation has been performed. Very good overall agreement is observed with available experimental data for thin-walled sections without embedded actuators. Good agreement is also observed between the developed theory and results obtained using NASTRAN for thick-walled sections without actuators. The results show that the embedded piezoelectric actuators significantly reduce the deflection along the box beam span and therefore can be used to control the magnitude of blade vibrations. In extreme cases, the actuators can compensate almost all deflections along the span due to external loads. It is also shown that the nonlinear actuation effect on smart composite box beams is closely related to the composite material stiffness. The lower the stiffness, the higher is the nonlinear actuation effect.

The research was supported by the U.S. Army Research Office, Grant number DAAH04-96-1-0163, Technical monitor, Dr. Gary Anderson.

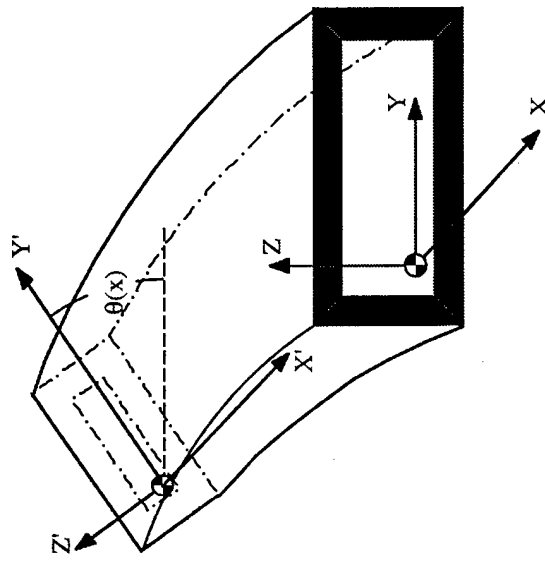
---

<sup>†</sup> Professor, Associate Fellow AIAA, Member ASME, AHS, SPIE, AAM, ISSMO

<sup>\*</sup> Postdoctoral Fellow, Member AIAA, ASME

<sup>\*\*</sup> Graduate Research Associate

# Modeling of Smart Composites Box Beams with Nonlinear Induced Strain



## Key Issues

Develop a general theory for smart composite boxbeam to include

1. Accurate evaluation of piezoelectric actuators
2. Transverse shear effect evaluation
3. Cross-sectional warping
4. Computational efficiency



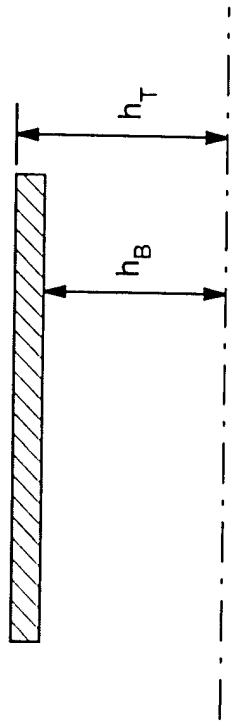
*Department of Mechanical and Aerospace Engineering  
Arizona State University, Tempe, Arizona*

# FORMULATION

## Refined Higher Order Displacement Field

$$u_1(\chi, \eta, \zeta) = u_o(\chi, \eta) + \zeta \left[ \psi_x(\chi, \eta) - \frac{\partial w_0(\chi, \eta)}{\partial \chi} \right] - \frac{\zeta^2}{2} \frac{h_T + h_B}{h_T h_B} \psi_x(\chi, \eta) + \frac{\zeta^2}{2h_T h_B} \psi_x(\chi, \eta)$$
$$u_2(\chi, \eta, \zeta) = v_o(\chi, \eta) - \zeta \left[ \psi_y(\chi, \eta) - \frac{\partial w_0(\chi, \eta)}{\partial \eta} \right] - \frac{\zeta^2}{2} \frac{h_T + h_B}{h_T h_B} \psi_y(\chi, \eta) + \frac{\zeta^2}{2h_T h_B} \psi_y(\chi, \eta)$$
$$u_3(\chi, \eta, \zeta) = w_o(\chi, \eta)$$

(for individual wall with eccentricity)



## Constitutive Relations

$$\sigma = \bar{\mathbf{Q}}(\varepsilon - \Lambda)$$

## Nonlinear Induced Strain

$$\Lambda = \mathbf{d}^T(\varepsilon) \mathbf{E} \equiv (\mathbf{d}_0^T + \mathbf{d}_1^T \varepsilon) \mathbf{E}$$



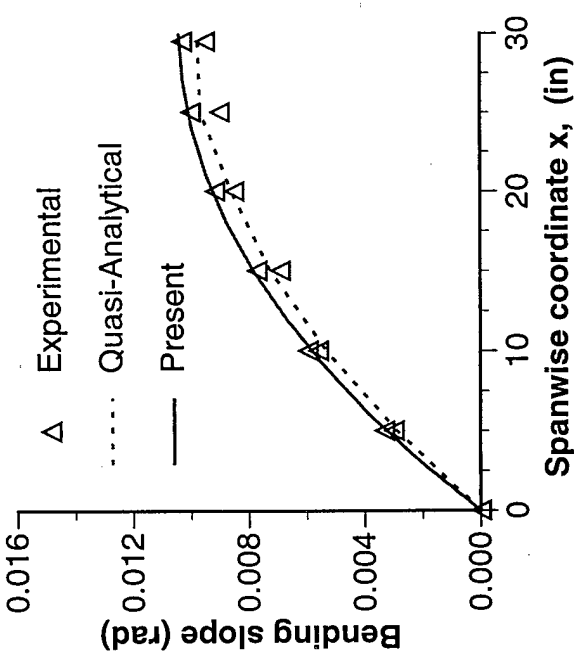
*Department of Mechanical and Aerospace Engineering  
Arizona State University, Tempe, Arizona*



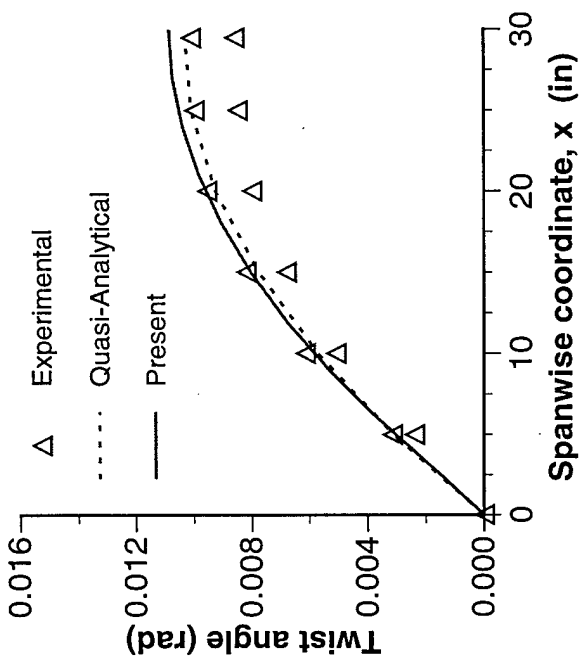
# BOX-BEAM MODEL CORRELATION

Symmetric  $[45^\circ]_6$  box beam, Tip bending load,  $F_z = 1 \text{ lb}$

Variation of bending slope along span



Variation of twist angle along span



*Department of Mechanical and Aerospace Engineering  
Arizona State University, Tempe, Arizona*

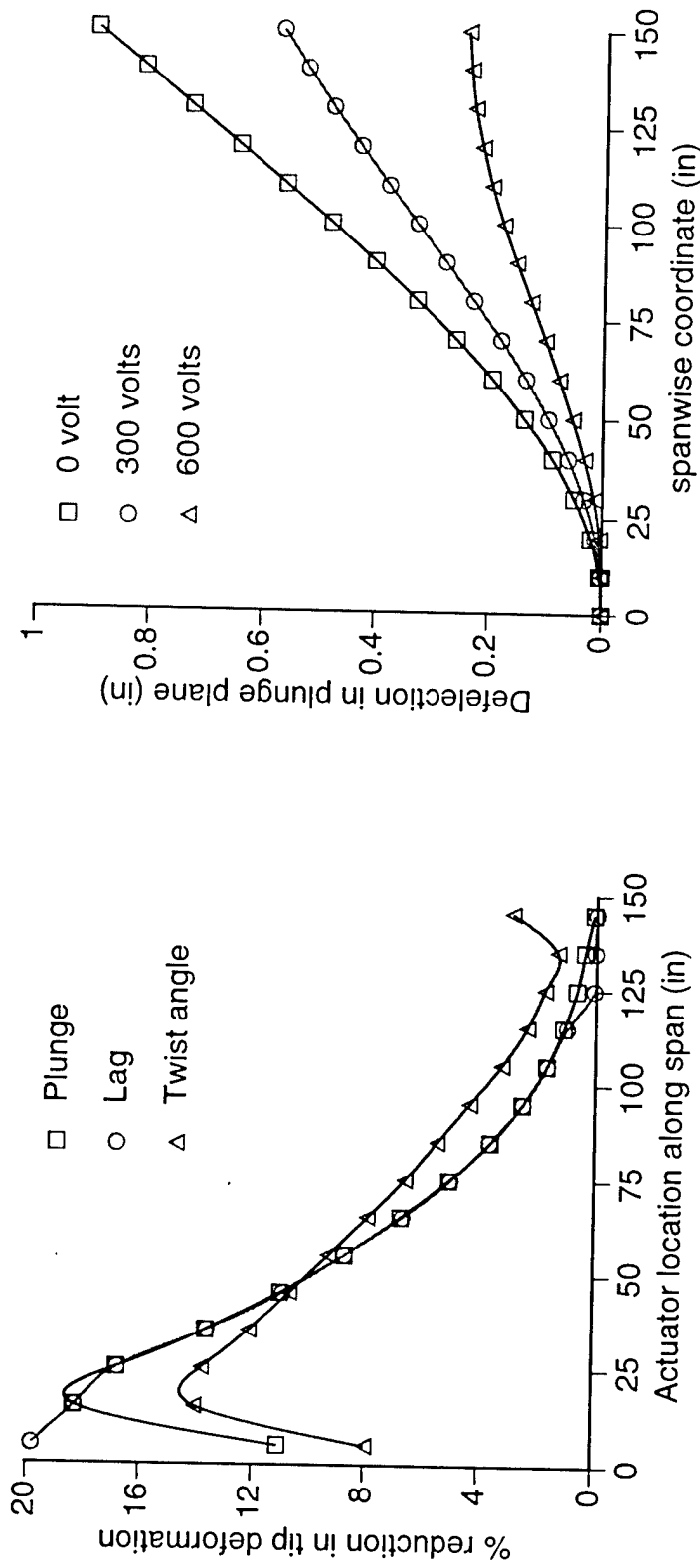


# DEFLECTION

Symmetric graphite/epoxy box-beam, external distribute load

One pair of actuator placed  
at different position

15 pairs of actuators covered  
all top and bottom surfaces

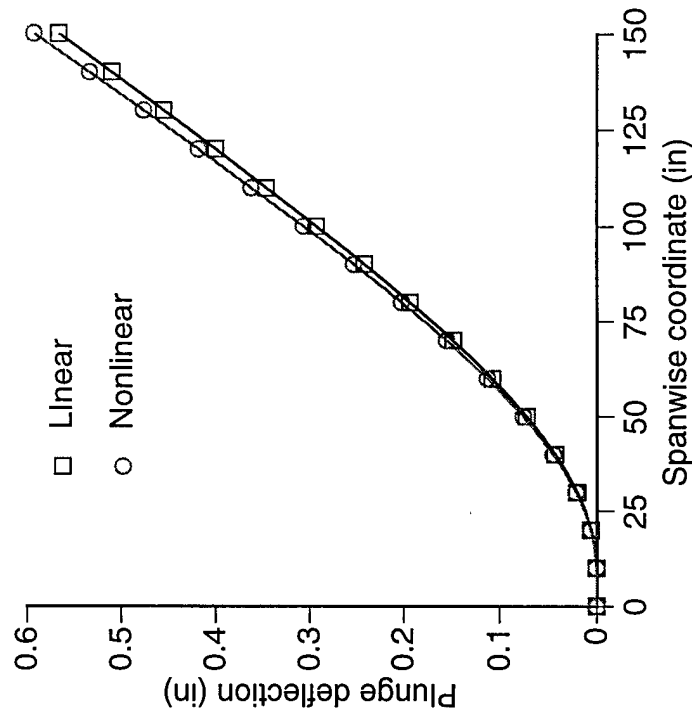


*Department of Mechanical and Aerospace Engineering  
Arizona State University, Tempe, Arizona*



# NONLINEAR INDUCED STRAIN EFFECT

Graphite/epoxy, External distribute load, 600 volts



*Department of Mechanical and Aerospace Engineering  
Arizona State University, Tempe, Arizona*



# Characterization of Semi-Active Magnetorheological Helicopter Lag Mode Dampers

Gopalakrishna M. Kamath \* Norman M. Wereley †

Mark R. Jolly ‡

Alfred Gessow Rotorcraft Center  
Department of Aerospace Engineering  
Rm. 3181, Engineering Classroom Bldg.,  
University of Maryland, College Park, MD 20742

Lord Corporation  
Thomas Lord Research Center  
405 Gregson Drive  
Cary, NC 27511

## Introduction

Aeromechanical stability of helicopters is a nonlinear phenomenon involving complex interactions of aerodynamic, inertial and elastic forces. Current advanced rotor designs tend towards hingeless and bearingless rotors with the objective of reducing life-cycle costs, improving hub designs, and achieving superior handling qualities. Due to stress and weight considerations, advanced rotors are designed as soft in-plane rotors. These rotor systems are susceptible to aeromechanical instabilities such as air and ground resonance [1]. In conventional articulated rotors, these instabilities are usually mitigated using hydraulic dampers. But hingeless and bearingless helicopter rotor designs have elastomeric lag dampers. Elastomeric dampers have the advantage of having no moving parts and no leakage problems that are present in hydraulic dampers. However, elastomeric dampers exhibit nonlinear behavior which is strongly dependent on frequency, temperature and loading conditions such as preloads and amplitude of motion. Also, the damping in elastomeric dampers reduces drastically for low amplitudes, thus causing limit-cycle oscillations that are detrimental to the operation of the rotor system. In order to circumvent the problems associated with the elastomeric dampers, Fluidlastic® dampers have been proposed [2]-[4]. Fluidlastic® dampers use elastomers in conjunction with fluids. The fluids add a viscous component to the energy dissipation mechanism in the dampers. But the existing damper designs discussed are all passive in nature. Augmentation of damping in the lag mode is required during specific flight conditions which can be achieved with a semi-active magnetorheological (MR) fluid damper. Matched sets of dampers are

\*Graduate Research Asst., Tel: (301) 405-1141, Fax: (301) 314-9001, E-mail: gmkamath@eng.umd.edu

†Assistant Professor, Tel: (301) 405-1927, Fax: (301) 314-9001, E-mail: wereley@eng.umd.edu

‡Senior Engineering Specialist

used to minimize the impact of varying damper mechanical properties on rotor tracking and trim conditions. Therefore, a damper that could adapt its properties to a fixed mechanical property specification would be of tremendous benefit. Thus, MR fluid dampers are attractive choices for augmenting lag mode damping in advanced rotor systems.

This paper presents a comparative study of the properties of Fluidlastic® dampers and MR fluid dampers that are crucial for their implementation in an advanced rotor system. The benchtop tests to study the various properties and the analytical efforts to model them are on-going [5]. During the second phase of this project, the dampers will be incorporated in a bearingless rotor system and tested on the hover stand.

## Benchtop Testing of Dampers

In order to study the hysteresis characteristics of the Fluidlastic® and the MR fluid dampers, an experimental setup was designed and built as shown in Fig. 1. The setup was designed to excite the dampers in the shear direction, which translates to lead-lag motion when mounted in a bearingless rotor system. A shaker was used to excite the damper and a load cell and an LVDT were used to measure the force and displacement time histories respectively. A sinusoidal signal of 10 Hz frequency was input to the shaker. The force amplitudes were changed and the corresponding displacement time histories recorded. Sample hysteresis curves for the MR fluid damper in the ON and OFF conditions are shown in Fig. 2.

## Modeling of Damper Hysteresis

A nonlinear model is proposed whose schematic is shown in Fig. 3. The model consists of three nonlinear elements: a spring, a dashpot and a rolling friction element. The rolling friction element differs from the conventional Coulomb friction element in that the force in the former does not change as abruptly as in the latter. The model coefficients, which are functions of displacement and velocity, are determined using a system identification procedure wherein the error between the model predictions and the experimental hysteresis data is minimized. Having estimated the model parameters, the hysteresis curves are predicted using the model. Sample results are shown in Fig. 4 for the MR fluid damper in the ON and OFF condition for a displacement amplitude of 1.25 mm (0.05 inches). The model predicts the nonlinear characteristics fairly well.

## Hover Stand Tests

The Alfred Gessow Rotorcraft Center has a 6 ft. diameter 1/8 Froude-scaled Bell 412 model bearingless rotor currently being experimentally evaluated for vibration performance. The lag mode damping of this rotor model will be evaluated on the hover stand for the passive dampers

and the semi-active MR fluid dampers in both the ON and OFF conditions. Test data will be used to compare the performances of the different dampers.

## Trademarks

Fluidlastic® is a registered trademark of Lord Corporation.

## Acknowledgments

This work was supported by the U.S. Army Research Office under a Short Term Innovative Research Award, Contract No. DAAH04-49610078 with Dr. Gary Anderson serving as the technical monitor.

## References

- [1] Chopra, I., "Perspectives in Aeromechanical Stability of Helicopter Rotors," *Vertica*, Vol. 14, No. 4, pp. 457-508.
- [2] McGuire, D.P., "Fluidlastic® Dampers and Isolators for Vibration Control in Helicopters," Presented at the 50th *Annual Forum of American Helicopter Society*, Washington D.C., May 1994.
- [3] Panda B., and Mychalowycz, E., "Aeroelastic Stability Wind Tunnel Testing with Analytical Correlation of the Comanche Bearingless Main Rotor," Presented at the 52nd *Annual Forum of American Helicopter Society*, Washington D.C., June 1996.
- [4] Panda B., Mychalowycz, E., and Tarzanin, F.J., "Application of Passive Dampers to Modern Helicopters," *Smart Materials & Structures*, Vol. 5, October 1996, pp. 509-516.
- [5] Kamath, G.M., Wereley, N.M., and Jolly, M.R., "Analysis and Testing of a Model-Scale Magnetorheological Fluid Helicopter Lag Mode Damper," Presented at the *American Helicopter Society Forum 53*, Virginia Beach, VA, April 29 - May 1, 1997.

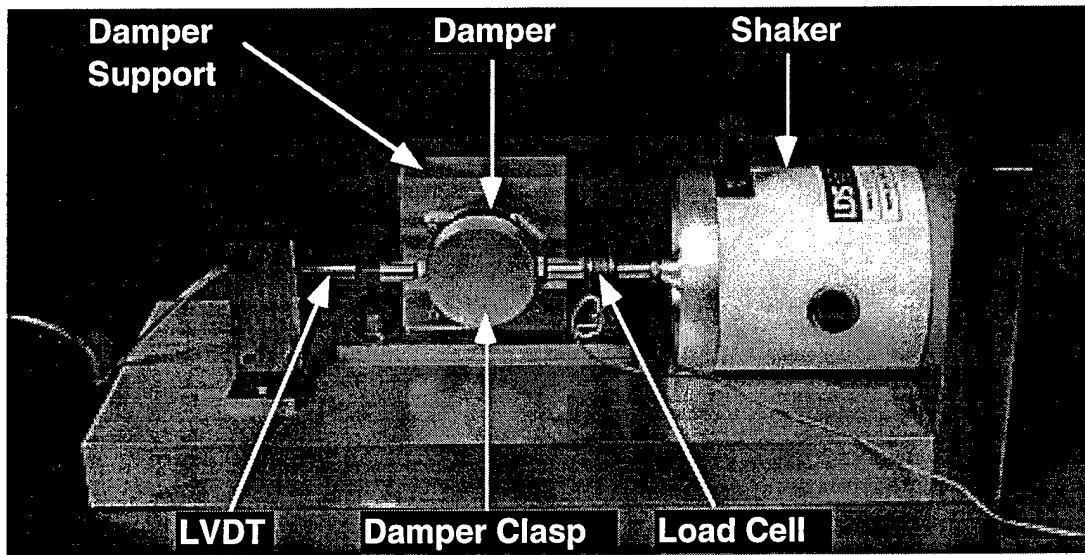


Figure 1: A photograph of the benchtop experimental setup.

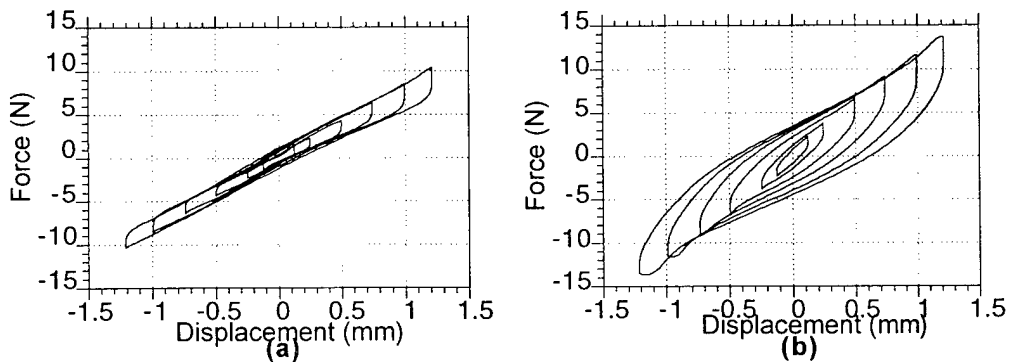


Figure 2: Force-displacement hysteresis plots for (a) MR fluid damper (OFF condition) and (b) MR fluid damper (ON condition) for varying displacement amplitudes.

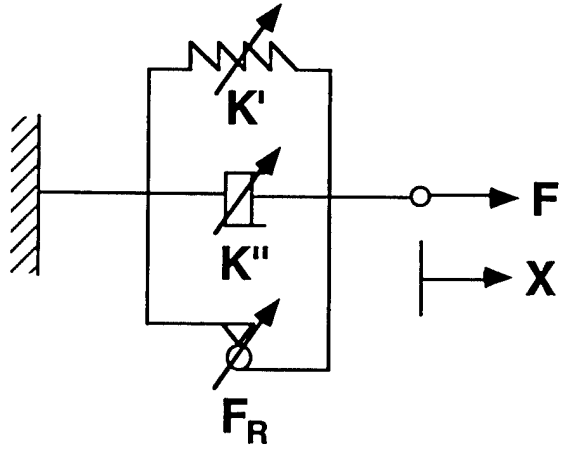


Figure 3: Schematic of the damper model consisting of nonlinear spring, dashpot and rolling friction elements.

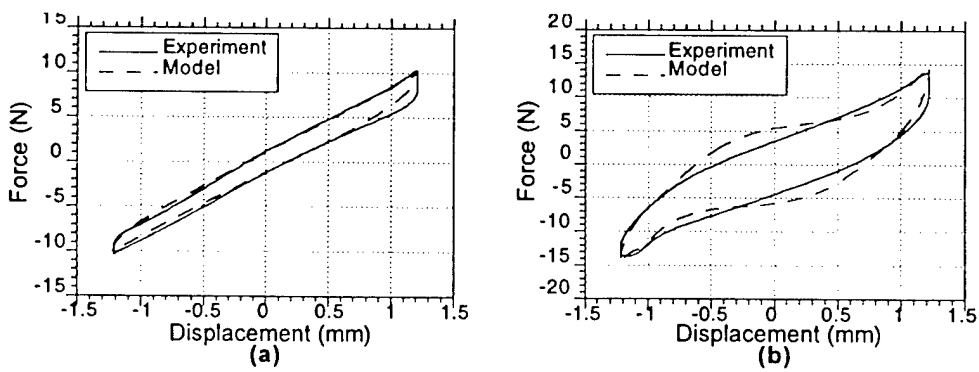


Figure 4: Model predictions of hysteresis plots for (a) MR fluid damper (OFF condition) and (b) MR fluid damper (ON condition) for displacement amplitude of 1.25 mm.

## ARL ACTIVE TWIST ROTOR RESEARCH

W. Keats Wilkie\*

K. C. Park<sup>†</sup>

W. Keith Belvin<sup>‡</sup>

Matthew L. Wilbur<sup>§</sup>

Paul H. Mirick<sup>\*\*</sup>

An overview of active twist rotor blade research being performed by the Army Research Laboratories, in cooperation with the University of Colorado at Boulder and NASA Langley Research Center, will be given. Two analytical efforts will be discussed in detail. The first is an in-house numerical analysis for examining the flap-torsion aeroelastic response of a helicopter rotor blade incorporating interdigitated electrode piezoelectric fiber composite plies. The derivation and capabilities of this analysis will be briefly discussed, and some applications involving open-loop twist actuation in hovering flight, and dynamic stall suppression at high thrust, high-speed forward flight conditions will be shown. A parallel active twist rotor analysis effort using the CAMRAD II comprehensive rotorcraft code will also be outlined. For this analysis, the piezoelectric-induced twist control loads acting upon the blades are represented by periodic torsional couples applied at the blade root and tip. The assumed magnitudes of the torsional couples are calculated separately using a static piezoelectric actuation beam analysis of the blade structure. Open-loop twist actuation results for a conceptual full-scale active twist rotor blade obtained with the CAMRAD II analysis will be compared with those generated using the in-house analysis. Plans for the construction of a 1/5th scale active twist rotor model to be tested in the Langley Transonic Dynamics Tunnel will also be described.

---

\* ARL/Vehicle Technology Center, NASA Langley Research Center, Mail Stop 340, Hampton, VA 23681-0001. Tel: 757/864-1260. Fax: 757/864-8678. E-mail: w.k.wilkie@larc.nasa.gov

† University of Colorado at Boulder, Center for Aerospace Structures, Campus Box 429, Boulder, CO 80309-0429. Tel: 303/492-6330. Fax: 303/492-4990. E-mail: kcpark@titan.colorado.edu

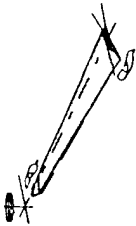
‡ NASA Langley Research Center, Structural Dynamics Branch, Mail Stop 230, Hampton, VA 23681-0001. Tel: 757/864-4319. Fax: 757/864-8540. E-mail: w.k.belvin@larc.nasa.gov

§ ARL/Vehicle Technology Center, NASA Langley Research Center, Mail Stop 340, Hampton, VA 23681-0001. Tel: 757/864-1268. Fax: 757/864-8678. E-mail: m.l.wilbur@larc.nasa.gov

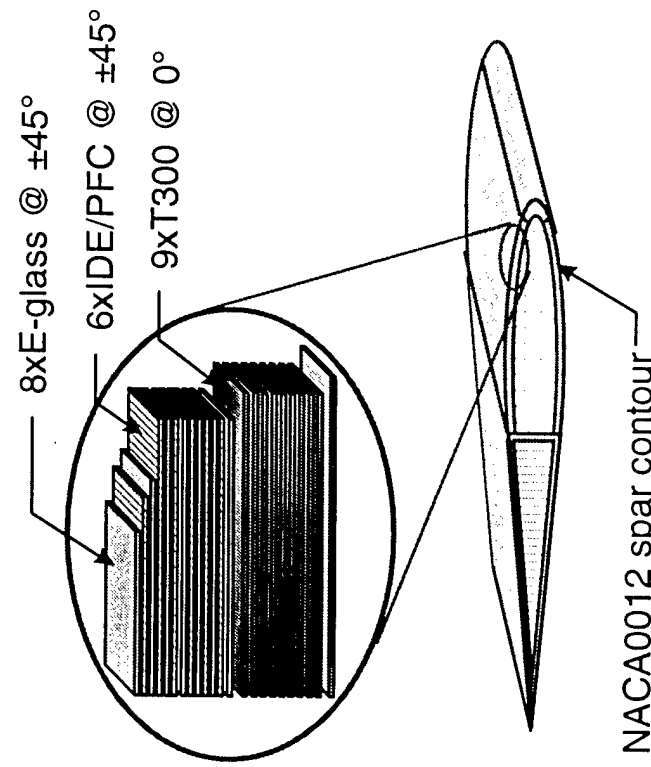
\*\* ARL/Vehicle Technology Center, NASA Langley Research Center, Mail Stop 340, Hampton, VA 23681-0001. Tel: 757/864-1269. Fax: 757/864-8678. E-mail: p.h.mirick@larc.nasa.gov

# AR

## Active Twist Rotor Blade (ATR)



**Conceptual full-scale ATR piezoelectric-fiber-composite blade**



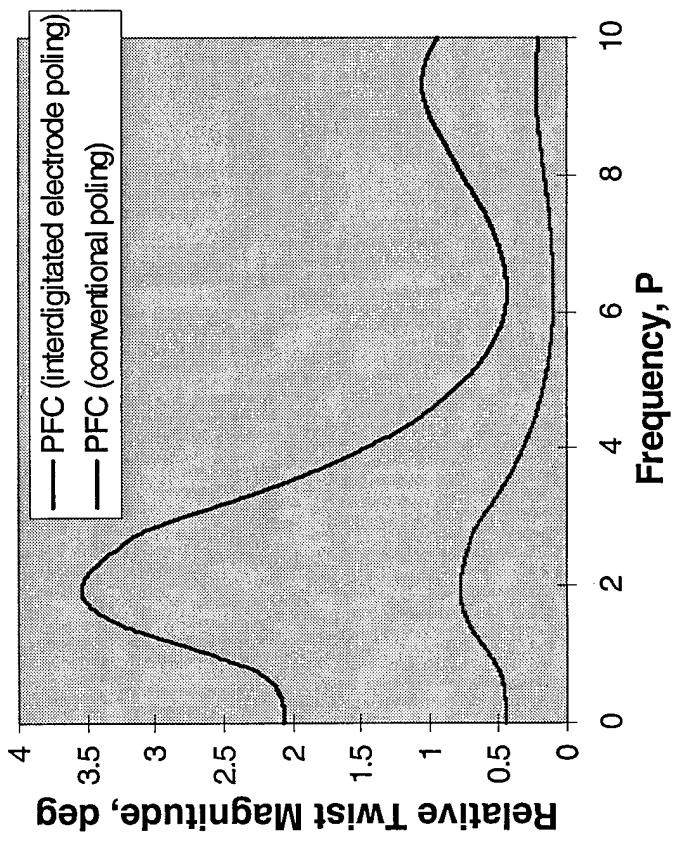
- MIT/Boeing concept
- Piezoelectric fiber composite (PFC) laminae easily incorporated into composite blades
- Interdigitated electrode poling (IDEP) enables large in-plane actuation strains

# PiezoElectric Twist Rotor Analysis (PETRA)

- Linearized flap-torsion blade dynamics
  - CLPT for blade active/pассивные properties
  - finite-state unsteady aerodynamics (includes ONERA dynamic stall)
  - Galerkin (modal) solution
- MATLAB-based code
  - state equations integrated in time
  - automatic trim included

**PETRA open-loop twist actuation frequency responses for ATR blade; (IDE vs. conventional poling)**

(4 deg collective pitch; hovering flight)

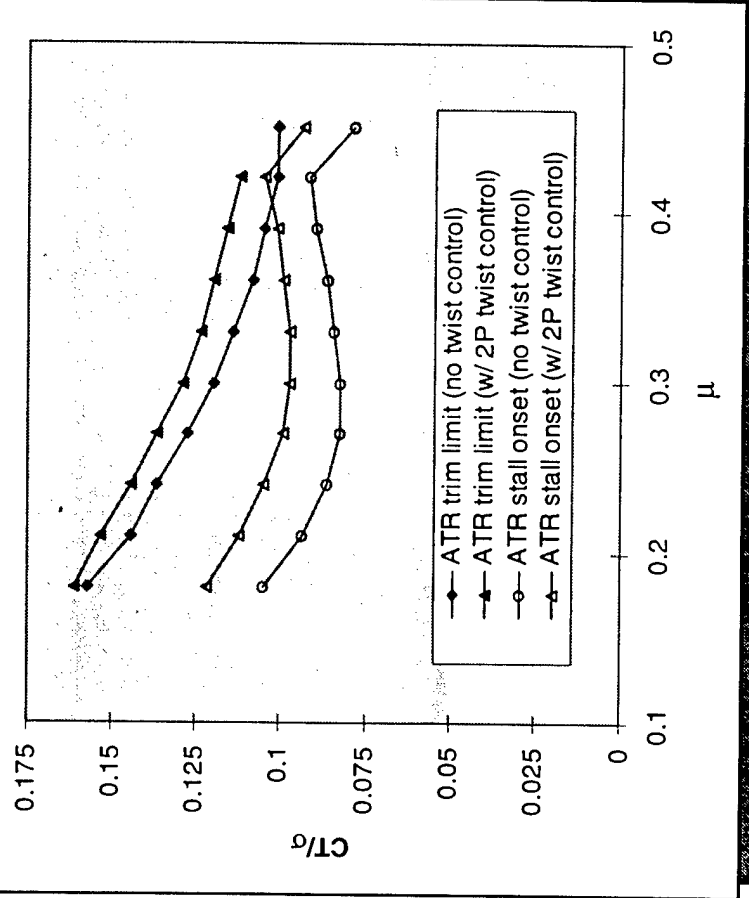




# Dynamic Stall Study (PETRA)

AR

## Thrust vs. forward-flight speed stall boundaries for ATR blade; (control off vs. 2P twist control on)



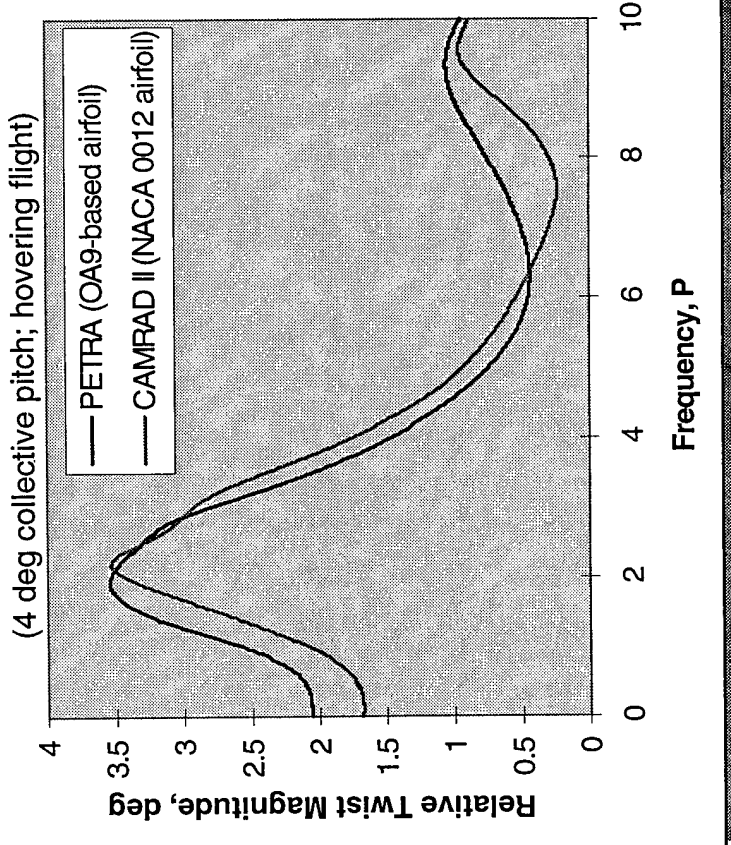
- Effect of simple active twist control scheme on ATR blade forward-flight stall boundaries
  - piezoelectric twist command at frequency  $\omega_{PE}=2\Omega$  (i.e., "2P")
- Stall onset delayed by 15% in  $C_T$  (constant  $\mu$ )
  - Max rotor  $C_T$  increased by 5-10% (constant  $\mu$ )



## CAMRAD II Active Twist Analysis

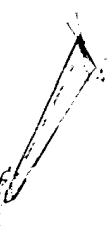
ARL

### Numerical open-loop twist actuation frequency responses for ATR blade; (CAMRAD II vs. PETRA)

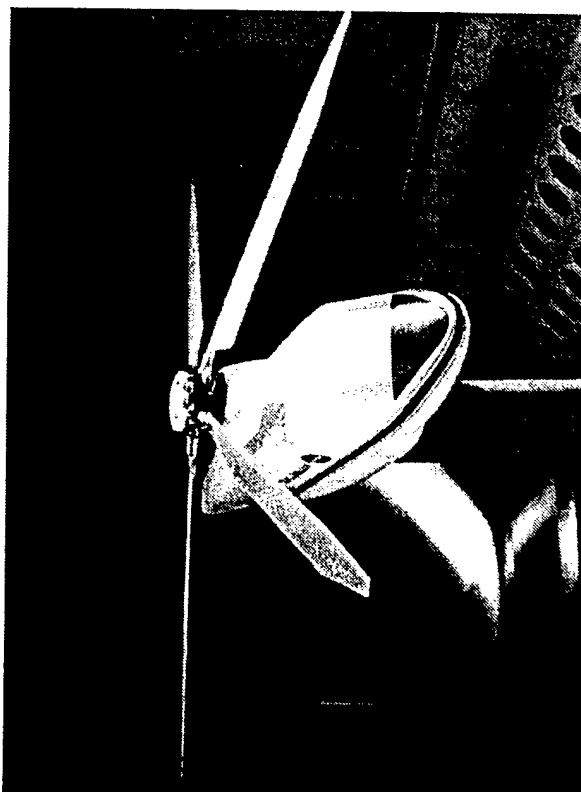


- Passive blade properties modeled using finite element beams
  - reduced to flap-torsion DOF model for comparison with PETRA
- Active twist control loads represented by torsional couple at blade root and tip
- Linearized system model used for frequency response analysis

# *Experimental Efforts*



## Aeroelastic Experimental Rotor System (ARES) in Langley Transonic Dynamics Tunnel (TDT)



- 1/5 scale ATR model blade under development
  - IDEPF composite spar (*with MIT Active Materials and Structures Laboratory*)
  - ARES power electronics (*with EMF, Inc.*)
- forward flight testing of ATR testbed in Langley Transonic Dynamics Tunnel (3/99)

# **Development of an Active Trailing Edge Flap for a Rotor using Piezostacks**

Taeoh Lee\*

Inderjit Chopra†

Alfred Gessow Rotorcraft Center

Department of Aerospace Engineering

University of Maryland, College Park, MD 20742

Actuation of trailing edge flap of helicopter rotor blade is being pursued intensely to alter the blade aerodynamics and hence to control its performance. Studies have been conducted to investigate the feasibility of the actuators using the piezo-materials to minimize vibration. A piezostack device has high actuation force but low actuation displacement. Trading the actuation force by the actuation displacement using mechanical devices makes it possible to use the piezostacks for the actuation of the trailing edge flap of a full-scale blade. This research is to systematically investigate the feasibility of the active trailing edge flap operating in rotating environment using piezostack actuators in conjunction with refined mechanical amplification devices.

To select the appropriate piezostack device among commercially available candidates, the force-strain behaviors as well as the strain-voltage behaviors for numerous piezostacks were evaluated by experiment. Such a comparative study was used for the final selection of piezostack device. Quasi-steady, incompressible aerodynamic calculations were carried out for a rotor to obtain an estimate of the magnitude of the flap hinge moment such that the hinge offset and force requirement of the flap can be achieved. The design point was determined to achieve both larger hinge offset and reasonably lower amplification factor, which corresponds to 30 lbs actuation force, 21 mils displacement, and 0.17 inch hinge offset. A blade section model with NACA0012 airfoil section has been designed and being built to investigate the feasibility of the piezostack actuator with newly designed mechanical amplification system.

To evaluate the performance of the trailing edge flap under different test conditions, investigations will be conducted under static conditions and in vacuum chamber. The performance of the flap will be evaluated at different actuation frequency, angles of attack, and rotational speed. This will help develop a full-scale rotor blade with trailing edge flap actuated using piezostacks.

---

\* Graduate Research Assistant

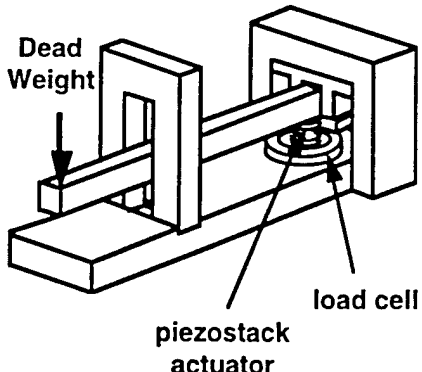
† Minta Martin Professor and Director



## Piezostack Testing



- To select the appropriate actuator among commercially available candidates
- Essential to design active trailing edge flap using piezostacks
- Testing device was developed in-house



## Piezostack Selection



Piezostack Actuator	Max. App. Voltage (V)	Max. Strain ( $\mu$ -strain)	Max. Block Force (bs)	B. Force per unit area (psi)
Morgan Matroc 7011 8(8M)	360	254	128	1.05
Morgan M.70023-1(5H)	200	449	101	0.83
Morgan M. 70023-2(4S)	360	497	143	1.17
Polytec PI P-915.8 55	100	1006	1325	8.55
Xinetics XIRE0410 L	100	468	95	5.16
Xinetics XIPZ0410L	100	910	70	3.58
EDO E100P-1 (EC-98)	800	838	154	2.00
EDO E100P-1 (EC-69)	800	472	50	0.66
Sumitomo PSA-15C (H5D)	150	940	266	7.47



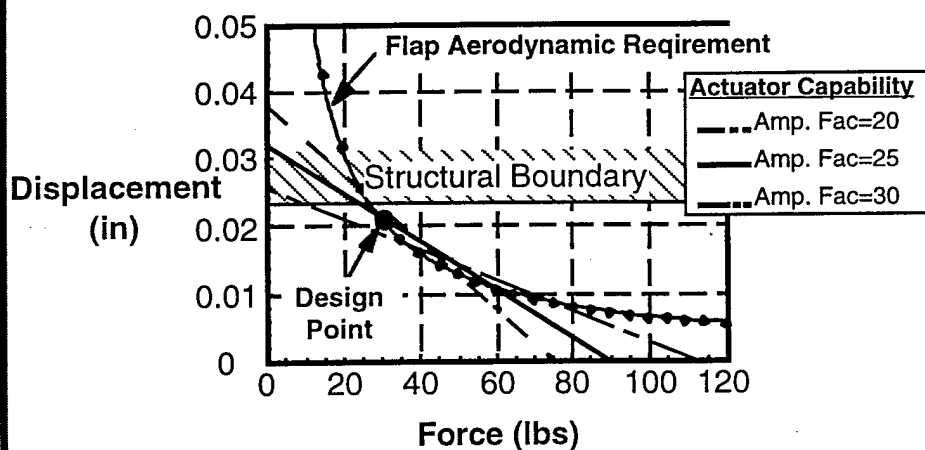
## Trailing Edge Flap Actuated with Piezostack



- Design Goal:  
flap amplitude of  $\pm 7$  deg in rotating environment
- Operational Environment  
MD Explorer in hover condition
- Trailing edge flap: located at .75R  
flap chord = 20% of blade chord, flap span= 4 inch
- Quasi-steady, incompressible analysis to calculate aerodynamic requirement
- Blade Section Model  
8 inch chord and 16 inch span

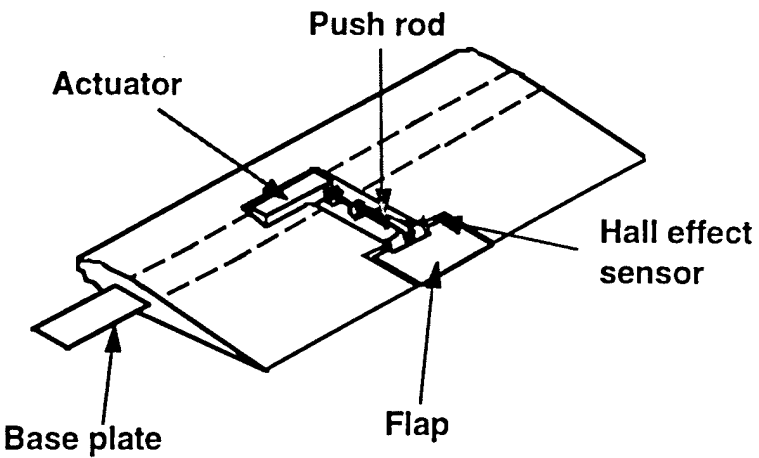


## Flap Actuator Requirement

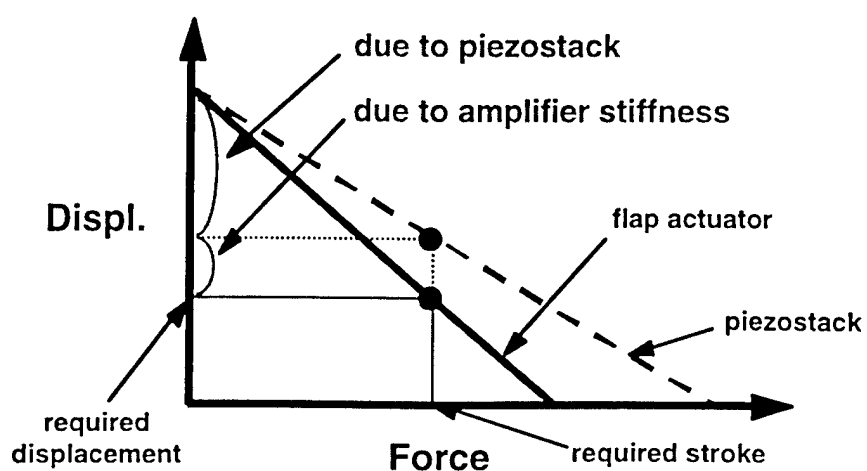




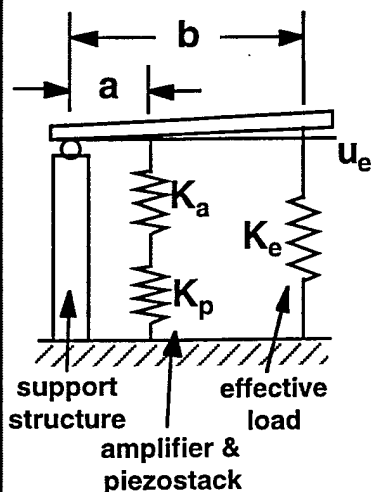
## Blade Section Model



## Flap Actuator Force vs. Displacement Trade



## Flap Actuator Modeling of Elastic Losses



Ideal Case ( $K_a = \infty$ )

$$\frac{u_e}{x_0} = \frac{(b/a)^2}{1 + (b/a)^2 (K_e/K_p)}$$

Considering  $K_a$

$$\frac{u_e}{x_0} = \frac{(b/a)^2}{1 + (b/a)^2 (K_e/K_p + K_e/K_a)}$$

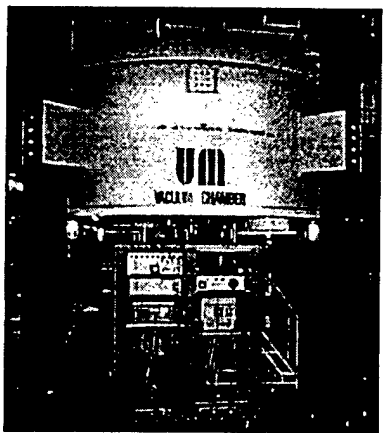
$x_0$ : free displacement

## Mechanical Amplification

- **Advantages**
  - Flexure at the high-load end is eliminated
  - can reduce the effect of the centrifugal force by the component of actuation force towarding blade root
  - can minimize the spanwise component of the actuator output by moving the location of fulcrum of outer lever
- **Disadvantages**
  - energy loss due to additional lever / flexure
  - relative complexity

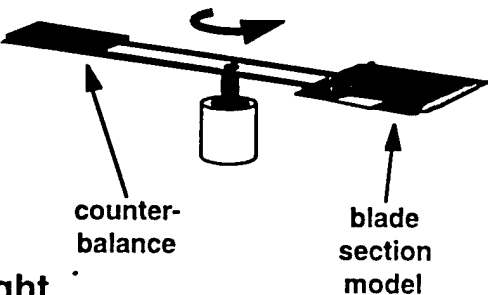


## Vacuum Chamber Testing



10 ft diameter X 4 ft height

Rotor Speed: 986 rpm  
Accel. at .75R: 700g



## Conlcuding Remarks & Future Work



- Comparative study on numerous actuators based on the testing was conducted to choose the appropriate piezostack for flap actuator
- Quasi-steady, incompressible analysis was performed to evaluate the aerodynamic requirement for the trailing edge flap
- Improved amplification device was designed and is currently under fabrication, and blade section model was designed to test the flap actuator in rotating environment

Future work: Investigations in vacuum chamber

# Characteristics of Enhanced Active Constrained Layer Damping Treatments with Edge Elements

**W. H. Liao**  
Graduate Assistant

**K. W. Wang**  
Professor

Structural Dynamics and Controls Lab  
Mechanical Engineering Department  
The Pennsylvania State University  
University Park, PA 16802  
(814)865-2183, FAX (814)863-7222  
kwwang@psu.edu

Abstract submitted for the Third ARO Workshop on Smart Structures

## Abstract

A new and *enhanced* active constrained layer (EACL) configuration has recently been developed to improve the active action transmissibility of the current active constrained layer (ACL) treatment<sup>1</sup>. Introducing *edge elements*, the active action from the piezoelectric cover sheet can be transmitted to the host structure more directly. Results from this study illustrated that, compared to the current ACL, the new configuration could improve the active action transmissibility while retaining a similar level of passive damping ability. While the results are indeed promising, more research is needed to understand the effects of the edge elements such that an effective active-passive hybrid system can be achieved.

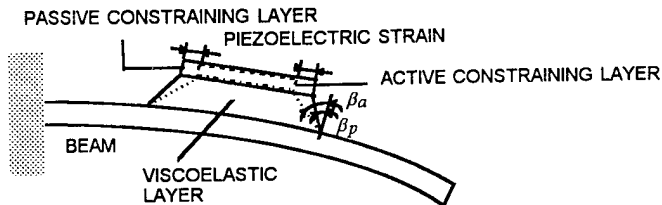
This paper presents some important characteristics of enhanced active constrained layer damping (EACL) treatments for vibration controls. The investigation also provides us with understandings

---

<sup>1</sup> W.H.Liao and K.W.Wang, "A New Active Constrained Layer Configuration with Enhanced Boundary Actions," *IOP Journal of Smart Materials and Structures*, Vol. 5, pp. 638-648, 1996.

on the edge elements and their effects. Specific interests are on understanding how the edge elements will influence the active action transmissibility, the passive damping ability, and their combined effects in EACL. It is concluded that the system performance is very related to the stiffness of the edge elements. Analysis results indicate that the edge elements could significantly improve the active action transmissibility of the ACL due to the so-called *bypass* effect. Although the edge elements will slightly reduce the viscoelastic material (VEM) passive damping, the EACL will still have significant damping from the VEM. Combining the overall active and passive actions, the EACL with sufficiently stiff edge elements not only can achieve better performance with less control effort compared to the ACL systems, but also could perform better than a purely active configuration. With careful analysis, the required critical stiffness of the edge elements are derived. In addition, the analysis also shows that the EACL treatment is a more robust design. That is, it can outperform both the purely passive and active systems throughout a broader design space than the current ACL configuration. With these desirable characteristics, the EACL concept could be used to realize an overall optimal active-passive hybrid system.

## CURRENT ACTIVE CONSTRAINED LAYER (ACL) CHARACTERISTICS



- Active piezoelectric cover sheet on passive viscoelastic (VEM) constrained damping layer
  - (a) Passive damping will be enhanced due to increase in shear angle [Baz, Inman, Shen, Van Norstrand, Wang....].
  - (b) Active action will be degraded by the viscoelastic layer due to transmissibility reduction [Bailey, Van Norstrand, Liao and Wang].

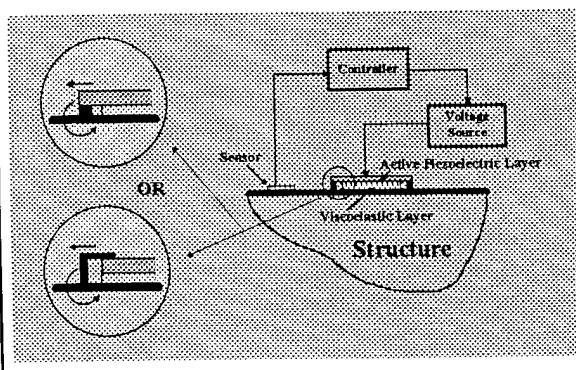
*Structural Dynamics and Controls Lab*

## ENHANCED ACL (EACL) IDEA (Liao and Wang, 1996)



Create new configuration to increase transmissibility

- Both active and passive actions can be effectively utilized
- Outperform both active and passive structures in most cases - a more robust design



- Edge elements to increase transmissibility and enhance active action contribution  
=> More effective than current ACL and outperform PCL
- Still maintain passive VEM damping  
=> Outperform purely active systems

*Structural Dynamics and Controls Lab*



## PROJECT OVERVIEW

### PROBLEM STATEMENT

- Feasibility study on EACL configuration shows promising results
- More understanding of the effect of the edge elements is needed

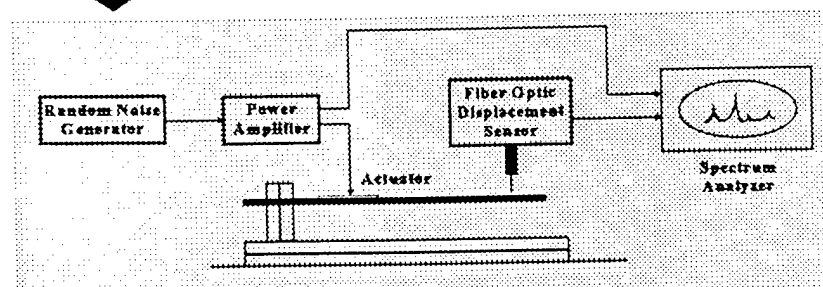
**OBJECTIVE** - To provide more insights on the characteristics of EACL

### TASKS

- EACL model development and validation
- System analysis
  - open loop and closed loop
  - active action authority, passive damping ability, and combined hybrid effect

*Structural Dynamics and Controls Lab*

## EXPERIMENTAL SETUP



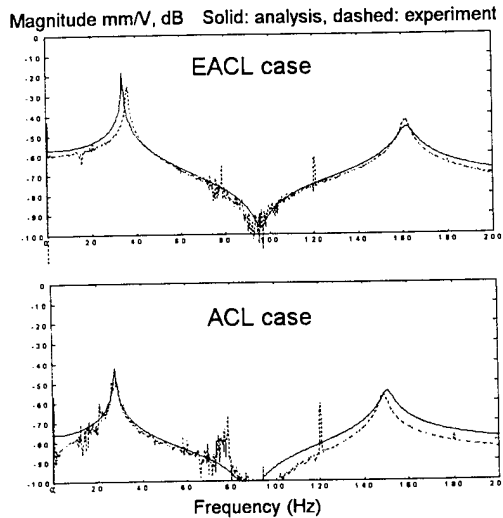
- Validate model and evaluate transmissibility
- Drive structure with actuator and measure beam vibration
- Given same level of input excitation,
  - Larger vibration amplitude = Higher transmissibility
  - = More effective active action

*Structural Dynamics and Controls Lab*

PENNSTATE



## OPEN LOOP ACTUATION -- Analysis and Experimental results



- Experimental and analytical results match nicely => model is valid
- Given same level of voltage input, larger magnitude indicates higher transmissibility of direct active control actions => more effective actuator
- EACL improves the effectiveness of the actuator significantly

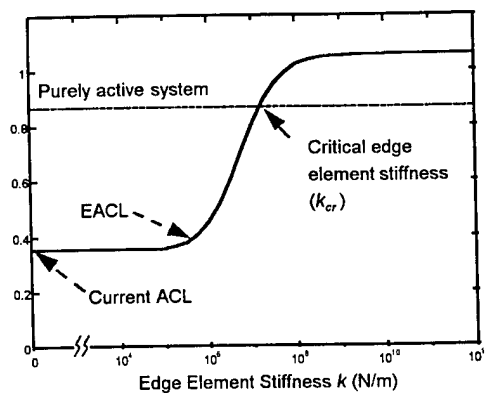
*Structural Dynamics and Controls Lab*

PENNSTATE



## EACL CLOSED LOOP ANALYSIS

Hybrid Control Index (Vibration Reduction / Control Effort)  
vs. Edge Element Stiffness



- Hybrid control index increases with increasing edge element stiffness  $k$
- With sufficient large edge element stiffness, the EACL can outperform current ACL
- For edge element stiffness  $> k_{cr}$  => effectiveness of the EACL better than the purely active system

*Structural Dynamics and Controls Lab*

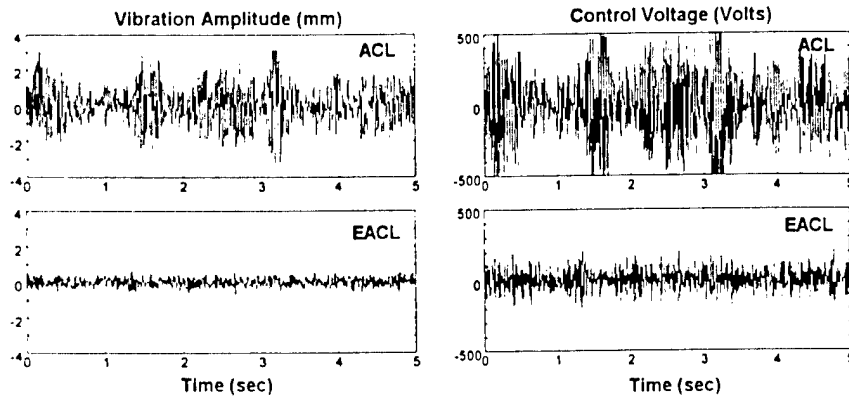
## PENNSTATE CLOSED LOOP COMPARISON STUDY



Comparing the EACL approach with the current ACL system

- Vibration reduction
- Control effort (voltage) requirement

Standard Deviations	$\sigma_w$ (mm)	$\sigma_v$ (volts)
ACL	1.05	217.93
EACL	0.285	89.49



Structural Dynamics and Controls Lab

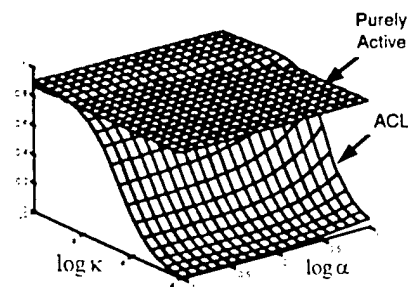
## PENNSTATE



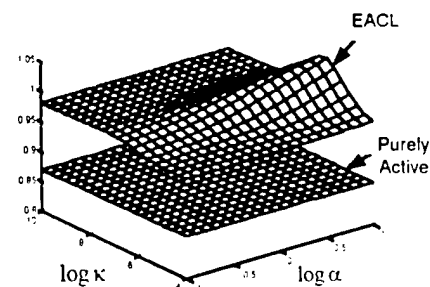
## DESIGN SPACE

Hybrid Control Index (Vibration Reduction / Control Effort)  
vs. VEM parameters

### CURRENT ACL



### EACL



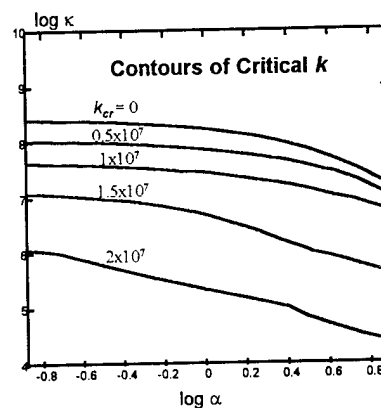
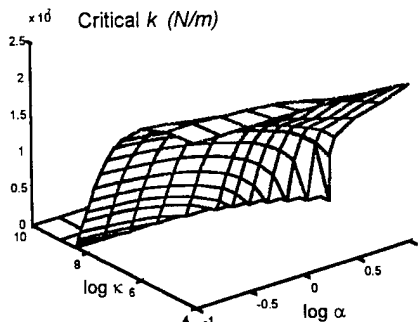
EACL Has a Broader Design Space to Outperform Both  
Purely Active and Passive Configurations

Structural Dynamics and Controls Lab

PENNSTATE



## A STUDY ON CRITICAL EDGE ELEMENT STIFFNESS ( $k_{cr}$ )



- Critical  $k$  decreases with increasing VEM shear modulus and loss factor
- For robust design => select  $k > \text{Max } k_{cr}$

Structural Dynamics and Controls Lab

PENNSTATE



## CONCLUSIONS

- EACL configuration created and analyzed
  - FE model developed and validated
  - Edge elements to enhance active action transmissibility
    - By-pass effect
  - Still maintain sufficient passive damping
    - Fail safe and more stable than purely active
  - More effective and robust than current ACL
    - Can outperform both PCL and purely active cases in a broader design space
- Edge element stiffness
  - Plays an important role
  - Need to be sufficiently large to be effective
  - Critical stiffness can be mapped for design guideline

Structural Dynamics and Controls Lab

# **Segmented Active Constrained Layer Damping Treatments for Structural Vibration Damping**

Grzegorz Kawiecki (gmk@utk.edu)

Peter F. Cento (centu@pauli.enr.utk.edu)

Department of Mechanical and Aerospace Engineering and Engineering Science

University of Tennessee, Knoxville, TN 37996-2210

tel. 423 974 5115

fax 423 974 5274

## **EXTENDED ABSTRACT**

The objective of this paper is to demonstrate the effect of Active Constrained Layer segmentation on the enhancement of low frequency vibrations damping in flexible beams. This presentation is based on the work by Kapadia and Kawiecki, 1996. The concept of Active Constrained Layer damping has been studied by Baz and Ro, 1993; Huang, Inman, and Austin, 1996; Shen, 1994; Smith and Wereley, 1996a; Van Nostrand and Inman, 1994; Wang and Liao, 1996. The presented work verifies a following assumption: since the passive constrained viscoelastic layer treatment segmentation has a beneficial effect on passive damping of low frequency vibrations (Parfitt, 1962; Plunkett and Lee, 1970), the segmentation of an active constraining layer may improve the performance of active damping treatments. Experimental results showing that this assumption is correct will be presented. Finite element modeling results supporting this assumption have been published by Lesieutre and Lee, 1996.

The effect of constraining layer segmentation has been tested using a stand shown in Fig. 1 where 1 is a shaking table, 2 denotes a shaker, 3 identifies the tested specimen, and 4 is a laser displacement sensor. Tested specimens were aluminum beams partially treated with active constraining layer treatments divided into a number of segments. Two types of specimens were tested: 1 mm x 25.4 mm x 330 mm beams with a fundamental bending frequency of 6.7 Hz and 1 mm x 50.8 mm x 565 mm beams with a fundamental bending frequency of 2.1 Hz. Tested beams were clamped at one end. The fixture was excited with a sinusoidal displacement signal using the shaker. Displacements of the free end were measured using the laser displacement sensor. Transient and steady state responses of both types of beams were examined. Tests were performed with the control system on and off, what corresponded to Active Constrained Layer Damping and Passive Constrained Layer Damping, respectively. Tested beams are shown in Fig. 2, where 1 represents beams with a higher natural frequency and 2 indicates beams with a lower natural frequency. One of the higher frequency beams shown in Fig. 2 has an unsegmented constraining layer and the remaining three beams have constraining layers divided into two, three and four segments. Constraining layers of lower frequency beams are divided into four, five, six and seven segments, respectively. Two testing sessions, approximately eight months apart, were conducted. Each of the sessions was completed by a different group of students. Not all of the configurations were tested again during the second testing session, mainly due to the deterioration of electrical connections between wire terminals and piezofilm. Results obtained during each of the sessions are denoted with numbers 1 and 2, respectively.

The performance of segmented active constrained layer treatment, for the transient case, was analyzed by evaluating the damping ratios for each specimen. Time histories were recorded using a data acquisition system consisting of a 486 PC with a Computer Boards, Inc. data acquisition card. Damping performance of passive treatments with various segment lengths was compared to the performance of the same treatments with activated constraining layers.

Three methods were considered for damping coefficient computations: the classical logarithmic decrement technique, a method based on Hilbert transform (Smith and Wereley, 1996b), and a moving block method (Tasker and Chopra, 1990). The moving block method has been reported to have problems with frequency resolution and with higher damping ratios (Smith and Wereley, 1996b). While the former was not a problem for the tested specimens, the latter was, due to the excellent performance of segmented active constrained layer damping treatments. Although the Hilbert transform method has been shown to outperform the logarithmic decrement approach for time histories with high noise levels, the results produced by those two techniques were very close for low noise levels (Smith and Wereley, 1996b). The level of noise in the vibration records analyzed in the present study was very low, mainly due to the RC filter installed in the feedback loop. Therefore, the simpler logarithmic decrement technique has been chosen for the computation of damping coefficients. The effect of noise was further reduced by analyzing only the first half of each time history.

Percentage improvements for transient vibrations damping were calculated using the formula given below.

$$\% \text{ Improvement} = \frac{\xi_{\text{active}} - \xi_{\text{passive}}}{\xi_{\text{passive}}} \cdot 100\% \quad (1)$$

Percentage improvements in reducing the amplitude of steady state vibrations were calculated using the following equation.

$$\% \text{ Improvement} = \frac{A_{\text{passive}} - A_{\text{active}}}{A_{\text{active}}} \cdot 100\% \quad (2)$$

Figs. 3 - 6 allow us to compare the transient vibrations damping capability of Segmented Active Constrained Layer treatments with the performance of Segmented Passive Constrained Layer treatments. We can clearly see that active constraining layers perform much better than passive treatments, and that the level of improvement depends on the length of constraining layer segments. Also, constraining layer segmentation gives better effects for lower frequencies than for higher frequencies. Fig. 4 shows that Segmented Active Constraining Layer treatment is capable of increasing the structural damping ratio by a factor of eight, compared to the passive equivalent.

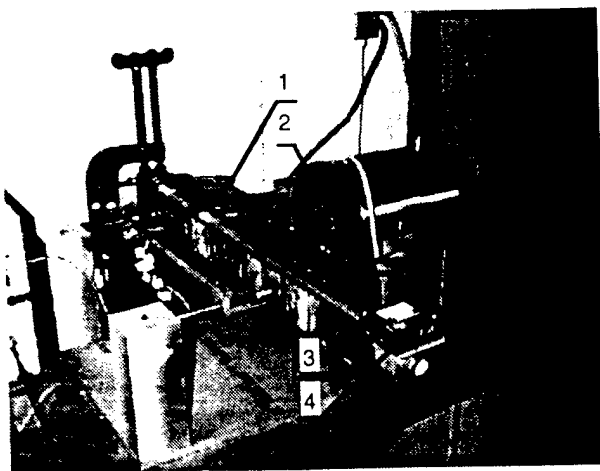


Fig. 1 Experimental set-up.

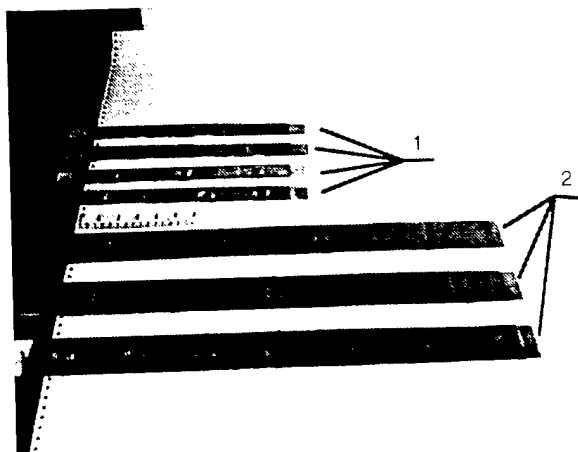


Fig. 2 Tested beams.

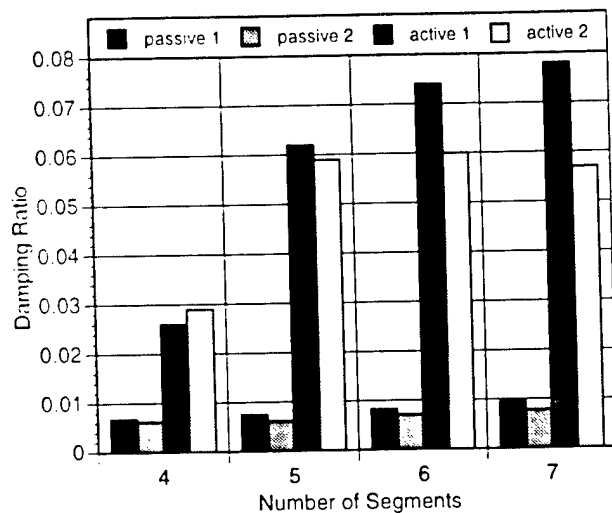


Fig. 3 Damping ratios for transient vibrations of beams with natural frequencies  $f_n = 2.1 \text{ Hz}$ .

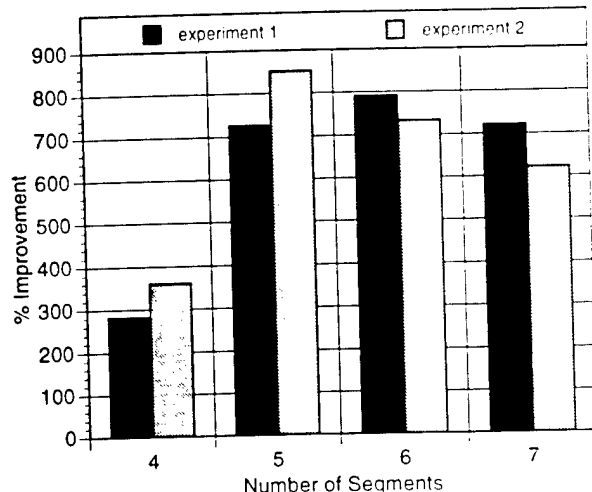


Fig. 4 Percentage improvement of transient vibrations damping ratio magnitude caused by constraining layer activation, beams with natural frequencies  $f_n = 2.1 \text{ Hz}$ .

The comparison of steady state vibrations damping capability of Segmented Active Constrained Layer treatments with the performance of Passive Constrained Layer treatments is shown in Figs. 7 and 8. Again, we can see that an appropriate segmentation of a constraining layer improves its performance substantially. As in the case of transient vibrations, segmented constraining layer treatments are more effective in reducing the amplitude of lower frequency vibrations. Fig. 7 shows that Segmented Active Constraining Layer treatment is capable of reducing the amplitude at resonance by a factor of ten. Sample time histories of passively and actively damped transient and steady state vibrations are shown in Figs. 9 and 10.

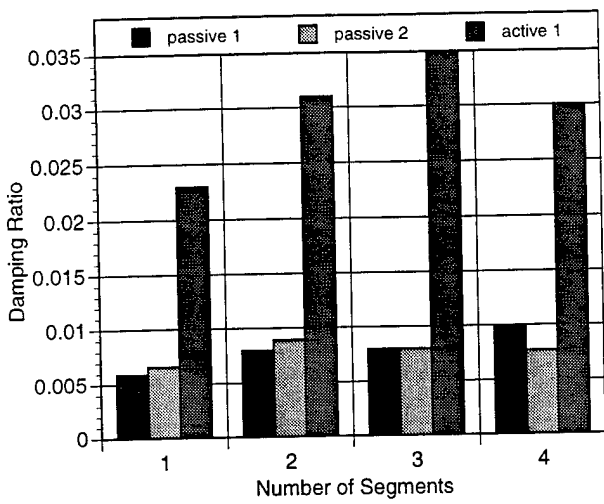


Fig. 5 Damping ratios for transient vibrations of beams with fundamental frequencies  $f_n = 6.7$  Hz.

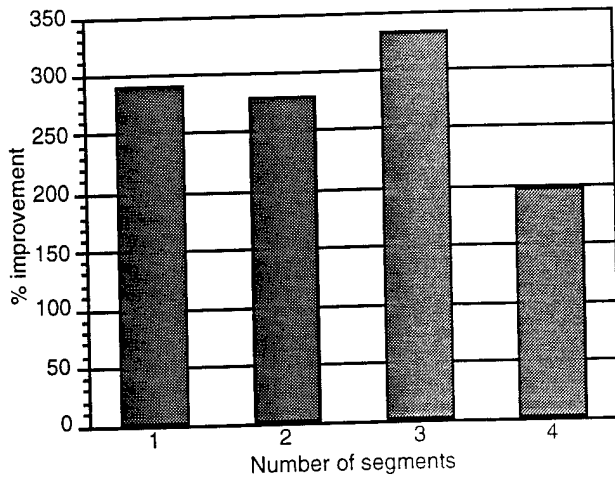


Fig. 6 Percentage improvement of transient vibrations damping ratio magnitude, caused by constraining layer activation, beams with fundamental frequencies  $f_n = 6.7$  Hz.

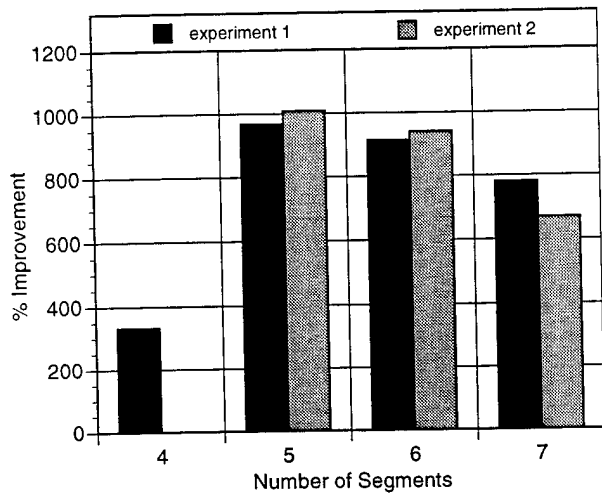


Fig. 7 Percentage reduction of steady-state tip displacement magnitude, caused by constraining layer activation, beams with fundamental frequencies  $f_n = 2.1$  Hz.

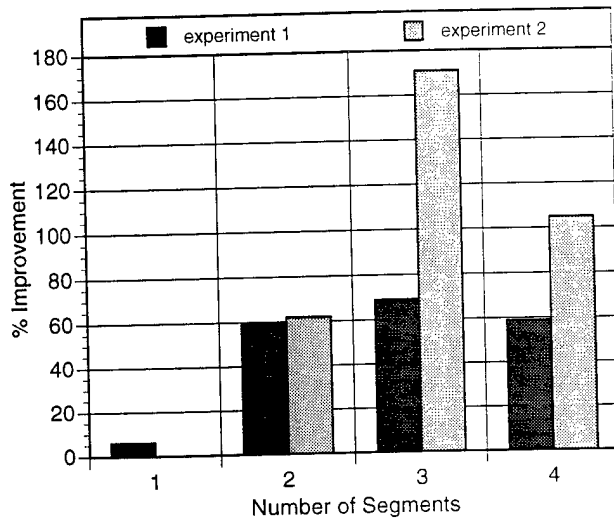


Fig. 8 Percentage reduction of steady-state tip displacement magnitude, caused by constraining layer activation, beams with fundamental frequencies  $f_n = 6.7$  Hz.

Therefore, the preliminary testing has demonstrated that Segmented Active Constrained Layer treatments are very effective in damping both transient and steady state vibrations. The presented results were achieved using a simple proportional feedback loop. It is expected that even a slightly more sophisticated control system based on a proportional-derivative feedback loop could improve the presented performance by at least a factor of two.

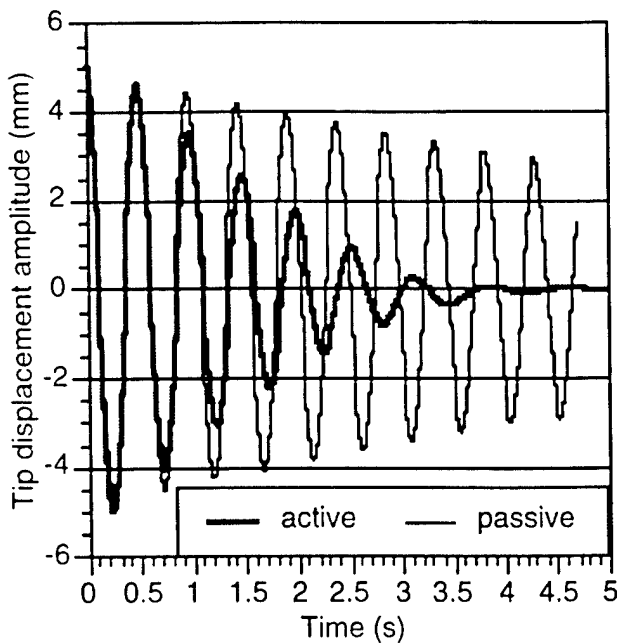


Fig. 9 Typical transient vibrations record.  
Passively vs. actively damped vibrations.

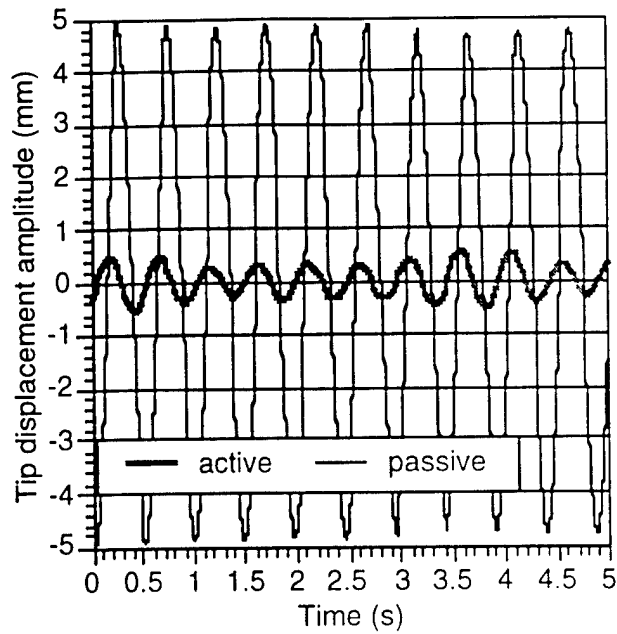


Fig. 10 Typical steady state vibrations record.  
Passively vs. actively damped vibrations.

The preliminary results of theoretical analysis are shown in Fig. 11. The approach used is being currently extensively modified, and the authors expect that a much better agreement between theoretical and experimental results will be obtained.

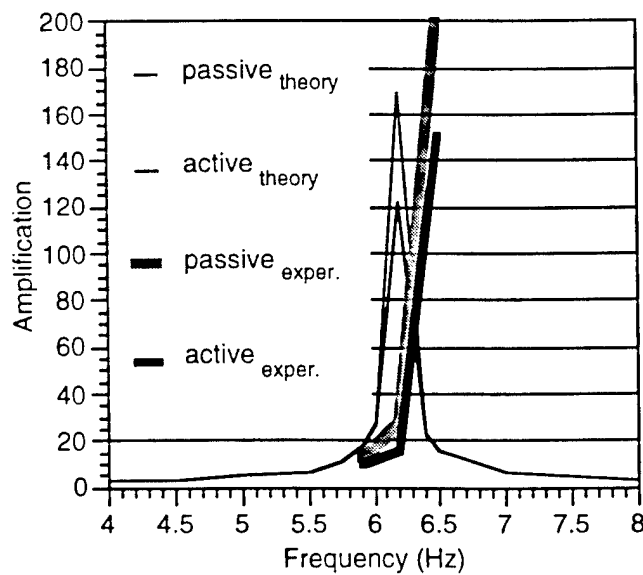


Fig. 11 Theoretical vs. experimental results.

## CONCLUSIONS

The active constrained layer treatment segmentation shows a great promise for vibration attenuation of slender beams with low natural frequencies. The presented study shows that even the proof-of-concept specimens controlled by a simple analog proportional feedback loop performed on average three times better when the

constraining layer was properly segmented. With an optimal selection of segment length, and with a better (e.g., displacement-velocity) control circuit, the damping ratios and displacement amplitude reduction could be significantly increased. Segmentation may be the only method to improve treatment effectiveness if the viscoelastic layer thickness cannot be increased because of weight limitations. Segmented active constrained layer treatments seem to be ideally suited to improve damping in structures with low resonant frequencies.

## REFERENCES

- Baz, A. and Ro, J., 1993, "Partial Treatment of Flexible Beams with Active Constrained Layer Damping," Conference of Engineering Science Society, ASME-AMD-Vol. 167, Charlottesville, VA, pp. 61-80.
- Huang, S. C., Inman, D. J., and Austin, E. M., 1996, "Some design considerations for active and passive constrained layer damping treatments," Smart Materials & Structures, Vol. 5, Number 3, pp. 301-313.
- Kapadia, R. and Kawiecki, G., 1996, "Low Frequency Vibration Attenuation Using Segmented Active Constrained Layer Damping Treatments," Proc. of the First European Conf. on Structural Control, Barcelona, Spain, May 29-31, pp. 378-385.
- Lesieurte, G. A., and Lee, U., 1996, "A finite element for beams having segmented active constrained layers with frequency-dependent viscoelastics," Smart Materials & Structures, Vol. 5, Number 5, pp. 615-627.
- Shen, I. Y., 1994, "Bending-vibration control of composite and isotropic plates through intelligent constrained-layer treatments," Smart Materials & Structures, Vol. 4, Number 1, pp. 59-70.
- Smith, C. B., and Wereley, N. M., 1996a, "Active-passive constrained layer damping of composite rotating flexbeams," AIAA/ASME/AHS Adaptive Structures Forum, Salt Lake City, UT, Apr. 18-19, pp. 207-216.
- Smith, C. B., and Wereley, N. M., 1996b, "Transient analysis for damping identification in rotating composite beams with integral damping layers," Smart Materials & Structures, Vol. 5, Number 5, October, pp. 540-550.
- Tasker, F. A., and Chopra, I., 1990, "Assessment of Transient Analysis Techniques for Rotor Stability Testing," Journal of the American Helicopter Society, Vol. 35, No. 1, January, pp. 39-50.
- Van Nostrand, W., C., and Inman, D. J., 1994, "Finite element Model for Active Constrained Layer Damping," Proceedings of the 31st annual technical meeting of the Society for Engineering Science, 10-12 October, Texas A&M University, College Station, Texas, SPIE Vol. 2427, Active Materials and Smart Structures.
- Wang, K. W., Liao, W. H., 1996, "A new active constrained layer configuration with enhanced boundary actions," Smart Materials & Structures, Vol. 5, Number 5, October, pp. 638-648.
- Parfitt, G. G., 1962, "The Effect of Cuts in Damping Tapes," Proceedings of the Fourth International Congress on Acoustics, Copenhagen, Denmark, August 21-28, pp. 21-24.
- Plunkett, R. and Lee, C. T., 1970, "Length Optimization for Constrained Viscoelastic Layer Damping," The Journal of the Acoustical Society of America, Vol. 48, No. 1 (Part 2) pp. 150-161.

**VIBRATION CONTROL OF LAMINATED PLATES  
WITH  
ACTIVE CONSTRAINED LAYER DAMPING**

C. Kim

NASA- Goddard Space Flight Center  
Code 712  
Greenbelt, MD 20771

T. Chen and A. Baz

Mechanical Engineering Department  
University of Maryland  
College Park, MD 20742

**Third ARO Workshop on Smart Structures**

VPI/SU  
Blacksburg, VA

August 27-29, 1997

# VIBRATION CONTROL OF LAMINATED PLATES WITH ACTIVE CONSTRAINED LAYER DAMPING

C. Kim

NASA- Goddard Space Flight Center  
Code 712  
Greenbelt, MD 20771

T. Chen and A. Baz

Mechanical Engineering Department  
University of Maryland  
College Park, MD 20742

## ABSTRACT

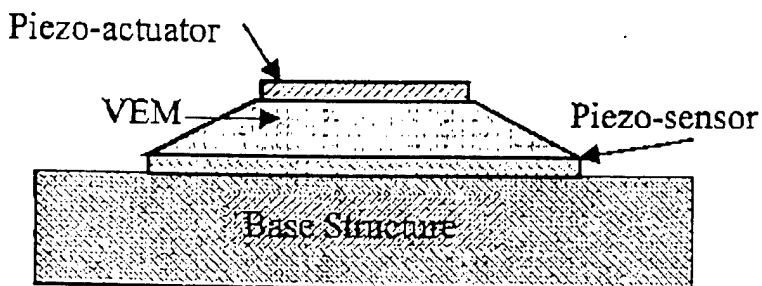
Bending vibration of thick laminated flat plates is controlled using Active Constrained Layer Damping (ACLD) treatments. The ACLD treatment consists of a visco-elastic damping layer which is sandwiched between two piezo-electric layers. The first layer is directly bonded to the plate to sense its vibration and the second layer acts as an actuator to actively control the shear deformation of the visco-elastic damping layer according to the plate response. With such active/passive control capabilities the energy dissipation mechanism of the visco-elastic layer is enhanced and the damping characteristics of the plate vibration is improved.

A finite element model is developed to analyze the dynamics and control of thick laminated plates which are partially treated with multi-patches of the ACLD treatments. The model is validated experimentally using an acrylic plates which are 3.75 cm thick, 20.0 cm long and 20. cm wide. The plates are fully treated with ACLD treatment which is made of SOUNDCOAT (Dyad 606) visco-elastic layer sandwiched between two layers of AMP/polyvinylidene fluoride (PVDF) piezo-electric films. The piezo-electric axes of the patches are set at zero degrees relative to the plate longitudinal axis to control the bending mode. The effect of the control gains on the system performance is presented. Comparisons between the theoretical predictions and the experimental results suggest the validity of the developed finite element model. Also, comparisons are made with the performance of conventional Passive Constrained Layer Damping (PCLD). The comparisons clearly demonstrate the merits of the ACLD as an effective means for suppressing the vibration of flat plates. [Work is funded by ARO]

## OUTLINE OF PRESENTATION

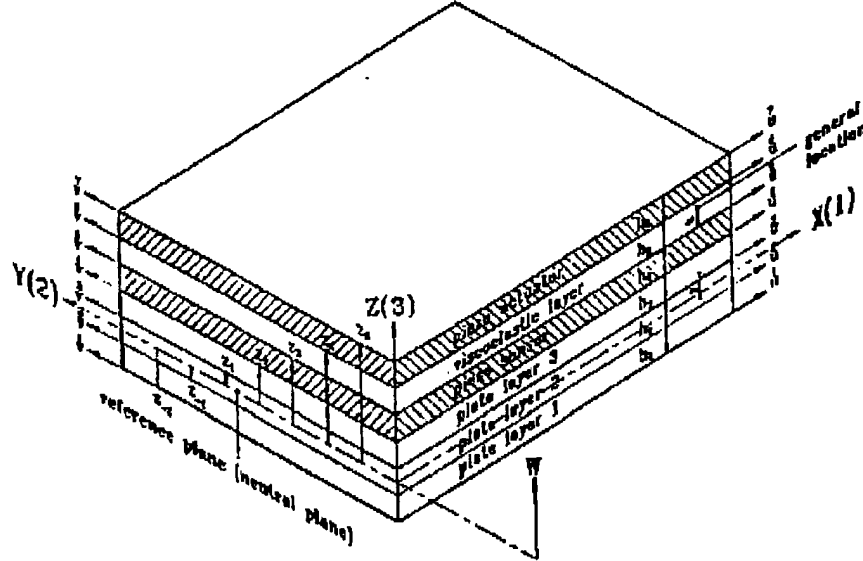
1. Introduction
2. Active Constrained Layer Damping
3. Finite Element Modeling
4. Experimental Performance
5. Comparison between theory & experiments
6. Summary & Conclusions

## ACTIVE CONSTRAINED LAYER DAMPING



- \* Combines active & passive damping controls
- \* Enhances energy dissipation characteristics
- \* Particularly suitable for control of **THICK** structures

## FINITE ELEMENT MODELING



Geometry of Laminated Plate/ACLD system

## DISPLACEMENT FIELD

The displacements  $(u_1, u_2, u_3)$  at any point  $(x, y, z)$  in the laminated plate/ACLD are:

$$u_1(x, y, z, t) = \overset{0}{u}(x, y, t) + \sum_{j=0}^{|k-N|} \psi_{N\pm j}(z) \phi_{1_{N\pm j}}(x, y, t), \quad (1.a)$$

$$u_2(x, y, z, t) = \overset{0}{v}(x, y, t) + \sum_{j=0}^{|k-N|} \psi_{N\pm j}(z) \phi_{2_{N\pm j}}(x, y, t), \quad (1.b)$$

$$\text{and} \quad u_3(x, y, t) = \overset{0}{w}(x, y, t). \quad (1.c)$$

where  $\overset{0}{u}$ ,  $\overset{0}{v}$  and  $\overset{0}{w}$  are the displacements of a point  $(x, y, 0)$  on the neutral plane of the laminated plate/ACLD in  $x$ ,  $y$ , and  $z$  direction respectively.  $k$ th layer and  $N$  indicates the layer of the reference plane. The  $\pm$  sign inside the summation depends on  $k - N$ .

The functions of the thickness  $\psi_i(z)$  are defined as follows:

$$\begin{aligned}\psi_i(z) &= z - z_{-i}, \quad z_{-i} \geq z \geq z_{-i-1} \\ &= z, \quad z_0 \leq z \leq z_1 \text{ or } z_{-i} \leq z \leq z_0 \\ &= z - z_i, \quad z_i \leq z \leq z_{i+1}\end{aligned}\quad (2)$$

where  $z_i$ 's are measured from the reference plane.

Also, the functions  $\phi_{1i}(x, y, t)$  and  $\phi_{2i}(x, y, t)$  are defined as follows:

$$\phi_{1i}(x, y, t) = -a_{1i} \frac{\partial w(x, y, t)}{\partial x}, \quad (3.a)$$

and

$$\phi_{2i}(x, y, t) = -a_{2i} \frac{\partial w(x, y, t)}{\partial y}, \quad (3.b)$$

where  $a_{1i}$ 's are adjustment coeff's. Physically,  $a_{1i} \frac{\partial w}{\partial x}$  and  $a_{2i} \frac{\partial w}{\partial y}$  define the slopes of the  $i$  th layer due to bending in the  $x$  and  $y$  directions, respectively

## STRAIN-DISPLACEMENT RELATIONS

The mechanical strains can be computed from:

$$\overset{\rho}{\epsilon}_{x,x_i} = \overset{\rho}{\epsilon}_{z,z_i} = \frac{1}{2} \left( \frac{\partial u_i}{\partial x_j} + \frac{\partial u_j}{\partial x_i} \right) \quad (i, j = 1, 2, 3). \quad (4)$$

The strain-displacement relationships for extension, bending and in-plane shear are:

$$\begin{bmatrix} \overset{\rho}{\epsilon}_1 \\ \overset{\rho}{\epsilon}_2 \\ \gamma_6 \end{bmatrix} = \begin{bmatrix} 0 \\ \overset{\rho}{\epsilon}_1 \\ 0 \\ \overset{\rho}{\epsilon}_2 \\ 0 \\ \gamma_6 \end{bmatrix} + \sum_{i=1}^{i=k} \psi_i \begin{bmatrix} K_1 \\ K_2 \\ K_3 \\ K_4 \\ K_5 \\ K_6 \end{bmatrix}_i. \quad (5)$$

Also, the strain-displacement relationships for the transverse shear strains are:

$$\begin{bmatrix} \gamma_5 \\ \gamma_4 \end{bmatrix} = \begin{bmatrix} (1 - a_{1i}) \frac{\partial w}{\partial x} \\ (1 - a_{2i}) \frac{\partial w}{\partial y} \end{bmatrix}, \quad (6)$$

where  $k$  viscoelastic layer.

## INDUCED PIEZO-ELECTRIC STRAINS

The induced strains are given by:

$$\begin{bmatrix} \tilde{\epsilon}_1 \\ \tilde{\epsilon}_2 \\ \tilde{\gamma}_6 \end{bmatrix} = \begin{bmatrix} d_{31} E_3 \Lambda(x, y) \\ d_{32} E_3 \Lambda(x, y) \\ 0 \end{bmatrix}, \quad (7)$$

and

$$\begin{bmatrix} \tilde{\gamma}_4 \\ \tilde{\gamma}_5 \end{bmatrix}_{\text{vcm}} = \begin{bmatrix} \frac{d_{31} E_3 [\Lambda(x, y) dx]}{h_{\text{vcm}}} \\ \frac{d_{31} E_3 [\Lambda(x, y) dy]}{h_{\text{vcm}}} \end{bmatrix}, \quad (8)$$

where  $\Lambda(x, y)$  is a spatial distribution function of the PVDF

## STRESS-STRAIN RELATION

The stress-strain relation are:

$$\begin{bmatrix} \sigma_1 \\ \sigma_2 \\ \sigma_6 \end{bmatrix}_k = \begin{bmatrix} \bar{Q}_{11} & \bar{Q}_{12} & \bar{Q}_{16} \\ \bar{Q}_{12} & \bar{Q}_{22} & \bar{Q}_{26} \\ \bar{Q}_{16} & \bar{Q}_{26} & \bar{Q}_{66} \end{bmatrix}_k \begin{bmatrix} \epsilon_1^T \\ \epsilon_2^T \\ \gamma_6^T \end{bmatrix}_k, \quad (9.a)$$

and

$$\begin{bmatrix} \sigma_5 \\ \sigma_4 \end{bmatrix}_k = \begin{bmatrix} \bar{Q}_{55} & \bar{Q}_{45} \\ \bar{Q}_{45} & \bar{Q}_{44} \end{bmatrix}_k \begin{bmatrix} \gamma_5^T \\ \gamma_4^T \end{bmatrix}_k. \quad (9.b)$$

## CONTROL LAW

The sensor voltage  $V_s$  generates control voltage  $V_c$  as follows:

$$V_c = -(K_p + i\omega K_d)V_s, \quad (10)$$

where  $K_p$  and  $K_d$  are proportional and derivative control gains, respectively.

## PIEZO-ELECTRIC FORCES

The external forces exerted by the piezoelectric actuator layer are given by:

$$\begin{bmatrix} f_1 \\ f_2 \\ f_6 \end{bmatrix} = \begin{bmatrix} \int_s \tilde{\sigma}_{xx} ds \\ \int_s \tilde{\sigma}_{yy} ds \\ \int_s 0 \end{bmatrix} = \begin{bmatrix} \bar{Q}_{11} & \bar{Q}_{12} & \bar{Q}_{16} \\ \bar{Q}_{12} & \bar{Q}_{22} & \bar{Q}_{26} \\ \bar{Q}_{16} & \bar{Q}_{26} & \bar{Q}_{66} \end{bmatrix} \begin{bmatrix} bd_{31}^0 V_C \\ ad_{32}^0 V_C \\ 0 \end{bmatrix}, \quad (11.a)$$

and

$$\begin{bmatrix} f_5 \\ f_4 \end{bmatrix} = \begin{bmatrix} \int_s \tilde{\tau}_x ds \\ \int_s \tilde{\tau}_y ds \end{bmatrix} = \sum_{\text{vom}} \begin{bmatrix} \bar{Q}_{33} & \bar{Q}_{43} \\ \bar{Q}_{43} & \bar{Q}_{44} \end{bmatrix}_{\text{vom}} \left\{ \begin{array}{l} bd_{31} E_3 \int \Lambda dx \\ ad_{32} E_3 \int \Lambda dy \end{array} \right\}, \quad (11.b)$$

where  $s$  is the actuator area with  $a$  is the length and  $b$  is the width of the piezoelectric actuator layer.

## OUTPUT OF PIEZO-ELECTRIC SENSOR

The total charge  $q(t)$  developed on the sensor is given by:

$$q(t) \int_A = \int_A \begin{bmatrix} d_{31}^0 \\ d_{32}^0 \\ 0 \end{bmatrix}^T \begin{bmatrix} \sigma_1 \\ \sigma_2 \\ \sigma_6 \end{bmatrix} dA. \quad (12.a)$$

and the sensor voltage  $V_s$  is given by:

$$V_s = \frac{1}{C} q(t) = \frac{1}{C} \int_A \begin{bmatrix} d_{31}^0 \\ d_{32}^0 \\ 0 \end{bmatrix}^T \begin{bmatrix} \sigma_1 \\ \sigma_2 \\ \sigma_6 \end{bmatrix} dA, \quad (12.b)$$

where  $C$  is the sensor capacitance  $C = \frac{8.854 * 10^{-12} A \cdot k_{31}}{h_a}$ ,  $A$  is the sensor surface area and  $k_{31}$  is dielectric constant.

## EQUATIONS OF MOTION

The dynamics of the composite sandwiched plate/ACLD is described by:

$$[M_G] \left\{ \frac{\partial^2 \Delta_G}{\partial t^2} \right\} + [K_G] \{ \Delta_G \} = \{ F_G \} + \{ \tilde{F}_G \}, \quad (13)$$

where  $\{ \Delta_G \}$  is global displacement vector.

The corresponding eigenvalue problem is:

$$\{ K_G \} - \omega^2 \{ M_G \} \{ \Phi \} = 0 \quad (14.a)$$

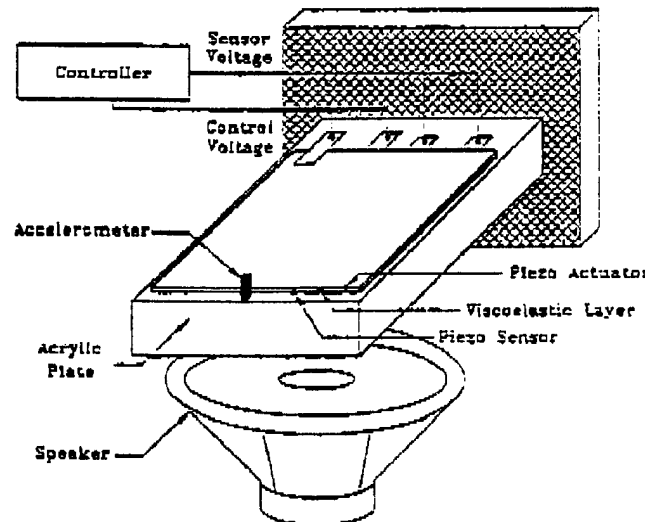
where  $\omega^2$  are complex eigenvalues.

The  $n$  th eigenvalue is written as follows:

$$\omega_n^2 = \omega_n^2 (1 + i\eta_n) \quad (14.b)$$

where  $\omega_n$  is the natural frequency and  $\eta_n$  loss factor for  $n$  th mode.

## EXPERIMENTAL PERFORMANCE



Schematic Drawing of Experimental Set-Up

## RESPONSE TO RANDOM EXCITATIONS

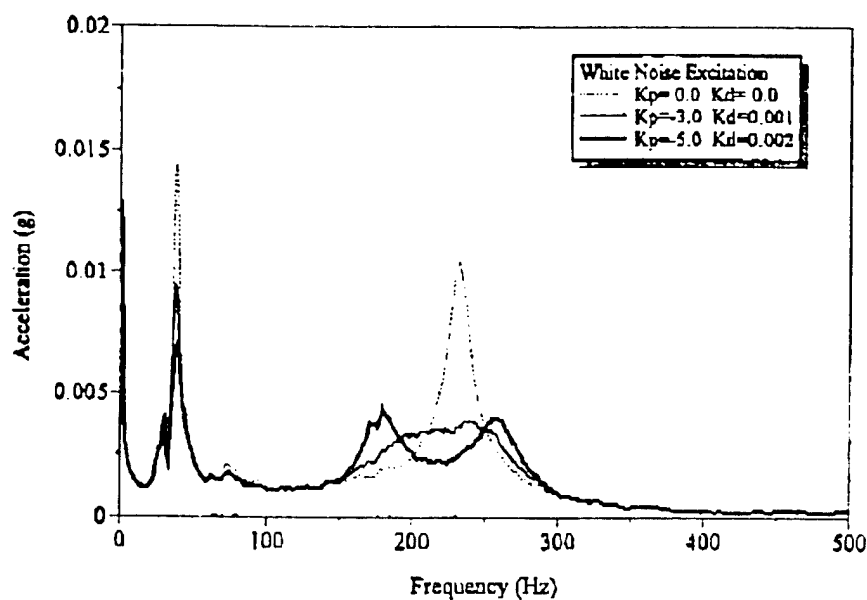


PLATE THICKNESS = 1 Inch

## RESPONSE TO RANDOM EXCITATIONS

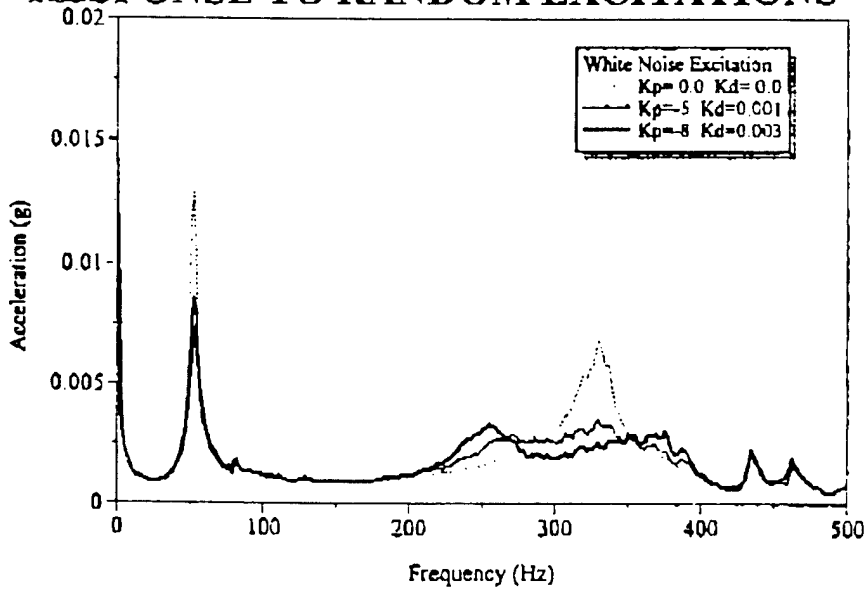


PLATE THICKNESS = 1.5 Inches

## COMPARISON BETWEEN THEORY & EXPERIMENTS

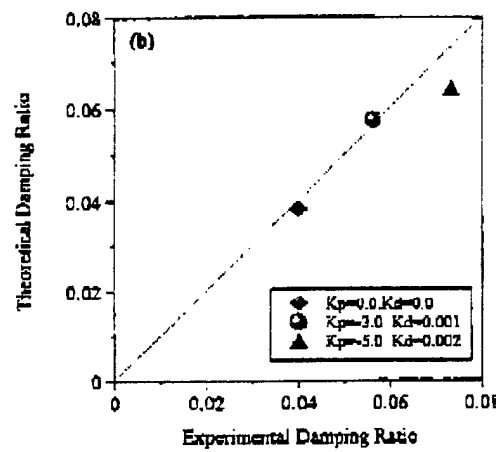
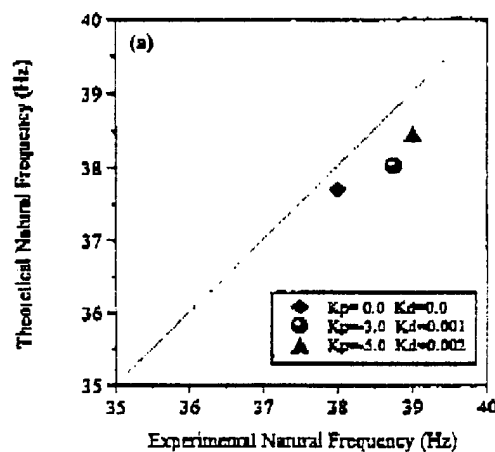


PLATE THICKNESS = 1 Inch

## COMPARISON BETWEEN THEORY & EXPERIMENTS

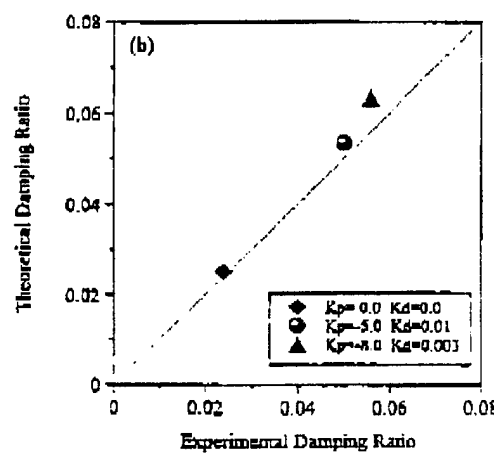
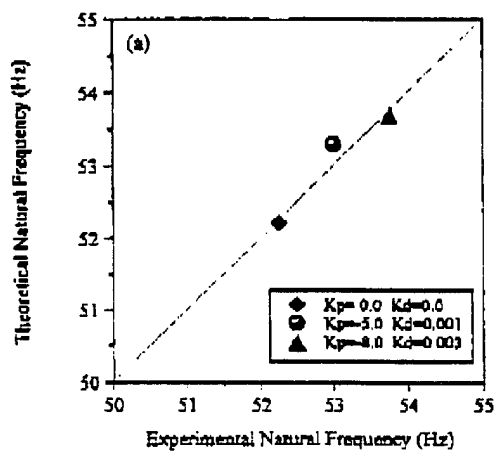


PLATE THICKNESS = 1.5 Inches

## **SUMMARY**

- 1.** A Finite element model is developed for laminated plate/ACLD system.
- 2.** The model is validated experimentally for six-layered plates.
- 3.** The ACLD is found to be effective in controlling the vibration of the multi-layered plates over a frequency range up to 300 Hz.
- 4.** The enhanced damping characteristics of the ACLD treatment plays an important role in attenuating the vibration of multi-layered plates.

# DAMPING USING A SOLID-STATE TUNABLE PIEZOCERAMIC VIBRATION ABSORBER

George A. Lesieutre  
Christopher L. Davis

Penn State University

A method for actively tuning the natural frequency and damping of a piezoceramic passive vibration absorber (PVA) was developed and experimentally verified. PVAs typically minimize vibration at a specific frequency often associated with a lightly damped structural mode or tonal disturbance. Large response reductions, however, may only be achieved if the PVA is lightly damped and accurately tuned to the frequency of concern. Thus, an important feature of a PVA is the ability to be accurately tuned to a possibly varying vibration or disturbance frequency.

Tuning an absorber generally requires a change in either the mass or stiffness of the device. Because the apparent stiffness and damping of a piezoelectric material depends on the electrical boundary conditions, the effective stiffness of a piezoceramic PVA can be modified using an external passive electrical shunt circuit. Some moduli of typical piezoceramics can change by a factor of 2 under different boundary conditions.

Capacitive shunting alters the natural frequency of the PVA only, while resistive shunting alters both the natural frequency and damping. Small shunt capacitances or large resistances correspond to an open circuit condition and have a stiffening effect, while large capacitances or small resistances correspond to a short circuit electrical boundary condition and have a softening effect.

A model was developed to predict changes in natural frequency and damping due to passive electrical shunting. Experiments using both passive capacitive and passive resistive shunt circuits verified the ability to predictably shift the natural frequencies of a particular piezoceramic inertial actuator by nearly 10%.

A tuning circuit was also developed to automatically adjust the shunt capacitance and the natural frequency of the vibration absorber to track a tonal disturbance. The absorber was passively tuned to an approximate frequency by choosing an appropriate reaction mass and then actively fine-tuned by the shunt circuit. An experiment was performed to evaluate the performance of the semi-active PVA on a structure subject to a tonal disturbance having a time-varying frequency. By keeping the absorber accurately tuned, a high degree of narrow-band vibration attenuation was maintained, with improvement over a purely passive PVA approaching 20 dB.

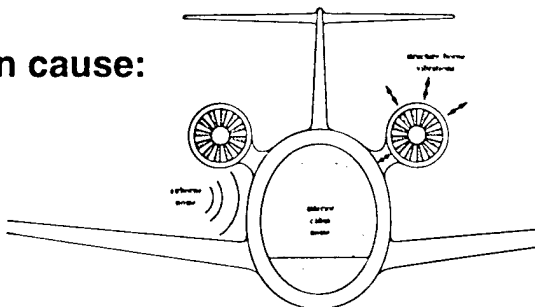
Penn State University  
Aerospace Engineering / Center for Acoustics and Vibration  
153G Hammond  
University Park, PA 16802

814-863-0103  
814-865-7092 (fax)  
[g-lesieutre@psu.edu](mailto:g-lesieutre@psu.edu)  
[cld103@psu.edu](mailto:cld103@psu.edu)

# Motivation

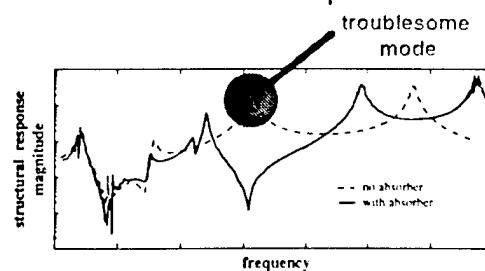
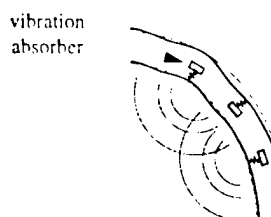
- **Vibrations result from disturbances:**
  - airborne sources (e.g., propwash, engine whine)
  - structure-borne sources (e.g., spool imbalance)

- **Vibrations can cause:**
  - fatigue
  - noise



## Passive Vibration Absorbers (PVAs)

- **Minimize vibration at a specific frequency**
  - changing mass or stiffness tunes device
  - tuning is critical for high performance
  - varying disturbance or mode can cause problems



## Problem Overview

---

- PROBLEM: need readily tunable PVAs
- EXISTING SOLUTIONS: AVAs
- POTENTIAL SOLUTION: shunted PIA
  - exploit piezo electromechanical coupling
  - tune without additional sensors
  - increase performance by using capacitive shunting

## Shunted Piezoceramic Stiffness

---

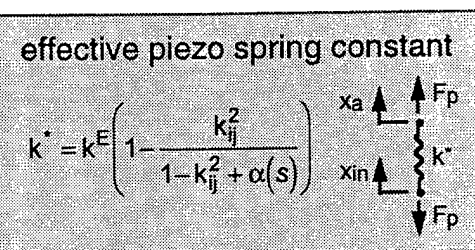
shunted compliance:  $S = s^E \left( 1 - s \frac{Ad_{31}^2}{s^E t} \right) T$       coupling coefficient:  $k_{ij} = \frac{d_{ij}^2}{s_{jj}^E \epsilon_i}$

short circuit stiffness:  $k^E = \frac{A}{s^E L}$

effective load:  $F_p = TA$

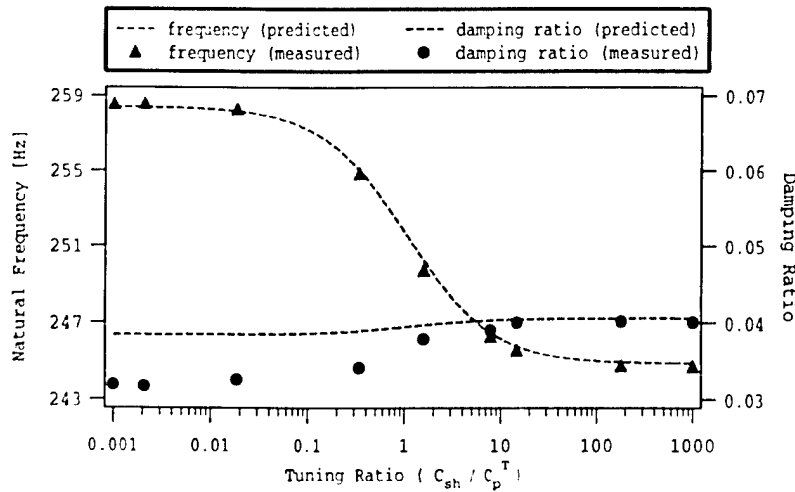
effective strain:  $S = \frac{x_a - x_{in}}{L}$

effective piezo spring constant  
$$k' = k^E \left( 1 - \frac{k_{ij}^2}{1 - k_{ij}^2 + \alpha(s)} \right)$$



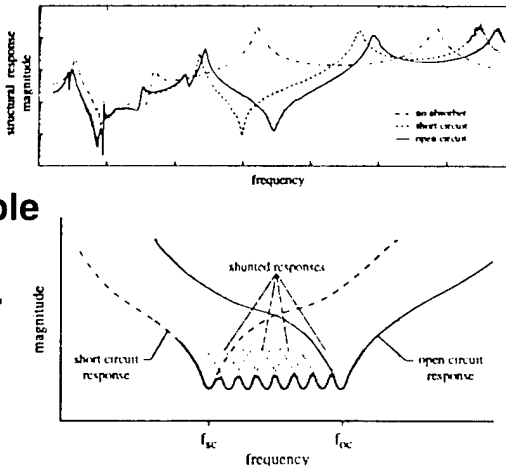
tuning ratio:  $\alpha(s) = \frac{Z_{oc}^T}{Z_{sh}}$

# Passive Capacitive Shunting

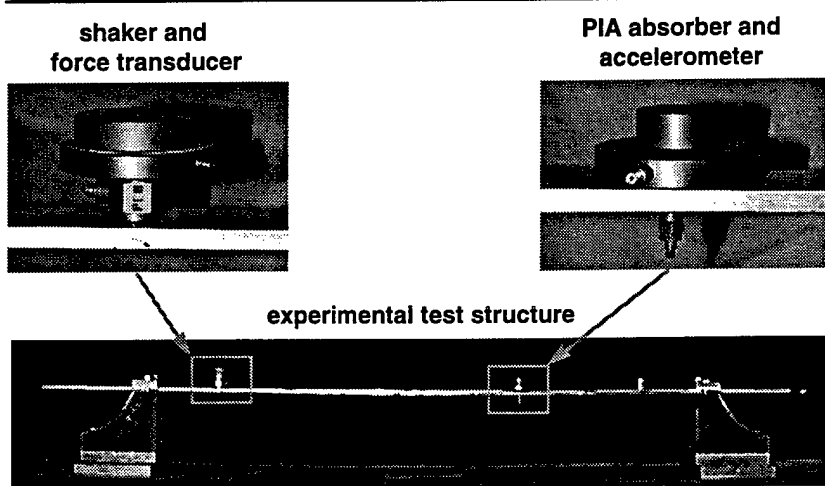


## Tuning Approach

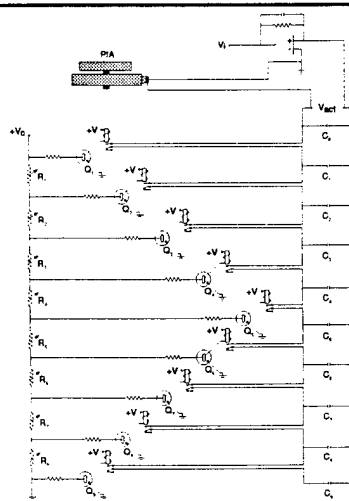
- Define tuning band ( $f_{sc}$  &  $f_{oc}$ )
- Measure dynamic variable to estimate  $f_d$
- Choose proper shunt to maintain min. response at  $f_d$



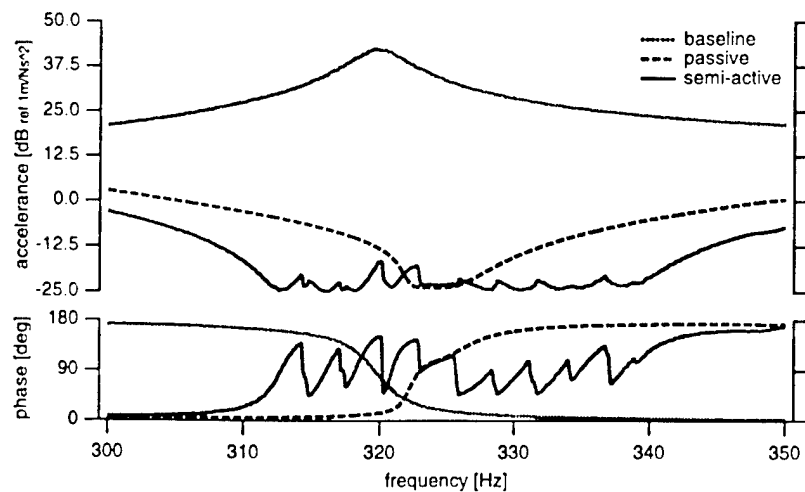
## Experimental Setup



## Tuning Control Circuit



## Passive & Semi-Active Performance



## Summary

- Developed a semi-active tunable vibration absorber
  - Tuned frequency of PIA with capacitive shunt
  - Changed natural frequency by more than 7%
  - Implemented controller for real-time tonal tuning
- Increased performance
  - $\pm 3.7\%$  tunable frequency band
  - additional attenuation effects beyond  $\pm 7\%$
  - increased performance by as much as 20 dB, averaging 10 dB across tuning band

# On the Structural Damping Characteristics of Active-Passive Piezoelectric Shunt Networks

**M. S. Tsai**  
Graduate Assistant

**K. W. Wang**  
Professor

Structural Dynamics and Controls Lab  
Mechanical Engineering Department  
The Pennsylvania State University  
University Park, PA 16802  
(814)865-2183, FAX (814)863-7222  
[kwwang@psu.edu](mailto:kwwang@psu.edu)

Abstract submitted for the Third ARO Workshop on Smart Structures

## Abstract

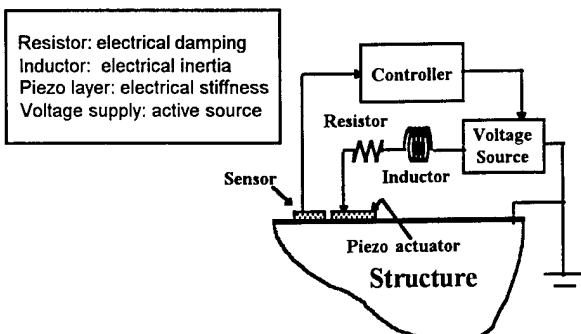
Due to their active and passive features, piezoelectric materials have been explored for their active-passive *hybrid* damping abilities, which could have the advantages of both the passive (stable, fail-safe, low power requirement) and active (high performance, feedback or feedforward actions) systems. Such a hybrid structural control concept normally integrates piezoelectric materials with an active voltage source and a passive RL circuit. Based on sensor feedbacks, the control voltage will drive the piezo-layer, together with the external shunting circuit, to suppress vibration of the host structure. While the results are promising, the functions of the various active and passive components and the interactions between them are not clearly understood.

This paper presents new insights obtained from analyzing the active-passive hybrid piezoelectric network (APPN) concept. It is shown that the shunt circuit not only can provide passive damping, they can also enhance the active action authority if tuned correctly. Therefore, the integrated APPN design is more effective than a system with separated active and passive elements.

However, it is also recognized that a systematic design/control method is needed to ensure that the passive and active actions are optimally synthesized. Such a method is developed and presented. The actuator bandwidth issue is addressed, and the possible benefits of integrating APPN with the active constrained layer (ACL) or enhanced active constrained layer (EACL) concepts are explored.

## Active-Passive Hybrid Piezoelectric Networks (APPN)

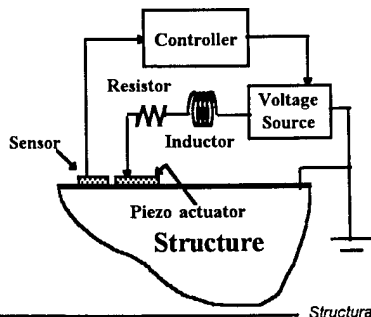
Piezoelectric Materials with Active Voltage Source  
 and  $RL$  Shunt Circuit (Agnes, 1994; Kahn and  
 Wang, 1994; Tsai and Wang, 1996)



*Structural Dynamics and Controls Lab*

## Observations From Previous Studies on APPN

- (a) By integrating the passive and active actions, the APPN could have the advantages of both active (high performance, feedback) and passive (stable, fail safe, low power requirement) approaches
- (b) One could achieve more vibration/noise reductions with less control effort than a purely active system



*Structural Dynamics and Controls Lab*



## Issues and Problem Statement

- (a) Interactions between the active and passive elements are not yet clear. Do the passive elements always complement the active action ? If yes, how ?
- (b) If not, should the active and passive elements be separated ? Will this enhance or reduce the hybrid action ?
- (c) APPN could outperform a purely active system, but since tuned damper concept -> bandwidth limitation ?

## Objective

To address the above issues and provide more insights to the APPN configuration

*Structural Dynamics and Controls Lab*

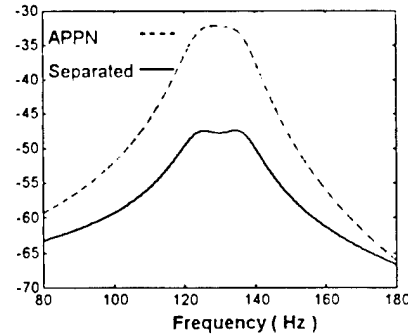
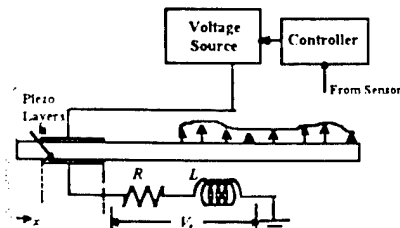


## Open Loop Analysis

How about separating the active and passive elements ?

- Active control on an optimized passive system
- Same passive damping ability
- Reduced active authority

Active authority index



*Structural Dynamics and Controls Lab*

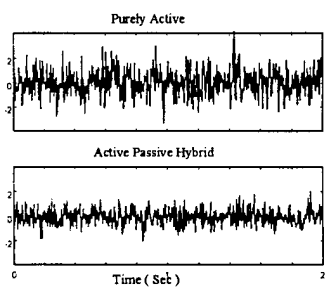
PENNSTATE



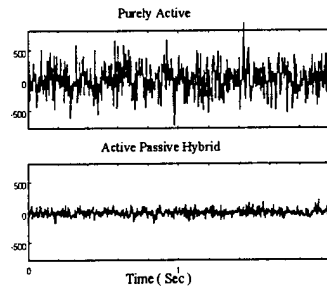
## Closed Loop Results

	$\sigma_w$ (mm)	$\sigma_{V1}$ (volts)	$\sigma_{V2}$ (volts)	$\sigma_{V3}$ (volts)
Uncontrolled	10.23	-	-	-
Purely Active Case	1.08	379	244	244
Active-Passive Hybrid Case	0.67	79.3	61.8	97.4

Vibration amplitude (mm)



Control effort (volts)

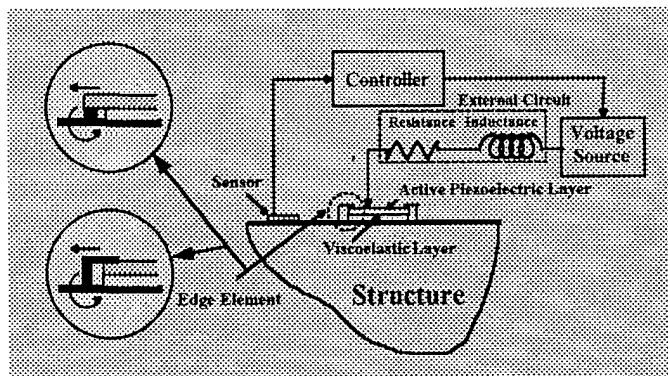


Structural Dynamics and Controls Lab

PENNSTATE



## Integrate APPN with Enhanced Active Constrained Layer (EACL)



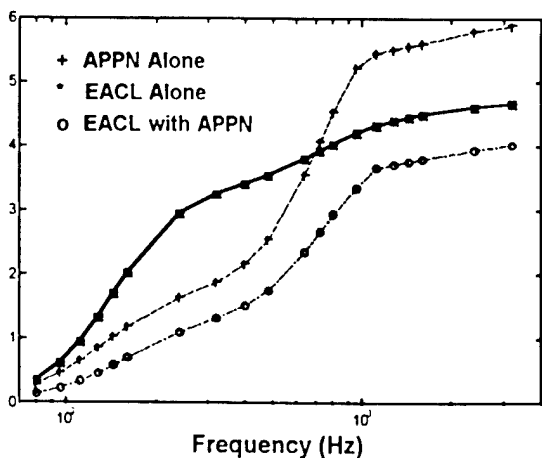
- Dual functional effect: wide and narrow band vibration controls
- Enhanced Active Constrained Layer (EACL): *edge elements* to increase transmissibility
  - enhance active authority (Liao & Wang 1996)
  - shunt action ?

Structural Dynamics and Controls Lab



## Comparison Study

Cost Function



- Cost function reflects vibration amplitude and control voltage requirements
- The integrated EACL/ APPN approach outperforms the other cases in a wide frequency range

Structural Dynamics and Controls Lab



## Conclusions

- Comparing to a purely active arrangement, the APPN shunt circuit not only can provide passive damping, it can also enhance the active authority around the tuned frequency
- The integrated APPN design is more effective than a system with separated active and passive elements
- Active authority will be degraded if the inductance is mistuned or if the resistance is too high -> a systematic design/control method is developed to ensure that the passive and active actions are optimally synthesized
- Method to enhance the actuator's broadband performance
  - integrate APPN with EACL

Structural Dynamics and Controls Lab

Third ARO Workshop on Smart Structures  
August 27-29, 1997, Virginia Tech, Blacksburg, VA

Nondimensional Analysis of Semi-Active  
Electrorheological and Magnetorheological Dampers

Li Pang  
*Research Assistant*

Norman M. Wereley  
*Assistant Professor*

Alfred Gessow Rotorcraft Center  
Department of Aerospace Engineering  
University of Maryland, College Park, MD 20742

**Abstract**

We develop nonlinear quasi-steady electrorheological (ER) and magnetorheological (MR) damper analysis using idealized Bingham plastic shear flow. Dampers with cylindrical geometry are investigated, where damping forces are developed in an annular bypass via Couette (shear mode), Poiseuille (flow mode) flow, or combined Couette and Poiseuille flow (mix mode). Models are based on parallel plate or rectangular duct geometry, and are compared to our prior 1D axisymmetrical analysis. Three nondimensional groups are introduced for damper analysis, namely, the Bingham number,  $Bi$ , the nondimensional plug thickness,  $\bar{\delta}$ , and the area coefficient, which is the ratio of the piston head area,  $A_p$ , to the cross-sectional area of the annular bypass,  $A_d$ . The approximate parallel plate analysis compares well with the 1D axisymmetrical model. The damping coefficient is the ratio of the equivalent viscous damping constant,  $C_{eq}$ , to the Newtonian viscous damping constant  $C$ . Using parallel plate analysis, in shear mode, the damping coefficient is a linear function of the Bingham number. In flow mode the damping coefficient is a function of nondimensional plug thickness only. In mixed mode, the damping coefficient reduces to the flow mode case when the area coefficient is large. The quasi-steady damping coefficient vs. nondimensional plug thickness diagram is validated using measured 10 Hz hysteresis cycles for an ER mode damper. LMS fit of the experiment data is compared with the analysis result which is shown in figure 2 (for approximate parallel plate analysis) and figure 3 (for more precise 1D axisymmetric analysis).

Because the damper was tested at 10 Hz which is not truly a quasi-steady loading condition, the analysis does not agree with the experiment. But the trends agree. It is expected that as the frequency of oscillation decreases and the loading condition more closely resembles quasi-steady loading, the agreement will improve substantially. We will further validate this analysis during the summer using an MR damper. Oscillatory loading will be applied to the MR damper in the 0.1 – 0.5 Hz frequency range, in order to obtain quasi-steady hysteresis cycle data.

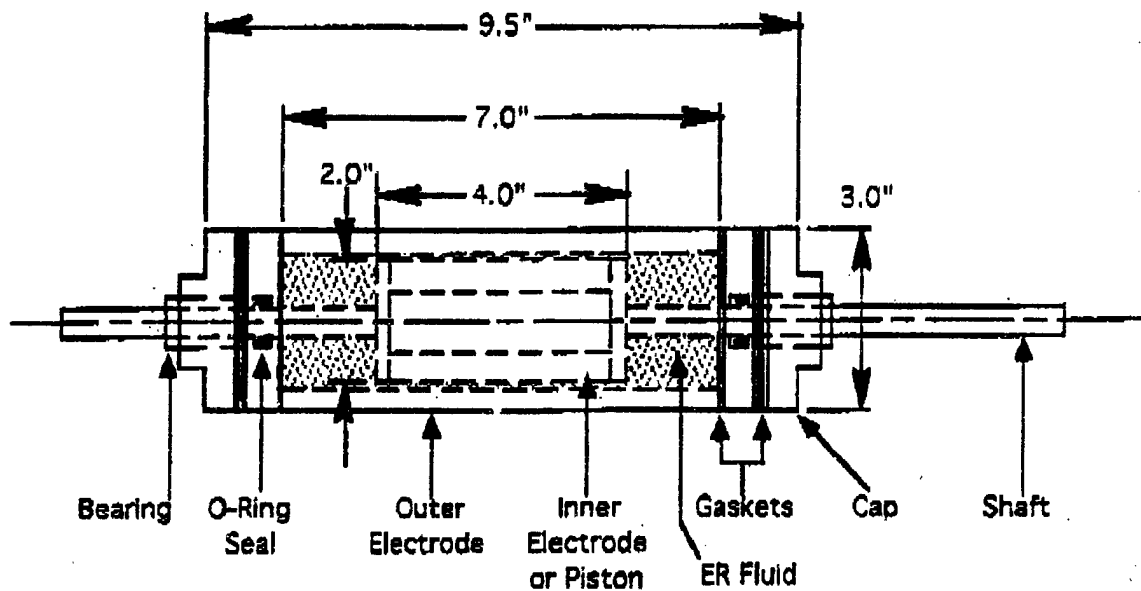


Figure 1: Schematic of the ER fluid mixed mode or moving electrode dashpot damper. The nominal design has a piston head that is 4.0 inches in length, a maximum stroke of 3.0 inches, a piston of diameter 2.0 inches, and an electrode gap of 0.1 inches.

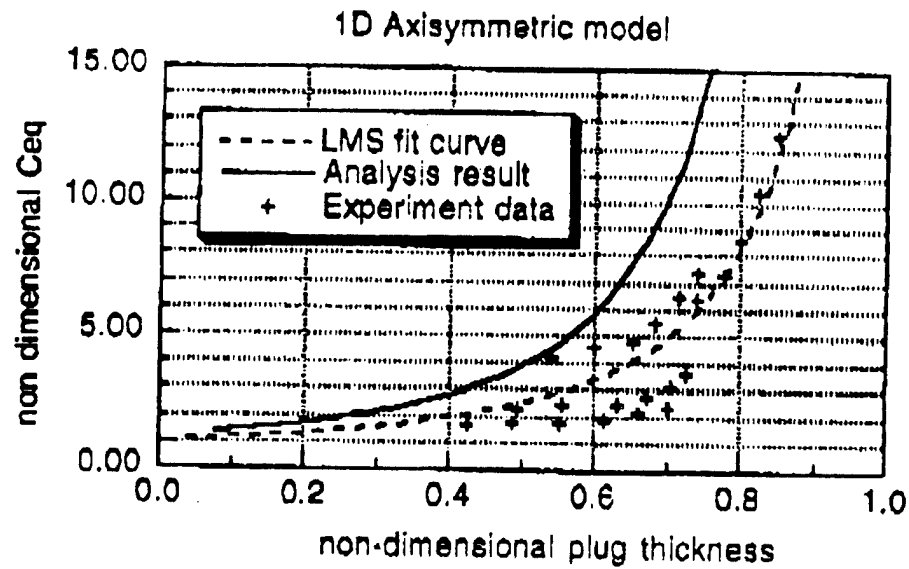


Figure 2: Damping coefficient vs. nondimensional plug thickness for the electrorheological mixed mode damper via 1D axisymmetrical analysis. A fit to 10 Hz hysteresis cycle data exhibits the same trend as quasi-steady analysis, and magnetorheological

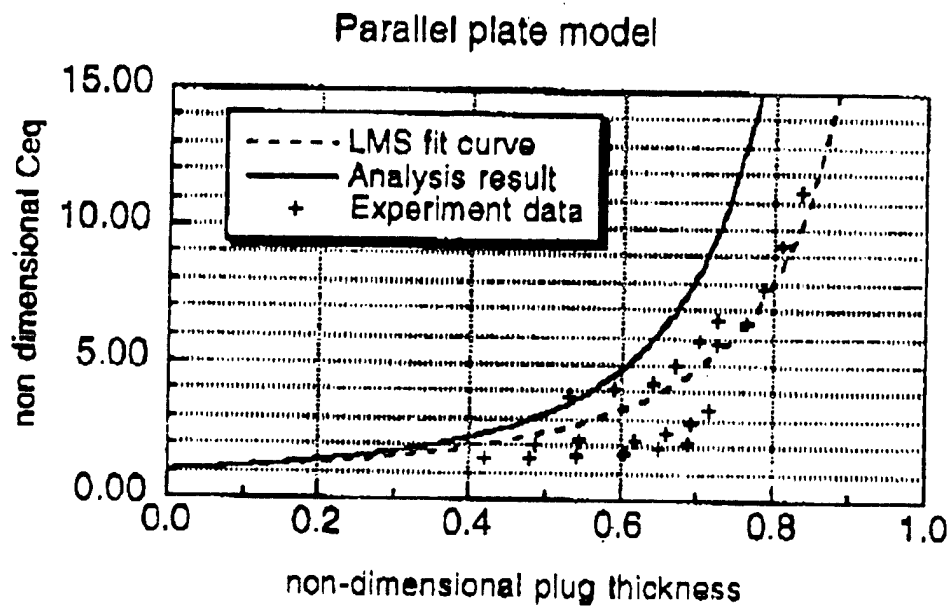


Figure 3: Damping coefficient vs. nondimensional plug thickness for the electrorheological mixed mode damper via parallel plate analysis. A fit to 10 Hz hysteresis cycle data exhibits the same trend as quasi-steady analysis, and magnetorheological

# DAMPING PROPERTIES OF MAGNETO-RHEOLOGICAL FLUIDS

Mehdi Ahmadian, Xubin Song, and Brian Reichert  
Advanced Vehicle Dynamics Laboratory  
Department of Mechanical Engineering

Virginia Tech

Blacksburg, VA 24061-0238 USA

## ABSTRACT

The damping properties of magneto-rheological (MR) fluids are investigated, both analytically and experimentally. A nonlinear mathematical simulation model for MR fluids is developed, and used to predict the damping behavior of MR fluids. The model is validated, using experimental results for a prototype MR damper. It is shown that the analytical model is able to accurately predict the damper behavior. Then, the model is used to investigate how various aspects of MR fluids, such as viscosity, magnetic properties, and shear strain effect the damping characteristics of the fluid. In addition to providing a better understanding of the damping properties of MR fluids, the result of the study show that it is possible to adjust the fluid properties to better suit various applications where MR dampers are commonly used.



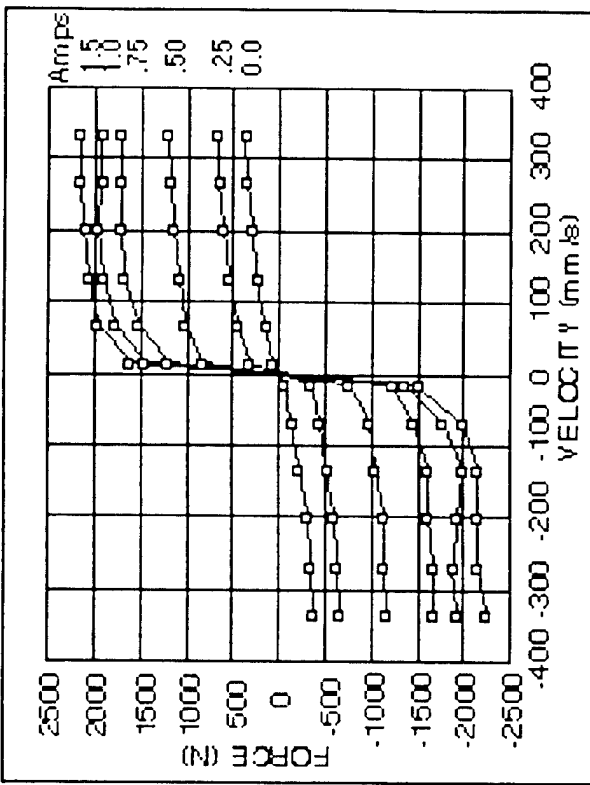
Advanced Vehicle  
Dynamics Laboratory

# MR Dampers



- Provide varying levels of damping, according to the voltage (current) supplied to the damper
- Fast acting; can be used for real-time, embedded control of noise and vibrations
- Mostly used in vehicle applications for improving suspension performance
- Some applications for seismic damping of tall buildings have been investigated

Light Duty Damper (SD-1000-2)  
with Single Controllable Fluid Valve

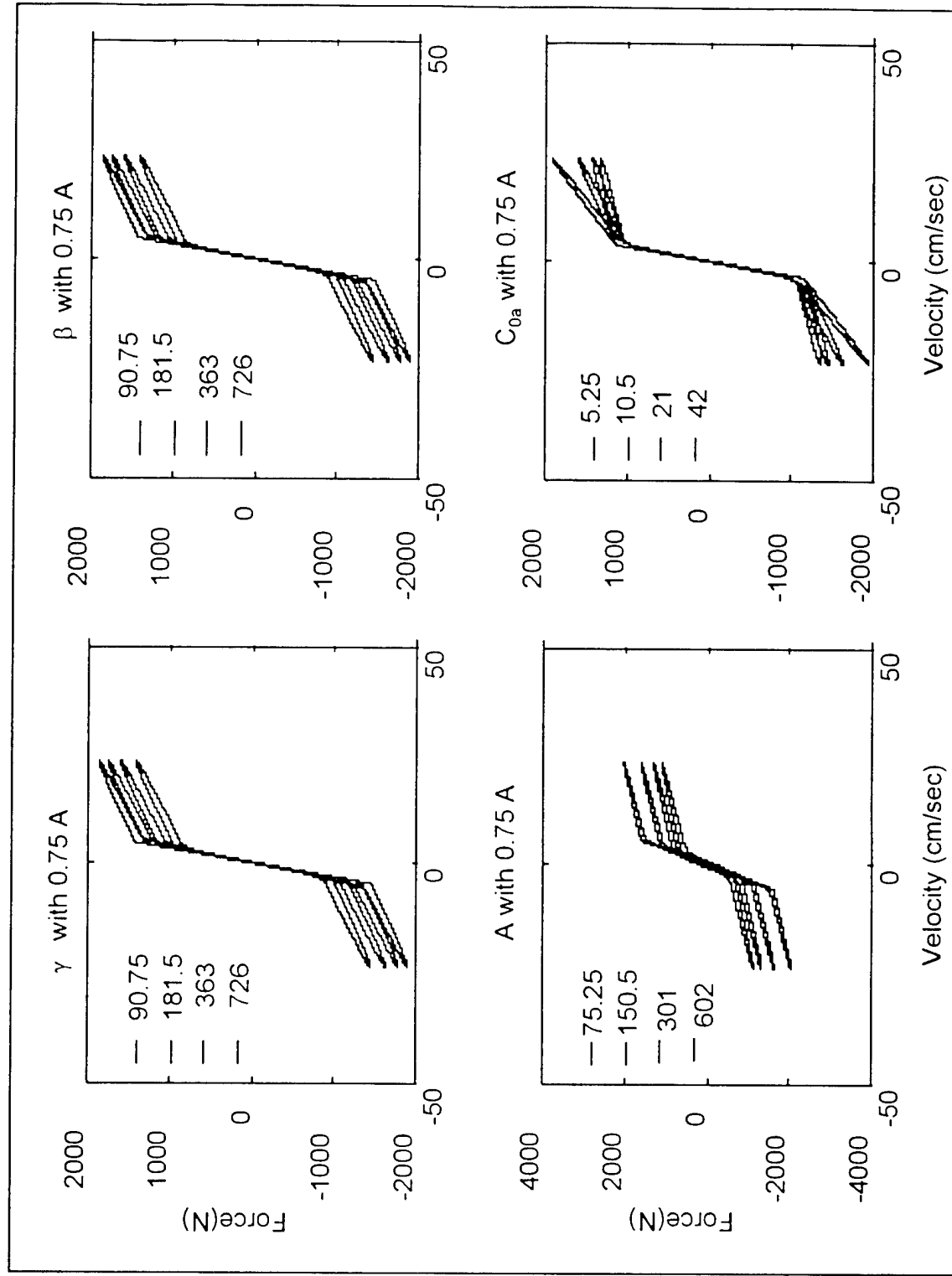


# MVR Damper Models

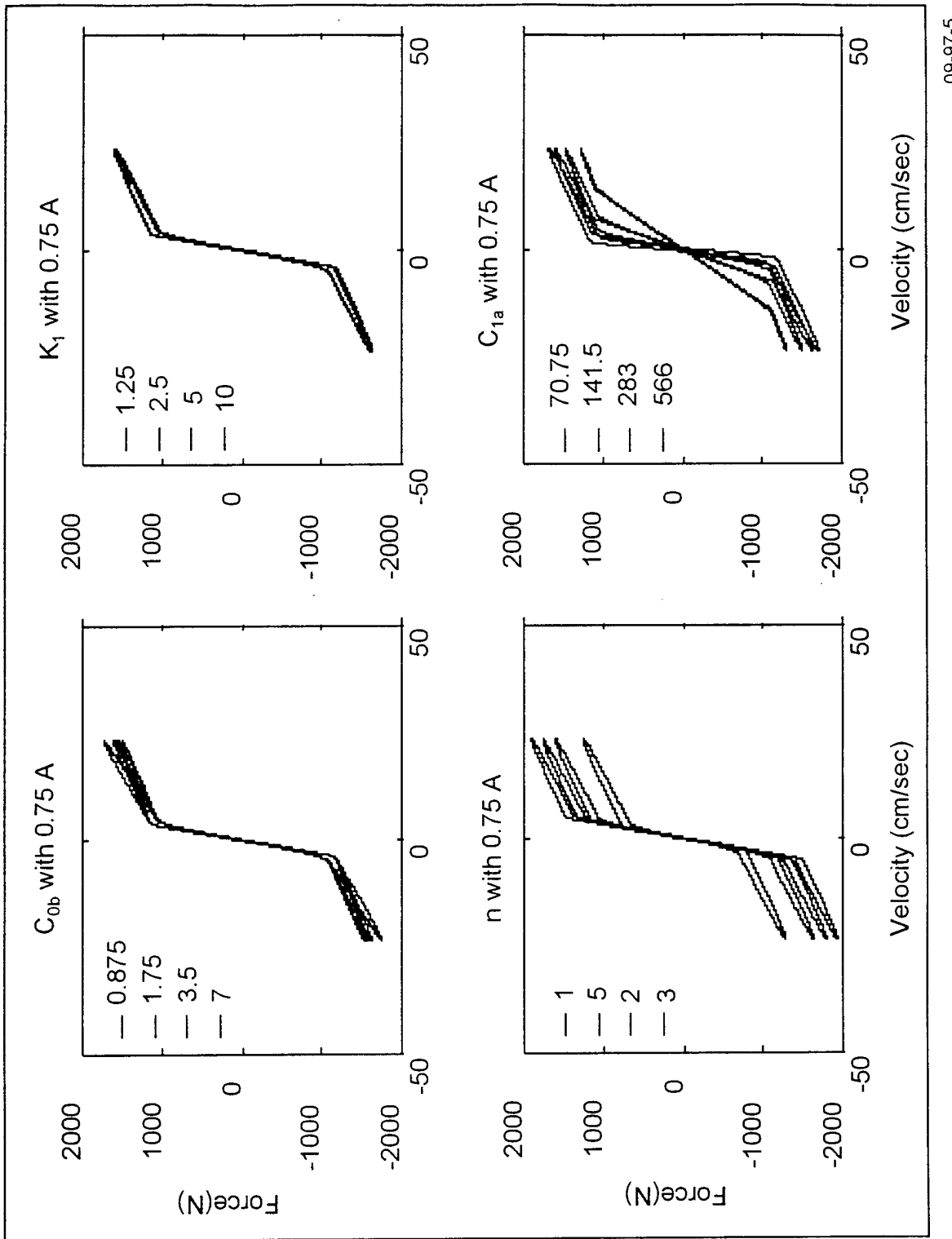
- Several models have been proposed
  - ◆ B.F. Spencer, Notre Dame
  - ◆ N.M. Wereley, Maryland
  - ◆ others
- Most models are discontinuous and complex, due to the nonlinearities and non-newtonian behavior of MVR dampers
- For some applications it may be possible to describe the damper behavior based on continuous functions, to make the numerical solution of the equations easier

$$\begin{cases} \dot{u} = -\eta(u - v) \\ \alpha = \alpha(u) = \alpha_a + \alpha_b u \\ c_1 = c(u) = c_{1a} + c_{1b} u \\ c_0 = c(u) = c_{0a} + c_{0b} u \end{cases}$$
$$\begin{cases} \dot{z} = -\gamma |\dot{x} - \dot{y}| z^{n-1} - \beta(\dot{x} - \dot{y}) |z|^n + A(\dot{x} - \dot{y}) \\ \dot{y} = \frac{1}{c_0 + c_1} \{ \alpha z + c_0 \dot{x} + k_0(x - x_0) \\ F_{mr} = c_1 \dot{y} + k_1(x - x_0) \end{cases}$$

# Parametric Analysis of MR Dampers

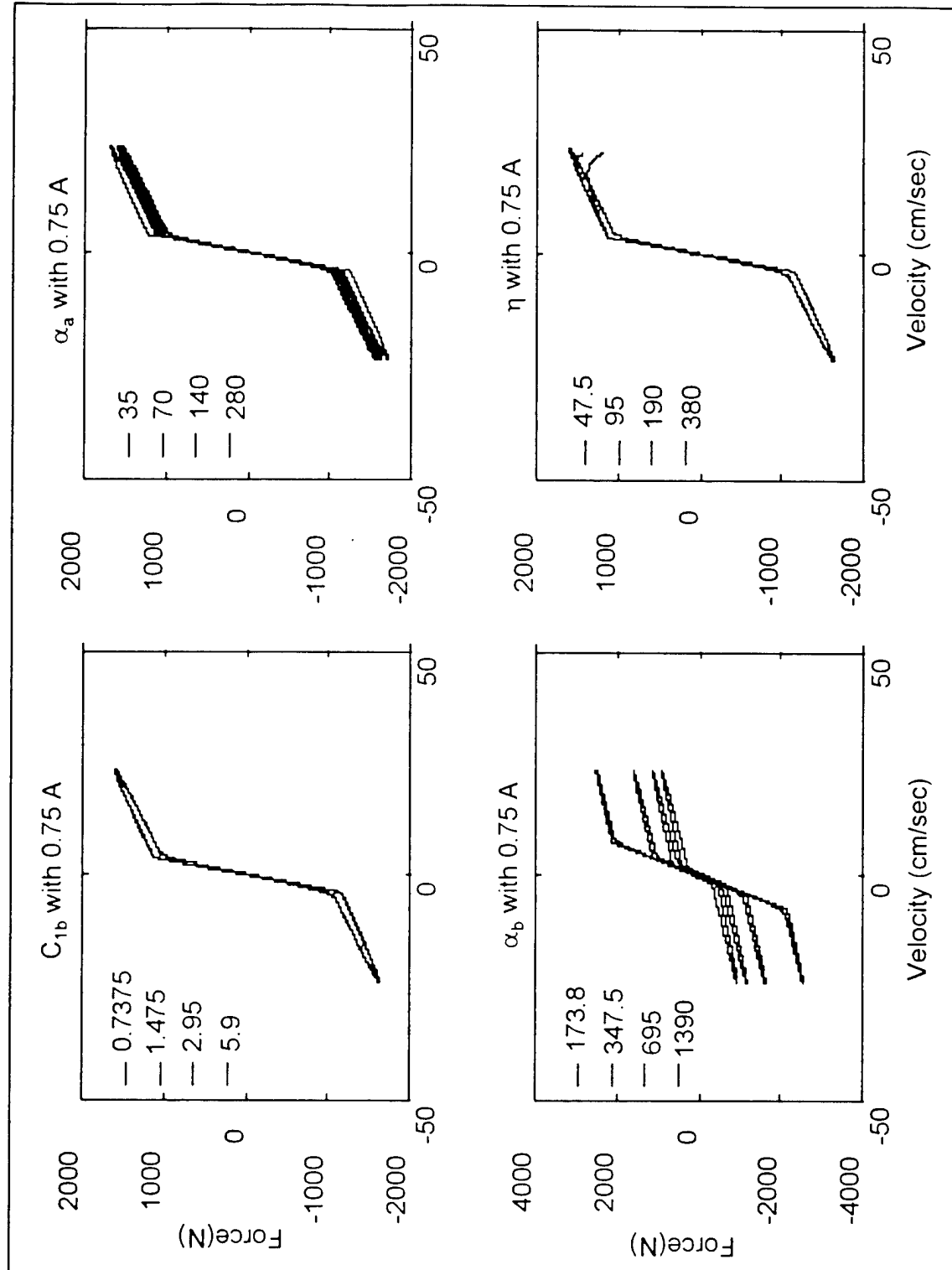


# Parametric Analysis of MR Dampers



09-97-5

# Parametric Analysis of MR Dampers



# Conclusions

- It is possible to use simple functions to represent force-velocity behavior of MR dampers
- For some applications, the non-linear models are necessary to analyze the damper behavior
- The mechanical tolerances and clearances of the damper significantly affect the damping achieved with MR dampers

# Helicopter Blade Response and Aeromechanical Stability with Magnetorheological Fluid Based Lag Dampers

Sameer Marathe\* Farhan Gandhi\*\* Kon-Well Wang\*\*\*

Rotorcraft Center of Excellence  
The Pennsylvania State University  
University Park, PA 16802

## ABSTRACT

Helicopters have traditionally been equipped with auxiliary hydraulic or elastomeric lead-lag dampers to alleviate aeromechanical instabilities due to the interaction of the poorly damped rotor lag modes with the fuselage pitch and roll modes. These passive dampers provide a fixed amount of damping over the entire flight envelope, although damping augmentation may really be required only in a limited number of operating conditions. At high speed forward flight the passive dampers then produce high periodic loads, leading to high dynamic stresses and fatigue of the blade root region. Additionally, the performance of passive dampers can significantly deteriorate at extreme temperatures, or they can produce small amplitude limit cycle oscillations of the blade. In recent years, there have been rapid developments in magnetorheological (MR) fluids. The high damping forces that MR fluid dampers can produce, along with the ability to control these forces by the application of a magnetic field, make MR fluid dampers attractive candidates for helicopter lag damping applications. The present study is the first to analytically examine the influence of MR lag dampers on rotor aeroelasticity. Results indicate that an MR damper of size approximately equal to that of a typical elastomeric damper can produce sufficient damping to alleviate ground resonance. The damper can be used in an ON-OFF mode or with continuous feedback linearization. With the former approach, the magnetic field is held at a high value when damping augmentation is required (as in the case of ground resonance), and reduced or eliminated in other conditions. At a given value of magnetic field, the available damping decreases as the perturbation size increases, and it is shown that a *secant approximation* can be used to obtain a conservative estimate of the equivalent linear system damping. Using a feedback linearization approach, the magnetic field is continuously changed to maintain a desired damping value, up to saturation. Using either scheme, the periodic damper loads in forward flight are considerably lower than that of a conventional passive damper. The study examines damper sizing issues, as related to the magnetic field saturation limits and lag perturbation amplitudes, to produce the desired damping.

\* Graduate Student

\*\* Assistant Professor, Aerospace Engineering

\*\*\* Professor, Mechanical Engineering

PENNSTATE



---

**Helicopter Blade Response and  
Aeromechanical Stability with  
Magneto Rheological Fluid Based Lag Dampers**

**Sameer Marathe**  
Graduate Research Assistant

**Farhan Gandhi**                   **Kon-Well Wang**  
Asst. Professor, Aerospace Engr.   Professor, Mechanical Engr.

**Rotorcraft Center of Excellence, Penn State University**

Presented at the 3rd ARO Workshop on Smart Structures  
Blacksburg, VA, August 27 - 29, 1997

**Background and Motivation**

PENNSTATE



- At present passive lag dampers used to alleviate aeromechanical instabilities of soft inplane rotors
- Lag damping augmentation is really required in only a limited number of operating conditions
- Passive dampers produce fixed damping in the entire envelope. In high speed forward flight, high damping (which is no longer required) increases the periodic damper and blade loads and decreases component fatigue life



## Background and Motivation

- Desirable to have controllable lag damping
- Then periodic loads in forward flight can be reduced while at the same time ensuring enough damping to stabilize ground resonance
- Additionally, passive elastomeric damper performance can significantly degrade at extreme temperatures, small amplitudes, etc. Controllable damping can compensate for this
- MR Fluid based dampers are attractive candidates for controllable lag damping



## Previous Work

- Considerable amount of work has been done in the ER and MR material modeling and control  
Carlson, Spencer, Jolly, DuClos, Coulter,  
Wang, Wereley, Stanway, others
- Application to helicopter rotor lag damping relatively unexplored, with NO WORK on influence of MR dampers on rotorcraft aeromechanics
  - Damper sizing and design issues to obtain required damping, saturation concerns
  - Control schemes
  - Periodic damper loads in forward flight

PENNSTATE



## Goals of Present Research & Approach

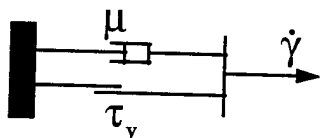
- Examine the effectiveness of MR lead-lag dampers for lag damping augmentation and reduction of periodic damper loads in forward flight
- Since damper is nonlinear, identify means of calculating equivalent linear system damping
- Determine relation between damper size, amplitude of perturbations, required field levels, and available damping
- Examine different control schemes for the MR lag damper
- Bingham-plastic model for MR damper integrated into a rotor aeroelastic analysis (blades undergoing flap, lag, and torsion motions about root springs, with periodic response calculated using finite element in time)

PENNSTATE



## A Review of the Semi-Active Damping Action of MR Fluids

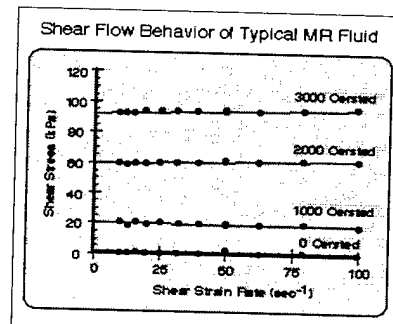
- Since pre-yield region is limited to very small strains, a large number of MR Fluid devices operate predominantly in post-yield
- Therefore behavior of MR lag damper can be effectively modelled as Bingham-Plastic



$$\tau = \tau_y \operatorname{sign}(\dot{\gamma}) + \mu \dot{\gamma}$$

$\tau_y$  - Yield stress

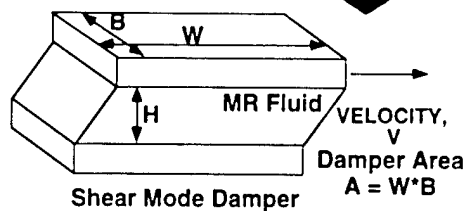
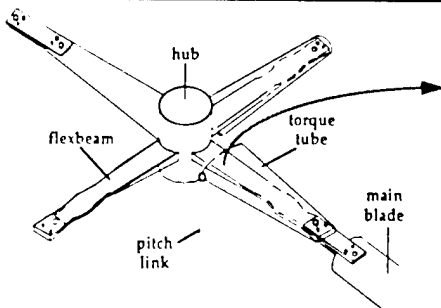
$\mu$  - Post-yield viscosity



PENNSTATE

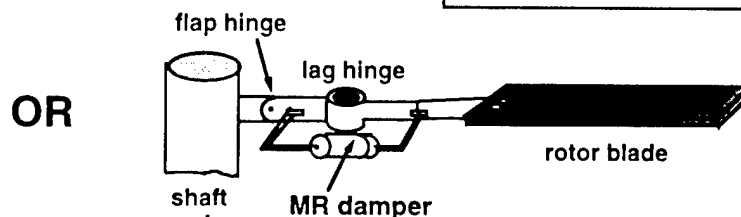


### MR Lead-Lag Damper on Rotor



#### Force Produced by Damper

$$F = \tau_y * A * \text{sgn}(V) + \mu * A / H * V$$



### Strategies for use of MR damper

#### 1. ON-OFF Operation (Constant Field)

PENNSTATE



- Turn ON the magnetic field for ground/hover operations where high damping is required
- Turn OFF the magnetic field when damping augmentation is not required

#### Questions:

- How large of a field should be applied?
- How much damping available? (amplitude dependent)
- What is the size of the damper as compared to an elastomeric lead-lag damper?
- How much reduction will it provide in periodic damper loads in forward flight?

## Linearization

PENNSTATE



- The friction element in the MR-damper model makes the system nonlinear

**Q. What is the magnetic field required to obtain a specified amount of damping?**

(for a given lag perturbation size, say 2 deg.)

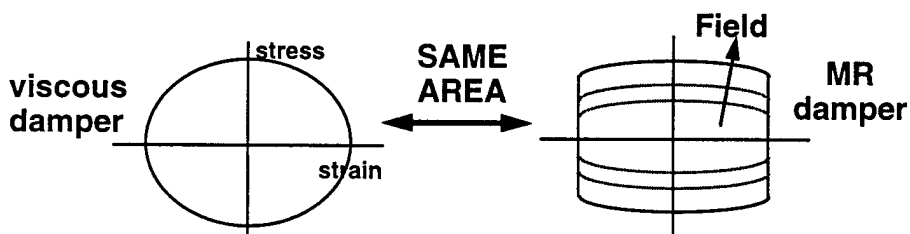
- In general, useful to obtain equivalent “linear” viscous damping for different perturbation amplitudes
- Two different approximation schemes are used:
  - (I) Equivalence of ENERGY DISSIPATED per cycle
  - (II) SECANT APPROXIMATION

## Equivalence of ENERGY DISSIPATED per cycle

PENNSTATE

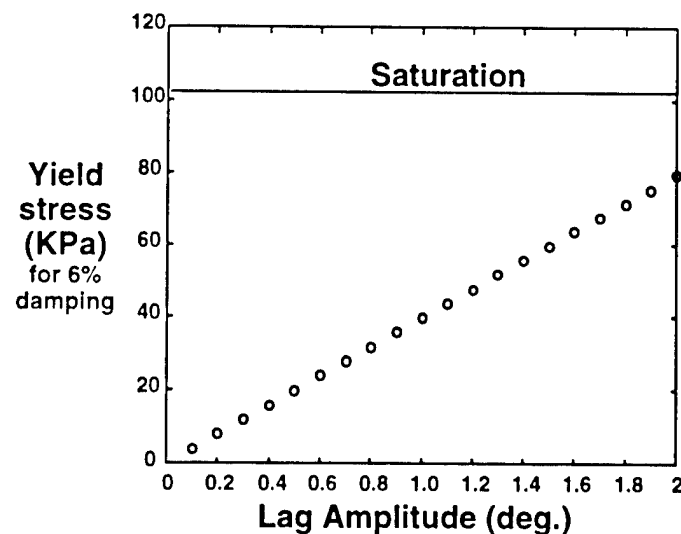


- For a 6% viscous damper, blade lead-lag motion of a prescribed amplitude is applied, and the area under the hysteresis loop (energy dissipated per cycle) is calculated.
- For the SAME lead-lag motion, the magnetic field (or yield stress) required, such that the MR damper hysteresis loop has the SAME area is determined



## Equivalence of ENERGY DISSIPATED per cycle

PENNSTATE



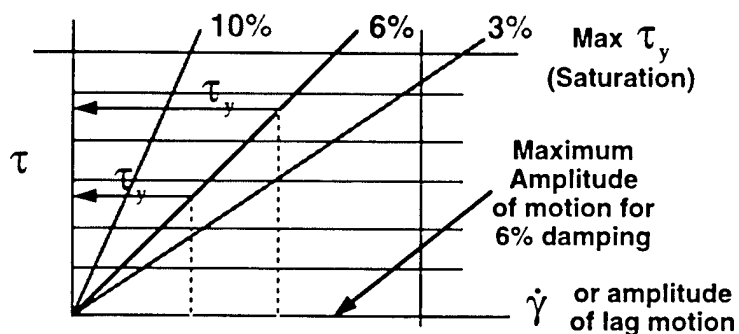
Graph shows the field (yield stress) required for 6% equivalent viscous damping for any amplitude of lag motion

## SECANT APPROXIMATION

PENNSTATE



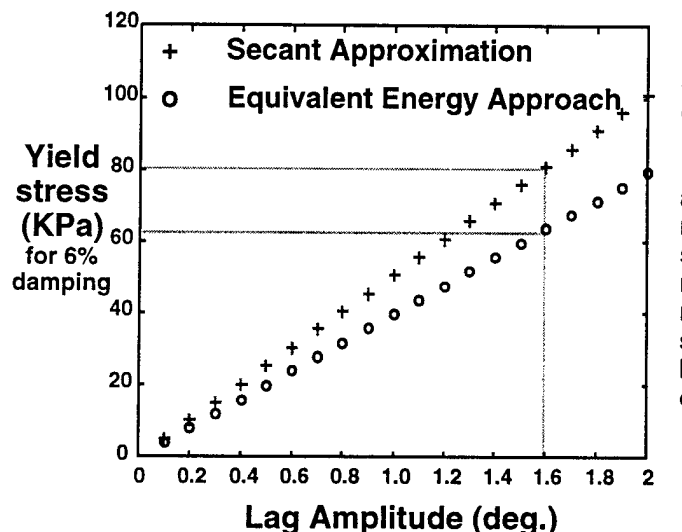
- On the stress versus strain rate curve, draw a line corresponding to 6% damping
- For every strain rate (corresponding to an amplitude of lag motion) determine the corresponding yield stress and magnetic field required



PENNSTATE



## Secant Aproximation is Conservative

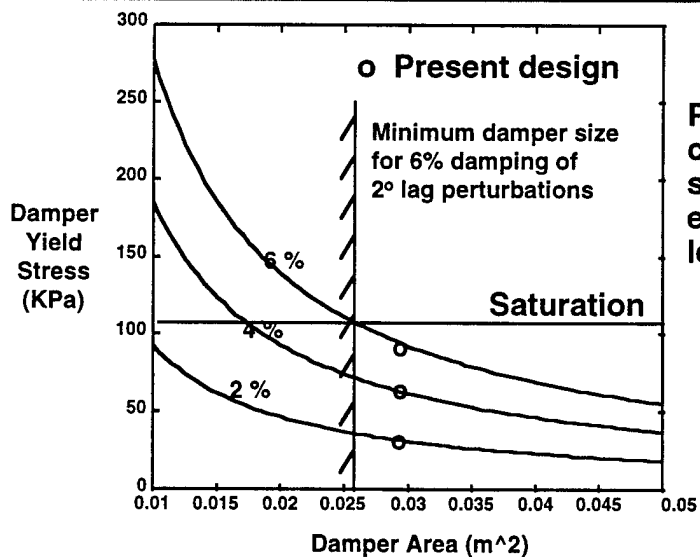


Secant Approx.  
convenient to use

For a given  
amplitude of lag  
motion and  
specified damping  
requirement, the  
required yield  
stress (field) can  
be directly  
obtained

## Damper Sizing Considerations

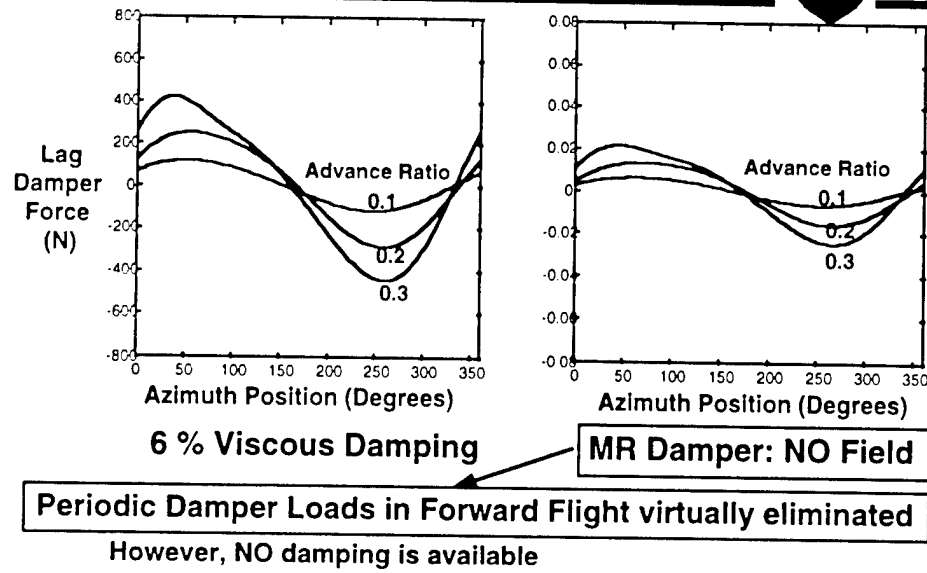
PENNSTATE



Present design  
comparable in  
size to a typical  
elastomeric  
lead-lag damper

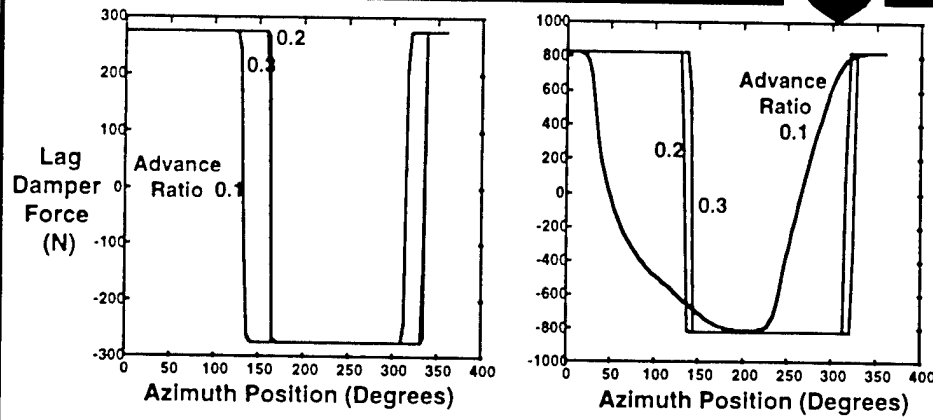
## Periodic Damper Loads in Forward Flight

PENNSTATE



## Periodic Damper Loads in Forward Flight

PENNSTATE



Even for modest values of magnetic field,  
Periodic Damper Loads can be very high

## Strategies for use of MR damper

PENNSTATE

### 2. Variable Field based on Feedback Linearization



MR Constitutive Law :  $\tau = \tau_y \operatorname{sign}(\dot{\gamma}) + \mu \dot{\gamma}$

→ Controllable

Previously,  $\tau_y$  (or magnetic field) held constant

If  $\tau_y = K|\dot{\gamma}|$  then  $\tau = (K + \mu) \dot{\gamma}$

This is just like a linear viscous damper,  $\tau = C \dot{\gamma}$   
where the damping constant, C, can be controlled

The control gain, K, can be set to provide 6% damping for ground resonance, and a lower value in forward flight

No energy equivalence or secant approximation required

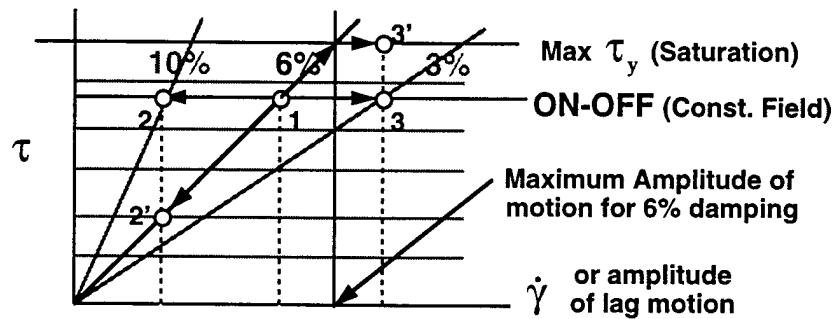
## ON-OFF versus Feedback Control

PENNSTATE



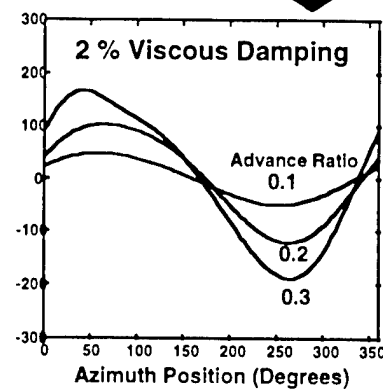
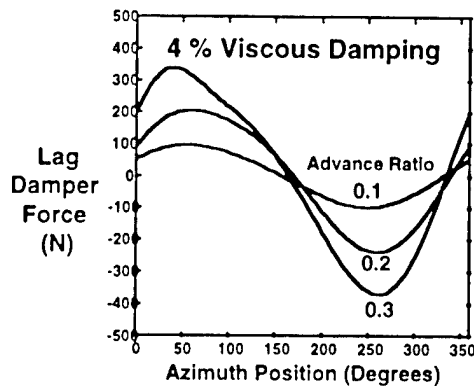
ON-OFF: Larger damping for smaller perturbations,  
Lower damping for larger perturbations  
(for a given field)

Feedback: The field is continuously changing so that  
damping is maintained at prescribed value (6%)  
before saturation



## Periodic Damper Loads in Forward Flight

PENNSTATE



With feedback linearization, lower but finite values of damping can be retained in forward flight, with reduced damper loads

## Summary and Concluding Remarks

PENNSTATE



- An MR damper of the approximate size of a typical elastomeric damper can provide the required lag damping to stabilize ground resonance
- With reduced (or zero) damping in forward flight, periodic damper loads may be reduced (or eliminated)
- Convenient approaches such as the 'Secant Approx.' are examined to quantify the 'equivalent linear damping'
- MR dampers can be used either as ON-OFF devices, or with a feedback linearization control scheme, as needed
- Damper area can be increased to obtain larger "equivalent damping ratios" or to damp larger perturbations

Qualitative Analysis of the Bulk Ferromagnetic  
Hysteresis Model

R. Venkataraman, P.S. Krishnaprasad

*Department of Electrical Engineering*

*and Institute for Systems Research*

*University of Maryland, College Park, MD 20742.*

August 27, 1997

## Abstract

In 1983, D.C. Jiles and D.L. Atherton proposed a model for ferromagnetic hysteresis from phenomenological and thermodynamic considerations. It is a low dimensional model with five parameters, and is appealing from the control point of view, because it aims to describe ferromagnetic hysteresis as a solution of four differential equations. To date, there has not been a mathematical demonstration that this intuition is indeed correct. The main difficulties in analyzing these differential equations seem to stem from the complicated nature of the equations. While verification of the periodic nature of the hysteresis curves produced by the sinusoidal inputs has been done by computer simulation, and also by the heuristic technique of harmonic balancing as in the work of V. Rizzoli et al., these are not a sufficient guide to the effectiveness of the Jiles-Atherton model.

In the present work, we show, via a careful analysis of the equations, that (a) they do admit a limit cycle for a range of periodic inputs, and (b) it is orbitally asymptotically stable (using the Poincaré map). There are two inequalities that the parameters of the Jiles-Atherton model must satisfy for our conclusions to hold. These inequalities also prove to be sufficient conditions for existence of a periodic solution.

We also, discuss these results in relation to some experimental data on the hysteretic behavior of Terfenol-D actuators.

# The Bulk Ferromagnetic Hysteresis Model

$$\frac{dM}{dH} = \frac{\frac{k\delta}{\mu_0} c \frac{dM_{an}}{dH_e} + \delta_M (M_{an} - M)}{\frac{k\delta}{\mu_0} - \delta_M (M_{an} - M) \alpha - \frac{k\delta}{\mu_0} \alpha c \frac{dM_{an}}{dH_e}} \quad (1)$$

$$\dot{M} = \frac{dM}{dH} \dot{H} \quad (2)$$
$$M_{an}(H_e) = M_s \left( \coth \left( \frac{H_e}{a} \right) - \frac{a}{H_e} \right). \quad (3)$$

$$H_e = H + \alpha M. \quad (4)$$

$$\delta_M = \begin{cases} 0 & : \dot{H} < 0 \text{ and } M_{an}(H_e) - M(H) > 0 \\ 0 & : \dot{H} < 0 \text{ and } M_{an}(H_e) - M(H) > 0 \\ 1 & : \text{otherwise.} \end{cases} \quad (5)$$

## The Bulk Ferromagnetic Hysteresis Model (Contd.)

$M$  is the average magnetization of a thin ferromagnetic rod.  
 $H$  is the magnetic field.

$k, \alpha, c, a, M_s$  are non-negative parameters.  
 $\delta, \delta_M$  are discrete states.

Conditions on Parameters to ensure Existence and  
Uniqueness of Solutions

$$0 < c < 1 \quad (6)$$

$$\frac{c\alpha M_s}{3a} < 1 \quad (7)$$

$$\frac{k}{\mu_0} \left(1 - \frac{\alpha c M_s}{3a}\right) - \alpha (\sup |\delta_M (M_{an} - M)|) > \varepsilon > 0 \quad (8)$$

## Key Property of the System

**Lemma 1** Consider the system described by Equations 1–5. Let the initial condition  $(M_0, H_0)$  be on the anhysteretic curve.

$$M_0 = M_{an}(H_0 + \alpha M_0). \quad (9)$$

If  $H(t)$  is a monotonically increasing function of time for  $t \in [a, b]$  where  $b > a \geq 0$ , then  $(M_{an} - M) \geq 0 \quad \forall t \in [a, b]$ . Else if  $H(t)$  is a monotonically decreasing function of time for  $t \in [c, d]$  where  $d > c \geq 0$ , then  $(M_{an} - M) \leq 0 \quad \forall t \in [c, d]$ .

## Main Theorem

**Theorem 1** Consider the system of equations 1-5, with the input given by  $u(t) = \dot{H}(t) = b \cos(\omega t)$ . If  $(H, M)(0) = (0, 0)$ , then the  $\Omega$ -limit set of the system is an asymptotically orbitally stable periodic orbit.

### Method of Proof for Periodicity of the Bulk Ferromagnetic Hysteresis Model for Sinusoidal Inputs

- Starting from  $(H, M) = (0, 0)$ ,  $M(t)$  increases for  $t \in [0, \frac{\pi}{2\omega}]$ , but lies below the anhysteretic magnetization curve.
- For  $t \in [\frac{\pi}{2\omega}, \frac{3\pi}{2\omega}]$ ,  $M(t)$  first intersects the anhysteretic curve, then lies above it.
- For  $t \in [\frac{3\pi}{2\omega}, \frac{5\pi}{2\omega}]$ ,  $M(t)$  first intersects the anhysteretic curve, then lies below it.

## Main Theorem (Contd.)

By repeating the analysis in Steps 2, 3, we can conclude that the solution trajectory to the ferromagnetism model lie within the compact set  $[-\frac{b}{\omega}, \frac{b}{\omega}] \times [-M_s, M_s]$ .

- We then look at  $\{M(\frac{2n\pi}{\omega})\}; n = 0, 1, 2, \dots$ . This sequence of points lie on the  $M$  axis ( $H = 0$  line). We then show that the sequence has a unique accumulation point. This shows the existence of an asymptotically stable periodic orbit in the  $H - M$  plane. Since  $\delta$  and  $\delta_M$  depend on  $H, M$ , we conclude that the system of equations 1-5 produce asymptotically stable periodic solutions, for the given input.

## References

- [1] D. Jiles and D. Atherton, "Ferromagnetic hysteresis," *IEEE Transactions on Magnetics*, vol. MAG-19, pp. 2183–2185, September 1983.
- [2] D. Jiles and D. Atherton, "Theory of magnetisation process in ferromagnets and its application to the magnetomechanical effect," *Journal of Physics-D:Applied Physics*, vol. 17, pp. 1265–1281, 1984.
- [3] D. Jiles and D. Atherton, "Theory of ferromagnetic hysteresis," *Journal of Applied Physics*, vol. 55, pp. 2115–2120, March 1984.
- [4] D. Jiles and D. Atherton, "Theory of ferromagnetic hysteresis," *Journal of Magnetism and Magnetic Materials*, vol. 61, pp. 48–66, 1986.
- [5] V. Rizzoli, D. Masotti, and F. Mastri, "General-purpose analysis of nonlinear circuits containing saturating/hysteretic inductors by the harmonic-balance technique," *IEEE Trans. Magnetics*, vol. 31, pp. 2290–2303, May 1995.

# Active Nonlinear Vibration Absorber

Shafic S. Oueini and Ali H. Nayfeh

Department of Engineering Science and Mechanics  
Virginia Polytechnic Institute and State University  
Blacksburg, VA 24061-0219

## 1 Introduction

A novel active nonlinear vibration absorber is being developed. The technique is based on exploiting the saturation phenomenon exhibited by multidegree-of-freedom systems with quadratic nonlinearities possessing autoparametric resonances. The strategy consists of introducing a second-order controller and coupling it to the plant through a sensor and an actuator, where both the feedback and control signals are quadratic. Once the plant is forced near resonance, its response saturates to a small value, and the remaining oscillatory energy is channeled and absorbed through the actuator. We have conducted experiments and showed that the strategy can be very effective in suppressing the vibrations of one or several modes of a multidegree-of-freedom plant. We built the absorber with electronic components and regulated the responses of flexible cantilever beams using piezoelectric and magnetostrictive actuators.

## 2 Development of the Control Law

We consider the problem of controlling the response of a second-order damped oscillator to a harmonic excitation. We express the motion of the plant as

$$\ddot{u} + f(\dot{u}) + \omega_p^2 u = F \cos(\Omega t) + G, \quad (1)$$

where  $u$  is the generalized plant coordinate,  $f(\dot{u})$  represents dissipative terms,  $\omega_p$  is the plant's natural frequency, and  $G$  is the control force. We consider the case when  $\Omega \approx \omega_p$  and introduce a second-order nonlinear controller and a control law in the form

$$\ddot{v} + 2\zeta_c \dot{v} + \omega_c^2 v = \alpha u v \quad \text{and} \quad G = \gamma v^2, \quad (2)$$

where  $\zeta_c$  and  $\omega_c$  are, respectively, the controller's damping coefficient and natural frequency, and  $\alpha$  and  $\gamma$  are positive constants. An autoparametric-resonance condition is created by choosing  $\omega_c$  so that  $2\omega_c \approx \omega_p$ . The form of the quadratic coupling in equations (2) is not unique. Coupling involving other combinations of nonlinear terms can induce the saturation phenomenon, and hence they can also be used to formulate adequately the control law. The choice of nonlinearities depends on the available feedback signal from the plant.

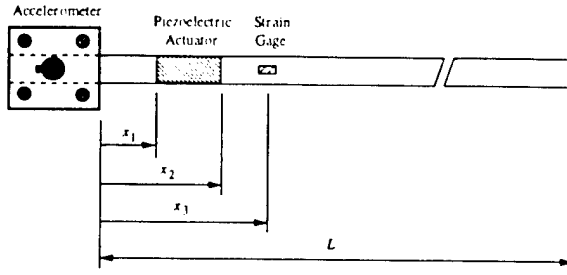


Figure 1: The locations of the PZT actuators and the strain gage.

To implement experimentally the technique, we developed an electronic circuit to emulate the equation of the controller. The circuit is assembled with operational amplifiers, analog multipliers, and various other electronic hardware. Its design enables the user to adjust the natural frequency  $\omega_c$ , the damping coefficient  $\zeta_c$ , and the nonlinear coupling gains  $\alpha$  and  $\gamma$ .

### 3 Application of the Strategy

We used the technique to suppress the vibrations of flexible cantilever beams. The actuation is achieved with linear piezoelectric (PZT) and nonlinear magnetostrictive (Terfenol-D) actuators.

We model the dynamics of a cantilever beam by

$$\rho A \frac{\partial^2 w}{\partial t^2} + C \frac{\partial w}{\partial t} + EI \frac{\partial^4 w}{\partial x^4} = F_a + F_e, \quad (3)$$

where  $A$  is the cross-sectional area of the beam,  $\rho$  is the mass density,  $EI$  is the flexural rigidity,  $C$  is a damping coefficient,  $F_a$  is the actuator force, and  $F_e$  is the excitation force.

#### 3.1 Piezoelectric Actuator

We consider a beam mounted on a shaker and fitted with two patches of PZT ceramics and a strain gage, as illustrated in Figure 1. Then, the excitation and control forces are defined by

$$F_e = -\rho A \frac{d^2 w_0}{dt^2} \quad \text{and} \quad F_a = \frac{\partial^2 M}{\partial x^2}, \quad (4)$$

respectively,  $w_0(t)$  is the motion of the shaker head, and

$$M(x, t) = KV_a(t) [H(x - x_1) - H(x - x_2)]. \quad (5)$$

Here,  $K$  is a constant that depends on material properties and the piezoamplifier gain,  $V_a(t)$  is a control voltage, and  $H(x)$  is the Heaviside step function.

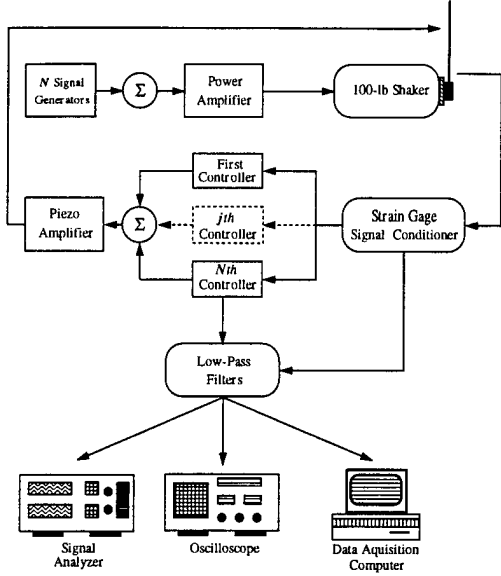


Figure 2: The experimental setup.

For the case of primary resonances, we define the shaker acceleration  $\ddot{w}_0$  by

$$\ddot{w}_0 = \sum_{j=1}^N f_j \cos(\Omega_j t), \quad (6)$$

where the  $f_j$  and the  $\Omega_j$  are the amplitudes and frequencies of the excitation, respectively, and  $N$  is the number of resonant modes. We assume, without loss of generality, that the first  $N$  modes of the beam are excited. Therefore, we let  $\Omega_j \approx \omega_j$ , where the  $\omega_j$  are the natural frequencies of the beam, and introduce a series of controllers taking the form

$$\ddot{v}_j + 2\zeta_j \dot{v}_j + \lambda_j^2 v_j = \alpha_j v_j e(x_3, t), \quad j = 1, 2, \dots, N \quad (7)$$

and a control signal

$$V_a(t) = \sum_{j=1}^N \gamma_j v_j^2, \quad (8)$$

where the controllers' natural frequencies  $\lambda_j$  are chosen such that  $2\lambda_j \approx \omega_j$ , and  $e(x_3, t)$  is the strain at the surface of the beam at location  $x_3$ . We carried out two experiments to control independently and simultaneously the first and second modes of two steel cantilever beams. The experimental setup is depicted in Figure 2. The setup consists of a 100-lb permanent magnet shaker and its driving power amplifier, a piezoamplifier, the controller circuit(s), a strain gage signal conditioner, an accelerometer, and signal generators.

The first experiment consisted of controlling the response of the first mode of the first beam. We subjected the beam to an initial base excitation of  $5.8 mg$  and increased it in five steps to

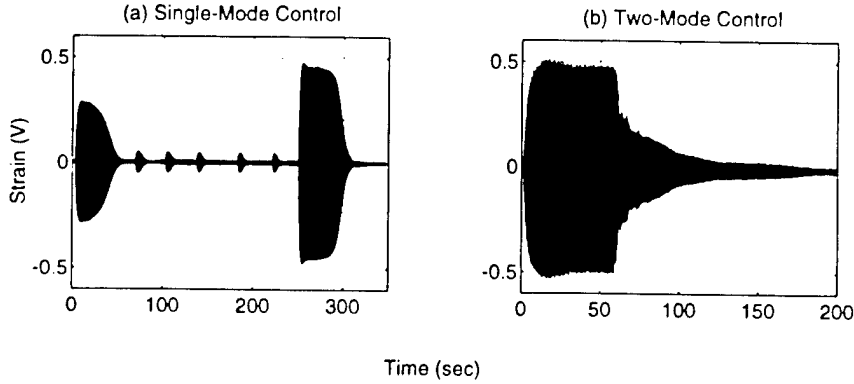


Figure 3: Control using PZT actuators. (a) Single-mode control when  $\Omega \approx 11.5$  Hz and (b) two-mode control when  $\Omega_1 \approx 4.3$  Hz and  $\Omega_2 \approx 26.5$  Hz.

$8.9\ mg$ . In Figure 3a, we illustrate the response of the system when the controller is activated at  $t \approx 20$  sec. At  $t \approx 250$  sec, the controller was deactivated allowing the response to fully develop at  $8.9\ mg$ . The controller was activated again at  $t \approx 260$  sec.

In the second experiment, we simultaneously excited the first and second modes of another beam, and we used two controller circuits. In Figure 3b, we show the time response when the controllers are activated at  $t \approx 60$  sec.

### 3.2 Magnetostriuctive Actuator

Terfenol-D is a magnetostriuctive material that exhibits a nonlinear quadratic constitutive relation between the applied magnetic field (current) and the strain. Thus, it is naturally suited for application with the nonlinear absorber. Though we develop the technique for Terfenol-D, the method can be easily applied to electrostrictive materials, such as PMN, that have quadratic constitutive laws.

In this case, the plant consists of a flexible cantilever beam stiffened near its base with an active strut and subjected to an external excitation delivered by an electrodynamic shaker. The setup is illustrated in Figure 4.

The control force is applied using an unbiased Terfenol-D actuator. Ignoring temperature effects, we define the actuation and excitation forces by

$$F_a(t) = \delta(x - x_a) K_a i_a(t)^2 \quad \text{and} \quad F_e = \delta(x - x_e) f \cos(\Omega t), \quad (9)$$

where  $K_a$  is a constant,  $i_a(t)$  is the control current, and  $x_a$  and  $x_e$  are the positions of the actuator and exciting shaker, respectively.

We let  $\Omega \approx \omega_i$ , where  $\omega_i$  is the natural frequency of the  $i^{th}$  mode, introduce a controller

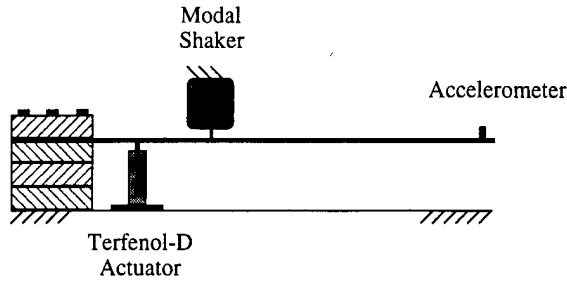


Figure 4: A description of the Terfenol-D beam-actuator setup.

taking the form

$$\ddot{v} + 2\zeta_c \dot{v} + \omega_c^2 v = \alpha v \left. \frac{\partial^2 w}{\partial t^2} \right|_{x=L} \quad (10)$$

and a control signal

$$i_a(t) = \gamma v, \quad (11)$$

where the controller's natural frequency  $\omega_c$  is chosen such that  $2\omega_c \approx \omega_j$ . We note that, in this example, we used the tip acceleration of the beam as a feedback signal, and we defined a linear control signal, equation (11).

We performed two experiments where we controlled the first and second modes of a cantilever beam. The results are shown in Figure 5.

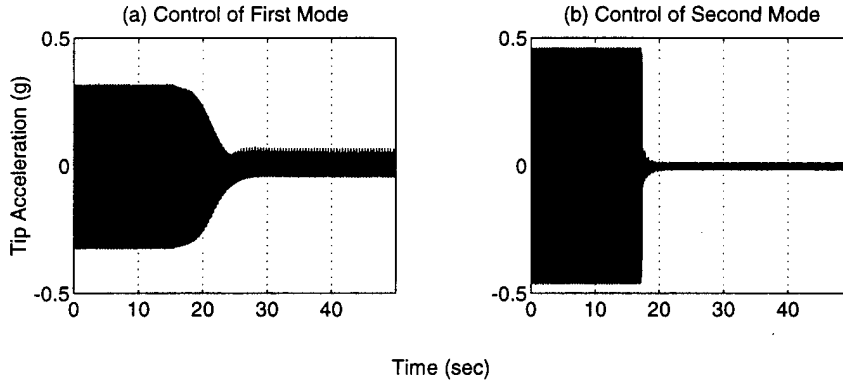


Figure 5: Control using a Terfenol-D actuator. (a) Response of the first mode when  $\Omega \approx 6.8$  Hz and (b) response of the second mode when  $\Omega \approx 47.5$  Hz

# Active Control of Enclosed Sound Fields

B. Balachandran and C. W. Ahn  
Department of Mechanical Engineering  
A. James Clark School of Engineering  
University of Maryland  
College Park, MD 20742

and

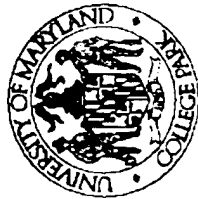
A. Sampath  
Scientific Systems, Inc.  
500 W. Cummings Pk.  
Suite 3950  
Woburn, MA 01801

A collective summary of analytical and experimental investigations into active control of multiple tones in a three-dimensional enclosure is presented. The enclosure has five rigid boundaries and a flexible boundary. Piezoelectric actuators and polyvinylidene fluoride (PVDF) film sensors are located on the flexible boundary through which noise is transmitted into the enclosure. Microphones, which are located inside and outside the enclosure, serve as error sensors. A mechanics-based state-space model is developed to model the structural-acoustic system and this model is used to study local vibration control on the flexible boundary and/or local noise control inside the enclosure. The analytical predictions, which are based on a filtered-U algorithm, are found to compare well with the experimental observations. The use of active constrained layer damping treatments are also explored in the experiments. The results of the efforts point to the strong possibilities for (spatially) local noise control in three-dimensional enclosures such as helicopter cabins.

Acknowledgements : ARO/URI Program and ARO/MURI Program  
Dr. Gary Anderson and Dr. Tom Doligalski

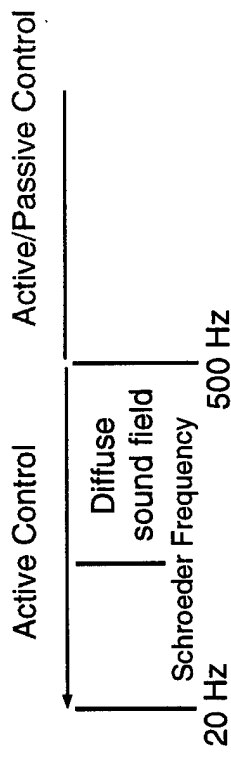
# Motivation

- Undesirable interior noise levels in rotorcraft
  - Noise due to main rotor, tail rotor, and turbines: Frequency range of 40 Hz to 500 Hz
  - Noise due to gear mechanisms: Frequency range of 500 Hz to 6000 Hz
  - Noise levels in 100–120 dBA range; desired target: 75 dBA
  - Unacceptable Speech Interference Level (SIL)
  - Discrete peaks in power spectrum of noise
- Passive control of noise over the whole frequency range is limited by space, weight, and cost
- Active control of bandlimited noise feasible at low frequencies

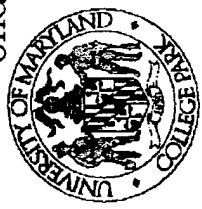


# Research Objectives

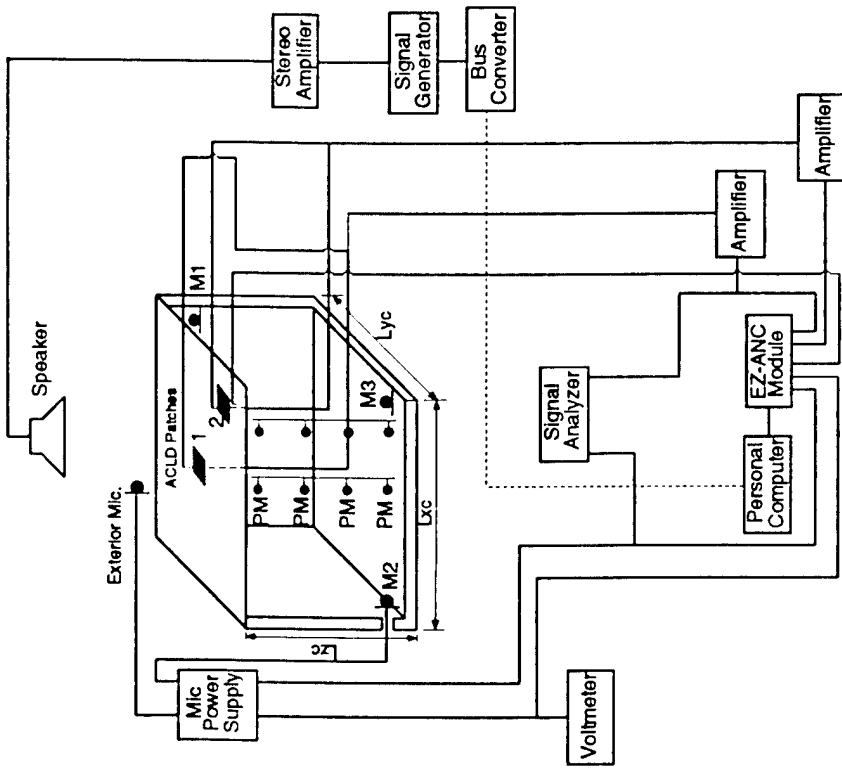
- Development of viable control schemes by using smart materials for reducing rotorcraft interior noise



- Development and validation of structural-acoustic models for trim panels and fuselage structure
- Development of combined feedback and feedforward control strategies for creating multiple quiet zones by using secondary acoustic sources and/or secondary force inputs

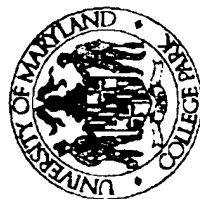


# Experimental Arrangement



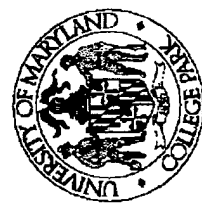
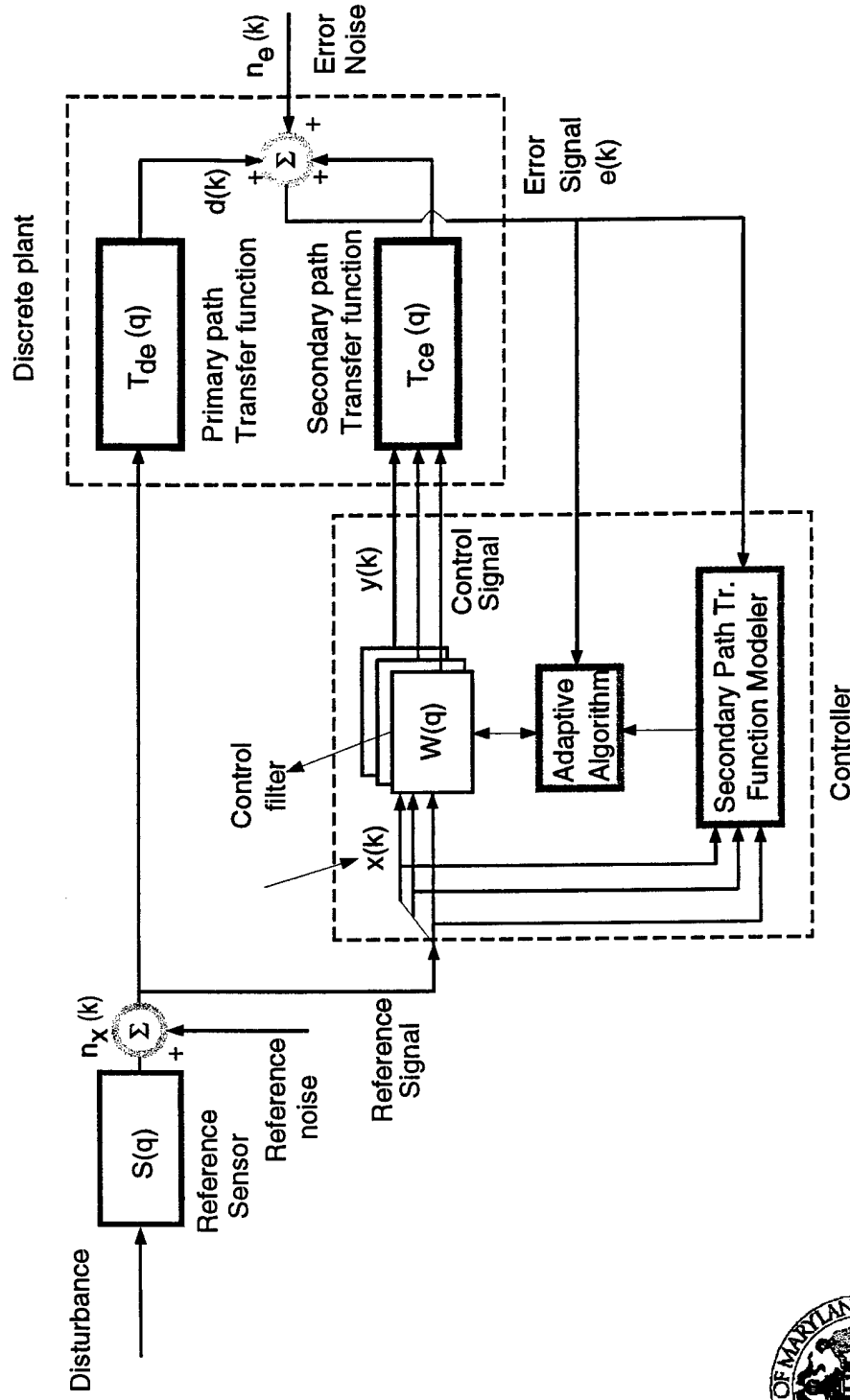
Acrylic cavity: 24" x 18" x 20"  
Aluminum panel: 26" x 20" x 1/16"

- Digital, local noise control

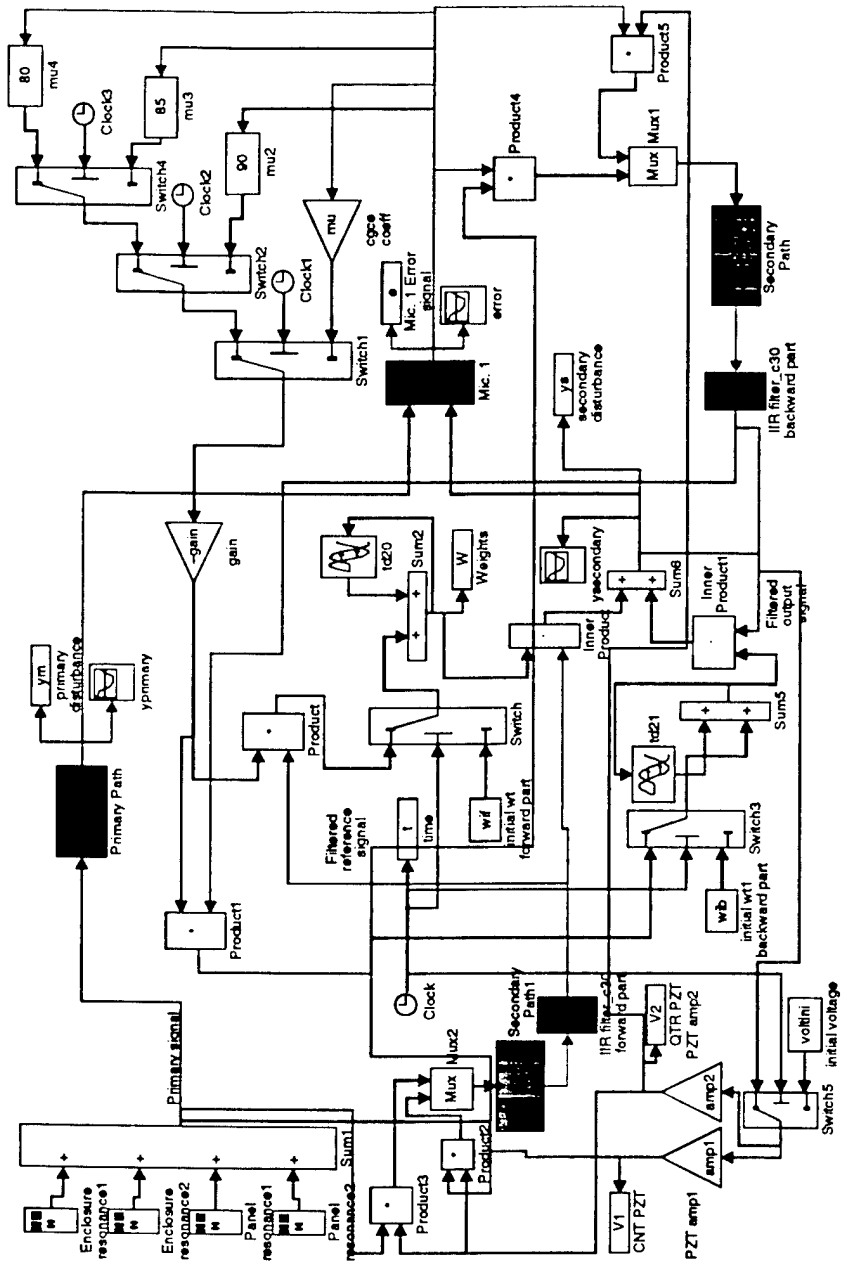


# Arrangement for Feedforward

## Adaptive Control

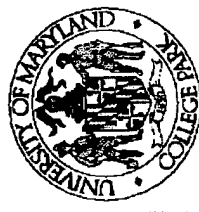


# Arrangement for Numerical Implementation of Feedforward Adaptive Control



## Concluding Remarks

- Developed a state-space model for panel-enclosure system that accommodates structural-acoustic interactions and carried out numerical studies of feedforward active noise control with distributed actuators and acoustic sensors for deterministic bandlimited disturbances
- Good comparisons between numerical predictions and experimental observations
- Noise reductions upto 35 dB achieved using ACILD treatment and noise reductions upto 32 dB achieved without ACILD treatment
- Lower voltage inputs into actuators required with ACILD treatment



# A Generalized Theory for Distributed Active-Passive Beam Structures for Vibration and Sound Radiation Control

Pierre Cambou, François Charette, and Chris R. Fuller

V.A.L., Mechanical Engineering Department, Virginia Polytechnic Institute and State University

This presentation is based upon research concerning generic active-passive systems. The goal is to develop a distributed treatment for vibration and sound radiation control. A theoretical model for the response of a beam with active-passive devices such as piezoelectric layers, constrained layers and tunable vibration absorbers is presented. These devices can be distributed and positioned anywhere along the beam. The axial and transversal motions of the beam are taken into account and any boundary condition can be considered at the beam-ends. The model is developed using a variational approach based on Hamilton's principle. The displacement field is approximated with a particular set of trial functions, called "Psin", which are based on trigonometric functions. The model permits to investigate the potentials of an active distributed absorber.

## List of Symbol

### Upper case

A	displacement Coefficient (m)
E	Energy (J)
F	Force (N)
G <sub>3</sub>	Electric Field (IEEE compact notation) (V/m)
K	Stiffness (N/m)
L	Length (m)
M	Mass (Kg)
N	Order of precision for displacement function(-)
S <sub>1</sub>	Strain (IEEE compact notation) (-)
U	Total displacement in the 1 direction (m)
W	Total displacement in the 3 direction (m)
Z	Mechanical impedance (Ns/m)

### Lower case

c <sub>11</sub>	Module of Elasticity (IEEE compact notation) (Pa)
e <sub>11</sub>	Piezoelectric Stress/Charge coefficient (IEEE compact notation) (N/Vm)
f	Unknown function (-)
h	Thickness (m)
u	Displacement in the 1 direction of the beam neutral axis (m)

w	Displacement in the 3 direction of the beam neutral axis (m)
x	Coordinate in the 1 direction (m)
z	Coordinate in the 3 direction (m)

### Subscripts or Superscripts

b	Beam
c	Constrained layer
d	Device
e	Elastic layer
m	Mass layer
p	Potential energy
r	Resonance
z	Piezoelectric layer

### Greek letters

$\alpha$	Tuning ratio (-)
$\alpha_n$	Psin coefficient (1/m)
$\beta_n$	Psin coefficient (-)
$\gamma_n$	Psin coefficient (1/m)
$\delta_n$	Psin coefficient (-)
$\epsilon$	Piezoelectric material permittivity (F/m)
$\omega$	Angular frequency (rad/s)

## Motivations

- Reduction of transmitted/radiated noise by panels still remains an important challenge in the transportation industry.
- Recently active/passive system have shown much potential to solve those problems (less electrical power requirements, fail safe control...).

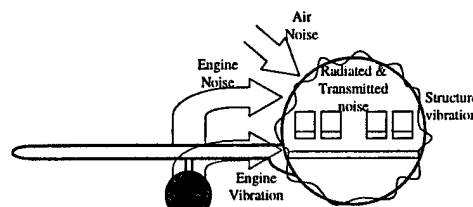


Fig. 1 : Interior noise in aircrafts.

## Objectives

- Create a 1-Dimensional model for an active distributed dynamic vibration absorber (DVA).
- Study the effect of distributed absorber to minimize a structure vibration or its associated sound radiation.
- Analyze the use of active excitation.

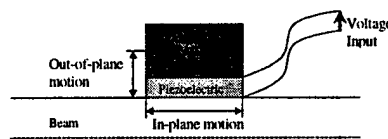


Fig. 2 : The active/passive DVA.

## Model principles and requirements

- Several sub-structures for a beam are developed :
  - Mass distribution
  - Piezoelectric layer
  - Constrained Layer (CL)
  - Absorber (DVA)
- The model is derived using a variational methods based on Hamilton's principle. Both axial and transversal motion of the beam is taken into account (asymmetrical actuation).
- The unknown displacement functions are approximated using the Rayleigh-Ritz method. The trial functions are expressed as :

$$f(x) = \sum_{i=1}^n A_i \frac{1}{2} \left\{ \cos \left( \alpha_i \frac{2x}{L_b} + \beta_i \right) - \cos \left( \gamma_i \frac{2x}{L_b} + \delta_i \right) \right\}$$

The coefficients  $\alpha_n, \beta_n, \gamma_n$ , and  $\delta_n$  are found Table I.

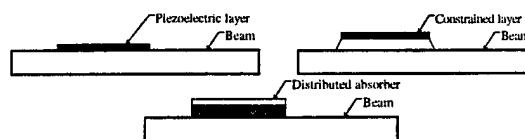


Fig. 3 : Beam structures

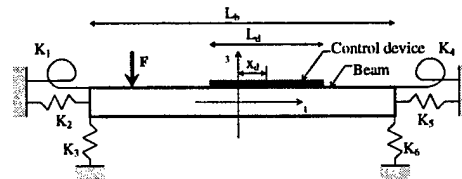


Fig. 4 : Modeled structure

$n$	$\alpha_n$	$\beta_n$	$\gamma_n$	$\delta_n$
1	0	0	$\frac{\pi}{2}$	$-\frac{\pi}{2}$
2	$\frac{3\pi}{4}$	$\frac{\pi}{4}$	$-\frac{\pi}{4}$	$-\frac{3\pi}{4}$
3	0	0	$\frac{\pi}{2}$	$\frac{\pi}{2}$
4	$-\frac{\pi}{4}$	$\frac{3\pi}{4}$	$\frac{3\pi}{4}$	$-\frac{\pi}{4}$
$\geq 5$	$\frac{\pi}{2}(n-5)$	$\frac{\pi}{2}(n-5)$	$\frac{\pi}{2}(n-3)$	$\frac{\pi}{2}(n-3)$

Table I : Trial function coefficients.

## Derivation procedure

- Assume a displacement field
- Determine the stress field using solid mechanics
- Compute the potential and kinetic energy (Lagrangian)
- Replace the unknown functions by a series of trial functions
- Differentiate the Hamiltonian (definite time integral of the Lagrangian) in respect to the serie's coefficients
- Solve the linear system of equations using matrix manipulation
- Compute the displacement of the beam
- Determine vibration and acoustic response (Mean square velocity , radiated power ...)

## Displacement fields & model assumptions

- Beam

The displacement field is derived according to Bernoulli's assumptions.

$$\begin{cases} U_b(x, z_b, \tau) = u_b(x, \tau) - z_b \frac{\partial v(x, \tau)}{\partial x} \\ W_b(x, z_b, \tau) = w(x, \tau) \end{cases}$$

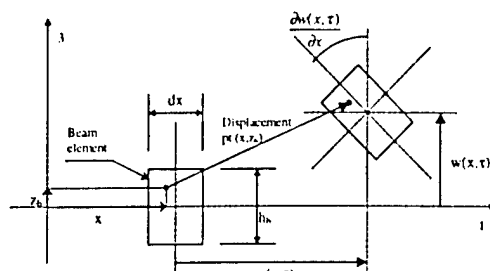


Fig. 5 : Displacement field for the beam.

- Piezoelectric layer

Continuity of displacement is assumed at the beam/piezo interface. The potential energy formulation (IEEE std) is :

$$E_p = \int_v \left[ \frac{1}{2} c_{ij} S_i S_j - e_k G_k S_l - \frac{1}{2} \epsilon_{mn} G_m G_n \right] dv$$

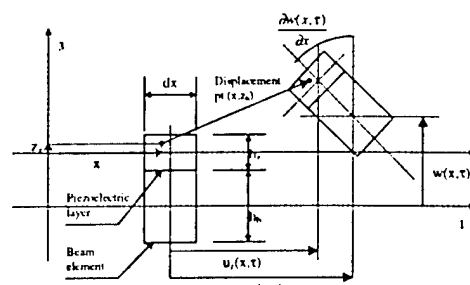


Fig. 6 : Displacement field for the beam with a piezoelectric layer.

- Constrained layer

The new variable  $\phi$  has to be introduced in order to model the shear in the constrained layer.

$$\begin{cases} U_c(x, z_c, \tau) = u(x, \tau) - \left( z_c + \frac{1}{2}(h_b + h_c) \right) \frac{\partial w(x, \tau)}{\partial x} - \left( z_c + \frac{h_c}{2} \right) \phi(x, \tau) \\ W_c(x, z_c, \tau) = w(x, \tau) \end{cases}$$

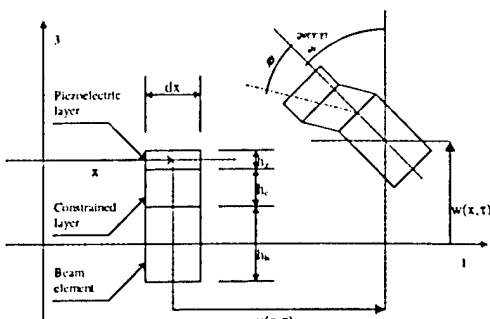


Fig. 7 : Displacement field for the beam with a constrained layer.

- Vibration absorber

The elastic layer is constrained in the 3-direction. For this model  $w_m$  can not be approximated by  $w$ .

In order to determine  $w_m$  without introducing a new variable in our system the absorber is considered as added impedance on the beam.

$$K(w_m - w) = Z(-j\omega w)$$

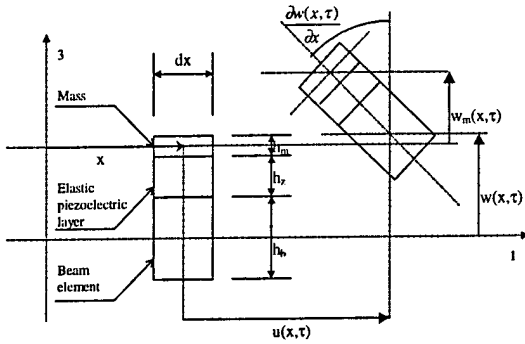


**Fig. 8 :** Displacement field for the beam with a distributed active-passive absorber.

These models can be combined very easily since the variational approach allows to add sub-systems by introducing their mass and stiffness matrices into the global beam equation :

$$\{-\omega^2[M] + [K]\}\{A\} = \{F\}$$

Solving for the vector  $\{A\}$  using LU decomposition, the vibration and acoustic fields can be determined.

The variational approach allows for the increase in the number of devices on top of the beam without changing the size of the matrices. Different combination of devices can then be investigated without CPU penalties.

## Preliminary Results for the absorber case

The advantages and issues related to a distribution of active-passive absorbers along a beam is now investigated in terms of the associated radiated power. The beam dimensions are 300x25x3.25mm. The total mass of the absorbers is 10% of the beam mass. Their resonant frequency is 772 Hz (3<sup>rd</sup> mode of the beam).

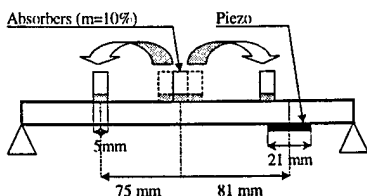


**Fig. 9 :** Steel beam excited with a piezo, with 3 active/passive DVAs

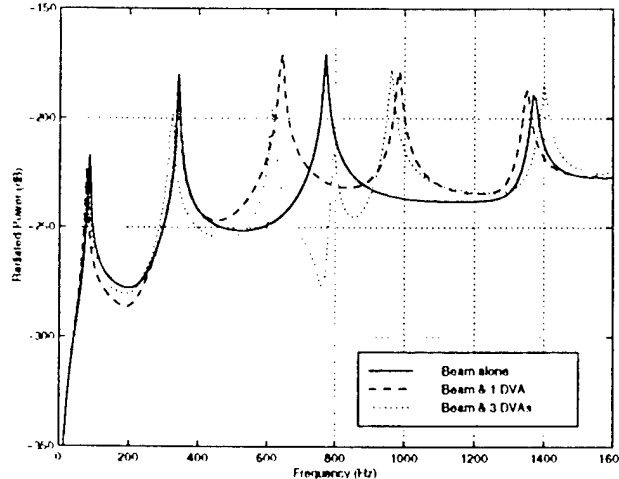


**Fig. 10 :** Influence of DVA's positioning for the control of 3<sup>rd</sup> mode sound radiations.

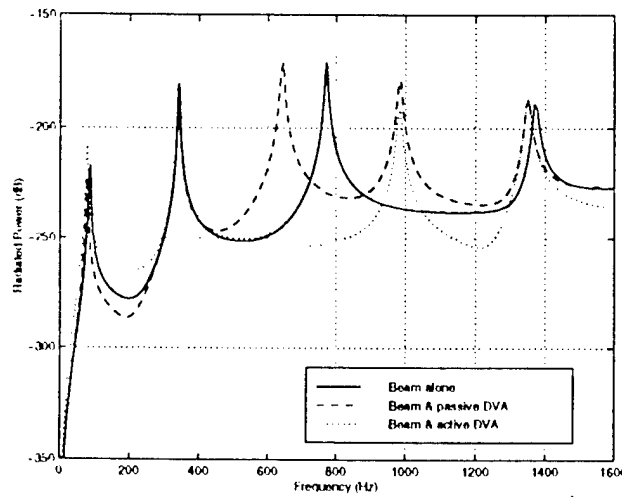


**Fig. 11 :** Influence of active force (constant phase) for the control of 3<sup>rd</sup> mode sound radiations.

- Distributing the absorbers increases power attenuation
- Introducing active control improves the performance of the absorber

## Tuning Optimization

To improve the performance of passive absorbers, their tuning ratio is optimized. this tuning ratio is defined as  $\alpha = \omega/\omega_r$  where  $\omega$  is the beam excitation frequency and  $\omega_r$  the resonant frequency of the absorber. As an example, a beam excited at its 2<sup>nd</sup> natural frequency (342 Hz) is considered.

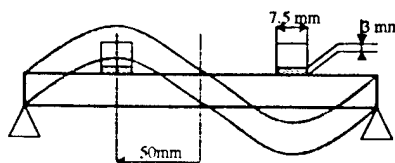


**Fig. 12 :** SS beam (same as Fig. 8) with 2 passive DVAs

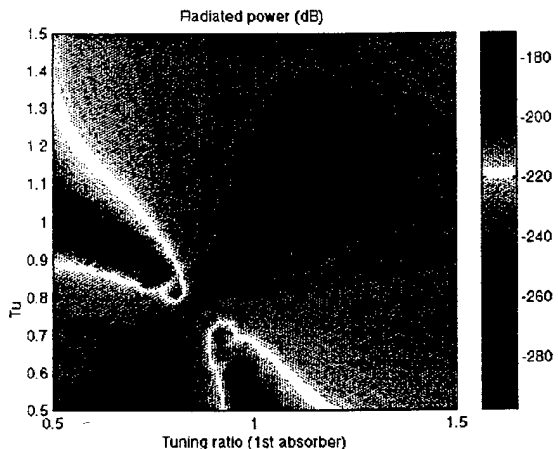


**Fig. 13 : Tuning optimum at 2<sup>nd</sup> mode**

The elastic layer is unchanged and the absorber masses vary from 1.5% to 15% of the beam mass. In this example the optimal tuning is (1.07,0.97). With a greater number of absorbers, the tuning problem has to be solved with an optimization algorithm since an exhaustive search becomes quickly impossible.

## Conclusions

- Distributing & tuning of the absorbers optimizes the sound reduction.
- Active absorbers improve reduction performances.
- The control in phase and magnitude has to be optimized for every frequency.

## Future work

- Optimize the control for multiple absorbers and broadband applications.
- Optimize the absorber distribution.

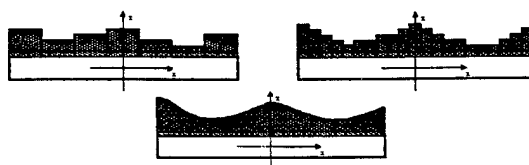


**fig. 14: Approximation of continuous absorber distribution**

# **Control of Low Frequency Structurally Radiated Noise with an Array of Weak Radiating Cells**

Bradley W. Ross and Ricardo A. Burdisso

Vibration and Acoustic Laboratories  
Department of Mechanical Engineering  
Virginia Polytechnic Institute and State University  
Blacksburg, VA 24061-0238

Third ARO Workshop on Smart Materials  
August 27, 1997

## **Introduction**

In the past, extensive research has been carried out to gain a better understanding of the acoustic behavior of structures such as helicopters [1], airplanes [2], and power transformers [3]. The attenuation of structurally radiated noise, in particular at low frequencies, from these systems has been intensively pursued. Recently, active control has emerged as a viable technology to solve this problem. Unfortunately, the complexity, power requirement, unreliability, and high cost of active control systems has significantly limited their practical application to realistic systems.

Here the concept of a weak radiating cell as a low frequency passive noise control device is developed and verified both analytically and experimentally. The uniqueness of the concept lies in the fact that the cells convert the motion of the vibrating structure into inefficient dipole acoustic sources. This leads to the passive reduction of low frequency sound without the adverse effects introduced by active control. The performance of the concept is demonstrated on a plate excited with white noise. An overall power reduction of 10.2 dB is achieved over the 0-1600 Hz range.

## **Weak Radiating Cell Concept**

At frequencies for which the acoustic wavelength exceeds the dimensions of a source, the radiated power is essentially determined by the volume velocity of the source. The radiated power can consequently be minimized by reducing the volume velocity of the source [4]. Thus, an efficient method to reduce the sound radiation from a structure would be to partition the surface of the structure into small sectors each of which would independently respond as a dipole with zero volume velocity. To this end, the concept of a weak sound radiating cell is introduced to reduce the low frequency radiated noise from structures.

The weak radiating cell consists of two mechanically coupled surfaces such that, when placed on a vibrating structure, the responses of the two surfaces are nearly out-of-phase and of equal strength over a wide frequency range. This leads the surfaces to behave as an acoustic dipole, and thus, as a poor sound radiating source. Figures 1a through 1d illustrates the concept. The sound power radiated by a small area,  $S_s$ , with dimensions smaller than the

acoustic wavelength, is determined by its volume velocity  $Q_s = v_s S_s$  where  $v_s$  is the average velocity over the small area. Note that the total radiated power from the plate is due to the contribution of all the areas of the structure including their far-field coupling. Figure 1b illustrates a weak radiating cell covering the surface  $S_s$ . The concept of the weak radiating cell is to convert the motion of the small area from that of a monopole into a dipole acoustic source. To this end, the motion of the nearly uniform velocity  $v_s$  of the surface  $S_s$  is transformed into the motion of the two surfaces  $S_{c1}$  and  $S_{c2}$  with velocities  $v_{c1}$  and  $v_{c2}$ , respectively. The cell is then designed so that the motion of these two surfaces is out-of-phase and of such relative magnitude so that the volume velocity is minimized, i.e.  $v_{c1}S_{c1} + v_{c2}S_{c2} \equiv 0$ . Conceptually, by covering the structural surface with an array of cells as shown in Figure 1c, the response of the structure is converted to that of an array of dipoles. Thus, leading to an essentially zero volume velocity structural source and minimum sound radiation.

An implementation of the weak radiating cell concept is illustrated in Figure 1d. The cell consists of a rigid element of area,  $S_{c2}$ , which is mounted to the radiating structure. Because this element is assumed to be very stiff, the velocity of the surface  $S_{c2}$  is nearly the same as the velocity of the structure,  $v_{c2} \approx v_s$ . The second radiating surface of the cell,  $S_{c1}$ , is obtained by attaching a rigid plate to the rigid element through a thin flexible shim which creates a sealed cavity. Figure 1d illustrates the shim as a simplified mechanical model where the stiffness and damping of the shim are denoted by  $k$  and  $c$ , respectively. The simplest mechanical behavior of the cell can then be depicted as a single degree of freedom lumped parameter system with a base excitation. Figure 2 illustrates the response of the cell in terms of the complex source strength of each radiating surface. Above the resonant frequency of the system, the two sources are out-of-phase and their source strengths are of approximately equal magnitude. Notice the nearly perfect cancellation at the frequency ratio of 2.2 where the source strengths from each surface are equal.

## Plate Experiments

To investigate the performance of an array of weak radiating cells applied to a structure, nine cells are mounted to the surface of a 380 x 300 x 9.5mm steel plate, as shown in Figure 3. The plate is attached to an enclosed box that houses the excitation shaker, which is driven with white noise in the 0-1600 Hz frequency range. A force transducer and accelerometer are attached at the driving point to monitor the plate response. The plate was placed in a reverberant chamber and ten microphones were used to measure the radiated sound power level. In addition, a laser vibrometer was used to measure the velocity distribution that in turn was used to determine source strength. The experiments were performed on the plate with and without the weak radiating cells and the results were compared to determine the performance of the proposed weak radiating cell concept.

All the cells have the same dimensions of 125 x 99 x 57mm. Figure 4 is a bottom view photograph of a single weak radiating cell. The outside rigid element that forms the surface  $S_{c2}$  is made of polyvinyl chloride (PVC). The rigid plate that forms the surface  $S_{c1}$ , also made of PVC, is mounted to the flexible thin brass shim which in turn is mounted to the rigid element. The cells are then mounted to the plate using double-sided adhesive tape. The

cells were designed to be effective in the 400-1600 Hz frequency range. To this end, the natural frequencies of the cells were placed at 200 Hz.

Only a few of the most important results of the experiments are summarized in Figures 5 and 6. Figure 5 illustrates the magnitude and phase of the displacement of the radiating cells at the first mode of the plate. In Figure 5a, the magnitude clearly shows the response of the cells follows the same general trend as the first mode shape of the plate. Figure 5b shows the response of the cell center surfaces,  $S_{c1}$ , are approximately 180° out-of-phase with respect to the rigid elements. This demonstrated that the cells behave as acoustic dipole sources. Similar behavior occurs over a wide frequency range. Figure 6 shows the sound power level reduction achieved by applying the array of cells to the plate as compared to the original untreated plate. An overall power reduction of 10.2 dB was realized in the 0-1600 Hz range with reduction peaks of up to 25 dB at the resonant frequencies of the plate. It is important to mention that the cells reduced the radiated power at all frequencies in the targeted 400-1600 Hz range. Additional results can be found in reference 5.

## Conclusions

The concept of a weak radiating cell as a low frequency passive noise control device was introduced and experimentally validated. When an array of weak radiating cells was applied to a vibrating rectangular plate, an overall sound power level reduction of 10.2 dB was achieved between 0-1600 Hz. This performance rivals the achievements of active control without the cost and complexity penalties of these systems.

## References

- [1] B. S. Murray and J. F. Wilby, *Proceedings of an International Specialist Symposium* held at NASA Langley Research Center, Hampton, Va., May 22-24, 1978, NASA Conference Publication 2052. *Helicopter Cabin Noise – Methods of Source and Path Identification and Characterization*, 1978.
- [2] J. F. Wilby, *Journal of Sound and Vibration*, 190(3), pp. 545-564, *Aircraft Interior Noise*, 1996.
- [3] K. Brungardt, J. Vierengel, K. Wiessman, *Active Structural Acoustic Control of Noise from Power Transformers*, Noise-Con '97, Pennsylvania State University, June 15-17, 1997, pp. 173-182.
- [4] L. E. Kinsler, A. R. Frey, A. B. Coppens, and J. V. Sanders, *Fundamentals of Acoustics*, Third Edition, Canada, John Wiley & Sons, 1982.
- [5] B. W. Ross, *Attenuation of Structurally Radiated Noise with an Array of Weak Radiating Cells*, Master's Thesis, Virginia Polytechnic Institute and State University, 1997.

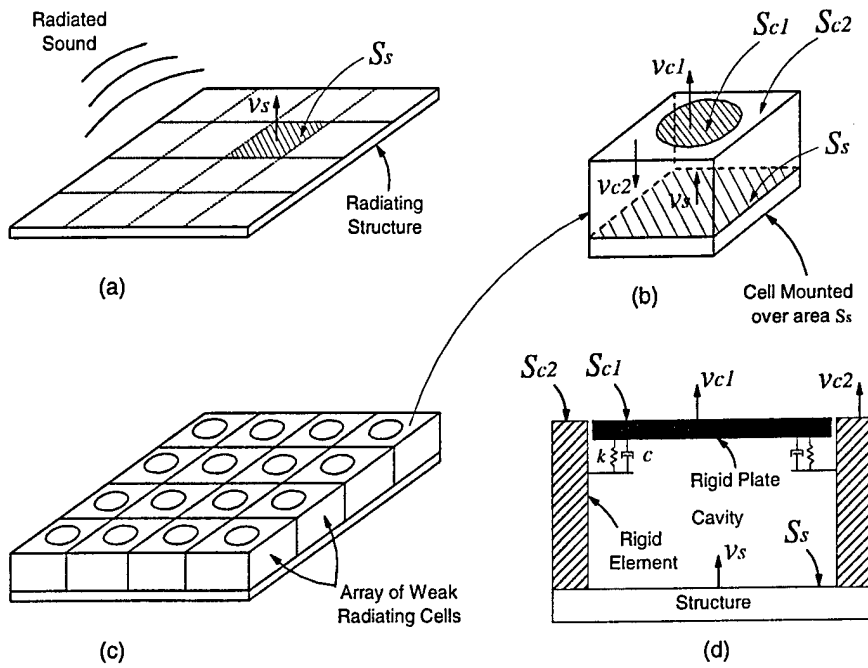


Figure 1: Attenuation of structurally radiated sound using weak radiating cell concept.

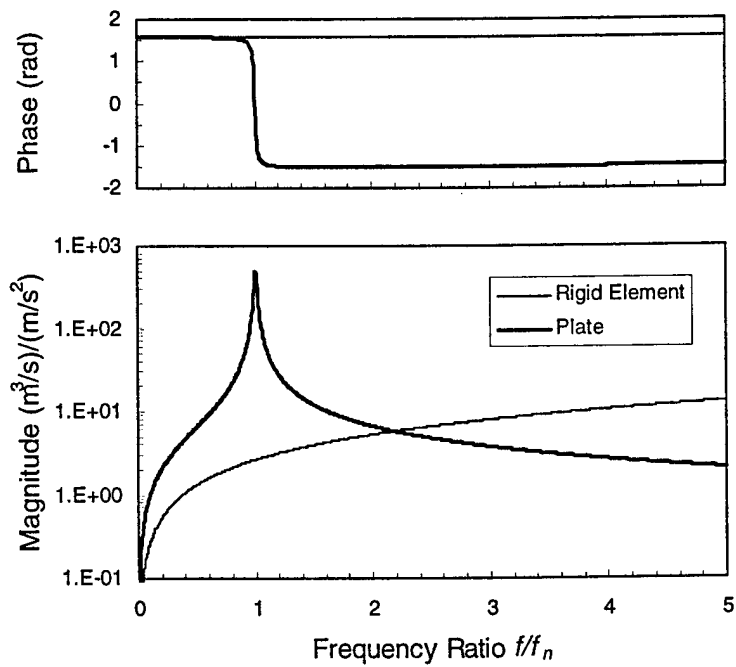


Figure 2: Source strength of surface areas  $S_{c1}$  and  $S_{c2}$  as a function of frequency,  $f$ , normalized by the cell natural frequency,  $f_n$ .

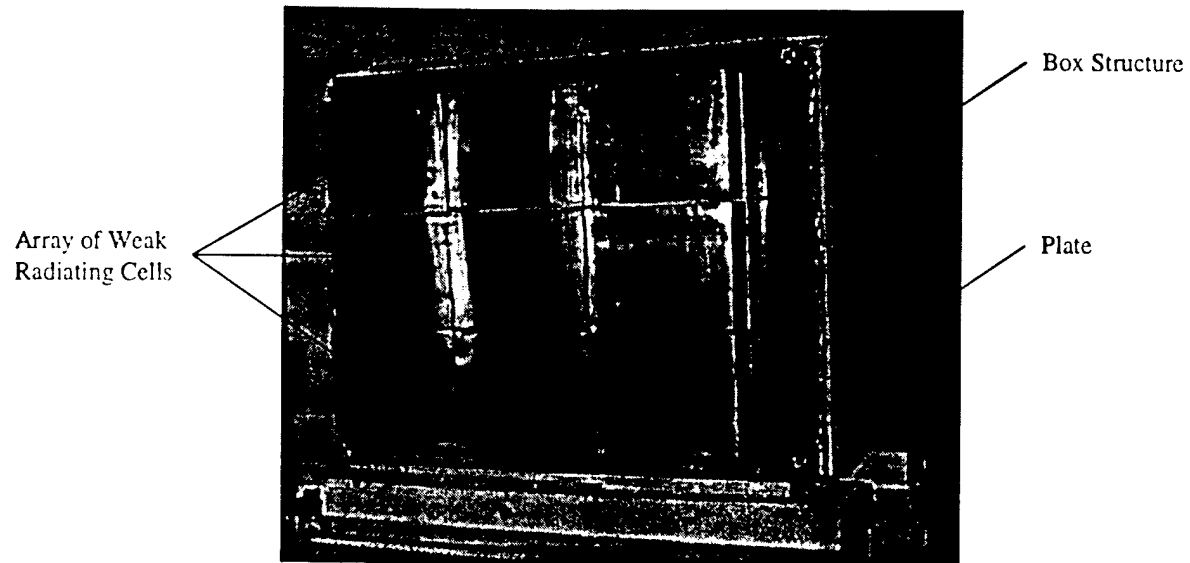


Figure 3: Plate with array of weak radiating cells test apparatus.

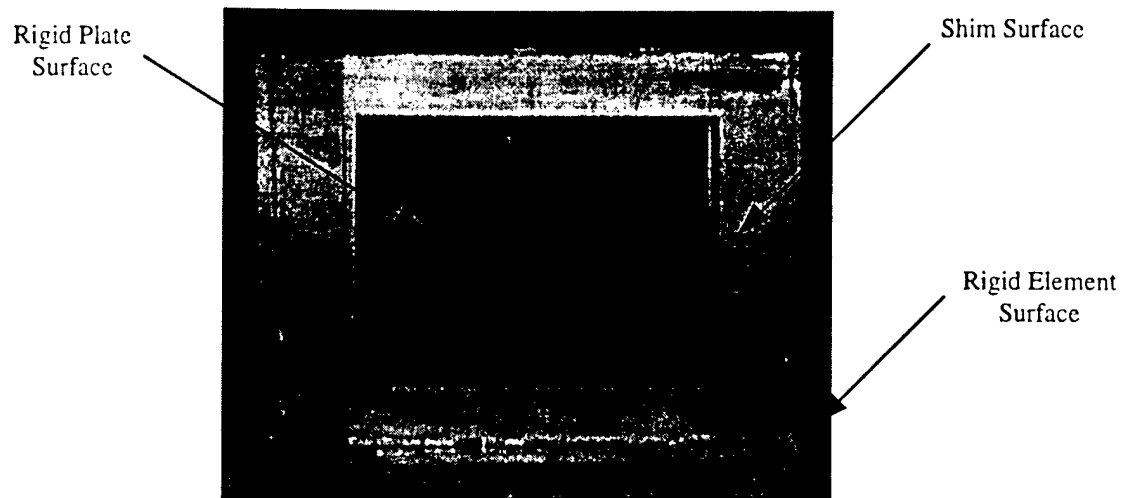
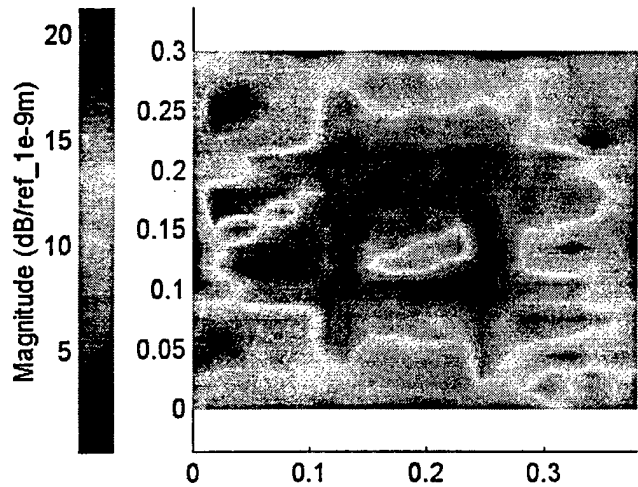
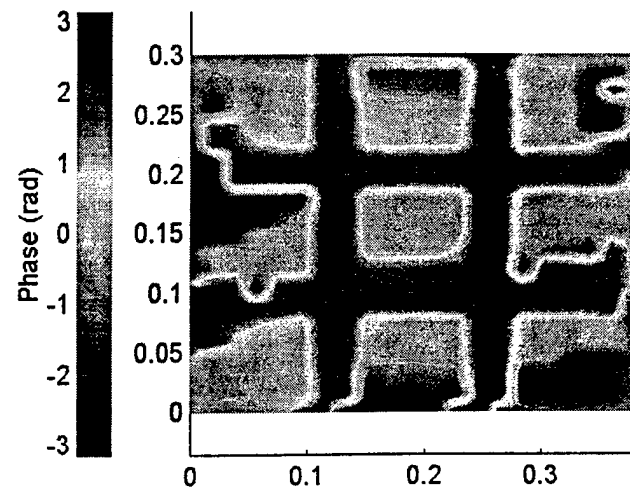


Figure 4: Bottom view of cell (plate and shim surfaces is  $S_{c1}$ , rigid element surface is  $S_{c2}$ ).



(a) Magnitude



(b) Phase

Figure 5: Cell displacement distribution at first mode of plate (388 Hz).

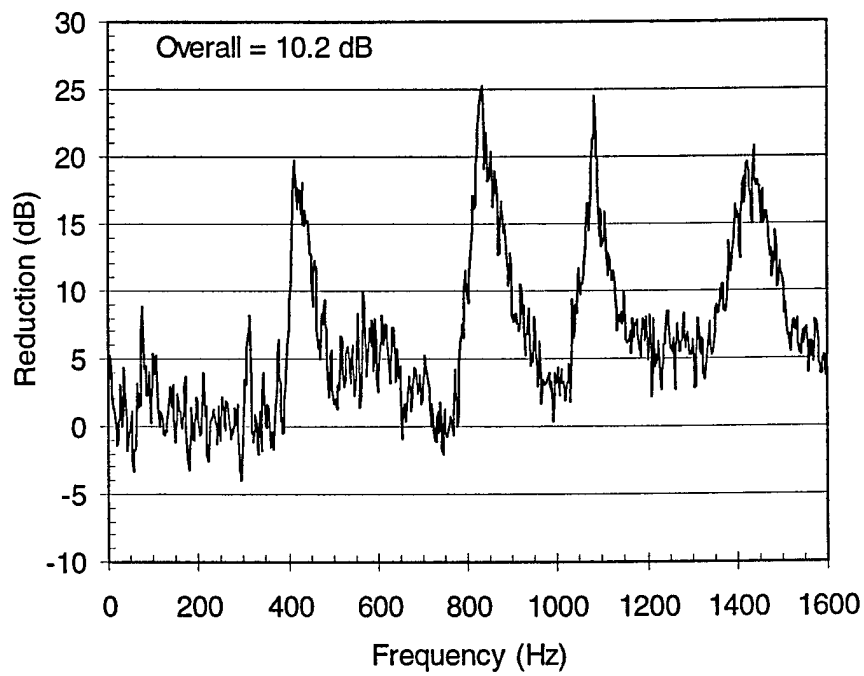


Figure 6: Sound power level reduction.

# **ARMARKOV/Toeplitz Models: A New Paradigm for Model Identification and Adaptive Cancellation**

James C. Akers, Ravinder Venugopal, and Dennis S. Bernstein  
Aerospace Engineering Department  
University of Michigan, Ann Arbor, MI

Conventional wisdom has it that there are two paradigms for linear system representation, namely, state space models and frequency response functions. These paradigms are dual in both their advantages and disadvantages. While state space models involve a finite number of parameters, their internal parameterization is ambiguous and distracts from the essential input-output behavior of the system. On the other hand, while frequency response functions focus on input-output behavior, they are infinite-dimensional objects represented by curves that can only be handled by gridding or sampling. What is needed is an input-output characterization of the system that is also finite-dimensional.

In this talk we will present an approach to linear system identification and adaptive cancellation that is distinct from state space and frequency response methods. The essential ingredient of this approach is the Markov parameters of a system. Given a state space realization  $(A, B, C, D)$ , the Markov parameters are the quantities  $D, CB, CAB, CA^2B, CA^3B, \dots$ , which are also the impulse response coefficients. The Markov parameters are independent of the choice of state space basis, and no more than  $2n+1$  Markov parameters are needed to represent a linear system of order  $n$ . Therefore, the Markov parameters provide a finite-dimensional representation of the input-output behavior of a system. If desired, the ERA algorithm can be used with the Markov parameters to construct a state space realization of the system.

To show how Markov parameters can be used for modeling and control, we first review ARMARKOV/Toeplitz models which have the form of structurally constrained and overparameterized ARMA models some of whose coefficients are Markov parameters. ARMARKOV/Toeplitz models, which are related to d-step-ahead predictive models, provide the basis for an identification algorithm that yields estimates of the Markov parameters of the system. This algorithm, which uses time-domain data either recursively or in batch mode, is easy to implement, has low sensitivity to measurement noise, and works well with modally dense, lightly damped systems. In addition, the algorithm is applicable to multiple-input/multiple-output systems where multiple actuators are simultaneously excited and multiple sensors are simultaneously sampled. Convergence of the Markov-parameter estimates is guaranteed for noise-free measurements and for sufficiently rich excitation. However, the excitation need only be persistent in a specific deterministic sense and need not be white noise or a sine sweep.

Next, we apply the ARMARKOV/Toeplitz representation to adaptive cancellation. It turns out that the ARMARKOV/Toeplitz system representation lends itself readily to adaptive cancellation due to its treatment of input and output signals by means of "sliding data windows". To exploit this feature, we apply a novel gradient update procedure to recursively refine the feedback gains as each additional measurement becomes available. In this way the algorithm continually evaluates performance based upon past data and adjusts the controller to improve closed-loop performance.

In applications, the ARMARKOV/Toeplitz adaptive cancellation algorithm 1) does not require a measurement of the disturbance, that is, does not require an uncontrolled reference or sync signal, 2) does not require any knowledge of the spectrum of the disturbance such as whether the disturbance is tonal or broadband, 3) does not require knowledge of the transfer functions from the disturbance source to the performance and measurement, that is, the primary and reference paths, and 4) does not require knowledge of the transfer function from control to measurement, that is, the feedback path. A suitable model of the transfer function that is required, namely, the secondary path (control-to-performance), can be efficiently identified using the ARMARKOV/Toeplitz identification algorithm described above.

We demonstrate the adaptive cancellation algorithm by means of noise control experiments. First we consider closed-loop performance for several classes of machine-generated disturbances including single tone, dual tone, and broadband signals. In addition, we consider more realistic, possibly nonstationary disturbances such as a single tone and dual tone disturbances with variable frequencies, fan noise and AM radio static.

## ARMARKOV/TOEPLITZ IDENTIFICATION

- ARMARKOV model

$$y(k) = \sum_{j=1}^n -\alpha_j y(k-\mu-j+1) + \sum_{j=1}^{\mu} H_{j-2} u(k-j+1) + \sum_{j=1}^n \mathcal{B}_j u(k-\mu-j+1)$$

- ARMA model with Markov parameters ( $H_k = CA^k B$ )
- Stack time-delayed ARMARKOV models

$$\underbrace{\begin{bmatrix} y(k) \\ \vdots \\ y(k-p+1) \end{bmatrix}}_{Y(k)} = \underbrace{\begin{bmatrix} -\mathcal{A} & 0_l & \dots & 0_l & H_{-1} & \dots & H_{\mu-2} & \mathcal{B} & 0_{l \times m} & \dots & 0_{l \times m} \\ 0_l & \ddots & \ddots & \vdots & 0_{l \times m} & \ddots & \ddots & \ddots & \ddots & \ddots & \vdots \\ \vdots & \ddots & \ddots & 0_l & \vdots & \ddots & \ddots & \ddots & \ddots & \ddots & 0_{l \times m} \\ 0_l & \dots & 0_l & -\mathcal{A} & 0_{l \times m} & \dots & 0_{l \times m} & H_{-1} & \dots & H_{\mu-2} & \mathcal{B} \end{bmatrix}}_W \underbrace{\begin{bmatrix} y(k-\mu) \\ \vdots \\ y(k-\mu-p-n+2) \\ u(k) \\ \vdots \\ u(k-\mu-p-n+2) \end{bmatrix}}_{\Phi(k)}$$

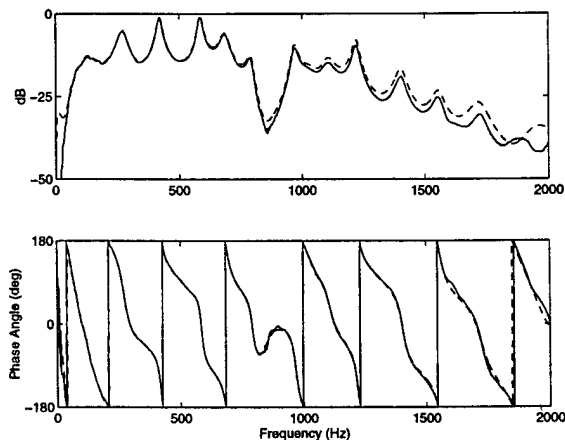
- Recursive update law

$$\widehat{W}(k+1) = \widehat{W}(k) - \eta(k) \frac{\partial J(k)}{\partial \widehat{W}(k)}$$

\*  $\eta(k)$  = adaptive step size

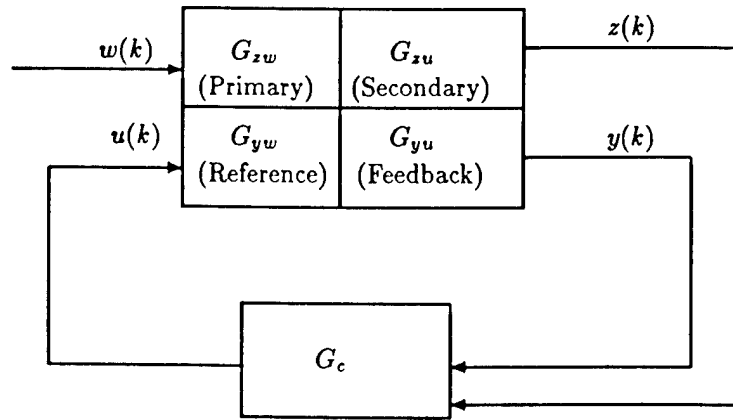
- Acoustic duct experimental results

- \* Measured frequency response (solid line)
- \* Frequency response of 44th-order realization (dashed line)



## ARMARKOV Representation of the Standard Problem

---



- State space form

$$\begin{aligned} x(k+1) &= Ax(k) + Bu(k) + D_1w(k) \\ z(k) &= E_1x(k) + E_2u(k) + E_0w(k) \\ y(k) &= Cx(k) + Du(k) + D_2w(k) \end{aligned}$$

- Goal: Synthesize  $u(k)$  to minimize a performance measure involving  $z(k)$ .
- Constraints
  - Minimal plant and disturbance modeling
  - $w(k)$  is not measured
- Weight matrix representation of standard problem

$$Z(k) = W_{zw}\Phi_{zw}(k) + B_{zu}U(k)$$

$$Y(k) = W_{yw}\Phi_{yw}(k) + B_{yu}U(k)$$

$$\begin{aligned} Z(k) &= \begin{bmatrix} z(k) \\ \vdots \\ z(k-p+1) \end{bmatrix} & Y(k) &= \begin{bmatrix} y(k) \\ \vdots \\ y(k-p+1) \end{bmatrix} & U(k) &= \begin{bmatrix} u(k) \\ \vdots \\ u(k-p_c+1) \end{bmatrix} \\ p_c &= \mu + p + n - 1 \end{aligned}$$

- $W_{zw}, W_{yw}, B_{zu}, B_{yu}$  are block Toeplitz

## Adaptive Disturbance Rejection Algorithm

---

- ARMARKOV controller

$$u(k) = \sum_{j=1}^{n_c} -\alpha_{c,j}(k)u(k-\mu-j+1) + \sum_{j=1}^{\mu_c-1} H_{c,j-1}(k)y(k-j+1) + \sum_{j=1}^{n_c} B_{c,j}(k)y(k-\mu-j+1)$$

- $\mu$ -step ahead predictor form

- Control window

$$U(k) = \sum_{i=1}^{p_c} L_i \theta(k-i+1) R_i \Phi_{uy}(k)$$

- $\theta(k)$  is a block vector of controller parameters

- Estimated performance

$$\hat{Z}(k) \triangleq W_{zw} \Phi_{zw}(k) + B_{zu} \sum_{i=1}^{p_c} L_i \theta(k) R_i \Phi_{uy}(k)$$

- based on past data with **current** controller

- Cost function and gradient

$$\begin{aligned} J(k) &= \frac{1}{2} \hat{Z}^T(k) \hat{Z}(k) \\ \frac{\partial J(k)}{\partial \theta(k)} &= \sum_{i=1}^{p_c} L_i^T B_{zu}^T \hat{Z}(k) \Phi_{uy}^T(k) R_i^T \end{aligned}$$

- Requires model of  $G_{zu}$

- Compute estimated performance

$$\hat{Z}(k) = Z(k) - B_{zu} \left( U(k) - \sum_{i=1}^{p_c} L_i \theta(k) R_i \Phi_{uy}(k) \right)$$

- Controller parameter update law

$$\theta(k+1) = \theta(k) - \eta(k) \frac{\partial J(k)}{\partial \theta(k)}$$

## Theoretical Results

---

- Assumption:

There exists  $\theta^*$  that minimizes  $J(k)$  for all  $k$ .

- Error matrix

$$E(k) \triangleq \theta^* - \theta(k)$$

- Desired performance

$$Z^*(k) \triangleq W_{zw}\Phi_{zw}(k) + B_{zu} \sum_{i=1}^{p_c} L_i \theta^* R_i \Phi_{uy}(k)$$

- Performance error

$$\varepsilon(k) \triangleq Z^*(k) - \hat{Z}(k)$$

- Theorem

Let

$$\eta_{\text{opt}}(k) \triangleq \frac{\|\varepsilon(k)\|_2^2}{\left\| \frac{\partial J(k)}{\partial \theta(k)} \right\|_F^2}.$$

Suppose  $\theta^*$  exists. Then

$$\|E(k+1)\|_F < \|E(k)\|_F$$

if and only if

$$0 < \eta(k) < 2\eta_{\text{opt}}(k).$$

In particular,  $\eta(k) = \eta_{\text{opt}}(k)$  minimizes  $\|E(k+1)\|_F - \|E(k)\|_F$ .

- Note:  $\eta_{\text{opt}}(k)$  is not computable

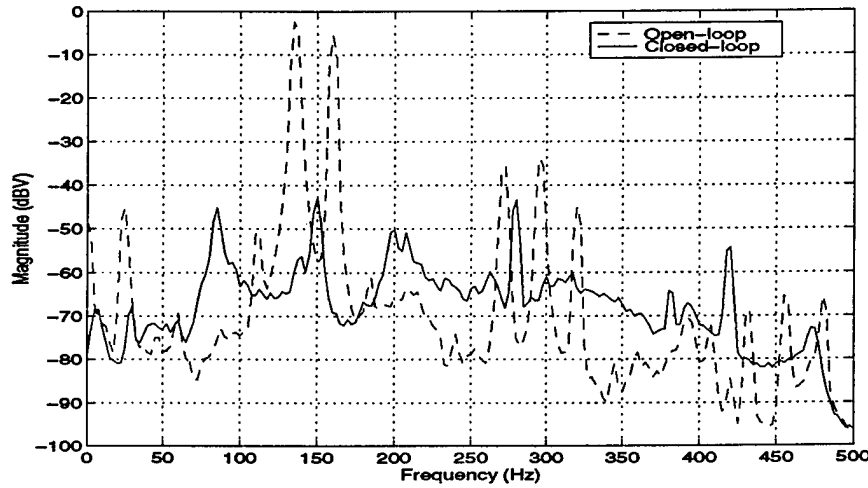
- Implementable adaptive step size

$$\eta_{\text{imp}}(k) \triangleq \frac{1}{p_c \|B_{zu}\|_F^2 \|\Phi_{uy}(k)\|^2}, \quad 0 < \eta_{\text{imp}}(k) \leq \eta_{\text{opt}}(k)$$

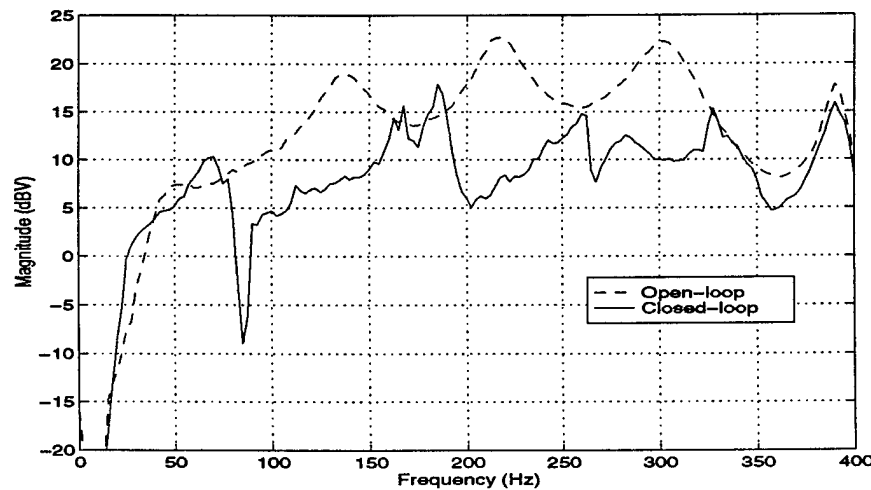
## Experimental Results on Acoustic Duct

---

- Dual Tone (139.65 Hz and 160.4 Hz)



- White Noise



# DEVELOPMENT OF A SMART MOVING-BLADE-TIP AND AN ACTIVE-TWIST ROTOR BLADE DRIVEN BY A PIEZO-INDUCED BENDING-TORSION COUPLED BEAM

Andreas P.F. Bernhard\*

Inderjit Chopra\*\*

Alfred Gessow Rotorcraft Center  
Department of Aerospace Engineering, University of Maryland  
College Park, MD 20742

## ABSTRACT

This paper presents the design, development, manufacture and testing of an active rotor blade that can be flown in two different configurations: either with a moving blade tip or as a controllable twist blade. For both blade types the inboard 90% of the blade with the bending-torsion coupled actuator located in the spar is common. The actuator, used in both blades, is a piezo-induced bending-torsion coupled composite beam. A spanwise variation in the beam layup and piezoceramic element phasing is used to maximize the twist response, while minimizing the bending response. Two operational 1/8<sup>th</sup> scale model rotor blades, with a 90% main blade section and 5% and 10% span active tips were manufactured for hover testing. In the controllable twist configuration, a non-rotating twist amplitude of 0.8 deg is achieved, at 100V<sub>rms</sub> and 75Hz. In hover, at 875 rpm, this reduces to 0.5 deg at 5/rev. The actuation power per blade is estimated at 1.2% of the hover power required at 8 deg collective. In the moving blade tip configuration, a non-rotating deflection amplitude of 1.7 deg is achieved at 100V<sub>rms</sub>. Non-rotating dynamic tests show resonant amplification for all frequencies up to 5/rev. The deflection at 120V<sub>rms</sub> increases from a low frequency 2.25 deg to 3.5 deg at 4/rev, and for 90V<sub>rms</sub> the low frequency deflection amplitude of 1.5 deg doubles to 3.0 deg at 5/rev. The rotor blades with non-activated moving tips were successfully flown in hover, at 900 rpm and collective setting from 4-8 deg.

## THE SMART MOVING-BLADE-TIP CONCEPT

In order to reduce vibration, it is proposed to generate new unsteady aerodynamic airloads, using a controllable blade tip. Correctly phased, these airloads can be used to cancel the rotor vibration directly on the rotor blade. A schematic of the rotor blade with a Smart Active Blade Tip (SABT) is shown in Figure 1. The SABT is rigidly connected to the actuator beam and as the tip of the actuator beam twists, so the SABT is deflected nose up or down.

A spanwise variation in beam layup and piezoceramic element phasing is used to convert the bending-torsion coupled beam into a pure twist actuator. Piezoceramic elements are surface bonded on top and bottom and are excited so as to induce spanwise and chordwise bending of the beam. The structural coupling, in turn, results in an induced twist, which is used to deflect the blade tip. The actuator is located spanwise in the box-beam cavity with the inboard end directly attached to the rotor flexbeam (via the blade root bolts). The moving tip, in turn, is attached to the outboard end of the beam via a rigid adaptor. This is supported in a radial bearing, that is used to carry the lift and drag of the tip while the centrifugal force and torsional loads are transferred to the actuator beam. As the tip of the beam twists relative to the inboard clamped end, the SABT is deflected. The SABT tip can be modeled as a blade tip section, attached to the hub flex beam via a secondary flex beam, that only has a torsional degree of freedom.

## THE ACTIVE TIP-TWIST CONCEPT

In the design phase for this project it became evident, that by locking the outboard end of the actuator beam in a rib at the end of the blade, the actuator would tend to twist the entire blade. Figure 2 shows a schematic of the controllable twist concept. The actuator beam, applies a torque at the tip, thereby inducing a linear twist over the blade length. See Figure 3 for a schematic of the blade tip deflection. In contrast to the moving tip, this configuration presents an active rotor blade with no aerodynamic discontinuities. Furthermore, the large centrifugal load imposed by the moving tip on the beam is eliminated, improving the beam twist performance. From a modeling perspective, the actuator beam can be represented as a torsional spring at the tip of the rotor blade.

---

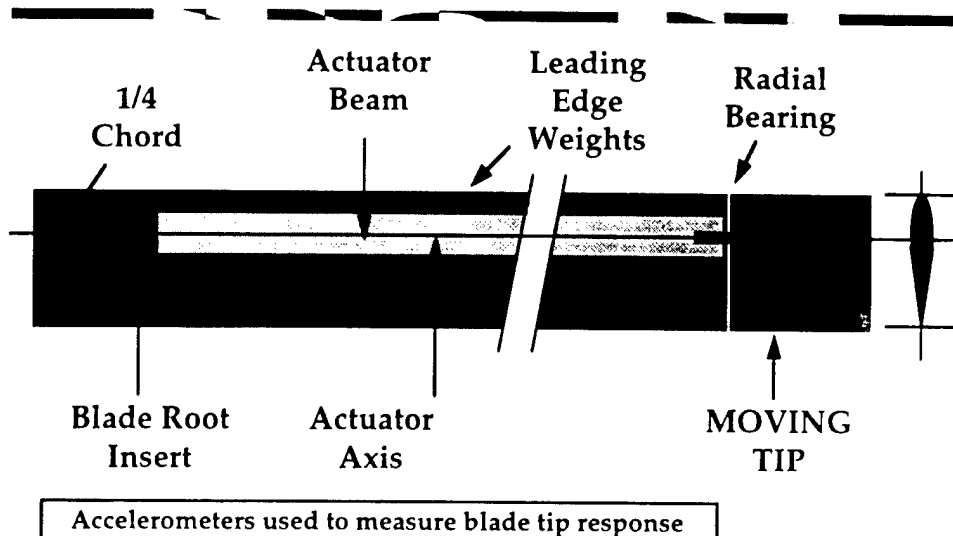
Presented at the Third ARO Workshop on Smart Structures, Virginia Tech, Blacksburg, VA, August 1997

\* Gustave J. Hokenson Fellow, Member AHS

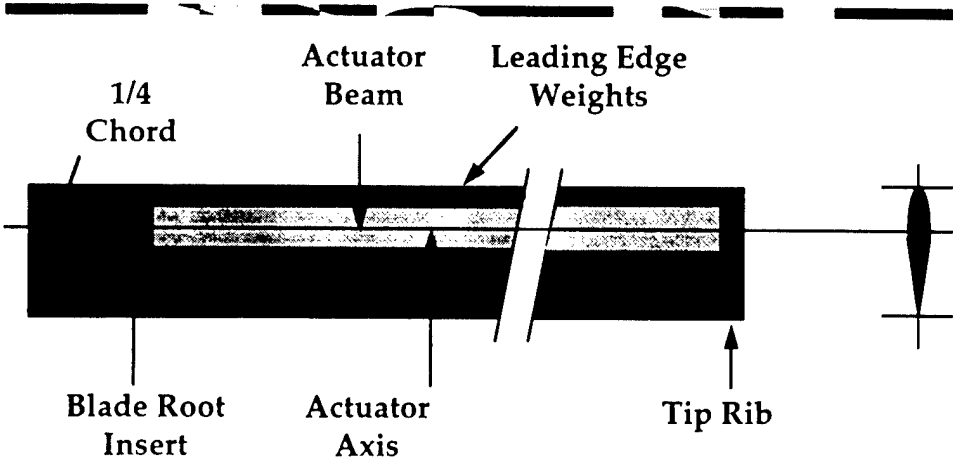
\*\* Professor and Director, Fellow AHS



## SMART ACTIVE BLADE TIP (SABT)



## ACTIVE BLADE TWIST





## Advantages & Disadvantages

- Advantages

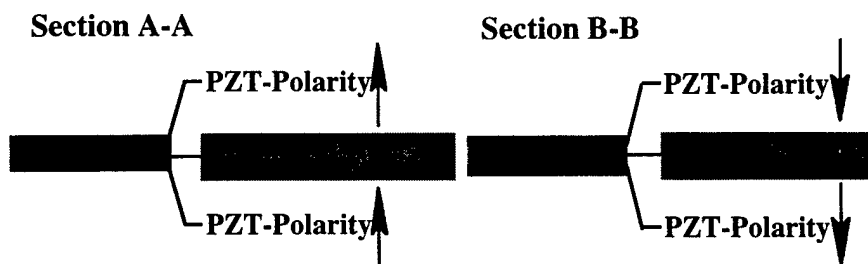
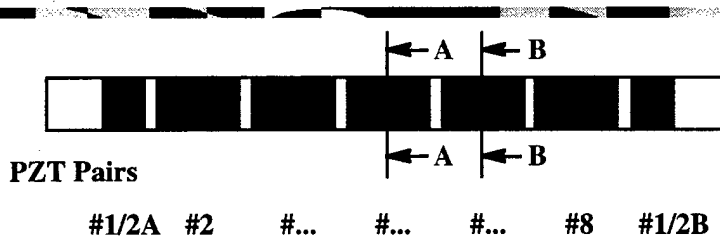
- Entire blade span can be used for actuation
- System can be mounted on 1/4 chord
- No amplification mechanism or thrust bearings

- Disadvantages

- Localized active blade system

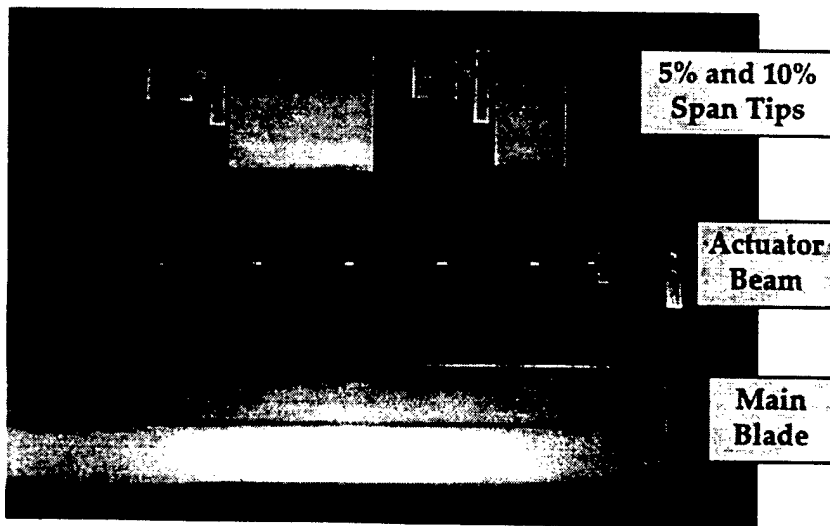


## Actuator Beam

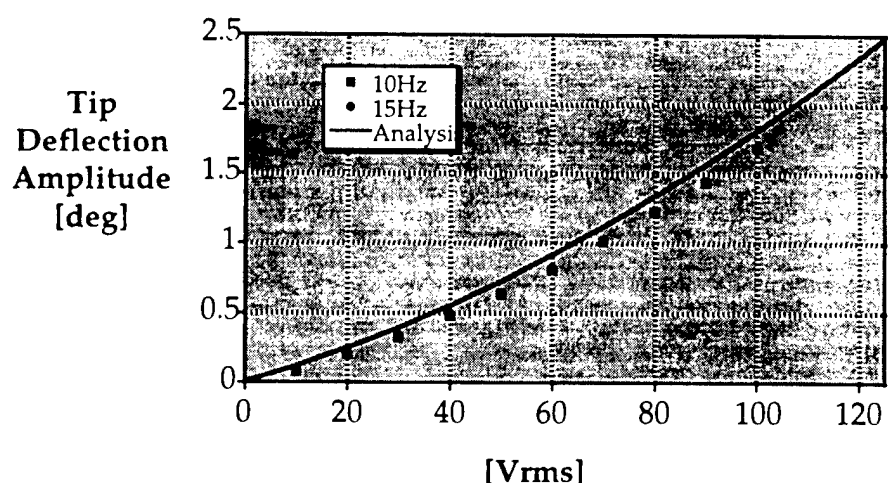




## Active Blade Components

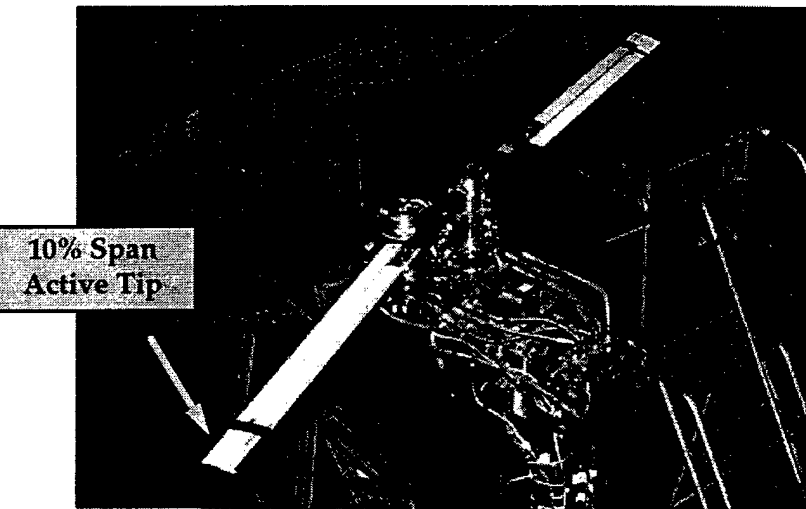


## SABT Non Rotating Test: Low Frequency Excitation

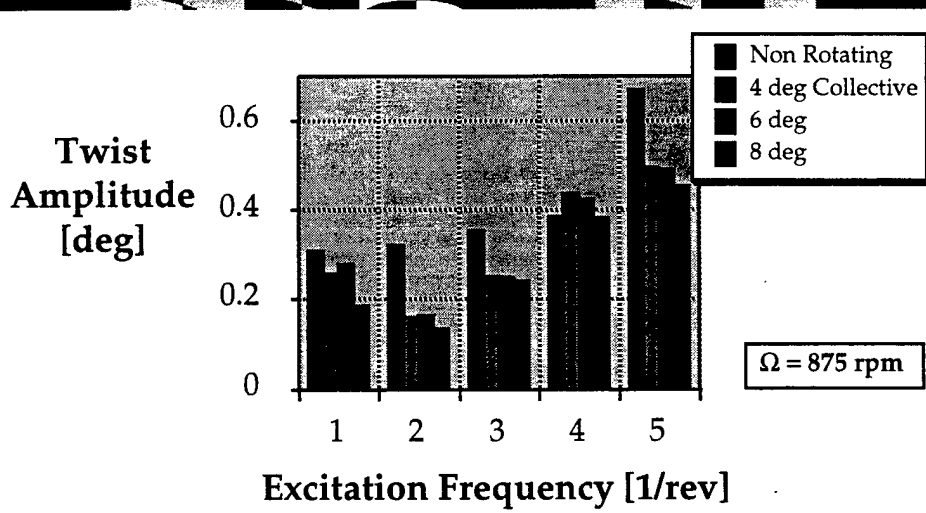




## SABT Hover Test



## Active Twist Hover Test 2: 100Vrms Excitation





## Conclusions: Active Tips

---

### Non rotating tests

- Low frequency amplitude of 1.7deg @ 100Vrms
- Analytic model shows good correlation with low frequency response
- Amplitude of 3.5 deg @ 120Vrms & 75Hz
- The active tip rotor, with zero tip excitation, was successfully flown at 900rpm with collective settings from 4-8 deg



## Conclusions: Active Twist

---

### Non rotating tests

- Natural frequency near 5/rev
- Twist amplitude of 0.8deg @100Vrms & 75Hz

### Hover tests

- Twist amplitude increases from 0.25deg at 3/rev to 0.4 deg at 4/rev and 0.5 deg at 5/rev, @100Vrms
- Twist amplitude does not change significantly with collective

# **DESIGN, MANUFACTURE, AND HOVER TESTING OF AN INTEGRAL TWIST-ACTUATED ROTOR BLADE**

John P. Rodgers and Nesbitt W. Hagood  
Active Materials and Structures Laboratory  
MIT Department of Aeronautics and Astronautics  
Cambridge, Massachusetts

## **ABSTRACT**

Helicopter rotor blades experience significant vibration levels as a result of variations in rotor blade aerodynamic loads with blade azimuth angle. Actively controlled rotor blades are currently being investigated as a means of reducing these detrimental vibrations. A reduction in the vibration levels will improve pilot effectiveness and passenger comfort, and reduce maintenance and operating costs. Performance benefits may also be achieved through increased payload and cruise speed.

Active twist control of the rotor blades may be used to reject the aerodynamic disturbances affecting the blades. These disturbances are the most severe during transitional and forward flight, manifesting in the form of N/rev vertical hub loads. Individual blade control (IBC) of blade twist or angle of attack enables the implementation of active vibration control strategies.

Active fiber composites offer a means of directly twisting the rotor blade. Anisotropic active plies may be embedded within the composite spar of the blade to induce shear stresses which create the twist. In addition, the dense electroceramic active material is positioned near the quarter-chord of the blade section, thus minimizing the weight penalty. The benefits of this concept are the significant actuation authority, high bandwidth, and potential reliability. This concept is an alternative to trailing edge flap concepts which induce an aerodynamic twisting moment to deflect the blade. The integral actuation concept distributes the active material through the spar and eliminates the need for a complex, highly efficient actuation amplification mechanism.

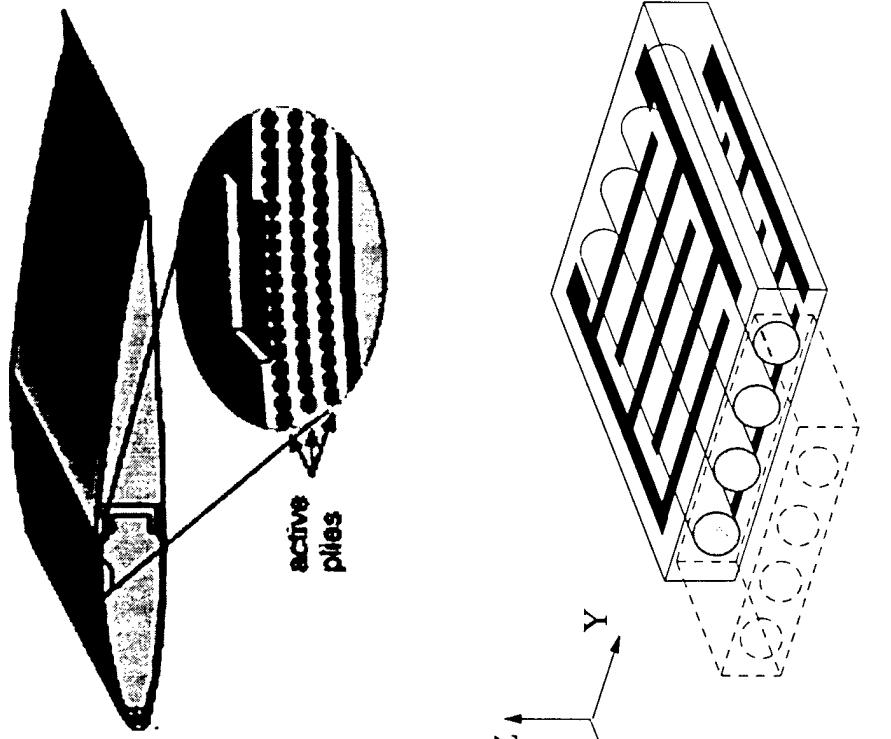
The primary objective of this research is to develop a twist-actuated rotor blade for helicopter vibration control. By controlling the pitch of individual blades at harmonic frequencies, unsteady aerodynamic disturbances can be rejected. As a result, the vibrations transferred to the hub can be reduced. This project will demonstrate the integral twist actuation concept and its advantages over other actuation methods. Active fiber composite plies will be integrated into a modified 1/6th Mach scale CH-47D spar to induce twist in the blade. This application takes advantage of the anisotropic actuation, conformability, and reliability of active fiber composites. Active fiber composites technology will be advanced in order to satisfy the actuator requirements of the project.

A half-span spar section of the prototype design was fabricated and tested to evaluate performance and characterize structural and electrical integrity. Actuation tests have demonstrated benchtop active twist capability and have revealed the need for fabrication improvements to address electrical insulation issues. Structural testing for the axial and torsional stiffness were used to validate both design predictions and manufacturing methods. Actuation under tensile loading tests have supported previous actuator reliability studies. Minimal degradation was recorded in actuator performance in repeated cycles to simulated Mach scale centrifugal loads.

The next prototype will incorporate improved insulation and higher performance requirements for the packs in order to achieve the design objectives for the integral blade. Design and manufacturing modifications resulting from this first integral spar will be discussed. Finally, progress in the manufacture of the complete integral blade will be discussed.

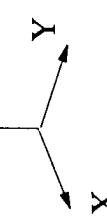
## *Introduction*

- Objective: Integrate active materials within rotor blades to control vibrations



- Concept

- Active fiber composite plies incorporated in composite spar lay-up
- Actuators induce shear stresses in spar walls to develop twisting moment

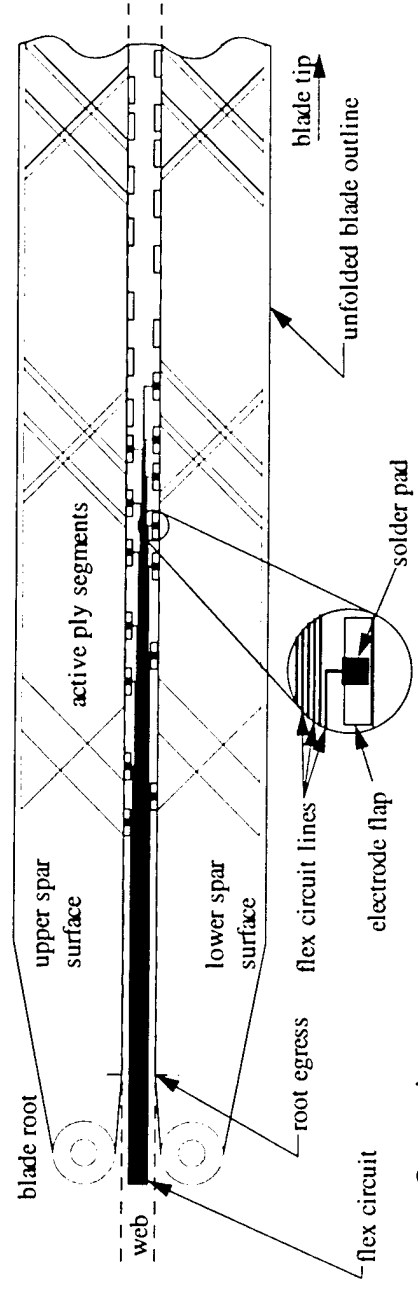


# *Actuator Development*

- Alternative fiber compositions investigated
  - PZT 5H, PZT 5A, PZT 4
  - Extruded round fibers compared with cut square fibers
- Comparison based on:
  - Fiber quality / reliability
  - Manufacturability
  - Free strain and laminate induced stress capability
  - Damage tolerance to 4000 and 6000 microstrain load
  - Compressive Stress Depolarization
- Investigated electrode material: etched copper vs. screen printed
- Investigated matrix additives
- PZT 5A selected along with copper / kapton electrodes and a pure epoxy matrix

## *Blade Design*

- 42 AFC packs in 3 active plies from 0.27 to 0.95R
- Independant electrical connections to packs along web (heel of spar)
- Flex circuit designed to interface with electrode flaps
  - 84 leads in 6 layers, 4000 V between leads
  - Conductive epoxy bond between electrode and flex circuit solder pads



Spar laminate unwrapped showing interface with flex circuit



MIT ACTIVE MATERIALS AND STRUCTURES LABORATORY (AMSL)

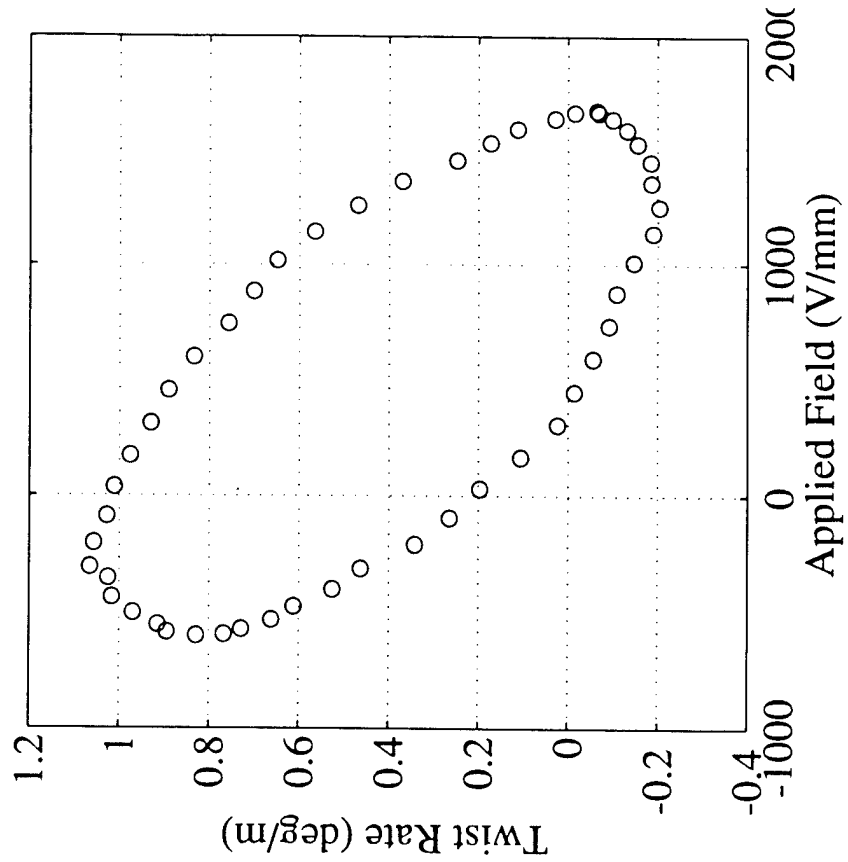
## *Integral Spar Section*

- Section of spar from root to 0.54R
- Incorporates 12 AFC packs
- Interfaces with flex circuit
- 6 full strain gage bridges on foam core
- Tip fixture for tensile testing



## *Twist Data*

- Preliminary twist data at 20 Hz and 600 Vdc + 2550 Vpp cycle
- $1.26 \text{ deg/m}$  peak-to-peak twist rate
- Dielectric breakdown between 2 packs in different plies limited data--improved pack insulation to correct problem
- Estimated average pack actuation was 460 microstrain (free) based on proof test data - $1.69 \text{ deg/m}$  predicted



# **DEVELOPMENT OF NEURAL NETWORK CONTROLLER FOR SMART STRUCTURE ACTIVATED ROTOR BLADES**

Michael G. Spencer  
*Graduate Research Assistant*

Robert M. Sanner  
*Assistant Professor*

Inderjit Chopra  
*Professor*

Alfred Gessow Rotorcraft Center  
Department of Aerospace Engineering  
University of Maryland, College Park, MD 20742

## **ABSTRACT**

### Introduction

This paper describes the research into development of an adaptive neurocontrol algorithm that can be used with distributed actuators and sensors to control the vibrations of flexible structures. In particular, this controller is being developed as a new method of individual blade control to reduce vibrations in rotorcraft. The new control method is based on nonlinear adaptive control techniques and neural network algorithms developed for rigid link robot manipulators[1]. The approach utilizes a finite dimensional FEM model of the structure, viewing it as an assembly of segmented elements with possibly unknown physical properties and subject to unknown time-periodic disturbances. By learning in realtime the material properties of the blade and the nature of the external disturbances, the controller learns the inputs to the piezoactuators necessary to adaptively cancel the induced blade vibrations. The controller is thus able to maintain consistent performance of the system in the presence of uncertainty or variations in the plant parameters or external disturbances[2].

Recent research applications of neural networks to rotorcraft problems have been directed toward identification of various helicopter characteristics[3,4], including the use of multiple smart structure sensors and actuators with artificial neural networks for structural identification[5]. The common aspect of these efforts is that they train the networks offline with known sets of test data and then use the networks to identify or predict structural characteristics. In contrast, however, our algorithm uses a neural network adapting in *realtime* to learn to compensate for unknown periodic disturbance forces and blade dynamics. The controller uses real time sensor signals as inputs for the networks and continuously adjusts the network parameters as necessary to control the blade and achieve vibration reduction.

### Preliminary Efforts

This controller has already been successfully tested on a cantilevered beam with piezoceramic actuators/sensors controlling the bending motion. As shown in Figure 1, two sets of piezoactuators were used to generate the bending moments at two active "joint" positions on the beam. The joint nearest the clamped end was location 3 and the outer joint was location 4. Beam disturbance motion was induced by a smaller piezoactuator set at the root of the beam (location 2). The applied control moments were determined from the complete control law developed in [2]:

$$\tau = -k_d s(t) + \mathbf{Y}\hat{\mathbf{a}} + N(x, \hat{c}) \quad (1)$$

where  $\tau$  is the vector of moments commanded at each piezo location, and  $k_d s(t)$  is a linear feedback term which augments the beam stiffness and damping. The term  $\mathbf{Y}\hat{\mathbf{a}}$  is a parameterization of the model dependent part of the controller structure, where  $\hat{\mathbf{a}}$  is a vector of estimates of the beam physical properties (inertia, stiffness, damping). Finally,  $N(x, \hat{c})$  represents the neural network component which approximates the unknown disturbance moments; the vector  $\hat{c}$  contains estimates of the network parameters required to cancel the vibration. The various estimates,  $\hat{\mathbf{a}}$  and  $\hat{c}$ , are then updated in realtime according to the learning rules [2]

$$\dot{\hat{\mathbf{a}}} = -\Gamma_a \mathbf{Y}^T s(t) \quad (2)$$

$$\dot{\hat{c}}_{ij} = -\Gamma_c g_{ij} s(t) \quad (3)$$

where the  $g_{ij}$  are basis functions ("neurons") used in the network construction, and  $\Gamma_a$  and  $\Gamma_c$  control the learning rates of the estimates. The computed moments are then converted to voltages by the linear relationship  $\tau = v * K_a$  where the gain  $K_a$  is based on the piezoactuator properties.

Figures 2 and 3 show examples of the controller's ability to learn and account for unknown periodic disturbances. Figure 2 shows the outputs from each piezo sensor as the controller attempts to suppress the vibrations at each joint. Without the network; that is, only the linear feedback and adaptive terms, a factor of six reduction in vibration was achieved, whereas with the neural network, a further order of magnitude reduction was obtained. In each test, all parameter estimates were initially zero reflecting a complete lack of prior knowledge about the beam properties or the nature of the external disturbances. The results show that the controller was able to learn within 40 seconds the parameters necessary to achieve vibration suppression.

Figure 2 shows the local vibrations at the "joint", locations 3 and 4. Of course, the segments of the beam beyond these "joints" are also flexible and will still exhibit some vibrations. As shown in Figure 3, this strategy still results in an asymptotic reduction of a factor of 7 in the vibration observed at the tip of the beam. Increasing the number of active piezo locations would allow an even greater vibration reduction along the beam.

### Current Research

Our current work extends this control concept to actively controlling the vibrations of Froude scale rotor blades. In the previous work described above, the control voltages resulted in application of direct bending moments to the beam to control its vibration. However, this method cannot be scaled up for rotor blades because the piezoactuators cannot generate the necessary structural bending moments. Instead, control of rotor flap vibration requires controlling the aerodynamic lift profile. Research has shown that incorporating active smart structure devices into rotor blades provides a means of changing the lift profile of individual blades[6,7]. One method to accomplish this uses trailing edge flaps on scale rotor blades [8,9]. Milgram and Chopra [10] performed a comprehensive rotor analysis with the UMARC code which included unsteady aerodynamics, and showed that rotors with trailing edge flaps are capable of vibration reduction. Another method of blade activation uses embedded piezoactuators to change the twist profile of the individual blades [11]. Tests have proven these devices capable of changing the aerodynamic loads of the rotor blades. To date these efforts have involved open-loop tests at various rotor harmonics to evaluate the effectiveness and validate the modeling of these new smart structure applications. Our current research will extend the utility of these devices by providing a new *closed-loop* control system based on neural networks that will actively reduce the rotor blade vibrations by varying the aerodynamic loading on the blades.

To actively control a rotor blade in this fashion requires extending the use of the neural networks from the algorithm described above [2]. For a lightweight structure, piezoactuators can provide the moments required to control the vibrations; however, with a rotor blade the bending moments must now be generated by the varying lift profile of the blade. The lift profile is a nonlinear function of the blade rotation ( $\Psi$ ) and local twist ( $\theta$ ) which includes the deflection of any flap surface. The blade flapping moments induced by any set of applied piezo voltages,  $v$ , are thus complex functions given by

$$\tau = M(L(\Psi, \theta(v))) = g(\Psi, v) \quad (4)$$

Unlike the assumed linear case considered above,  $\tau = v * K_a$ , the piezo voltages required to produce the necessary bending moments are now nonlinear functions of the applied piezo voltages. Thus, in order to adaptively cancel vibration, the network must also learn the dynamic relationship between the voltage applied to the piezoactuators and the resulting lift profile and induced bending moments.

By using dynamic extension and backstepping techniques [12,13], our previous algorithm has been extended to cover this more general, and indeed, more practical case. Computer simulation tests will be used to demonstrate the controller capability using the comprehensive UMARC code. Ultimately, these efforts will be validated by testing of scale model smart structure actuated rotor blades in hover and in forward flight at the University of Maryland test facilities.

The significance of this research is that it provides a new approach for closed-loop vibration control of flexible rotor blades. By combining adaptive nonlinear control theory and neural network techniques this controller adapts to poorly modeled nonlinear effects and can learn to anticipate and counter external periodic aerodynamic disturbances that deflect the blade. The controller also provides robustness by being able to detect and compensate for changes in the physical properties of the blade (mass, length, or stiffness) when changes occur such as due to damage to the rotor.

#### REFERENCES

1. Sanner, R. M., and Slotine, J.-J. E., "Stable Adaptive Control of Robot Manipulators Using Neural Networks", *Neural Computation*, Vol. 7, (4), 1995.
2. Spencer, M.G., Sanner, R.M., and Chopra, I., "Adaptive Nonlinear Neural Network Controller for Rotorcraft Vibration", *Proceedings of the 1997 SPIE's North American Symposium n Smart Structures and Materials*, San Diego, CA, March 1997.
3. Haas, D. J., Milano, J., and Flitter, L., "Prediction of Helicopter Component Loads Using Neural Networks", *Journal of the American Helicopter Society*, Vol. 40, (1), pp. 72-82, Jan. 1995.
4. Ganguli, R., Chopra, I., and Haas, D. J., "Detection of Helicopter Rotor System Simulated Faults Using Neural Networks", *Proceedings of the 37th Structures, Structural Dynamics and Materials Conference*, Salt Lake City, UT April 1996.
5. Damle, R., Rao, V., and Kern, F., "Multivariable Neural Network Based Controllers for Smart Structures", *Journal of Intelligent Material Systems and Structures*, Vol. 6, pp. 516-528, July 1995.

6. Chopra, I., "Development of a Smart Rotor," *Proceeding of the 19th European Rotorcraft Forum, Cernobbio Como, Italy*, September 1993
7. Straub, F. K., "A Feasibility Study of Using Smart Materials for Rotor Control" *Smart Materials and Structures*, Vol. 5, No. 1, February 1996, pp. 1-10.
8. Ben-Zeev, O. and Chopra, I., "Advances in the Development of an Intelligent Helicopter Rotor Employing Smart Trailing-Edge Flaps," *Smart Materials and Structures*, Vol. 5, No. 1, February 1996, pp. 11-25.
9. Koratkar, N. A., and Chopra, I., "Testing and Validation of a Froude Scaled Helicopter Rotor Model with Piezo-Bimorph Actuated Trailing Edge Flaps" *Proceedings of the 1997 SPIE's North American Symposium n Smart Structures and Materials*, San Diego, CA, March 1997.
10. Milgram, J. and Chopra, I., "A Comprehensive Rotorcraft Aeroelastic Analysis with Trailing-Edge Flaps: Validation with Experimental Data, 52nd Annual Forum of the American Helicopter Society, Washington D.C., June 1996.
11. Chen, P.C., and Chopra, I., "Hover Testing of Smart Rotor with Induced-Strain Actuation of Blade Twist", *AIAA Journal*, Vol. 35 (1), pp. 6-16, Jan. 1997.
12. Nijmeijer, H. and van der Shaft, A. J., *Nonlinear Dynamical Control Systems*, Springer-Verlag, New York, 1990.
13. Krstic, M., Kanellakopoulos, I., Kokotovic, P., *Nonlinear and Adaptive Controller Design*, John Wiley and Sons, New York, 1995.

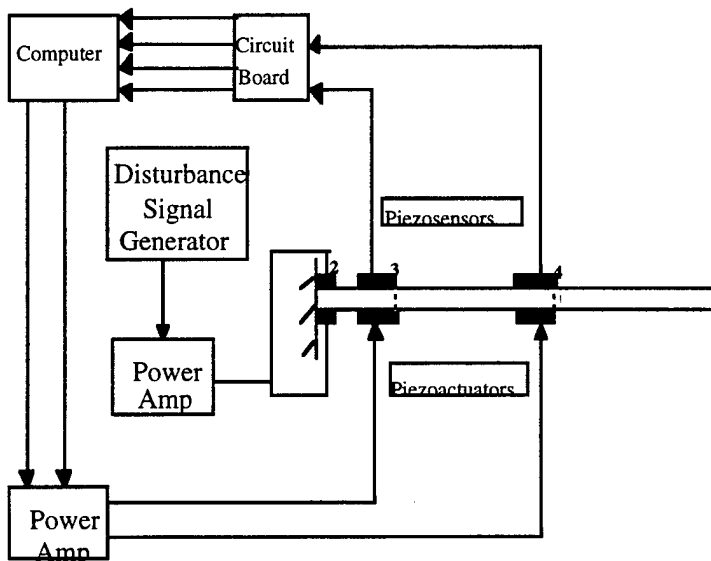


Figure 1. Fixed Beam Test Set-Up

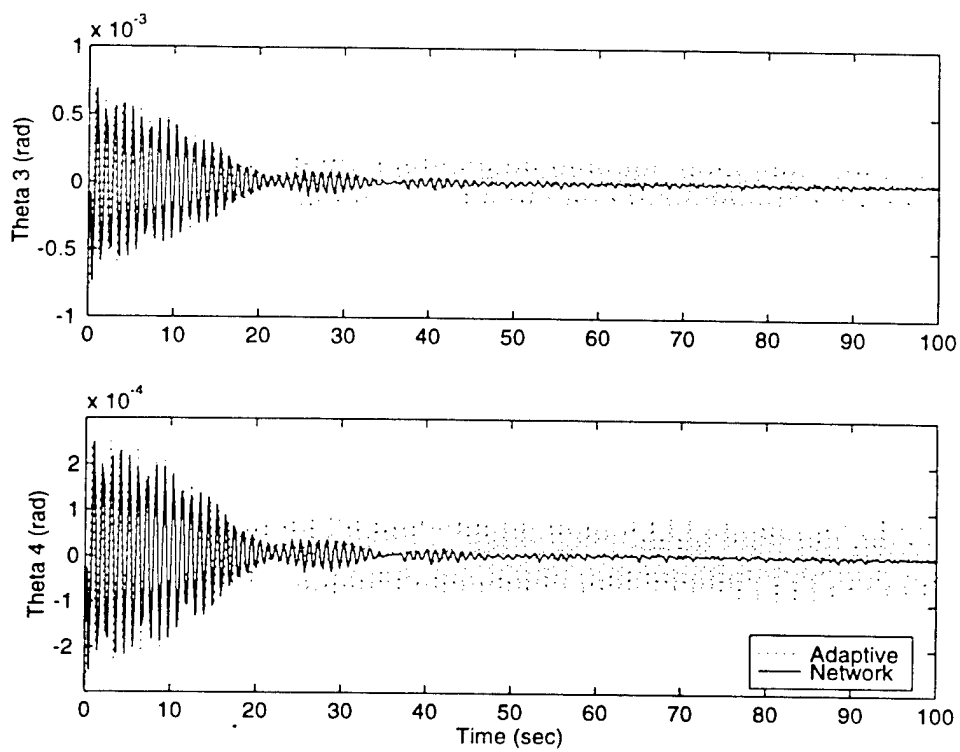


Figure 2. Joint Angles for Periodic Disturbance Suppression Test

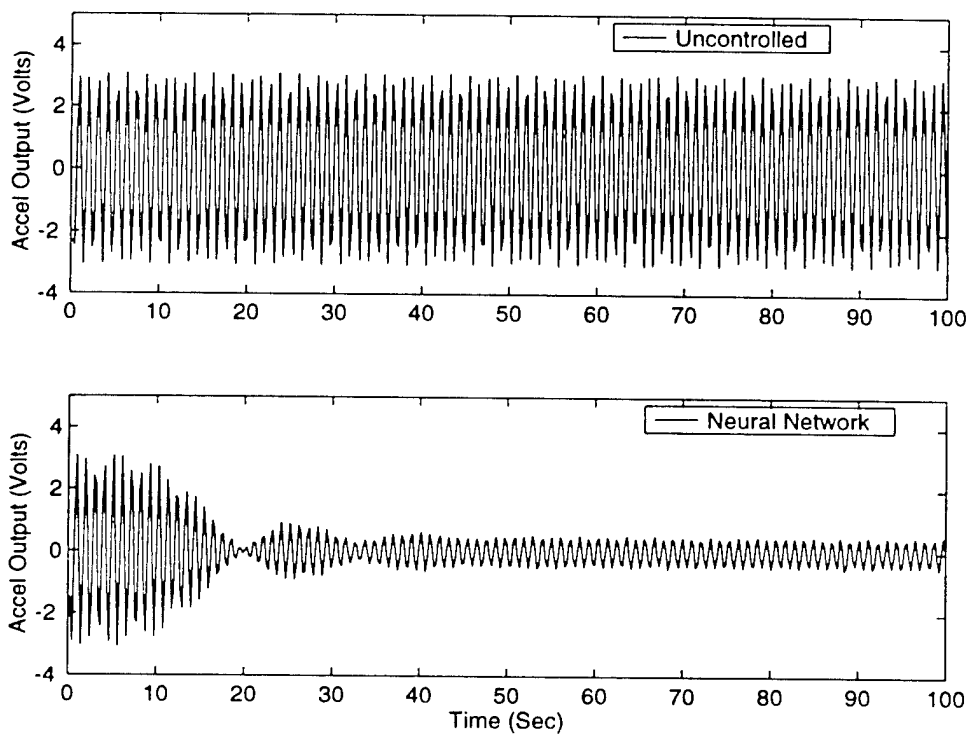


Figure 3. Tip Accelerometer Output

# APPLICATION OF LARIS PRINCIPLE TO DIRECTLY-DEFORMABLE AERODYNAMICS SURFACES

Victor Giurgiutiu and Craig A. Rogers

Mechanical Engineering Department  
University of South Carolina  
Columbia, SC 29208

## Abstract

The large-amplitude rotary induced strain actuator (LARIS) principle utilizes the twist-warping coupling of thin wall tubes to produce a significant rotary deflection at the tip of the open tube in response to a small axial input at the root of the tube. The viability of this concept has already been proved through extensive laboratory tests on the LARIS Mk 1 and LARIS Mk 2 proof-of-concept demonstrators. The LARIS Mk 1 experiments showed that the LARIS principle is capable of producing  $8^0$  of static deflection over a 1.2 m (4-ft) tube length while the shorter-built LARIS Mk 2 experiments explored the dynamic characteristics. A consistent  $6^0$  rotary deflection was demonstrated over the frequency range 0-50 Hz. The LARIS concept is an ideal candidate for active vibration control applications utilizing aerodynamic response to pitch or angle-of-attack variations.

In recent period, significant effort has been invested by other researchers in creating deformable aerodynamic surfaces that can display a distributed time-varying twist along their span with beneficial smart control results. Northrop Grumman has developed this concept utilizing SMA torque-tube motors to induce wing rotation, and have built a 1/7 scale model that was successfully tested in the Transonic Wind-Tunnel Facility at NASA Langley, VA. They observed that the inherent stiffness of the wing opposed considerable reaction stiffness to the applied rotational input from the SMA torque-tube motors, and hence some significant loss of input was experimentally recorded. Wright Labs at the Wright Patterson Air Force Base, OH, have started the Twist Adaptive Wing System (TAWs) experimental program utilizing an uninhabited aerial vehicle with torsion activated wings that respond to control signals and prevent aileron reversal and other aeroelastic instabilities. The actuation mechanism consists of a conventional rotary actuator and a stiff steel tube designed to transmit the rotation input through the wing structure to the wing tip. Again, significant reaction moments are expected from the wing structure itself that resulted in the need for a stiff torque tube of steel construction to overcome them without too much loss of active deflection. The feasibility of this principle to utilization of induced-strain actuation is not yet clear.

In our work, we propose a direct extension of the LARIS principle to achieve direct twist and torsion control of deformable aerodynamic surfaces. This application will utilize the differential warping imposed at the root of the aerodynamic surface to create a rotation at its tip. Consistent with the LARIS principle, the rotation of the aerodynamic surface will be linearly distributed along its span and directly controllable through a single parameter input, the root linear deflection applied as differential warping. Since the structure itself is producing the deformation, a good balance will be achieved between the active and reactive structural forces and moments, and the corresponding deformations. The principle will be directly applicable to both fixed-wing and rotor-blade applications. A patent disclosure pertinent to this application of the LARIS principle is under review with the University of South Carolina.

(Presented at 3<sup>rd</sup> ARO Workshop on Smart Structures, Virginia Tech, Blacksburg, VA, 24061, August 27-29, 1997)

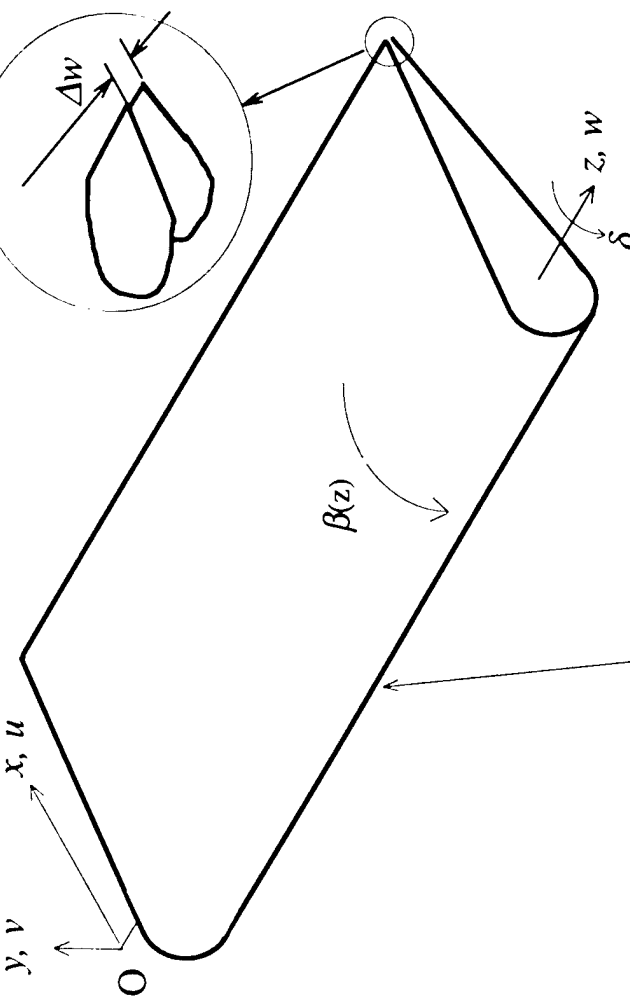


USC

College of Engineering

# LARIS Mk3 Linear-to-Angular Converter-Amplifier Concept

$$\vec{u} = [\beta(z)\vec{k}] \times \vec{r} + w(x, y, z)\vec{k}$$



$$u(x, y, z) = -\theta \cdot zy$$

$$v(x, y, z) = \theta \cdot zx$$

$$w(x, y, z) = \theta \cdot \psi(x, y)$$

$$\Delta \psi \approx 2A$$

$$w(x, y, z) = \theta \cdot \psi(x, y)$$

$$\Delta w \approx 2A\theta$$

$$\beta(z) = \frac{z}{2A} \Delta w$$

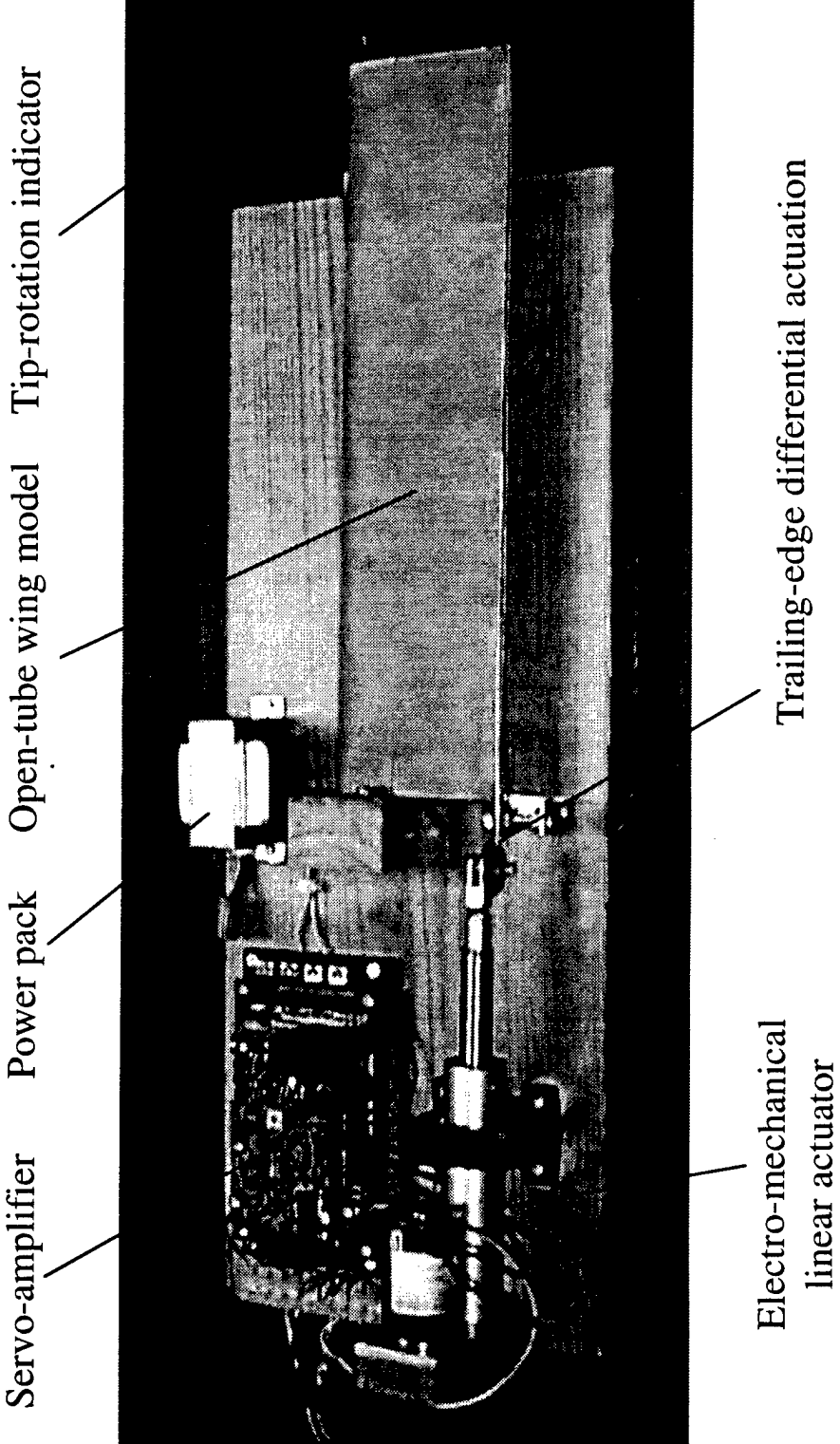
At the tip:

$$\boxed{\delta = \frac{L}{2A} \Delta w}$$

Open-tube wing of length,  $L$ ,  
thickness,  $t$ , cross-sectional contour,  
 $\Gamma$ , and enclosed cross-sectional  
 $\delta$

# Proof-of-Concept

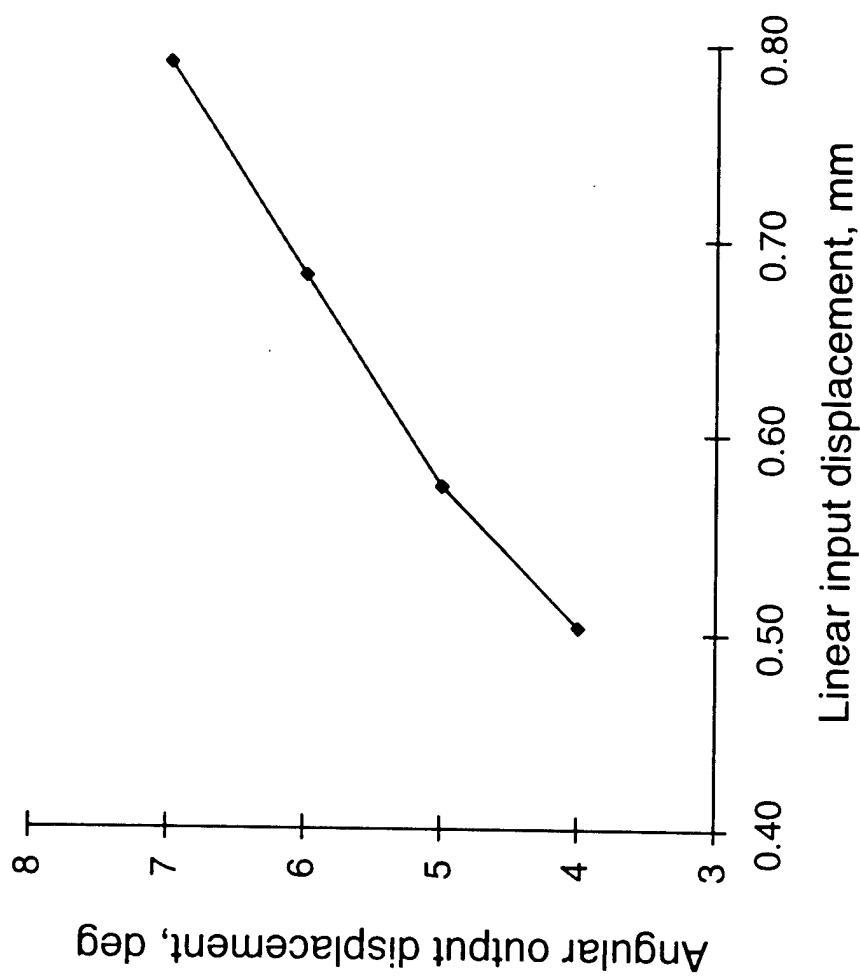
## LARIS Mk 3 Demonstrator



USC

College of Engineering

# Output Wing-Tip Rotation vs. Input Root Displacement



- Linear dependence of the wing tip rotation with input displacement was observed.
- Maximum rotation values over 7 deg. were recorded.



USC

College of Engineering

# Conclusions

- LARIS concept of solid-state linear-to-rotary conversion-amplification can applied to wing and rotor blade adaptive control
- Proof-of-concept laboratory experiments have shown excellent results with tip rotation angles above  $7^{\circ}$ .
- The proposed concept is scalable to full-size wings and rotor blades.
- Further theoretical and experimental investigation, including full-scale prototype, is warranted.



# Acknowledgments

- Previous LARIS work was supported by the US Army Research Office - University Research Initiative Program, Grant No. DAAL03-92-0181, Dr. Gary Anderson, Program Manager
- Current work has been partially supported by the South Carolina Research Institute.
- The dedicated and inspired experimental work of Mr. Brian Seat, Undergraduate Research Assistant at USC, is gratefully acknowledged.



# WIND TUNNEL TESTING OF A SMALL-SCALE ROTOR WITH ON-BLADE ELEVONS

Mark V. Fulton  
Aeromechanics Branch  
Army/NASA Rotorcraft Division

and

Robert A. Ormiston  
Aeroflightdynamics Directorate  
US Army Aviation RD&E Center (AMCOM)

Ames Research Center  
Moffett Field, California

## Introduction

There has long been a desire to reduce helicopter vibration. Considerable effort is now being directed toward on-blade aerodynamic control concepts. The present investigation uses a trailing-edge control surface, or elevon, to generate local aerodynamic lift and pitching moment.

In the present investigation a two-blade, 7.5-ft diameter hingeless rotor with 10% chord on-blade elevons driven by piezoceramic bimorph actuators was tested in forward flight for advance ratios from 0.1 to 0.3 at low to moderate thrust coefficients. The objective was to explore fundamental dynamic response characteristics and determine the effectiveness of elevon control in reducing blade vibratory loads. All elevon excitations were open loop. Primary measurements included elevon deflection and blade root bending and torsion moments. The design and development of the model rotor blades, piezoceramic actuators and elevons, and quasi-steady and dynamic test data for nonrotating and rotating conditions in hover were reported in Ref. 1. Preliminary results of forward flight wind tunnel testing will be presented herein.

## Experimental Model

A low tip-speed (298 ft/sec), small-scale dynamic model of low cost and complexity was suitable for this exploratory investigation. Fundamental structural dynamic characteristics were emphasized; evaluation of rotor performance and compressibility or stall effects would require a more sophisticated model. The model is shown in Fig. 1 installed on the Small Scale Rotor Test Rig (RTR) in the Army/NASA 7-by 10-Ft. Wind Tunnel.

The 7.5-ft diameter rectangular, untwisted rotor blades are uniform in mass and stiffness except at the blade root and the elevon "active section". Chordwise mass and aerodynamic centers are located near the quarter chord of the symmetrical NACA 0012 airfoil section. The blades are constructed of composite materials including a fiberglass spar, foam filled core, and fiberglass wrapped skin construction. Each blade has two bimorph actuators driving a single, 10% chord, plain elevon with a span of 12% blade radius, centered at the 75% radial location. Model physical properties and operating conditions are listed in Table 1. Additional construction details are available in Ref. 1.

The two piezoceramic, lead zirconate titanate (PZT), bimorph bender beam actuators are cantilevered to the rear of each blade spar. Fiberglass lever arms project forward from the elevon to engage the tip of the cantilever PZT beam to produce elevon rotational motion. In order to minimize mechanical losses, considerable attention was devoted to the design and construction of the elevon hinge and lever mechanism. To reduce friction, steel pins bonded to the ends of the PZT bender beams engaged the elevon lever arms. Slots in the lever arms accommodated small translations of the bender beam pins caused by the opposing arc motion of the two components, Fig. 2. Steel elevon hinge pins were mounted in low friction Delrin bearing blocks attached to the blade, with brass and Teflon thrust washers reacting the elevon centrifugal force. A photograph of the actuator and elevon installation is shown in Fig. 3.

Elevon motion was measured with a Hall-effect transducer and blade moment responses were measured through full strain gage bridges at the root flexure of each blade. The flap and chord strain gage bridges were at 0.114 R, and the torsion strain gage

bridge was at 0.128 R. In addition, the root pitch of blade 1 was measured with a potentiometer.

### Rotor Blade Structural Dynamic Characteristics

The rotor blade frequency fan plot (in air at 0° collective pitch), Fig. 4, illustrates the structural dynamic characteristics of the rotor blades. The frequencies were predicted by Second Generation Comprehensive Helicopter Analysis System (2GCHAS) using blade properties adjusted to match measured nonrotating frequencies. The nominal rotor speed (760 RPM, 12.7 Hz) results in a representative first-flap frequency (1.11/rev). The rotor is stiff inplane, with a first lead-lag frequency of 1.08/rev, and was somewhat sensitive to 1/rev loads. The second flap bending mode is above 3/rev unlike most blades, where this mode is below 3/rev. The first torsion frequency is 4.6/rev. Both the first elevon/actuator and third flap bending frequencies are between 6/rev and 7/rev at nominal rotor speed. The bimorph/elevon fundamental natural frequency was estimated assuming quasi-static 2-D airfoil aerodynamics and ignoring mechanical friction.

### Synopsis of Previous Hover Test Data

The hover testing was conducted in the AFDD Hover Test Chamber on the RTR. The principal results of the hover testing are summarized in this section. Additional details can be found in Ref. 1.

The model succeeded in demonstrating the practical feasibility of using piezoceramic bimorph actuators to provide reasonable elevon deflections for a small-scale low tip speed model by achieving deflections of +/- 10 deg nonrotating and +/- 5 deg up to 4/rev at the nominal rotor speed of 760 RPM.

Low-frequency blade torsion moment response to elevon deflection indicated that elevon effectiveness was lower than predicted by thin airfoil theory, largely due to the effects of low Reynolds number on elevon control power,  $c_{m\delta}$ .

Low frequency blade root bending response exhibited an "elevon reversal speed" slightly above 760 RPM, due to elastic blade twist induced by the negative elevon aerodynamic pitching moment.

Aeroelastic and structural dynamic response characteristics were evaluated over a wide rotor speed range using sine sweep excitation of the elevon up to 105 Hz (8/rev). CIFER<sup>\*</sup> (Refs. 2 and 3) was used to calculate the frequency response function magnitude, phase and coherence of measured blade

flap bending and torsion moments to elevon input and elevon response to actuator input voltage.

Frequency response measurements indicated that blade torsion moment response at resonance was amplified approximately five times the steady-state amplitude.

Blade flap bending responses produced by the available range of elevon deflection suggested that it would be possible to achieve significant reductions of anticipated 3, 4, and 5/rev vibratory flap bending moments in forward flight.

### Wind Tunnel Test Procedures

Forward flight testing was conducted in the Army/NASA 7-by 10-Ft. Wind Tunnel. Testing was typically performed at 760 and 450 RPM, with 760 being the "nominal" rotor speed, although limited testing was also performed at 600 RPM. Most of the data was taken at zero deg shaft angle, although a few points were also taken with 3 deg forward shaft tilt.

Steady-state data was obtained to quantify the variation of the root blade vibratory loads with flight speed. The steady-state test envelope is shown in Fig. 5 for both 760 and 450 RPM at 0 deg shaft angle and a range of advance ratios from 0 to 0.3. Since at 760 RPM the maximum achievable collective pitch was lower than desired and constrained by allowable blade loads, testing at 450 RPM was performed to obtain higher nondimensional blade loading. Figure 6 illustrates the theoretical nondimensional blade loading (thrust coefficient/solidity) reached during testing as predicted using 2GCHAS.

In addition to the steady-state testing, phase sweeps of elevon excitation were performed. First, a flight condition was established, including shaft angle, rotor speed, advance ratio, and collective pitch, with cyclic pitch adjusted to minimize 1/rev flap bending. Next, a discrete harmonic of the rotor speed (from 1/rev to 5/rev) was chosen for PZT actuator voltage excitation. A phase sweep of the PZT voltage was then performed, acquiring a data point for each discrete elevon phase angle (at the same cyclic pitch). The collective pitch used for each voltage harmonic and advance ratio is given in Table 2 for 760 RPM. For 450 RPM, all phase sweeps were at an advance ratio of 0.2 for a collective of 6.25 deg. This phase sweep data provides a measurement of elevon effectiveness and identifies the elevon phase required to minimize flap bending moment.

For a few flight conditions and elevon frequencies, a voltage sweep was performed. For these cases, a phase would be selected and the PZT voltage would be swept, with a data point being acquired for each discrete voltage level. This provides evidence of the elevon amplitude required for minimization of a flap bending harmonic.

Finally, frequency response data was acquired using frequency sweeps from 1 to 105 Hz. These frequency sweeps were performed for a range of advance ratios (up to  $\mu = 0.6$ ) at 0 deg collective, although some sweeps were also performed at higher collective pitch angles. It is hoped that this data will indicate any influence of advance ratio on elevon effectiveness in changing the blade root flap bending and torsion moments.

### Wind Tunnel Data

Data presented in this paper is limited to 760 RPM, 0 deg shaft angle, 4 deg collective pitch, and an advance ratio of 0.2.

The basic concept of vibratory loads reduction is that aerodynamic induced blade loads generated at one elevon harmonic will cancel the steady-state periodic load at the same frequency if the amplitude and phase of the elevon excitation is properly adjusted. This assumes, of course, that the elevon has sufficient effectiveness to cancel the steady-state blade root bending. If periodic motion is assumed, with the fundamental period equal to one rotor revolution, then the steady-state moment can be represented as

$$Ms = Ms_0 + \sum_{i=1}^n Ms_i * \cos(i\psi + \phi_{Ms_i}) \quad (1)$$

where  $Ms_0$  is the steady term and  $Ms_i$  is the amplitude of the  $i^{\text{th}}$  harmonic. The same form can be used for the elevon-induced moment,  $M\delta$ , and the total resultant moment,  $Mt$ . If the rotor is assumed to respond linearly, then

$$Mt = Ms + M\delta \quad (2)$$

In this case, the total vibratory load response can be shown to be a function of the steady-state and elevon-induced response :

$$Mt_n = \sqrt{Ms_n^2 + 2 * Ms_n * M\delta_n * \cos(\phi_{Ms_n} - \phi_{M\delta_n}) + M\delta_n^2} \quad (3)$$

This linear model is illustrated in Fig. 7, where the amplitude of the total response ( $Mt_n$ ) is plotted as a function of the phase of the elevon-induced moment

( $\phi_{Ms_n}$ ) for various amplitudes of the elevon-induced moment ( $M\delta_n$ ). This figure illustrates two principal effects. First, both "underdriven" and "overdriven" conditions are shown, where the excitation input is either insufficient or excessive for countering the steady-state response, respectively. Second, cancellation is shown to require 180 deg phasing of the elevon-induced moment relative to the steady-state moment.

Several results for the phase sweeps are now described. For each case, the amplitude of the response is obtained using an FFT of the response at the excitation harmonic. In each case, the amplitudes for blade "j" are plotted against the phase of elevon "j" (relative to blade "j" aft, for  $j = 1$  or 2). The 5/rev elevon deflection amplitude, Fig. 8, shows that there is only a small variation of the elevon amplitude with elevon phase.

The resultant variation in the 5/rev flap bending moment, however, is significant (Fig. 9). Note that the two blades show significantly different steady-state response, but that they also both show significant sensitivity to elevon phase angle. Similar flap bending results are shown in Figs. 10 and 11 for 4/rev and 3/rev excitation, respectively. Note, however, that the 3/rev elevon motion is of the proper magnitude to provide nearly complete cancellation of the 3/rev flap bending moment for a phase of about 90 deg (Fig. 11).

Figures 9 - 11 include curve fits based on the linear model of Eq. 3, with the magnitude of the steady-state harmonic specified but the remaining variables left as free parameters. This approach provides good curve fits and permits the identification of the amplitude and phase of the elevon-induced moment. Both the steady-state harmonic and the elevon-induced harmonic are plotted for 1/rev - 5/rev in Fig. 12. (Each amplitude is at the frequency of the PZT voltage.) Comparing the relative amplitudes of these two components provides an indication of elevon effectiveness for each response harmonic. The results in Fig. 12 indicate that, at this flight condition ( $\mu = 0.2$  and  $\theta_0 = 4$  deg), elevon effectiveness is sufficient to cancel the flap bending moment at all harmonics except 2/rev. Although the test data was obtained at different voltage levels, this comparison is useful since only the 1/rev and 2/rev voltage levels were at the maximum allowable value of 110 Vrms.

The measured flap bending moment response characteristics derived from the curve fits will now be used to illustrate how vibratory loads vary as a function of elevon excitation amplitude. The average

elevon amplitude ( $\delta_e$ ) at the PZT excitation frequency of each harmonic shown in Fig. 12 can be used to normalize the results. First, assume that the elevon-induced moment is proportional to elevon angle. Next, assume that the phase of the elevon motion is chosen to minimize the total response. The steady-state response at each harmonic can then be used with the elevon effectiveness at each harmonic to predict the variation of the total response at any given harmonic with elevon angle:

$$Mt_e = \left| Ms_e - \left( \frac{M\delta_e}{\delta_e} \right) * \delta_e \right| \quad (4)$$

The results of using this procedure are shown in Fig. 13 where the flap bending moment is reduced for increasing elevon deflection amplitude until cancellation is achieved; for larger elevon motions, an "overdriven" condition begins, causing the total response to increase.

The azimuthal time history shown in Fig. 14 illustrates several features of the elevon motion response. Consider two data points corresponding to the 4/rev harmonic line in Fig. 13: first the steady-state response and, second, the point with the 4P elevon excitation amplitude chosen to cancel the 4P flap bending harmonic. The elevon motion shown in Fig. 14 for the steady-state case is very small, as would be expected. The large 4/rev elevon motion required to cancel the 4/rev flap bending moment exhibits moderate 1/rev content as well as other harmonics. This is due in part to the azimuthal variation of elevon aerodynamic "stiffness" opposing the PZT actuator deflection; these nonsinusoidal elevon motions may complicate future correlations with analytical predictions.

Nonetheless, the desired effect of significantly reducing the 4/rev flap bending moment was accomplished as shown in Fig. 15. The fact that harmonics other than 4/rev are affected is likely caused by interharmonic coupling induced by the periodic coefficients of forward flight. Likewise, the nonsinusoidal elevon motion may well be affected by the blade motion through aerodynamic and inertial effects. Further detailed data analysis and correlation with analytical predictions will be required to better determine the exact cause of the observed behaviors.

## Concluding Remarks

Preliminary examination of the experimental data from this wind tunnel test indicates the on-blade elevon concept may have significant potential for reducing rotor system vibratory loads. Further evaluation of the data together with analytical studies are planned. A complete evaluation of the practical effectiveness and suitability of active on-blade elevon controls will require additional testing with more sophisticated rotor models.

## References

1. Fulton, M.V., and Ormiston, R.A., "Hover Testing of a Small-Scale Rotor with On-Blade Elevons," *Proceedings of the 53rd Annual Forum of the American Helicopter Society*, Virginia Beach, Virginia, April 29-May 1, 1997.
2. Tischler, M.B., Cauffman, M.G., "Frequency-Response Method for Rotorcraft System Identification: Flight Applications to BO-105 Coupled Rotor/Fuselage Dynamics," *Journal of the American Helicopter Society*, Vol. 37, No. 3, July 1992, pp. 3-17.
3. Tischler, M.B., Driscoll, J.T., Cauffman, M.G., and Freedman, C.J., "Study of Bearingless Main Rotor Dynamics from Frequency-Response Wind Tunnel Test Data," *Presented at the American Helicopter Conference*, San Francisco, CA, January 19-21, 1994.

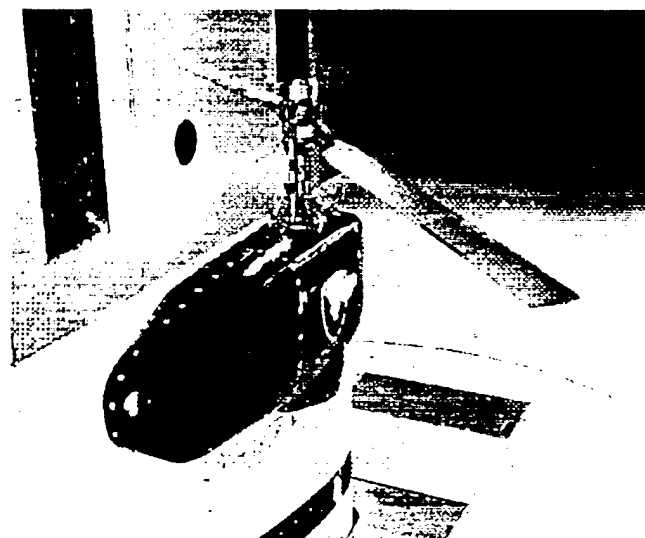


Fig. 1 Rotor with on-blade elevons in the Army/NASA 7- by 10-Ft. Wind Tunnel.

Table 1. Rotor Characteristics & Operating Conditions.

Description	Variable	Value
No. of Blades	b	2
Rotor Radius	R	45 in (3.75 ft)
Airfoil		NACA 0012
Airfoil Chord	c	3.4 in
Elevon Chord	$c_{elv}$	0.34 in (10% c)
Elevon Span	$S_{elv}$	5.55 in (12% R)
Solidity	$\sigma$	0.048
Lock No.	$\gamma$	5 -- 7.5
Precone	$\beta_0$	0.0
Nominal Rotor Speed	$\Omega_0$	760 RPM (12.7 Hz)
1st Flap Mode	$\omega\beta_1$	1.11/rev*
1st Lag Mode	$\omega\zeta_1$	1.08/rev*
1st Torsion Mode	$\omega\phi_1$	4.6/rev*
Airspeed	$V_{tip}, V_{elv}$	298, 224 ft/s
Dynamic Pressure	$q_{tip}, q_{elv}$	106, 60 lb/ft <sup>2</sup>
Reynolds Number	$Re_{tip}, Re_{elv}$	540,000; 400,000
Mach Number	$M_{tip}, M_{elv}$	0.27, 0.20

\*  $\theta_0=0^\circ$ , 760 RPM, in air

Table 2. Collective pitch angles for elevon phase sweep test matrix at 760 RPM (0 deg shaft angle).

$\omega/\mu$	0.1	0.2	0.3
1		0°, 2°, 3°, 4°	
2		0°, 2°, 3°, 4°	
3	2°	0°, 2°, 3°, 4°	2°
4	2°, 3°	0°, 2°, 3°, 4°	2°, 3°
5	2°	0°, 2°, 3°, 4°	2°

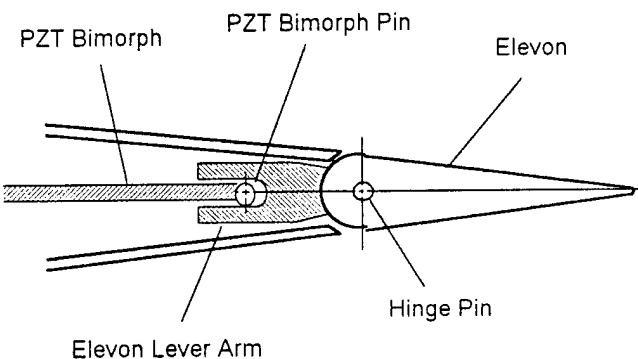


Fig. 2 Airfoil cross section, PZT bimorph bender beam and elevon lever arm mechanism.

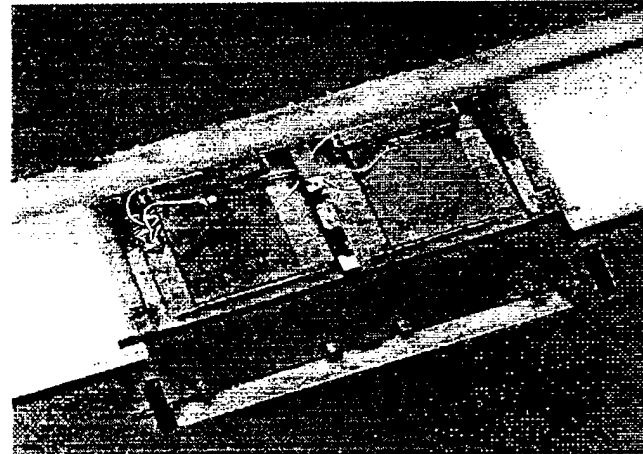


Fig. 3 Close-up of the active section with the access panel removed and the elevon disassembled.

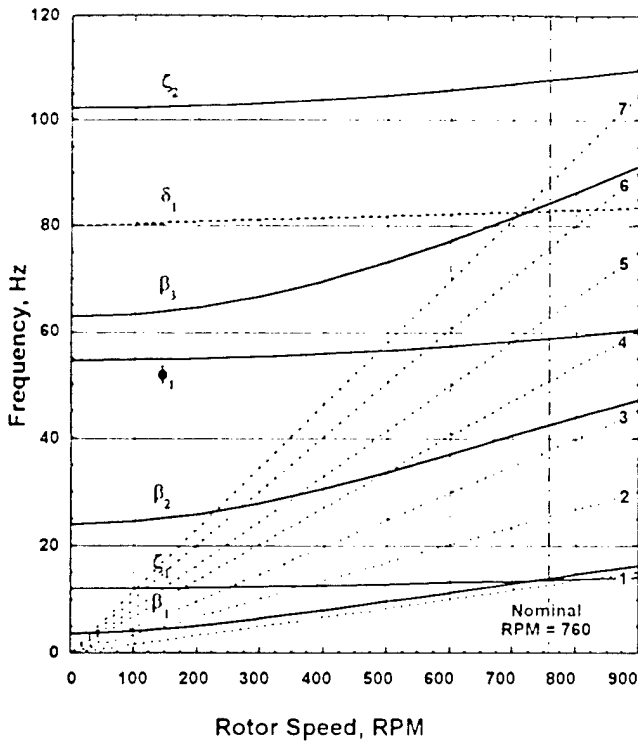


Fig. 4 Rotor blade frequencies versus rotor speed in air at zero collective pitch.

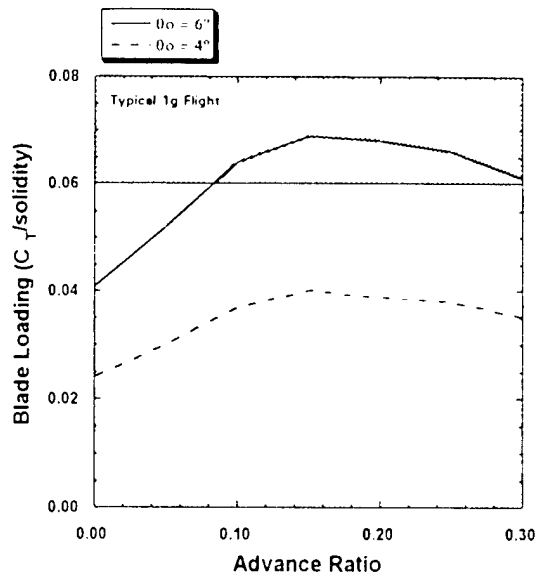


Fig. 6 Representative blade loading (760 RPM).

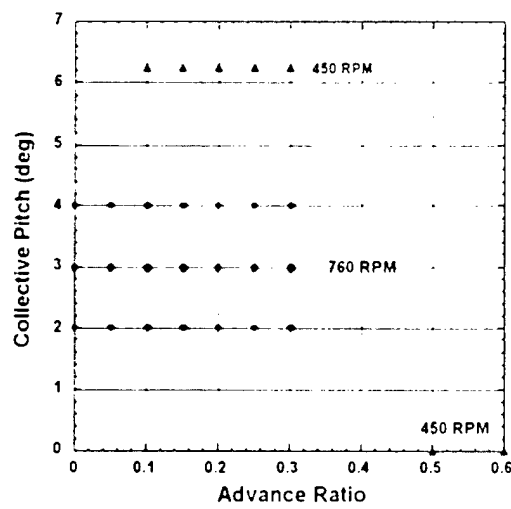


Fig. 5 Steady-state test matrix (760 and 450 RPM at 0 deg shaft angle).

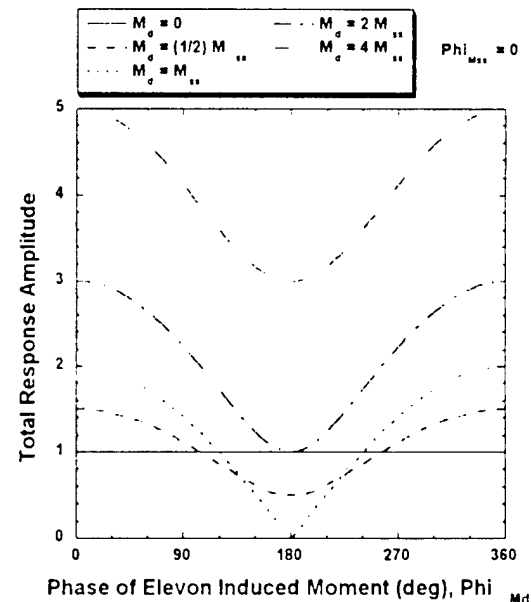


Fig. 7 Linear model of sine wave summation.

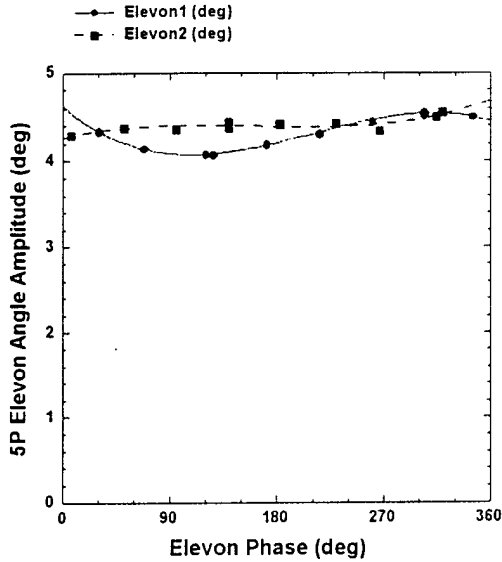


Fig. 8 Relative insensitivity of 5/rev elevon motion to elevon phase (5/rev PZT voltage).

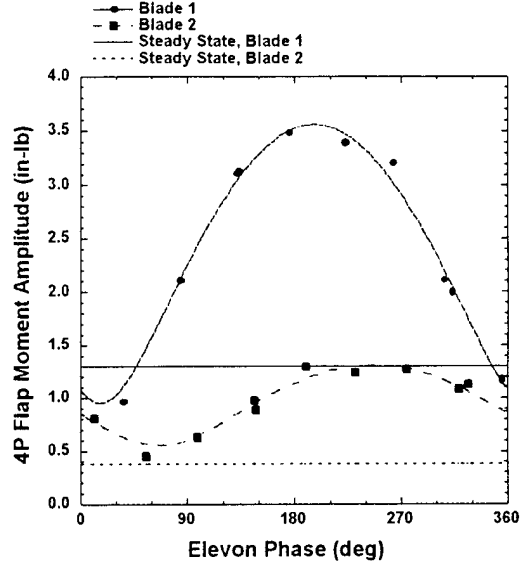


Fig. 10 Sensitivity of 4/rev flap bending moment to elevon phase (4/rev PZT voltage).

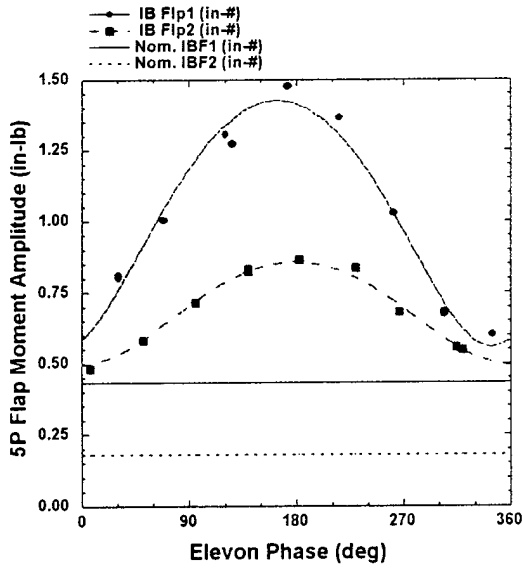


Fig. 9 Sensitivity of 5/rev flap bending moment to elevon phase (5/rev PZT voltage).

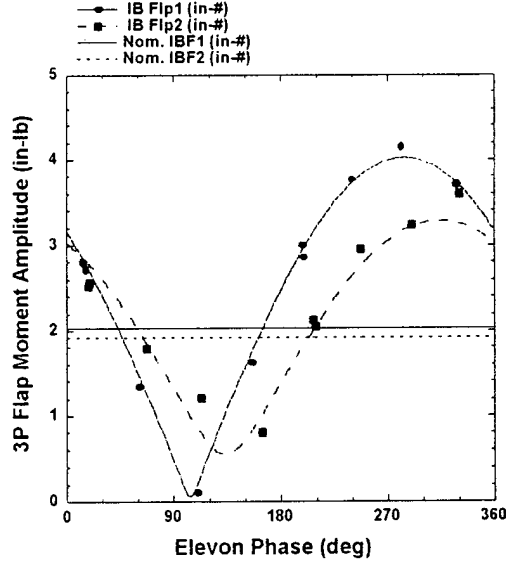


Fig. 11 Sensitivity of 3/rev flap bending moment to elevon phase (3/rev PZT voltage).

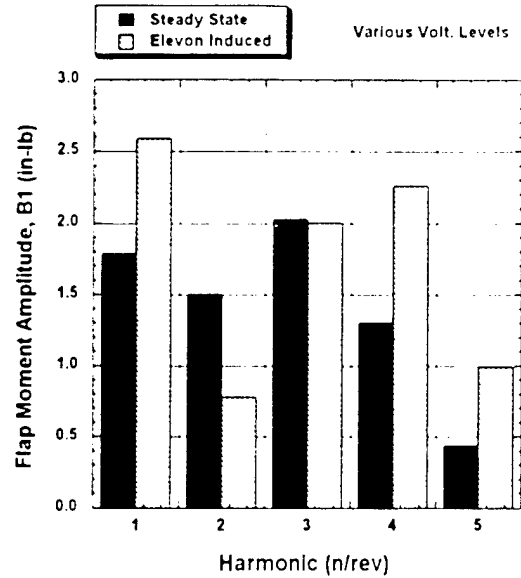


Fig. 12 Elevon effectiveness for various harmonics.

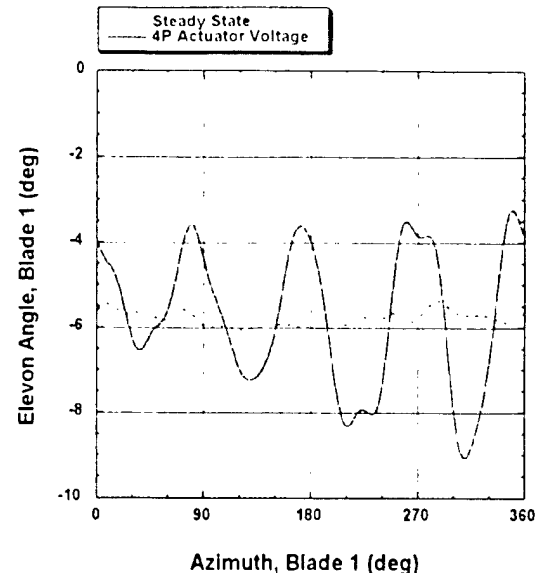


Fig. 14 Elevon motion over one rotor revolution for two cases, one with 4/rev PZT voltage and the other without.

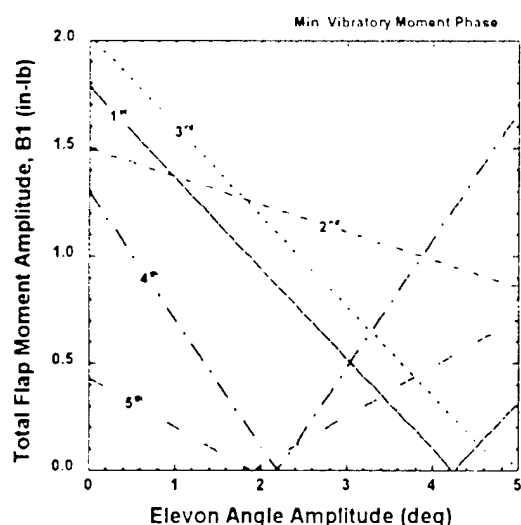


Fig. 13 Effect of elevon excitation amplitude on flap bending moment harmonics; derived from experimental measurements.

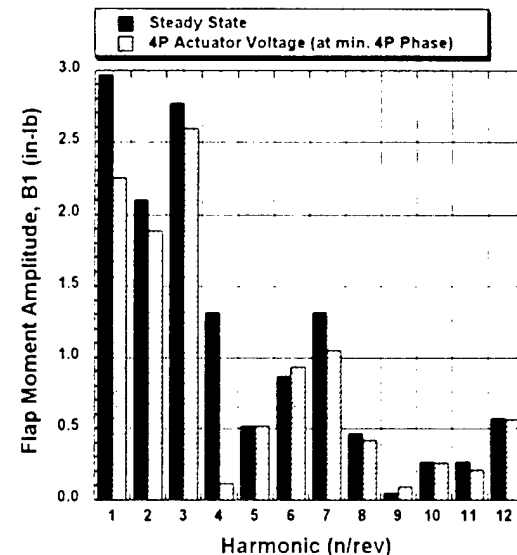


Fig. 15 Comparison of flap bending moment amplitudes for steady-state condition and case with 4/rev PZT voltage.

# Electromechanical Tuning of Self-Sensing Piezoelectric Transducers\*

Eugenio Brusa, Stefano Carabelli, Fulvio Carraro, Andrea Tonoli

Mechatronics Laboratory  
Politecnico di Torino  
Corso Duca degli Abruzzi 24, I-10129 Torino, Italy  
E-mail: tonoli@polito.it

*3rd ARO Workshop on Smart Structures*

## Introduction

The application of the self-sensing technique show to be promising for the vibration control of structures including piezoelectric transducers. Sensing and actuating functions are concentrated in the same device avoiding the inclusion in the structure of separate sensors. Due to the intrinsic colocation, the system exhibits a zero-pole alternating pattern that guarantees stability for a purely proportional output rate feedback, at least for ideal actuators.

The self-sensing operation of a piezoelectric is usually obtained by including it in the measure arm of a passive bridge network [1]. Both strain and strain rate information can be obtained from the output depending on how is devised the bridge network. The accurate balancing of the bridge is the key point to attenuate the direct link of the input on the output signal, increasing the observability and controllability of the mechanical subsystem. Nonidealities affecting the analog components of the bridge strongly degrade the performance of the system mainly for what the open loop transfer function zeros is concerned. The losses can be partly compensated by using a combination of a dummy piezoelectric and a low loss capacitor in the reference arm [2].

The use self sensing piezoelectric transducers within a simple strain rate feedback has shown to be effective for the vibration control of structures [1]. The closed loop performance achievable with balanced self-sensing networks is comparable with that obtained by means of separate sensors and actuators [3]. Better results can be achieved on the lower frequency modes with positive position feedback [1] and LQG controllers [2]. Positive position feedback and LQG show a higher robustness of the closed loop system relative to a variation of the bridge parameters from the nominal values.

Considering the model of a piezoelectric included in a bridge readout network, in the present paper is shown that the electrical poles of the bridge are shifted due to the piezoelectric interaction with the mechanical system. A design of the bridge impedances aimed to compensate the shift and to place the poles of the bridge at the same frequency leads to a balancing technique that can be referred to as "electromechanical balancing" to distinguish it from the usually adopted one (electrical balancing).

Even if lossless models show that the electromechanical balancing leads to a significant shift of the zeros from the poles, the unavoidable nonidealities strongly attenuate the differences between electrical and electromechanical balancing evidenced by lossless models. The compensation of the losses is essential to get satisfying results in both cases of electrical and electromechanical balancing. To overcome the difficulties in an analog realization of a loss compensation network using discrete electric components, the reference arm has been implemented by real-time software on a digital signal processor (DSP).

A pair of state feedback controllers have then been designed to increase the damping of the first bending mode of the beam. The controllers are based on a Luemberger's observer which estimates the mechanical modal states of lower frequency and the electrical states of the bridge network. Exploiting the compensation of the losses obtained with a proper assignment of the reference arm of the bridge, the observer has been designed based on an ideal, lossless model reduced to one and two modes, respectively.

\*This work was partially supported by the Italian Space Agency under Contract ASI 1994 RS77.

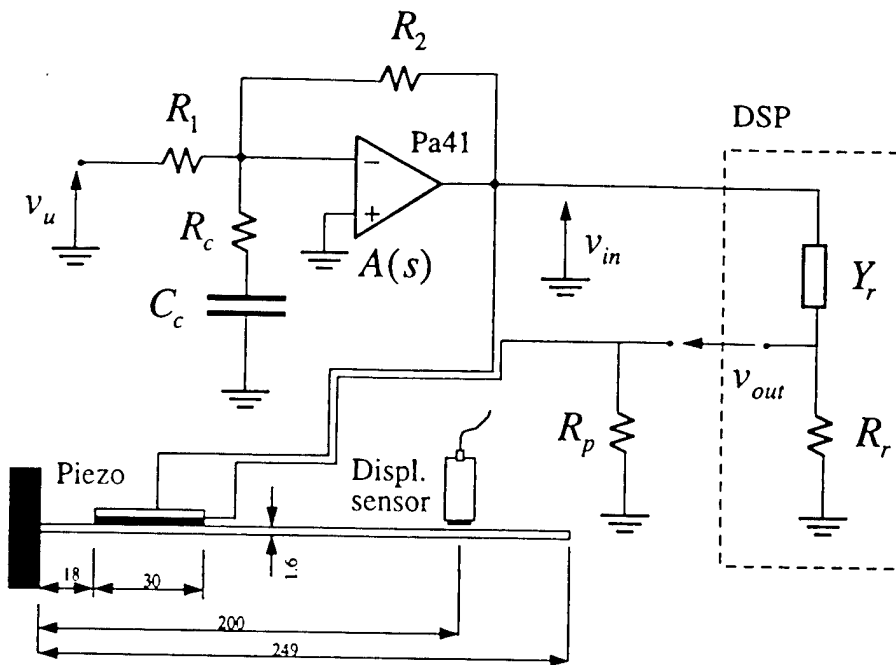


Figure 1: Beam experimental setup with bridge readout network.

## The concept of electromechanical balancing

Assuming that the piezoelectric interaction is conservative, the equations of motion of a simplified layout with a single piezoelectric are the following:

$$[M]\{\ddot{x}\} + [C]\{\dot{x}\} + [K]\{x\} + [\Theta]v_p = \{F\} \quad (1)$$

$$-[\Theta]^T\{x\} + C_p v_p = q_p \quad (2)$$

where  $[M]$ ,  $[C]$  and  $[K]$  are the mass, the damping and the stiffness matrices and  $C_p$  is the capacitance of the piezoelectric. Matrix  $[\Theta]$  is responsible of the coupling between the voltage  $v_p$  acting on the piezoelectric and the mechanical displacements  $\{x\}$ .

### Bridge balancing

Making reference to figure 1, in the case the reference admittance  $Y_r$  is that of an ideal capacitor  $C_r$ , the Laplace transform  $V_{out}$  of the output voltage  $v_{out}$  is given by:

$$V_{out} = \left( \frac{R_p C_p}{1 + R_p C_p s} - \frac{R_r C_r}{1 + R_r C_r s} \right) s V_{in} - \frac{R_p [\Theta]^T}{1 + R_p C_p s} s \{X\} \quad (3)$$

In the case of "electrical balancing", i.e.

$$C_p R_p = C_r R_r \quad (4)$$

the direct link between the output and the input  $V_{in}$  is eliminated and the output becomes proportional to the velocities  $s \{X\}$ .

By eliminating the mechanical states  $\{x\}$  from equations 1 and 2, the coupled electromechanical dynamics of the bridge is determined by the poles and the zeros of the input-output transfer function. Considering the piezoelectric as an electric dipole its admittance  $Y_p = I_p/V_p$  is obtained as:

$$Y_p = \left[ C_p + [\Theta]^T ([M] s^2 + [C] s + [K])^{-1} [\Theta] \right] s \quad (5)$$

Assuming that the high voltage amplifier is a pure gain and using Kirchoff's laws, the transfer function between the input  $V_{in}$  and the output  $V_{out}$  is:

$$\frac{V_{out}}{V_{in}} = \frac{R_r Y_{Cr} - R_p Y_p}{(1 + R_r Y_{Cr})(1 + R_p Y_p)} \quad (6)$$

Being  $n$  the number of the mechanical degrees of freedom of the system, the bridge exhibits  $2n + 2$  poles. Two of them are pure real, while  $2n$  are complex and conjugate. One of the real poles ( $s_r$ ) is uncoupled from the mechanical behaviour and can be associated to the reference arm:

$$s_r = -1/(R_r C_r) \quad (7)$$

The remaining  $2n + 1$  poles are given by the measure arm of the bridge. They are the roots  $s_p$  of the following equation:

$$1 + R_p C_p s_p + R_p [\Theta]^T ([M] s_p^2 + [C] s_p + [K])^{-1} [\Theta] s_p = 0 \quad (8)$$

If the electromechanical interaction is null ( $[\Theta] = 0$ ) equation 8 reduces to  $s_p = -1/(R_p C_p)$  and the mechanical states are unobservable from  $V_{out}$ . By converse, if  $[\Theta] \neq 0$ , the poles of the measure arm are  $2n$  complex conjugate and one real  $s_{pRe}$ . Exploiting the uncoupling of the reference from the measure arm of the bridge, it is possible to design  $R_r$  and  $C_r$  such that

$$s_r = s_{pRe} \quad (9)$$

The condition of equation 9 is indicated hereafter as "electromechanical balancing".

## Test beam

The aluminum alloy cantilever beam of figure 1 has been built for the experimental validation of the proposed balancing. The measured bending modes of lower frequency in open loop conditions are 20.8, 122.44, 332.5 650.3 and 1087 Hz with the modal damping values of 0.31, 0.21, 0.21, 0.18 and 0.22 %, respectively.

A PCE5 square piezoceramic, 30 mm wide and 0.3 mm thick, is bonded using AE10 epoxy resin. The input voltage  $v_{in}$  is supplied by an Apex PA41 high voltage operational amplifier. A voltage divider with output  $v_1$  avoids overvoltage on the DSP input circuitry while two unity gain buffers avoid loading of the bridge. The reference arm is software implemented within the DSP sampling the voltage  $v_1$ .

Two different kind of models have been used to describe the system: a complete one (analysis model) for simulation and analysis and a highly reduced one (design model) for the dual design of the observer and state feedback.

The analysis model is based on a modal reduction of the beam which retains 20 bending modes along with the electrical dynamics of the amplifier and of the components of the bridge. The model of the amplifier includes the characteristic open loop pole at low frequency of the PA41, its output resistance and the compensation network  $R_c C_c$ . The leakage and the hysteretic behavior of the piezoelectric are included as a loss resistor  $R_{lp}$  in parallel with a complex capacitance:

$$C_p = |C_p| (\cos \theta - j \sin \theta) \quad (10)$$

The design model is based on a modal reduction retaining a small number of modal co-ordinates (2 to 5 modes). All nonidealities of the piezoelectric and of the high voltage amplifier are not accounted for. This corresponds with the assumption that all nonidealities of the bridge are closely compensated.

## Open loop experimental results

The upper curves of figures 2 and 3 show that in the case an ideal capacitor is implemented within the reference arm of the bridge, the measured transfer functions show negligible differences between the electrical and electromechanical balancing. The zeros are damped out because of the small phase and amplitude variations between the two arms of the bridge induced by the losses at the antiresonance frequencies. The effect of the losses can be compensated by including them as a parallel resistor in the reference arm

$$Y_{lr} = j\omega C_r + 1/R_{lr} \quad (11)$$

To obtain a compensation over a wide frequency range of the hysteretic losses of equation 10, resistance  $R_{lr}$  should include a frequency dependent term. Due to the difficulties in implementing a frequency dependent resistance, a frequency independent value has been included. The loss compensation can then be achieved at that single frequency while in the rest of the frequency range it is just approximated.

The extreme sensitivity of the system to the electric parameters of the piezoelectric makes necessary their identification starting from the experimental response. The parameters of the piezoelectric have been determined by using the following procedure:

1. The nominal capacitance  $|C_p|$  of the piezoelectric has been implemented as the reference capacitor  $C_r$ . The parallel loss  $R_{lp}$  has been initially set according to the loss data  $\theta$  and  $R_{lp}$  available on the piezoelectric datasheets. The system transfer function has been experimentally measured in electrical balancing conditions.
2. The piezoelectric capacitance  $|C_p|$  and its loss parameters  $\theta$  and  $R_{lp}$  have been identified by minimizing the least square difference between the theoretical and the measured transfer functions.
3. The identified values have been employed to design the admittance  $Y_{lr}$  to be implemented as reference arm in the DSP.

In the case of the test beam the identification gave the following results:  $|C_p| = 27.4 \text{ nF}$ ,  $\theta = 6 \cdot 10^{-3} \text{ rad}$  and  $R_{lp} = 15.1 \text{ M}\Omega$ . At the first resonance frequency these values are equivalent to  $C_r = 27.4 \text{ nF}$  and to  $R_{lr} = 11.4 \text{ M}\Omega$ . Figure 2 relative to the electrical balancing ( $R_r = R_p$ ) shows that the compensation of the losses decreases the damping of the antiresonance and makes the experimental transfer function close to that predicted by the lossless model.

Including the identified values for the piezoelectric in the analysis model, electromechanical balancing condition of equation 9 are met for  $R_r = 1.02 \cdot R_p$ . The approximate conditions of electromechanical balancing could not be reached with the previously identified losses. The loss compensation resistor  $R_{lr}$  has been adjusted to the value of  $9.84 \text{ M}\Omega$  to obtain figure 3. The considerable shift of the zero frequencies predicted by the model are just roughly approximated during experiments even with elaborate adjustment procedures. The loss compensation demonstrates in this case to be a much more difficult task probably because of the higher significance of the losses in proximity of the antiresonance.

Taking into account of equation 5, the admittance of the piezoelectric increases by increasing the operating frequency while the leakage losses in parallel to it remain approximately constant and thus decreasing their relative importance. In this condition, the electromechanical balancing has shown to be easier to approximate experimentally. A series of measurements has been performed on the beam in open loop conditions in the frequency range  $0.5 \div 1 \text{ kHz}$  corresponding to the fourth bending mode. The parameters of the piezoelectric have been identified following the above outlined procedure and resulted to be the following:  $|C_p| = 25.6 \text{ nF}$ ,  $\theta = 2.1 \cdot 10^{-3} \text{ rad}$  and  $R_{lp} = 2.7 \text{ M}\Omega$ . The corresponding values implemented in the reference arm are  $C_r = 25.6 \text{ nF}$  and  $R_{lr} = 1.7 \text{ M}\Omega$ .

Figures 4 and 5 show that the electromechanical balancing is more effectively approached in practice even without any further tuning of the loss resistance  $R_{lr}$ . The value of the reference resistor is kept at  $R_r = 1.02 \cdot R_p$ .

## Control system design and closed loop results

The goal of the closed loop control is to add damping to the first bending mode of the beam. Two controllers are designed with a classical dual pole placement for the state feedback and the observer. The first controller is obtained including the first two mechanical modes in the observer, the second includes the first mode only. The state feedback mainly attempts to increase (more than 10 times) the damping of the first mode while leaving almost unchanged the others. The observer natural frequencies are placed only slightly higher in frequency than those of the open loop system. Two additional poles are included in the observers model to account for the electrical dynamics of the bridge. In practice, they make the regulator to roll off at frequency higher than the third mode and so gain stabilize the higher modes. To be noted that the third mechanical mode is almost unobservable and uncontrollable due to the spatial filtering properties of the actual location of the piezoelectric on the beam.

The resulting regulators are discretized using a bilinear transformation and implemented on a DSP board equipped with a Texas Instruments TMS320C32 floating point DSP sampling at 10 kHz. The DSP board is interfaced to the Matlab computing environment [4] for rapid prototyping and data collection.

The closed loop tests are meant to show the influence of the balancing configuration adopted for the sensing bridge when the same controller is used to close the feedback loop. The experimental results are obtained exciting the system with a sinusoidal voltage command at the first mode resonant frequency. The achieved closed loop damping is obtained measuring the displacement during the free response after the excitation is switched off.

With the single mode observer and the electrically balanced bridge the first mode is stiffened to 21.2 Hz increasing its damping nearly 3 times from 0.3 to 0.9 % (figure 8). Under electromechanical balancing, the first mode is moved to 21.5 Hz and its damping is increased almost 10 times to 2.95 % (figure 9). With the two modes observer and the electromechanical balancing the results are almost identical with a damping of 2.99 % (figure 7) while with the electrically balanced bridge the first mode damping increases to 1.41 % (figure 6).

## Conclusions

The analysis of piezoelectric transducers included in a bridge circuit has been studied taking into account of the dynamic coupling between mechanical and electrical subsystems due to the piezoelectric effects. The analytical model evidences that due to the electromechanical interaction the open loop poles of the bridge network are shifted at a lower frequency relative to the case no coupling occurs. A balancing condition referred to as "electromechanical balancing" is introduced placing the electric dynamics of the two arms of the bridge at the same frequency. Relative to the usually adopted  $RC$  balancing (electrical balancing), this allows to significantly shift the antiresonances towards higher frequencies while preserving the pole-zero pattern typical of colocated systems.

In order to obtain experimentally the performances predicted by the theoretical models the compensation of the nonidealities within the bridge has shown to be of essential importance. In a first step the parameters of the piezoelectric has a lossy and hysteretic capacitor have been identified starting from experimental data, then the reference arm of the bridge has been designed to compensate the nonidealities of the piezoelectric. To avoid the difficulties in the analog realization of the reference arm, it has been implemented within a digital signal processor. The open loop results show that the loss compensation can be achieved in the frequency range of the first mode only in part after a fine tuning.

The operation in the frequency range of the fourth mode makes the system less sensitive to the dielectric losses within the piezoelectric. Both the electrical and the electromechanical balancing are more closely approximated in this case by the experimental system.

A pair of observer based state feedback controllers have been designed to increase the damping on the first mode of the test beam. As the loss compensation implemented in DSP make the system perform as if the lossless were strongly attenuated, a Luemburger's state observer has been designed based on a lossless model. The experiments performed on the beam structure showed that a shift from electrical to electromechanical balancing leads to an increase in the closed loop damping of the first mode for both controllers. Moreover, in the case of electromechanical balancing, the lower order controller (4th order) nearly achieve the same results of the higher order controller (6th order).

## References

- [1] J. Dosch and D. Inman, "A self-sensing piezoelectric actuator for collocated control," *Journal of Intelligent Material Systems and Structures*, vol. 3, pp. 166–185, January 1992.
- [2] E. Anderson and N. Hagood, "Simultaneous piezoelectric sensing/actuation : Analysis and application to controlled structures," *Journal of Sound and Vibration*, vol. 174, no. 5, pp. 617–639, 1994.
- [3] S. Yang and C. Jeng, "Structural vibration suppression by concurren piezoelectric sensor and actuator," *Journal of Smart Materials and Structures*, vol. 5, pp. 806–813, 1996.
- [4] S. Carabelli, "MatDSP – Matlab and Simulink interface to floating point DSP systems," in *Matlab Connections*, (The MathWorks Inc.), p. 43, <http://www.mathworks.com/connections/toc.html>, Summer 1996. Third-party products.

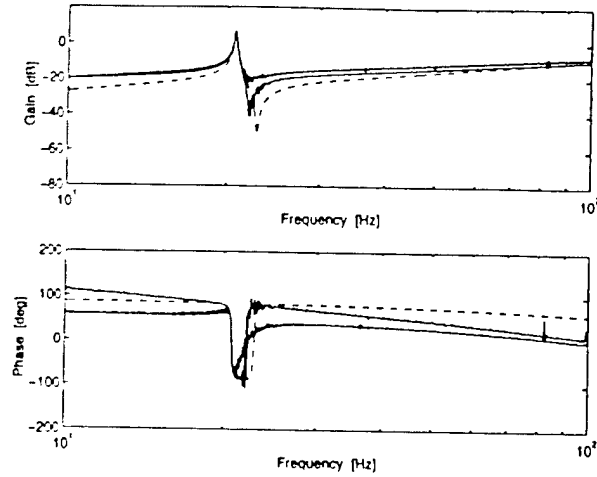


Figure 2: Electrical balancing: transfer functions of lossless theoretical model (dashed) and experimental with and without loss compensation (solid) in the first mode frequency region.

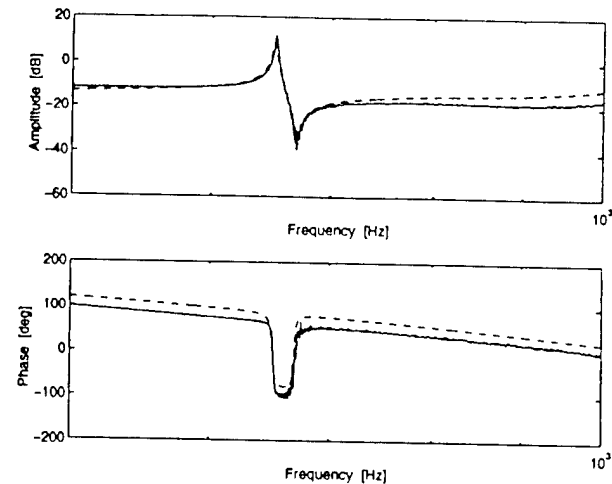


Figure 4: Electrical balancing: transfer functions of lossless theoretical model (dashed) and experimental with loss compensation (solid) in the fourth mode frequency region.

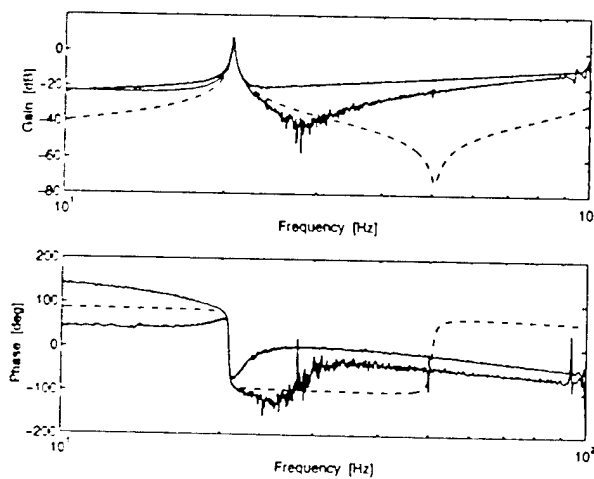


Figure 3: Electromechanical balancing: transfer functions of lossless theoretical model (dashed) and experimental with and without loss compensation (solid) in the first mode frequency region.

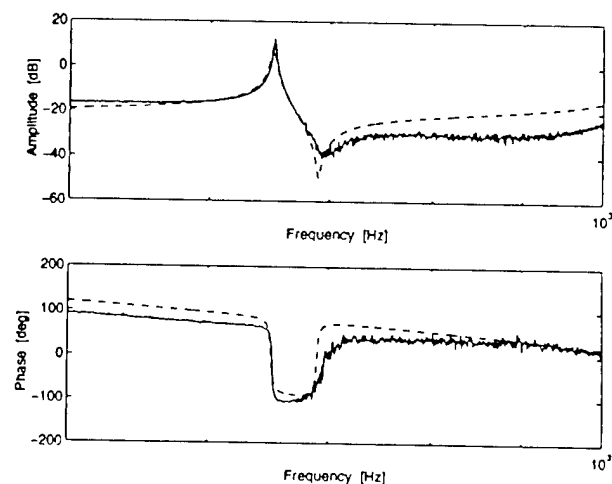


Figure 5: Electromechanical balancing: transfer functions of lossless theoretical model (dashed) and experimental with loss compensation (solid) in the fourth mode frequency region.

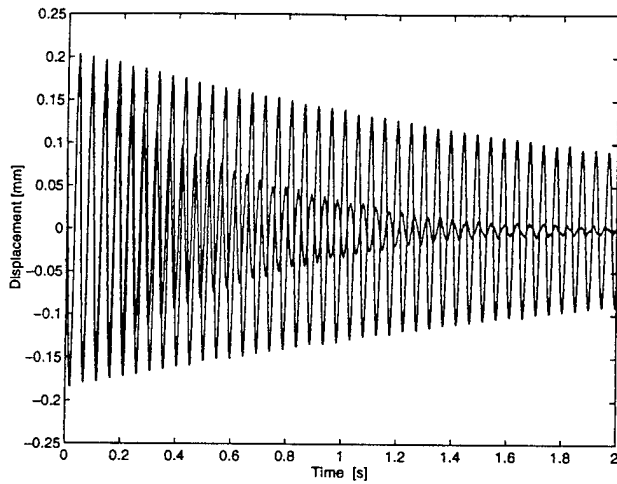


Figure 6: Electrical balancing: open versus closed loop free response with two modes observer based controller.

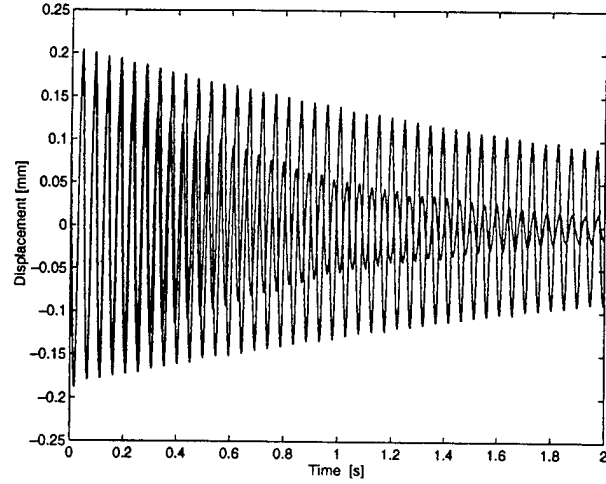


Figure 8: Electrical balancing: open versus closed loop free response with single mode observer based controller.

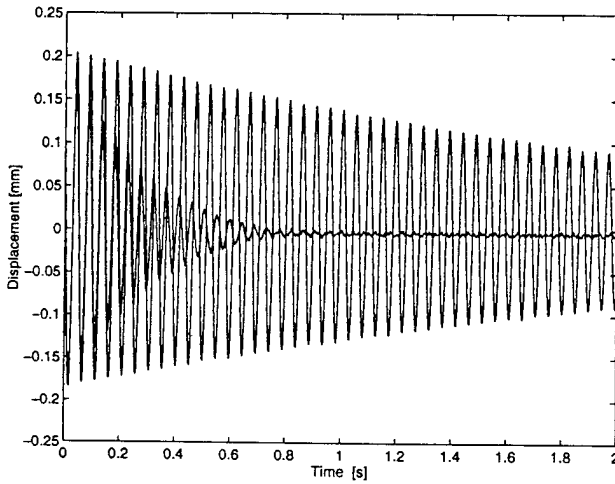


Figure 7: Electromechanical balancing: open versus closed loop free response with two modes observer based controller.

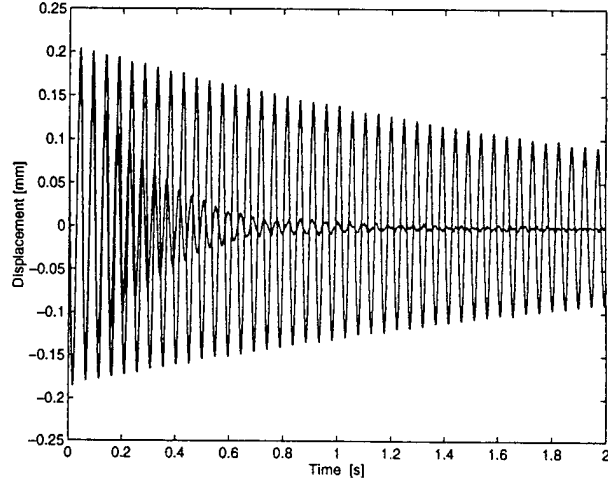


Figure 9: Electromechanical balancing: open versus closed loop free response with single mode observer based controller.

# **CONTROLLABLE RESONANCE IN STRUCTURES AND FLUIDS AND THE RECTIFICATION OF OSCILLATORY MOTION**

by

Prof. Roger W. Brockett  
Division of Engineering and Applied Sciences  
Harvard University  
Cambridge, Massachusetts 02138  
Phone: (617) 495-3922  
Fax: (617) 496-6404  
E-Mail: brockett@framian.harvard.edu

## **ABSTRACT**

In this talk we will discuss systematic approaches for the analysis and design of structures that can be excited so as to resonate in two or more modes. We will emphasize structures that can be easily driven by piezoelectric and/or magnetostrictive materials. The idea of rectification will be introduced and the properties of high-frequency mechanical rectifiers will be discussed. Time permitting, there will be a discussion of fluid systems that rectify vibratory motion.

## Actuator Limited Multivariable Controllers for Smart Structural Systems

Monika Jadi, Sridhar Sana, and Vittal Rao

Department of Electrical Engineering and  
Intelligent Systems Center  
University of Missouri-Rolla, Rolla, MO 65409

[ Rao, Ph: 573-341-6371, Fax: 573-341-6512, e-mail:rao@isc.umr.edu]

### Abstract

In recent studies, many robust controllers have been successfully designed and implemented on smart structural systems. However the actuators limits ( available control force, bandwidth, etc.) are not integrated with the controller design methodologies. It is well known that actuator limits can introduce performance degradation and possible instability in the closed loop systems. It is difficult to incorporate the actuator limits in the design of robust controllers using LQG/LTR and H<sub>2</sub>/H<sub>inf</sub> methods. In this paper, we propose to develop a actuator limited multivariable controller using Linear Matrix Inequalities(LMI) formulation. Availability of advanced computational techniques for solving convex optimization problems in LMI formulation, makes this approach very attractive.

In this study, we have investigated a two different techniques for designing actuator limited controllers for smart structural systems. In the first method, we determined the minimum amount of control effort required for a specified performance of the system by using LMI formulation. We then modified these results for maximization of the performance for a given limit on the actuator forces. In the second method we design a robust controller to meet the desired performance in the absence of actuator limits. In order to provide a graceful degradation of performance due to actuator limits, an additional compensator will be augmented to the nominal controller.

The proposed design methodology is demonstrated by designing actuator limited controllers on a two input-two output experimental test article. The designed controllers were implemented using d-space system. The open-loop and closed-loop response of the structure are verified by using experimental results. The control effort required for the implementation of the robust controllers is verified to be within the limits of the actuators. The robustness properties of the controller are also verified. The experimental results will be presented in the workshop.

University of Missouri-Rolla



# ACCURATOR LIMITED MULTIVARIABLE CONTROLLERS FOR SMART STRUCTURAL SYSTEMS

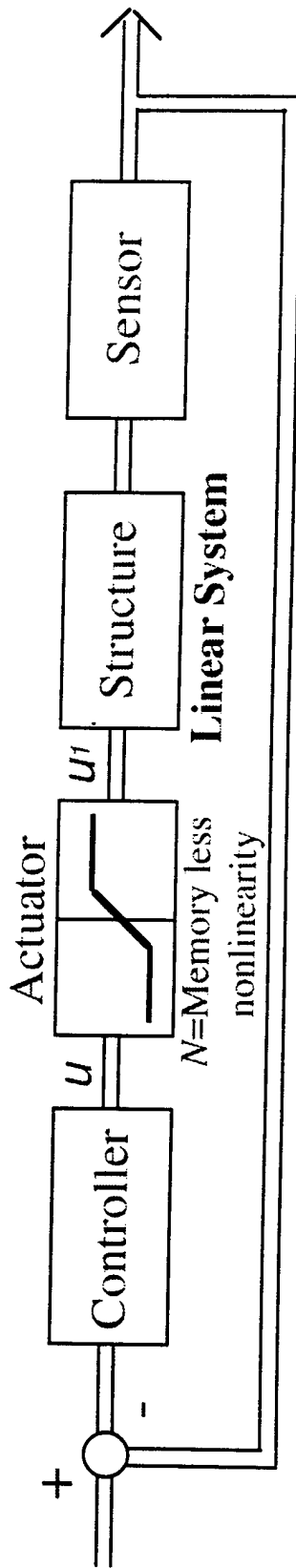
*Sridhar Sana, Monika Jadi and Vittal S. Rao*  
Department of Electrical Engineering and  
Intelligent Systems Center  
University of Missouri-Rolla

Research Sponsored by the Army Research Office

Third AFRO Workshop on Smart Structures  
Blacksburg, VA August 27-29, 1997



## Actuator-Limited Multivariable Controllers



- The limitations cause the actual structure input,  $u'$ , to be different from the controller output,  $u$ .
- In the absence of actuator constraints, the controller stabilizes and provides acceptable performance.
- Actuator constraints (nonlinearities) can produce
  - significant performance degradation
  - possible instability (limit cycles) in the control system.





# Linear Matrix Inequalities (LMIs)

What is an LMI ?

An LMI is a constraint of the form

$$L(x) < 0 \quad \text{-- (1)}$$

where  $L(x)$  is

- a symmetric matrix
- depends *affinely* on vector  $x \in R^p$  of unknown scalar variables ( called *decision variables* )

A set of LMIs,  $L_i(x) < 0 ; i = 1, 2, 3, \dots M$ , in the same decision variables can be treated as a single LMI as follows

$$L(x) = \text{Diag}((L_1(x), L_2(x), \dots, L_M(x))) < 0 \quad \text{-- (2)}$$

What does “solving an LMI” involve ?

- Finding some *feasible* vector  $x$  for which eq(2) holds.
- As  $L(x)$  depends affinely on  $x$ , finding a solution is a convex optimization problem.

## Schur's Complement Lemma

For any matrices  $\Phi_{11}$ ,  $\Phi_{12}$  and  $\Phi_{22}$  where  $\Phi_{11}$  and  $\Phi_{22}$  are symmetric, the following are equivalent.



## The Three Generic LMI problems

(1) Feasibility Problem :

To find an  $x$  such that it satisfies the LMI

$$L(x) < 0 \quad \text{-- (6)}$$

or to determine that the LMI is infeasible.

(2) Linear Objective Minimization Problem :

Minimize  $c^T x$  subject to the LMI  $A(x) < 0$ .

(3) Generalized Eigenvalue Problem :

Minimize  $\lambda$  subject to

$$A(x) < \lambda B(x)$$

$$B(x) > 0$$

$$C(x) < 0$$

### Examples in Control Theory :

(i) LQG or  $H_2$  performance :

Finding the LQG or  $H_2$  performance of a stable LTI system given by

$$\dot{x} = Ax + Bw ; \quad y = Cx$$

## Multi-Objective $H_\infty$ Synthesis

In many real-world applications, standard  $H_\infty$  synthesis cannot adequately capture all design specifications. For instance, noise attenuation or regulation against random disturbances are more naturally expressed in LQG terms. Similarly, pure  $H_\infty$  synthesis only enforces closed-loop stability and does not allow for direct placement of the closed-loop poles in more specific regions of the left-half plane. Since the pole location is related to the time response and transient behavior of the feedback system, it is often desirable to impose additional damping and clustering constraints on the closed-loop dynamics. This makes multi-objective synthesis highly desirable in practice, and LMI theory offers powerful tools to attack such problems.

Mixed  $H_2/H_\infty$  synthesis with regional pole placement is one example of multi-objective design addressed by the LMI Control Toolbox. The control problem is sketched in Figure 5-5. The output channel  $z_\infty$  is associated with the  $H_\infty$  performance while the channel  $z_2$  is associated with the LQG aspects ( $H_2$  performance).

Denoting by  $T_\infty(s)$  and  $T_2(s)$  the closed-loop transfer functions from  $\omega$  to  $z_\infty$  and  $z_2$ , respectively, we consider the following multi-objective synthesis problem:

### Multi-Objective $H_\infty$ Synthesis

be state-space realizations of the plant  $P(s)$  and controller  $K(s)$ , respectively, and let

$$\begin{cases} \dot{x}_{cl} = A_{cl} x_{cl} + B_{cl} w \\ z_\infty = C_{cl1} x_{cl} + D_{cl1} w \\ z_2 = C_{cl2} x_{cl} + D_{cl2} w \end{cases}$$

be the corresponding closed-loop state-space equations.

Our three design objectives can be expressed as follows:

- **$H_\infty$  performance:** the closed-loop RMS gain from  $w$  to  $z_\infty$  does not exceed  $\gamma$  if and only if there exists a symmetric matrix  $\mathcal{X}_\infty$  such that

$$\begin{pmatrix} A_{cl}\mathcal{X}_\infty + \mathcal{X}_\infty A_{cl}^T & B_{cl} & \mathcal{X}_\infty C_{cl1}^T \\ B_{cl}^T & -I & D_{cl1}^T \\ C_{cl1}\mathcal{X}_\infty & D_{cl1} & -\gamma^2 I \end{pmatrix} < 0$$

$$\mathcal{X}_\infty > 0$$

- **$H_2$  performance:** the  $H_2$  norm of the closed-loop transfer function from  $w$  to  $z_2$  does not exceed  $\nu$  if and only if  $D_{cl2} = 0$  and there exist two symmetric matrices  $\mathcal{X}_2$  and  $Q$  such that

$$\begin{pmatrix} A_{cl}\mathcal{X}_2 + \mathcal{X}_2 A_{cl}^T & B_{cl} \\ B_{cl}^T & -I \end{pmatrix} < 0$$

$$\begin{pmatrix} Q & C_{cl2}\mathcal{X}_2 \\ \mathcal{X}_2 C_{cl2}^T & \mathcal{X}_2 \end{pmatrix} > 0$$

$$\text{Trace}(Q) < \nu^2$$

- **pole placement:** the closed-loop poles lie in the LMI region

$$\mathcal{D} = \{z \in \mathbb{C} : L + Mz + M^T \bar{z} < 0\}$$

with  $L = L^T = [\lambda_{ij}]_{1 \leq i,j \leq m}$  and  $M = [\mu_{ij}]_{1 \leq i,j \leq m}$  if and only if there exists a symmetric matrix  $\mathcal{X}_{\text{pol}}$  satisfying

$$[\lambda_{ij}\mathcal{X}_{\text{pol}} + \mu_{ij}A_{cl}\mathcal{X}_{\text{pol}} + \mu_{ji}\mathcal{X}_{\text{pol}}A_{cl}^T]_{1 \leq i,j \leq m} < 0$$

$$\mathcal{X}_{\text{pol}} > 0$$



# Limit Protected Multivariable Controller design using LMIs

## Problem Statement

To design a copensator in addition to a Nominal Controller which ensures *graceful degradation* of the performance upon limitation on the multivariable control input.

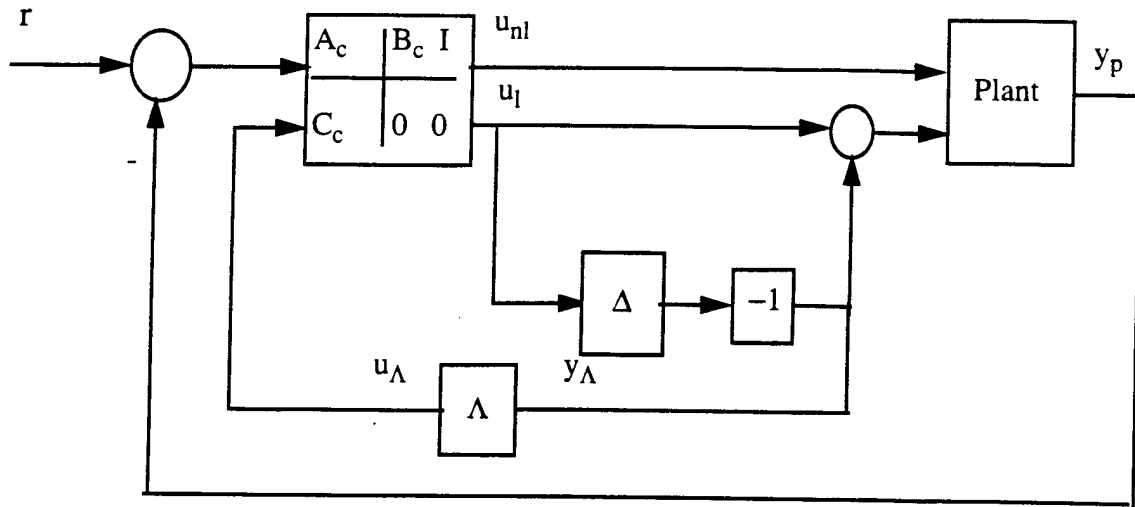
### Marcopoli and Phillips Method :

#### Assumptions and Terminology

- The nominal controller ( $A_C, B_C, C_C, D_C$ ) is strictly proper i.e  $D_C = 0$
- The multivariable nonlinearity  $N$  is decoupled, sector bounded and possibly time varying. Hence the nonlinearity can characterised as

$$N(u, t) = \begin{bmatrix} n_1(u_1, t) & & & 0 \\ & n_2(u_2, t) & & \\ 0 & & \dots & \\ & & & n_l(u_l, t) \end{bmatrix} \quad -- (12)$$

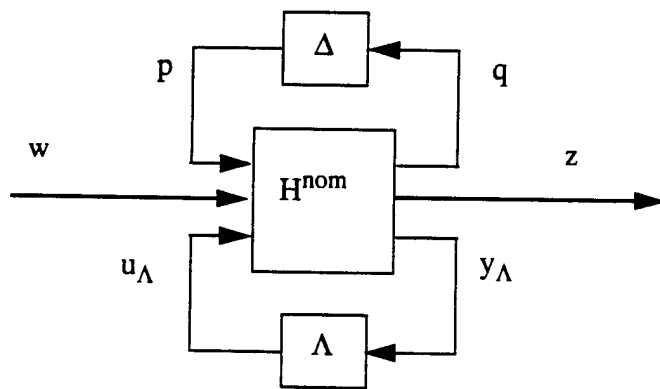
where  $l$  is the number of control inputs and  $n_j(u_j, t)$  belongs to the sector  $[0,1]$ .



By representing the nonlinearity as a perturbation  $\Delta = I - N$ , the nonlinear operator  $\Delta$  can be expressed as,

$$\Delta(q, t) = 1 - \begin{bmatrix} 1 - n_1(u_1, t) & & & 0 \\ & 1 - n_2(u_2, t) & & \\ 0 & & \dots & \\ & & & 1 - n_l(u_l, t) \end{bmatrix} \quad -- (13)$$

the limit protection control system can be equivalently represented in the LFT form as,





Equivalently the absolute stability can be defined as finding a matrix  $P = P^T$  such that,

$$A_i^T P + PA_i < 0 \text{ for } i = 1, 2, \dots, 2^l \quad -- (18)$$

### Limit Protection Design:

#### Problem Statement :

Determination of  $\Lambda$  for providing desired performance in the presence of actuator limitation.

Two approaches have been considered here for the limit protection design.

#### Design by $H_\infty$ norm minimization :

From the LFT formulation of the limit protected control system, the  $L_2$  gain of the operator having input  $w$  and output  $z$  is given by

$$\sup_{w \neq 0, \|w\|_2 < \infty} \frac{\|z\|_2}{\|w\|_2} \quad -- (19)$$

The  $L_2$  gain is less than  $\gamma$  if,

$$\begin{bmatrix} A_i^T P + PA_i + C_{zi}^T C_{zi} & PB_w + C_{zi}^T D_{zw} \\ B_w P + D_{zw} C_{zi} & -\gamma^2 I + D_{zw}^T D_{zw} \end{bmatrix} < 0, \text{ for all } i = 1, 2, \dots, 2^l \quad -- (20)$$

To obtain *graceful degradation* of performance, it is required that  $\gamma$  is minimized subject to the above constraints by optimizing with respect to  $\Lambda$ .



Design by Maximization of decay rate :

The approach considered here is that of Maximization of the decay rate ( $\alpha$ ) of the output of the plant.

Using the result of absolute stability, the problem now becomes

minimize  $\frac{1}{\alpha}$

$$\text{subject to } A_i^T P + PA_i + 2\alpha P < 0 ; P > 0 \quad -- (22)$$

where  $A_i = A_{k_i} - B_u \Lambda K_i C_q$  and  $A_{k_o} = A + B_p K_i C_q$

or equivalently

minimize  $\frac{1}{\alpha}$  subject to

$$2P < \frac{1}{\alpha}(-A_{k_i}^T P - PA_{k_i} + (B_u \Lambda K_i C_q)^T P + PB_u \Lambda K_i C_q) ; P > 0 \quad -- (23)$$

This is a GEVP problem for a Bilinear Matrix Inequality (BLMI) for which solution has to be found by iteration

Iterative Procedure :

Start : Initialize  $\Lambda$  to 0 and  $\alpha$  to 0

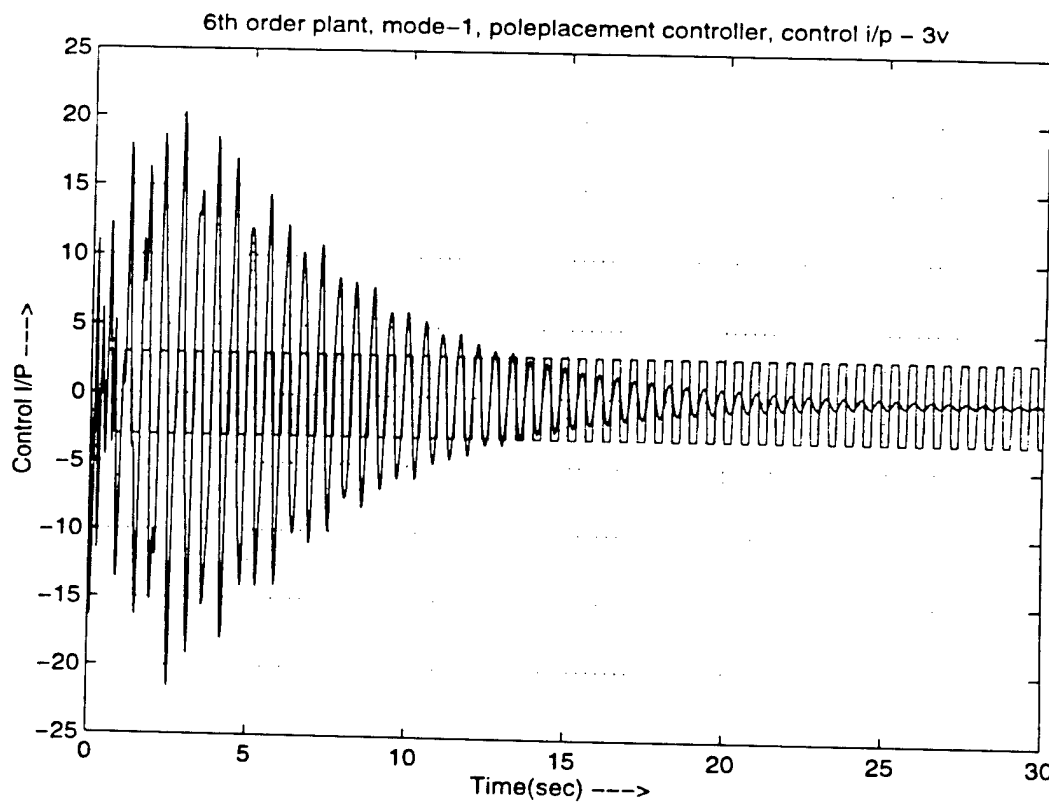
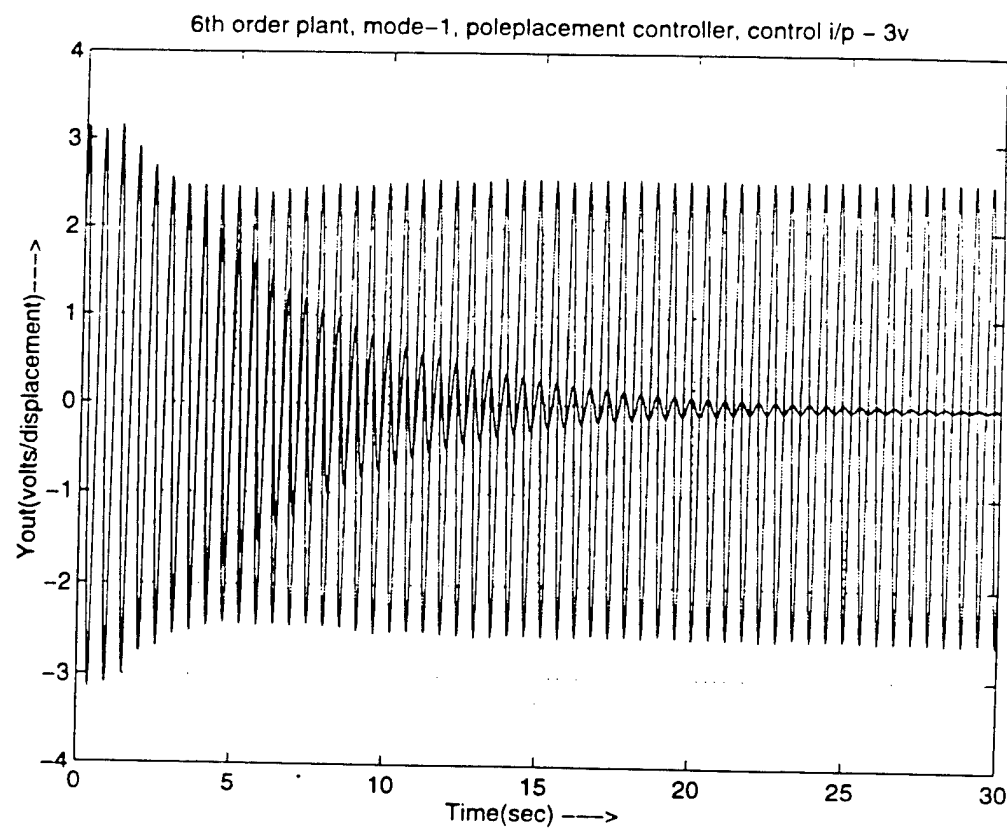
Step 1 : Fix  $\Lambda$  and  $\alpha$ ; solve for  $P$

Step 2: Fix  $P$  and solve for  $\Lambda$ , while minimizing  $\alpha$ .

The iterations are continued until there is convergence. The iterative procedure can alternatively start from initializing  $P$  with some feasible starting value.

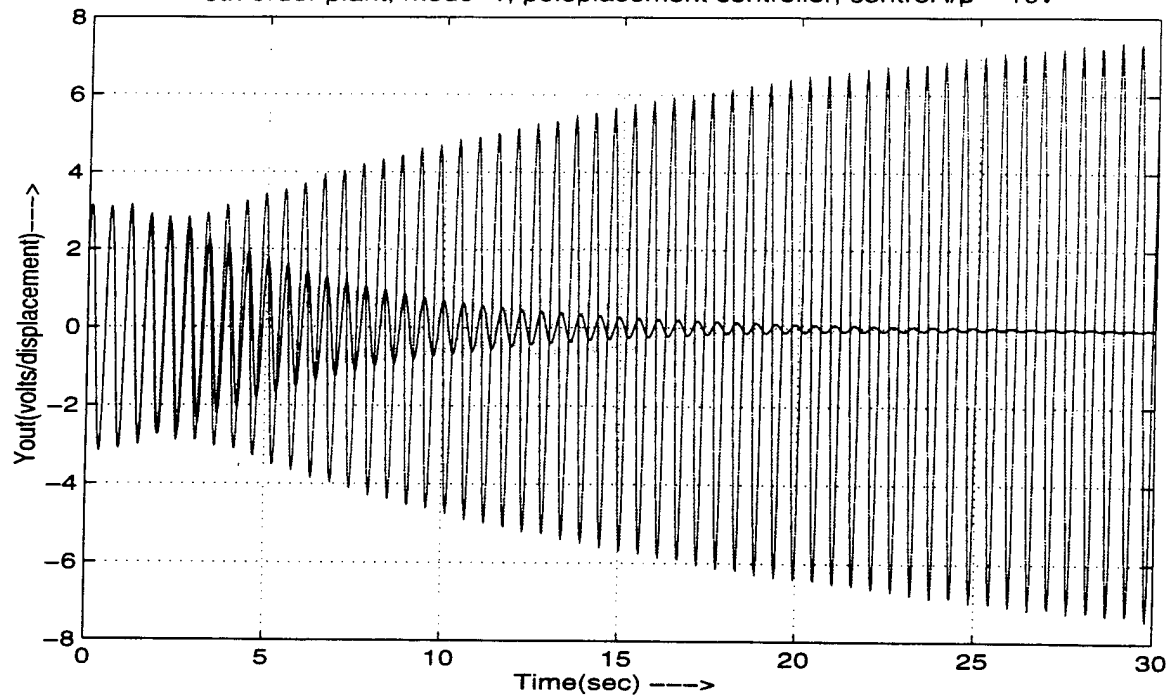


## Simulation Results

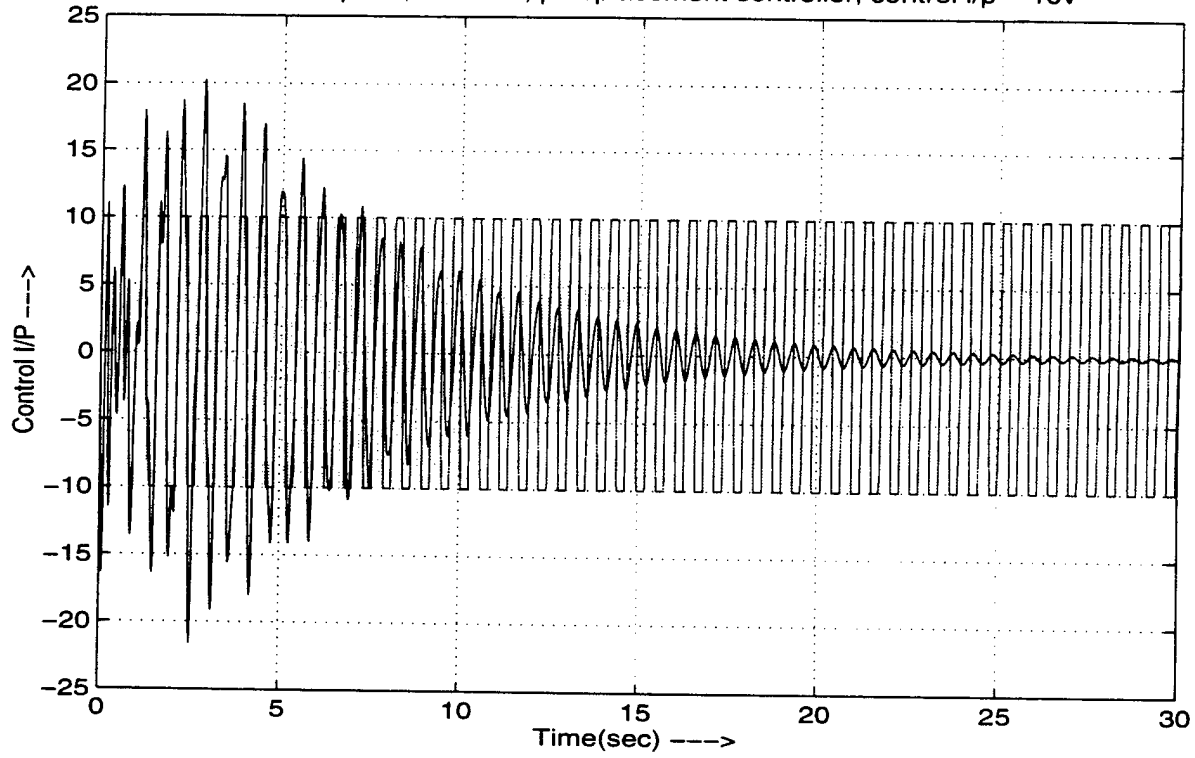




6th order plant, mode-1, poleplacement controller, control i/p - 10v

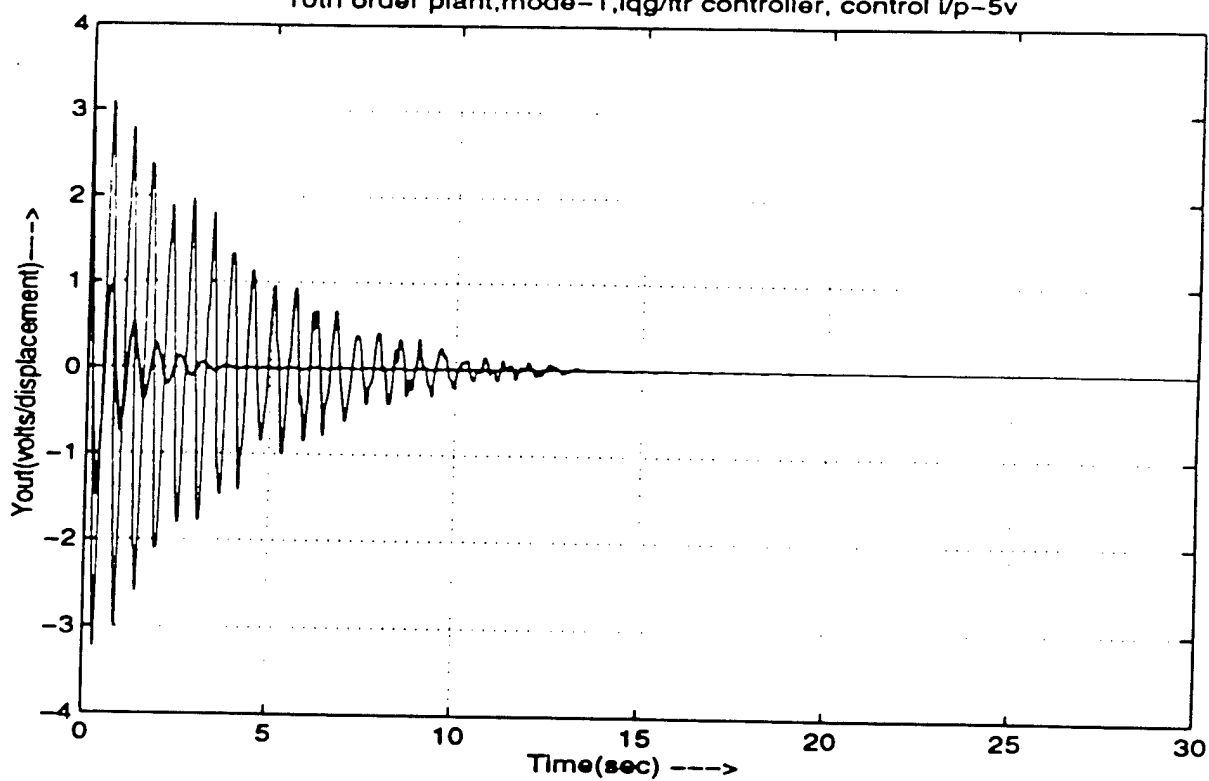


6th order plant, mode-1, poleplacement controller, control i/p - 10v

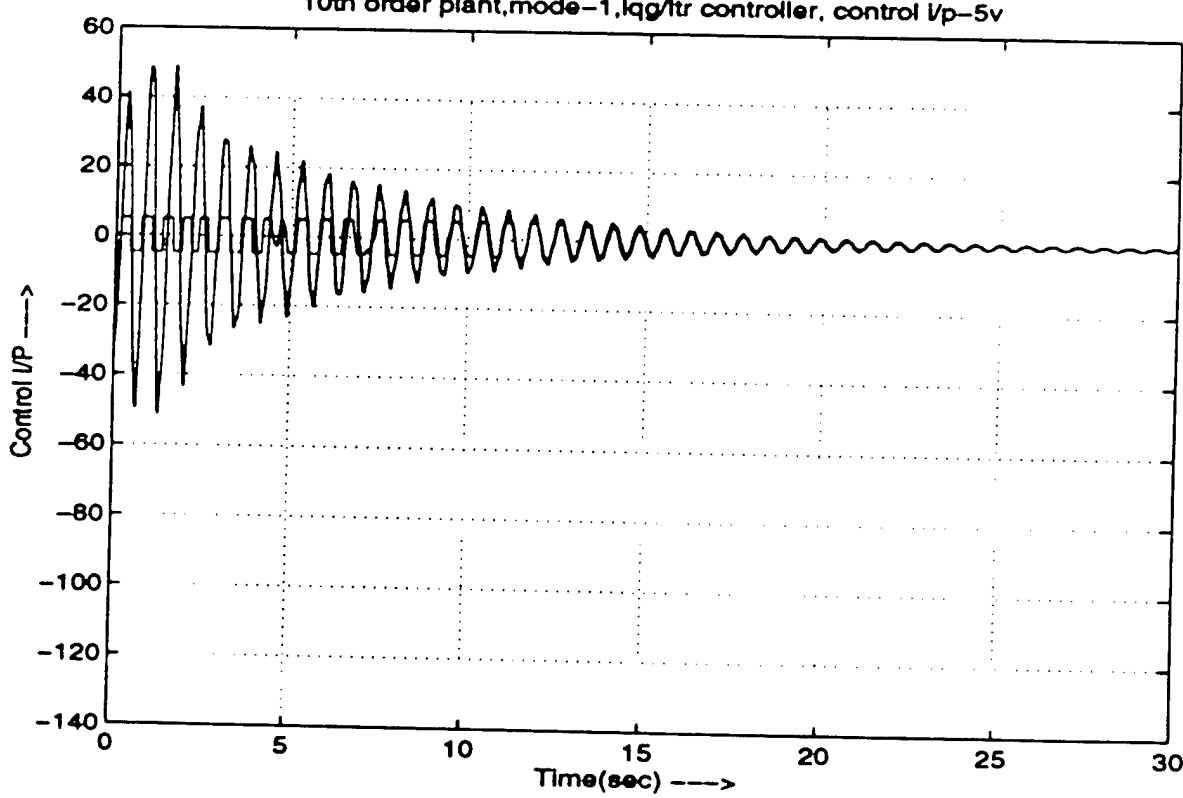


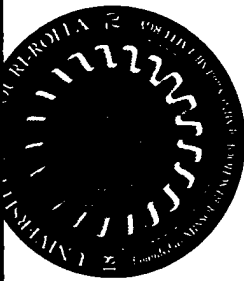


10th order plant, mode-1, lqg/ltr controller, control Vp=5v



10th order plant, mode-1, lqg/ltr controller, control Vp=5v





## Conclusions

- Actuator limits are incorporated in the controller design
- LMI formulations to design multivariable controllers
- Numerical solutions of bilinear LMI equations
- Very good simulation results
- Currently implementing on experimental systems
- Multivariable Nonlinear Controllers

# POWER FLOW ANALYSIS OF AN ELECTROSTRICTIVE ACTUATOR DRIVEN BY A PWM AMPLIFIER

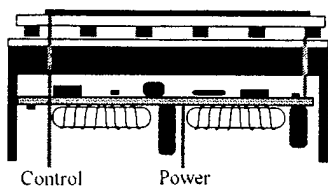
Douglas K. Lindner  
Gregory A. Zvonar

Bradley Department of Electrical Engineering  
Virginia Tech

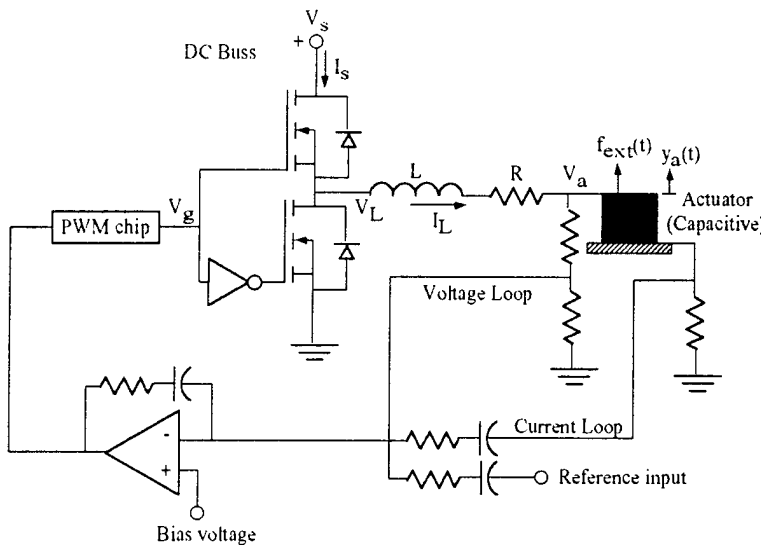
**Virginia Tech**

## ABSTRACT

We analyze the power flow between stacked electrostrictor actuators and a pulse-width-modulated switching amplifier. An integrated model is developed which includes a dynamic structural model of the actuator, a dynamic model of the power electronics and a nonlinear electromechanical coupling mechanism. By analyzing the conversion of mechanical power to and from electrical power, a better understanding is gained of the interaction between the electrical amplifier and the actuators. Furthermore, this new insight provides for the design of more efficient closed loop controllers. This work focuses on the behavior of electrostrictive actuators with nonlinear actuator models. Also, with the inclusion of the dynamic model of the switching amplifier, the power flow can be traced directly back into the original power bus. The effect on the power flow of a nonlinear amplifier controller is also investigated. It is shown that the nonlinear controller, which reduced actuator velocity distortion, also reduces the maximum required power that the amplifier must process.



Smart Material



Simplified Circuit Diagram

**Virginia Tech**

#### DESCRIPTION OF THE SMART MATERIAL

A cross-section of the Smart Material we will consider is shown above. This material consists of a graphite-epoxy box which contains the amplifier that drives the actuators. This box also provides a rigid base on which are mounted stacked electrostrictor actuators. To the top of these actuators is mounted a rigid headmass. A PVDF sensor is mounted on top of the headmass. This whole device would be covered with a polyurethane coating to seal it from the water. The purpose of this device is to cancel incoming underwater acoustic waves. These pressure waves are detected by the PVDF sensor and communicated to the control system (not shown above). The control system generates a control signal to the amplifier. The amplifier, in turn, drives the electrostrictor actuators and vibrates the headmass in such a way as to cancel the incoming acoustic wave.

#### MODEL OF ELECTRONICS

The circuit for the pulse-width-modulated (PWM) amplifier which we will consider is also shown above. Power is delivered to the actuator from the 32 Volt DC power bus by opening and closing the two MOSFET switches. At any one time the inductor is either connected to the power bus or ground. The voltage that appears across the actuators is the average of this square wave voltage on the positive side of the inductor,  $v_L(t)$ . This average is, in turn, controlled by the duty cycle of the square wave. Since these switches have very low losses, this configuration allows for a two-way power flow between the power bus and the actuator. This operation is quite different from a conventional Class A amplifier which dissipates the power that flows into the amplifier in heat.

The purpose of the voltage loop is to maintain a constant bias voltage on the actuator below the frequency band of interest. The purpose of the current loop is to control the current entering the actuator to be proportional to an external reference command input. This reference input originates from the smart material control system in response to the incoming acoustic wave.

## COUPLED STRUCTURAL/MATERIAL/AMPLIFIER MODEL

In this section we develop the model of the actuator. The model development is motivated by the desire to integrate an actuator material model with the electronics model and the structural dynamics of the actuator. The actuator material, PMN, is characterized by a set of coupled constitutive equations postulated by Hom and Shankar<sup>\*</sup> shown in Eq.'s (1) and (2).

$$\epsilon = \frac{\sigma}{Y} + Q_{11}P^2 \quad (1)$$

$$E = -2Q_{11}P\sigma + \frac{1}{k} \tanh^{-1}\left(\frac{P}{P_s}\right) \quad (2)$$

These constituent equations assume polarization, P, and stress,  $\sigma$ , as the independent variables and strain,  $\epsilon$ , and electric field, E, as the dependent variables.

Recognizing that polarization is charge per area, electric field is voltage per distance, and strain is displacement per length, we find an approximate expression for the voltage across the actuator in terms of displacement and charge.

$$v_a = -2dQ_{11}\left(\frac{q}{A_e}\right)\left(Y\frac{y_a}{h} - YQ_{11}\left(\frac{q}{A_e}\right)^2\right) + \frac{d}{k} \tanh^{-1}\left(\frac{q}{A_e P_s}\right) \quad (3)$$

Where  $y_a$  is the displacement of the top of the actuator relative to the bottom of the actuator, h is the height of the actuator,  $A_e$  is the total charge surface area, and d is the actuator layer thickness. Assuming a lump mass equivalent model of the actuator with stiffness  $k_a$  and mass  $m_a$ , the model of the coupled system can be found using standard energy methods

$$m_a \ddot{y}_a + c_a \dot{y}_a + k_a y_a = f_{ext} + k_a N_c d Q_{11}\left(\frac{q}{A_e}\right)^2 \quad (4)$$

$$L \ddot{q} + R \dot{q} + \frac{d}{k} \tanh^{-1}\left(\frac{q}{A_e P_s}\right) + v_L(t) = v_L(t) \quad (5)$$

where

$$v_L(t) = -2dQ_{11}\left(\frac{q}{A_e}\right)\frac{1}{\Lambda}\left(k_a y_a - k_a N_c d Q_{11}\left(\frac{q}{A_e}\right)^2\right) \quad (6)$$

and where  $N_c$  is the number of layers per actuator,  $f_{ext}$  is an external disturbance force acting of the actuator,  $c_a$  is the damping of the actuator,  $v_L(t)$  is the positive inductor voltage, and R is the series resistance of the inductor. Eq.'s (4), (5), and (6) were simplified using the following relations:

$$k_a = \frac{YA}{h}, \quad h = N_c d, \quad A_e = N_c A \quad (7)$$

These relations come from the equivalent lumped stiffness relationship, the fact that the height of the actuator is its number of plates,  $N_c$ , times the distance between the plates, d, and that the charge surface area is the area of the actuators times the number of plates, respectively.

Note that from Eq. (5), the actuator voltage,  $v_a(t)$  is equal to

$$v_a(t) = \frac{d}{k} \tanh^{-1}\left(\frac{q(t)}{A_e P_s}\right) + v_L(t) \quad (8)$$

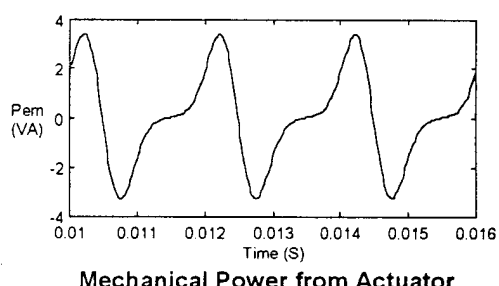
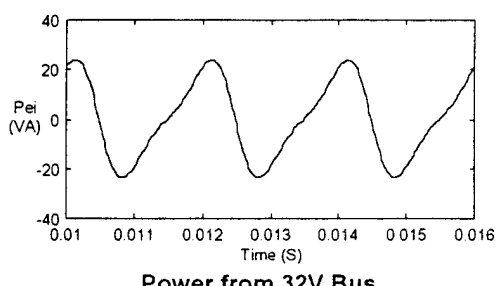
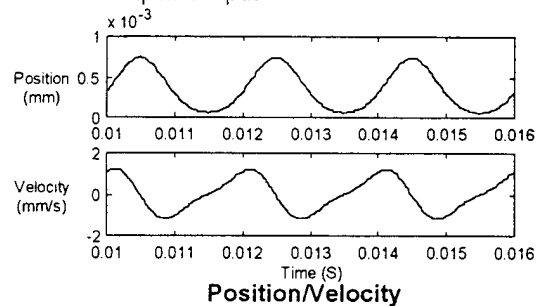
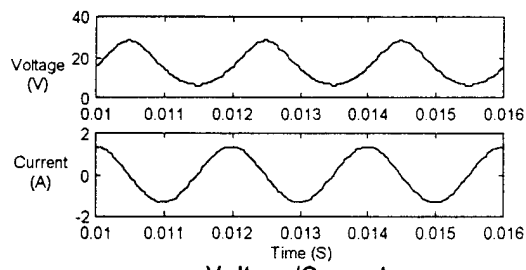
We now have a dynamic coupled model of the interactions between the amplifier and the actuator. With this model we can analyze the power flow of the system from the power bus to the external forces on the actuator.

---

<sup>\*</sup> Hom, Craig L., Shankar, Natarajan. "Fully coupled constitutive model for electrostrictive ceramic materials." *Journal of Intelligent Material Systems and Structures*, vol. 5, no. 6, Nov. 1994, pp. 795-801.

## Simulation Results (No external force)

No External Force Input - Sinusoidal Amplifier Input



**Virginia Tech**

### NO EXTERNAL FORCE

First, we examine the flow of power through the system when there is no external force applied to the system and the amplifier is driven with a sinusoidal input. The figure above shows the voltage and current waveforms of the actuator. Note that the amplifier is configured for current control so the current signal is sinusoidal like the input signal. The nonlinearity in the actuator is exhibited in the voltage signal.

For this condition the power delivered from the power bus is also shown above, bottom left. Note that the power from the bus is found by multiplying the bus current by the bus voltage. The power flow is both positive and negative indicating a reactive (capacitive) load. The mean value of this signal is about 0.1 W which is mostly due to the small resistive losses in the amplifier. Little real power is consumed since there is no mechanical loading on the actuator.

Next we look at the mechanical power signals. The top right of the above figure shows the position and velocity of the actuator under this condition. Note that due to the nonlinearity in the material model these signals are not sinusoidal.

The bottom right figure shows the mechanical power from the actuator or the electromechanical power. The electromechanical power is defined as the mechanical force due to the charge on the actuator multiplied by the actuator velocity:

$$P_{em} = \dot{y}_a(t) k_a N_c dQ_{11} \left( \frac{q(t)}{A_e} \right)^2 \quad (9)$$

The electromechanical power is both positive and negative much like the electrical power but with smaller amplitude. Therefore, this cyclic signal represents only a portion of the electrical potential energy as it is converted to mechanical potential energy, the remaining power remains as electrical reactive power.

## Power Signal Definitions

Constituent Equations for Electrostrictive Actuators

$$\sigma = \frac{\pi}{V} \cdot Q_{11} P^2$$

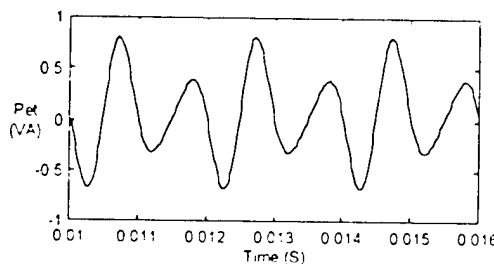
Source of Electromechanical Power

$$E = -2Q_{11}P\sigma + \frac{1}{k} \tanh^{-1}\left(\frac{P}{P_s}\right)$$

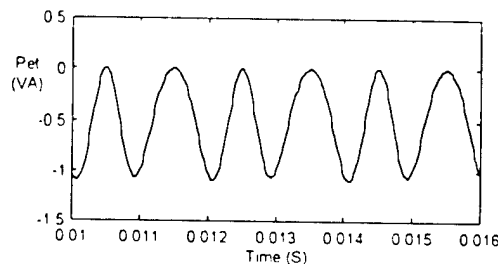
Source of Transfer Power

## Transfer Power Simulation

Sinusoidal Amplifier Input and Sinusoidal External Force



Sinusoidal External Force (Out of Phase)



Sinusoidal External Force (In Phase)

**Virginia Tech**

### TRANSFER POWER UNDER SINUSOIDAL FORCE EXCITATION

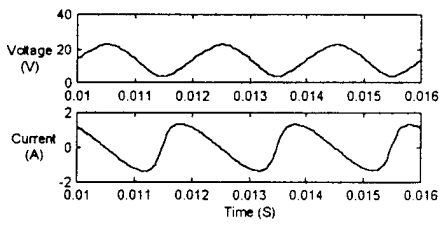
Since the electromechanical power, defined on the previous page, contains a significant portion of reactive power being cycled from electrical to mechanical power, it is difficult to measure the net power transfer between the electrical and mechanical systems. By examining the *transfer power* signal, this information is more easily gleaned from the waveform. The transfer power is the electrical power generated from the electrostrictive converse effect. The converse effect is the appearance of an electrical field in the actuator due to an externally applied force. The second constituent equation shown above shows the source of the transfer power. The transfer power is the electrical analog to the electromechanical power which originates from the first constituent equation shown above. The voltage generated from the field due to the converse effect times the actuator current is defined to be the transfer power. Since the system is nonlinear, this signal is not equal to the electromechanical power. However, due to the conservation of energy, the average value of this signal must be equal to the average value of the electromechanical power.

The plot in the lower section of the above figure shows the transfer power when a sinusoidal force is applied to the actuator. The left figure shows the transfer power when the external force and the amplifier input (or equivalently the actuator velocity) are out of phase. Since velocity and external force are ninety degrees out of phase, the transfer power shows no net power transfer from electrical to mechanical power. Rather, electrical and mechanical power are cycled between each other.

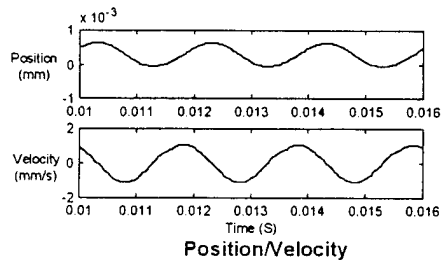
The lower right figure shows the transfer power when the external force and the amplifier input are in phase. Since the input signal (and the velocity) are in phase, we now have a net power transfer. In this case net power is flowing from the actuator, through the amplifier, and into the power bus. The mean power transfer is around -0.5 W (power flowing back to amplifier). If this external force were from an acoustic wave, this configuration would reduce the energy of the wave.

### Simulation Results (Nonlinear Control)

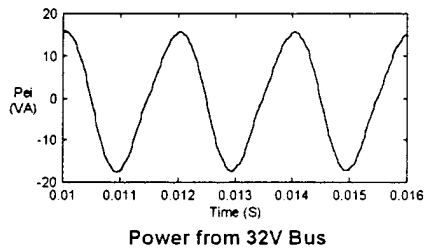
Sinusoidal Amplifier Input and In-Phase Sinusoidal External Force



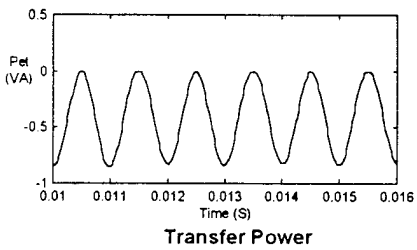
Voltage/Current



Position/Velocity



Power from 32V Bus



Transfer Power

**Virginia Tech**

#### NONLINEAR CONTROL

In a previous paper, we proposed a nonlinear controller for the PWM amplifier which reduces the distortion in the actuator velocity caused by the quadratic nonlinearity in electrostrictive actuators. In this paper we showed that the velocity of the actuators is approximately

$$\dot{y}_a(t) = \frac{2d N_c Q_{11}}{A_c^2} Q_{DC} \left( i_L(t) + \frac{1}{Q_{DC}} \tilde{q}(t) i_L(t) \right) \quad (10)$$

where  $\tilde{q}(t)$  is the AC portion of the charge on the actuator and  $Q_{DC}$  is the DC portion of the charge. Therefore by configuring the amplifier to control not solely current but current plus a correction factor, then the actuator's velocity will be directly proportional to the external input into the amplifier

The top left figure above shows the voltage and current with the nonlinear controller implemented. Note that neither the voltage nor the current waveforms are sinusoidal since the amplifier is no longer controlling current, rather the amplifier is, in effect, controlling velocity. This can be seen in the upper right hand figure since the velocity is now sinusoidal like the external input.

The lower right figure shows the transfer power under this condition. The average power transfer from mechanical to electrical power has decreased in magnitude from about -0.5 W, as shown on the previous slide, to about -0.4 W. Therefore, given the same desired fundamental velocity amplitude, the amplifier with the nonlinear control needs to transfer less mechanical to electrical real power.

As an added benefit of nonlinear control, the amplitude of the reactive power processed by the amplifier has been decreased as well as shown in lower left figure. With the nonlinear control, the maximum reactive power has decreased from over 20 VA to less than 16 VA. Therefore, given an actuator with a given velocity specification, the amplifier with the nonlinear control is required to process less power over a linearly controlled amplifier, hence it can be constructed with smaller electrical components.

---

Zvonar, G. A. and D. K. Lindner, "Nonlinear Electronic Control of an Electrostrictive Actuator," to be published in *Proceedings of the SPIE's 1997 North American Symposium on Smart Structures and Materials*, San Diego, CA, March, 1997.

# Deflection Response for Series Configurations of Piezoceramic Unimorph C-Block Actuators

Andrew J. Moskalik, Diann Brei, and Simon J. Palko

Department of Mechanical Engineering and Applied Mechanics, The University of Michigan

2250 G. G. Brown Building, Ann Arbor, MI 48109-2125

Phone: (313) 763-6617 FAX: (313) 647-3170 E-mail: dibrei@engin.umich.edu

Ron Barrett  
Aeronautical Engineering Department, Auburn University

## ABSTRACT

### Introduction

Rotorcraft are prematurely aged because they are plagued with high levels of vibration, mostly attributable to rotor dynamics and aerodynamics. To reduce these levels of vibration, researchers have investigated the use of active servoflaps driven by piezoceramic actuators. Most piezoelectric actuators used in active rotor blade flaps are either stacks, which produce high forces and small deflections; or straight benders, which generate large deflection and small forces. This leaves a midrange gap in actuator capabilities in which many of these flaps operate. To fill this gap, a number of new architectures have been proposed. A common scheme used to create a mid-range stiffness actuator for many applications involves mechanical leveraging of stacks to improve deflection performance at the expense of force generation capability, thereby making the overall stack actuator package more compliant. However, this approach frequently suffers from transmission losses and may create difficulties in packaging the additional external leveraging mechanisms.

To overcome these problems, internally leveraged actuators called C-blocks have been developed. C-blocks are solid-state curved laminate piezoelectric actuators, that can generate over twice the force of a straight bender with some reduction in deflection. To compensate for this loss of deflection, individual C-blocks can be combined in series to increase the total output deflection (Fig. 1a). The piezoceramic C-block series shown in Fig. 1 are piezoceramic semicircles bonded to a continuous steel substrate and poled in the radial direction. They are activated in the circumferential direction and when a voltage is applied across the thickness of the piezoceramic, the strain produced creates a bending moment within each individual C-block. This causes the entire actuator architecture to flex as shown in Figure 1b. One of the foremost attractions of series C-blocks is the diverse number of architectures that can be constructed by

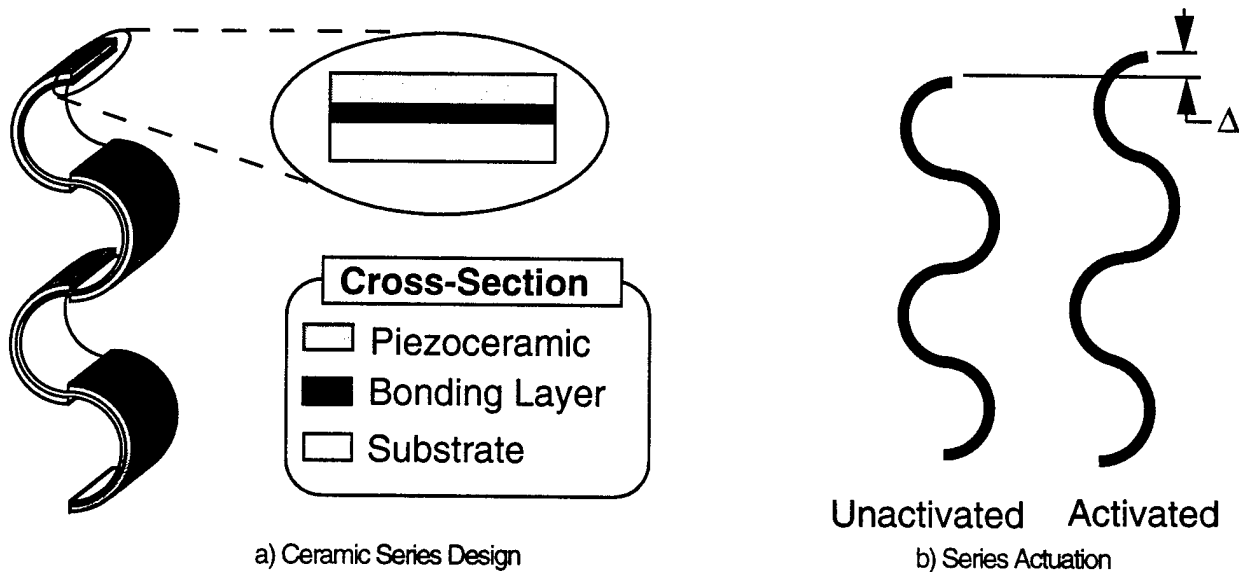


**Figure 1. Piezoceramic C-block Series Actuator Design and Operation.** Series C-block actuators can be constructed by joining individual C-blocks in an array form. The deflection of the series C-block is the sum of the deflections of individual C-blocks.

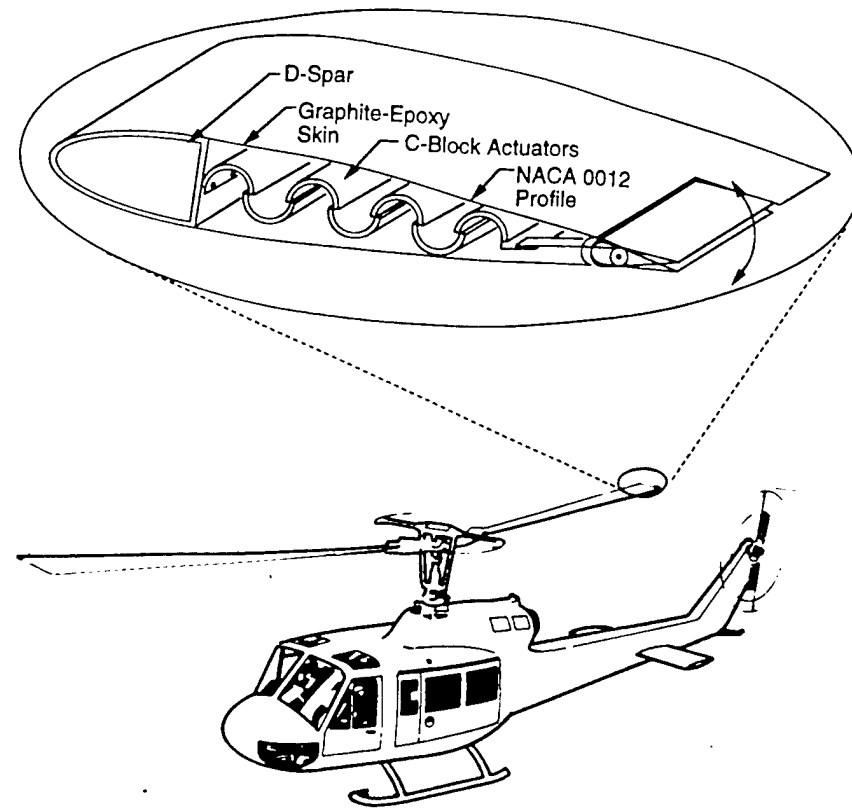


**Figure 2. Piezoceramic C-block Series Actuators Used for Actuation of Servoflaps.**  
Series C-block actuators are being developed to drive a balanced active rotor blade flap.

altering the geometry and number of C-blocks in the array. This versatility allows the series C-block to be easily tailored to produce a broad range of force and deflection characteristics, while fitting within confined application spaces. Thus, C-blocks are an ideal candidate for space-limited applications, such as rotor blade servoflap actuation (Fig. 2).

Before C-blocks can be used in an active rotor blade flap application, the general performance of these actuators must be characterized. The quasi-static deflection-voltage behavior for piezoceramic C-blocks is presented. Details are given on the derivation of a fundamental analytical model for the deflection-voltage performance. The fabrication process for prototypes is outlined and experimental results for a variety of piezoceramic series C-block actuators are presented.

### Modeling

To investigate the quasi-static deflection capabilities of series C-block actuators, an analytical model for the deflection-voltage performance was derived using Castigliano's theorem. During the derivation, the C-block was assumed to be a thin, perfectly bonded laminate curved beam with three layers: piezoceramic, bonding, and substrate. The nomenclature used is shown in Fig. 3, where  $\Delta$  is the tip deflection,  $R_n$  is the neutral axis radius,  $b$  is width, and  $z$  is distance from the neutral axis to the outside of a layer. The subscripts  $p$ ,  $b$ ,  $s$ , and  $i$  refer to the piezoelectric layer, bonding layer, substrate layer, and inside of the C-block, respectively. To derive the model, the internal strain energy in individual C-blocks in the series was determined. The strain energy was used in Castigliano's theorem to derive the quasi-static deflection-voltage behavior of the C-block series,

$$\Delta = \frac{2nM^P R_n^2}{D} = \frac{3nY_p d_{31} V b_p (z_p + z_b) R_n^2}{Y_p b_p (z_p^3 - z_b^3) + Y_b b_b (z_b^2 - z_s^3) + Y_s b_s (z_s^3 - z_i^3)}$$

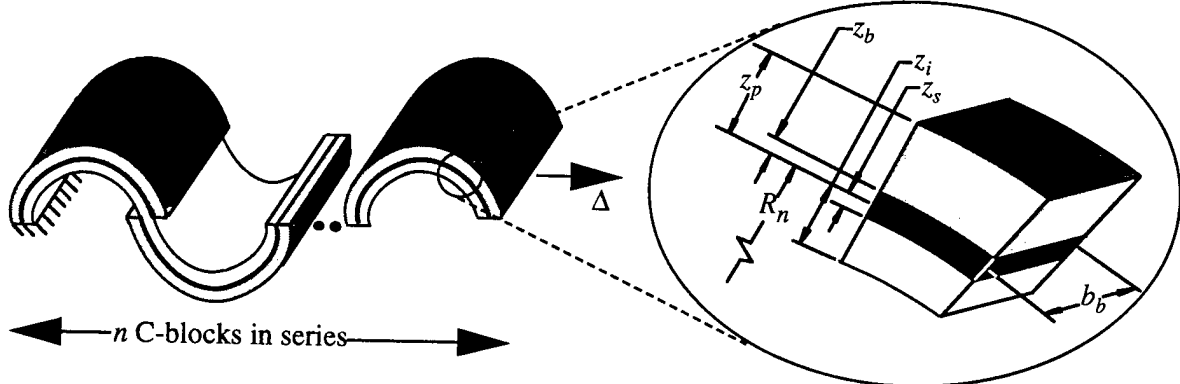


**Figure 3. Nomenclature Used in Analytical Model Derivation.** The series C-block is made up of  $n$  individual C-blocks, each with a neutral axis of  $R_n$  and identical cross-section. The total tip deflection is  $\Delta$ ,  $z$  is the distance to the outside of a layer, and  $b$  is the layer width.

where this simple model relates the tip deflection,  $\Delta$ , to the number of C-blocks in series,  $n$ , and the radius,  $R_n$ , bending stiffness,  $D$ , and internal moment,  $M^P$ , of each C-block.

Substituting in the expressions for moment and bending stiffness for the unimorph cross-section, the model can be explicitly written in terms of geometric and material parameters, where  $d_{31}$  is the piezoelectric constant and  $V$  is the applied voltage. The resulting simple model predicts that the total

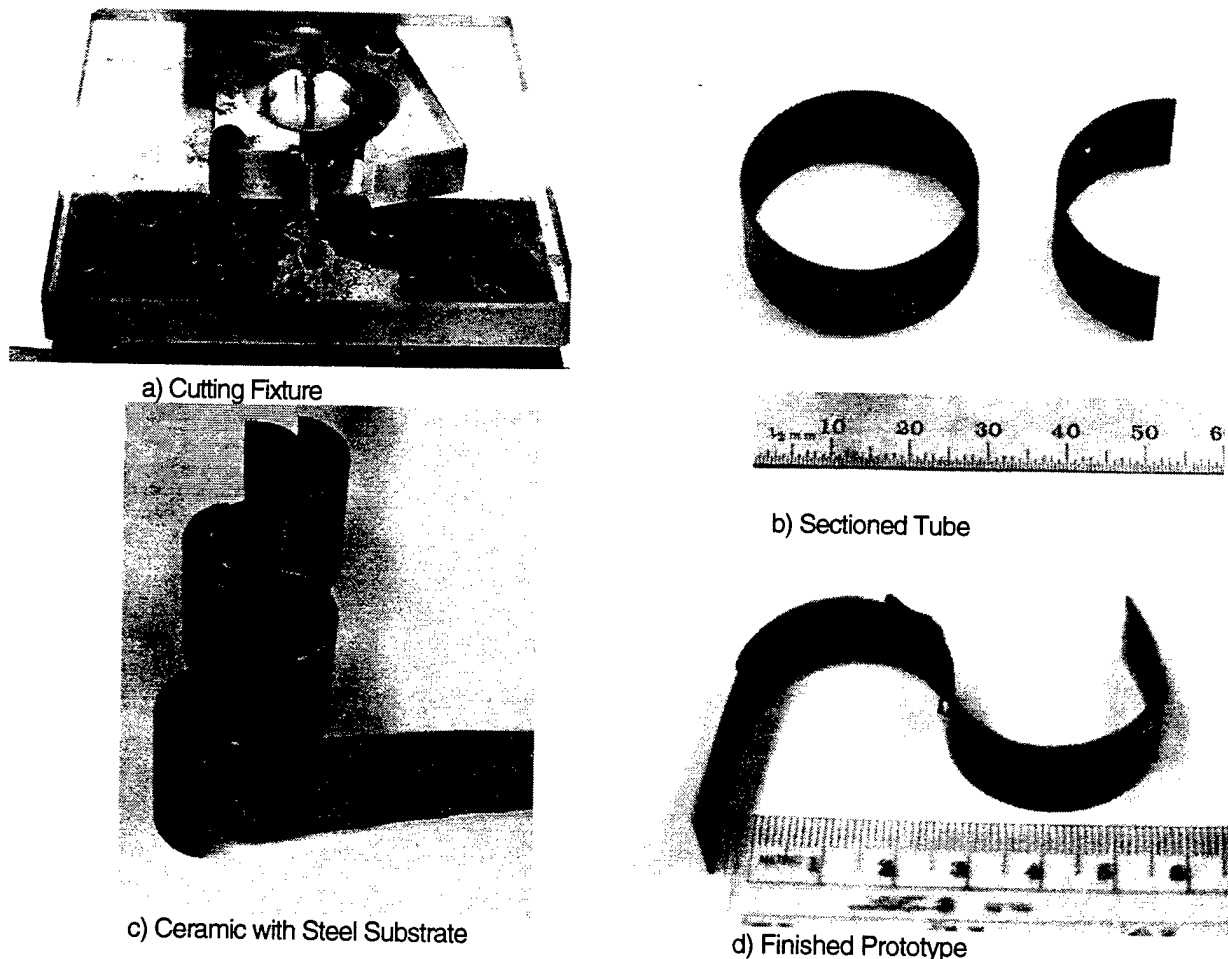


**Figure 4. Fabrication of Piezoceramic Series C-blocks.** The series C-block actuators were fabricated from tubes of PZT-5H or PZT-8 piezoceramic. These tubes were placed in a fixture and sectioned into semicircles using a diamond saw. The resulting piezoceramic semicircles were bonded to a steel substrate to form the finished prototype.

deflection of the series is a linear addition of the deflections of the individual C-blocks making up the array.

### Prototype Fabrication

This model was experimentally verified by constructing C-block series prototypes. These prototypes were constructed as unimorphs as shown in Fig. 4. Each prototype was fabricated from circular piezoceramic tubes, either of PZT-5H or of PZT-8. The inner and outer radii of the tubes were pre-plated with a silver electrode a few microns thick. To fabricate the piezoceramic actuator, each tube was placed in a fixture, shown in Fig. 4a, and cut into two semicircular sections using a diamond saw. A sectioned tube is shown in Fig. 4b. A steel strip was formed into an S-shape, shown in Fig. 4c, to conform to the inner diameter of the piezoceramic tubes, with loops in the steel equal to the number of C-blocks in the final prototype. After the epoxy had cured, the individual ceramics were jumpered together to form the final prototype, shown in Fig. 4d.

Three different types of prototypes were fabricated using this process. The first was a series of two 15.9 mm radius PZT-8 C-blocks of 0.76 mm thickness with a 0.41 mm thick steel substrate. The second was a series of two 9.5 mm radius PZT-5H C-blocks of 1.00 mm thickness with a 0.71 mm thick substrate. The third was a series of four 9.5 mm radius PZT-5H C-blocks of 1.00 mm thickness with a 0.46 mm thick substrate.

### Experimental Testing

The prototypes were tested experimentally to determine their deflection-voltage performance. To perform the experimental testing, each prototype was securely clamped in a vise and connected to a voltage supply as shown in Fig. 5. For the PZT-8 prototype, the voltage was increased in intervals of 25 V to a maximum of 400 V, and then returned to zero volts, again in intervals of 25 V. For the PZT-5H prototypes, the voltage was increased in intervals of 10 V to a maximum of 150 V, and then returned to zero volts, again in intervals of 10 V. At each interval, the deflection of the tip of the C-block was measured using a fiber optic probe. The results of this experimental run are compared to the analytical model in Fig. 6 for all prototypes.

### Discussion

For the series of two C-blocks fabricated from PZT-5H (Fig. 6a), the average difference between the experimentally determined data and the theoretically predicted values was 0.46 microns, corresponding to 5.4% of the full-scale deflection output. For the series of two C-blocks fabricated from PZT-8 (Fig. 6b), the average difference between the experimentally determined data and the theoretically predicted values was 0.69 microns, corresponding to 1.4% of the full-scale deflection output. For the series of four C-blocks fabricated from PZT-5H (Fig. 6c), the average difference between the experimentally determined data and the theoretically predicted values was 0.77 microns, corresponding to 3.8% of the full-scale deflection output. This close match indicates good correlation between the analytically predicted behavior and the experimental results. Most of the difference between the analytical model and experimental data is

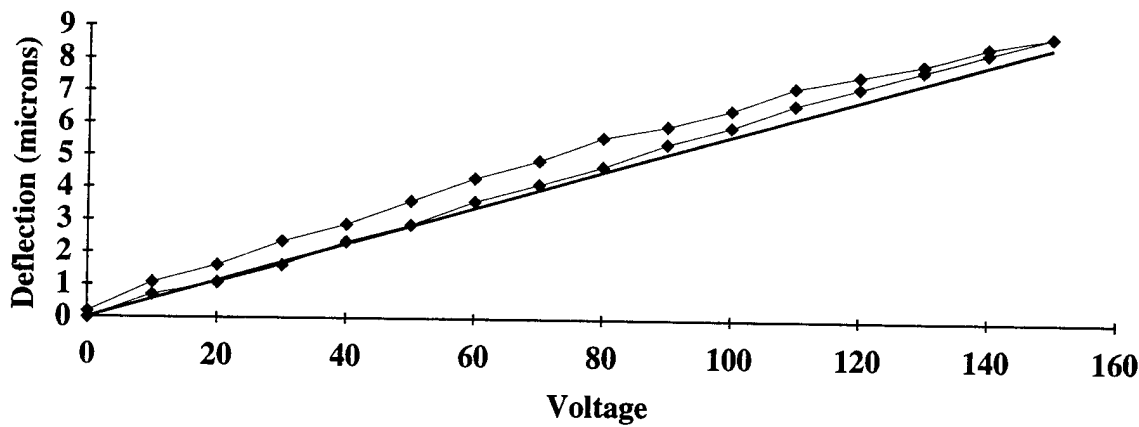


a) Test Setup

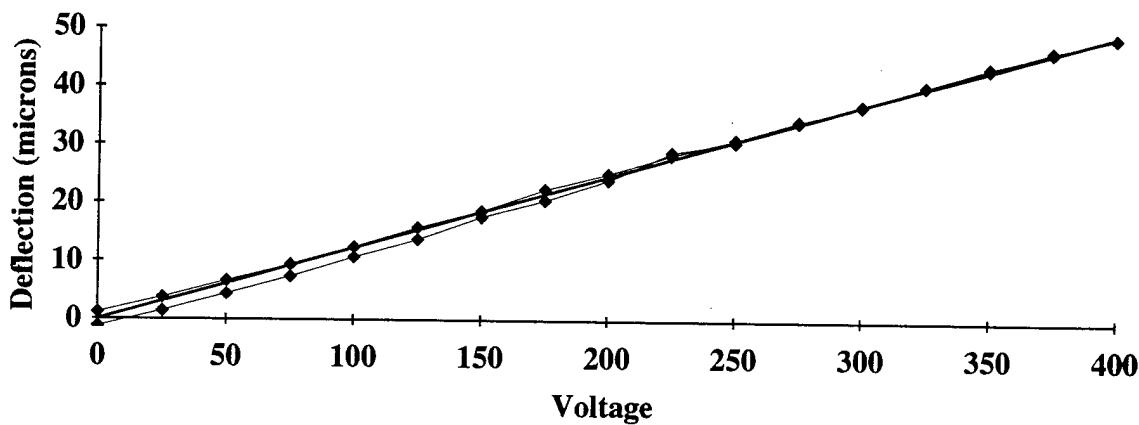


b) Close-Up of Prototype in Test Setup

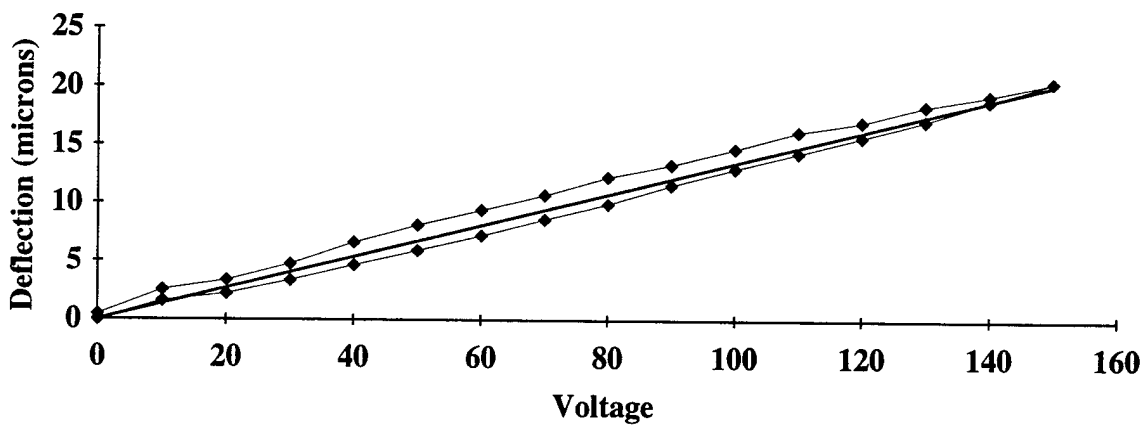
**Figure 5. Experimental Test Setup for Piezoceramic Series C-blocks.** The series C-blocks were clamped in a vise and connected to a high-voltage power supply. Tip displacement is measured with a fiber-optic probe.



a) Series of two PZT-5H C-blocks;  $R_{out} = 9.5$  mm,  $t_p = 1.00$  mm,  $t_s = 0.71$  mm



b) Series of two PZT-8 C-blocks;  $R_{out} = 15.9$  mm,  $t_p = 0.76$  mm,  $t_s = 0.41$  mm



c) Series of four PZT-5H C-blocks;  $R_{out} = 9.5$  mm,  $t_p = 1.00$  mm,  $t_s = 0.46$  mm

**Figure 6. Deflection-Voltage Experimental Results.** Three prototypes were experimentally tested to determine their deflection-voltage performance. The experimental results are graphed along with the deflection determined by the analytical model.

attributable to the presence of hysteresis, a common second-order phenomenon in piezoelectric materials. Hysteresis was not accounted for in the analytical derivation to ensure that the final model was as simple as possible. Experimental results show the PZT-5H prototypes exhibit greater hysteresis, as would be expected from the soft ceramic.

The three prototypes tested show the versatility of the C-block architecture. The series of two PZT-5H C-blocks (Fig. 6a) give a total of 9 microns in deflection. This deflection output can be increased by changing the material and geometric properties, as shown by the series of two PZT-8 C-blocks (Fig. 6b). Alternatively, the number of C-blocks in series can be increased, as shown by the series of four PZT-5H C-blocks in Fig. 6c, to increase the deflection. Thus, not only can C-block actuators be tailored using geometric and material parameters similar to other conventional technologies, it can also be tailored using architecture parameters such as the number of C-blocks in series. This capability broadens the design space and is helpful for volume constrained applications.

## Conclusion

The close agreement of the experimental results with the analytical model shows that the deflection of series C-blocks can be accurately predicted with a simple model. The deflection for the series is a simple sum of the deflections of the individual C-blocks within the series. The fabrication and testing of series C-blocks demonstrate the versatility of the architecture. The quasi-static models are currently being used to design and develop a series C-block actuator to be used as an actuation source for a balanced active rotor blade flap.

## Acknowledgment

The authors would like to thank the Army Research Office for sponsoring this research under grant number DAAH04-96-1-0186.

# **Fiber Optic Sensors for Soldier's Smart Uniform**

## **(An Overview)**

**Mahmoud A. El-Sherif**

**Fiber Optics and Photonics Laboratory**  
**Drexel University**  
**Philadelphia, PA 19104**

### **Abstract**

Advancements in chemical and biological warfare and other battlefield threats have stimulated interest in the development of novel systems for early warning and counteraction to battlefield threats. Soldier survivability can be enhanced and improved by giving the soldier's uniform the ability to sense environmental conditions. Along with the idea of smart structures and smart materials,<sup>1</sup> a "smart" uniform can provide instantaneous warnings to the soldier and help to identify zones of biological threats on the battlefield. It is an integration of smart materials within smart structures. These uniforms can be constructed of embedded sensors, actuators, and feedback control signals, giving the uniforms the capability to sense and respond to battlefield threats in an appropriate and timely manner.

Although conventional sensors are highly developed and tested in many applications, they are not well suited for battledress applications. However, fiber optics technology offers significant potential for this application. Optical fibers have the advantage of small size, light weight, immunity to electromagnetic interference, flexible and compatible with textile structures. Therefore, the focus of this study is to develop fiber optic sensors that can be used to sense a number of environmental threats such as chemical and biological warfare battlefield threats, electromagnetic fields, temperature, and so forth. The sensor output can be used to actuate devices that can provide warning signals or other functions. This system can be modified in the future to provide camouflage and signature suppression from visible to multiple infrared (IR) wavebands imaging threat sensors.

To this end, Drexel University, in collaboration with the University of Akron (UA) and North Carolina State University (NCSU), is working on the development of fiber optic sensors that can be integrated into a battlefield uniform. Specifically, Drexel is developing a fiber optic biological sensor using novel multifunctional materials as a modified cladding for the sensing fiber. This multifunctional materials is under development by UA Department of Polymer Science.<sup>2-4</sup> Drexel is also working with NCSU's College of Textiles on the integration of this system into textile structures. An overview of the proposed fiber optic system is presented and preliminary results are discussed.

## Executive Summary

The sensor design is based on two primary components. The first component is an on-fiber structure that has the optical fiber passive cladding been replaced by a multifunctional smart material(s) sensitive to battlefield threats. Such materials must be innovative with regards to structure, functionality, and design.<sup>1,5</sup> The second component uses the modal power distribution variation within the fiber core as an indication of induced variation in the properties of the modified cladding. This technique is defined as spatial intensity modulation (SIM) within the fiber core. The advantage of using the SIM technique is that a regular light emitting diode (LED) and photodetector are the main sensor components. Therefore, this technique is very sensitive and inexpensive, and the required components can be assembled into a very small micro-structure.<sup>6</sup> The SIM has been tested for measuring stress distribution within composite materials.<sup>7</sup> In this paper, a brief description of the spatial intensity modulation technique is presented, and the sensor manufacturing procedure as well as investigations on innovative techniques to incorporate optical fiber sensors within soldiers' uniforms are discussed.

### Spatial Intensity Modulation

The principle of operation of the SIM technique has been reported in previous publications.<sup>6,8</sup> In short, within a multimode optical fiber, modal power is distributed according to the boundary conditions and the beam launching properties. Altering the multifunctional cladding induces modal coupling between guided modes and evanescent field and results in modal power redistribution within the fiber core. Measurements of the modal power distribution and redistribution can be accomplished by scanning the far-field pattern at the fiber end, as shown in Figure 1. This figure shows the function diagram of the sensor system. The modal launcher is a light source coupled to a number of micro-lenses to selectively excite a limited number of propagating modes within the fiber core. The modal analyzer is an array of photo-detectors or a CCD camera. A sample of the far-field pattern for an optical fiber excited with an optical beam, at an angle 8° off-axis, is shown in Figure 2a.

Spatial intensity distribution of an optical signal propagating within the fiber core depends on fiber properties, excitation angle, and the bandwidth of the optical source. Changing the properties of the multifunctional material will result in changing the intensity distribution of the optical signals at the fiber end, as shown in Figure 2b. The SIM technique has been successfully tested with embedded sensors for stress analysis in composite materials.<sup>9</sup> Theoretical analysis performed earlier shows that this technique is highly sensitive to changes in the cladding materials.<sup>10</sup> Therefore, the application of this technique to sense changes induced in the multifunctional materials by battlefield biological threats or others is promising.

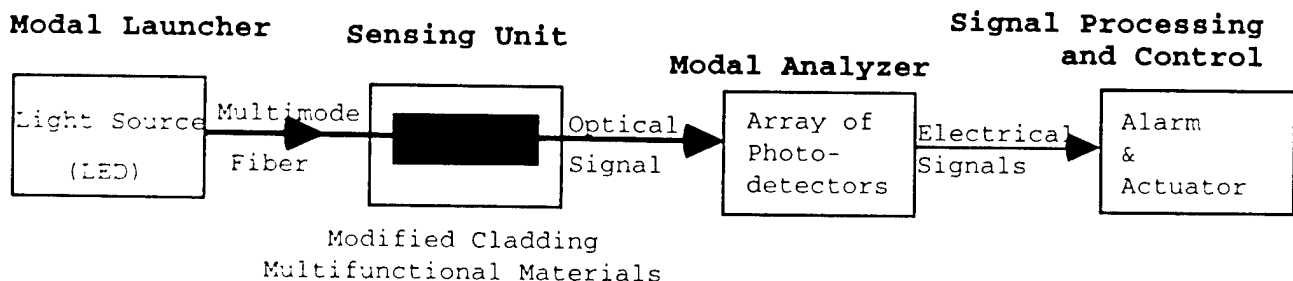


Figure 1. Block diagram of the experimental set up for a sensor based on the spatial intensity modulation technique.

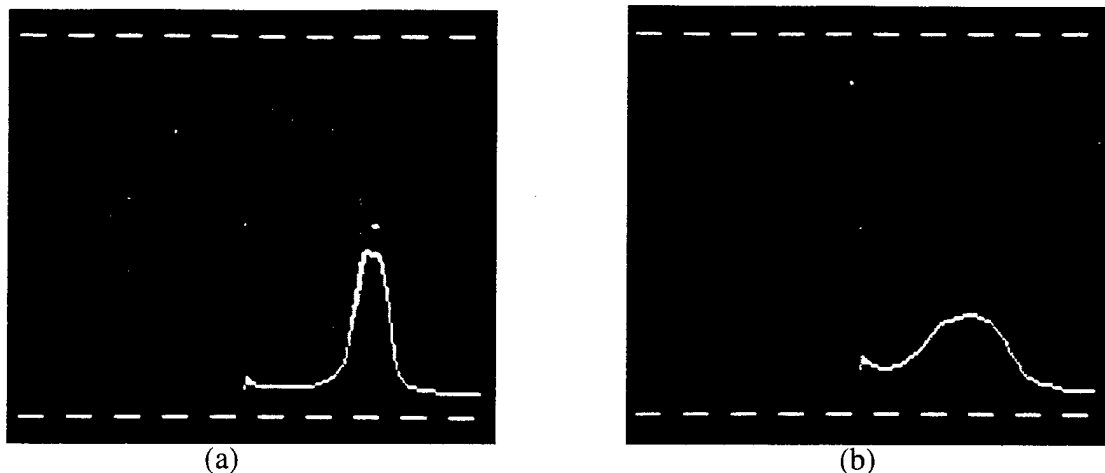


Figure 2. The 2-D image and the horizontal intensity profile of the far-field pattern before (a) and after (b) the presence of perturbation.

### Multifunctional Materials Preparation and Testing

Using multifunctional materials is one of the key components in developing these novel smart uniforms. Innovative synthesis and novel processing are being investigated, and the material properties will be carefully identified. For a feasibility study, the multifunctional polyurethanes developed by D. Reneker, R. Quirk, and W. Brittain of the University of Akron are being used as the modified cladding for the optical fiber sensors. In the near future, the properties and functionality of these materials will be tuned for specific applications. These materials exhibits the combination of thermochromic, photochromic and mechanochromic functionality.<sup>2,3</sup> Samples of the developed polyurethanes (polyurethane-diacetylene segmented copolymers prepared from polyisoprene diols) have been received from UA and tested. The testing procedure and results obtained will be published in as soon as this study is completed. The study includes thin film processing and characterization as well as thin film coating of optical fibers constructing a modified cladding.

Since the prepared polyurethanes materials have a spongy structure, these materials were first dissolved in THF (tetrahydrofuran), and the absorption spectrum of solutions with different concentration were examined carefully. The dissolving process were carried out at room temperature using magnetic stirring. As the polymer concentration increased, the color of the solution changed from colorless to yellow. A spectrophotometer (HITACHI-U 2000) was used to test the solution absorption by wavelength scanned from 190 nm to 1100 nm.

Then, thin films were processed from these materials and tested under three different conditions: a) as prepared, b) after UV exposure, and c) after being heated to different temperature levels. The testing procedure were designed carefully sothat the photo-thermo-chromic properties of these materials could be fully examined. These materials will be applied as the fiber modified cladding.

Two methods are used to prepare thin films one is the solvent casting technique; the other is the spinning technique, in which the dissolved polymer solution is uniformly distributed on a glass substrate. The advantage of the latter method is that more uniform and thinner films can be easily made. Both of these techniques were examined for coating optical fibers to select the appropriate one for application. Prepared thin films were cross-polymerized by exposure to UV light source. After being irradiated by UV, the thin film became blue. Then, the blue films were heated up to 135°C, the blue color changed to yellow, orange, and to red/purple. When the samples were cooled down to

room temperature, the film appeared purple blue. After repeating this procedure several times, it became clear that the absorption spectrum and the color of the material change several times during the heating cycle and it is reversible if the heating temperature does not exceed 50-60°C. Both UV exposure and heat treatment increase the absorption in the visible range and near IR, and shift the absorption edge from about 300 nm to about 650 nm. A sample of the absorption spectrum for one of the thin films is shown in Figure 3, which shows the absorption spectrum of the film as prepared, after UV exposure, and after UV exposure and heated to 110°C.

Also, the thin films were tested by X-rays. The X-ray diffraction pattern shows that the amorphous halo is centered at  $19^\circ$  ( $2q$ ) in all three samples but the crystallinity peak centered at  $23.5^\circ$  ( $2q$ ) overlaps the amorphous halo in both as-spun and after UV exposure samples. After heating, however, the crystallinity peak is almost lost, which indicates some amount of disorder is introduced during the heating process. The results obtained on the absorption measurements and on X-ray diffraction will be discussed in the presentation.

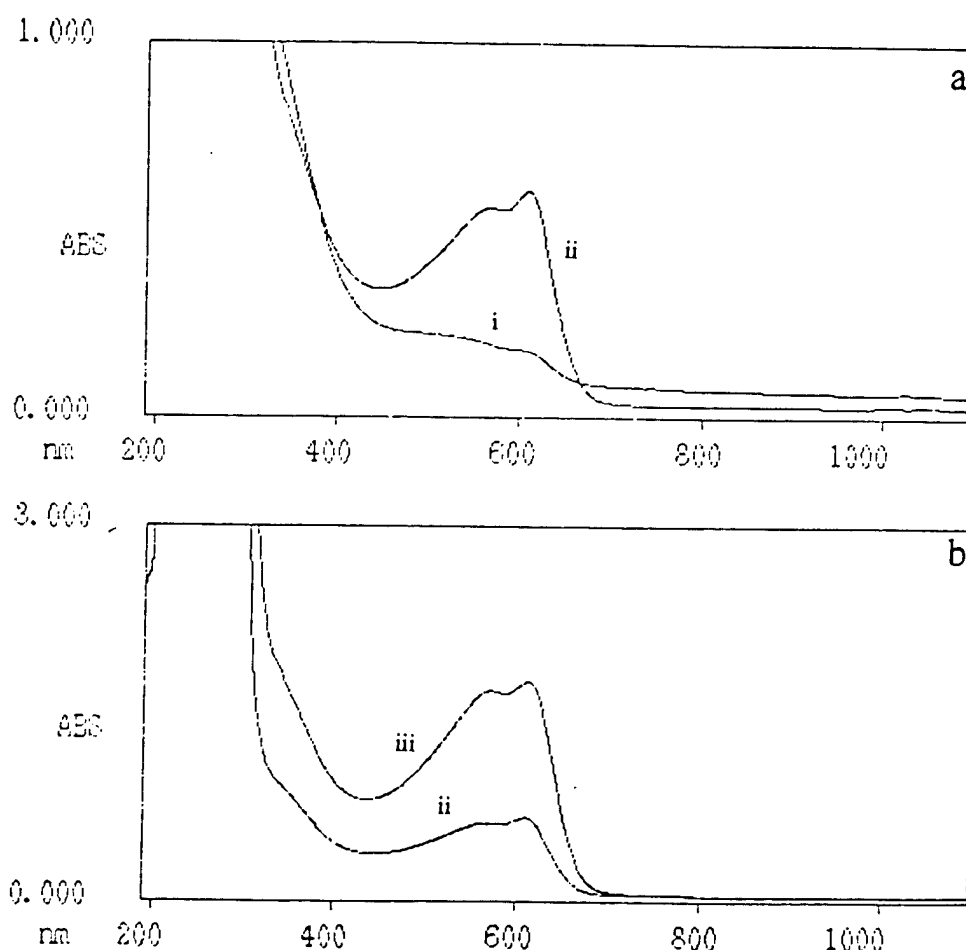


Figure 3. The normalized absorption spectrum for a thin film (i) before and (ii) after exposure to UV light, and (iii) after UV exposure and heated to 110°C.

## **Development of Smart Materials/Structures**

Smart uniforms do not currently exist, but there is a strong need to develop such smart materials/structure system. The developed systems design for this application is based on three major steps; (a) development of smart/multifunctional materials that can detect battlefield threat gases and others; (b) applying these materials to a fiber optic sensory system acting as an information gathering network; and (c) integration of these fiber optic nervous system with soldiers' uniforms for on-line monitoring of battlefield conditions. In order to achieve direct interaction between the multifunctional materials and the optical fibers, the multifunctional materials are used as a modified cladding, by replacing the passive fiber cladding with these active materials. General requirements for the developed system will be high sensitivity, short response time, reversibility and high selectivity, resulting in low false-alarm rates. In addition, compatibility with textile materials, long operational life and low cost are important factors for materials selection. To this end the study on development of smart material/structures will focus on the following:

- Innovative synthesis and novel processing to develop multifunctional materials for the proposed application. The properties of the materials will be carefully investigated.
- Multifunctional materials will be applied on optical fibers in a pre-selective areas, to replace passive cladding material. This requires stripping the fiber jacket and etching part of the clad material.
- These optical fibers will be integrated into the uniform textile fabrics in an appropriately intelligent fashion. Other microelectronics components will be designed for signal processing and control, as shown in Figure 1.

A number of optical fibers has been prepared for the sensor application. For these fibers, the jacket and the cladding materials have been removed. A novel chemical etching process has been developed to uniformly remove part of the fiber cladding without changing the quality of the structure. Akron thermo- and photochromic polyurethanes materials were applied to these fibers in the etched regions. Testing is underway in order to identify the required light source as well as the sensor sensitivity and dynamic range, and to explore the possibility of using these materials in sensor applications.

In addition, a number of optical fibers have been prepared and shipped to NCSU College of Textiles to perform study on the integration of these fibers in textile structures. Samples of the optical fibers were embedded in specially designed seams, via an ultrasonic technique. These samples were sent back to Drexel for optical testing and evaluation. Preliminary optical test results were encouraging, and more work in this direction is underway.

Finally, to make full use of the optical fiber sensors for these embedded structures, the mechanical behaviors of the materials system must be thoroughly understood. With this in mind, mechanical testing on various optical fibers were performed; specifically, tensile and bending tests were performed to obtain the moduli of elasticity for various optical fibers (silica core with silica clad, hard plastic clad, or soft plastic clad, all with a plastic jacket). These results are essential to model the mechanical behavior of the smart structure. To precisely evaluate the properties of each of the fiber core, cladding and jacket, tensile tests were performed on various optical fibers both with the fiber jacket and without the jacket, also, with fibers having the jacket and the cladding been removed. The initial data are listed in the progress reports published by the U.S. Army Research Office, Contract/Grant NO. DAAH04-96-1-0018.

## **Conclusion**

This study presents a novel approach to develop an embedded fiber optic sensor for on-line monitoring of battlefield threats. The sensor design is based on on-fiber devices, where multifunctional materials are used as the fiber modified cladding. The detection mechanisms are based on spatial intensity modulation induced by changes in the multifunctional cladding materials.

Testing and characterization of multifunctional materials, developed by the UA, to identify the dynamic range and the bandwidth of the fiber optic sensor. Preliminary attempts to incorporate the optical fiber into textile structures are promising. More research and development is underway to enhance the multifunctional properties and integrate the system components as well as to improve the embedding process.

### Acknowledgments

This work was supported by the U.S. Army Research Office (Contract/Grant NO. DAAH04-96-1-0018), Research Triangle Park, NC. Special thanks to both Andrew Crowson and Ed Chen of the ARO for supporting this effort and for valuable discussions. This effort is a multidisciplinary collaborative research integrating Drexel University team with both UK and NCSU. Thanks to R. Quirk, W. Brittain, D. Reneker, M. Foster and Q. Zhuo of the UK for providing the multifunctional materials used in the study. Also, thanks to T. Little, H. Davis, and A. James of the NCSU College of Textiles for collaboration on the integration of the optical fibers into textile structures. Special thanks to J. Yuan the graduate student of DU, who is concentrating on the experimental measurements.

### References

1. Andrew Crowson, "Smart Materials Based on Polymeric Systems", Proc. SPIE Smart Structures and Materials 1996, Smart Materials Technologies and Biomimetics, Vol. 2716, p.2-7.
2. Reneker, D.H.; Mattice.,W.L.; Quirk, R.P.; Kim, S.J., "Macromolecular smart materials and structures", Smart Materials and Structures, vol.1, no.1, p.84-90, March 1992.
3. L.M. Siewierski and W.J. Brittain, Am. Chem. Soc., 35(1), 1994.
4. S.J. Kim and D.H. Reneker, Polym. Bull., 31, p.367, 1993.
5. I. Ahmad, Smart Materials, Structures, and Mathematical Issues, Technomic Publishing Co., Inc., 1. 1989
6. M. A. El-Sherif, "Spatial light modulators in multimode fibers," Technical Digest, Spatial Light Modulators and Applications, Optical Society of America, Vol. 8, 200-203, 1988.
7. M. A. El-Sherif, "Smart composites with embedded sensors for in situ monitoring and diagnostic systems," Materials Technology, Vol. 9, Nos. 7/8, 141-143, 1994.
8. J. Radhakrishnan and M. A. El-Sherif, "Analysis on spatial intensity modulation for fiber optic sensor applications," *J. Optical Fiber Technology*, Vol. 2, No. 1, pp 114-126, January 1996.
9. M. A. El-Sherif and F. K. Ko, "Spatial modulation within embedded fiber-optic sensors for smart structures characterization," Technical Digest of the First European Conference on Smart Structures and Materials, Glasgow, SPIE, Vol. 1777, 85-88, 1992.
10. El-Sherif, M. A. and Radhakrishnan, J., "Advanced Composites With Embedded Fiber Optic Sensors For Smart Applications," *J. of Reinforced Plastics and Composites*, Vol. 16, No. 2/1997, pp. 144-154.

## Optical Fiber Sensors Used in Smart Structural Systems

K. A. Murphy, M. F. Gunther, R. O. Claus

Fiber & Electro-Optics Research Center

Bradley Department of Electrical Engineering

Virginia Tech, Blacksburg, VA 24061

540-231-7203, fax 540-231-4561, email <kemurphy@vt.edu>

P. G. Duncan, M. E. Jones and M. B. Miller

F&S Inc., 2801 Commerce Street, Blacksburg, VA 24062

540-552-5128, fax 540-951-0760, email <pduncan@f-s.com>

Optical fiber sensors that have been developed over a period of several years by our group and used on a number of large government-industry smart structure demonstration programs are described.

We have developed several classes of optical fiber sensors and popularized their use for smart structural systems and other applications. Major classes of optical fiber sensors now used for the analysis of structural systems include Fabry-Perot and grating-based devices. In the area of Fabry-Perot sensors we developed the first extrinsic Fabry-Perot interferometric (EFPI) sensor elements as early as 1988, for the mapping of strain on mullite and corderite ceramic cross-flow filters at temperatures exceeding 700 °C in coal-fired combustor systems. The EFPI sensor element consists simply of two cleaved optical fiber ends inserted into a hollow-core fiber tube to form an air-gap cavity between the two fiber ends. Advantages of EFPI devices for this and similar applications is that the construction allows zero sensitivity to non-longitudinal strain and low sensitivity to temperature because the air in the cavity cannot support shear and its index of refraction does not vary significantly with temperature. Other groups have built on this design more recently to demonstrate similar air-gap Fabry-Perot sensor elements with similar sensitivities.

Networks of EFPI-based strain and temperature sensors, and other sensors, have been used on several major government/industry smart structures programs, including the Northrop-Grumman "Smart Metallic Structures" and "Smart Wing" programs, and the Lockheed-Martin "Smart Material Systems" and "Composite Smart Materials" programs, and those applications, and corresponding sensor performance, are summarized.

More recently, we also have worked to demonstrate grating-based fiber sensors, and to develop and demonstrate our own special version of those sensors with special advantages for structural instrumentation. Fiber Bragg gratings (FBGs) were developed in the late 1980s by several groups, and consist of periodic index of refraction variations along the core of the fiber that lead to optical backreflection at a wavelength determined by the spatial period of the index variation. Perturbations such as temperature or strain vary this spatial period and thus the backreflected wavelength, making it possible to measure the temperature or strain. We have worked in cooperation with Bell Laboratories/Lucent Technology to develop and demonstrate instead long-period

grating (LPG) sensors that act as wavelength specific attenuators rather than reflectors. Major advantages of LPGs as sensors include larger sensitivity and the ability to tailor the properties of the core and the cladding of the fiber to implement a strain sensor with zero temperature sensitivity, or a temperature sensor with zero strain sensitivity.

We describe recent laboratory and large government/industry program test articles we have instrumented using FBG and LFG sensors, and outline results.

This work has been supported by sponsors including DARPA, the Air Force, Navy, NASA and DoE.

# Distributed Modal Sensors

Prof. Hartono Sumali  
Agricultural and Biological Engineering  
Purdue University  
West Lafayette IN 47907

Prof. Harley H. Cudney  
Center for Intelligent Materials, Systems, and Structures  
Department of Mechanical Engineering  
Virginia Polytechnic Institute and State University  
Blacksburg VA 24061-0261

## ABSTRACT

The sensing technique described in this dissertation produces modal coordinates for monitoring and active control of structural vibration. The sensor array is constructed from strain-sensing segments. The segment outputs are transformed into modal coordinates by a sensor gain matrix.

An adaptive algorithm for computing the sensor gain matrix with minimal knowledge of the structure's modal properties is proposed. It is shown that the sensor gain matrix is the modal matrix of the segment output correlation matrix. This modal matrix is computed using new algorithms based on Jacobi rotations. The procedure is relatively simple and can be performed gradually to keep computation requirements low.

The sensor system can also identify the mode shapes of the structure in real time using Lagrange polynomial interpolation formula.

An experiment is done with an array of piezoelectric polyvinylidene fluoride (PVDF) film segments on a beam to obtain the segment outputs. The results from the experiment are used to verify a computer simulation routine. Then a series of simulations are done to test the adaptive modal sensing algorithms. Simulation results verify that the sensor gain matrix obtained by the adaptive algorithm transforms the segment outputs into modal coordinates.

# Distributed Modal Sensors

Dr. Anton Sumali  
Purdue University

Dr. Harley H. Cudney  
Virginia Polytechnic Institute & State  
University

Third ARO Workshop on Smart Structures  
August 1997



MMYY2

## Why modal sensors

- To monitor modal responses  
E.g., flutter analysis (Shelley, Freudinger, Allemand)
- To prevent observation spillover  
Control energy from one mode affects other modes, can cause instability (Balas, 1978)  
In feedforward control: degrades performance (Clark, 1995)
- To implement modal space control  
Independent modal space control (IMSC) (Meirovitch, 1982):  
Controls MDOF structures as independent SDOF systems.  
Adaptive feedforward modal space control (Clark, 1995):  
Decouples coefficient adaptation of adaptive filters.  
Integration with structural design (Canfield, 1994)

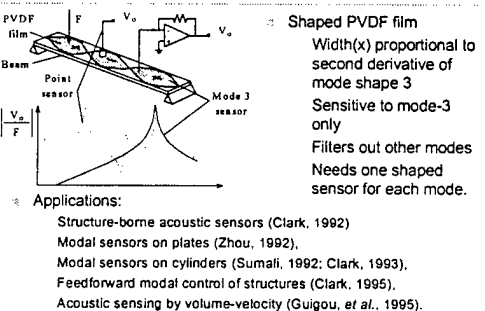
## Why modal sensors (cont'd)

- To create acoustic sensors  
Structure-borne acoustic sensors (Clark, 1992): Acoustic responses proportional to combinations of modal coordinates.  
Modal sensing of efficient acoustic radiators (Clark, 1992)  
Volume-velocity sensing (Guigou, 1996)

## The quest for modal sensors

- Shelley, Freudinger, Allemand (19xx)  
Transformed sensor outputs into modal coordinates in real time using a transformation matrix.
- Ouyang (1987), Davidson (1990)  
Used Voltage-Controlled-Oscillators to resynthesize modal coordinates.
- Lee (1987)  
Shaped piezoelectric PVDF film to sense one mode and filter out other modes.

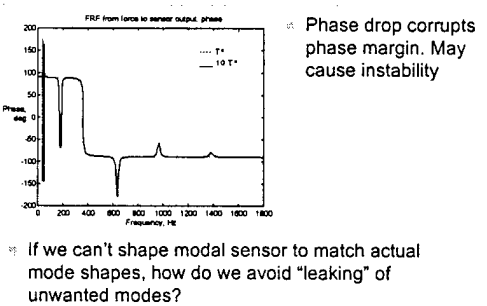
## Lee (1987)



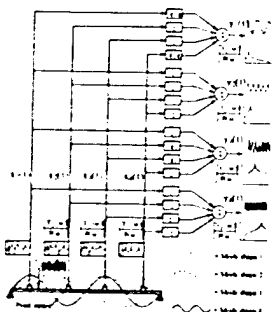
## Inadequate modal filtering

- Failure to filter out undesired modes may result from:  
Imperfect knowledge of mode shapes  
Imperfect sensor shape (even microscopic) Lee (1987)
- Example:  
  
Mode-3 sensor was designed for  $T''=1$ .  
( $0 < T < \infty$ ).  
Actual  $T'' = 10$

## Effect of inadequate modal filtering



### Discrete modal filters: basic idea

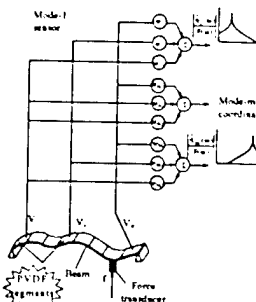


- Modal coordinates = Linear combination of sensor outputs Allemand (1980)

$y = Wx$

Gain matrix  $W$ :  
Proportional to eigenvectors  
If inaccurate, can be adjusted

### Segmented modal sensors



Rectangular piezoelectric film segments:  
Easy to build, cheap, little loading on structure  
One array can be used to sense many modes.  
Can be made adaptive by adjusting the weights.

### Outputs of segments

Segment outputs are proportional to difference between slopes at segment ends

$$V_{ij} = c_{ij} b \frac{h}{2} \left( \left. \frac{\partial^2}{\partial x^2} \right|_{x_i} - \left. \frac{\partial^2}{\partial x^2} \right|_{x_j} \right)$$

Slopes are proportional to modal coordinates

$$\frac{\partial^2}{\partial x^2} = \sum_{i=1}^n c_{ij} n_i(t) \\ C_s = \text{Matrix of slope differences}$$

Thus, segment outputs are proportional to modal coordinates. For an array of segments,

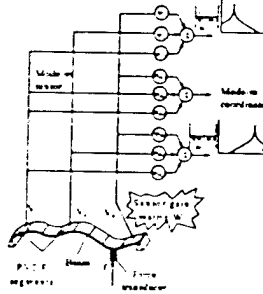
### Sensor gain matrix calculation

- Segment outputs are proportional to modal coordinates.
 
$$V = C_S n$$

Mode slope differences
- We want sensor gain matrix  $W$  to transform segment outputs into modal coordinates
 
$$y = WV$$

$$y = WC_S n$$
- Thus, we must set the gain matrix  $W$  to
 
$$W = C_S^{-1}$$

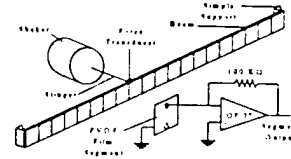
### Transforming segment outputs into modal coordinates



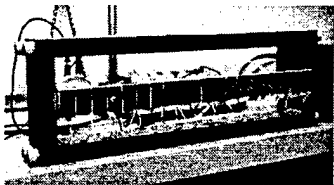
- Sensor gain matrix  $W$  transforms segment outputs  $V$  into modal coordinate estimate

- Modal coordinate estimate is not exactly the same as modal coordinates, because of modal truncation.  
More modes included in calculation → more accurate modal coordinates.

### Experiment setup



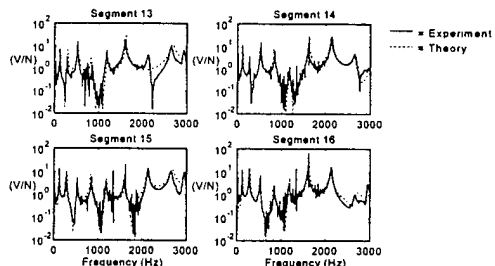
## Experiment setup



Property	Value	Unit	Property	Value	Unit
Length (L)	0.4500	m	Density ( $\rho$ )	2700	kg/m <sup>3</sup>
Width (b)	0.0381	m	Young's modulus	68(10 <sup>9</sup> )	Pa
Thickness	3.175	mm	Poisson's ratio	0.3	

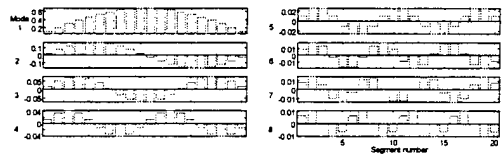
- Obtained FRF's from force to segment outputs.
- Twenty segments on beam. Point force burst random excitation.

## FRF's from force to segment outputs



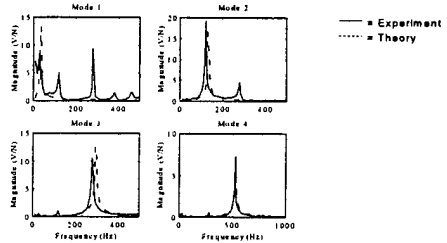
## Sensor gain matrix

- Gain matrix W to transform outputs of 20 segments into the first eight modal coordinates
- Each row = one mode filter



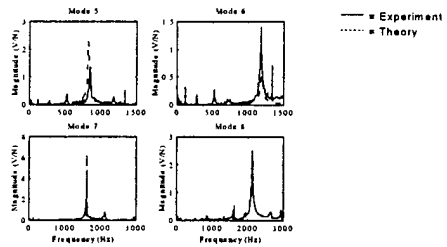
## Sensor outputs

- FRF's from force to modal coordinate estimates  $\hat{\eta} = WV$  should be SDOF (ideally)



## Sensor outputs (cont'd)

- Inadequate modal filtering results in a little "leaking" of unwanted modes.



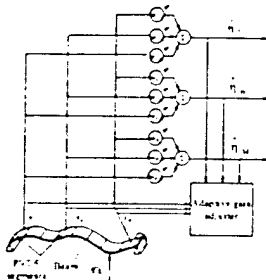
## Need for adaptive modal sensors



- Inaccuracy in structural parameters
  - Boundary conditions are not exactly zero-moment.
  - Segment dimensions and positions are not perfect.
  - Physical parameters are not exact.

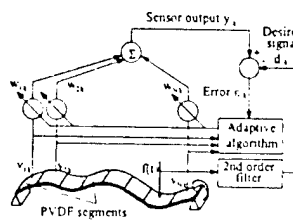
- Adaptive modal filters
  - Adjust gain matrix W automatically until outputs are true modal coordinates.
  - Can extract modal properties from W.

### Adaptive modal filter



**Adaptive algorithm**  
Adjusts gain matrix  $W$  until outputs are modal coordinates.  
Receives data from segment outputs  $V$ .  
Can use sensor outputs as performance feedback.

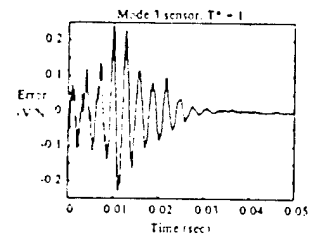
### Training the weights using known modal parameters



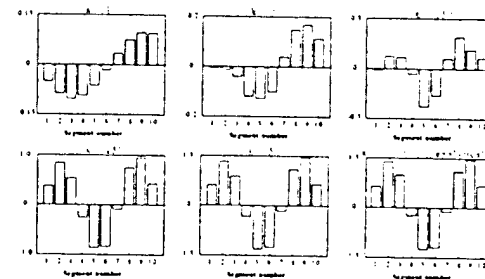
**Adaptation scheme**  
Each mode = a second-order filter.  
LMS Algorithm adjusts weights according to  
 $W_{k+1} = W_k + 2\mu r_k v_k$   
 $\mu$  = an adaptation parameter

Note: we need to program the natural frequency and damping into the filter.

### Error signal history

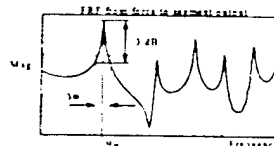


### Weight evolution: mode-3 filter



### Filter to train weights

- To obtain natural frequency and damping ratio



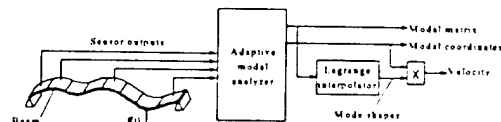
For a lightly damped lightly coupled mode:  

$$\Omega_n = \frac{\Delta_m}{2\pi m}$$

We need to program the natural frequency and damping into the filter

If we do not even have any FRF, can we still create a modal filter?

### Adaptive modal analyzers



Adjusts gain matrix  $W$  automatically until sensor outputs are modal coordinates.  
Extracts modal matrix (mode shapes).  
Also can produce velocity signal.

## Conclusions

- Modal sensors are very sensitive to inaccuracies.
- Array of strain sensors lends itself to adaptive modal filtering.
- Modal matrix of segment output correlation matrix transforms segment outputs to modal coordinates.
- Algorithms B and C compute sensor gain matrices efficiently.
- Lagrange interpolation estimates mode shapes from sensor gain matrix.



0-8974-3

Virginia Tech

## Future directions

- Solve problems with imperfect modal filtering, scaling, mode-ordering.
- Develop methods to filter out noise.
- Experiment with programmable digital signal processors.
- Build hard-wired adaptive modal analyzers.
- Use Lagrange interpolation circuits for estimating deflections and mode shapes.



0-8974-3

Virginia Tech

# WIRELESS MEMS SENSORS FOR MEASURING DEFLECTION, ACCELERATION AND ICE DETECTION ON SCALE MODEL ROTORBLADES

Vijay K. VARADAN and Vasundara V. VARADAN

Alumni Distinguished Professors of  
Engineering Science and Mechanics and Electrical Engineering  
Research Center for the Engineering of Electronic and Acoustic Materials  
Pennsylvania State University  
University Park, PA 16802

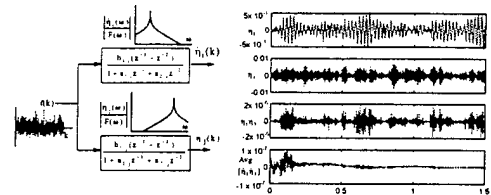
## ABSTRACT

Smart MEMS (MicroElectroMechanical Systems) in the form of integrated sensors and actuators offer significant potential for many rotorcraft applications. Sensing of flex beam deflection and acceleration, ice formation and deicing are major candidate areas where smart conformal MEMS based sensors can be exploited by the rotorcraft community. The major technical barrier of the present day smart structures technology is the need for wired communication between sensors and actuators in the rotating system and controllers, data storage units, and cockpit avionics. Many proposed sensors and actuators are commonly distributed either along the blade length or, in the active flap devices, out near the 75% blade radial station. Also they are not conformal to the airfoil shape of the rotor blades. The communication between rotating and fixed systems is typically accomplished using complex slip ring assemblies transferring electronic information down through the rotor shaft. Although advances have been made in wired communication, these complex assemblies are essentially similar to test hardware and present numerous reliability and maintainability limitations when implemented on a production scale. Considering these limitations, development of a wireless means of communication through a new generation of conformal sensors with built-in antenna, akin to telemetry, could have a dramatic beneficial payoff for rotorcraft applications.

In this talk, a summary of recent developments in MEMS sensors and wireless telemetry will be presented. The performance of the integrated sensor system will be shown on a scale model rotorblade.

The authors would like to acknowledge many helpful discussions with Dr. Gary Anderson and Professor Inderjit Chopra. The work is sponsored by US Army MURI program through the University of Maryland and NRTC through the Rotorcraft Center of Excellence of Penn State University.

### Correlations among modal coordinates



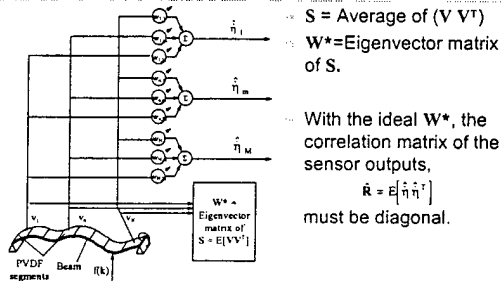
- Two different modal coordinates are uncorrelated.
- Average of the product converges to zero.

### Correlation matrix and eigenvectors

- Sensor output = gain matrix . segment outputs  
 $\hat{n} = WV$
- Define correlation matrix = Expected value of outer product of sensor outputs.  
 $\hat{R} = E[\hat{n}\hat{n}^T]$
- For "quasi-constant" gain matrix,  $\hat{R} = W E[VV^T]W^T$
- If  $W$  is the eigenvector matrix of  $E[VV^T]$   
then the correlation matrix  $\hat{R}$  is diagonal.

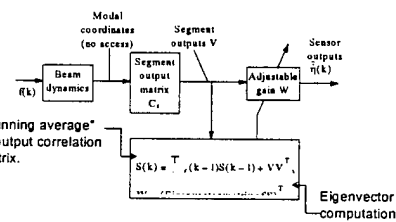
The gain matrix that transforms the segment outputs into uncorrelated signals is the eigenvector matrix of the expected value of the outer product of the segment outputs.

### The ideal gain matrix



- $S = \text{Average of } (V V^T)$
- $W^* = \text{Eigenvector matrix of } S$ .
- With the ideal  $W^*$ , the correlation matrix of the sensor outputs,  
 $\hat{R} = E[\hat{n}\hat{n}^T]$   
must be diagonal.

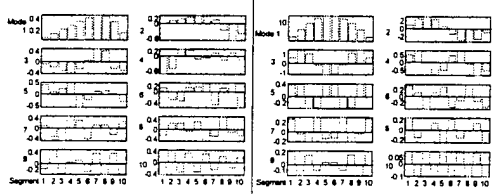
### Simulation



- "Running average" of output correlation matrix.
- Average  $S(k)$  gets better with time.
- So does the gain matrix  $W$ .

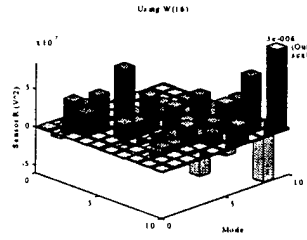
### Gain matrix $W$ .

- Computed with  $k = 16$  iterations



### Output correlation matrix $\hat{R} = E[\hat{n}\hat{n}^T]$

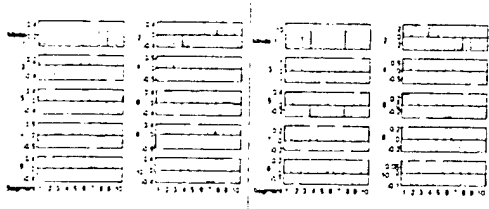
- Computed with  $k = 16$  iterations



Still far from being diagonal.

Gain matrix  $W$ .

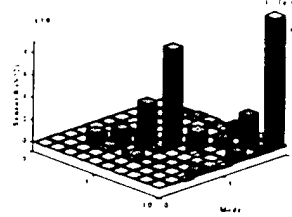
Computed with  $k = 256$  iterations



Ideal

Output correlation matrix  $\hat{R} = E[\hat{\eta}\hat{\eta}^T]$

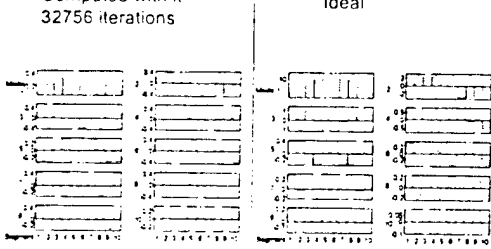
Computed with  $k = 256$  iterations



Still not diagonal.

Gain matrix  $W$ .

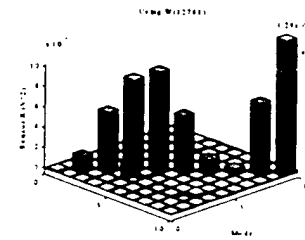
Computed with  $k = 32756$  iterations



Ideal

Output correlation matrix  $\hat{R} = E[\hat{\eta}\hat{\eta}^T]$

Computed with  $k = 32756$  iterations



Practically diagonal.

# Wireless MEMS sensors for measuring deflection, acceleration and ice detection on scale model rotor blades

V. K. Varadan and V. V. Varadan

Alumni Distinguished Professors of  
Engineering Science and Mechanics and Electrical Engineering  
Center for the Engineering of Electronic and Acoustic Materials  
Pennsylvania State University, University Park, PA 16802

3rd ARO WORKSHOP ON SMART STRUCTURES

Virginia Polytechnic Institute and State University  
August 27, 1997

PSU/CEEAM

## **OUTLINE**

- INTRODUCTION
- MOTIVATION
- SCALE MODEL ROTOR BLADES
- CONVENTIONAL MEMS VIBRATION AND ACCELERATION SENSORS
- IDT MICROSENSORS AND WIRELESS COMMUNICATION WITH SMART ELECTRONICS
- DEFLECTION AND STATIC AND DYNAMIC STRAIN MEASUREMENT; COMPARISON WITH STANDARD STRAIN GAUGE
- MEMS-IDT MICROACCELEROMETERS
- MICROFABRICATED IDT MICRO ICE SENSOR
- MICROFABRICATED ANTI-ICING DEVICE
- CONCLUSION



PENNSTATE  
SMART SKIN WITH  
MESOSENSORS AND  
MESOACTUATORS

↑  
CONTROLLED  
OSCILLATORY  
MOTION  
↓

AIRFOIL SECTION  
WITH SMART SKIN

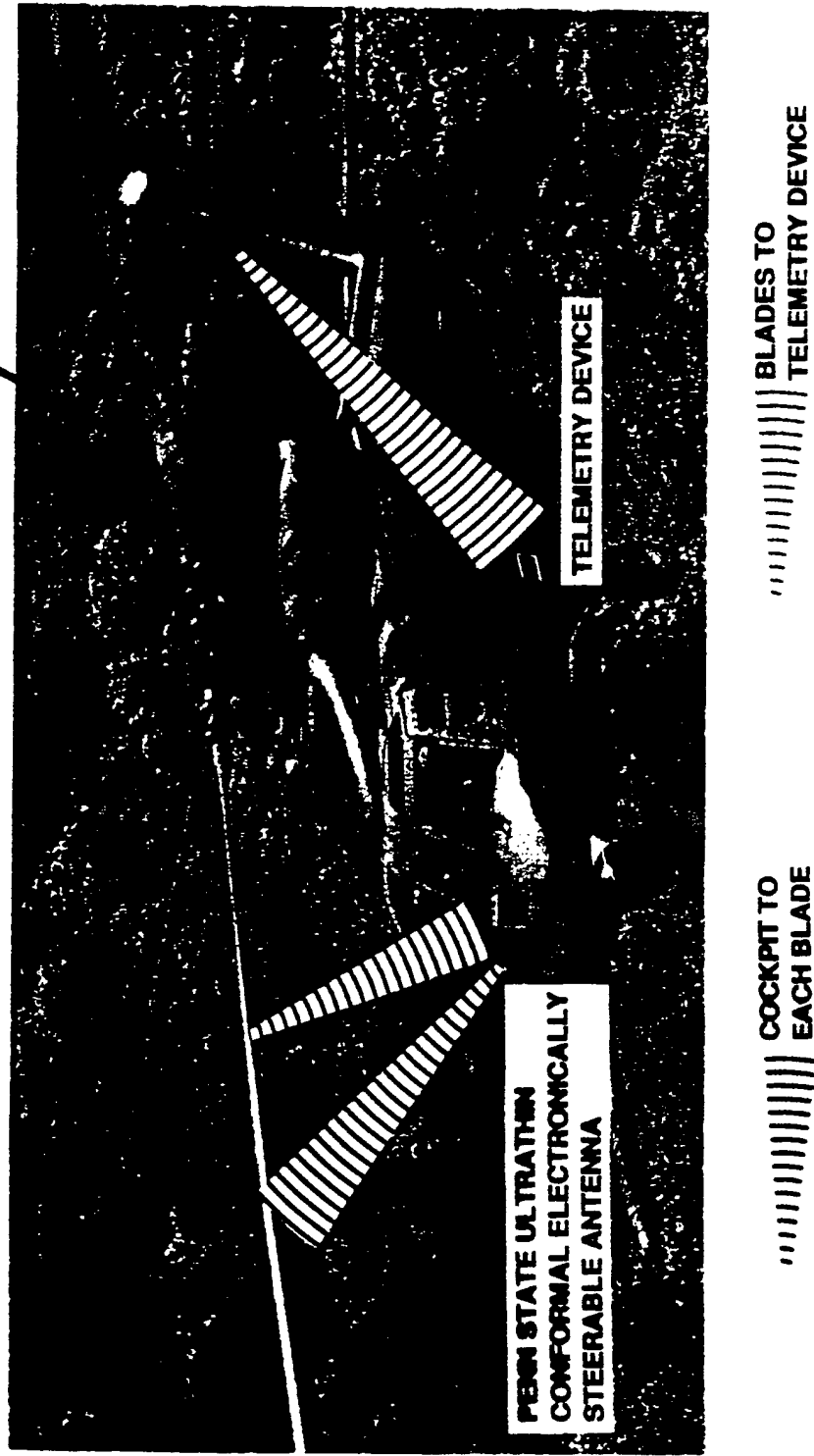
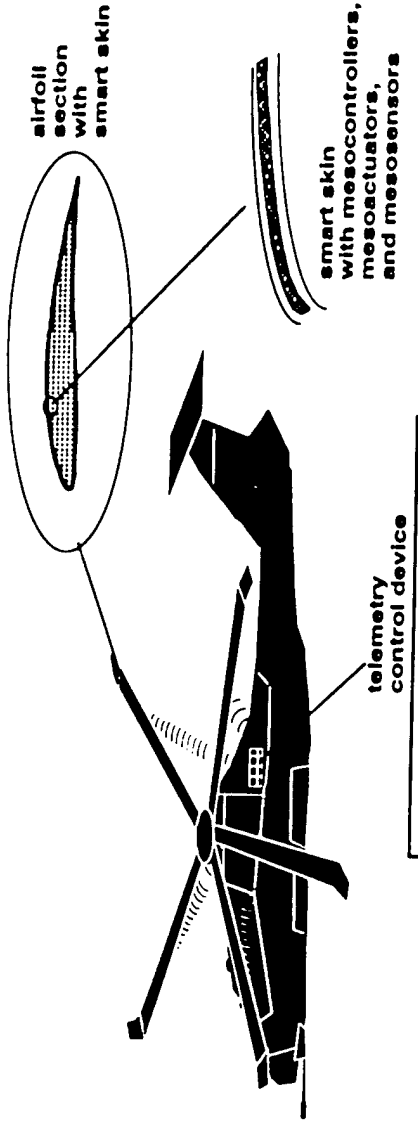


Figure 1.1a: Concept for Smart Rotor Blades allowing for Wireless Telemetry between Blade Sensors/Actuators and Cockpit using Antennas

AROMURI Mesoscale Integration for Smart Structures



## MOTIVATION

- Smart structures in the form of integrated sensors and actuators offer significant potential applications, such as sensing unsteady pressure, acceleration, shearing force, local strain and structural deflections, flow induced noise and vibration and BVI in rotor crafts

- A major technical barrier is the communication link between numerous sensors and actuators in the rotating system, and controllers, data processors, and power conditioning units in the fixed frame. This communication link between rotating and fixed systems is typically accomplished using complex slip-ring unit transferring electronic information down through the rotor shaft. The slip-ring unit is expensive and limited (in terms of number of connections), and is a source of maintenance problems.

- Considering these limitations, development of a wireless means of communication through a new generation of conformal MEMS sensors, could have a dramatic payoff for rotocraft applications

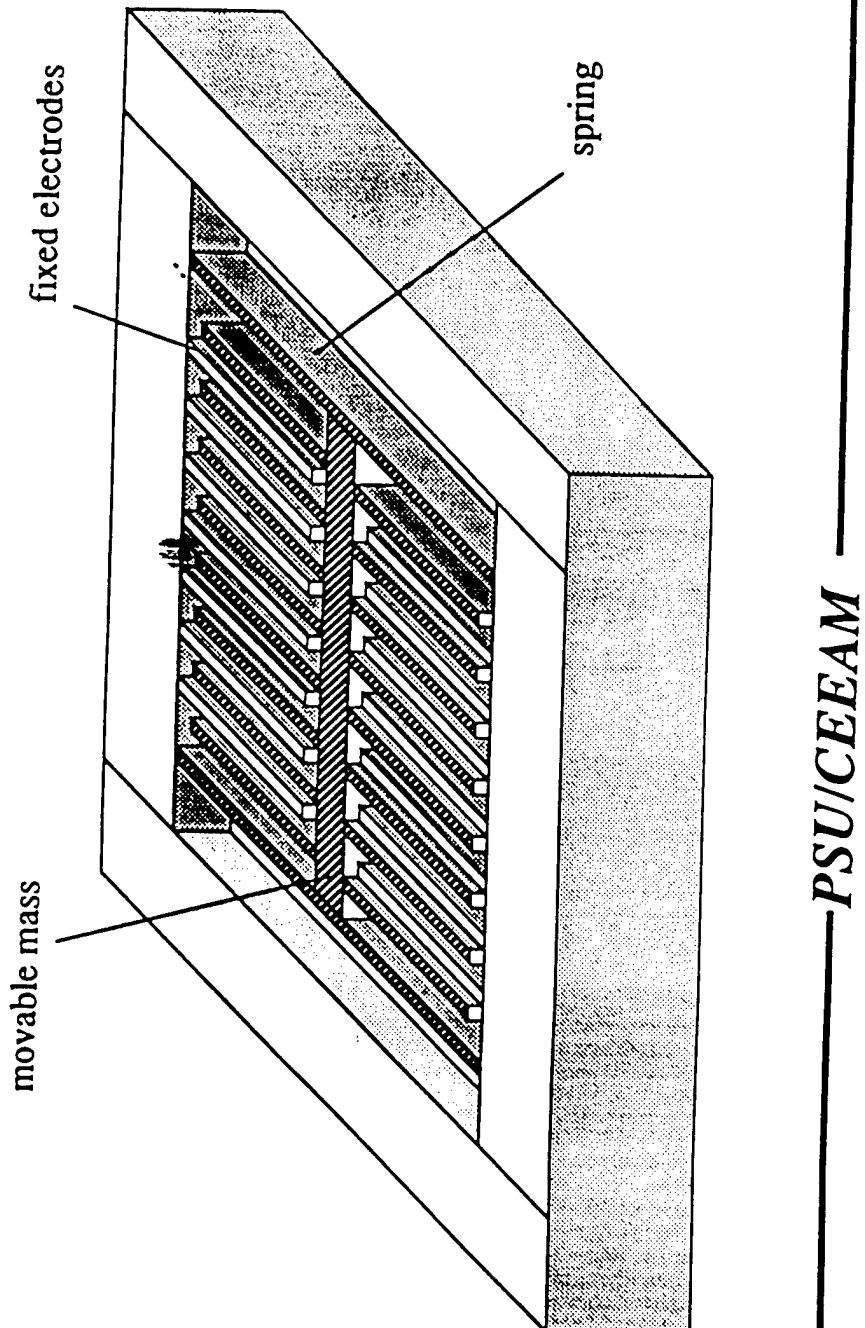
# Scale Modeling of Rotorblade

- The base strain for the S-76A rotorblade was calculated for its first vibrational mode using beam theory
- FEM Modeling, using ABAQUS, was applied to scale down the blade to approximately one-tenth its size thus simulating a base strain close to that of the original blade
- The experimental and theoretical base strains were compared



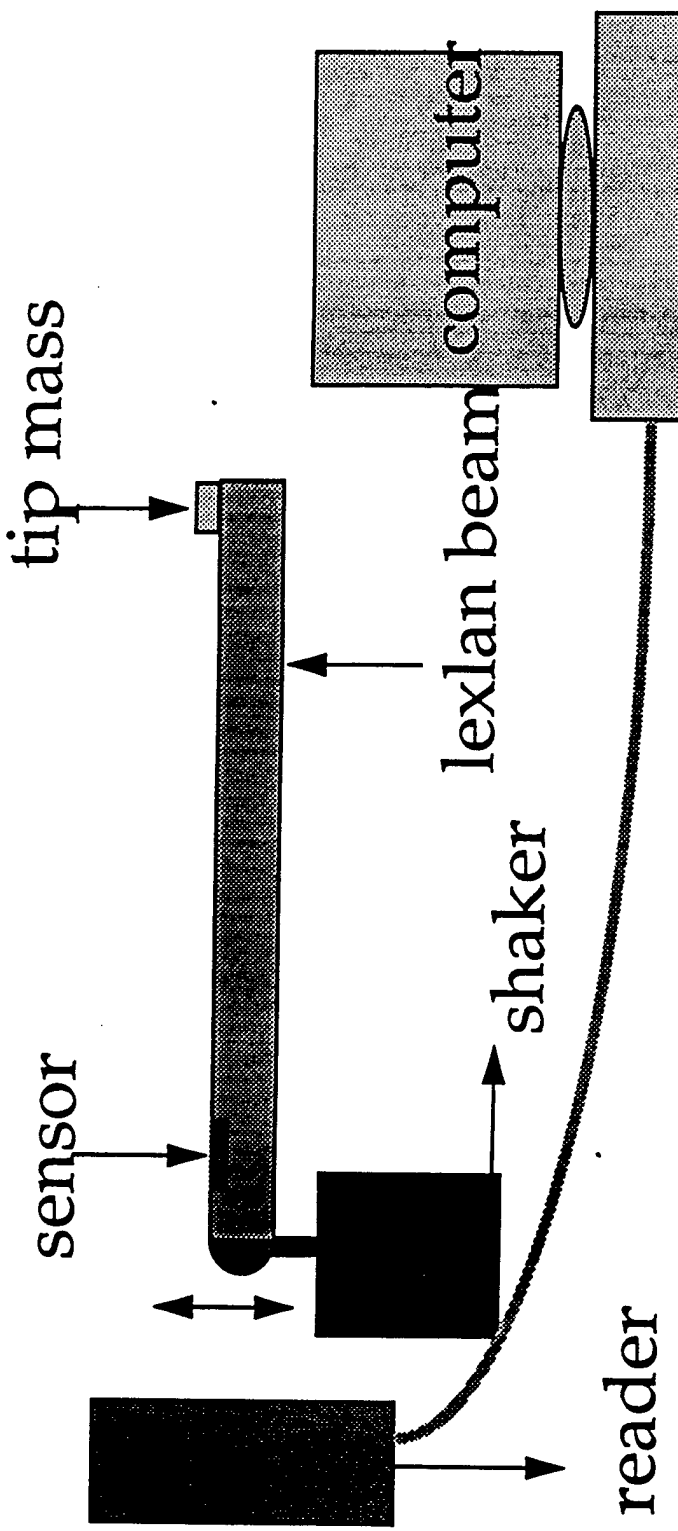
*Research Center for the Engineering of Electronic and Acoustic Materials*

## Three Dimensional View of the MEMS Sensor



PSU/CEEAM

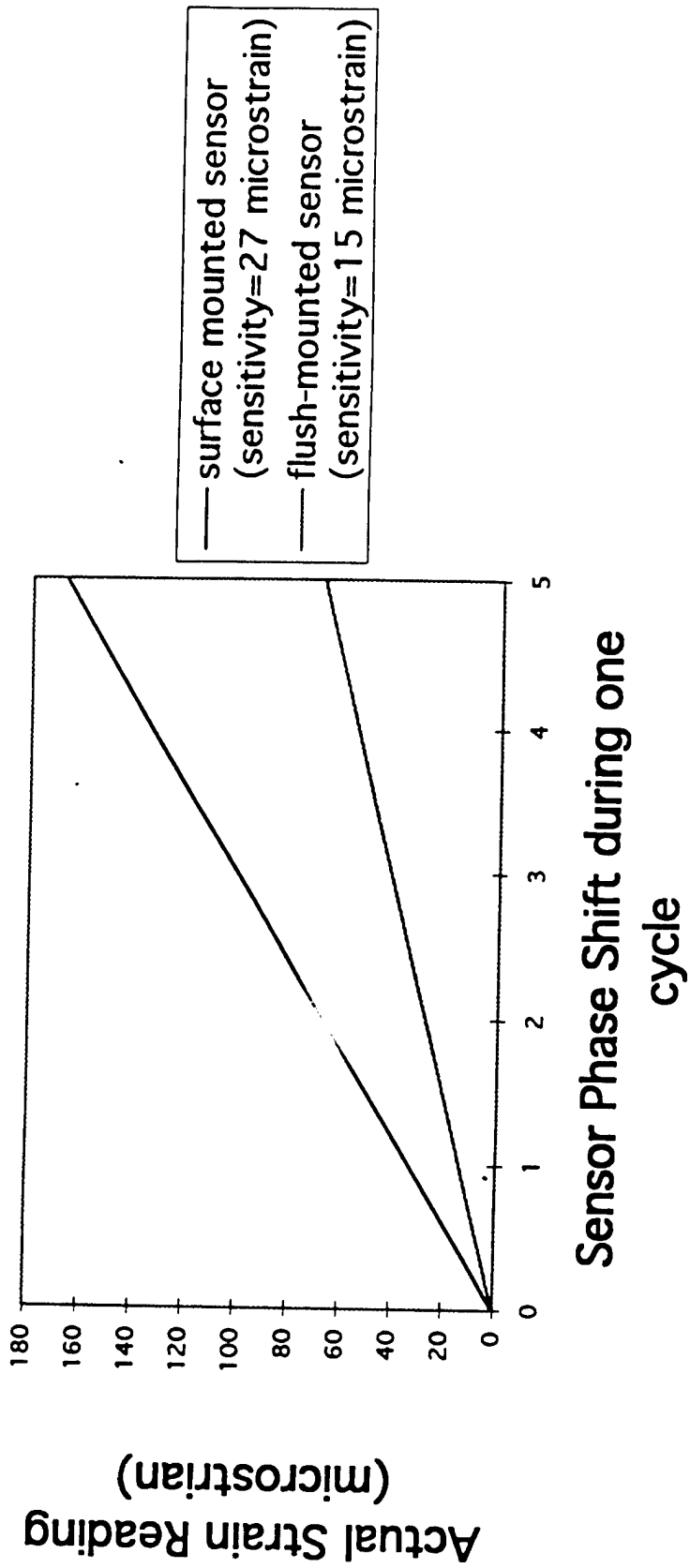
# Experimental setup of flush-mounted sensor



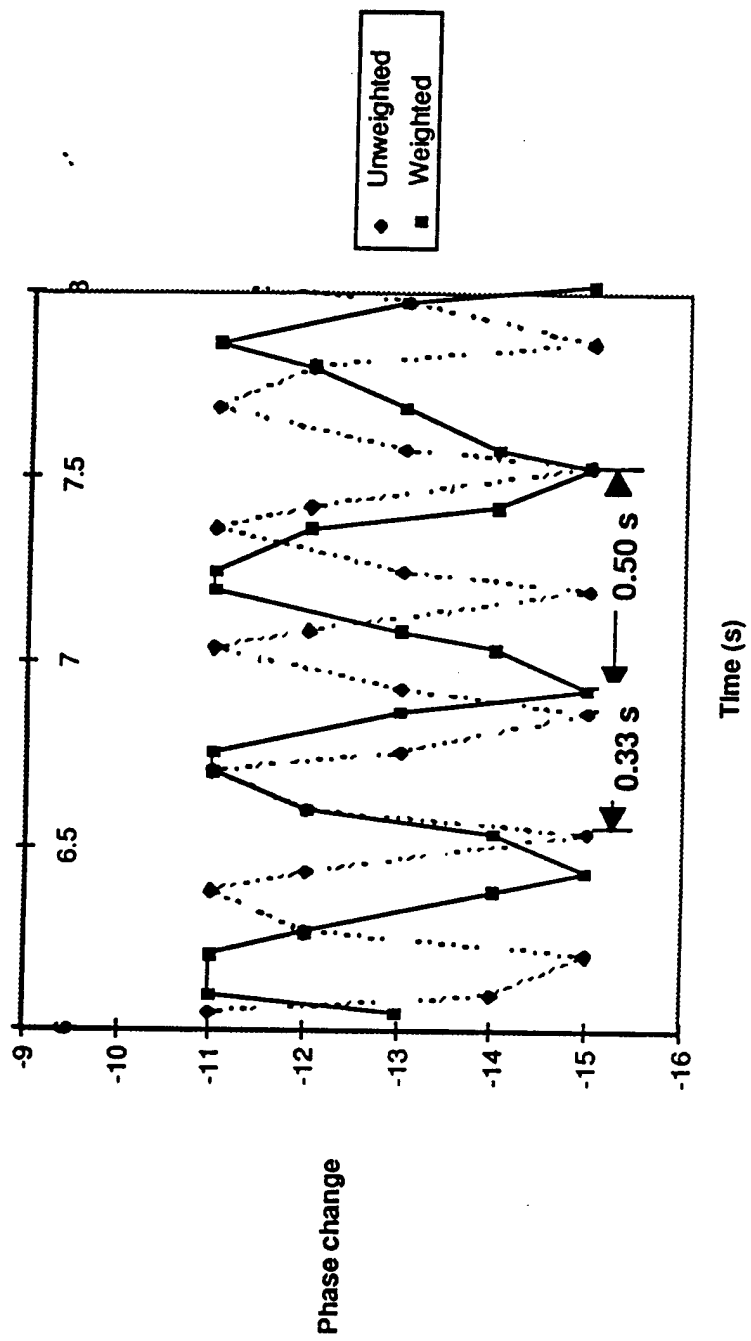
PENNSTATE  
Research Center for the Engineering of Electronic and Acoustic Materials



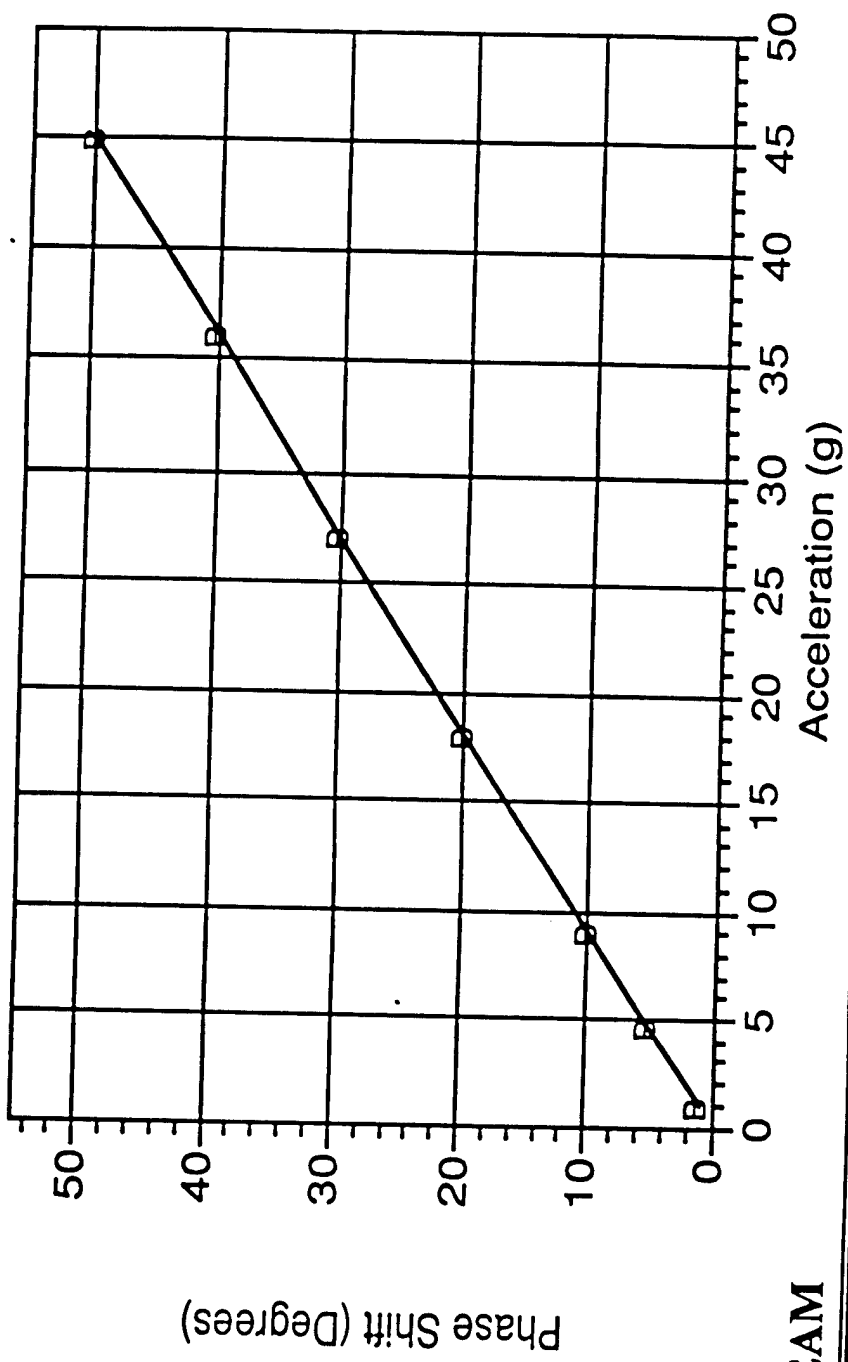
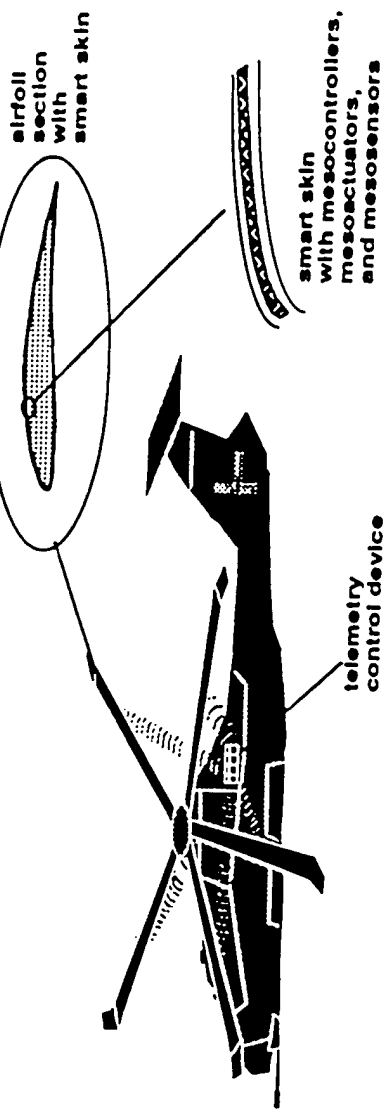
## Sensor Sensitivity Comparison for two different sensor mountings



# Dynamic Strain Measurement by Surface Mounted Sensor



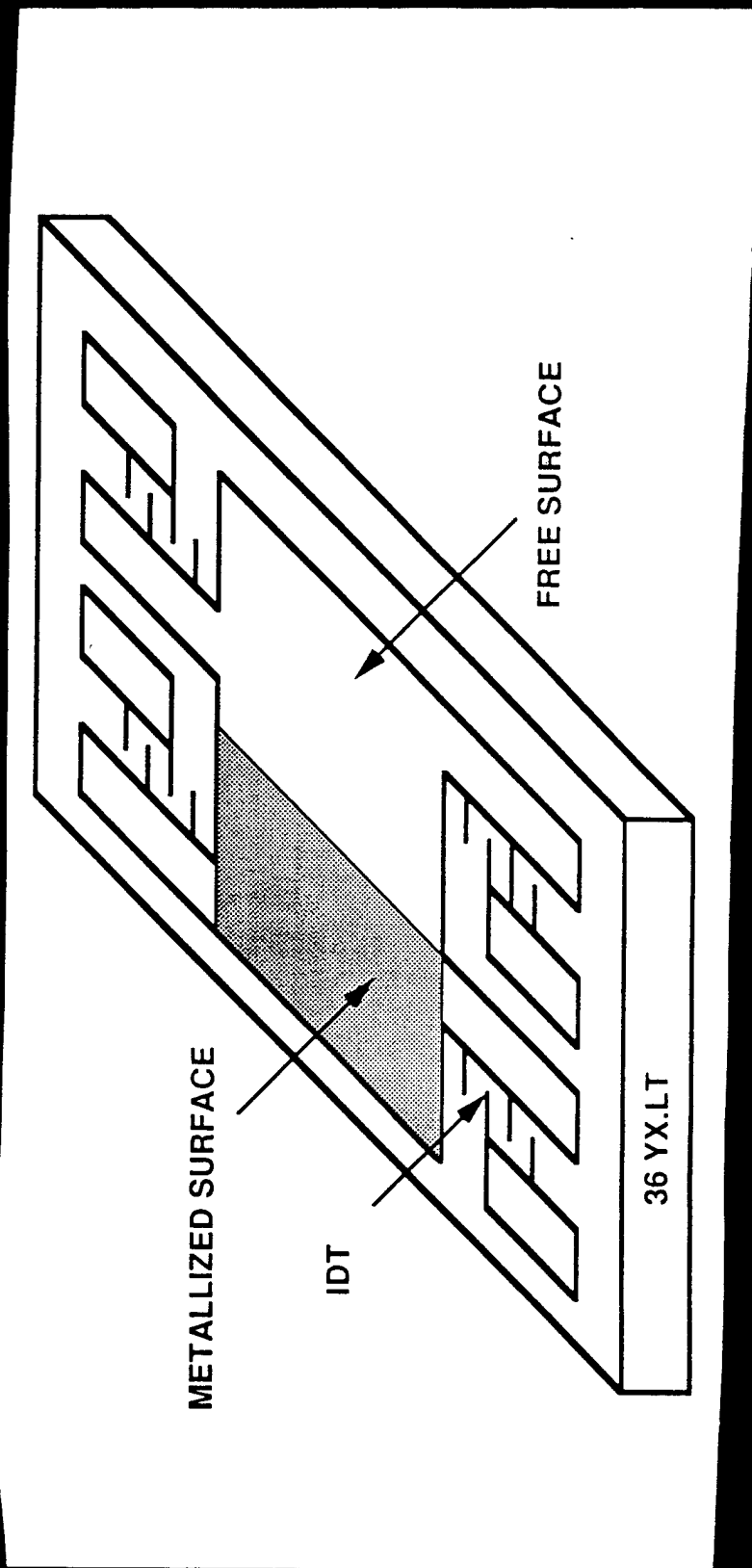
Graph of Phase Change v / s Strain



Phase Shift (Degrees)

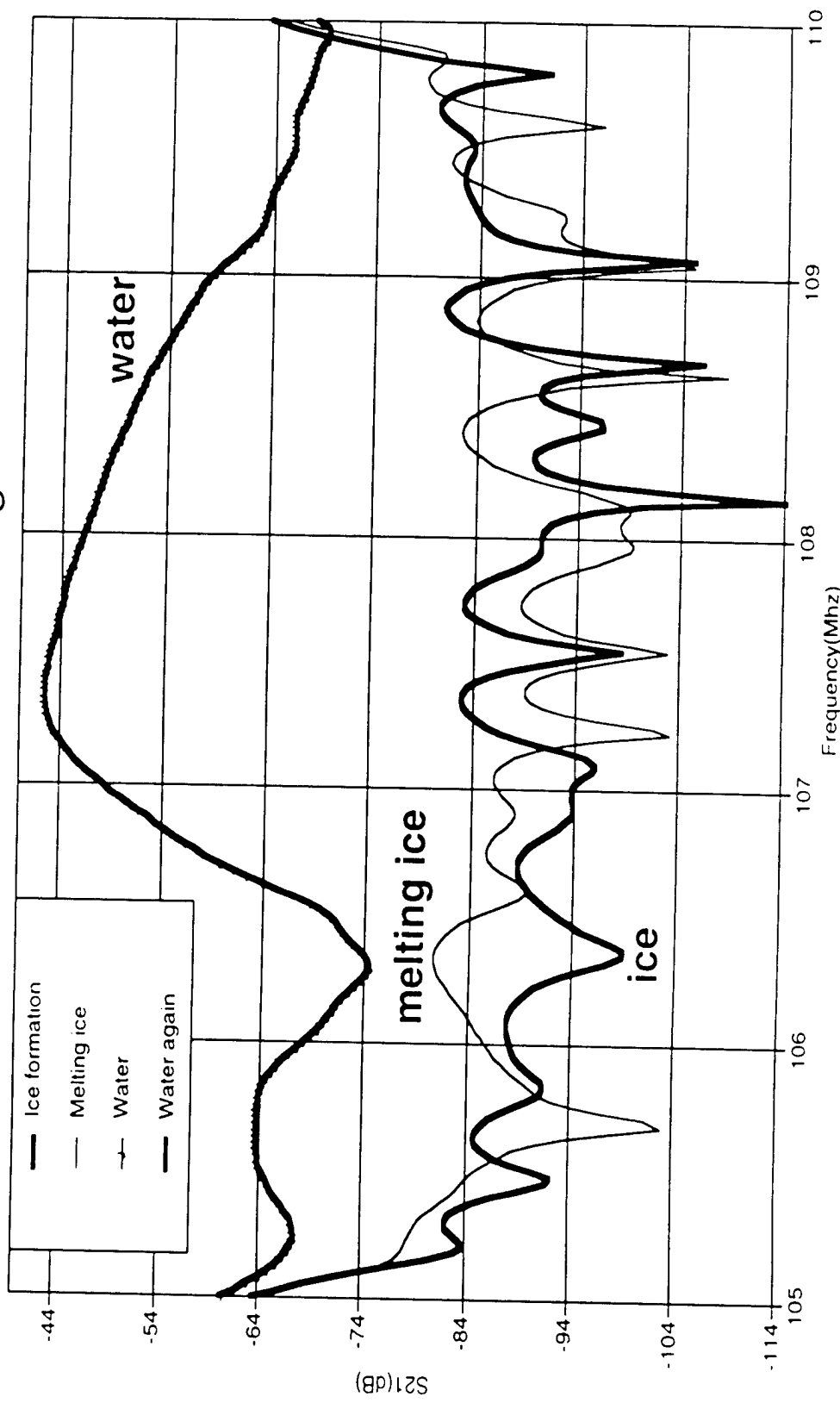
PSU/CEEAM

# *Love-Wave Delay Line*



# SMART ICE SENSOR

Ice Sensing



# Structurally Embedded Multifunction Fiber Optic Sensors

X. D. Jin and J. S. Sirkis

Smart Materials and Structures Research Center

Mechanical Engineering, University of Maryland, College Park, MD 20742

J. K. Chung

Department of Mechanical Engineering, Chosun University

375 Seosuk-dong, Kwangju, 501-759, Korea

## ABSTRACT

An optical fiber sensor for simultaneous measurement of axial strain and temperature is reported. This sensor configuration consists of an in-line fiber etalon (ILFE) cascaded with a in-fiber Bragg grating (BG) and is demultiplexed using a variation of coherence division multiplexing. The strain/temperature sensor is demonstrated by embedding it into a graphite/epoxy composite cantilever beam. They are found to agree with traditional strain and temperature sensors to within  $5\mu\epsilon$  and  $0.5^\circ\text{C}$ , respectively for a sensor gage length of  $\sim 1.0\text{cm}$ .

**Keywords:** in-line fiber etalon, Bragg grating, temperature, strain, F-P interferometer

## 1. INTRODUCTION

Considerable progress has been made on the development of fiber optic based temperature and strain sensors in the last few years<sup>1-6</sup>. The goal of many of these devices is to use a single transducer to measure strain and temperature at the same time. This is particularly true in smart structure applications where complex thermomechanical strain fields can be common. This paper describes the combination of an in-fiber Bragg grating (BG) and an in-line fiber etalon (ILFE) for the purpose of simultaneously measuring strain and temperature. The ILFE is sensitive to the axial strain, much less sensitive to temperature, and insensitive to transverse strain<sup>7</sup>. The low intrinsic thermal sensitivity of ILFEs results in a response that is primarily proportional to the thermomechanical axial strain in the structure. In contrast, Bragg grating sensors are intrinsically sensitive to axial strain, transverse strain and temperature because the refractive index of silica responds to temperature and all three principal strains in the fiber. The different sensitivities of ILFE and BG sensors enable the two sensors to be combined into a single transducer capable of decoding temperature and strain.

The ILFE/BG configuration described above can only be successful in measuring the axial strain and temperature if the signals from the two sensors can be separated. In the original incarnation of this strain and temperature sensor, Singh and Sirkis<sup>8</sup> decoded the sensor signals from the ILFE and BG sensors using two light sources with different wavelengths and using a WDM to separate the two sensor signals. An optical spectrum analyzer was used to measure the wavelength shift of the BG sensor and path-matched differential interferometry to measure the optical phase change generated in the ILFE sensor. While this WDM approach was effective in demonstrating the concept, the optical spectrum analyzer limits measurement resolution and bandwidth. The sensor system presented in this paper uses only one light source, interferometric demodulation for BG sensor interrogation<sup>9</sup>, and path matched differential interferometry (PMDI)<sup>10</sup> for ILFE sensor interrogation. The ILFE/BG signals are demodulated by using Pseudo-Heterodyne (Serrodyne) scheme with ramp mod-

ulation, and then used with the respective phase-strain-temperature equations to develop a well-conditioned system of two equations for the strain and temperature. The ILFE/BG sensor system is demonstrated in an embedded catilever beam which a simultaneous combination of both strain and temperature fields was applied to.

## 2. PRINCIPLE OF OPERATION

### 2.1 Path Matched Interferometry for the ILFE Sensor

ILFE sensors are formed by fusing a hollow capillary tube to a single fiber. This capillary, which has the same outer diameter as the standard single mode fiber, is cleaved under a microscope to the desired ILFE gage length, and then fused with the other single fiber<sup>7</sup>. The phase of the light propagating in this sensor cavity is primarily proportional to axial strain along the fiber length. Path matched differential interferometry (PMDI) is used to demodulate the ILFE signal. PMDI is implemented by illuminating an interferometer with a broadband source having a coherence length smaller than the optical path length of the sensor. The ILFE sensor is cascaded with another interferometer which has a path length almost equal to the path length of the sensor so that the coherent interference fringes are produced. The phase change in the ILFE sensor is given by

$$\Delta\Phi_{\text{ILFE}} = 2\beta_0(\Delta L_{\text{ILFE}} + \xi^a \Delta T L_{\text{ILFE}}); \quad (1)$$

where  $\Delta L_{\text{ILFE}}$  is the change in the ILFE sensor cavity length;  $L_{\text{ILFE}}$  is the ILFE cavity length;  $\xi^a$  is the normalized temperature coefficient of air;  $\beta_0$  is the propagation constant in air; and  $\Delta T$  is the temperature perturbation.

### 2.2 Fabry-Perot Read-out Interferometer for the In-Fiber Bragg Grating Sensor Interrogation

In-fiber Bragg grating sensors have attracted considerable interest because of their intrinsic nature and wavelength-encoded operation. The sensing signal is encoded directly into wavelength, which is an absolute parameter and does not depend on the light intensity. The dependence of the reflected wavelength on fiber strain and temperature lies in the detection of the wavelength shift. An optical spectrum analyzer or monochromator can be used to detect the wavelength shift, but they are unattractive due to their bulk-optical nature, big size, and limited resolution. A viable alternative to this instrument was proposed by Kersey<sup>9</sup> in which an unbalanced interferometer used as a wavelength discriminator. The experiments in this paper use a low-finesse Fabry-Perot readout interferometer for wavelength-shift determination of the return signal from the BG sensor. The wavelength component reflected back from the Bragg grating effectively becomes the monochromatic source launched into the Fabry-Perot interferometer. Wavelength shifts induced by strain and temperature resembles a wavelength modulation of this source. The Fabry-Perot readout interferometer converts the wavelength shift of the light into an optical phase shift given by:

$$\Delta\Phi_{\text{BG}} = 4\pi L_{\text{FP}} \Delta\lambda_{\text{B}} / \lambda_{\text{B}}^2; \quad (2)$$

where  $\lambda_{\text{B}}$  is the Bragg wavelength of the BG sensor;  $\Delta\lambda_{\text{B}}$  is the induced change in the reflected Bragg wavelength due to the strain and temperature perturbation; and  $L_{\text{FP}}$  is the F-P cavity length.

### 2.3 Axial Strain and Temperature Determination

The phase change of ILFE sensors depend primarily on axial strain component and has small dependence on temperature<sup>7</sup>. On the other hand, BG sensors have sensitivity to not only all the principal strain components, but also a strong dependence on the temperature. The following two equations show the functionality of phase changes in terms of the strain components and temperature for ILFE and BG sensors:

$$\Delta\Phi_{ILFE} = K_{1e}\varepsilon_1 + K_{1T}\Delta T \quad (3)$$

$$\Delta\Phi_{BG} = K_{2e}\varepsilon_1 + K_{2T}\Delta T \quad (4)$$

If two phase changes from ILFE and BG sensors are measured and four coefficients  $K_{ii}$ , representing the responsiveness of the two sensors, are known, then the strain and temperature can be determined from these two well-conditioned equations.

### 3. EXPERIMENTAL SETUP AND RESULTS

The experimental arrangement used for the ILFE/BG sensor system is shown in Fig. 1. Light from a super luminescent source is launched into one end of a 3dB coupler, with ILFE/BG on the other end. The signal reflected back from the ILFE/BG sensor is split into two parts using a second 3dB coupler. One output fiber of this second 2x2 coupler is sent to a Fabry-Perot cavity that is path-matched to the ILFE sensor, and the other output fiber is connected to a Fabry-Perot cavity used to demodulate the Bragg grating. The cavity length of this second Fabry-Perot cavity is selected to be more than three times larger than the ILFE readout cavity to prevent coherence division cross-talk and to increase the sensitivity of the unbalanced interferometer to changes in the Bragg wavelength.

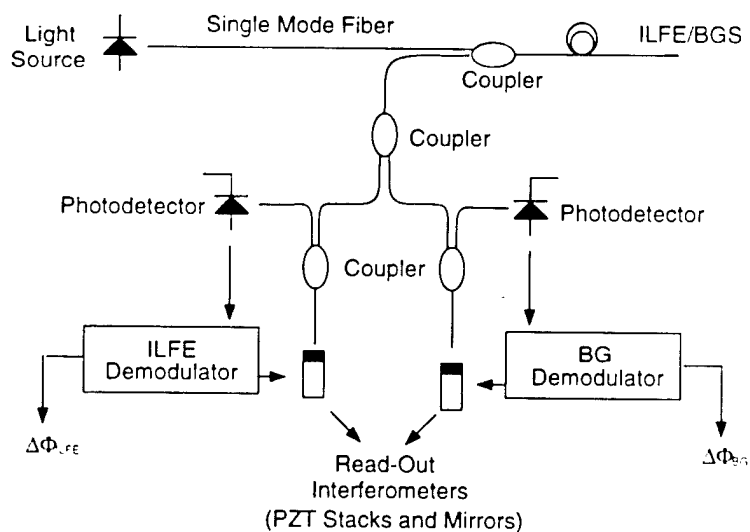


Fig. 1 Interferometric Configuration for Coherence Multiplexing and Demodulation

#### 3.1 Phase-Strain Models

The sensor system is embedded in the graphite/epoxy composite cantilever beam, and phase changes from ILFE and BG sensors due to both strain and temperature are still given by Eqs. (3) and (4), but in this case the four constants are given by<sup>12</sup>:

$$K_{1\epsilon} = 2\beta_0 L_{ILFE}, \quad (5)$$

$$K_{1T} = 2\beta_0 L_{ILFE}(\alpha_{zz}^c - \alpha_f + \xi^a), \quad (6)$$

$$K_{2\epsilon} = 2\beta L_{FP}(1 - 1/2n_0^2(P_{12} - v_{eff}(P_{11} + P_{12}))), \quad (7)$$

$$K_{2T} = 2\beta L_{FP}((1 - 1/2n_0^2P_{12})\alpha_{zz}^c - 1/2n_0^2\alpha_{eff}(P_{11} + P_{12}) + \xi); \quad (8)$$

where  $L$  stands for the Fabry-Perot cavity length;  $\alpha_{zz}^c$ ,  $\alpha_f$  are the coefficients of thermal expansion of the beam and the fiber;  $\xi^a$  and  $\xi$  are thermo-optic coefficients of the ILFE and BG, respectively;  $\beta_0 = 2\pi/\lambda_0$  and  $\beta = 2\pi/\lambda_B$  are propagation constants, where  $\lambda_0$  and  $\lambda_B$  are the central wavelengths of EDFA and Bragg grating, respectively;  $v_{eff}$  is the effective Poisson ratio of the embedded optical fiber subjected to uniaxial tension and  $\alpha_{eff}$  is the effective transverse coefficient of thermal expansion of the fiber;  $P_{11}$  and  $P_{12}$  are the strain-optic coefficients. The values of these constants are given in Table 1 except constants:  $v_{eff}=0.16$  and  $\alpha_{eff}=2.7\times 10^{-6}$ . These expressions were derived by combining strength of materials, composite laminated plate theory, and concentric cylinder micromechanical models with the appropriate phase-strain-temperature equations<sup>13</sup>.

Table 1 Constant Values

$\lambda_0$	1.553μm
$\lambda_B$	1.534μm
$n_0$	1.458
$P_{11}$	0.113
$P_{12}$	0.252
$\xi^a$	$0.112\times 10^{-6}/(^{\circ}\text{C})$
$\xi$	$8.916\times 10^{-6}/(^{\circ}\text{C})$
$\alpha_{zz}^c$	0.2μm/m·°C
$\alpha_f$	0.5μm/m·°C

In our experiments we used EDFA as light source with  $\lambda_0=1.553\mu\text{m}$ , a Bragg grating at a wavelength of  $\lambda_B=1.534\mu\text{m}$ , cavity length of the ILFE sensor of  $L_{ILFE}=164\mu\text{m}$ , and cavity length of the Bragg grating readout interferometer of  $L_{FP}=730\mu\text{m}$ . Therefore, four calculated values for the Eqs.(5)-(8) are:  $K_{1\epsilon}=1.33\times 10^{-3}\text{rad}/\mu\epsilon$ ,  $K_{1T}=-0.27\times 10^{-3}\text{rad}/^{\circ}\text{C}$ ,  $K_{2\epsilon}=4.75\times 10^{-3}\text{rad}/\mu\epsilon$ , and  $K_{2T}=47.9\times 10^{-3}\text{rad}/^{\circ}\text{C}$ .

### 3.2 Experimental Results

The response of the hybrid ILFE/BG sensor is tested by embedding it into a graphite/epoxy cantilever beam. The 14 ply unidirectional AS4/3501-6 graphite/epoxy composite beam had the dimensions of  $150\times 25\times 1.8\text{mm}$  and was fabricated using a standard curing cycle. The ILFE/BG sensor is located 0.4mm above the neutral surface of the beam and parallel to the reinforcing fiber direction. In order to verify the strain and temperature measured by the fiber sensor, a semi-conductor thermistor and a resistance strain gage were mounted on the surface of the beam directly above the fiber sensors. Finally a Peltier device (TE cooler) was used to control the temperature of the beam in the vicinity of the sensors. The interface between the Peltier device and the cantilever beam was filled with high thermal conductivity grease.

Simple vibration was applied to the beam so that the strain coefficients  $K_{1\epsilon}$  and  $K_{2\epsilon}$  could be measured while the ILFE/BG sensor were kept at a constant temperature. Then the sensor was held unstrained while applying a temperature field so that the thermal coefficients  $K_{1T}$  and  $K_{2T}$  could be measured. Table 2 provides measured values of the four coefficients as well as the calculated values given in the previous section. The comparison shows agreement between the calculated and experimental values to within 3.7%.

Table 2 Comparison of Theoretical and Experimental Values  
for Embedded ILFE/BG Sensor

	Theoretical	Experimental	Difference
$K_{1\epsilon}(\times 10^3 \text{ rad}/\mu\epsilon)$	1.33	1.31( $\pm 0.02$ )	1.5%
$K_{2\epsilon}(\times 10^3 \text{ rad}/\mu\epsilon)$	4.75	4.70( $\pm 0.05$ )	1.1%
$K_{1T}(\times 10^3 \text{ rad}/^\circ\text{C})$	-0.27	-0.26( $\pm 0.01$ )	3.7%
$K_{2T}(\times 10^3 \text{ rad}/^\circ\text{C})$	47.9	46.3( $\pm 0.5$ )	3.3%

With the strain and temperature coefficients known for the ILFE and BG sensors, the strain and temperature can be determined by measuring the respective phase changes and solving Eqs. (3) and (4). This concept was tested by subjecting the cantilever beam to a simultaneous combination of strain and temperature fields. The experimental results of the strain and temperature determined from the ILFE/BG sensor and the electrical gages are plotted in Fig.3 and 4, respectively. Fig.3 shows the mechanical strain measured by the ILFE/BG sensor and plotted with the strain recorded by the resistance strain gage after adjustment for the temperature change. In Fig.4, the temperature calculated from the ILFE/BG sensor is plotted along with the temperature measured by the temperature sensor. There is good agreement between the optical and electrical gages. The precision of the measurement is about  $5\mu\epsilon$  for the strain and  $0.5^\circ\text{C}$  for the temperature.

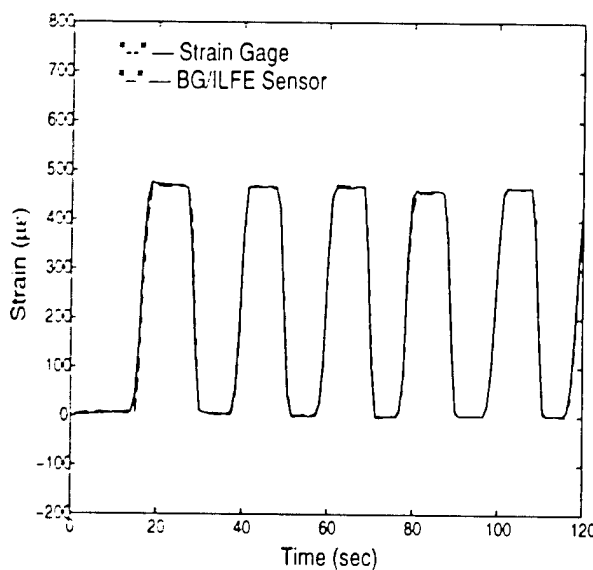


Fig. 3 Strain for ILFE/BG sensor  
compared with strain gage

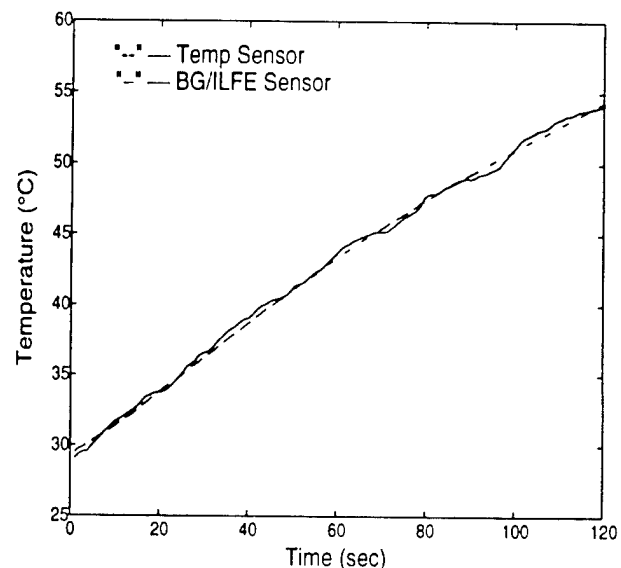


Fig. 4 Temperature for ILFE/BG sensor  
compared with temperature sensor

#### **4. CONCLUSION**

In this paper we have showed that an optical fiber sensor consisting of an ILFE sensor cascaded with a BG sensor can be used to measure strain and temperature simultaneously. The response of the ILFE sensor and the BG sensor was separated using coherence-based multiplexing. The two signals were demodulated using pseudo-heterodyne technique with ramp modulation, and then a well-conditioned system of two equations for the strain and temperature is developed. This fiber strain/temperature sensor was tested by embedding it into a graphite/epoxy composite cantilever beam. The measured strain and temperature are found to be within  $5\mu\epsilon$  and  $0.5^\circ\text{C}$ , respectively, by comparing with electrical strain and temperature sensors.

#### **5. ACKNOWLEDGMENT**

This financial support for this work provided by the Army Research Office under Grant DAAL 03-92-G-0121 (Dr. Gary Anderson, Technical Monitor) is gratefully acknowledged.

#### **6. REFERENCES**

- [1] G.Meltz, J.Dunphy, W.Glenn, J.Farina, and F.Leonberger, "Fiber Optic Temperature and Strain Sensors," in SPIE vol. 198, pp.104-112, 1987.
- [2] W.Michie, B.Culshaw, R.Roberts, and R.Davidson, "Fiber Optic Technique for Simultaneous Measurement of Strain and Temperature Variations in Composite Materials," in SPIE vol. 1588, pp.342-355, 1991.
- [3] A.M.Vengsarkar, W.C.Michie, L.Jankovic, B.Culshaw, and R.O.Claus, "Fiber-Optic Dual-Technique Sensor for Simultaneous Measurement of Strain and Temperature," Journal of Lightwave Technology, vol. 12, no.1, pp170-177, Jan. 1994.
- [4] V.Gusmeroli and M.Martinelli, "Nonincremental Interferometric Fiber-Optic Measurement Method for Simultaneous Detection of Temperature and Strain," Optics Letters, vol.19, no.24, pp2164-2166, Dec.15, 1994.
- [5] M.G.Xu, J.Archanbault, L.Reekie, and J.P.Dankin, "Discrimination Between Strain and Temperature Effects Using Dual-Wavelength Fibre Grating Sensors," Electronics Letters, vol. 30, no. 13, pp.1085-1087, 1994.
- [6] H.Singh and J.Sirkis, "Dual-Parameter Optical Fiber Sensor," in SPIE vol. 2443, pp258-265, 1995.
- [7] J. Sirkis, D. Brennan, M. Putman, T. Berkoff, A. Kersey, and E. Friebel, "In-Line Fiber Etalon(ILFE) for Optic Strain Measurement," Optics Letters, vol.18, pp.1973-1975, Nov. 1993.
- [8] H.Singh, "Simultaneous Measurement of Strain and Temperature Using Optical Fiber Sensors: Two Novel Configuration," OFS Conference, 1996.
- [9] A.D.Kersey, T.A.Berkoff, and W.W.Morey, "High-Resolution Fibre-Grating Based Strain Sensor with Interferometric Wavelength-Shift Detection," Electron. Lett., vol. 28, pp. 236-238, 1992.
- [10] A.D.Kersey and A.Dandridge, "Phase-Noise Reduction in Coherence-Multiplexed Interferometric Fibre Sensors," Electronic Letters, vol. 22, pp. 616-617, May 1993.
- [11] D. Jackson, A. Kersey, M. Corke, and J. Jones, "Pseudo-Heterodyne Detection Scheme for Optical Interferometers," Electronic Letters, vol. 18, pp.1081-1083, Dec. 1982.
- [12] J. S. Sirkis, "Unified Approach to Phase-Strain-Temperature Models for Smart Structure Interferometric Optical Fiber Sensors: Part I, Development," Optical Engineering, vol. 32, pp.752-761, April 1993.
- [13] X. D. Jin, J. K. Chung, and V. S. Venkateswaran, "Embedded In-Line Fiber Etalon/Bragg Grating Hybrid Sensor to Measure Strain and Temperature in a Composite Beam," submitted to the Journal of Intelligent Material Systems and Structures.

# **Compensation for hysteresis using KP integral operators**

W. Steven Galinaitis and Robert C. Rogers

Department of Mathematics, Virginia Tech, Blacksburg, Virginia 24061-0123

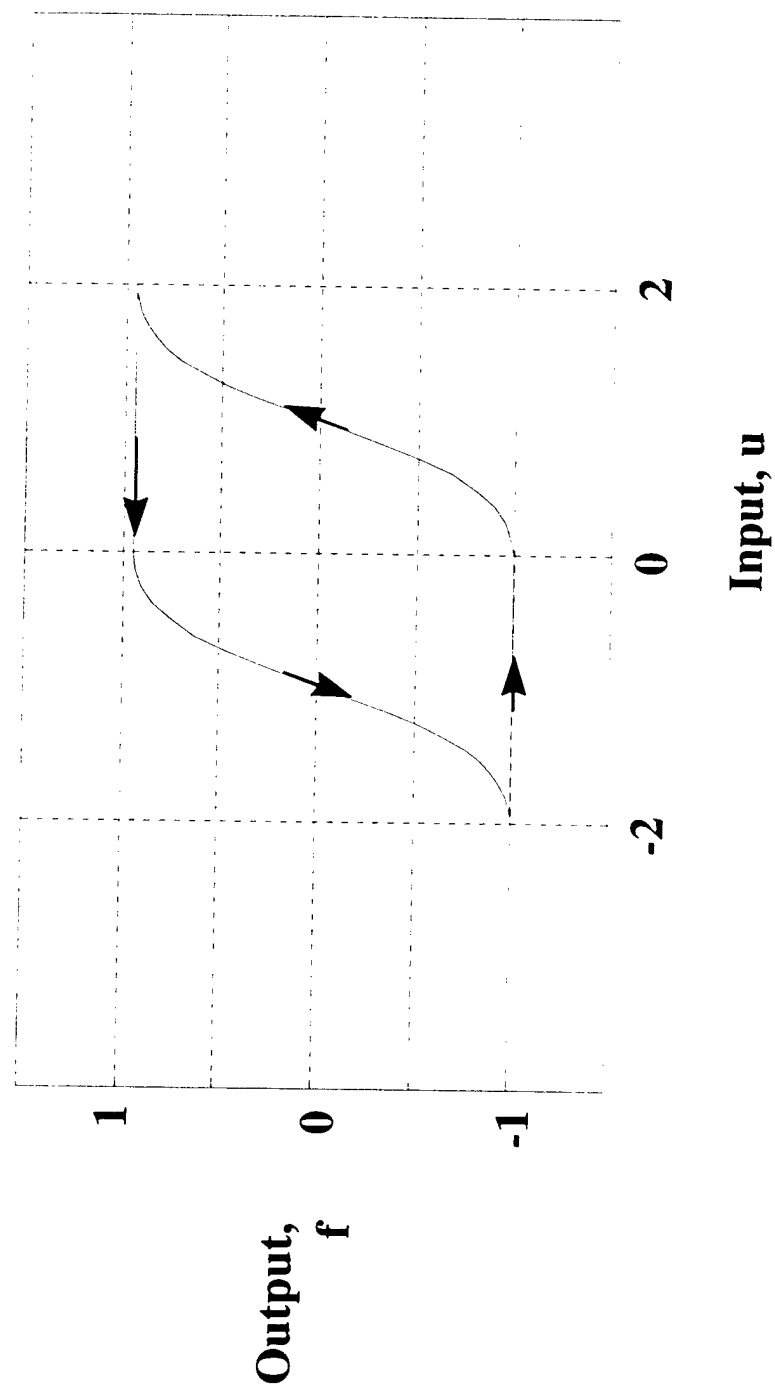
## **Abstract**

The accurate control of a system that exhibits hysteresis requires a control strategy that incorporates some form of compensation for the hysteresis. One approach is to develop a compensator based on the inverse of the hysteresis operator. This form of compensation uses the inverse operator to linearize the hysteresis effect. In this work, a system with hysteresis is modeled by a generalized Krasnoselskii - Pokrovskii integral operator. An approximation of the KP operator and its inverse are presented. The results of a computer simulation are then used to illustrate the properties of the KP operator, the inverse and a compensator based on the inverse.

Keywords: Hysteresis, KP integral operators, inverse operators, compensation.

**Problem definition:** Actuator hysteresis causes positioning error.

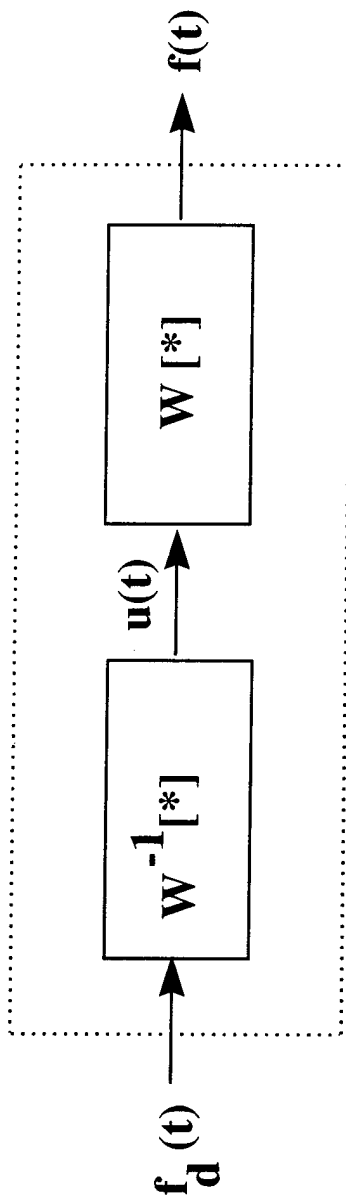
---



W.S. Galinatis  
R.C. Rogers  
Virginia Tech  
Mathematics Dept.

**Proposed Solution:** Use the inverse operator to linearize the actuator.

---



$$f(t) = W[u](t) = W[W^{-1}[f_d]](t) = f_d(t)$$

W.S. Galinaitis  
R.C. Rogers  
Virginia Tech  
Mathematics Dept.

## Issues

- 1. Modeling the hysteresis**
- 2. Does the model have an inverse?**
- 3. Realtime implementation**
- 4. Parameter estimation**
- 5. Robustness**

**W.S. Galinaitis  
R.C. Rogers  
Virginia Tech  
Mathematics Dept.**

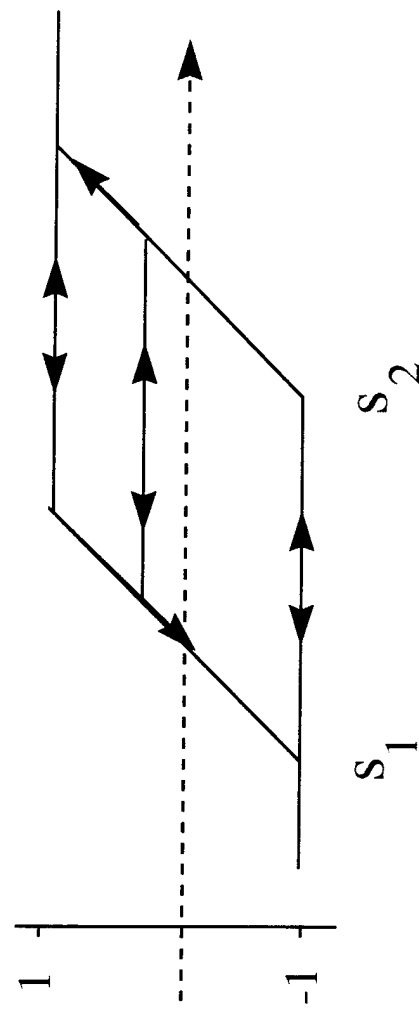
# Krasnosel'skii-Pokrovskii integral hysteresis operator

---

$$[W_\mu(u, \gamma)](t) \equiv \int_S [\mathcal{K}_s(u, \gamma(s))](\tau) d\mu(s)$$

$$S \equiv \{(s_1, s_2) \in R^2 : s_1 < s_2\}, \text{ Preisach plane}$$

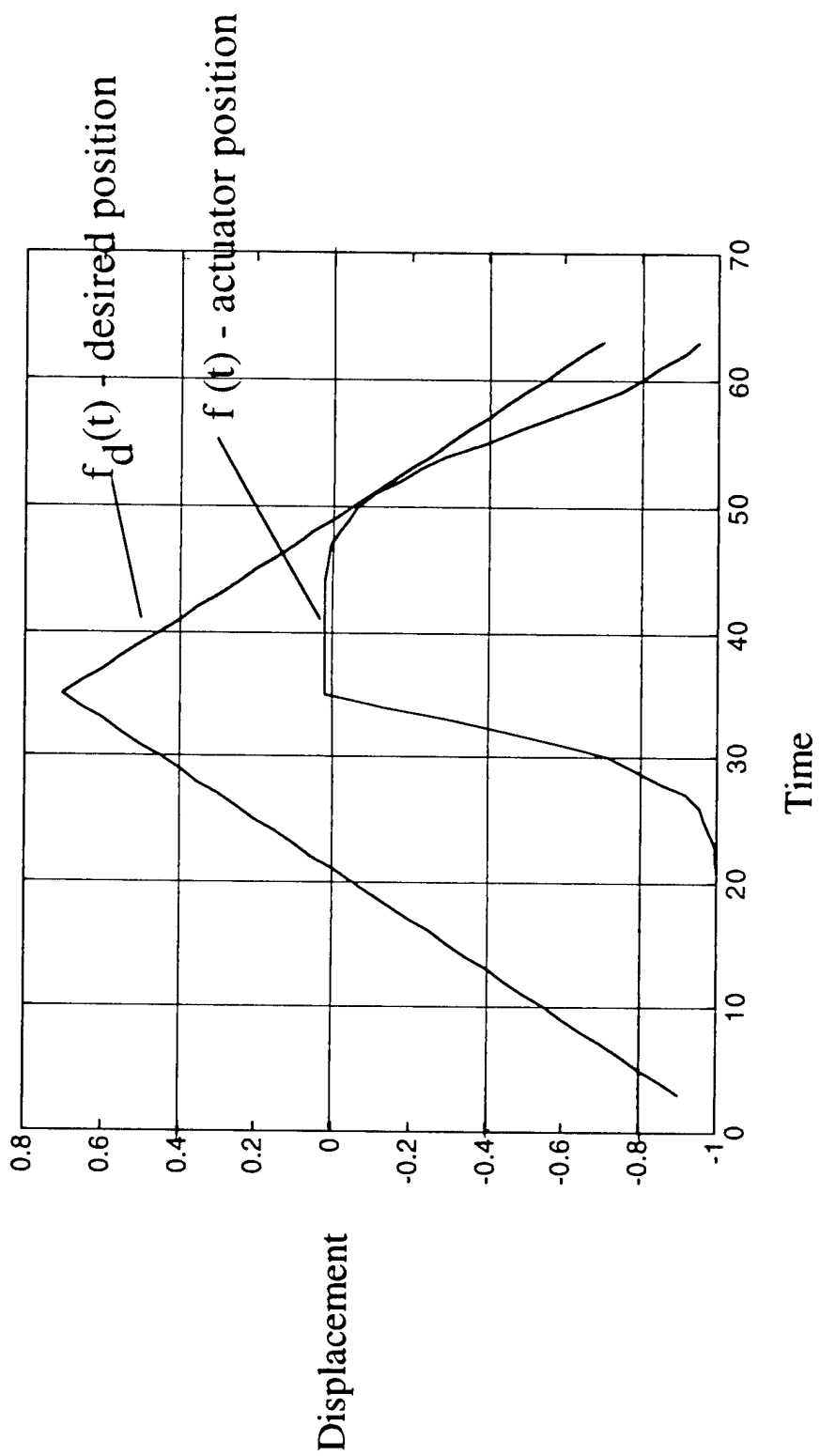
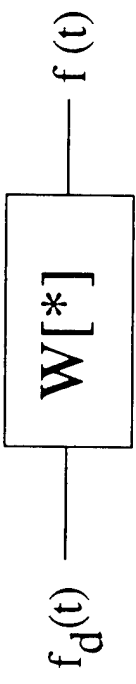
$[\mathcal{K}_s(u, \gamma(s))](t), \text{ KP kernel}$



W.S. Galinaitis  
R.C. Rogers  
Virginia Tech  
Mathematics Dept.

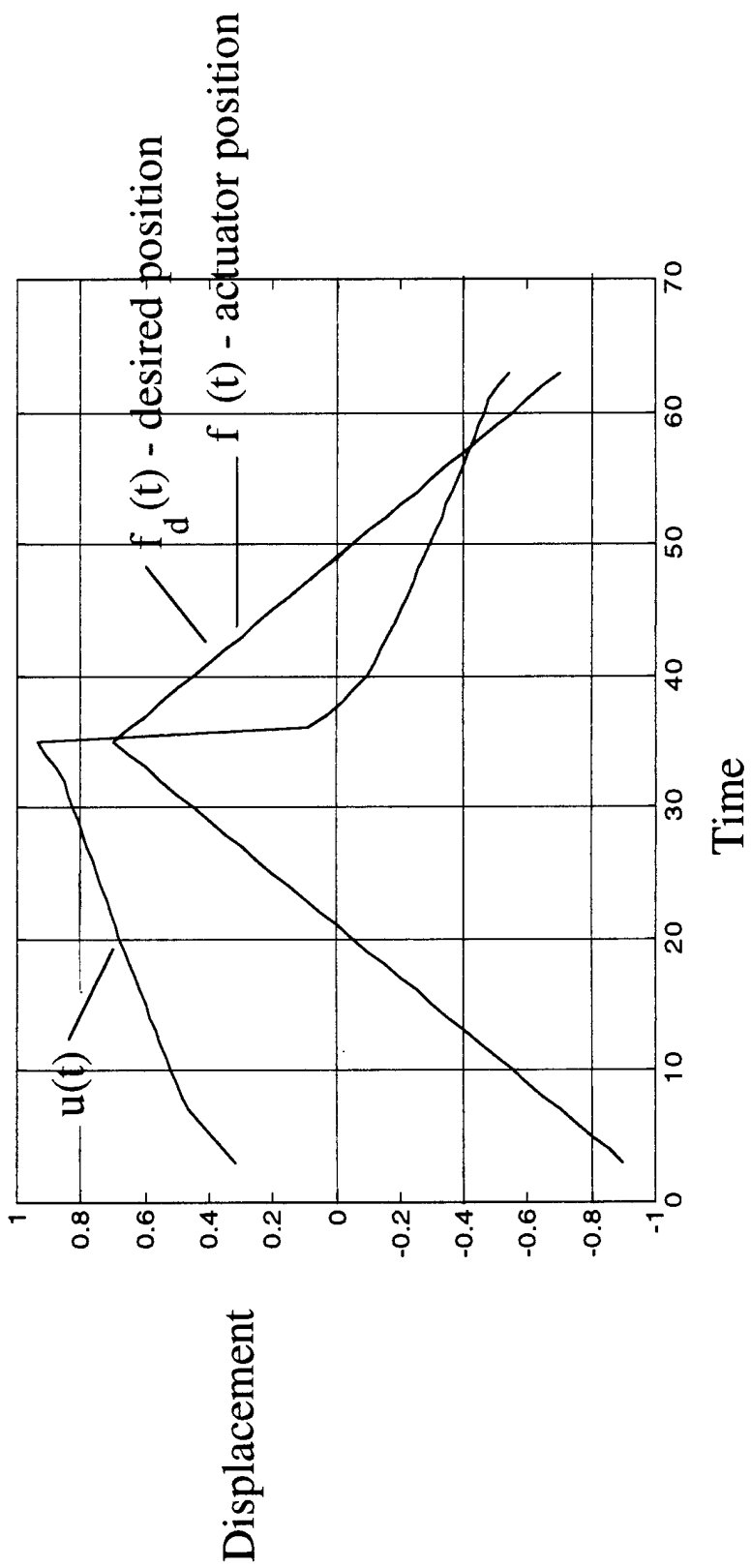
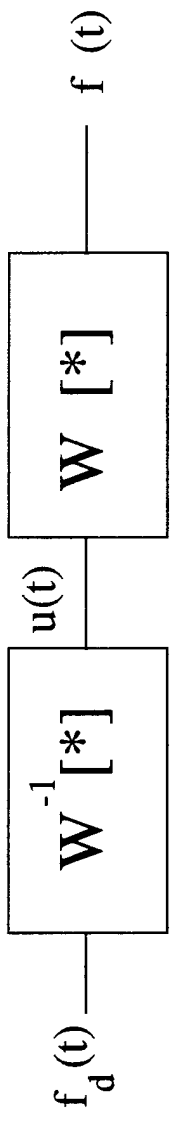
## No Compensation

---



# Compensated Actuator

---



# Micromechanics and Control of Hysteresis in Shape Memory Alloys

D. Lagoudas, Z. Bo

A. Kurdila, G. Webb

Aerospace Engineering Department  
Texas A&M University  
College Station, TX 77843-3141

August 29, 1997

RPI-TAMU ARO URI  
Smart Materials and Structures  
DAAL03-92-G-0123

**SMART**

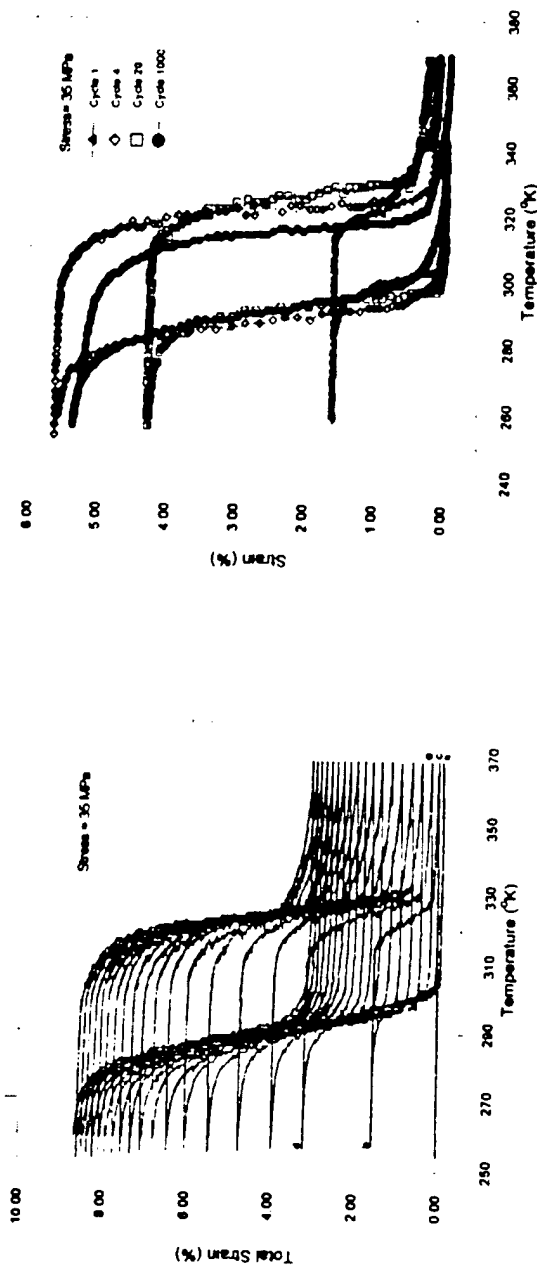
Texas A&M University

# Experimental Investigation and Constitutive Modeling of Cyclic Loading of SMAs

## • Research Objectives

- Investigate experimentally the accumulation of plastic strains, creation of the two way memory effect, and low cycle fatigue during thermally-induced cyclic phase transformations in SMAs
- Develop a constitutive model to predict the evolution of plastic strains and two way memory effect during cycling loading.
- Establish a model to predict minor hysteresis loops under arbitrary loading path and with evolving plastic strains.

# Strain Hysteresis Under Cyclic Loading



## ● Accomplishments

- The experimental results show that the rate of the accumulation of plastic strains is approximately proportional to the magnitude of the applied load.
- In the constitutive modeling of the cyclic loading of SMAs, a methodology similar to that used in viscoplasticity is adopted. As shown in figures, the model prediction agrees well with the experimental results.
- The minor hysteresis loops under arbitrary loading path and with evolving plastic strains can be described using the present constitutive model. Only one additional material constant is introduced to describe the evolving rate of the minor loops with respect to the major loops. The loading history path dependence is similar to that of Preisach model.
- The model prediction agrees well with the experimental data.

## Definitions of Field Variables and Material Constants

$E^P$ : Macroscopic plastic strain;

$E^m$ : Macroscopic transformation strain;

$E^\theta$ : Macroscopic thermal strain;

$\eta^P$ : Drag stress due to elastic interaction between plastic deformation and phase transformation;

$\eta^m$ : Drag stress due to elastic interaction between newly formed martensite region and existing martensite;

$\alpha_{ij}^P$ : Back stress due to elastic interaction between plastic deformation and phase transformation;

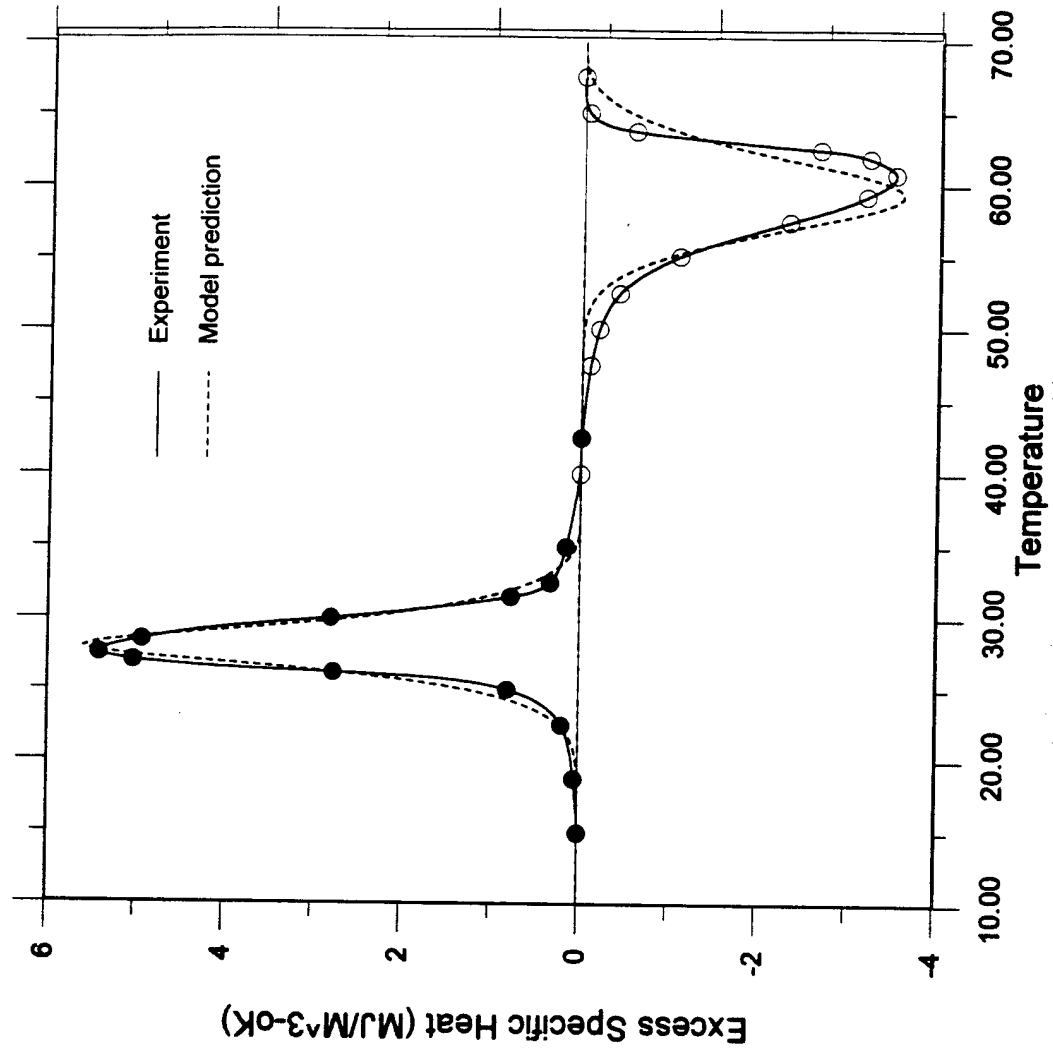
$\alpha_{ij}^m$ : Back stress due to elastic interaction between newly formed martensite region and existing martensite;

$\Delta G_0$ : Difference of Gibbs free energy of reference state between the two phases representing the material initial heterogeneity;

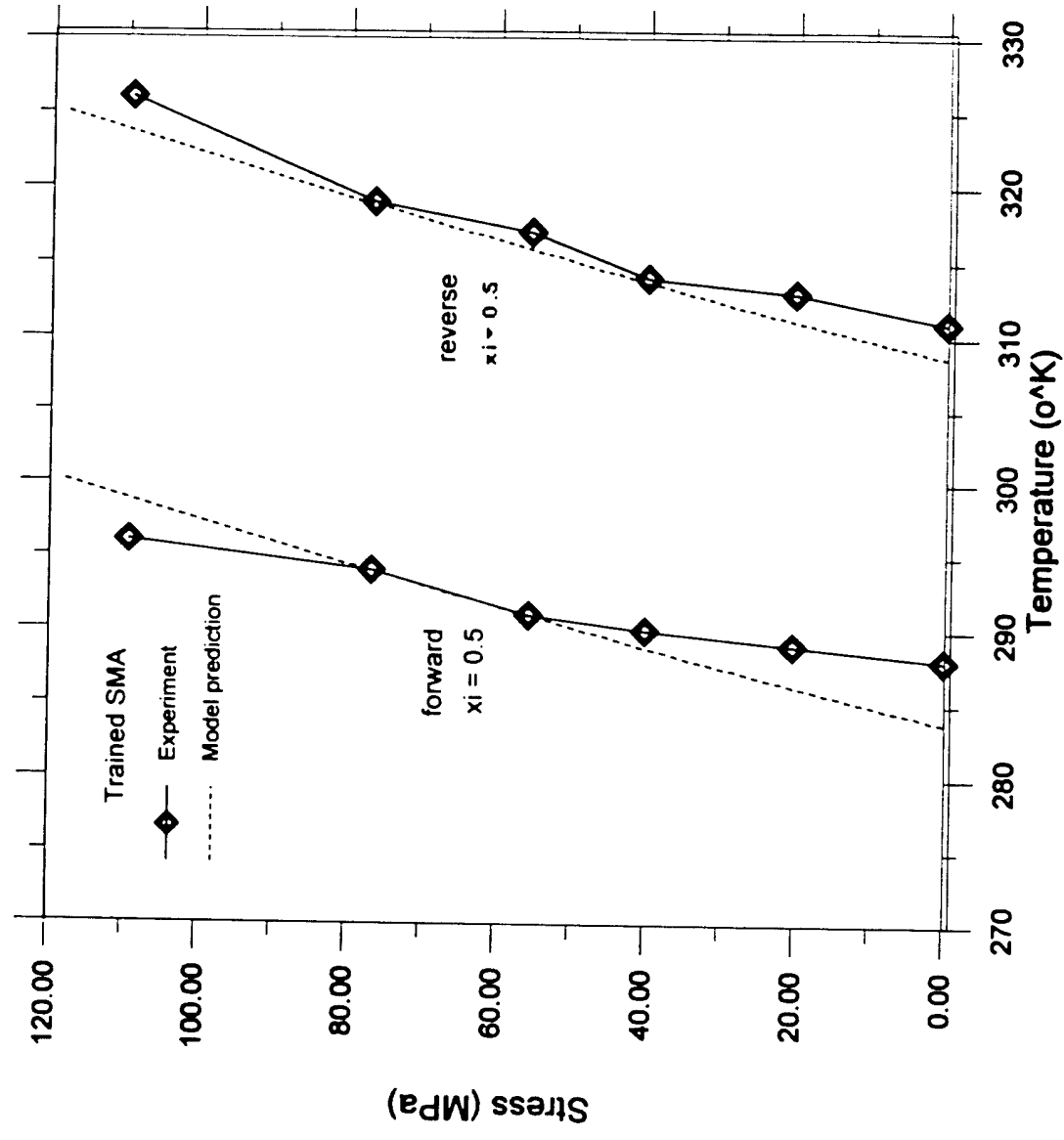
$\Delta c$ : Difference of the specific heat between the two phases

$\Delta s_0$ : Difference of specific entropy between the two phases

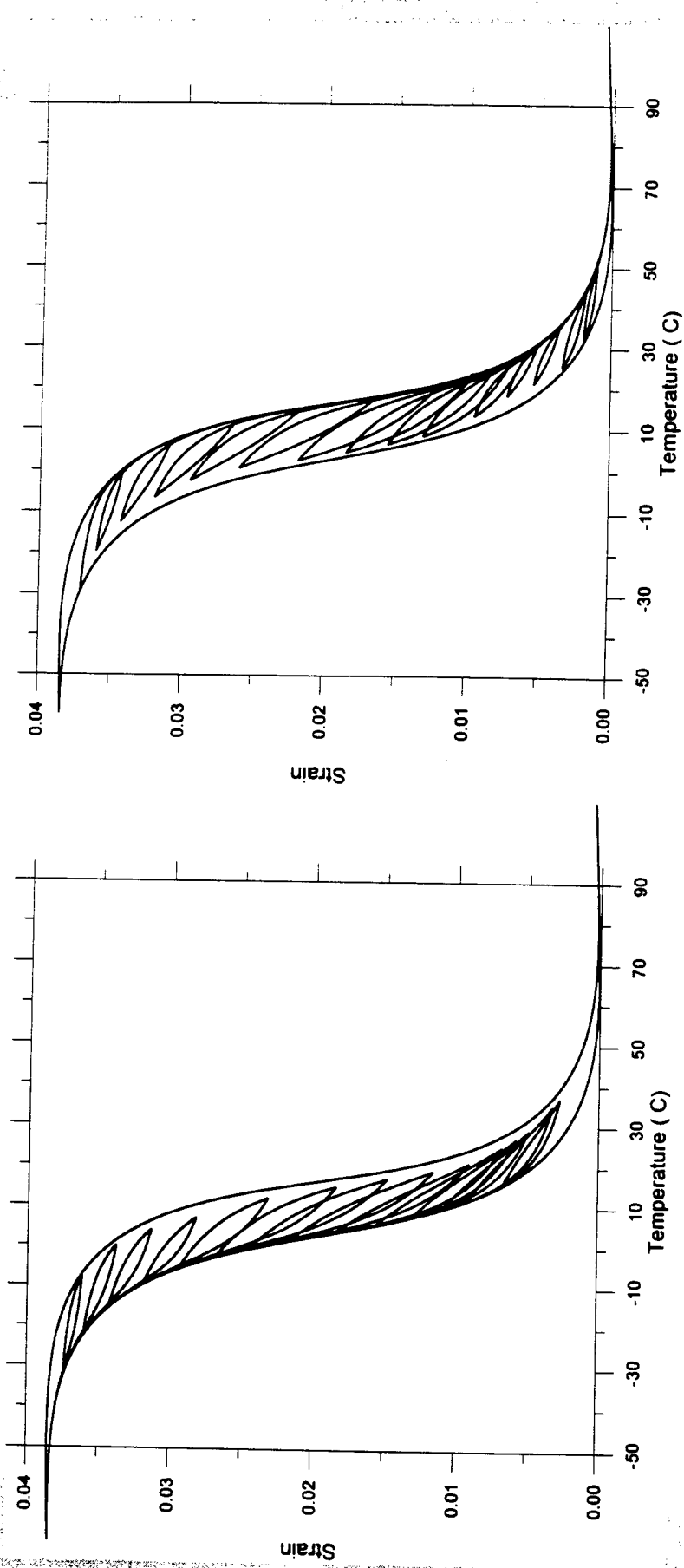
Comparison of the Excess Heat Rate,  $\rho Q_{ex}$ , Between a DSC Measurement and a Theoretical Prediction



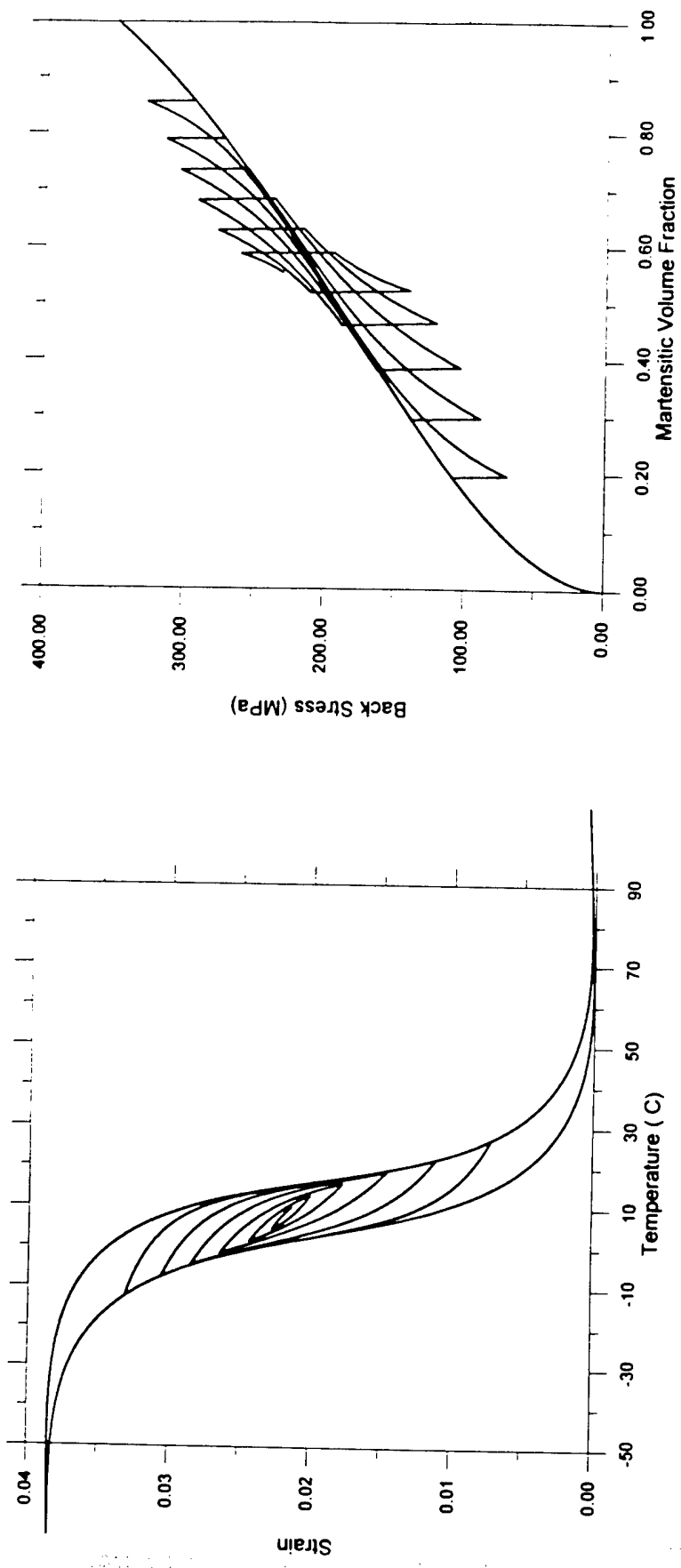
Comparison of Stress-Temperature Diagram predicted by model to experiment data for a trained SMA



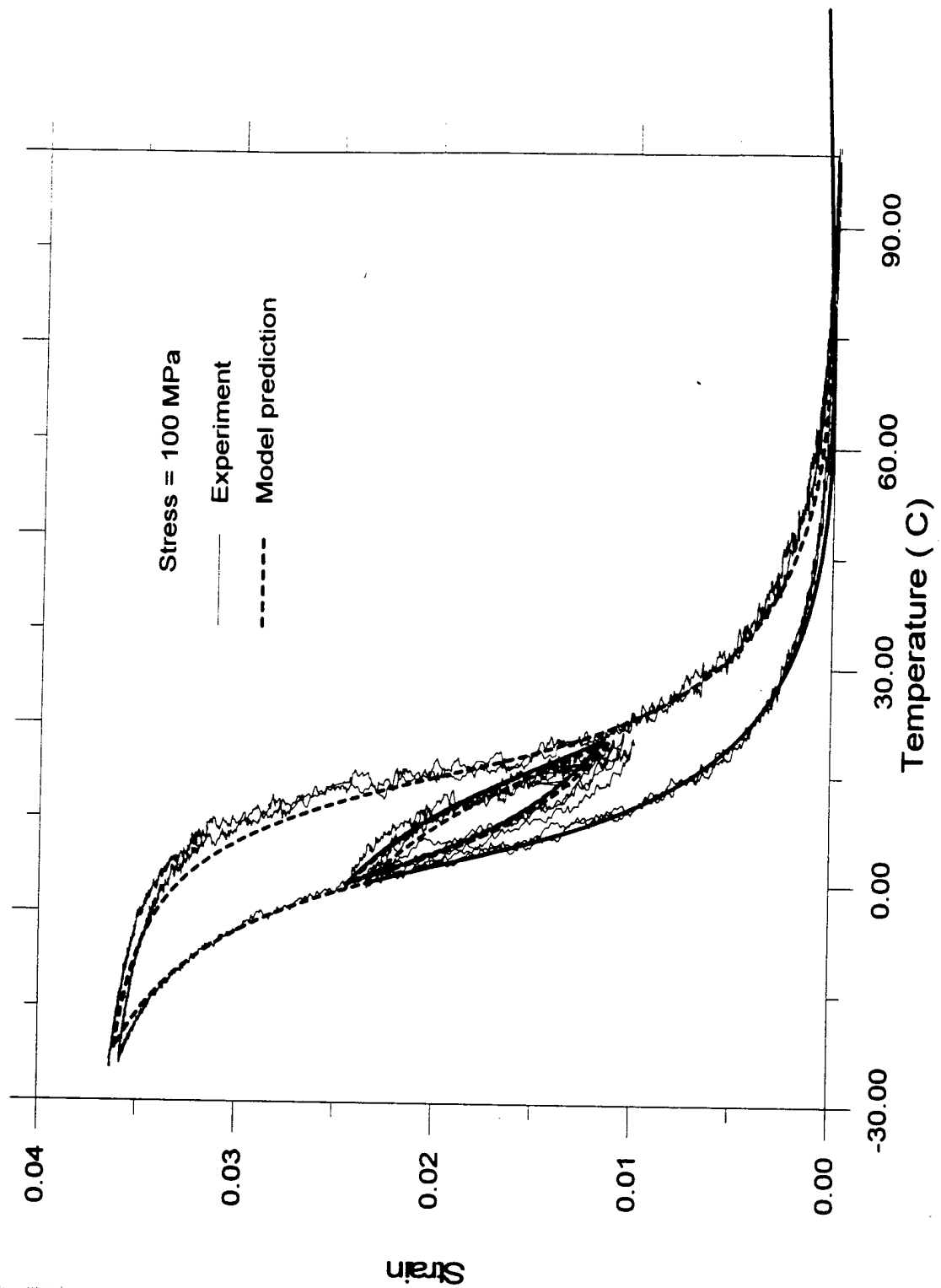
## Minor Hysteresis Loops



# Model Prediction of Minor Hysteresis Loops



# Comparison of Model Prediction with Experimental Data



# Micromechanics and Control of Hysteresis in Shape Memory Alloys

## Control Theoretic Background

Numerous Compensation Strategies

Hughes/Wen 1994, Ge 1996, Bekey/Hadaegh 1983...

## Systematic Framework

Tao/Kokotovic 1996

### Limitations

Low Dimensional  
Piecewise Linear

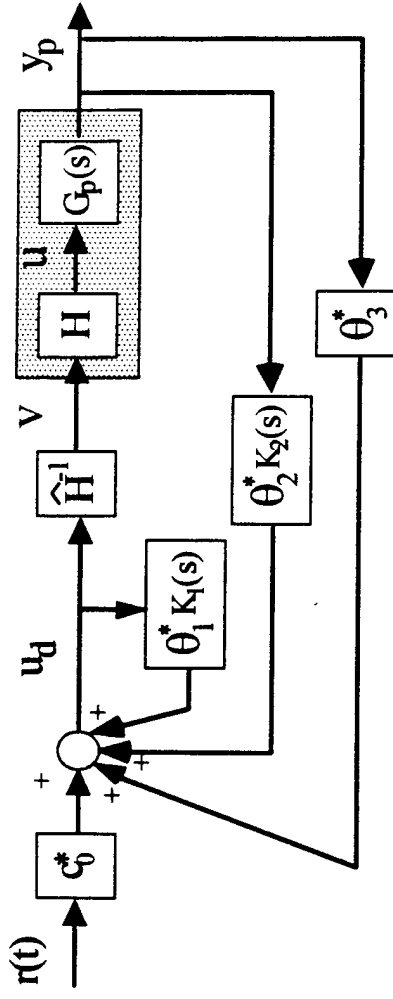
### Static Hysteresis Model

## Generalizations

- 1) Banks, Kurdila, Webb, 1996 "Identification of Hysteretic Control Influence Operators: Formulation," JMPE, (CRSC-TR96-14, CRSC-TR96-23)  
OI.S  
Offline  
Identification
- 2) Banks, Kurdila, Webb, 1997 "Identification of Hysteretic Control Influence Operators: Convergent Approximations" JIMSS (CRSC-TR97-7)  
(Compensation)
- 3) Kurdila and Webb, "Compensation for Classes of Distributed Hysteresis Operators and Representation of Active Structural Systems" AIAA JGCD, Nov. 1997  
Static Hysteresis  
(Compensation)
- 4) Webb, Kurdila, Lagoudas, Bo, "Identification and Adaptive Control for a Class of Hysteresis Operators," AIAA JGCD, 1997  
Adaptive Hysteresis  
(Compensation)

## Hysteresis Compensation: Fixed and Adaptive

### Fixed Hysteresis Compensation



$$[y_p] = G_p(s)[u_d], \quad [y_m] = W_m(s)[r]$$

$$u_d = K_1(s, \theta_1^*)[u] + K_2(s, \theta_2^*)[y_p] + \theta_3^* y_p + c_0^* r$$

When  $\hat{H} = H$ ,

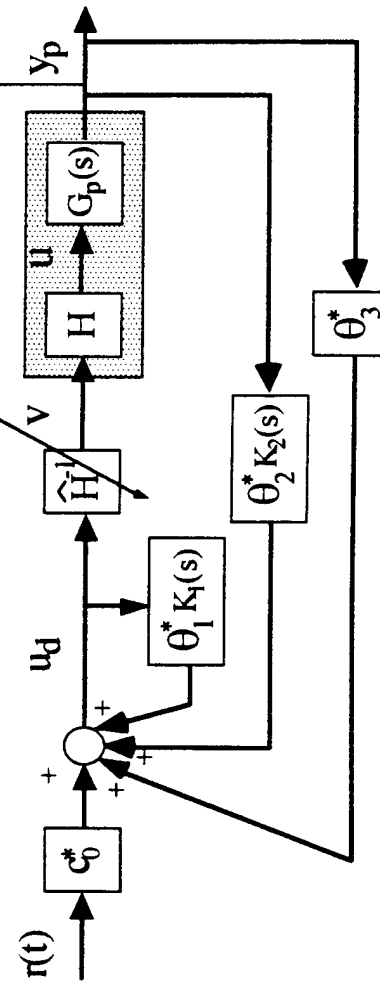
$$u = H(v) = H(\hat{H}^{-1}(u_d)) = H(H^{-1}(u_d)) = u_d$$

When  $\hat{H} \neq H$ ,

$$e_H = u - u_d = H(v) - \hat{H}(v)$$

$$u = u_d + e_H$$

### Adaptive Hysteresis Compensation



If we can express  $H(v)$  as linear in parameters,

$$H(v) = \theta_H^{*T} F(v), \quad \hat{H}(v) = \hat{\theta}_H^T F(v)$$

The adaptive update law for  $\hat{H}(v)$ :

$$\dot{\theta}_H(t) = \frac{\Gamma \xi_H(t) \epsilon_H(t)}{m_H^2(t)} + f_H(t)$$

$$e(t) = [y - y_m](t)$$

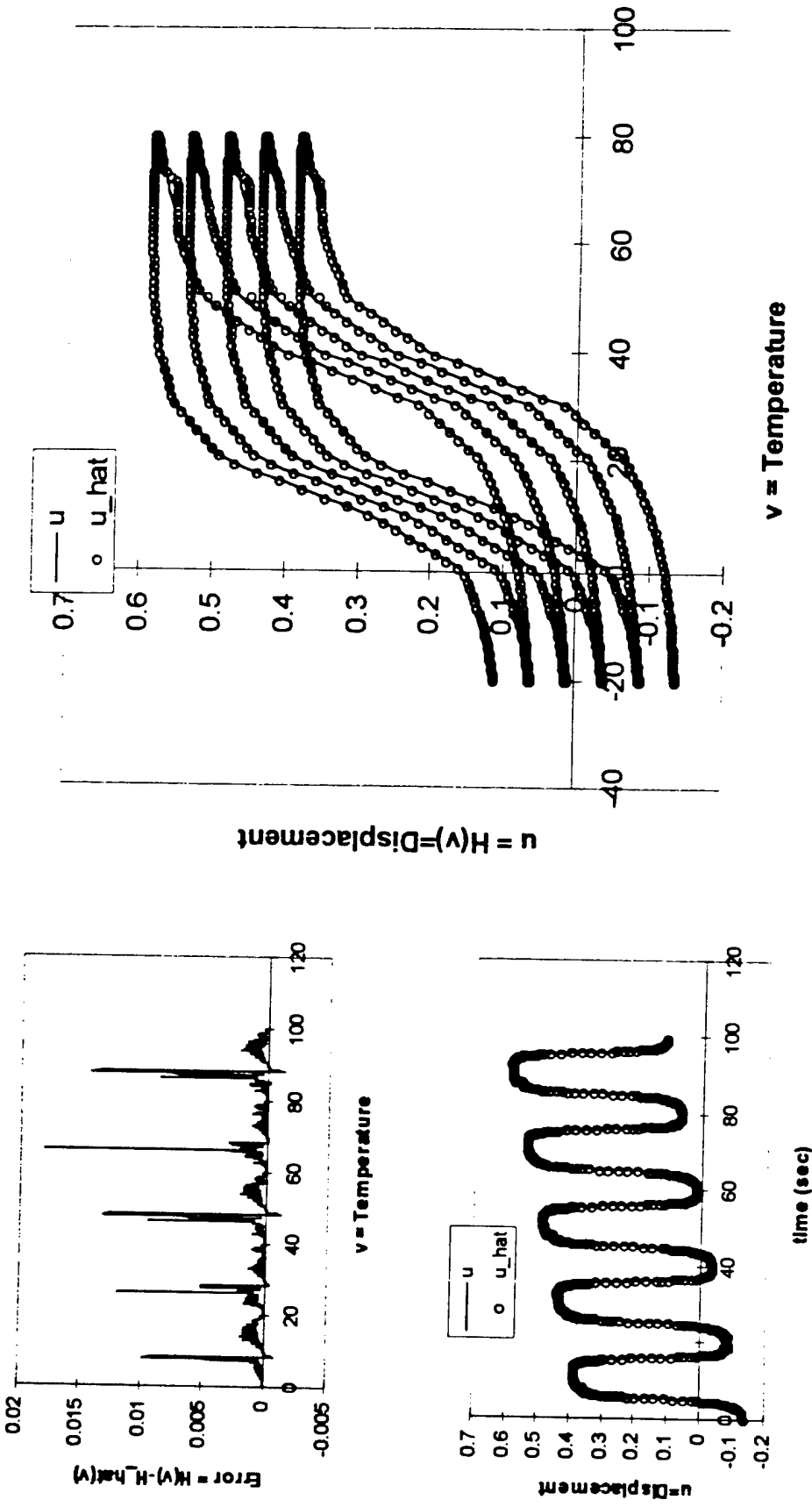
$$\epsilon_H(t) = e(t) + \xi_H(t)$$

$$\xi_H(t) = \theta_H^T(t) \xi_H(t) - W(s)[\theta_H^T F(v)](t)$$

$$\zeta_H(t) = W(s)[F(v)](t)$$

$$m_H^2(t) = 1 + [\xi_H^T \xi_H](t) + \xi_H^2(t)$$

# Adaptive Control, No Noise



# Adaptive Hysteresis Compensation: Goals

Define a hysteresis model such that:

- It can be parameterized linearly in coefficients.
- The inverse exists.
- An upper bound for the error between models with different coefficients exists, and

$$e_H(t) = \left[ H - \hat{H} \right](t) \rightarrow 0 \text{ as } \hat{\theta}_H \rightarrow \theta_H$$

For known plant parameters

- Adaptive law : Guarantee signal boundedness.
- Model estimate does not match the “true” model
  - Adaptive law should reduce the tracking error
    - Ideally,

$$\hat{\theta}_H \rightarrow \theta_H$$

$$e_H(t) \rightarrow 0$$

## Adaptive Hysteresis Compensation

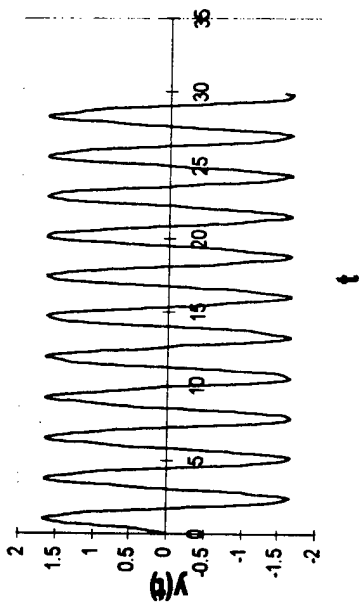
- Upper bound for error  $\delta = \max(\|\gamma_r - \hat{\gamma}_r\|, \|\gamma_i - \hat{\gamma}_i\|)$  where  $\|\gamma_r, \hat{\gamma}_r\| = \max_{i=1,2,\dots,N} |\theta_{r_i} - \hat{\theta}_{r_i}|$
- Let  $\delta > 0$
- If for some  $v$   $|\gamma_i(v) - \hat{\gamma}_i(v)| \leq \delta$  and  $|\gamma_r(v) - \hat{\gamma}_r(v)| \leq \delta$  for all  $v \in R$ 
  - ( $v, \xi^0 \in C^0[0, T] \times R$ )
- Then for any  $|k_s(v, \xi) - \hat{k}_s(v, \xi)| \leq 2\delta$
- Apply to  $H(v, \xi)$ 

$$\begin{aligned}
 |H - \hat{H}| &= |k_s + mv - \hat{k}_s - \hat{m}v| \\
 &\leq |k_s - \hat{k}_s| + |(m - \hat{m})v| \\
 &\leq 2\delta + |m - \hat{m}| \max_{v \in V} |v| = \delta^*
 \end{aligned}$$
- As  $\hat{\theta}_r \rightarrow \theta_r, \hat{\theta}_i \rightarrow \theta_i$  and  $\hat{m} \rightarrow m$  (i.e.,  $\hat{\theta}_H \rightarrow \theta_H$ )
 
$$\delta^* = 2\delta + |m - \hat{m}| \max_{v \in V} |v| \rightarrow 0 \Rightarrow e_H \rightarrow 0$$

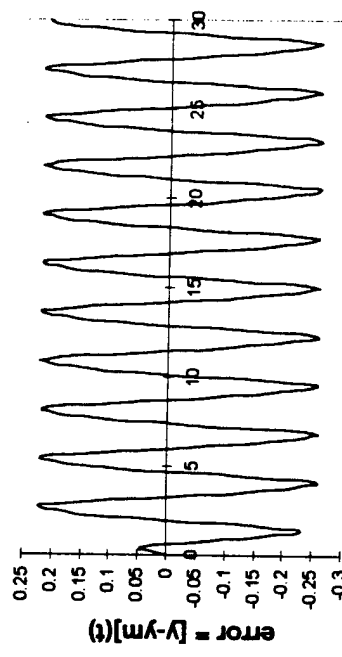
# Adaptive Hysteresis Compensation

## Numerical Example

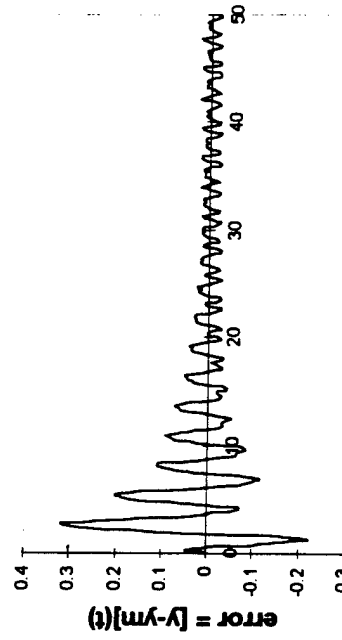
$\gamma_i(v)$  and  $\gamma_r(v)$  are represented by five nodes



Exact Hysteresis Estimate, Plant Response

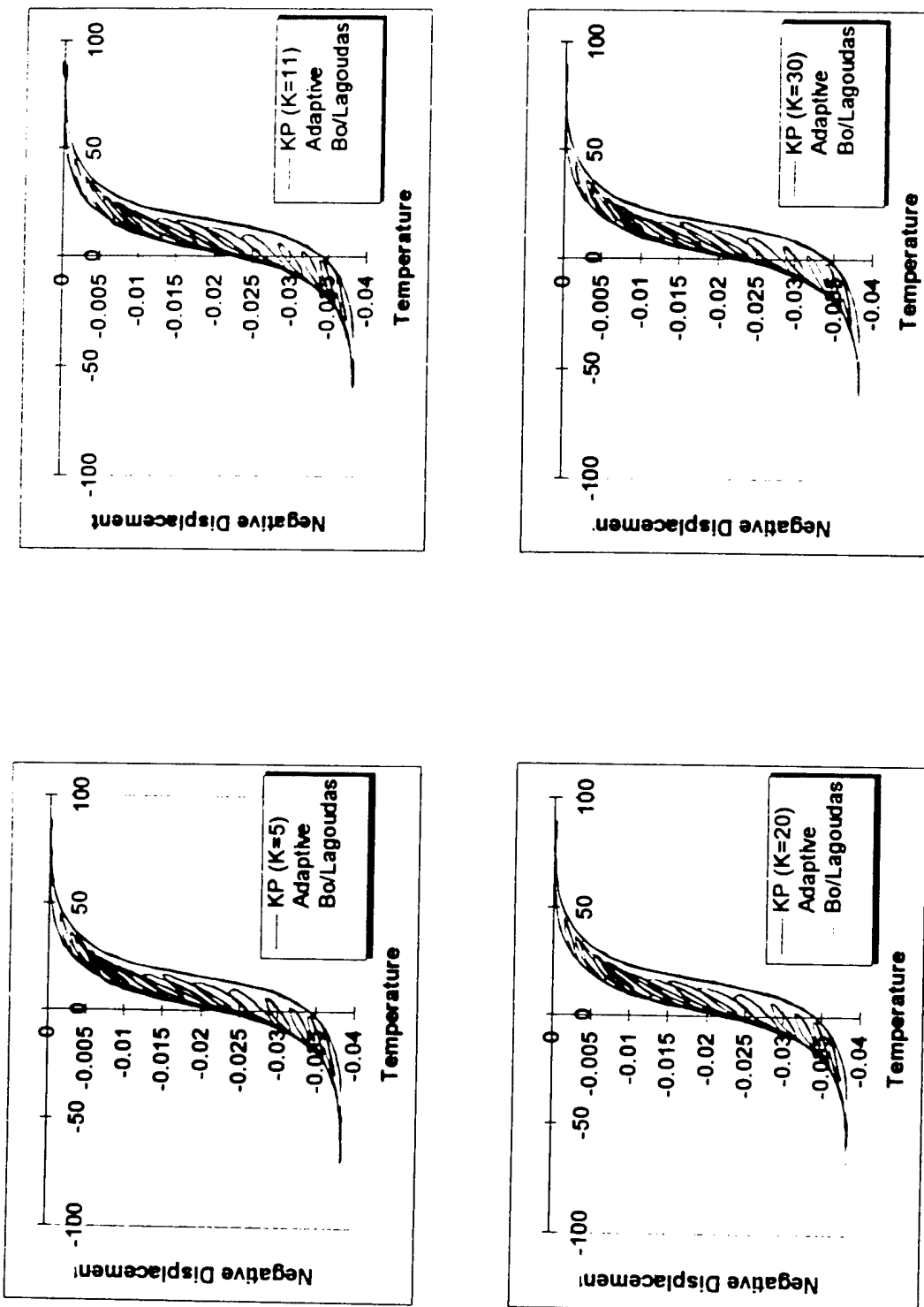


Mismatched Hysteresis Estimate,  
Tracking Error



Mismatched Hysteresis Estimate  
with Adaptive Update, Tracking Error

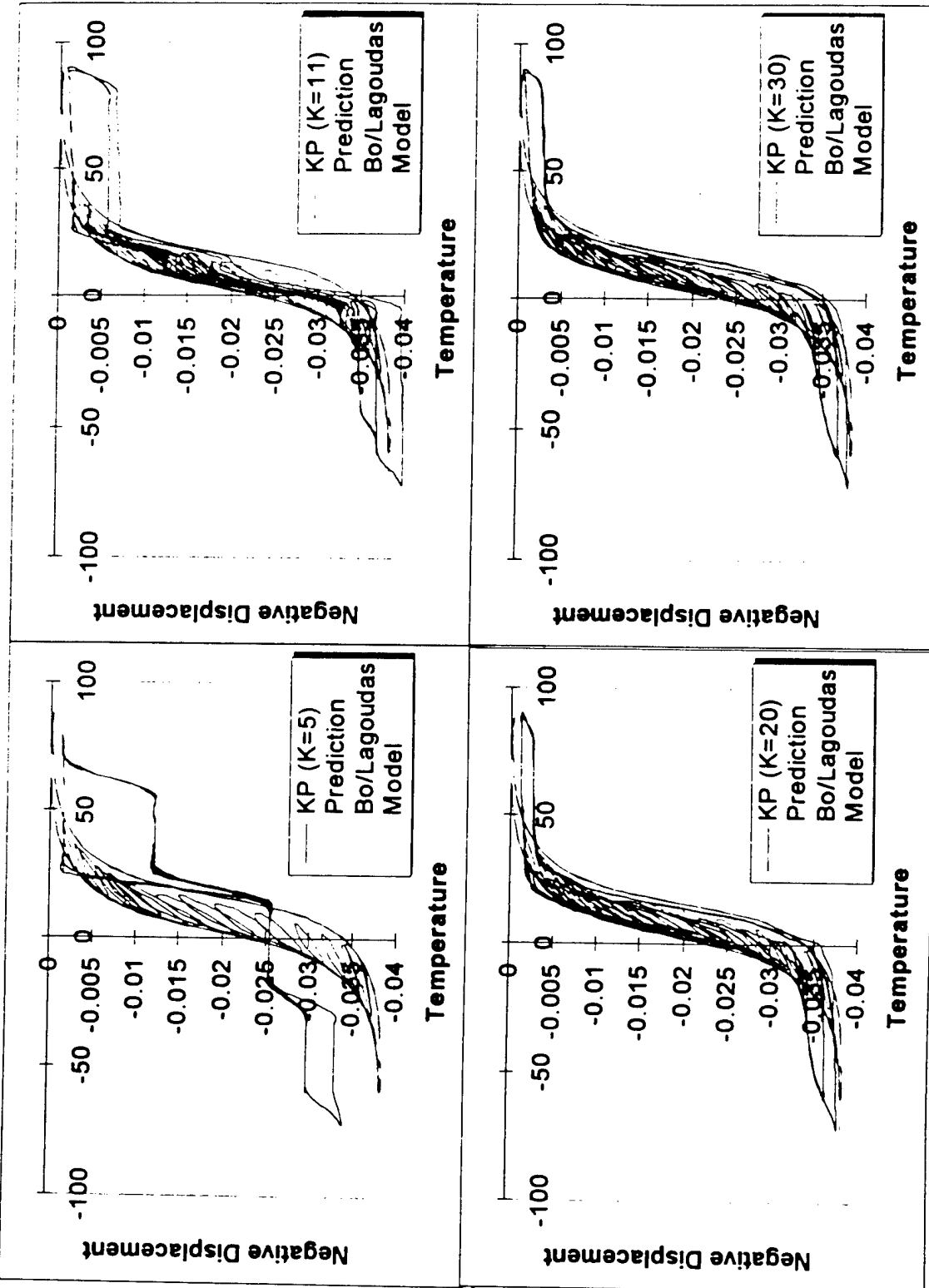
# Adaptive Tracking Results



# Adaptive Tracking Results

- $v$  = Input Variable = Temperature
- $u$  = Output Variable = Displacement
- $u = H(v)$
- The adaptive tracking results are displayed for various discretizations of the KP model ( $K=5, 11, 20, 30$ ) in the form of  $u-v$  hysteresis loops. They are plotted against the actual  $u-v$  data from Bo/Lagoudas Model.
- It can be seen that the adaptive tracking for  $K=5$  is almost as good as for  $K=30$ .
- The difference in performance due to discretization number becomes significant in 1D, as will be seen next.

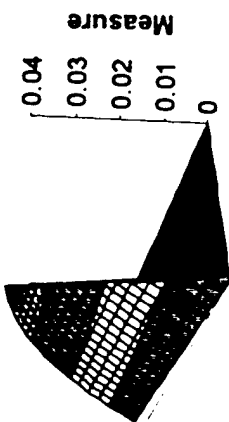
# Predicted Tracking Results



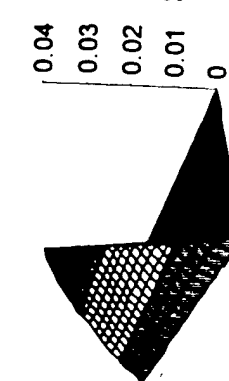
# Identified KP Measures

- First Page of Measure Plots: the ID'd KP measures are shown for discretizations of  $K=5, 11, 20, 30$  taken after 400 seconds of adaptation.
  - The measure surfaces can be seen to converge as  $K$  increases.
- Second Page of Measure Plots: the ID'd KP measures for  $K=20$  is shown to evolve from the initial guess at  $t=0$  seconds to the measure surface at  $t=400$  seconds.

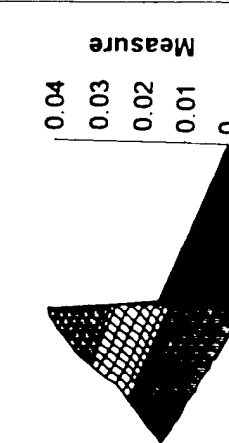
# Time Evolution of K=20 KP Measure ID



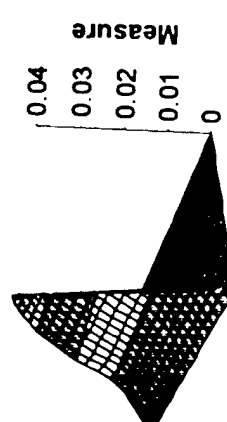
$t = 0$



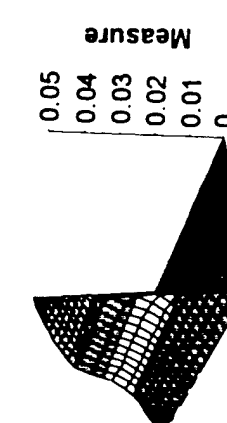
$t = 5$



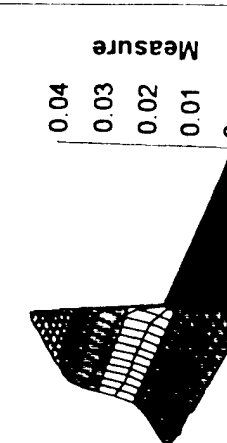
$t = 15$



$t = 30$



$t = 200$



$t = 400$

# SMA-Induced Deformations of General Unsymmetric Composite Laminates

Marie-Dano and Michael W. Hyer

Department of Engineering Science and Mechanics

Virginia Polytechnic Institute and State University

tel:540-231-5372 fax:540-231-4574 email:hyerm @ vt.edu

By way of background (first attached overhead), it is well known that when cured and cooled to room temperature, an epoxy-matrix unsymmetric laminate can have several equilibrium configurations. Perhaps the most well-known phenomenon in the category of unsymmetric laminates is the behavior of a cross-ply [0<sub>2</sub>/90<sub>2</sub>]<sub>T</sub> laminate. This laminate is, of course, flat at its elevated curing temperature, but when cooled to room temperature the laminate can assume one of two shapes. If when flat the laminate is in the x-y plane of an x-y-z coordinate system, one cured shape is cylindrical with its generator parallel to the x axis. The other cured shape is also cylindrical with a curvature equal in magnitude but opposite in sign to the first cylinder, and with its generator parallel to the y axis, namely perpendicular to the generator of the first cylindrical shape. The laminate can be changed from one cylindrical configuration to another by a simple snap-through action. There is a third configuration, a saddle shape, that is unstable and thus is never observed.

The existence of two equilibrium configurations, or structural shapes, presents interesting opportunities. It is possible to use SMA's to provide the snap-through moments and change from one cylindrical configuration to the other on command. Potential applications (second overhead) include using one or more unsymmetric laminates as portions of the walls of a conduit transporting a fluid. A change in the conduit cross section is possible by changing the wall laminate from one cylindrical configuration to another. This change in wall geometry could change the flow in the conduit on command. Other potential applications (third overhead) could result in an elastic system that exhibits a stiffness that can be changed from a high value to a low value by simply snapping the laminate from one configuration to another. The simplest concept for effecting a configuration change (fourth overhead) is to use SMA wires to provide the snap-through moments. With more general unsymmetric laminates, twist curvature is possible, resulting in an endless variety of structural shapes which can be changed by a snap-through action. In all cases the deformations of the laminate are quite large. Furthermore, because there are multiple equilibrium configurations, the problem is inherently nonlinear and stability is an issue. In particular, because of the large deformations, the nonlinearity is geometric in nature.

In the current research effort progress has been made on using SMA's, in wire form, as actuators to produce the configuration change. This accomplishment involved achieving a thorough understanding of the complex behavior of unsymmetric laminates. First, a methodology was developed to predict the multiple shapes that result for considering general unsymmetric laminates. The methodology was verified by fabricating a number of laminates and measuring their multiple shapes. The second step was to understand the conditions required to effect the snap through. Force levels and force directions were the primary concern. These results were then used to design the overall requirements for the SMA wire actuators. Thirdly, an acceptable SMA constitutive model was adopted and verified with experiments on simple aluminum plates. The predictions of SMA wire temperature vs. strains in the aluminum plate were very close to the experimental results, and thus the SMA model was applied to the unsymmetric laminate problem.

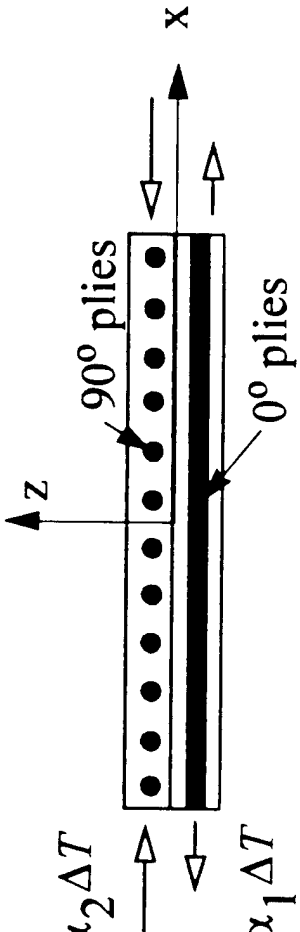
The results of using SMA actuators with unsymmetric laminates have been successful. The theory developed to predict the response of the laminates, particularly snap-through conditions, to the forces of SMA wire actuators correlates quite well with measurements (fifth overhead). In particular, strains vs. actuator temperature and snap-through temperature correlate well, and the results are repeatable.

## Background

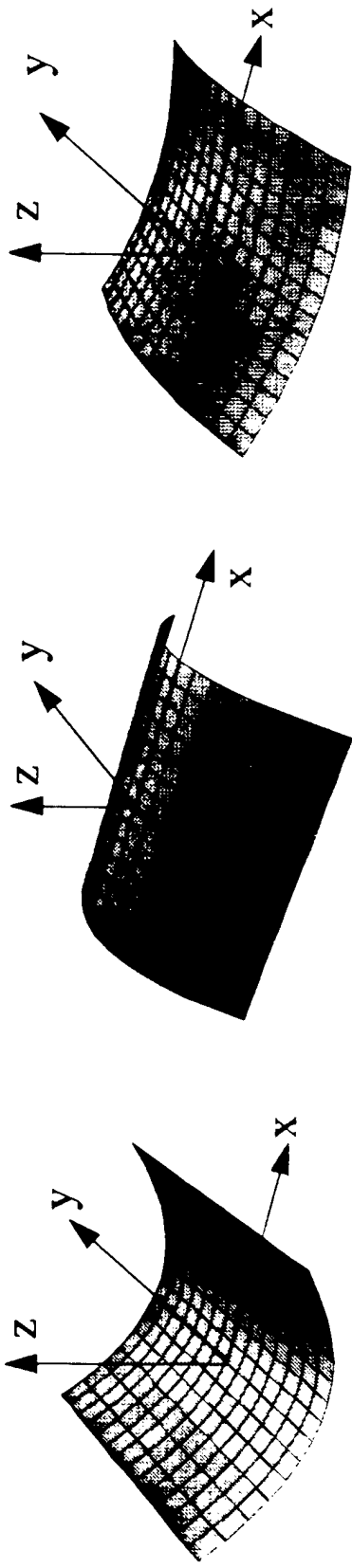
Shapes of a  $[0_2/90]_T$  unsymmetric laminate

$$\Delta T < 0$$
$$\varepsilon_x = \alpha_2 \Delta T$$
$$\varepsilon_x = \alpha_1 \Delta T$$

Curing temperature

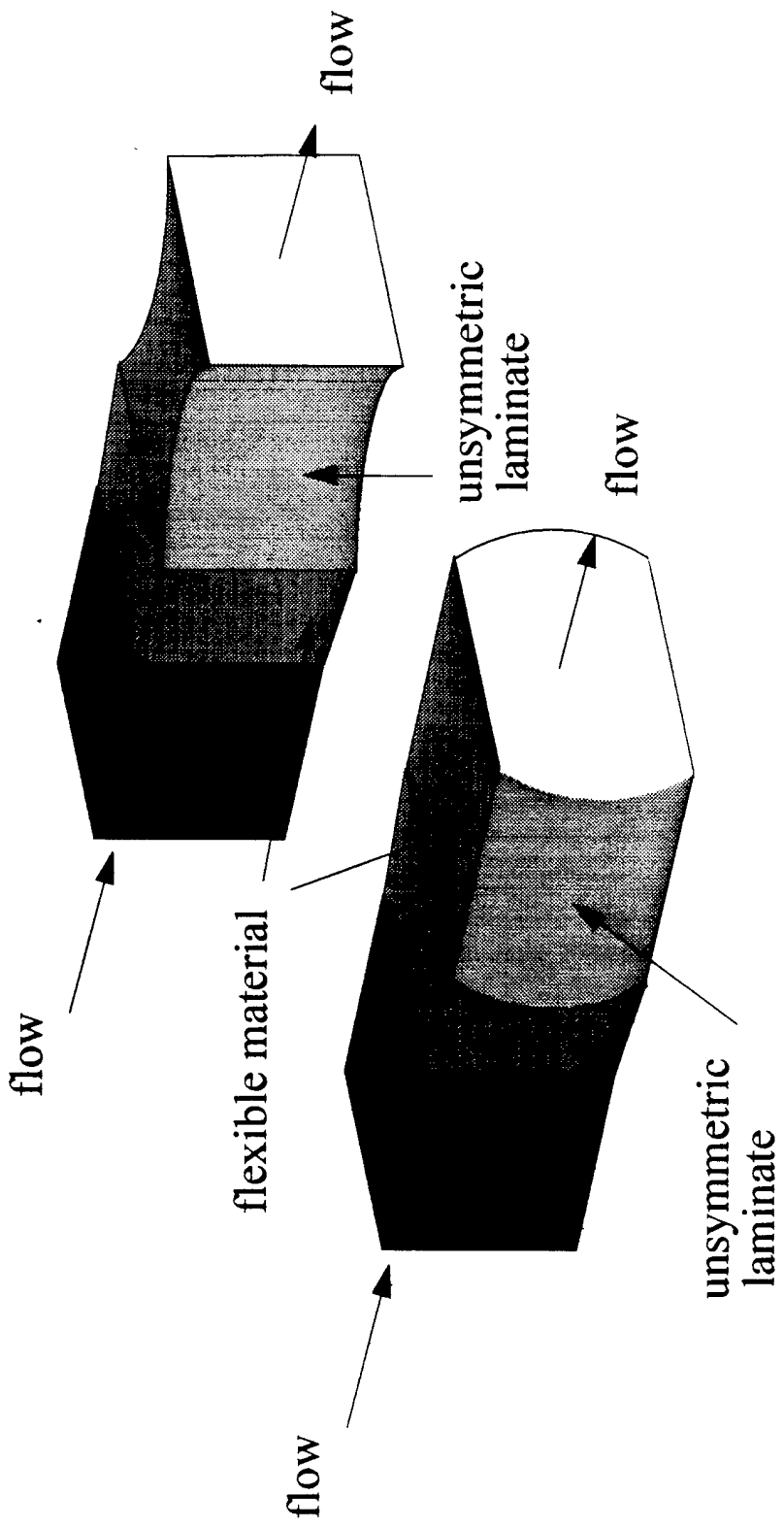


Room temperature



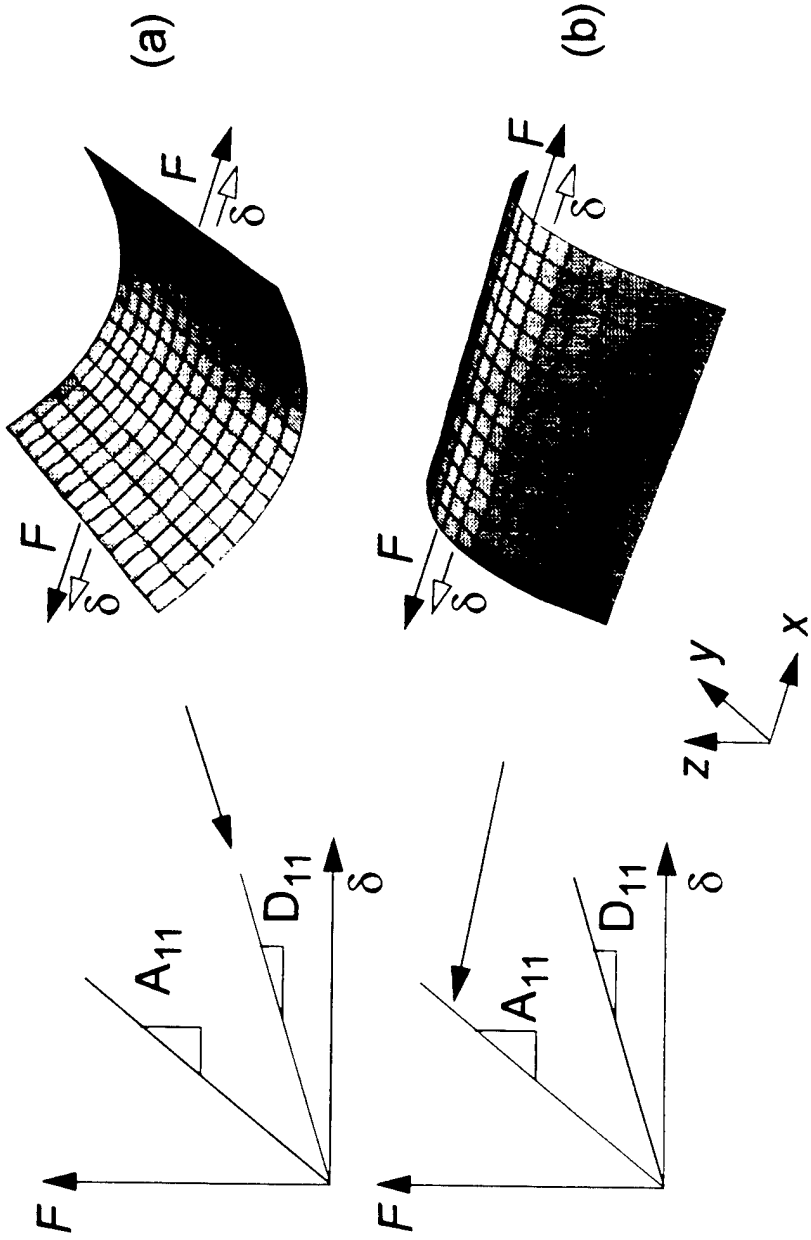
## Possible application

Use one or more unsymmetric laminates as portions of a variable-geometry conduit to transport fluid:

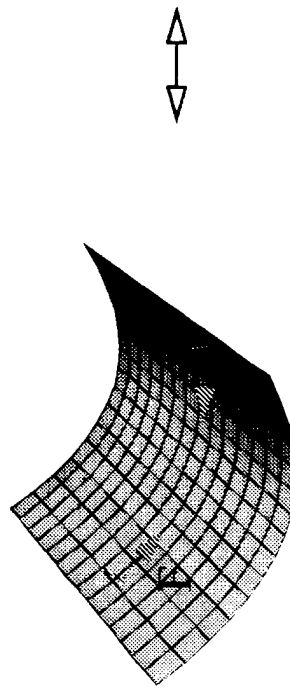
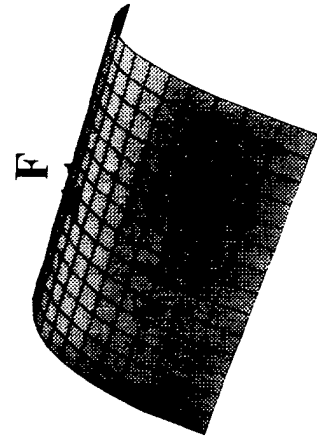
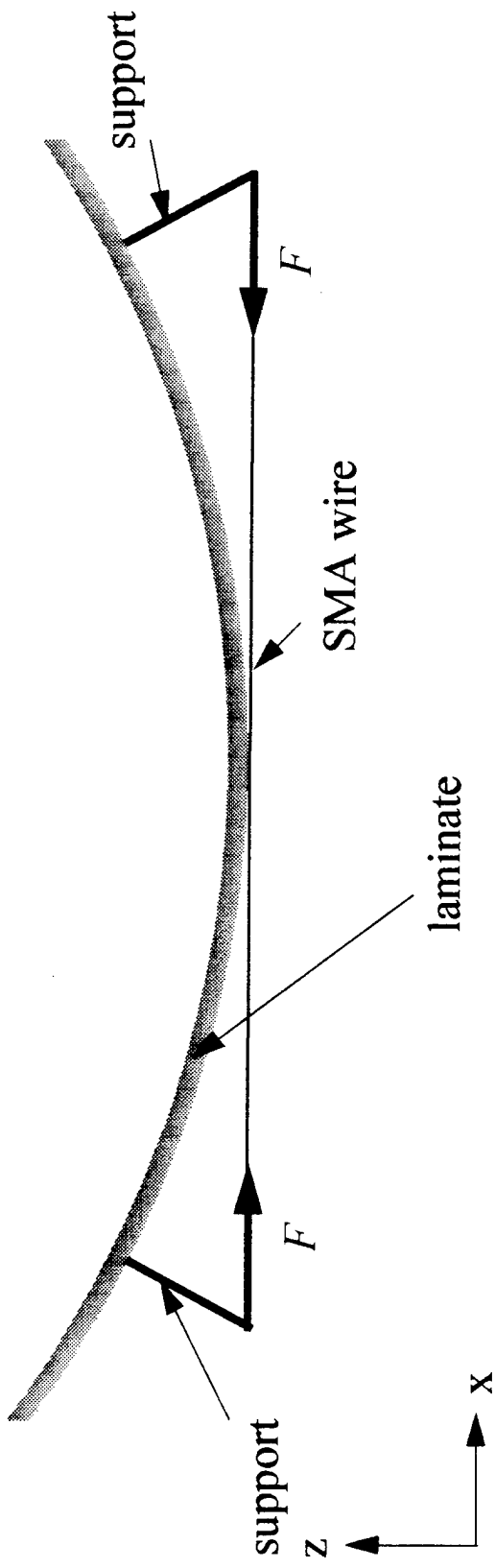


## Possible application (cont')

The combination of SMA-actuators used with unsymmetric laminates could result in a system that exhibit two highly contrasting stiffness:

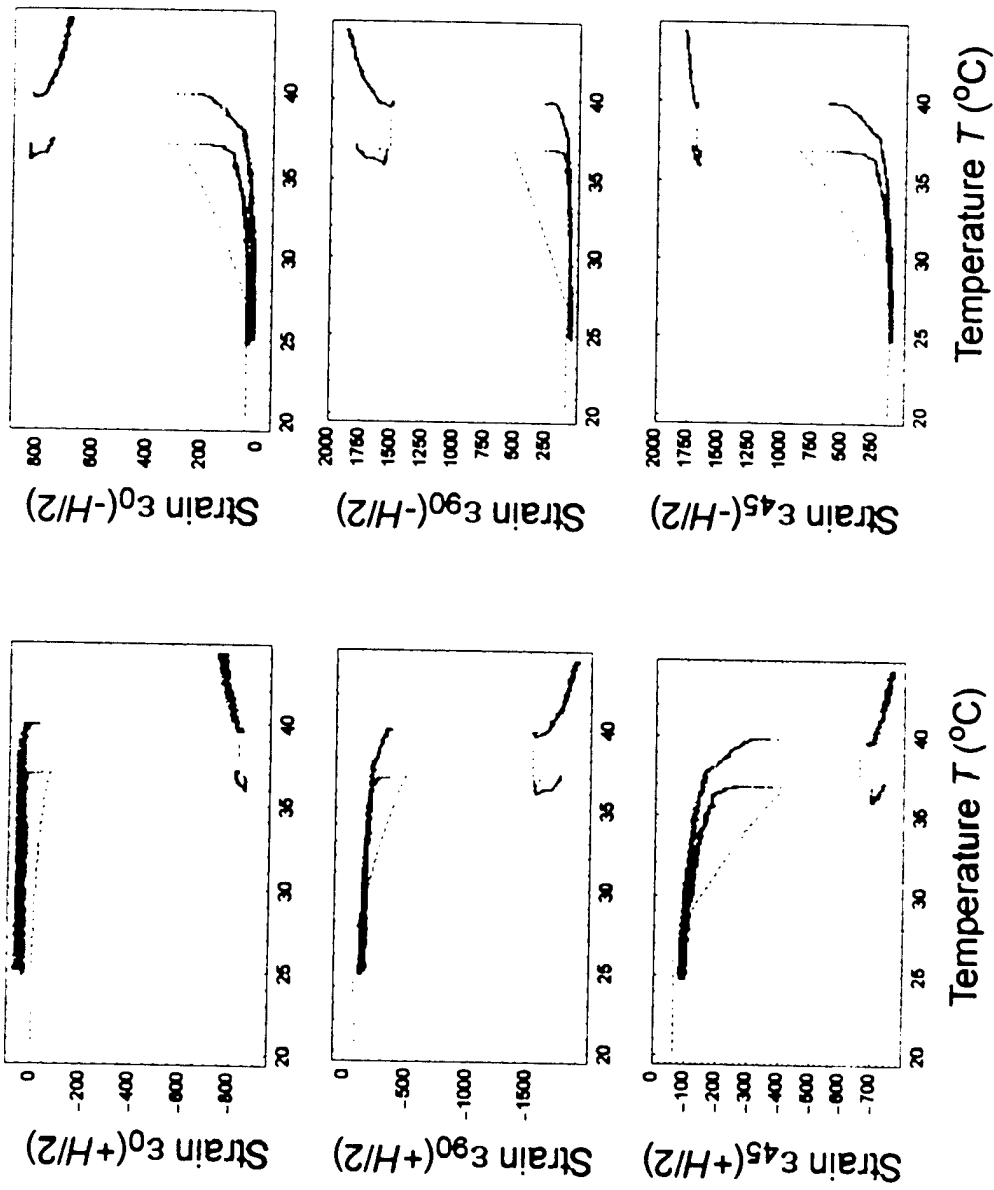


# Concept



# $[ -30_4 / 30_4 ]_T$ laminate

.... Theory  $A_{so}=25^\circ\text{C}$   
 — First experiment  
 — Second experiment



# **Comparative Evaluation of Shape Memory Alloy Constitutive Models with Test Data**

Jeanette J. Epps and Inderjit Chopra

Alfred Gessow Rotorcraft Center, Department of Aerospace Engineering  
University of Maryland, College Park, Maryland 20742  
Office Phone: (301)405-1142, Fax: (301)314-9001  
email: jeanette@eng.umd.edu

## **Abstract**

Shape memory alloys are being recognized as a revolutionary material to develop smart actuators for numerous aerospace, civil structures, marine, and medical applications since it is able to undergo large deformations and then recover its original shape upon heat activation. One potential application of SMA is a trailing edge tab adjustment for in-flight tracking of a helicopter rotor that is being pursued in this paper. One drawback is the lack of a reliable database for material properties of SMA. Another drawback is the unavailability of an accurate constitutive model for SMA. In this study, a comparative evaluation of several SMA constitutive models with test data was undertaken.

Various constitutive models were developed by researchers to characterize the thermo-mechanical behavior of SMA materials. These models are based on thermo-mechanics, or a combination of thermomechanics and SMA phenomenology, and/or statistical mechanics. Four constitutive models were compared and validated with experimental results. The four models were developed by Tanaka, Liang and Rogers, Boyd and Lagoudas, and Brinson.

To predict the thermo-mechanical properties of SMA, it was necessary to carry out careful testing of the SMA wire to determine the coefficients for the four constitutive models. Careful specimen testing is necessary since there is no reliable database available for the properties of SMA materials and the thermo-mechanical properties of the shape memory alloys depend on many variables, such as wire manufacturing, wire diameter, pre-strain, stress level, temperature, and whether or not the material has been cycled. Using the data obtained from testing the necessary coefficients for the four constitutive models were measured. Coefficients such as the Young's modulus for the martensite and austenite phase and the four phase transformation temperatures were determined.

All models showed good correlation with experimental stress-strain curves, however the model developed by Brinson showed the best correlation with all test data. None of the models, however, were able to predict the unloading curve accurately for most of the stress-strain curves in the austenite phase. It was noted that stress-strain curves at martensitic temperatures could not be calculated using the models developed by Tanaka, Liang and Rogers and Boyd and Lagoudas. It was theorized that this was due to the inability of these models to distinguish between temperature-induced and stress-induced martensite volume fraction.

Measured and calculated recovery stress-temperature characteristics were also compared. All models showed difficulty in predicting this behavior. Experimental results showed that the recovery stress becomes nearly constant after transformation whereas all predicted results showed an increase.

The present study will be used in the investigation of in-flight tracking of helicopter rotor blades. A rigid composite wing model of 8 inch chord, 16 inch span and NACA 0012 airfoil section will be built. The flap actuation will be achieved using SMA wires. The actuation system consists of two or more, pre-strained SMA wires mechanically constrained at the quarter chord spar, and hinged to a flap at the other end. A control feedback scheme will be developed to fine tune the flap. The wing section will then be tested in an open-jet tunnel and the performance of the flap under SMA actuation will be examined. The results will be used to validate predictions.

## Objective of Current Research

- *To conduct a comparative evaluation of several constitutive models for shape memory alloys based on correlation with test data.*
- *To investigate a trailing-edge tab actuated using SMA wire actuators for in-flight tracking of helicopter rotor blades.*

## Shape Memory Effect

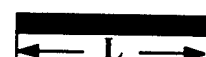
### 1. High Temperature

- Phase change - austenite phase
- SMA wire of length L



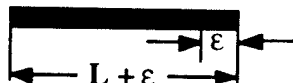
### 2. Room Temperature

- Undeformed wire
- Phase change - martensite phase



### 3. Room Temperature

- Plastically deformed wire
- Remains in the martensite phase



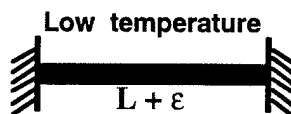
### 4. High Temperature

- Phase change - austenite phase
- Recovery of deformation
- undeformed wire of length L

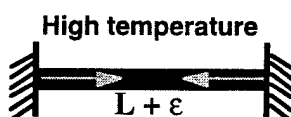


## Constrained Recovery

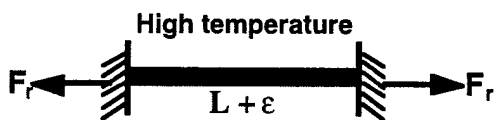
I. Initially the material is mechanically constrained at both ends and the material has a pre-strain,  $\epsilon$ .



II. When the material is heated a phase change takes place and the wire will try to recover  $\epsilon$  due to the shape memory effect.

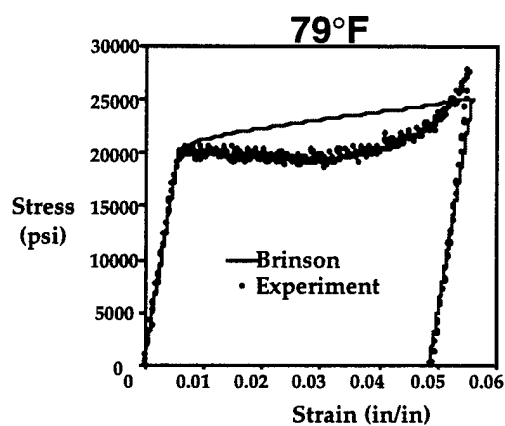


III. However a tensile force develops instead due to the mechanical constraints



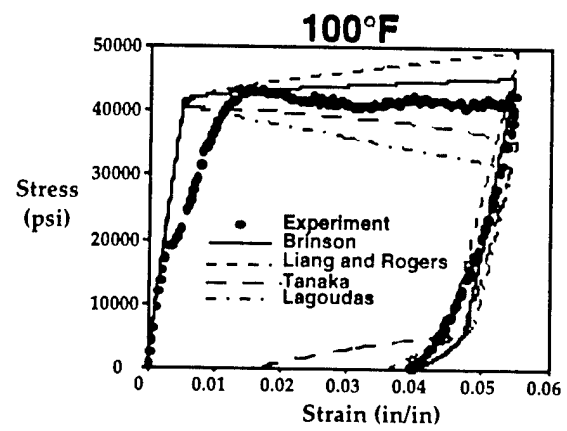
## Experimental-Theoretical Stress-Strain-Temperature Curves

- 100% Martensite Initially
- Only results from the Brinson model shown.
- Stress-strain curves at  $T < M_s$  could not be calculated using the models due to the inability of the models to distinguish between temperature- and stress-induced martensite.
- Good correlation between experiment and model

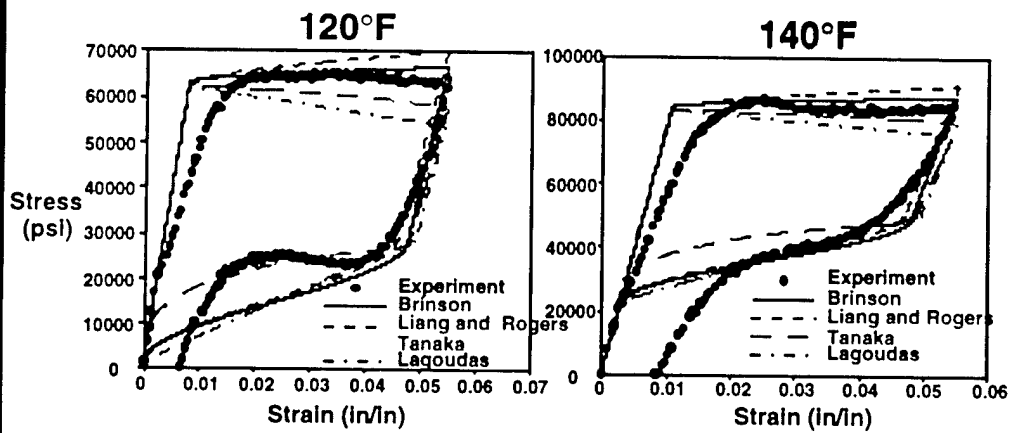


## Experimental-Theoretical Stress-Strain-Temperature Curves

- At this temperature the material resides in a mixed phase- difficult to predict.
- All models shown.
- Good correlation between experiment and models.
- Overall, the Brinson model showed the best correlation, however correlation for the other models improve for higher temperatures.



## Experimental-Theoretical Stress-Strain-Temperature Curves (con't)

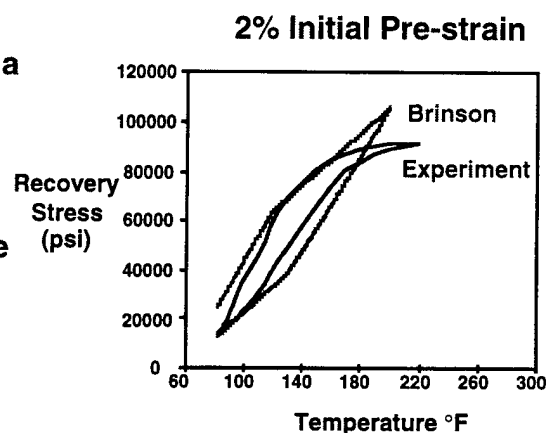


## Experimental-Theoretical Recovery Stress-Temperature Curves

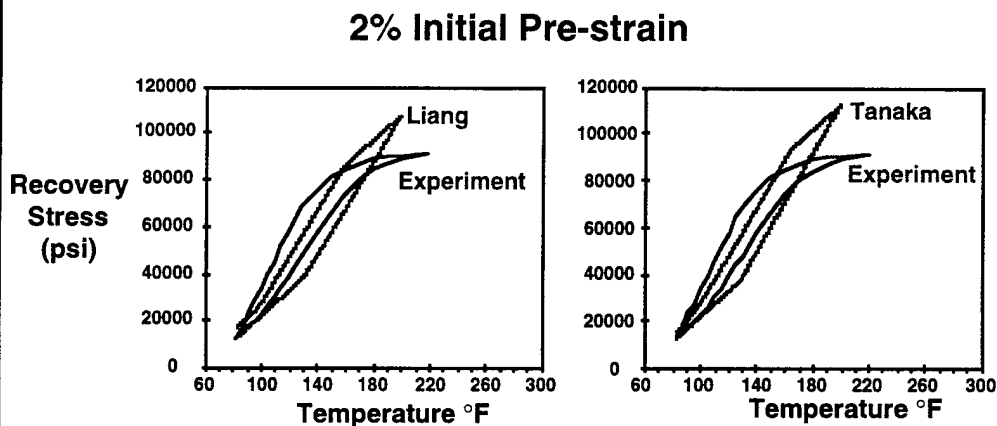
- The recovery stress-temperature characteristics are needed in the design of a tab actuator.

- All models showed difficulty in predicting the recovery stress-temperature characteristics.

- Further work will involve improvements in the prediction of the recovery stress.

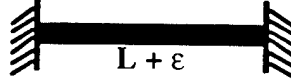


## Experimental-Theoretical Recovery Stress-Temperature Curves (con't)

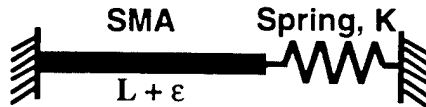


## Application of Shape Memory Alloys: Actuation of Trailing-Edge Tab for In-Flight Blade Tracking

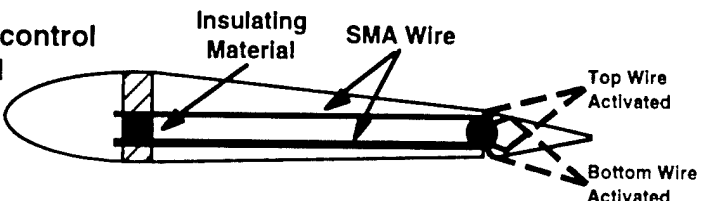
- Modeling of SMA actuation of a trailing edge tab is similar to constrained recovery except the amount of recovery is controlled.



- This can be modeled as a spring in series with a pre-strained SMA wire.



- To fine tune a tab, a control feedback scheme will be developed.



## Conclusions

- The Brinson model showed good correlation for SMA wire in the martensite phase ( $T < M_s$ ).
- Stress-strain curves at  $T < M_s$  could not be calculated for the Tanaka, Liang and Rogers and Boyd and Lagoudas models. This could be due to the inability of the models to distinguish between temperature- and stress-induced martensite.
- Good correlation between experiment and models for  $T > M_s$ .
- Overall, the Brinson model showed the best correlation, however correlation for the other models improve for higher temperatures.
- All models showed difficulty in predicting the recovery stress-temperature characteristics.

## Viscoelastic Effects in the Dynamics of Thick Beams

A. R. Johnson<sup>1</sup> and A. Tessler  
Computational Structures Branch  
NASA Langley Research Center, MS240  
Hampton, VA 23681-0001

### Summary

A viscoelastic higher-order thick beam finite element formulation is extended to include elastodynamic deformations. The material constitutive law is a special differential form of the Maxwell solid. In the constitutive model, the elastic strains and the conjugate viscous strains are coupled through a system of first-order ordinary differential equations. The total time-dependent stress is the superposition of its elastic and viscous components. The elastodynamic equations of motion are derived from the virtual work principle. Computational examples are carried out for a thick orthotropic cantilevered beam. A quasi-static relaxation problem is employed as a validation test for the elastodynamic algorithm. The elastodynamic code is demonstrated by analyzing the damped vibrations of the beam which is deformed and then released to freely vibrate.

### Introduction

The combination of highly viscous low-modulus materials with the traditional high-modulus materials produces stiff, highly damped load carrying structures. The quasi-static and dynamic analyses of such structures require improvements in the material damping representation over the velocity proportional damping schemes. Halpin and Pagano<sup>1</sup> demonstrated that the relaxation moduli for anisotropic solids produce symmetric matrices that can be expanded in a Prony series form (i.e., a series of exponentially decaying terms). Early viscoelastic models for small deformations of composites focused on computing the complex moduli for anisotropic solids from the elastic properties of the fibers and the complex modulus properties of the matrix.<sup>2,3</sup> Recently, various classical constitutive models have been used including generalized Maxwell and Kelvin-Voigt solids.<sup>4,5</sup> These constitutive models have practical value since they provide adequate approximations for the dynamic softening and hysteresis effects – the phenomena that are not directly proportional to strain rates.

Coleman and Noll<sup>6</sup> and Schapery<sup>7</sup> presented comprehensive discussions on the history integral form of the Maxwell solid. Johnson and Stacer<sup>8</sup> developed a differential form of the Maxwell solid constitutive law for large strain viscoelastic deformations of rubber. The formulation required additional viscous strain

---

<sup>1</sup> Vehicle Technology Center, Army Research Laboratory.

variables that are conjugate to the elastic strains. The same constitutive law was used by Johnson et al.<sup>9,10</sup> to formulate a viscoelastic, large-displacement shell finite element. In the work of Johnson and Tessler,<sup>11</sup> the differential constitutive law was implemented within Tessler's<sup>12</sup> higher-order beam theory, giving rise to a quasi-static viscoelastic thick beam finite element formulation. They presented several quasi-static numerical solutions demonstrating the relaxation, creep, and cyclic creep response of thick beams. They demonstrated that only minor modifications to an elastic finite element code are needed to produce a computationally efficient viscoelastic code.

In this paper, the quasi-static viscoelastic formulation of Johnson and Tessler<sup>11</sup> is extended to elastodynamics. The mass matrix for the higher-order beam is derived and a modified Newmark algorithm is employed to integrate the equations of motion. The modified Newmark algorithm contains an implicit trapezoidal integration scheme which enables accurate integration of the first-order differential equations for the viscous strains.

### Viscoelastic Higher-Order Beam

In this section, an internal variable formulation for a Maxwell solid higher-order beam theory<sup>11</sup> is outlined. The beam dimensions and sign convention are shown in Figure 1. The differential form of the viscoelastic constitutive model for the beam is written in matrix form as

$$\mathbf{s}(t) = \mathbf{C}\mathbf{e} + \mathbf{\dot{C}} \sum_{n=1}^N \mathbf{\dot{e}}_n(t) \quad (1)$$

$$\mathbf{\dot{e}}_n + \mathbf{\dot{e}}_n / \tau_n = \mathbf{\dot{e}} \quad \text{for each } n \quad (2)$$

where  $\mathbf{s}^T = (\sigma_{xx}, \sigma_{zz}, \tau_{xz})$ ,  $\mathbf{e}^T = (\varepsilon_{xx}, \varepsilon_{zz}, \gamma_{xz})$ ,  $\mathbf{\dot{e}}_n^T = (\dot{\varepsilon}_{xx}, \dot{\varepsilon}_{zz}, \dot{\gamma}_{xz})$

$$\mathbf{C} = \begin{bmatrix} C_{11} & C_{13} & 0 \\ C_{13} & C_{33} & 0 \\ 0 & 0 & C_{55} \end{bmatrix} \quad \text{and} \quad \mathbf{\dot{C}} = \begin{bmatrix} \dot{C}_{11} & \dot{C}_{13} & 0 \\ \dot{C}_{13} & \dot{C}_{33} & 0 \\ 0 & 0 & \dot{C}_{55} \end{bmatrix}$$

The vectors  $\mathbf{s}$  and  $\mathbf{e}$  are the engineering stresses and strains (geometrically nonlinear strain-displacement relations can be used for  $\mathbf{e}$ , see Ref. 9 for a nonlinear quasistatic model.) The vectors  $\mathbf{\dot{e}}_n$  ( $n = 1, 2, \dots, N$ ) are the internal variables, i.e., conjugate viscous strains, where  $N$  is the number of terms in a Prony series representation of the material's stress relaxation response. The matrices  $\mathbf{C}$  and  $\mathbf{\dot{C}}$  contain the elastic and viscous stiffness coefficients. In the higher-order beam

theory,<sup>12</sup> the components of the displacement vector are approximated through the beam thickness by way of five kinematic variables, i.e.,

$$u_x(x, z, t) = u(x, t) + h\zeta\theta(x, t) \quad (3)$$

$$u_z(x, z, t) = w(x, t) + \zeta w_1(x, t) + \left(\zeta^2 - \frac{1}{5}\right)w_2(x, t) \quad (4)$$

where  $\zeta = z/h$  denotes a nondimensional thickness coordinate and  $2h$  is the total thickness. The function  $u(x, t)$  represents the midplane (i.e. reference plane) axial displacement,  $\theta(x, t)$  is the bending rotation of the cross-section of the beam,  $w(x, t)$  is the weighted-average deflection, and  $w_1(x, t)$  and  $w_2(x, t)$  are the higher-order transverse displacement variables enabling a parabolic distribution of  $u_z(x, z, t)$  through the thickness.

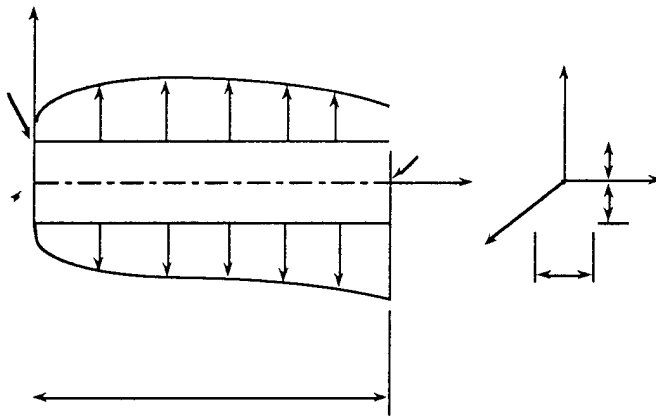


Figure 1. Thick-beam geometry, kinematics, and loading.

The above displacement assumptions give rise to the following thickness distributions for the strains: a linear axial strain, a cubic transverse normal strain, and a quadratic transverse shear strain. These strain components have the following form

$$\varepsilon_{xx} = u(x, t)_x + h\zeta\theta(x, t)_x \quad (5)$$

$$\varepsilon_{zz} = \frac{w_1(x, t)}{h} + \phi_z(\zeta) \frac{w_2(x, t)}{h^2} + \phi_x(\zeta) \theta(x, t)_x \quad (6)$$

$$\gamma_{xz} = \phi_{xz}(\zeta) (w(x, t)_x + \theta(x, t)) \quad (7)$$

where  $\phi_x(\zeta) = h\nu_{13}\zeta(4 - 7\zeta^2)/17$ ,  $\phi_z(\zeta) = 14\zeta h(3 - \zeta^2)/17$ ,  $\phi_{xz}(\zeta) = 5(1 - \zeta^2)/4$ ,

and  $\nu_{13}$  is Poisson's ratio. The simplest finite element approximation of this beam theory involves a three-node configuration (see Figure 2) which is achieved by the following interpolations

$$\begin{aligned} u(\eta, t) &= (1 - \eta)u_0^t(t) + \eta u_1^t(t), & \theta(\eta, t) &= (1 - \eta)\theta_0^t(t) + \eta\theta_1^t(t), \\ w(\eta, t) &= (1 - \eta)w_0^t(t) + \eta w_1^t(t) - \frac{\eta(1 - \eta)}{2}(\theta_0^t(t) - \theta_1^t(t)), \\ w_1(\eta, t) &= W_1^t(t), & w_2(\eta, t) &= W_2^t(t) \end{aligned} \quad (8)$$

where  $\eta = x/\ell$  is the nondimensional axial coordinate. The nodal degrees-of-freedom at the two ends of the element are subscripted with indices 0 and 1. Since the strains do not possess derivatives of the  $w_1(\eta, t)$  and  $w_2(\eta, t)$  variables, these variables need not be continuous at the element nodes and, hence, their simplest approximation is constant for each element. Their corresponding degrees-of-freedom are attributed to a node at the element midspan.

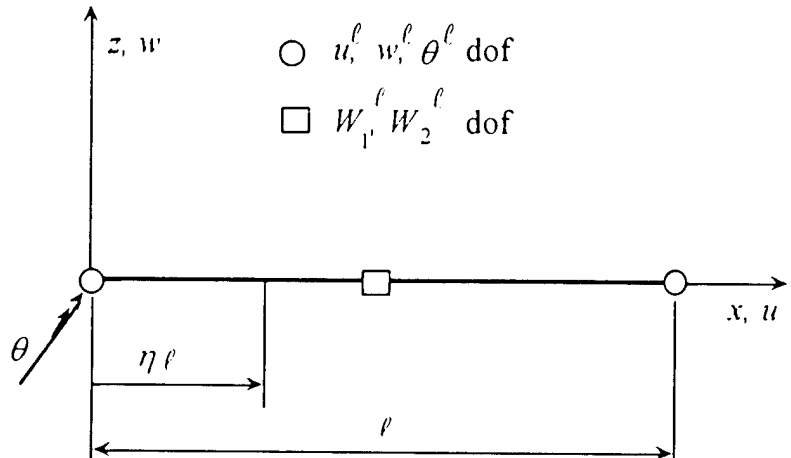


Figure 2. A three-node, higher-order theory thick-beam element.

For dynamic loading, the virtual work statement for an element of volume  $V$  with the differential Maxwell constitutive law can be written as

$$\int \rho (\ddot{u}_x \delta u_x + \ddot{u}_z \delta u_z) dV + \int \mathbf{e}^T \mathbf{C} \delta \mathbf{e} dV + \sum_{n=1}^N \int \mathbf{e}^T \mathbf{C} \delta \mathbf{e} dV - \delta W = 0 \quad (9)$$

where the first integral represents the virtual work done by inertial forces, the second is the internal virtual work done by the elastic stresses, the third is the internal virtual work done by the viscous stresses, and  $\delta W$  is the virtual work done by the external forces. Introducing (8) into (3)-(4) and substituting the

results into (5)-(7) yields finite element approximations of the strains in terms of the nodal variables, i.e.,

$$\mathbf{e} = \mathbf{B}\mathbf{u}, \quad (10)$$

$$\mathbf{B} = \begin{bmatrix} -\frac{1}{\ell} & 0 & -\frac{z}{\ell} & 0 & 0 & \frac{1}{\ell} & 0 & \frac{z}{\ell} \\ 0 & 0 & -\frac{\phi_x}{\ell} & \frac{1}{h} & \frac{\phi_z}{h^2} & 0 & 0 & \frac{\phi_x}{\ell} \\ 0 & -\frac{\phi_x}{\ell} & \frac{\phi_z}{2} & 0 & 0 & 0 & \frac{\phi_x}{\ell} & \frac{\phi_z}{2} \end{bmatrix} \quad (11)$$

and  $\mathbf{u}^T = (u_0, w_0, \theta_0, W_1, W_2, u_1, w_1, \theta_1)^T$  denotes the element nodal displacement vector. Next, a set of analogous nodal variables,  ${}_n^*\mathbf{u}$ , and corresponding viscous strains,  ${}_n^*\mathbf{e}$ , are introduced. These are related by

$${}^*\mathbf{e} = \mathbf{B} {}_n^*\mathbf{u} \quad (12)$$

The  ${}_n^*\mathbf{u}$  variables, which carry the time dependent information for the material within the element, are independent from element to element. The displacements  $u_x$  and  $u_z$  are then expressed in terms of the element nodal degrees-of-freedom using (3), (4) and (8), giving rise to  $u_x = \Phi_x^T \mathbf{u}$  and  $u_z = \Phi_z^T \mathbf{u}$ , where  $\Phi_x(\zeta, \eta)$  and  $\Phi_z(\zeta, \eta)$  are vectors of the interpolation functions. The virtual work statement for an element then becomes

$$\begin{aligned} & \tilde{\mathbb{W}} \int \rho (\Phi_x \Phi_x^T + \Phi_z \Phi_z^T) dV \delta \mathbf{u} + \mathbf{u}^T \int \mathbf{B}^T \mathbf{C} \mathbf{B} dV \delta \mathbf{u} \\ & + \sum_{n=1}^N {}_n^*\mathbf{u}^T \int \mathbf{B}^T {}^*\mathbf{C} \mathbf{B} dV \delta {}_n^*\mathbf{u} - \delta \mathcal{W} = 0 \end{aligned} \quad (13)$$

By defining the integrals in (13) as the mass,  $\mathbf{m}$ , elastic stiffness,  $\mathbf{k}$ , and viscous stiffness,  ${}^*\mathbf{k}$ , matrices, there results

$$[\tilde{\mathbb{W}} \mathbf{m} + \mathbf{u}^T \mathbf{k}] \delta \mathbf{u} + \left[ \sum_{n=1}^N {}_n^*\mathbf{u}^T {}^*\mathbf{k} \right] \delta {}_n^*\mathbf{u} - \delta \mathcal{W} = 0 \quad (14)$$

Since  $\delta \mathbf{u} = \delta {}_n^*\mathbf{u}$  when  $t$  is constant, the virtual work takes on a simpler form

$$\left[ \ddot{\mathbf{W}}^T \mathbf{m} + \mathbf{u}^T \mathbf{k} + \sum_{n=1}^N {}^n \mathbf{k}^T \cdot {}^n \mathbf{u} \right] \delta \mathbf{u} - \delta \mathcal{W} = 0 \quad (15)$$

This implies that at any time  $t$  the element equilibrium equations are

$$\mathbf{m} \ddot{\mathbf{Y}} + {}^n \mathbf{k} {}^n \mathbf{u} = \mathbf{f} - \sum_{n=1}^N {}^n \mathbf{k} {}^n \mathbf{u} \quad \text{for each element} \quad (16)$$

where  $\mathbf{f}$  denotes the element consistent load vector due to the external loading. Introducing (10) and (12) into the differential equations for the strain variables in (2) yields

$${}^n \dot{\mathbf{Y}} + {}^n \mathbf{u} / \tau_n = \dot{\mathbf{Y}} \quad \text{for each } n \quad (17)$$

The global equilibrium equations are determined by the standard assembly of the element equations, (16). Note, there is no assembly for (17). The global equations of motion are

$$\mathbf{M} \ddot{\mathbf{Y}}_g + \mathbf{K} \mathbf{u}_g = \mathbf{F}_{mech} - \mathbf{F}_{visc} \quad (18)$$

where  $\mathbf{u}_g$  denotes the global nodal variable vector,  $\mathbf{M}$  is the mass matrix,  $\mathbf{K}$  is the elastic stiffness matrix,  $\mathbf{F}_{mech}$  is the global force vector due to mechanical loads, and  $\mathbf{F}_{visc}$  is the assembled vector for  $\sum_{n=1}^N {}^n \mathbf{k} {}^n \mathbf{u}$ . The viscoelastic problem is solved by simultaneously integrating the first order differential equations, (17), and the second order equations, (18), where the latter is subject to the appropriate boundary restraints.

As far as the finite element implementation is concerned, a conventional linear elastic code can be readily adapted to perform a dynamic analysis for a structure made from a Maxwell material, i.e., a material whose relaxation stiffness coefficients can be modeled with a Prony series. First, the viscous stiffness coefficients,  ${}^n C_y$ , are used in place of the elastic values to compute the element viscous stiffness matrices,  ${}^n \mathbf{k}$ , which are stored for repeated use. The internal nodal variables for each element,  ${}^n \mathbf{u}$ , are set equal to their initial values. A modified Newmark algorithm is then used to integrate (18). The modification is required so that (17), stiff relaxation equations, are implicitly integrated.

### Applications

Two numerical solutions representative of quasi-static and free vibration deformations of a cantilevered thick orthotropic beam are presented. The beam dimensions are as follows:  $L = 0.1\text{ m}$ ,  $2h = 0.02\text{ m}$ , and  $b = 1.0\text{ m}$  (refer to Figure 1). The beam elastic stiffness coefficients for the state of plane stress can be written in terms of engineering material constants as

$$C_{11} = E_x / (1 - \nu_{xz} \nu_{zx}), \quad C_{33} = E_z / (1 - \nu_{xz} \nu_{zx}), \quad C_{13} = \nu_{xz} C_{33}, \quad C_{55} = G_{xz}$$

A unidirectional E-glass/epoxy laminate is considered for which the material constants are:  $E_x = 38.6\text{ GPa}$ ,  $E_z = 8.27\text{ GPa}$ ,  $G_{xz} = 4.14\text{ GPa}$ ,  $\nu_{xz} = 0.26$ , and  $\rho = 1.8\text{ g/cm}^3$ . The viscous relaxation properties are computed from complex modulus versus frequency data for the E-glass/epoxy.<sup>13</sup> The equations for the real and imaginary parts of the effective modulus for a ten term Maxwell solid<sup>14</sup> are least-squares fit to the measured data in a frequency range of 45 Hz – 145 Hz. The least squares minimization was performed using a quadratic programming method that enforced the constraint that each of the moduli in the Maxwell solid must be positive. The time constants for the ten terms are;  $\tau_n = 10^{-4}, 10^{-3.5}, 10^{-3}, 10^{-2.5}, 10^{-2}, \dots, 10^1$ , and infinity. The resulting Maxwell solid had its moduli scaled so that its equivalent nondimensional Prony series has the form

$$P(t) = 1.0 + 0.01755 e^{-0.0001t} + 0.000257 e^{-0.01t} + 0.072014 e^{-0.3162t}$$

The time dependent stiffness values for the E-glass/epoxy are then given by  

$${}^* \mathbf{C} = P(t) \mathbf{C}$$
.

Example 1. A cantilever beam (reference Figure 1) with  $w$ ,  $u$ ,  $\theta$  fixed at point A has a prescribed deflection  $w$  at point B that is ramped from 0 to -1 cm in 0.05 sec and then held constant at -1 cm. Figure 3 depicts the maximum axial stress at point C as a function of time. Also shown are the elastic and viscous stress components comprising the total stress. The decay of the total viscoelastic stress to its elastic value as time is increased demonstrates the expected step-strain relaxation behavior. Note, when this problem is solved with a velocity proportional viscous damping model the viscous stress for time greater than 0.05 sec is zero.

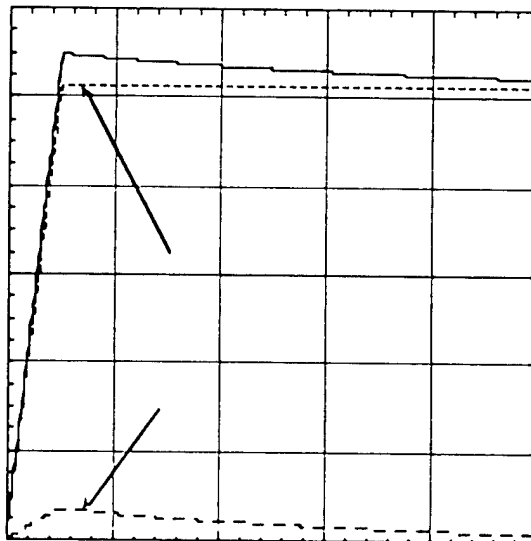


Figure 3. Cantilevered beam under prescribed tip deflection.  
Stress in top surface at support (point C).

Example 2. The cantilevered beam of Example 1 has its tip (point B) released at  $t = 0.1$  sec and is allowed to vibrate freely thereafter. The resulting tip deflection as a function of time is shown in Figure 4. Figure 5 depicts the value of the dynamic axial stress at point C as a function of time. Note that both relaxation and damped vibration response are obtained within the same finite element solution.

### Conclusions

An elastodynamic formulation, which includes a differential form of the Maxwell viscous solid constitutive theory, has been implemented in a higher-order-theory beam finite element. The attractive features of the formulation include: (1) The constitutive constants are the same as those needed in the classical history-integral model, and they are also readily available from step-strain relaxation tests, (2) The internal variables are conjugate to the elastic strain measures; hence, they are consistent with the kinematic assumptions of the elastic formulation, (3) The update of the state variables can be performed in a parallel computing environment, allowing the viscous force vector in the equations of motion to be determined efficiently within the modified Newmark algorithm,

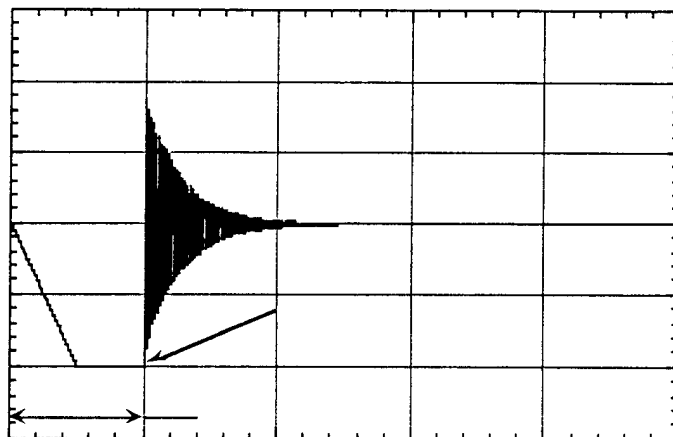


Figure 4. Cantilevered beam under prescribed tip deflection.  
Tip released - vibration of tip (Point B).

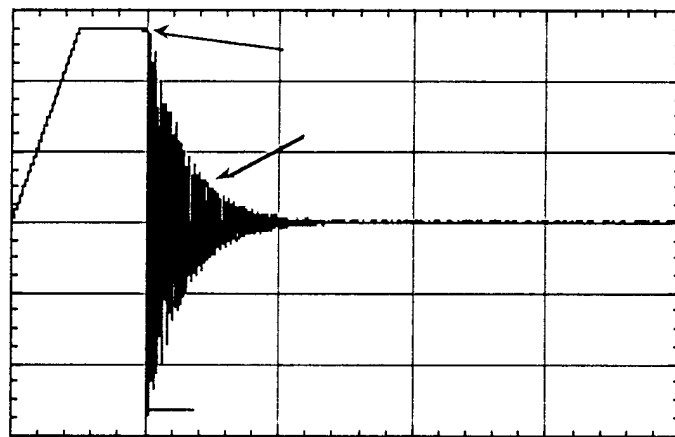


Figure 5. Cantilevered beam under prescribed tip deflection.  
Tip released - Stress on top surface at support. (Point C).

(4) Applications of time-dependent displacements and loads are performed within the same finite element algorithm, and (5) The higher-order beam theory accounts for both transverse shear and transverse normal deformations — the effects that need to be accounted for in thick and highly orthotropic beams, and in high-frequency dynamics.

Example 2, in which a quasi-static enforced deformation is followed by a high frequency free vibration, demonstrates the capability of this finite element formulation to simulate physically important phenomena that is computationally difficult to obtain.

**Acknowledgment:** The authors would like to thank Mr. Michael Dambach, of The George Washington University at the NASA Langley Research Center, for his help in the computational effort.

### References

1. Halpin, J. C., and Pagano, N. J., Observations on linear anisotropic viscoelasticity, *J. Composite Materials*, **2**, No. 1, 68-80 (1968).
2. Hashin, Z., Complex moduli of viscoelastic composites - I. General theory and applications to particulate composites, *Int. J. Solids Structures*, **6**, 539-552 (1970).
3. Hashin, Z., Complex moduli of viscoelastic composites - II. Fiber reinforced materials, *Int. J. Solids and Structures*, **6**, 797-807 (1970).
4. Argyris, J., St. Dolsinis, I., and da Silva, V. D., Constitutive modeling and computation of non-linear viscoelastic solids, Part I. Rheological models and numerical integration techniques, *Comput. Methods Appl. Mech. Engrg.*, **88**, 135-163 (1991).
5. Shaw, S., Warby, M. K., and Whiteman, J. R., Numerical techniques for problems of quasistatic and dynamic viscoelasticity, in "The Mathematics of Finite Elements and Applications," edited by J. R. Whiteman, John Wiley & Sons (1994).
6. Coleman, B. D., and Noll, W., Foundations of linear viscoelasticity, *Reviews of Modern Physics*, **33**, No.2, 239-249 (1961).
7. Schapery, R. A., Viscoelastic behavior and analysis of composite materials, in "Composite Materials", **2**, edited by G. P. Sendeckyj, Academic Press (1974).
8. Johnson, A. R., and Stacer, R. G., Rubber viscoelasticity using the physically constrained system's stretches as internal variables, *Rubber Chemistry and Technology*, **66**, No.4, 567-577 (1993).
9. Johnson, A. R., Tanner, J. A., and Mason, A. J., A kinematically driven anisotropic viscoelastic constitutive model applied to tires, in "Computational Modeling of Tires," compiled by A. K. Noor and J. A. Tanner, NASA Conference Publication 3306, August 1995.
10. Johnson, A. R., Tanner, J. A., and Mason, J. A., A viscoelastic model for tires analyzed with nonlinear shell elements, presented at the Fourteenth Annual Meeting and Conference on Tire Science and Technology, University of Akron, March 1995.
11. Johnson, A. R., and Tessler, A., A viscoelastic higher-order beam finite element, *NASA TM 110260*, June 1996.

12. Tessler, A., A two-node beam element including transverse shear and transverse normal deformations, *Int. J. for Numer. Methods Eng.*, **32**, 1027-1039 (1991).
13. Gibson, R. F., and Plunkett, R., Dynamic mechanical behavior of fiber-reinforced composites: Measurement and analysis, *J. Composite Materials*, **10**, 325-341 (1976).
14. Aklonis, J. J., MacKnight, W. J., and Shen, M., *Introduction to Polymer Viscoelasticity*, John Wiley & Sons, 1972.

# **Compensation for hysteresis using KP integral operators**

W. Steven Galinaitis and Robert C. Rogers

Department of Mathematics, Virginia Tech, Blacksburg, Virginia 24061-0123

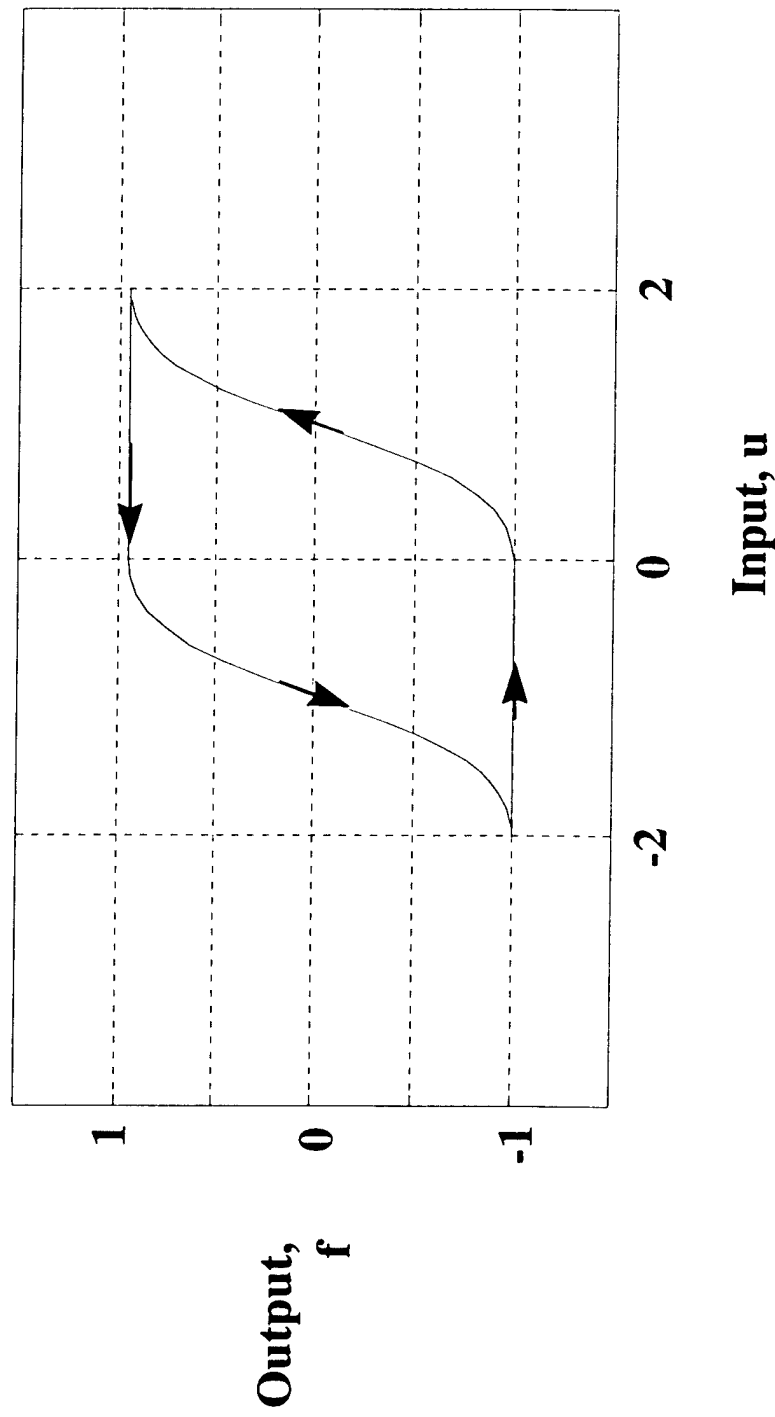
## **Abstract**

The accurate control of a system that exhibits hysteresis requires a control strategy that incorporates some form of compensation for the hysteresis. One approach is to develop a compensator based on the inverse of the hysteresis operator. This form of compensation uses the inverse operator to linearize the hysteresis effect. In this work, a system with hysteresis is modeled by a generalized Krasnoselskii - Pokrovskii integral operator. An approximation of the KP operator and its inverse are presented. The results of a computer simulation are then used to illustrate the properties of the KP operator, the inverse and a compensator based on the inverse.

**Keywords:** Hysteresis, KP intergral operators, inverse operators, compensation.

**Problem definition:** Actuator hysteresis causes positioning error.

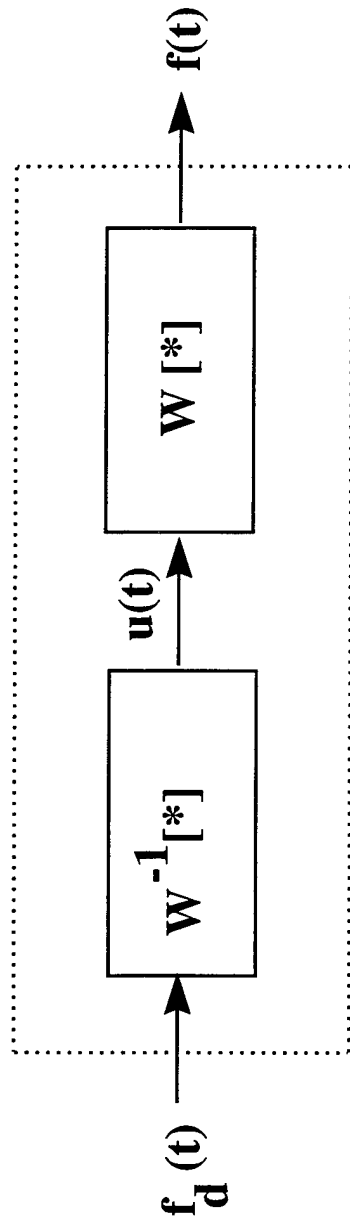
---



W.S. Galinaitis  
R.C. Rogers  
Virginia Tech  
Mathematics Dept.

**Proposed Solution:** Use the inverse operator to linearize the actuator.

---



$$f(t) = W[u](t) = W[W^{-1}[f_d]](t) = f_d(t)$$

W.S. Gallinaitis  
R.C. Rogers  
Virginia Tech  
Mathematics Dept.

# Issues

---

- 1. Modeling the hysteresis**
- 2. Does the model have an inverse?**
- 3. Realtime implementation**
- 4. Parameter estimation**
- 5. Robustness**

W.S. Gallinaitis  
R.C. Rogers  
Virginia Tech  
Mathematics Dept.

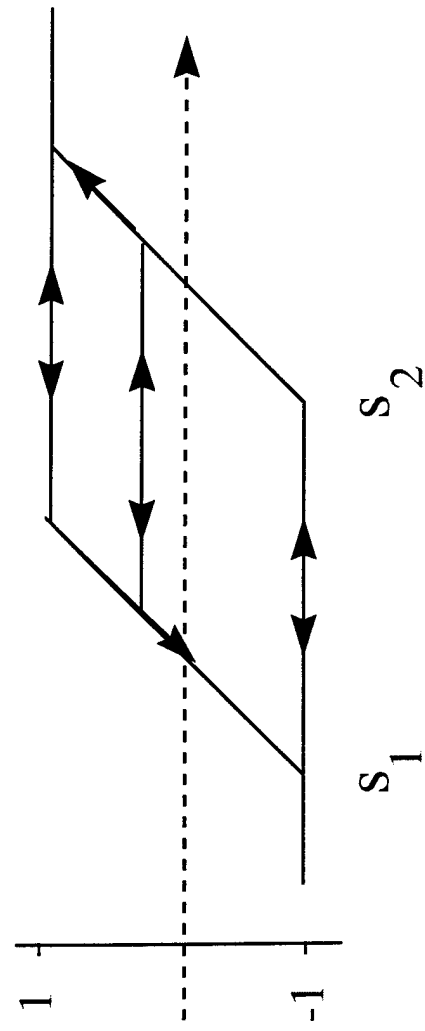
# Krasnoselskii- Pokrovskii integral hysteresis operator

---

$$[W_\mu(u, \gamma)](t) = \int_S [\kappa_s(u, \gamma(s))](\tau) d\mu(s)$$

$$S = \{(s_1, s_2) \in R^2 : s_1 < s_2\}, \text{ Preisach plane}$$

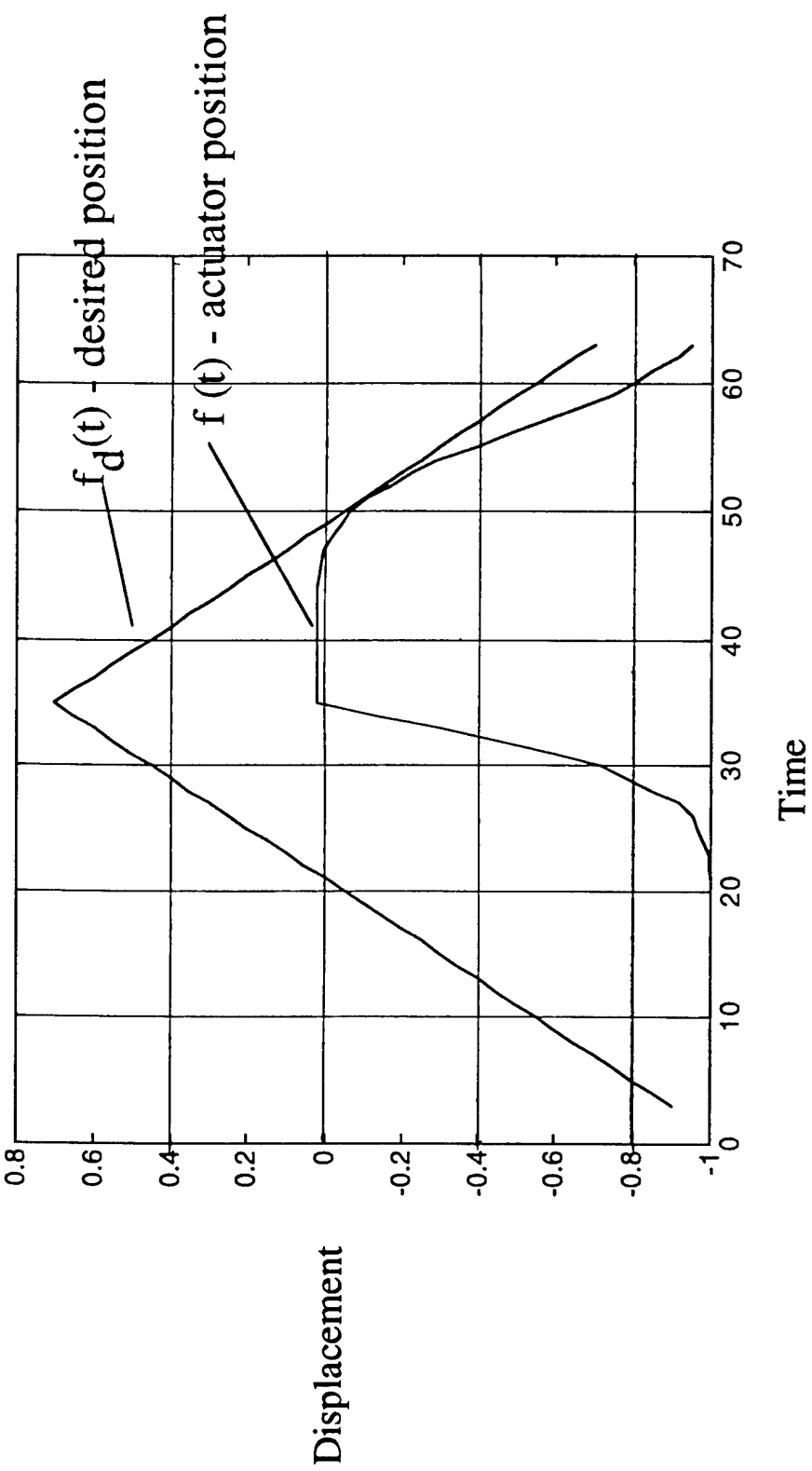
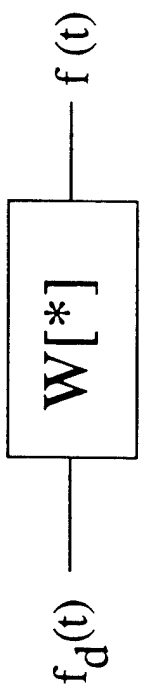
$$[\kappa_s(u, \gamma(s))](\tau), \text{ KP kernel}$$



W.S. Galinaitis  
R.C. Rogers  
Virginia Tech  
Mathematics Dept.

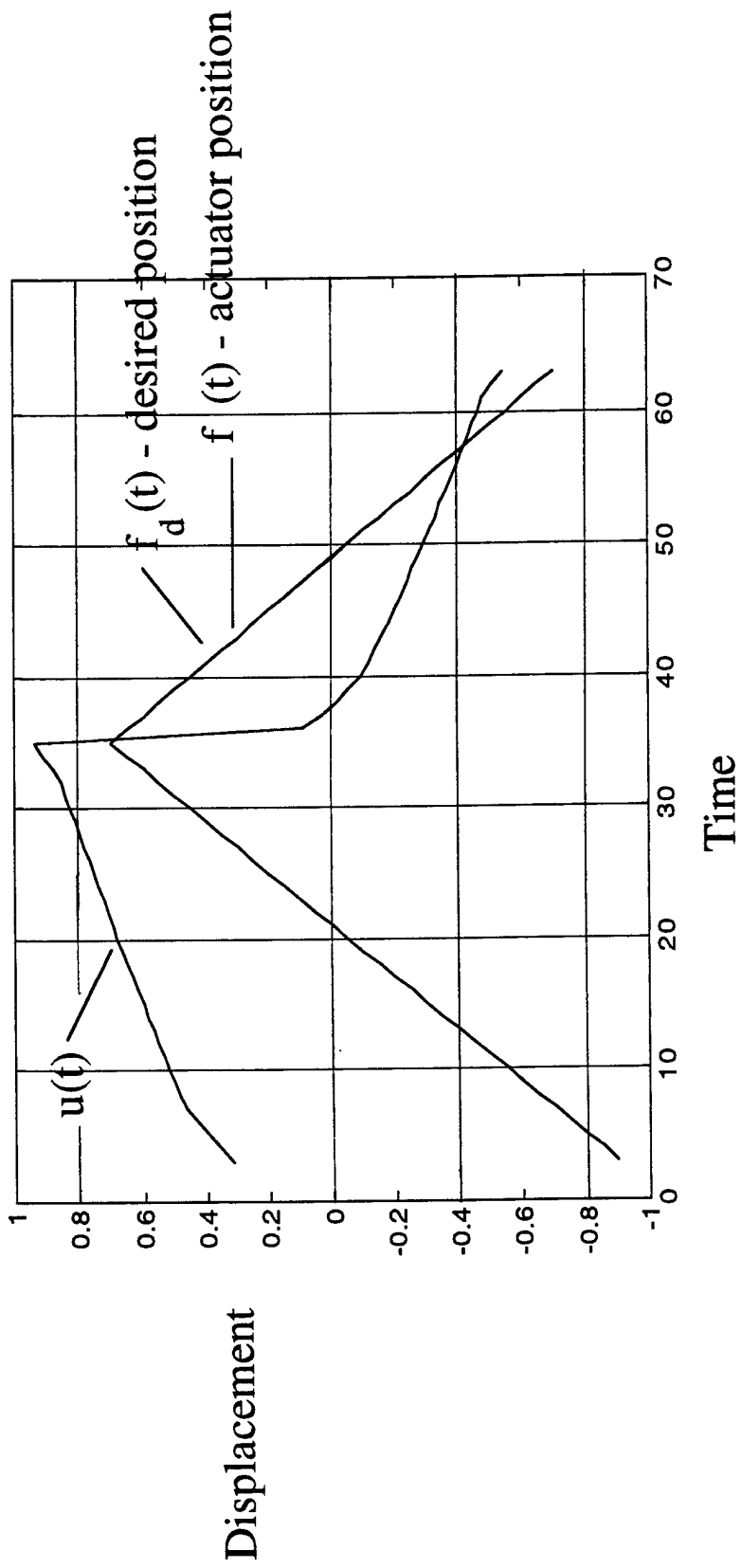
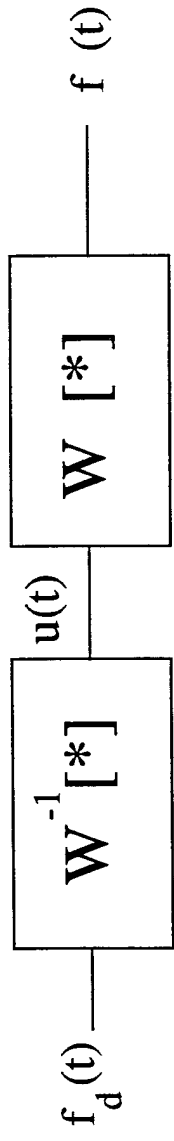
## No Compensation

---



## Compensated Actuator

---



# Micromechanics and Control of Hysteresis in Shape Memory Alloys

D. Lagoudas, Z. Bo

A. Kurdila, G. Webb

Aerospace Engineering Department  
Texas A&M University  
College Station, TX 77843-3141

August 29, 1997

RPI-TAMU ARO URI  
Smart Materials and Structures  
DAAL03-92-G-0123

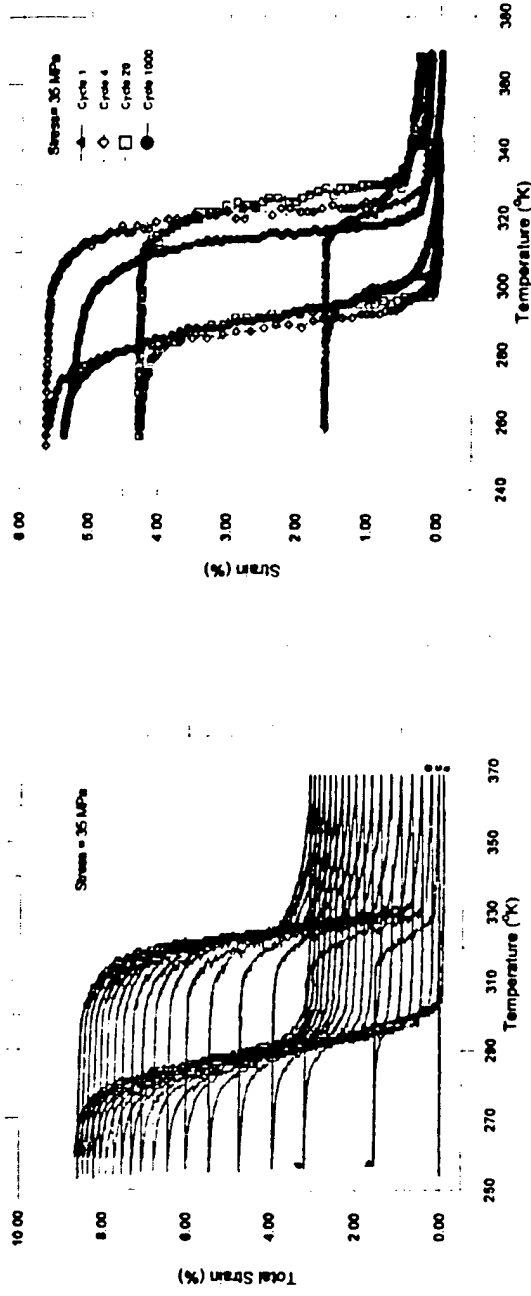


# Experimental Investigation and Constitutive Modeling of Cyclic Loading of SMAs

## Research Objectives

- Investigate experimentally the accumulation of plastic strains, creation of the two way memory effect, and low cycle fatigue during thermally-induced cyclic phase transformations in SMAs
- Develop a constitutive model to predict the evolution of plastic strains and two way memory effect during cycling loading.
- Establish a model to predict minor hysteresis loops under arbitrary loading path and with evolving plastic strains.

# Strain Hysteresis Under Cyclic Loading



## ● Accomplishments

- The experimental results show that the rate of the accumulation of plastic strains is approximately proportional to the magnitude of the applied load.
- In the constitutive modeling of the cyclic loading of SMAs, a methodology similar to that used in viscoplasticity is adopted. As shown in figures, the model prediction agrees well with the experimental results.
- The minor hysteresis loops under arbitrary loading path and with evolving plastic strains can be described using the present constitutive model. Only one additional material constant is introduced to describe the evolving rate of the minor loops with respect to the major loops. The loading history path dependence is similar to that of Preisach model.
- The model prediction agrees well with the experimental data.

## Definitions of Field Variables and Material Constants

$E^P$ : Macroscopic plastic strain;

$E^m$ : Macroscopic transformation strain;

$E^\theta$ : Macroscopic thermal strain;

$\eta^P$ : Drag stress due to elastic interaction between plastic deformation and phase transformation;

$\eta^m$ : Drag stress due to elastic interaction between newly formed martensite region and existing martensite;

$\alpha_{ij}^P$ : Back stress due to elastic interaction between plastic deformation and phase transformation;

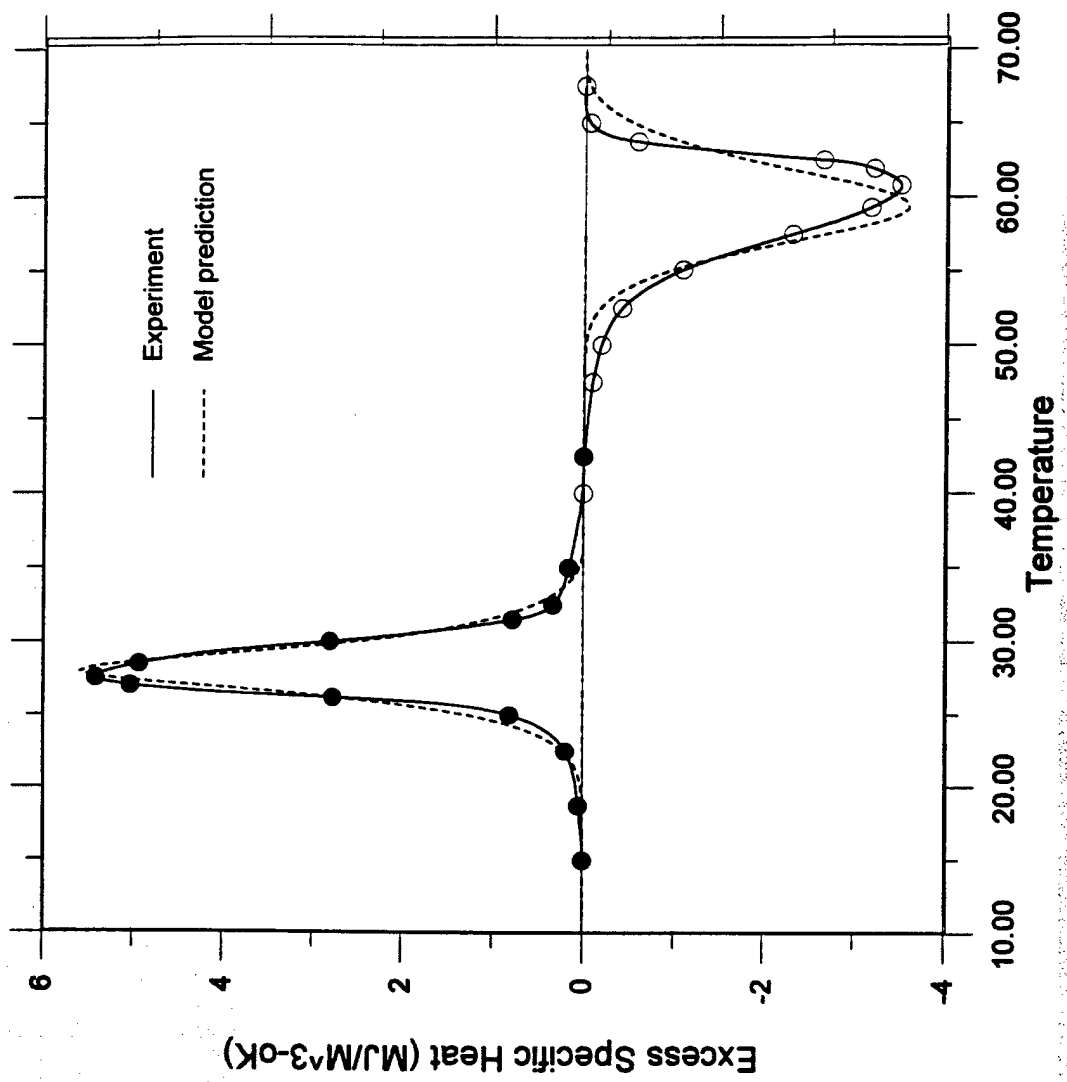
$\alpha_{ij}^m$ : Back stress due to elastic interaction between newly formed martensite region and existing martensite;

$\Delta G_0$ : Difference of Gibbs free energy of reference state between the two phases representing the material initial heterogeneity;

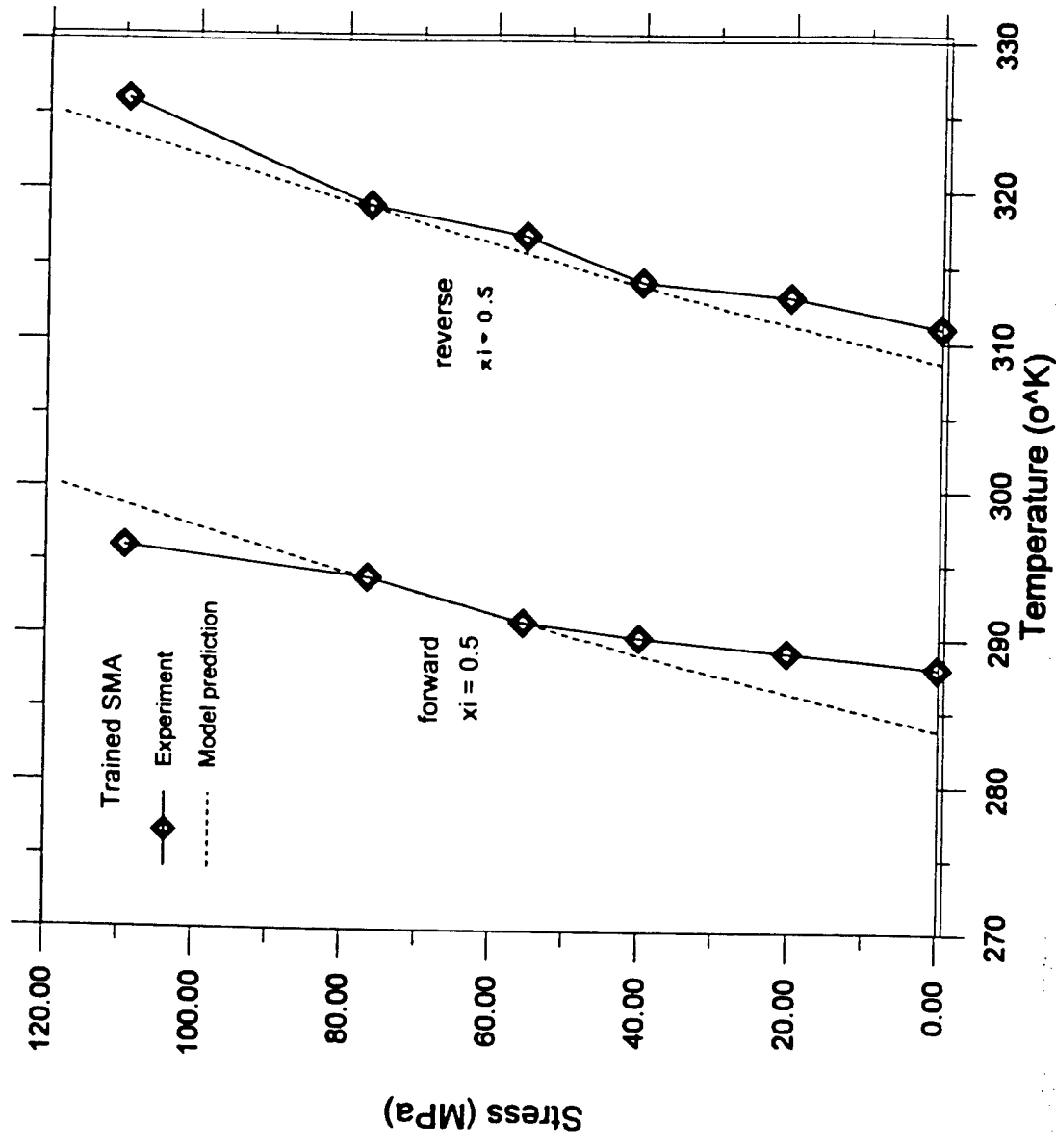
$\Delta c$ : Difference of the specific heat between the two phases

$\Delta s_0$ : Difference of specific entropy between the two phases

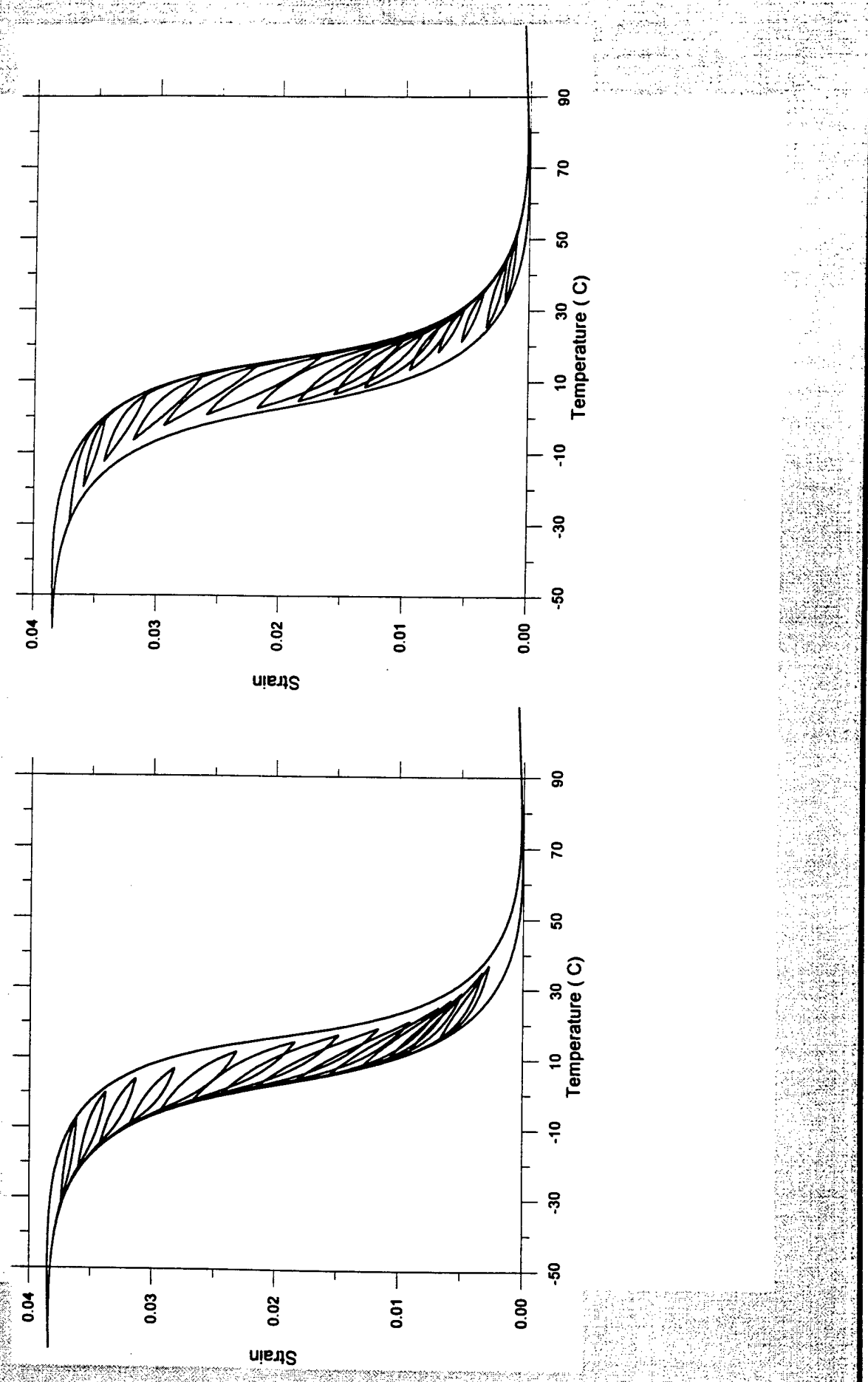
Comparison of the Excess Heat Rate,  $\rho Q^{ex}$ , Between a DSC Measurement and a Theoretical Prediction



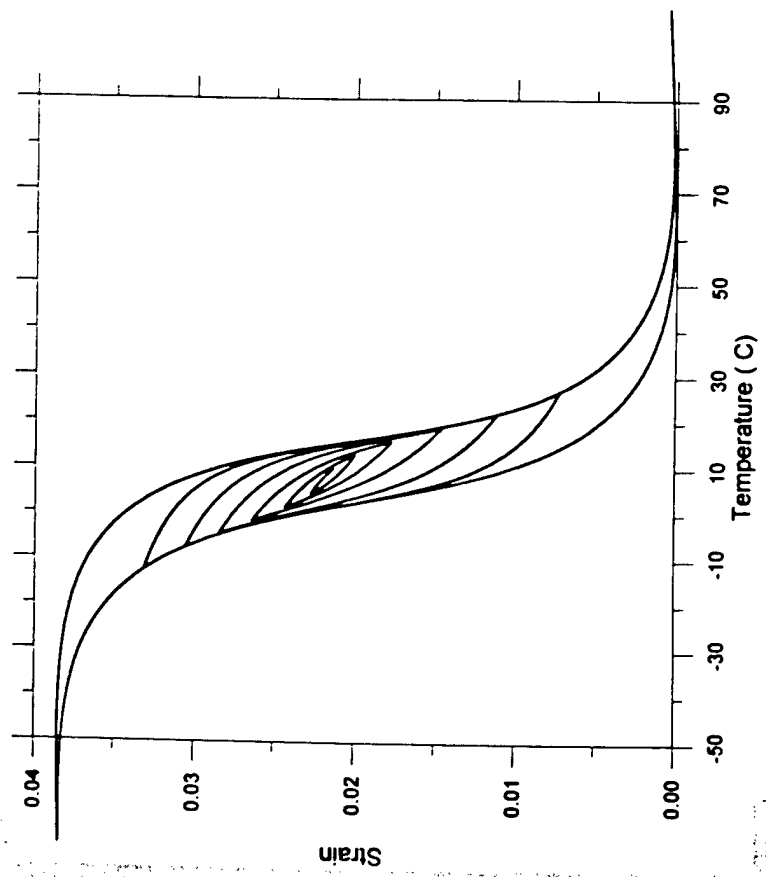
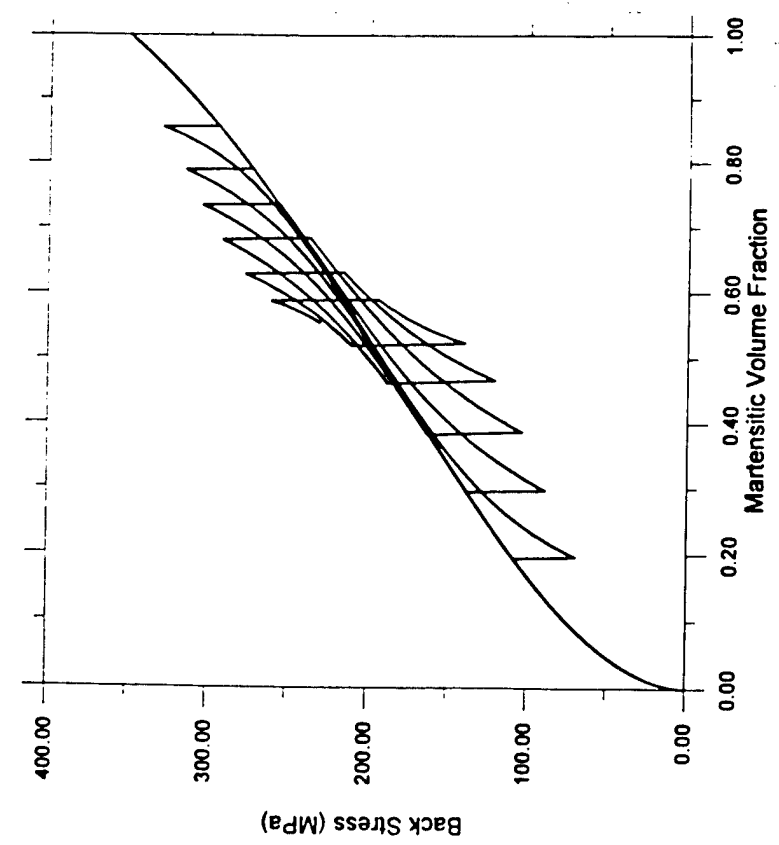
Comparison of Stress-Temperature Diagram predicted by model to experiment data for a trained SMA



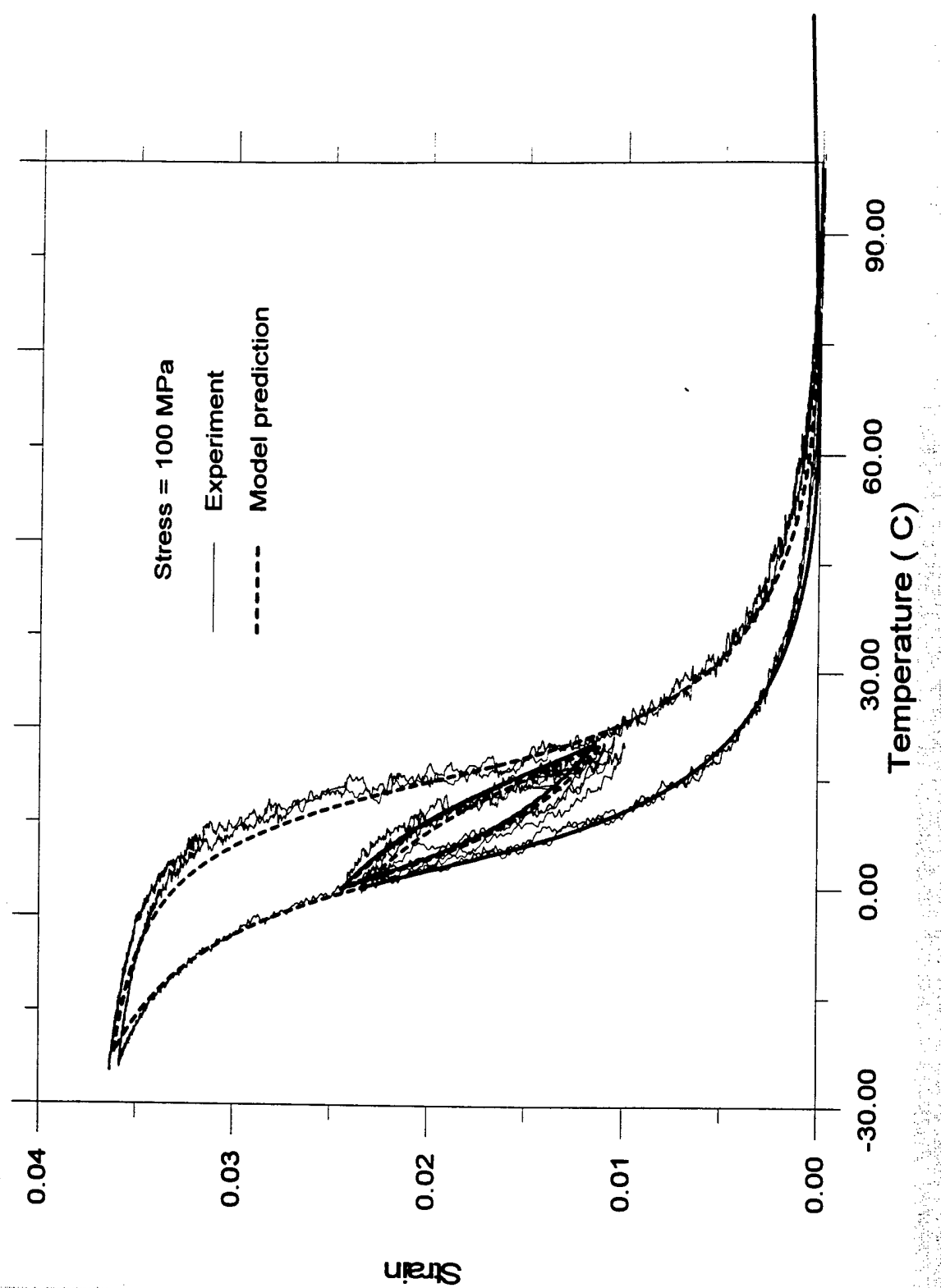
# Minor Hysteresis Loops



# Model Prediction of Minor Hysteresis Loops



# Comparison of Model Prediction With Experimental Data



# Micromechanics and Control of Hysteresis in Shape Memory Alloys

Control Theoretic Background  
Numerous Compensation Strategies

Hughes/Wen 1994, Ge 1996, Bekey/Hadaegh 1983...

## Systematic Framework

Tao/Kokotovic 1996

### Limitations

Low Dimensional

Piecewise Linear

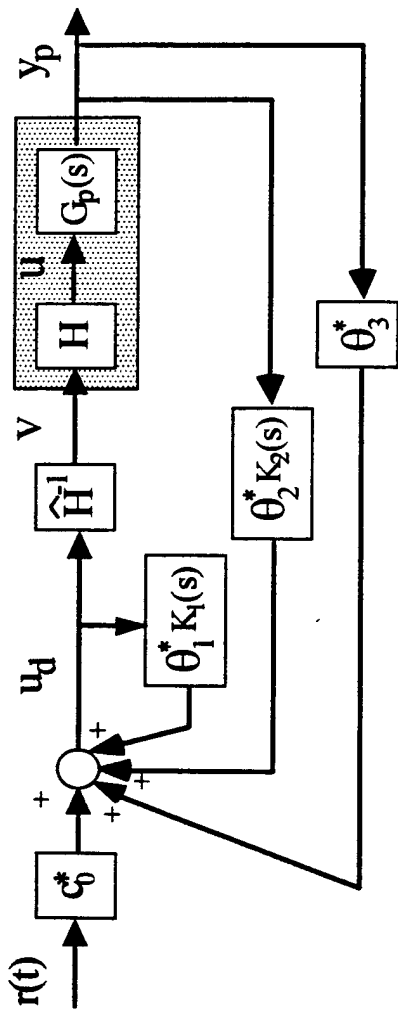
Static Hysteresis Model

## Generalizations

- 1) Banks, Kurdila, Webb, 1996 "Identification of Hysteretic Control Influence Operators: Formulation," JMPE, (CRSC-TR96-14, CRSC-TR96-23)  
OIS  
Offline  
Identification
- 2) Banks, Kurdila, Webb, 1997 "Identification of Hysteretic Control Influence Operators: Convergent Approximations," JIMSS (CRSC-TR97-7)  
Static Hysteresis  
Compensation
- 3) Kurdila and Webb, "Compensation for Classes of Distributed Hysteresis Operators and Representation of Active Structural Systems" AIAA JGCD, Nov. 1997  
Adaptive Hysteresis  
Compensation
- 4) Webb, Kurdila, Lagoudas, Bo, "Identification and Adaptive Control for a Class of Hysteresis Operators," AIAA JGCD, 1997

## Hysteresis Compensation: Fixed and Adaptive

### Fixed Hysteresis Compensation



$$[y_p] = G_p(s)[u_d], \quad [y_m] = W_m(s)[r]$$

$$u_d = K_1(s, \theta_1^*)[u] + K_2(s, \theta_2^*)[y_p] + \theta_3^* y_p + c_0^* r$$

When  $\hat{H} = H$ ,

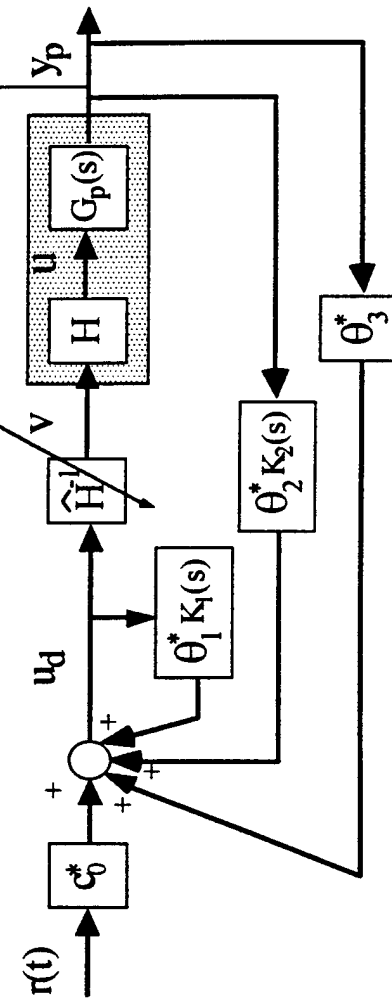
$$u = H(v) = H(\hat{H}^{-1}(u_d)) = H(H^{-1}(u_d)) = u_d$$

When  $\hat{H} \neq H$ ,

$$e_H = u - u_d = H(v) - \hat{H}(v)$$

$$u = u_d + e_H$$

### Adaptive Hysteresis Compensation



If we can express  $H(v)$  as linear in parameters,

$$H(v) = \theta_H^{*T} F(v), \quad \hat{H}(v) = \hat{\theta}_H^T F(v)$$

The adaptive update law for  $\hat{H}(v)$ :

$$\dot{\theta}_H(t) = \frac{\Gamma \xi_H(t) \epsilon_H(t)}{m_H^2(t)} + f_H(t)$$

$$e(t) = [y - y_m](t)$$

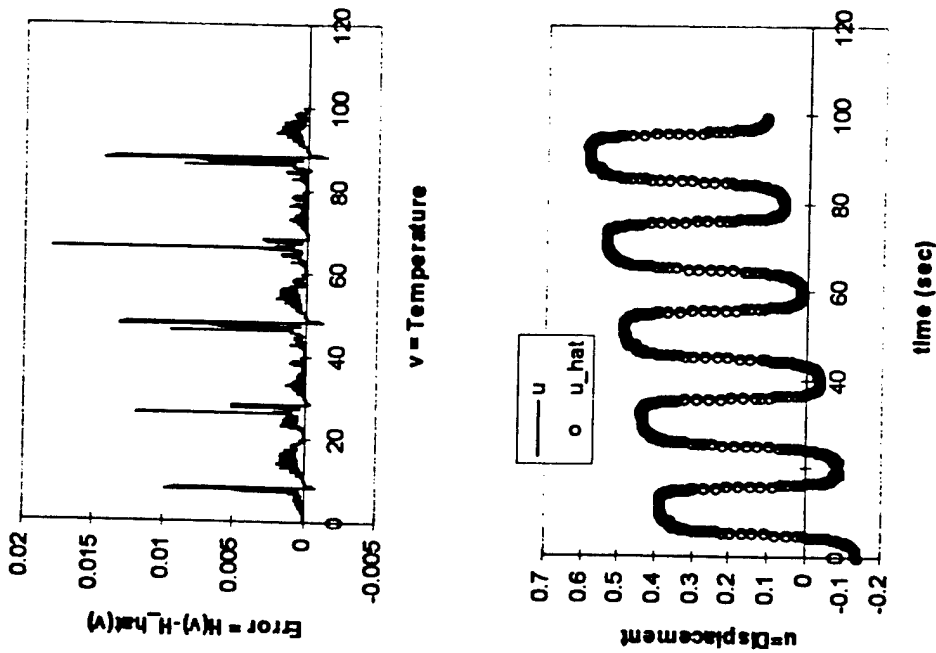
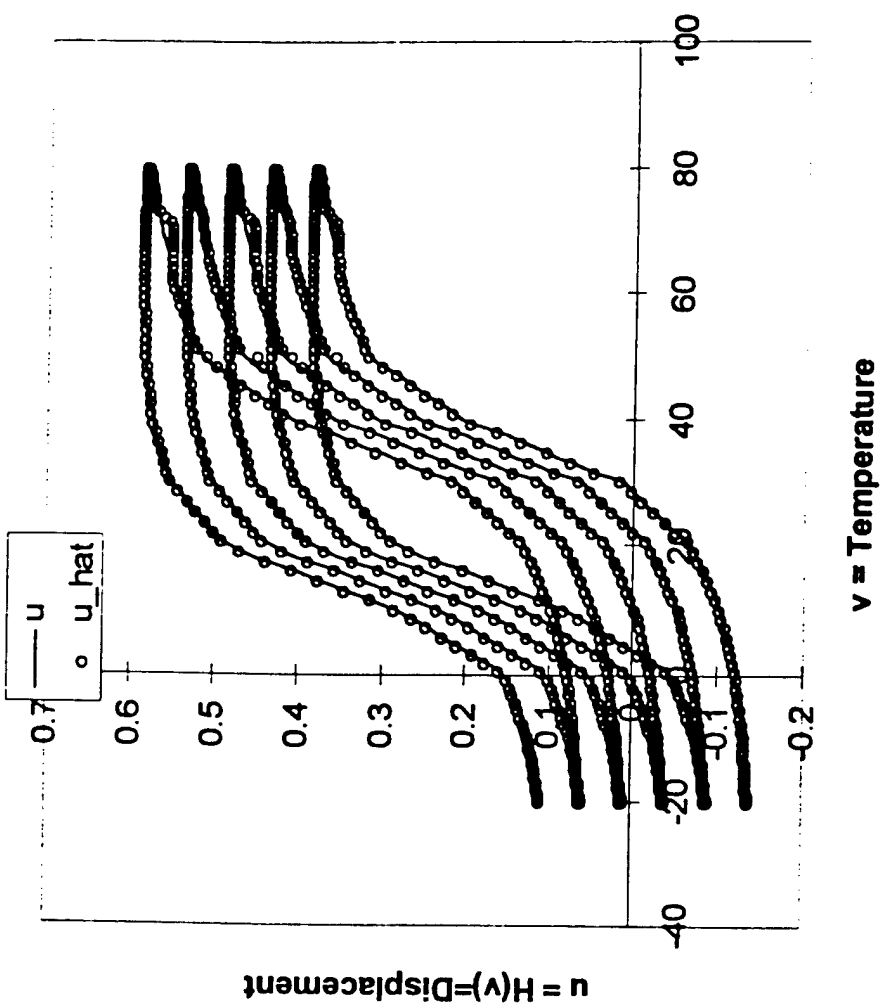
$$\epsilon_H(t) = e(t) + \xi_H(t)$$

$$\xi_H(t) = \theta_H^T(t) \xi_H(t) - W(s)[\theta_H^T F(v)](t)$$

$$\xi_H(t) = W(s)[F(v)](t)$$

$$m_H^2(t) = 1 + [\xi_H^T \xi_H](t) + \xi_H^2(t)$$

# Adaptive Control, No Noise



# Adaptive Hysteresis Compensation: Goals

Define a hysteresis model such that:

- It can be parameterized linearly in coefficients.
- The inverse exists.
- An upper bound for the error between models with different coefficients exists, and

$$e_H(t) = \left\| H - \hat{H} \right\|(t) \rightarrow 0 \text{ as } \hat{\theta}_H \rightarrow \theta_H$$

For known plant parameters

- Adaptive law : Guarantee signal boundedness.
- Model estimate does not match the “true” model
  - Adaptive law should reduce the tracking error
  - Ideally,

$$\hat{\theta}_H \rightarrow \theta_H$$
$$e_H(t) \rightarrow 0$$

# Adaptive Hysteresis Compensation

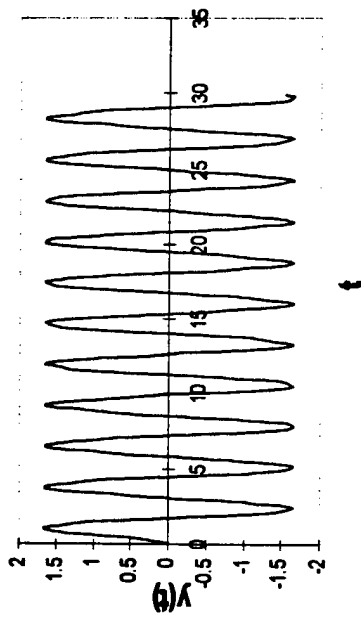
- Upper bound for error  $\delta = \max(\|\gamma_r, \hat{\gamma}_r\|, \|\gamma_s, \hat{\gamma}_s\|)$  where  $\|\gamma_r, \hat{\gamma}_r\| = \max_{i=1,2,\dots,N} |\theta_{r_i} - \hat{\theta}_{r_i}|$
- Let  $\delta > 0$
  - If for some  $v$ ,  $|\hat{\gamma}_s(v) - \hat{\gamma}_r(v)| \leq \delta$  and  $|\gamma_r(v) - \hat{\gamma}_r(v)| \leq \delta$  for all  $v \in R$   
 $(v, \xi^0) \in C^0[0, T] \times R$
  - Then for any  $|k_s(v, \xi) - \hat{k}_s(v, \xi)| \leq 2\delta$
  - Apply to  $H(v, \xi)$ 

$$\begin{aligned} |H - \hat{H}| &= |k_s + m v - \hat{k}_s - \hat{m} v| \\ &\leq |k_s - \hat{k}_s| + |(m - \hat{m})v| \\ &\leq 2\delta + |m - \hat{m}| \max_{v \in V} |v| = \delta^* \end{aligned}$$
  - As  $\hat{\theta}_r \rightarrow \theta_r, \hat{\theta}_s \rightarrow \theta_s$  and  $\hat{m} \rightarrow m$  (i.e.,  $\hat{\theta}_H \rightarrow \theta_H$ )
$$\delta^* = 2\delta + |m - \hat{m}| \max_{v \in V} |v| \rightarrow 0 \Rightarrow e_H \rightarrow 0$$

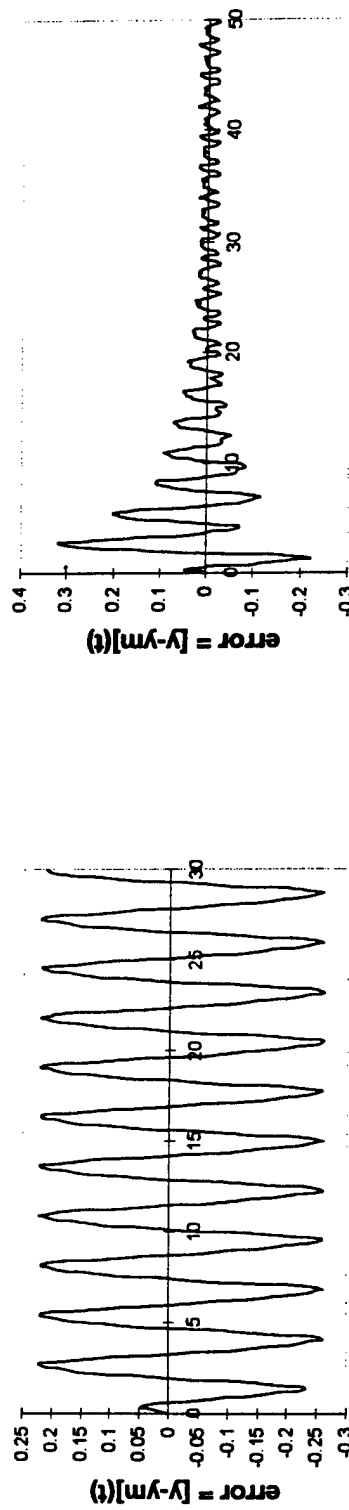
# Adaptive Hysteresis Compensation

## Numerical Example

$\gamma_i(v)$  and  $\gamma_r(v)$  are represented by five nodes



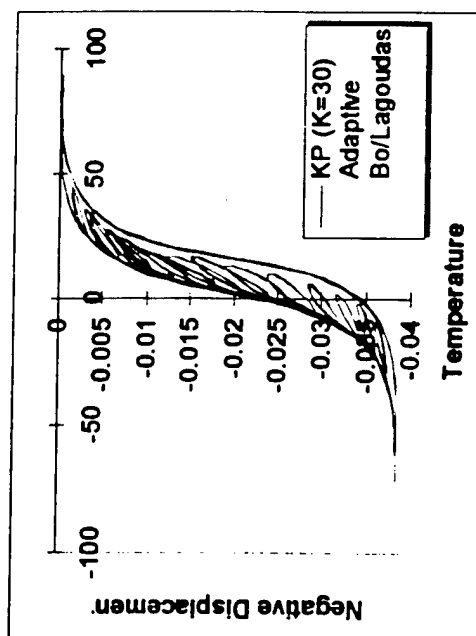
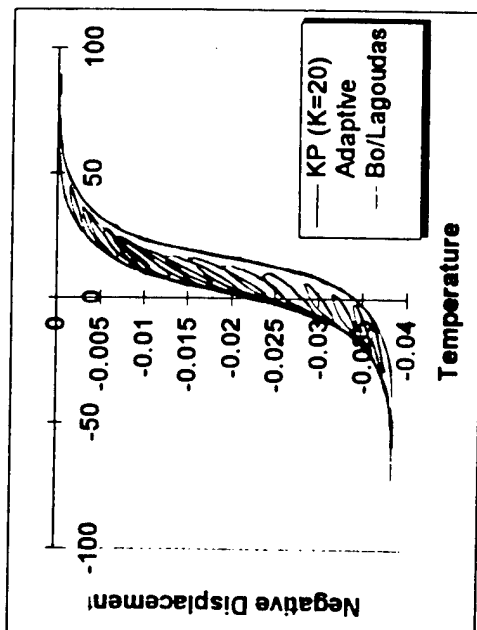
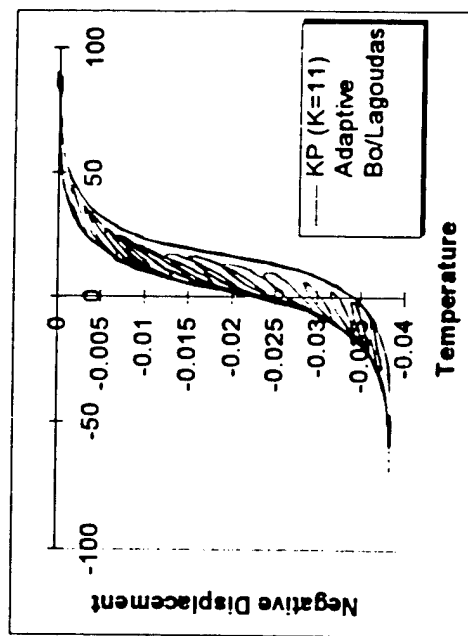
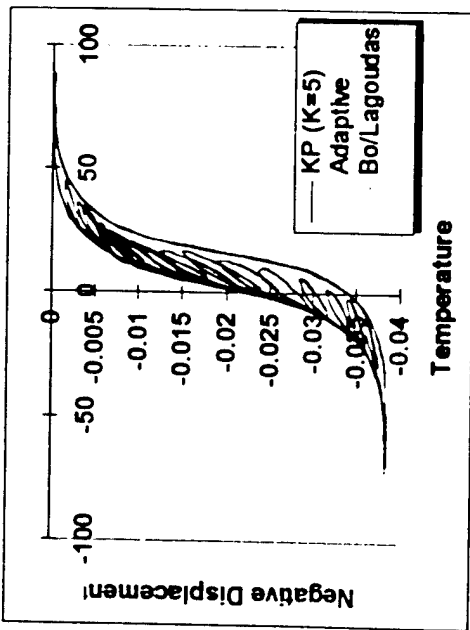
Exact Hysteresis Estimate, Plant Response



Mismatched Hysteresis Estimate,  
Tracking Error

Mismatched Hysteresis Estimate  
with Adaptive Update, Tracking Error

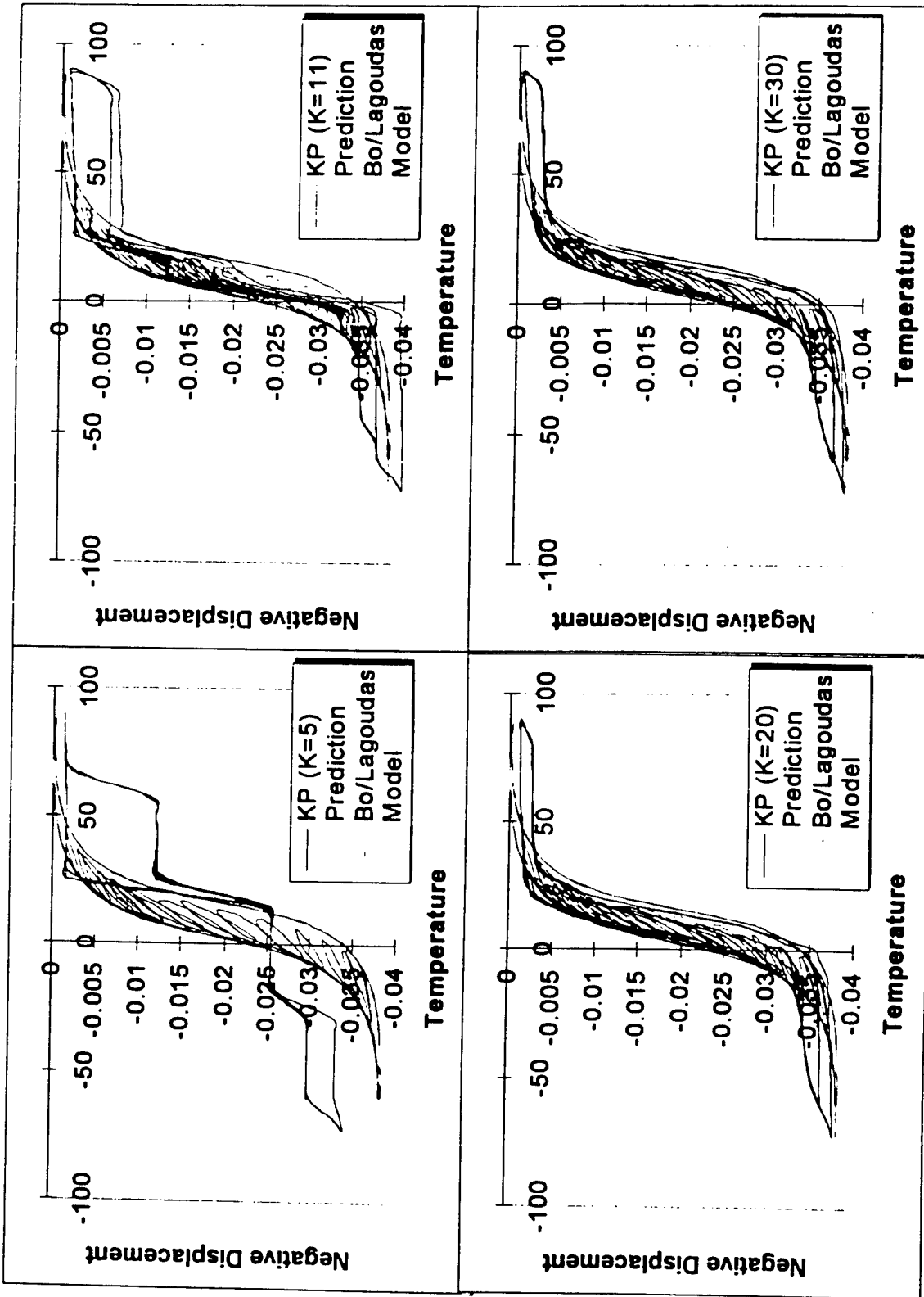
# Adaptive Tracking Results



# Adaptive Tracking Results

- $v = \text{Input Variable} = \text{Temperature}$
- $u = \text{Output Variable} = \text{Displacement}$
- $u = H(v)$
- The adaptive tracking results are displayed for various discretizations of the KP model ( $K=5, 11, 20, 30$ ) in the form of  $u-v$  hysteresis loops. They are plotted against the actual  $u-v$  data from Bo/Lagoudas Model.
- It can be seen that the adaptive tracking for  $K=5$  is almost as good as for  $K=30$ .
- The difference in performance due to discretization number becomes significant in 1D, as will be seen next.

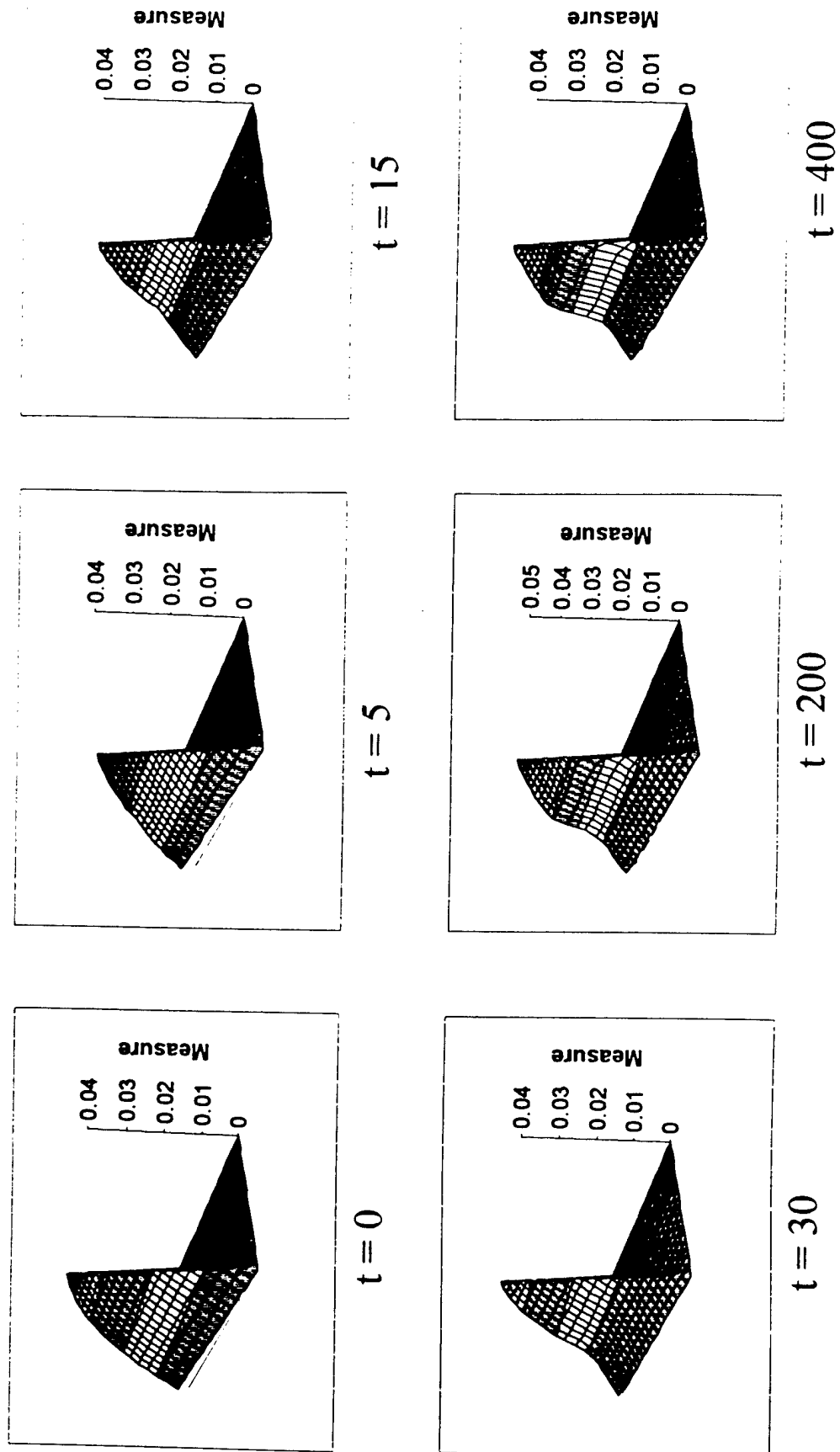
# Predicted Tracking Results



# Identified KP Measures

- First Page of Measure Plots: the ID'd KP measures are shown for discretizations of  $K=5, 11, 20, 30$  taken after 400 seconds of adaptation.
  - The measure surfaces can be seen to converge as  $K$  increases.
- Second Page of Measure Plots: the ID'd KP measures for  $K=20$  is shown to evolve from the initial guess at  $t=0$  seconds to the measure surface at  $t=400$  seconds.

# Time Evolution of K=20 KP Measure ID



# SMA-Induced Deformations of General Unsymmetric Composite Laminates

Marie-Dano and Michael W. Hyer

Department of Engineering Science and Mechanics

Virginia Polytechnic Institute and State University

tel:540-231-5372 fax:540-231-4574 email:hyerm @ vt.edu

By way of background (first attached overhead), it is well known that when cured and cooled to room temperature, an epoxy-matrix unsymmetric laminate can have several equilibrium configurations. Perhaps the most well-known phenomenon in the category of unsymmetric laminates is the behavior of a cross-ply [0<sub>2</sub>/90<sub>2</sub>]<sub>T</sub> laminate. This laminate is, of course, flat at its elevated curing temperature, but when cooled to room temperature the laminate can assume one of two shapes. If when flat the laminate is in the x-y plane of an x-y-z coordinate system, one cured shape is cylindrical with its generator parallel to the x axis. The other cured shape is also cylindrical with a curvature equal in magnitude but opposite in sign to the first cylinder, and with its generator parallel to the y axis, namely perpendicular to the generator of the first cylindrical shape. The laminate can be changed from one cylindrical configuration to another by a simple snap-through action. There is a third configuration, a saddle shape, that is unstable and thus is never observed.

The existence of two equilibrium configurations, or structural shapes, presents interesting opportunities. It is possible to use SMA's to provide the snap-through moments and change from one cylindrical configuration to the other on command. Potential applications (second overhead) include using one or more unsymmetric laminates as portions of the walls of a conduit transporting a fluid. A change in the conduit cross section is possible by changing the wall laminate from one cylindrical configuration to another. This change in wall geometry could change the flow in the conduit on command. Other potential applications (third overhead) could result in an elastic system that exhibits a stiffness that can be changed from a high value to a low value by simply snapping the laminate from one configuration to another. The simplest concept for effecting a configuration change (fourth overhead) is to use SMA wires to provide the snap-through moments. With more general unsymmetric laminates, twist curvature is possible, resulting in an endless variety of structural shapes which can be changed by a snap-through action. In all cases the deformations of the laminate are quite large. Furthermore, because there are multiple equilibrium configurations, the problem is inherently nonlinear and stability is an issue. In particular, because of the large deformations, the nonlinearity is geometric in nature.

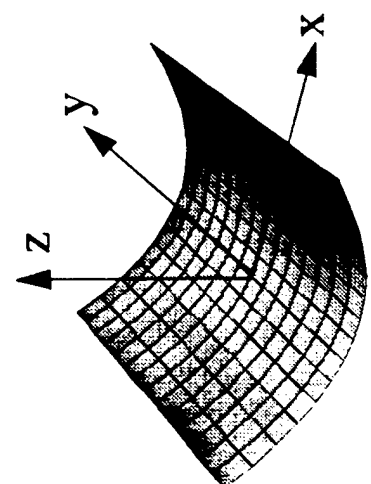
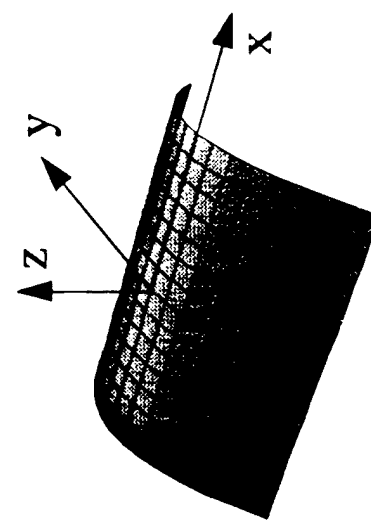
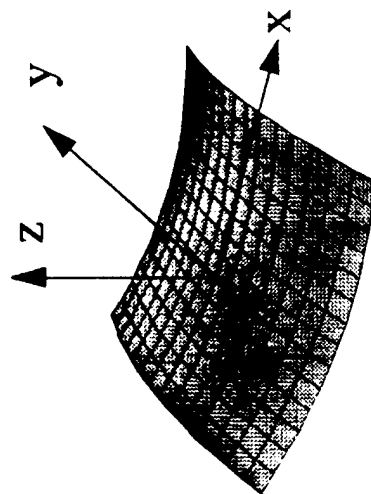
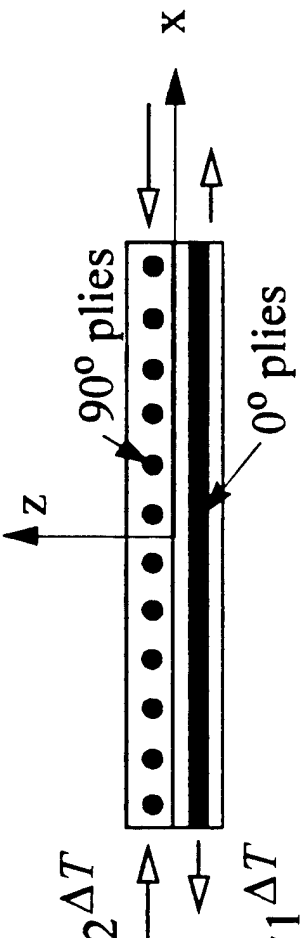
In the current research effort progress has been made on using SMA's, in wire form, as actuators to produce the configuration change. This accomplishment involved achieving a thorough understanding of the complex behavior of unsymmetric laminates. First, a methodology was developed to predict the multiple shapes that result for considering general unsymmetric laminates. The methodology was verified by fabricating a number of laminates and measuring their multiple shapes. The second step was to understand the conditions required to effect the snap through. Force levels and force directions were the primary concern. These results were then used to design the overall requirements for the SMA wire actuators. Thirdly, an acceptable SMA constitutive model was adopted and verified with experiments on simple aluminum plates. The predictions of SMA wire temperature vs. strains in the aluminum plate were very close to the experimental results, and thus the SMA model was applied to the unsymmetric laminate problem.

The results of using SMA actuators with unsymmetric laminates have been successful. The theory developed to predict the response of the laminates, particularly snap-through conditions, to the forces of SMA wire actuators correlates quite well with measurements (fifth overhead). In particular, strains vs. actuator temperature and snap-through temperature correlate well, and the results are repeatable.

## Background

Shapes of a  $[0_2/90]_T$  unsymmetric laminate

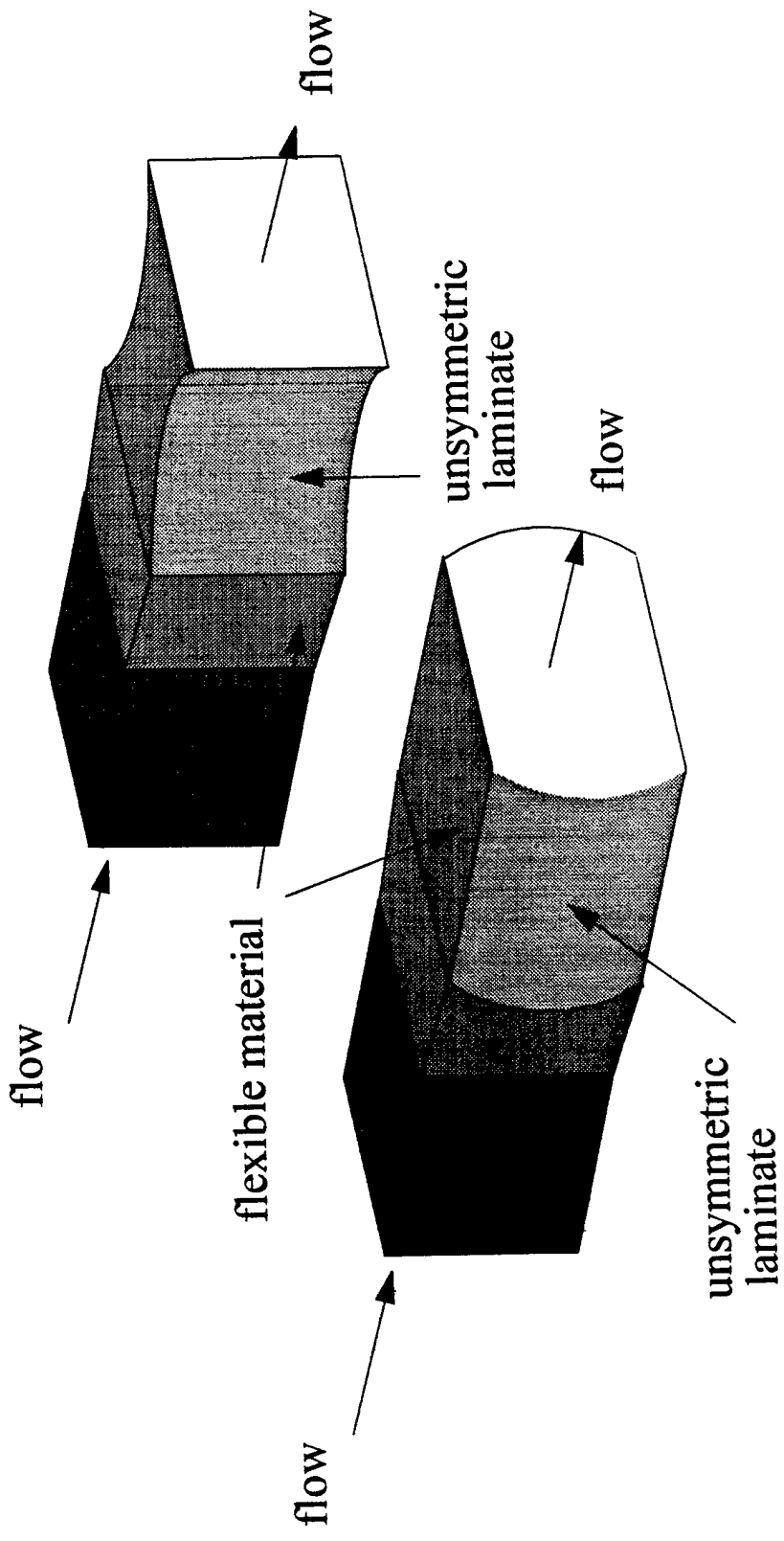
$$\Delta T < 0 \rightarrow \begin{aligned} \varepsilon_x &= \alpha_2 \Delta T \\ \varepsilon_x &= \alpha_1 \Delta T \end{aligned}$$



## Possible application

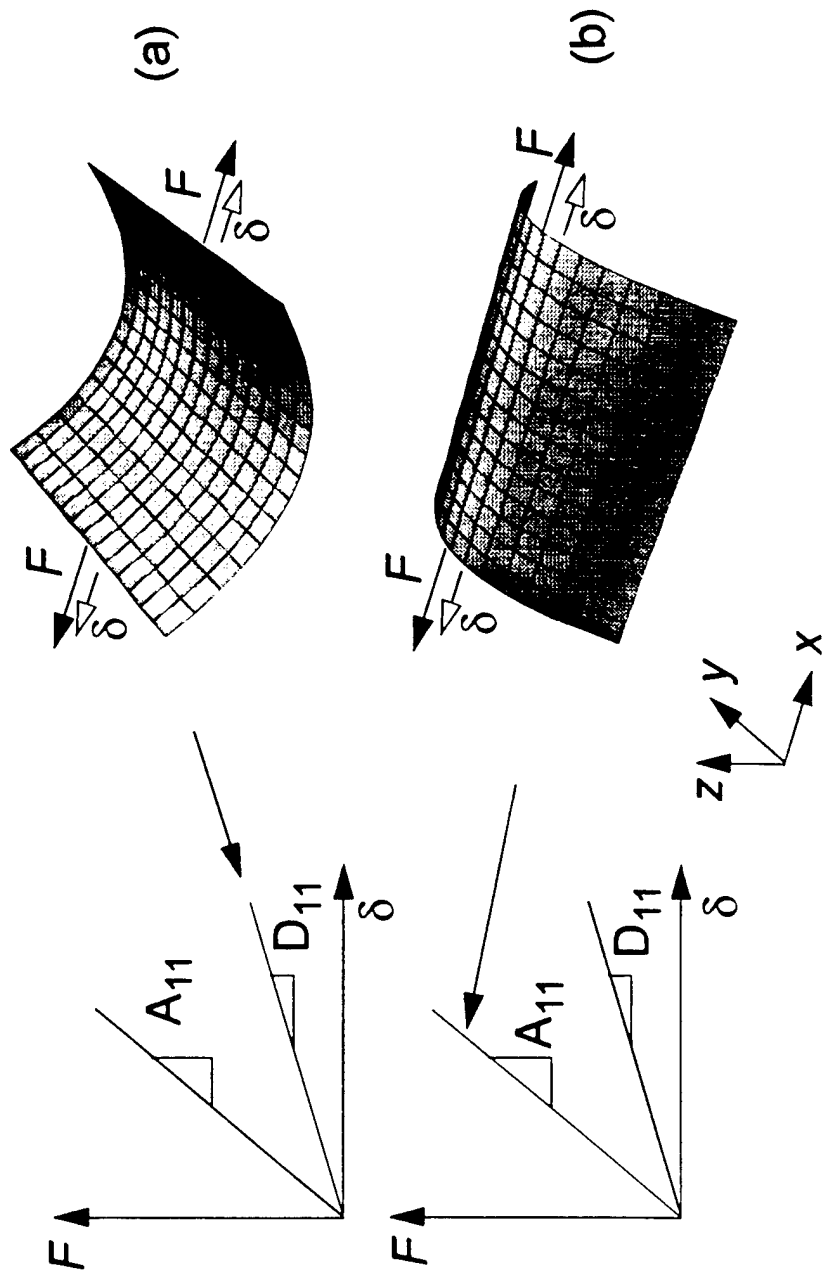
---

Use one or more unsymmetric laminates as portions of a variable-geometry conduit to transport fluid:

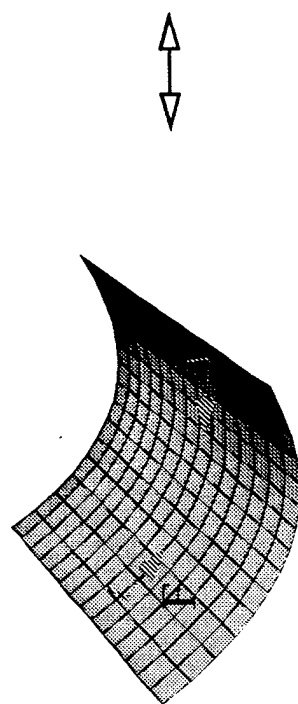
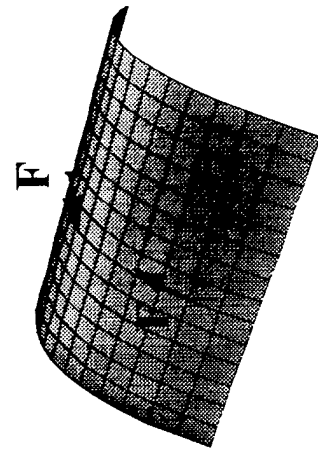
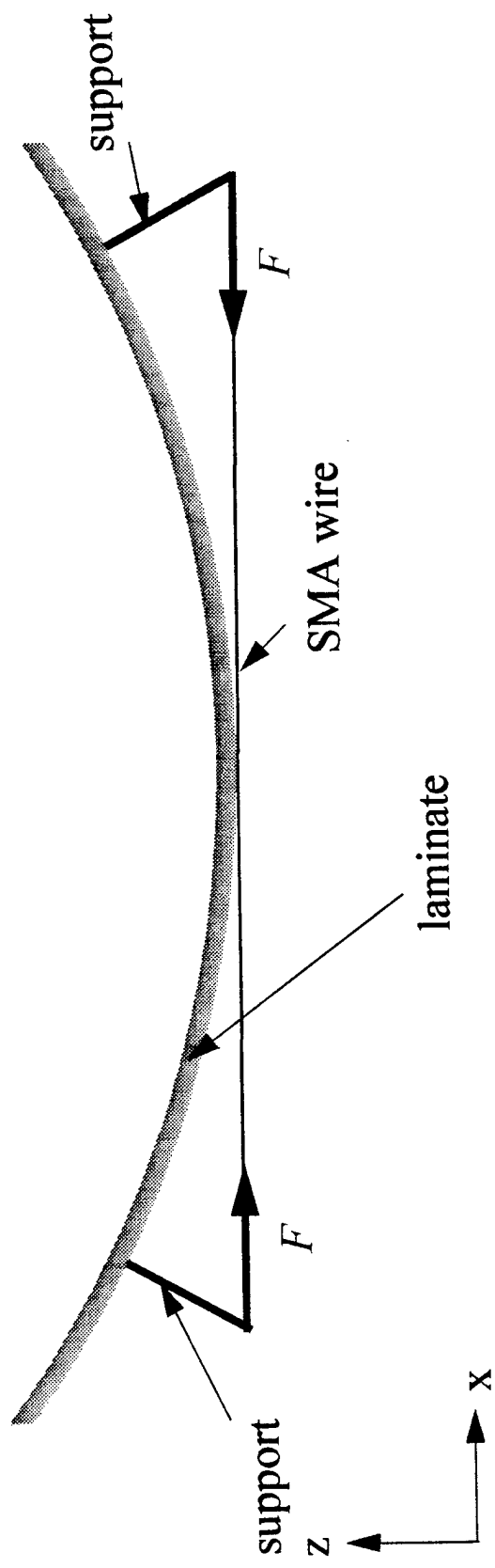


## Possible application (cont')

The combination of SMA-actuators used with unsymmetric laminates could result in a system that exhibit two highly contrasting stiffness:

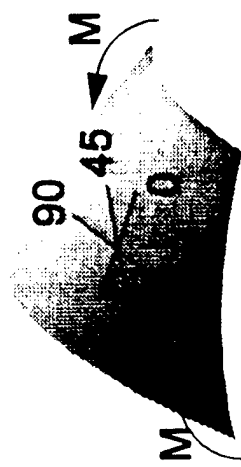
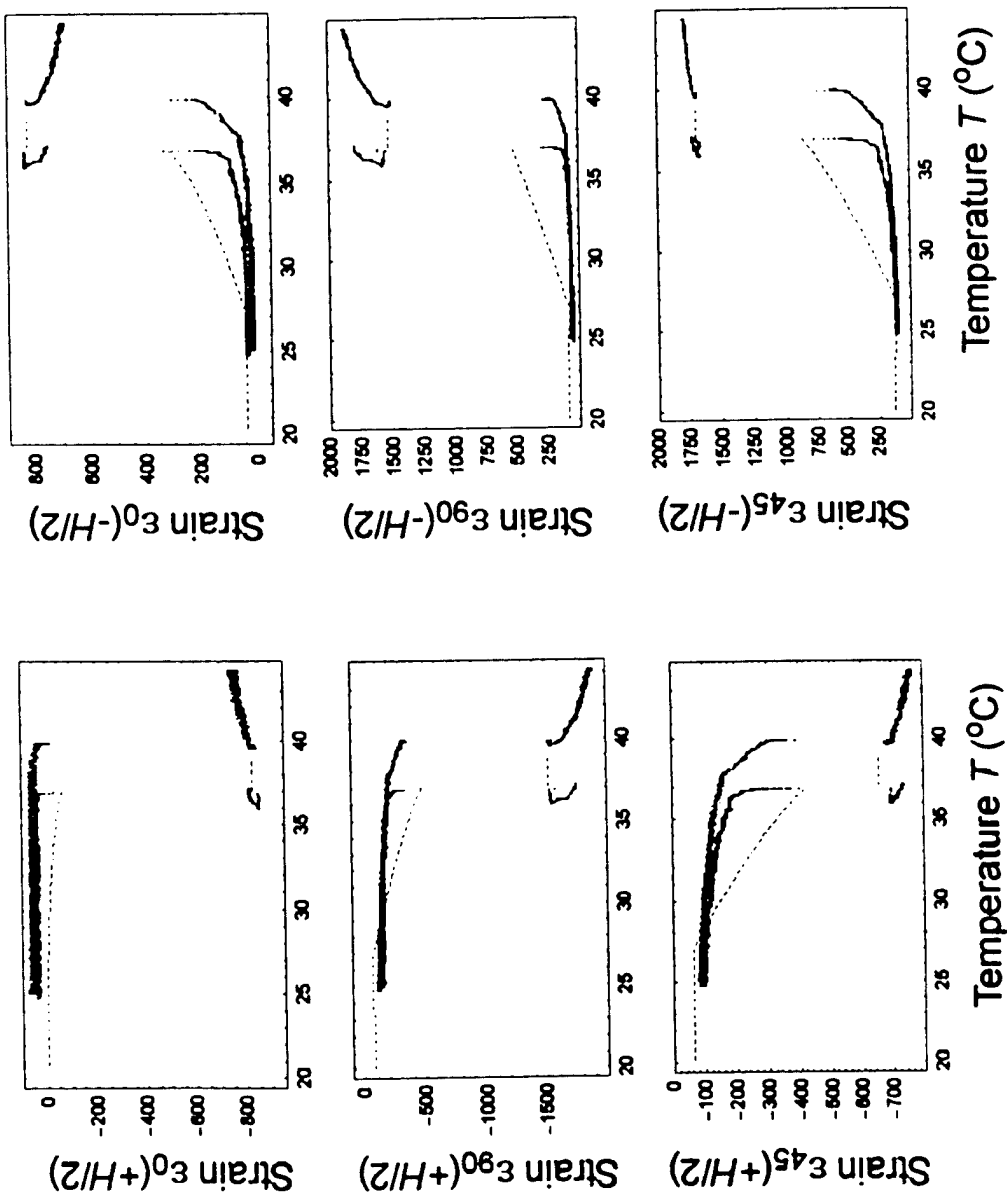


## Concept



# $[ -30_4 / 30_4 ]_T$ laminate

..... Theory  $A_{so}=25$  °C  
 — First experiment  
 — Second experiment



# **Comparative Evaluation of Shape Memory Alloy Constitutive Models with Test Data**

Jeanette J. Epps and Inderjit Chopra

Alfred Gessow Rotorcraft Center, Department of Aerospace Engineering  
University of Maryland, College Park, Maryland 20742  
Office Phone: (301)405-1142, Fax: (301)314-9001  
email: jeanette@eng.umd.edu

## **Abstract**

Shape memory alloys are being recognized as a revolutionary material to develop smart actuators for numerous aerospace, civil structures, marine, and medical applications since it is able to undergo large deformations and then recover its original shape upon heat activation. One potential application of SMA is a trailing edge tab adjustment for in-flight tracking of a helicopter rotor that is being pursued in this paper. One drawback is the lack of a reliable database for material properties of SMA. Another drawback is the unavailability of an accurate constitutive model for SMA. In this study, a comparative evaluation of several SMA constitutive models with test data was undertaken.

Various constitutive models were developed by researchers to characterize the thermo-mechanical behavior of SMA materials. These models are based on thermo-mechanics, or a combination of thermomechanics and SMA phenomenology, and/or statistical mechanics. Four constitutive models were compared and validated with experimental results. The four models were developed by Tanaka, Liang and Rogers, Boyd and Lagoudas, and Brinson.

To predict the thermo-mechanical properties of SMA, it was necessary to carry out careful testing of the SMA wire to determine the coefficients for the four constitutive models. Careful specimen testing is necessary since there is no reliable database available for the properties of SMA materials and the thermo-mechanical properties of the shape memory alloys depend on many variables, such as wire manufacturing, wire diameter, pre-strain, stress level, temperature, and whether or not the material has been cycled. Using the data obtained from testing the necessary coefficients for the four constitutive models were measured. Coefficients such as the Young's modulus for the martensite and austenite phase and the four phase transformation temperatures were determined.

All models showed good correlation with experimental stress-strain curves, however the model developed by Brinson showed the best correlation with all test data. None of the models, however, were able to predict the unloading curve accurately for most of the stress-strain curves in the austenite phase. It was noted that stress-strain curves at martensitic temperatures could not be calculated using the models developed by Tanaka, Liang and Rogers and Boyd and Lagoudas. It was theorized that this was due to the inability of these models to distinguish between temperature-induced and stress-induced martensite volume fraction.

Measured and calculated recovery stress-temperature characteristics were also compared. All models showed difficulty in predicting this behavior. Experimental results showed that the recovery stress becomes nearly constant after transformation whereas all predicted results showed an increase.

The present study will be used in the investigation of in-flight tracking of helicopter rotor blades. A rigid composite wing model of 8 inch chord, 16 inch span and NACA 0012 airfoil section will be built. The flap actuation will be achieved using SMA wires. The actuation system consists of two or more, pre-strained SMA wires mechanically constrained at the quarter chord spar, and hinged to a flap at the other end. A control feedback scheme will be developed to fine tune the flap. The wing section will then be tested in an open-jet tunnel and the performance of the flap under SMA actuation will be examined. The results will be used to validate predictions.

## Objective of Current Research

- *To conduct a comparative evaluation of several constitutive models for shape memory alloys based on correlation with test data.*
- *To investigate a trailing-edge tab actuated using SMA wire actuators for in-flight tracking of helicopter rotor blades.*

## Shape Memory Effect

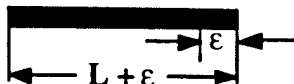
1. High Temperature
- Phase change - *austenite phase*
  - SMA wire of length L



2. Room Temperature
- Undefomed wire
  - Phase change - *martensite phase*



3. Room Temperature
- *Plastically deformed* wire
  - Remains in the martensite phase

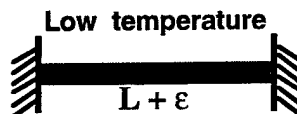


4. High Temperature
- Phase change - *austenite phase*
  - Recovery of deformation
  - undefomed wire of length L

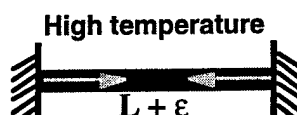


## Constrained Recovery

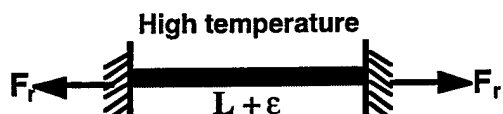
I. Initially the material is mechanically constrained at both ends and the material has a pre-strain,  $\epsilon$ .



II. When the material is heated a phase change takes place and the wire will try to recover  $\epsilon$  due to the shape memory effect.

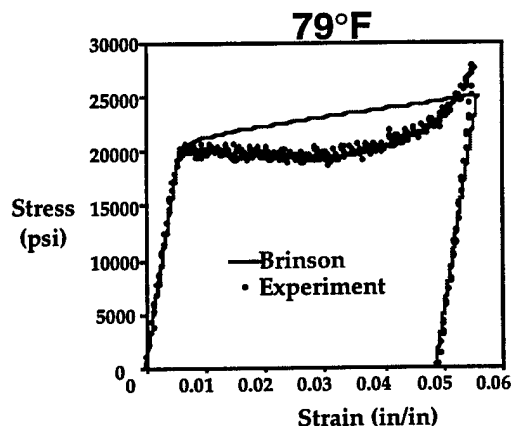


III. However a tensile force develops instead due to the mechanical constraints



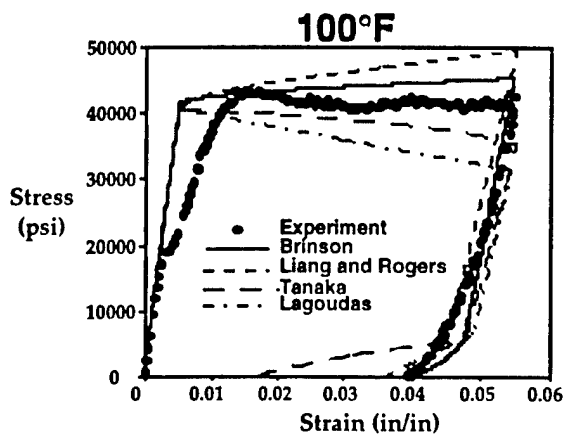
## Experimental-Theoretical Stress-Strain-Temperature Curves

- 100% Martensite Initially
- Only results from the Brinson model shown.
- Stress-strain curves at  $T < M_s$  could not be calculated using the models due to the inability of the models to distinguish between temperature- and stress-induced martensite.
- Good correlation between experiment and model

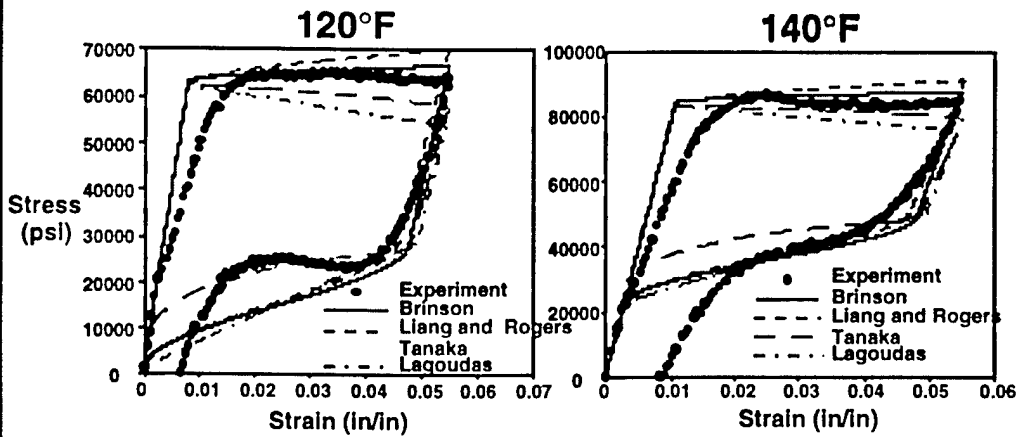


## Experimental-Theoretical Stress-Strain-Temperature Curves

- At this temperature the material resides in a mixed phase- difficult to predict.
- All models shown.
- Good correlation between experiment and models.
- Overall, the Brinson model showed the best correlation, however correlation for the other models improve for higher temperatures.



## Experimental-Theoretical Stress-Strain-Temperature Curves (con't)

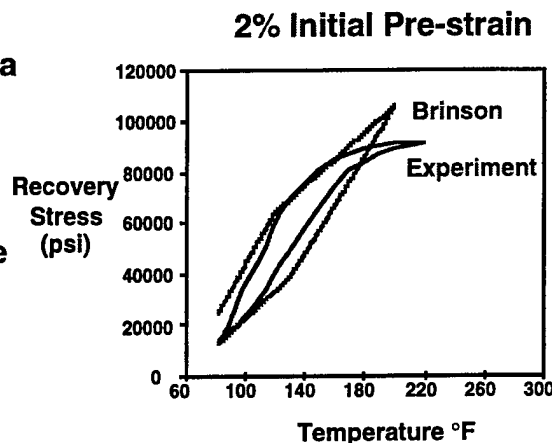


## Experimental-Theoretical Recovery Stress-Temperature Curves

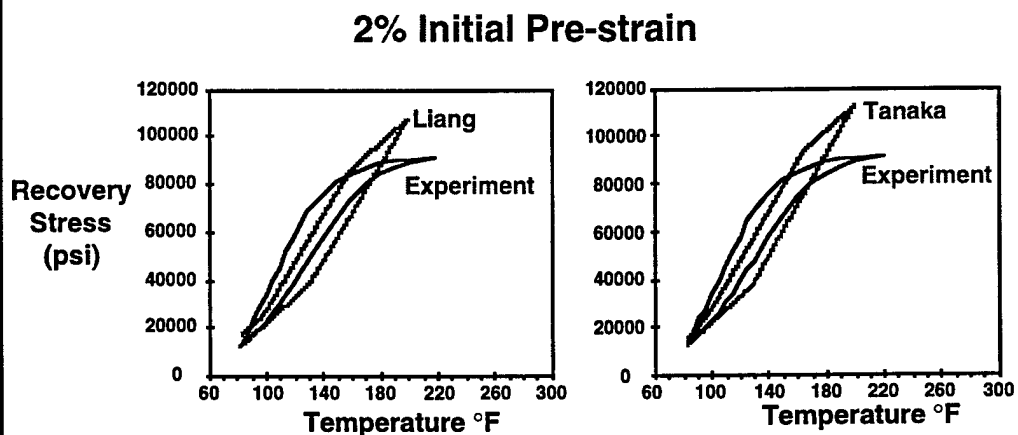
- The recovery stress-temperature characteristics are needed in the design of a tab actuator.

- All models showed difficulty in predicting the recovery stress-temperature characteristics.

- Further work will involve improvements in the prediction of the recovery stress.

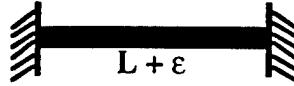


## Experimental-Theoretical Recovery Stress-Temperature Curves (con't)

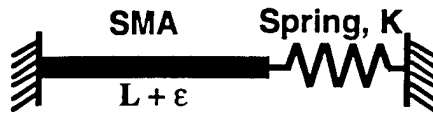


## Application of Shape Memory Alloys: Actuation of Trailing-Edge Tab for In-Flight Blade Tracking

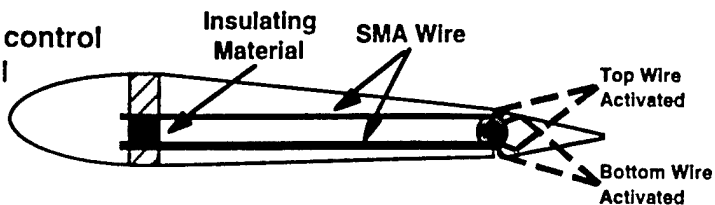
- Modeling of SMA actuation of a trailing edge tab is similar to constrained recovery except the amount of recovery is controlled.



- This can be modeled as a spring in series with a pre-strained SMA wire.



- To fine tune a tab, a control feedback scheme will be developed.



## Conclusions

- The Brinson model showed good correlation for SMA wire in the martensite phase ( $T < M_s$ ).
- Stress-strain curves at  $T < M_s$  could not be calculated for the Tanaka, Liang and Rogers and Boyd and Lagoudas models. This could be due to the inability of the models to distinguish between temperature- and stress-induced martensite.
- Good correlation between experiment and models for  $T > M_s$ .
- Overall, the Brinson model showed the best correlation, however correlation for the other models improve for higher temperatures.
- All models showed difficulty in predicting the recovery stress-temperature characteristics.

## Viscoelastic Effects in the Dynamics of Thick Beams

A. R. Johnson<sup>1</sup> and A. Tessler

Computational Structures Branch

NASA Langley Research Center, MS240

Hampton, VA 23681-0001

### Summary

A viscoelastic higher-order thick beam finite element formulation is extended to include elastodynamic deformations. The material constitutive law is a special differential form of the Maxwell solid. In the constitutive model, the elastic strains and the conjugate viscous strains are coupled through a system of first-order ordinary differential equations. The total time-dependent stress is the superposition of its elastic and viscous components. The elastodynamic equations of motion are derived from the virtual work principle. Computational examples are carried out for a thick orthotropic cantilevered beam. A quasi-static relaxation problem is employed as a validation test for the elastodynamic algorithm. The elastodynamic code is demonstrated by analyzing the damped vibrations of the beam which is deformed and then released to freely vibrate.

### Introduction

The combination of highly viscous low-modulus materials with the traditional high-modulus materials produces stiff, highly damped load carrying structures. The quasi-static and dynamic analyses of such structures require improvements in the material damping representation over the velocity proportional damping schemes. Halpin and Pagano<sup>1</sup> demonstrated that the relaxation moduli for anisotropic solids produce symmetric matrices that can be expanded in a Prony series form (i.e., a series of exponentially decaying terms). Early viscoelastic models for small deformations of composites focused on computing the complex moduli for anisotropic solids from the elastic properties of the fibers and the complex modulus properties of the matrix.<sup>2,3</sup> Recently, various classical constitutive models have been used including generalized Maxwell and Kelvin-Voigt solids.<sup>4,5</sup> These constitutive models have practical value since they provide adequate approximations for the dynamic softening and hysteresis effects – the phenomena that are not directly proportional to strain rates.

Coleman and Noll<sup>6</sup> and Schapery<sup>7</sup> presented comprehensive discussions on the history integral form of the Maxwell solid. Johnson and Stacer<sup>8</sup> developed a differential form of the Maxwell solid constitutive law for large strain viscoelastic deformations of rubber. The formulation required additional viscous strain

---

<sup>1</sup> Vehicle Technology Center, Army Research Laboratory.

variables that are conjugate to the elastic strains. The same constitutive law was used by Johnson et al.<sup>9,10</sup> to formulate a viscoelastic, large-displacement shell finite element. In the work of Johnson and Tessler,<sup>11</sup> the differential constitutive law was implemented within Tessler's<sup>12</sup> higher-order beam theory, giving rise to a quasi-static viscoelastic thick beam finite element formulation. They presented several quasi-static numerical solutions demonstrating the relaxation, creep, and cyclic creep response of thick beams. They demonstrated that only minor modifications to an elastic finite element code are needed to produce a computationally efficient viscoelastic code.

In this paper, the quasi-static viscoelastic formulation of Johnson and Tessler<sup>11</sup> is extended to elastodynamics. The mass matrix for the higher-order beam is derived and a modified Newmark algorithm is employed to integrate the equations of motion. The modified Newmark algorithm contains an implicit trapezoidal integration scheme which enables accurate integration of the first-order differential equations for the viscous strains.

### Viscoelastic Higher-Order Beam

In this section, an internal variable formulation for a Maxwell solid higher-order beam theory<sup>11</sup> is outlined. The beam dimensions and sign convention are shown in Figure 1. The differential form of the viscoelastic constitutive model for the beam is written in matrix form as

$$\mathbf{s}(t) = \mathbf{C}\mathbf{e} + {}^*\mathbf{C}\sum_{n=1}^N {}_n\dot{\mathbf{e}}(t) \quad (1)$$

$${}^*_n\dot{\mathbf{e}} + {}_n\dot{\mathbf{e}}/\tau_n = \dot{\mathbf{e}} \quad \text{for each } n \quad (2)$$

where  $\mathbf{s}^T = (\sigma_{xx}, \sigma_{zz}, \tau_{xz})$ ,  $\mathbf{e}^T = (\varepsilon_{xx}, \varepsilon_{zz}, \gamma_{xz})$ ,  ${}_n\dot{\mathbf{e}}^T = ({}^*_n\varepsilon_{xx}, {}^*_n\varepsilon_{zz}, {}^*_n\gamma_{xz})$

$$\mathbf{C} = \begin{bmatrix} C_{11} & C_{13} & 0 \\ C_{13} & C_{33} & 0 \\ 0 & 0 & C_{55} \end{bmatrix} \quad \text{and} \quad {}^*\mathbf{C} = \begin{bmatrix} {}^*C_{11} & {}^*C_{13} & 0 \\ {}^*C_{13} & {}^*C_{33} & 0 \\ 0 & 0 & {}^*C_{55} \end{bmatrix}$$

The vectors  $\mathbf{s}$  and  $\mathbf{e}$  are the engineering stresses and strains (geometrically nonlinear strain-displacement relations can be used for  $\mathbf{e}$ , see Ref. 9 for a nonlinear quasistatic model.) The vectors  ${}_n\dot{\mathbf{e}}$  ( $n = 1, 2, \dots, N$ ) are the internal variables, i.e., conjugate viscous strains, where  $N$  is the number of terms in a Prony series representation of the material's stress relaxation response. The matrices  $\mathbf{C}$  and  ${}^*\mathbf{C}$  contain the elastic and viscous stiffness coefficients. In the higher-order beam

theory,<sup>12</sup> the components of the displacement vector are approximated through the beam thickness by way of five kinematic variables, i.e.,

$$u_x(x, z, t) = u(x, t) + h\zeta\theta(x, t) \quad (3)$$

$$u_z(x, z, t) = w(x, t) + \zeta w_1(x, t) + \left(\zeta^2 - \frac{1}{5}\right)w_2(x, t) \quad (4)$$

where  $\zeta = z/h$  denotes a nondimensional thickness coordinate and  $2h$  is the total thickness. The function  $u(x, t)$  represents the midplane (i.e. reference plane) axial displacement,  $\theta(x, t)$  is the bending rotation of the cross-section of the beam,  $w(x, t)$  is the weighted-average deflection, and  $w_1(x, t)$  and  $w_2(x, t)$  are the higher-order transverse displacement variables enabling a parabolic distribution of  $u_z(x, z, t)$  through the thickness.

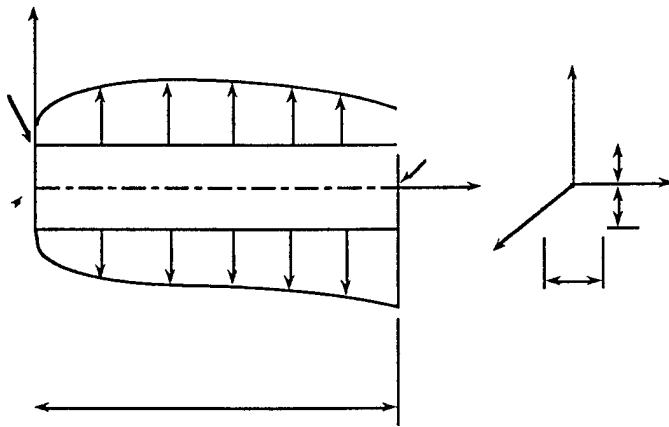


Figure 1. Thick-beam geometry, kinematics, and loading.

The above displacement assumptions give rise to the following thickness distributions for the strains: a linear axial strain, a cubic transverse normal strain, and a quadratic transverse shear strain. These strain components have the following form

$$\varepsilon_{xx} = u(x, t)_x + h\zeta\theta(x, t)_x \quad (5)$$

$$\varepsilon_{zz} = \frac{w_1(x, t)}{h} + \phi_z(\zeta) \frac{w_2(x, t)}{h^2} + \phi_x(\zeta) \theta(x, t)_x \quad (6)$$

$$\gamma_{xz} = \phi_{xz}(\zeta) (w(x, t)_x + \theta(x, t)) \quad (7)$$

where  $\phi_x(\zeta) = h\nu_{13}\zeta(4 - 7\zeta^2)/17$ ,  $\phi_z(\zeta) = 14\zeta h(3 - \zeta^2)/17$ ,  $\phi_{xz}(\zeta) = 5(1 - \zeta^2)/4$ ,

and  $\nu_{13}$  is Poisson's ratio. The simplest finite element approximation of this beam theory involves a three-node configuration (see Figure 2) which is achieved by the following interpolations

$$\begin{aligned} u(\eta, t) &= (1 - \eta)u_0^\ell(t) + \eta u_1^\ell(t), \quad \theta(\eta, t) = (1 - \eta)\theta_0^\ell(t) + \eta\theta_1^\ell(t), \\ w(\eta, t) &= (1 - \eta)w_0^\ell(t) + \eta w_1^\ell(t) - \frac{\ell}{2}\eta(1 - \eta)(\theta_0^\ell(t) - \theta_1^\ell(t)), \\ w_1(\eta, t) &= W_1^\ell(t), \quad w_2(\eta, t) = W_2^\ell(t) \end{aligned} \quad (8)$$

where  $\eta = x/\ell$  is the nondimensional axial coordinate. The nodal degrees-of-freedom at the two ends of the element are subscripted with indices 0 and 1. Since the strains do not possess derivatives of the  $w_1(\eta, t)$  and  $w_2(\eta, t)$  variables, these variables need not be continuous at the element nodes and, hence, their simplest approximation is constant for each element. Their corresponding degrees-of-freedom are attributed to a node at the element midspan.

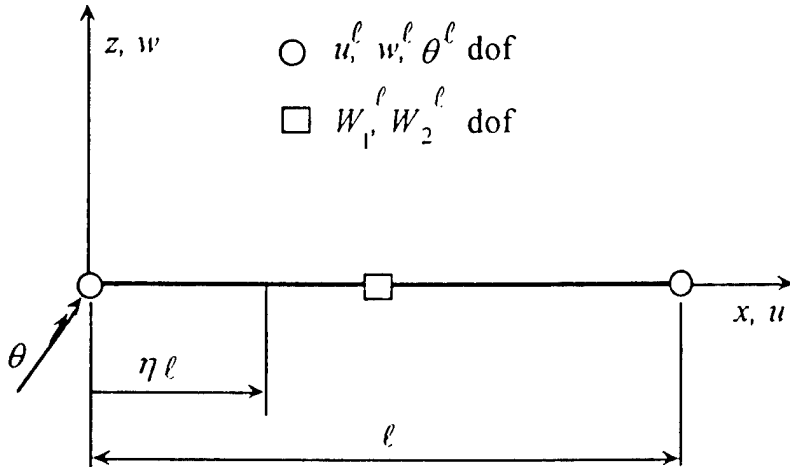


Figure 2. A three-node, higher-order theory thick-beam element.

For dynamic loading, the virtual work statement for an element of volume  $V$  with the differential Maxwell constitutive law can be written as

$$\int \rho (\ddot{u}_x \delta u_x + \ddot{u}_z \delta u_z) dV + \int \mathbf{e}^T \mathbf{C} \delta \mathbf{e} dV + \sum_{n=1}^N \int_n^* \mathbf{e}^T \mathbf{C} \delta_n^* \mathbf{e} dV - \delta W = 0 \quad (9)$$

where the first integral represents the virtual work done by inertial forces, the second is the internal virtual work done by the elastic stresses, the third is the internal virtual work done by the viscous stresses, and  $\delta W$  is the virtual work done by the external forces. Introducing (8) into (3)-(4) and substituting the

results into (5)-(7) yields finite element approximations of the strains in terms of the nodal variables, i.e.,

$$\mathbf{e} = \mathbf{B}\mathbf{u}, \quad (10)$$

$$\mathbf{B} = \begin{bmatrix} -\frac{1}{\ell} & 0 & -\frac{z}{\ell} & 0 & 0 & \frac{1}{\ell} & 0 & \frac{z}{\ell} \\ 0 & 0 & -\frac{\phi_x}{\ell} & \frac{1}{h} & \frac{\phi_z}{h^2} & 0 & 0 & \frac{\phi_x}{\ell} \\ 0 & -\frac{\phi_{xz}}{\ell} & \frac{\phi_{xz}}{2} & 0 & 0 & 0 & \frac{\phi_{xz}}{\ell} & \frac{\phi_{xz}}{2} \end{bmatrix} \quad (11)$$

and  $\mathbf{u}^T = (u_0, w_0, \theta_0, W_1, W_2, u_1, w_1, \theta_1)^T$  denotes the element nodal displacement vector. Next, a set of analogous nodal variables,  ${}^*\mathbf{u}$ , and corresponding viscous strains,  ${}^*\mathbf{e}$ , are introduced. These are related by

$${}^*\mathbf{e} = \mathbf{B} {}^*\mathbf{u} \quad (12)$$

The  ${}^*\mathbf{u}$  variables, which carry the time dependent information for the material within the element, are independent from element to element. The displacements  $u_x$  and  $u_z$  are then expressed in terms of the element nodal degrees-of-freedom using (3), (4) and (8), giving rise to  $u_x = \Phi_x^T \mathbf{u}$  and  $u_z = \Phi_z^T \mathbf{u}$ , where  $\Phi_x(\zeta, \eta)$  and  $\Phi_z(\zeta, \eta)$  are vectors of the interpolation functions. The virtual work statement for an element then becomes

$$\begin{aligned} \ddot{\mathbf{W}} \int \rho (\Phi_x \Phi_x^T + \Phi_z \Phi_z^T) dV \delta \mathbf{u} + \mathbf{u}^T \int \mathbf{B}^T \mathbf{C} \mathbf{B} dV \delta \mathbf{u} \\ + \sum_{n=1}^N {}^*\mathbf{u}^T \int \mathbf{B}^T {}^*\mathbf{C} \mathbf{B} dV \delta {}^*\mathbf{u} - \delta W = 0 \end{aligned} \quad (13)$$

By defining the integrals in (13) as the mass,  $\mathbf{m}$ , elastic stiffness,  $\mathbf{k}$ , and viscous stiffness,  ${}^*\mathbf{k}$ , matrices, there results

$$[\ddot{\mathbf{W}} \mathbf{m} + \mathbf{u}^T \mathbf{k}] \delta \mathbf{u} + \left[ \sum_{n=1}^N {}^*\mathbf{u}^T {}^*\mathbf{k} \right] \delta {}^*\mathbf{u} - \delta W = 0 \quad (14)$$

Since  $\delta \mathbf{u} = \delta {}^*\mathbf{u}$  when  $t$  is constant, the virtual work takes on a simpler form

$$\left[ \ddot{\mathbf{M}}^T \mathbf{m} + \mathbf{u}^T \mathbf{k} + \sum_{n=1}^N {}^* \mathbf{u}^T {}^* \mathbf{k}_n \right] \delta \mathbf{u} - \delta W = 0 \quad (15)$$

This implies that at any time  $t$  the element equilibrium equations are

$$\mathbf{m} \ddot{\mathbf{Y}}_n + {}^* \mathbf{k}_n \mathbf{u}_n = \mathbf{f}_n - \sum_{n=1}^N {}^* \mathbf{k}_n {}^* \mathbf{u}_n \quad \text{for each element} \quad (16)$$

where  $\mathbf{f}_n$  denotes the element consistent load vector due to the external loading. Introducing (10) and (12) into the differential equations for the strain variables in (2) yields

$${}^* \dot{\mathbf{Y}}_n + {}^* \mathbf{k}_n \mathbf{u}_n / \tau_n = \dot{\mathbf{Y}}_n \quad \text{for each } n \quad (17)$$

The global equilibrium equations are determined by the standard assembly of the element equations, (16). Note, there is no assembly for (17). The global equations of motion are

$$\mathbf{M} \ddot{\mathbf{Y}}_g + \mathbf{K} \mathbf{u}_g = \mathbf{F}_{mech} - \mathbf{F}_{visc} \quad (18)$$

where  $\mathbf{u}_g$  denotes the global nodal variable vector,  $\mathbf{M}$  is the mass matrix,  $\mathbf{K}$  is the elastic stiffness matrix,  $\mathbf{F}_{mech}$  is the global force vector due to mechanical loads, and  $\mathbf{F}_{visc}$  is the assembled vector for  $\sum_{n=1}^N {}^* \mathbf{k}_n {}^* \mathbf{u}_n$ . The viscoelastic problem is solved by simultaneously integrating the first order differential equations, (17), and the second order equations, (18), where the latter is subject to the appropriate boundary restraints.

As far as the finite element implementation is concerned, a conventional linear elastic code can be readily adapted to perform a dynamic analysis for a structure made from a Maxwell material, i.e., a material whose relaxation stiffness coefficients can be modeled with a Prony series. First, the viscous stiffness coefficients,  ${}^* C_y$ , are used in place of the elastic values to compute the element viscous stiffness matrices,  ${}^* \mathbf{k}$ , which are stored for repeated use. The internal nodal variables for each element,  ${}^* \mathbf{u}$ , are set equal to their initial values. A modified Newmark algorithm is then used to integrate (18). The modification is required so that (17), stiff relaxation equations, are implicitly integrated.

### Applications

Two numerical solutions representative of quasi-static and free vibration deformations of a cantilevered thick orthotropic beam are presented. The beam dimensions are as follows:  $L = 0.1\text{ m}$ ,  $2h = 0.02\text{ m}$ , and  $b = 1.0\text{ m}$  (refer to Figure 1). The beam elastic stiffness coefficients for the state of plane stress can be written in terms of engineering material constants as

$$C_{11} = E_x / (1 - \nu_{xz}\nu_{zx}), \quad C_{33} = E_z / (1 - \nu_{xz}\nu_{zx}), \quad C_{13} = \nu_{xz}C_{33}, \quad C_{55} = G_{xz}$$

A unidirectional E-glass/epoxy laminate is considered for which the material constants are:  $E_x = 38.6\text{ GPa}$ ,  $E_z = 8.27\text{ GPa}$ ,  $G_{xz} = 4.14\text{ GPa}$ ,  $\nu_{xz} = 0.26$ , and  $\rho = 1.8\text{ g/cm}^3$ . The viscous relaxation properties are computed from complex modulus versus frequency data for the E-glass/epoxy.<sup>13</sup> The equations for the real and imaginary parts of the effective modulus for a ten term Maxwell solid<sup>14</sup> are least-squares fit to the measured data in a frequency range of 45 Hz – 145 Hz. The least squares minimization was performed using a quadratic programming method that enforced the constraint that each of the moduli in the Maxwell solid must be positive. The time constants for the ten terms are;  $\tau_n = 10^{-4}, 10^{-3.5}, 10^{-3}, 10^{-2.5}, 10^{-2}, \dots, 10^1$ , and infinity. The resulting Maxwell solid had its moduli scaled so that its equivalent nondimensional Prony series has the form

$$P(t) = 1.0 + 0.01755 e^{-0.0001t} + 0.000257 e^{-0.01t} + 0.072014 e^{-0.3162t}$$

The time dependent stiffness values for the E-glass/epoxy are then given by  

$${}^*\mathbf{C} = P(t)\mathbf{C}.$$

Example 1. A cantilever beam (reference Figure 1) with  $w$ ,  $u$ ,  $\theta$  fixed at point A has a prescribed deflection  $w$  at point B that is ramped from 0 to -1 cm in 0.05 sec and then held constant at -1 cm. Figure 3 depicts the maximum axial stress at point C as a function of time. Also shown are the elastic and viscous stress components comprising the total stress. The decay of the total viscoelastic stress to its elastic value as time is increased demonstrates the expected step-strain relaxation behavior. Note, when this problem is solved with a velocity proportional viscous damping model the viscous stress for time greater than 0.05 sec is zero.

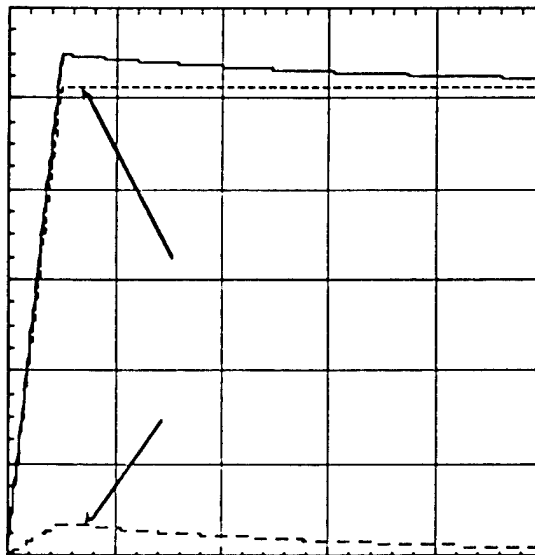


Figure 3. Cantilevered beam under prescribed tip deflection.  
Stress in top surface at support (point C).

Example 2. The cantilevered beam of Example 1 has its tip (point B) released at  $t = 0.1$  sec and is allowed to vibrate freely thereafter. The resulting tip deflection as a function of time is shown in Figure 4. Figure 5 depicts the value of the dynamic axial stress at point C as a function of time. Note that both relaxation and damped vibration response are obtained within the same finite element solution.

### Conclusions

An elastodynamic formulation, which includes a differential form of the Maxwell viscous solid constitutive theory, has been implemented in a higher-order-theory beam finite element. The attractive features of the formulation include: (1) The constitutive constants are the same as those needed in the classical history-integral model, and they are also readily available from step-strain relaxation tests, (2) The internal variables are conjugate to the elastic strain measures; hence, they are consistent with the kinematic assumptions of the elastic formulation, (3) The update of the state variables can be performed in a parallel computing environment, allowing the viscous force vector in the equations of motion to be determined efficiently within the modified Newmark algorithm,

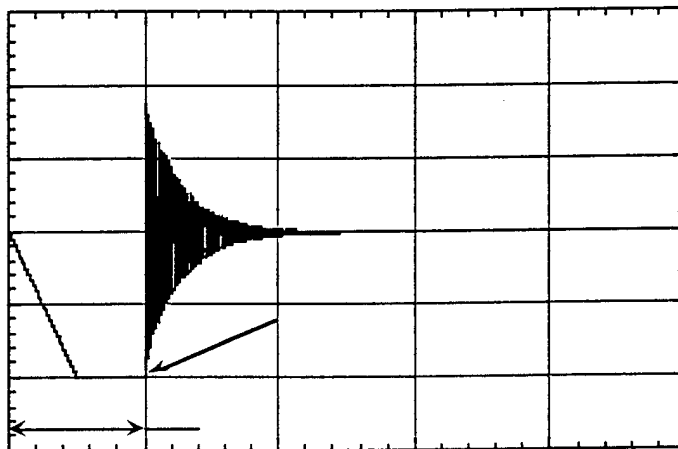


Figure 4. Cantilevered beam under prescribed tip deflection.  
Tip released - vibration of tip (Point B).

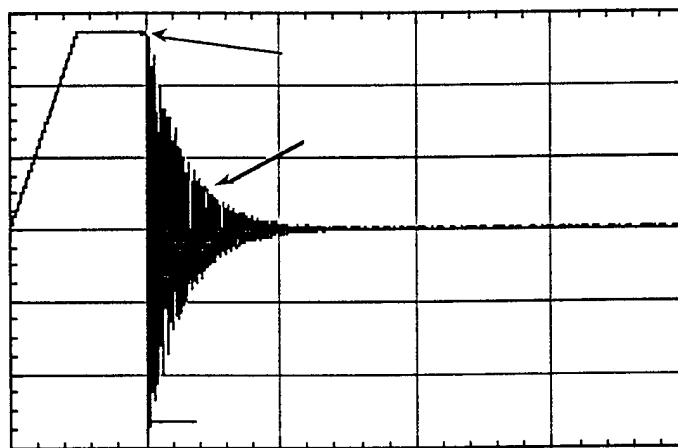


Figure 5. Cantilevered beam under prescribed tip deflection.  
Tip released - Stress on top surface at support. (Point C).

(4) Applications of time-dependent displacements and loads are performed within the same finite element algorithm, and (5) The higher-order beam theory accounts for both transverse shear and transverse normal deformations — the effects that need to be accounted for in thick and highly orthotropic beams, and in high-frequency dynamics.

Example 2, in which a quasi-static enforced deformation is followed by a high frequency free vibration, demonstrates the capability of this finite element formulation to simulate physically important phenomena that is computationally difficult to obtain.

**Acknowledgment:** The authors would like to thank Mr. Michael Dambach, of The George Washington University at the NASA Langley Research Center, for his help in the computational effort.

### References

1. Halpin, J. C., and Pagano, N. J., Observations on linear anisotropic viscoelasticity, *J. Composite Materials*, **2**, No. 1, 68-80 (1968).
2. Hashin, Z., Complex moduli of viscoelastic composites - I. General theory and applications to particulate composites, *Int. J. Solids Structures*, **6**, 539-552 (1970).
3. Hashin, Z., Complex moduli of viscoelastic composites - II. Fiber reinforced materials, *Int. J. Solids and Structures*, **6**, 797-807 (1970).
4. Argyris, J., St. Doltsinis, I., and da Silva, V. D., Constitutive modeling and computation of non-linear viscoelastic solids, Part I. Rheological models and numerical integration techniques, *Comput. Methods Appl. Mech. Engrg.*, **88**, 135-163 (1991).
5. Shaw, S., Warby, M. K., and Whiteman, J. R., Numerical techniques for problems of quasistatic and dynamic viscoelasticity, in "The Mathematics of Finite Elements and Applications," edited by J. R. Whiteman, John Wiley & Sons (1994).
6. Coleman, B. D., and Noll, W., Foundations of linear viscoelasticity, *Reviews of Modern Physics*, **33**, No.2, 239-249 (1961).
7. Schapery, R. A., Viscoelastic behavior and analysis of composite materials, in "Composite Materials", **2**, edited by G. P. Sendeckyj, Academic Press (1974).
8. Johnson, A. R., and Stacer, R. G., Rubber viscoelasticity using the physically constrained system's stretches as internal variables, *Rubber Chemistry and Technology*, **66**, No.4, 567-577 (1993).
9. Johnson, A. R., Tanner, J. A., and Mason, A. J., A kinematically driven anisotropic viscoelastic constitutive model applied to tires, in "Computational Modeling of Tires," compiled by A. K. Noor and J. A. Tanner, NASA Conference Publication 3306, August 1995.
10. Johnson, A. R., Tanner, J. A., and Mason, J. A., A viscoelastic model for tires analyzed with nonlinear shell elements, presented at the Fourteenth Annual Meeting and Conference on Tire Science and Technology, University of Akron, March 1995.
11. Johnson, A. R., and Tessler, A., A viscoelastic higher-order beam finite element, *NASA TM 110260*, June 1996.

12. Tessler, A., A two-node beam element including transverse shear and transverse normal deformations, *Int. J. for Numer. Methods Eng.*, **32**, 1027-1039 (1991).
13. Gibson, R. F., and Plunkett, R., Dynamic mechanical behavior of fiber-reinforced composites: Measurement and analysis, *J. Composite Materials*, **10**, 325-341 (1976).
14. Aklonis, J. J., MacKnight, W. J., and Shen, M., *Introduction to Polymer Viscoelasticity*, John Wiley & Sons, 1972.

# Damage detection methodology for composite rotorcraft flexbeams

K. A. Lakshmanan

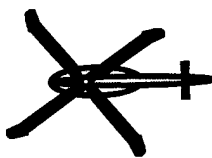
Graduate Research Assistant, Department of Aerospace Engineering  
University of Maryland, College Park, MD 20742

Darryll J. Pines

Assistant Professor, Department of Aerospace Engineering  
University of Maryland, College Park, MD 20742

## ABSTRACT

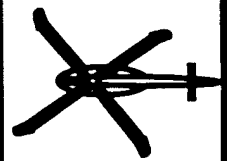
This paper presents the analytical modeling and experimental validation of a local wave model which can detect damage in the form of transverse cracks in composite rotorcraft flexbeams under rotation. The model is used to identify the location and extent of damage. Health and usage monitoring is increasingly gaining importance in the rotorcraft industry. Online detection of damage will make it possible to reduce maintenance intervals and costs since components will be replaced on an “as-required” basis rather than based on mandatory time-cycles. In this method, the principles of wave transmission and phase closure are used to study flapping wave propagation dynamics in a composite flexbeam. Scattering of incident waves across structural discontinuities are used to characterize the nature of the damage. Using the changes in a parameter called the scattering matrix, one can identify the crack size and location in conjunction with a least squares optimization. Experimental results on  $[0/90]_S$  Gr/Ep test specimens indicate that the model is able to detect transverse cracks in composite rotorcraft flexbeams in real time under centrifugal loading in vacuum. Both the damage location and size of crack depth are detectable to within 20% error for various RPM levels. This suggests that this type of model can potentially be used on a rotorcraft flexbeam for real time health monitoring.



## Objectives

UM

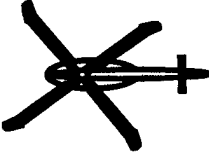
- Develop local wave models for one-dimensional composite structures (rotating and non-rotating).
- Detect presence of chordwise transverse cracks using the wave model.
- Detect through-width delaminations in beams.
- Identify location and extent of crack damage.
- Validate the concept of using wave models in damage detection methods for rotating beams.
- Carry out experiments on composite rotorcraft flexbeams in vacuum to validate the local wave model.



## Contributions of this Work

UVI

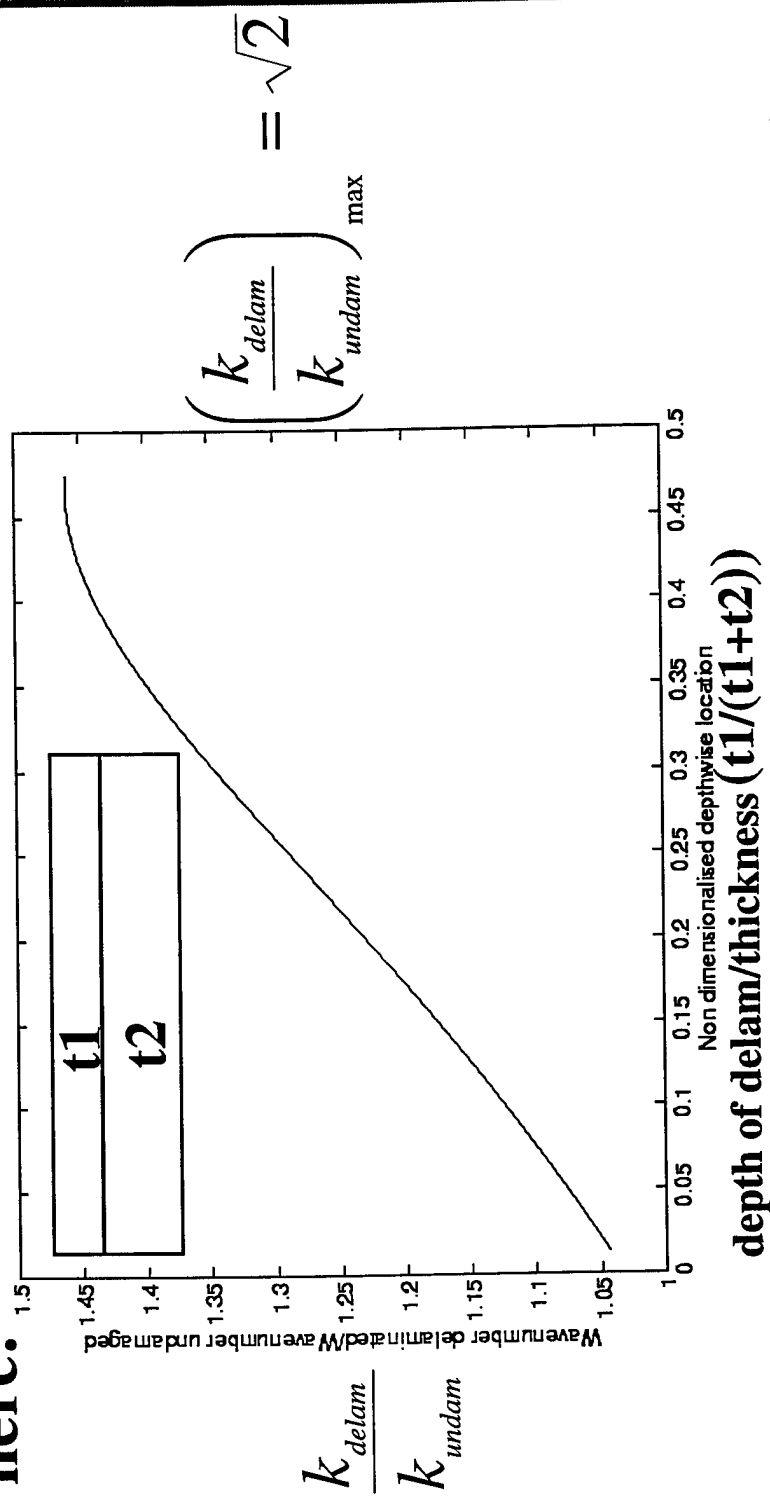
- A local-based wave propagation modeling approach to damage detection.
- Application to composite rotorcraft flexbeams with chordwise cracks and delamination.
- Use of wave scattering for damage identification (size and location).
- A potential real-time methodology for damage detection.



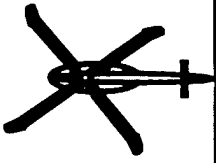
## Delamination: effect on wavenumber

UM

- The effect of delamination on the wavenumber is shown here:

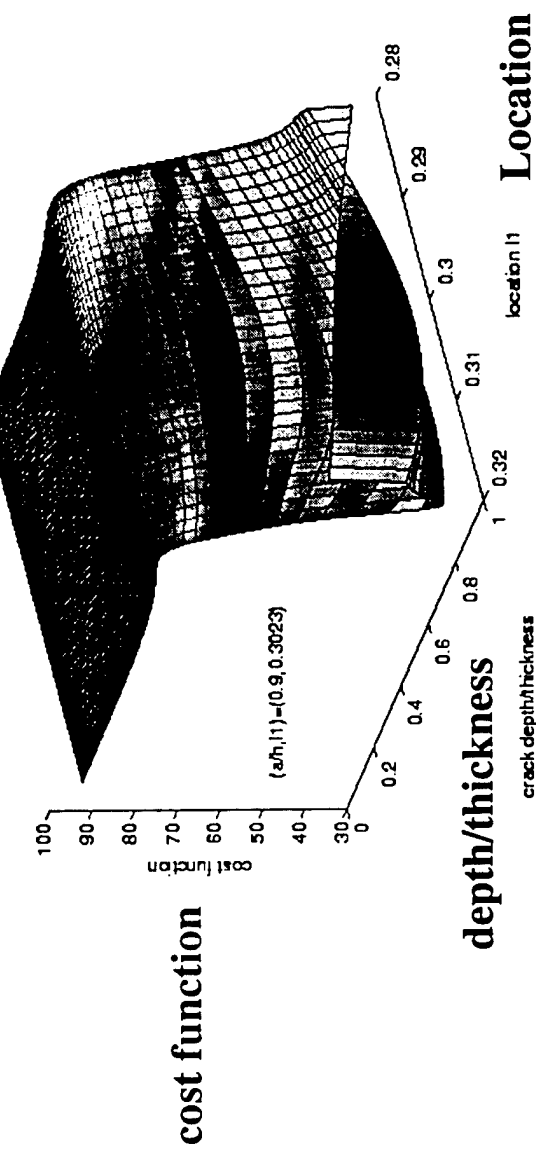


depth of delam/thickness ( $t1/(t1+t2)$ )

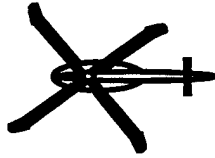


## Cost function at 0 RPM

( $a/h = 0.9$ , loc = 0.3023)



UMI



## Conclusions

UM

- Local wave models can be used to capture the dynamics of chordwise cracks and through-width delaminations.
- The scattering matrix can be used to identify damage.
- Experimental results on uncoupled composite flexbeams in vacuum confirm analytical predictions.
- Damage identification was used to detect crack size (to within 20 %) and location (to within 5 %) for uncoupled beam specimens.
- Non-dimensional wavenumber-frequency relation shows that as RPM increases, the evanescent components are attenuated and only the propagating terms need to be considered.
- It is possible to detect delamination based on constrained mode model. This model suggests that the worst case delamination results in a 75 % loss in stiffness EI.

# **ROTOR BLADE DAMAGE AND DETERIORATION DETECTION THROUGH THE WAVELET TRANSFORM METHOD**

**X. DENG<sup>1</sup>, C. A. ROGERS<sup>2</sup>, V. GIURGIUTIU<sup>1</sup>, and M. A. SUTTON<sup>2</sup>**

Center for Mechanics of Materials and NDE, Department of Mechanical Engineering  
College of Engineering, University of South Carolina, Columbia, SC 29208

## **SUMMARY**

In this presentation we will first review several common damage types in helicopter rotor-blade structures and then discuss our recent effort in developing new damage detection methods that may be applicable to rotor-blade structures.

### ***Typical Rotor Blade Damage Modes***

Current rotor blades in service with the Army and the National Guard span a variety of constructions. Conventional D-tube metallic type (e.g. Blackhawk helicopter) coexists with adhesively bonded multi-cell sheet-metal construction (e.g., Apache helicopter) and advanced composite lay-ups (e.g. Comanche). Rotor blade damage modes resulting from in-service operations depend to a certain degree on the blade construction solution.

#### **D-Tube Metallic Blades**

D-tube metallic blades are usually prone to through-thickness fatigue cracks in the extruded section. These cracks appear at locations of maximum dynamic bending moment and can lead to catastrophic failure if not detected early. The pressurized pop-up crack detection system that has become the norm on D-tube blades was intended to guarantee early detection of such cracks. However, an improved crack detection system capable of detecting cracks not yet at the through-thickness stage is needed to improve the safety and reliability of this blade type.

#### **Adhesively Bonded Multi-Cell Sheet-Metal Blades**

Adhesively bonded multi-cell sheet-metal blades are susceptible to a different type of fatigue-induced damage, *viz.* delamination (disbond) between adjacent cells. Disbonds longer than six inches have been recorded at the blade tip at the South Carolina National Guard helicopter detachment at McEntire Base in Sumter, SC. Figure 1 presents an overall view of an Apache blade showing two disbonds, at the second and third cross-sectional shear web, respectively. These damage could lead to excessive helicopter vibration and even flight events if not addressed early.

#### **Composite Blades**

Two types of damage often result from in-service operations of composites: (a) hidden accidental damage due to mishandling; (b) fatigue-induced disbond and delamination. Hidden accidental damage is especially dangerous since it can lead to subsurface defects that greatly reduce the local strength of the composite (especially the compression strength after impact) and can jeopardize the safe use of the blade. The situation is particular to composite material constructions

---

<sup>1</sup> Associate Professor

<sup>2</sup> Professor

that tend to have a "spring-back" capacity at the surface of the damaged area, unlike the damage response of metallic constructions that leave a permanent damage mark. Even when the static strength of the blade is not drastically affected, such hidden damage can become a fatigue crack initiation site that can eventually lead to catastrophic failure.

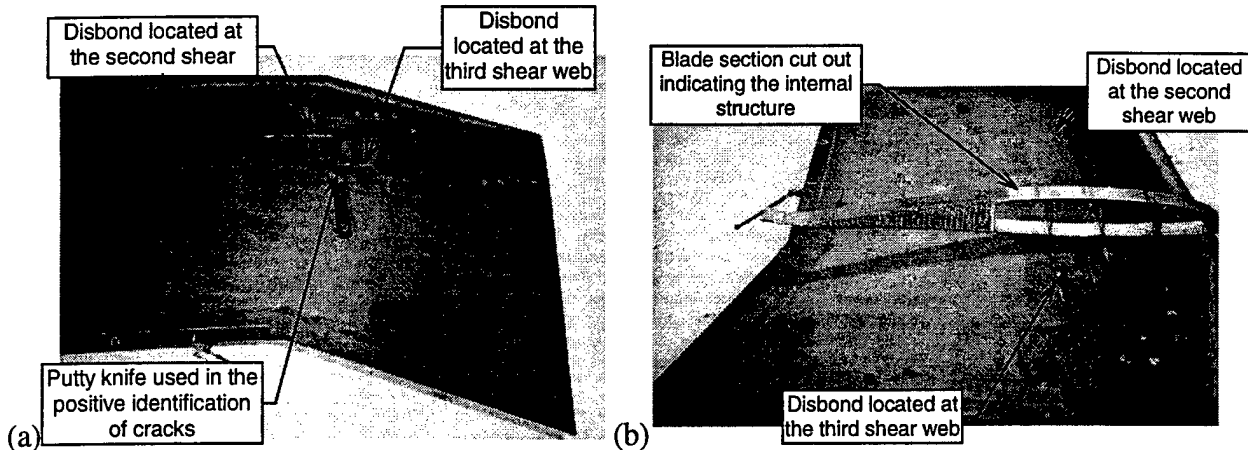


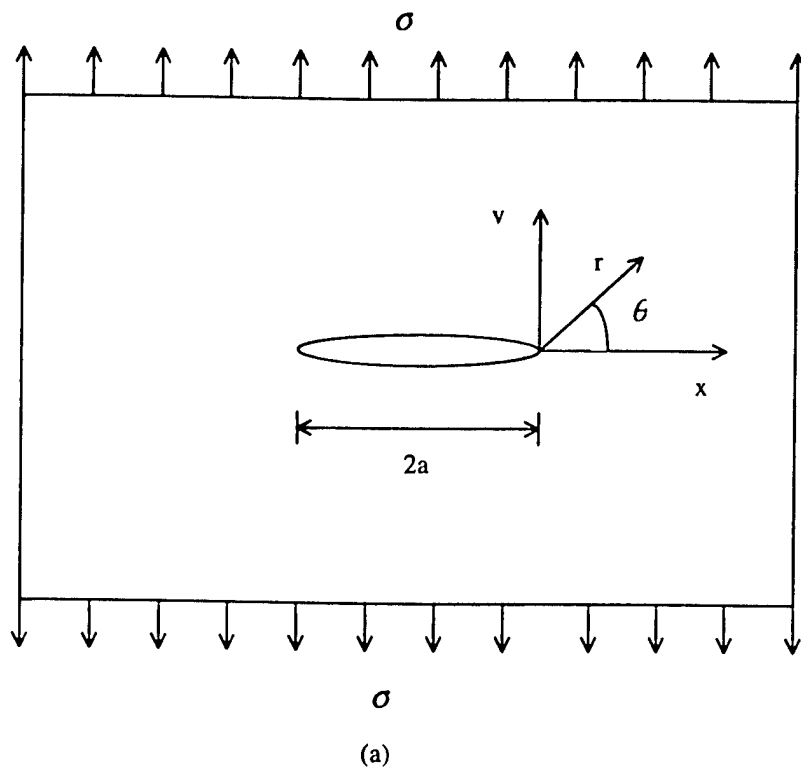
Fig. 1 Apache blade showing dramatic disbonds near the blade tip: (a) overall view of the swept-back blade; (b) details of the internal construction of the blade.

### ***Damage Detection Methods Based on Wavelet Transforms of Sensor Signals***

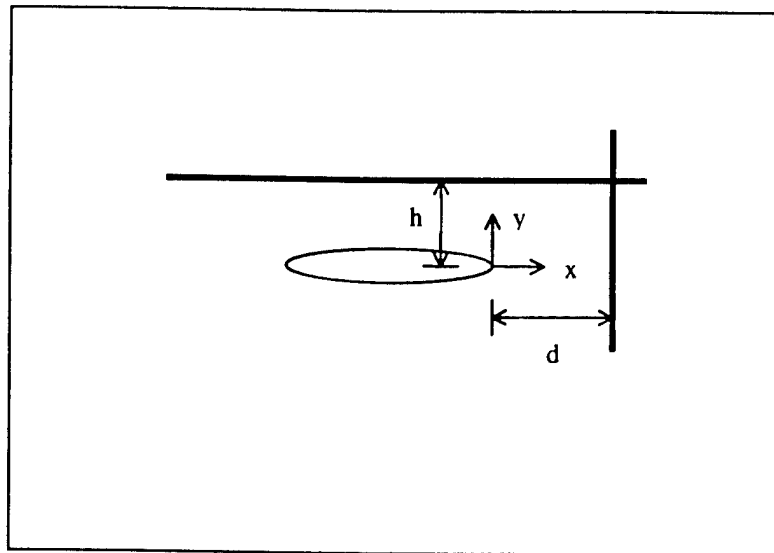
We present preliminary results of a recent explorative effort in using wavelet transforms of sensor signals to reveal damage information imbedded in the sensor signals. Our results so far are based on simulated, spatially distributed displacement signals in structures containing cracks. We will attempt to show that there are inherent perturbation features in the spatial signals that are induced by the presence of crack-like damage, and that the wavelet transform appears to be able to reveal these features and hence to locate the damage. We hope to shed light on the potential of the wavelet transform in damage detection and to stimulate interest and further effort in this area.

We first consider a large elastic plate containing a center crack and subject to a remote uniform tension (see Fig. 2). The displacement response along a vertical line segment, as shown in Fig. 2(b), is given in Fig. 3 for a typical case, based on a converged finite element solution under plane stress conditions. Although a dip can be seen in the  $u_x$  curve at the crack tip location, it is not apparent where the crack tip is from the  $u_y$  curve. The wavelet transforms of the two curves at scales 6 and 10 are shown in Fig. 4, where the crack tip location is clearly characterized by a special feature in the form of a sudden change in the wavelet transforms.

Similarly, we have examined problems involving a cantilever beam loaded at the free end, with either a transverse crack (Fig. 5) or a longitudinal sub-surface crack (Fig. 7) at the mid span of the beam. In both cases, the wavelet transforms of the displacement response are able to indicate the crack tip location (see Figs. 6 and 8) even though the original displacement curves tell little about the location of the crack tip.



(a)



(b)

Fig. 2 (a) A large plate with a center crack under remote uniform tension loading; (b) vertical and horizontal line segments along which the displacement response will be obtained and used in wavelet analysis.

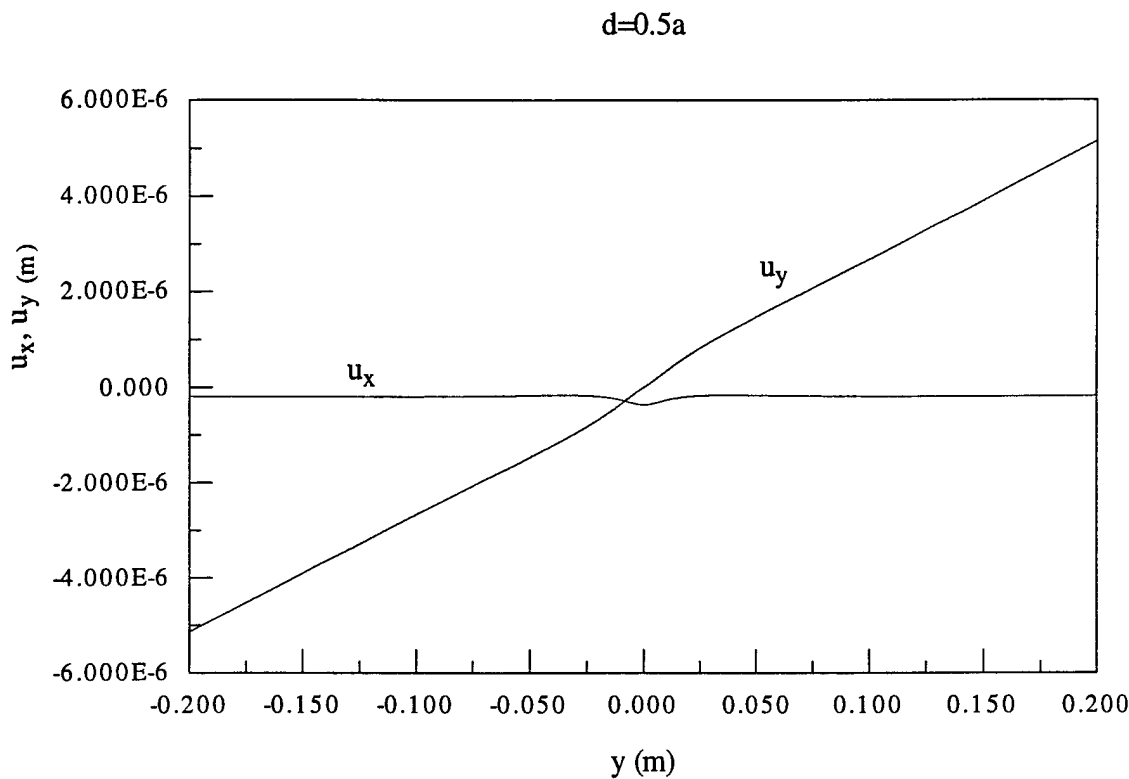


Fig. 3 Elastic displacement response along the vertical line segment in Fig. 2(b), with  $d=0.5a$  and  $a=40$  mm, and for a unit-thickness steel plate subject to  $\sigma = 5$  MPa.

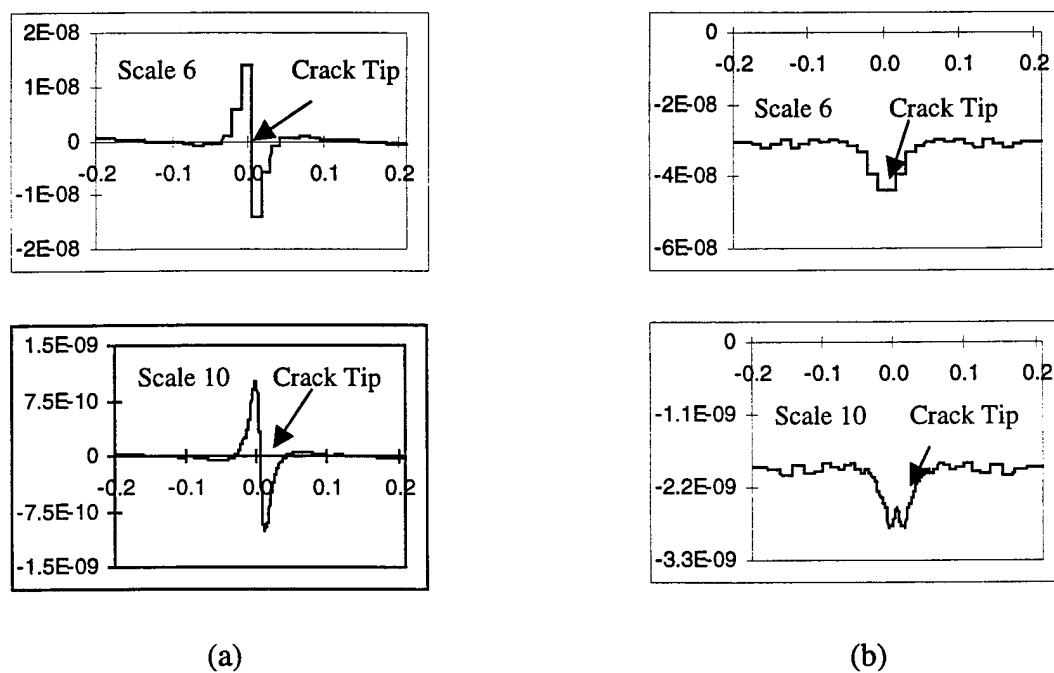


Fig. 4 Wavelet transforms of (a)  $u_x$  and (b)  $u_y$  in Fig. 3 at scales 6 and 10.

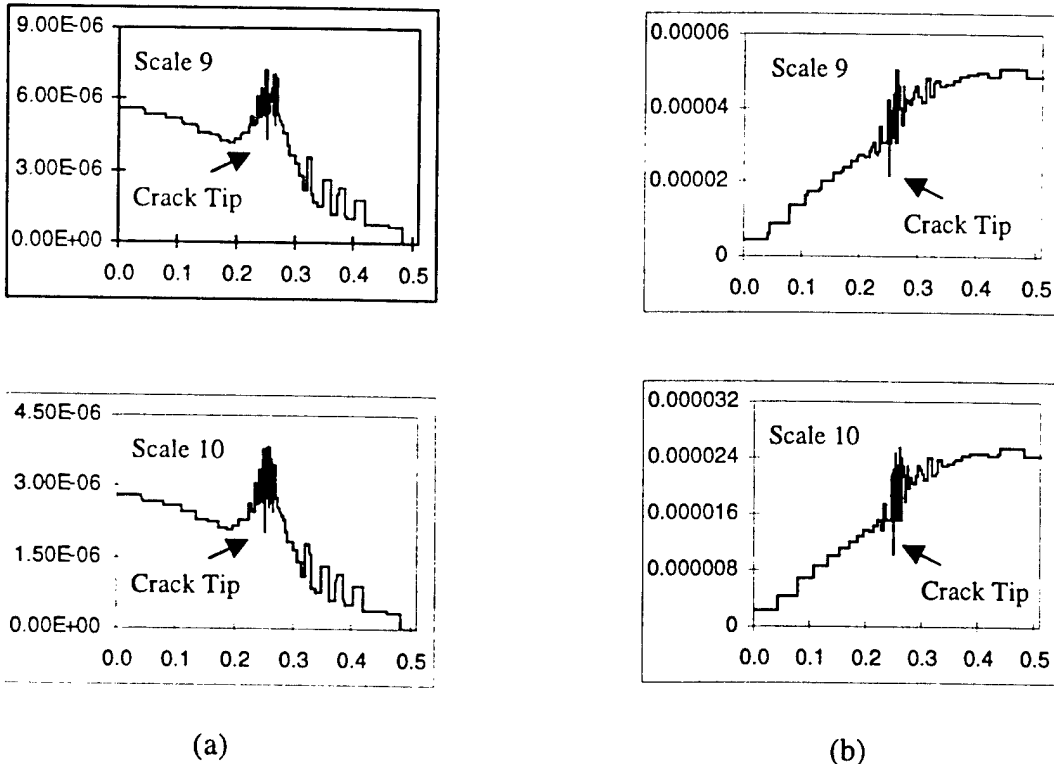
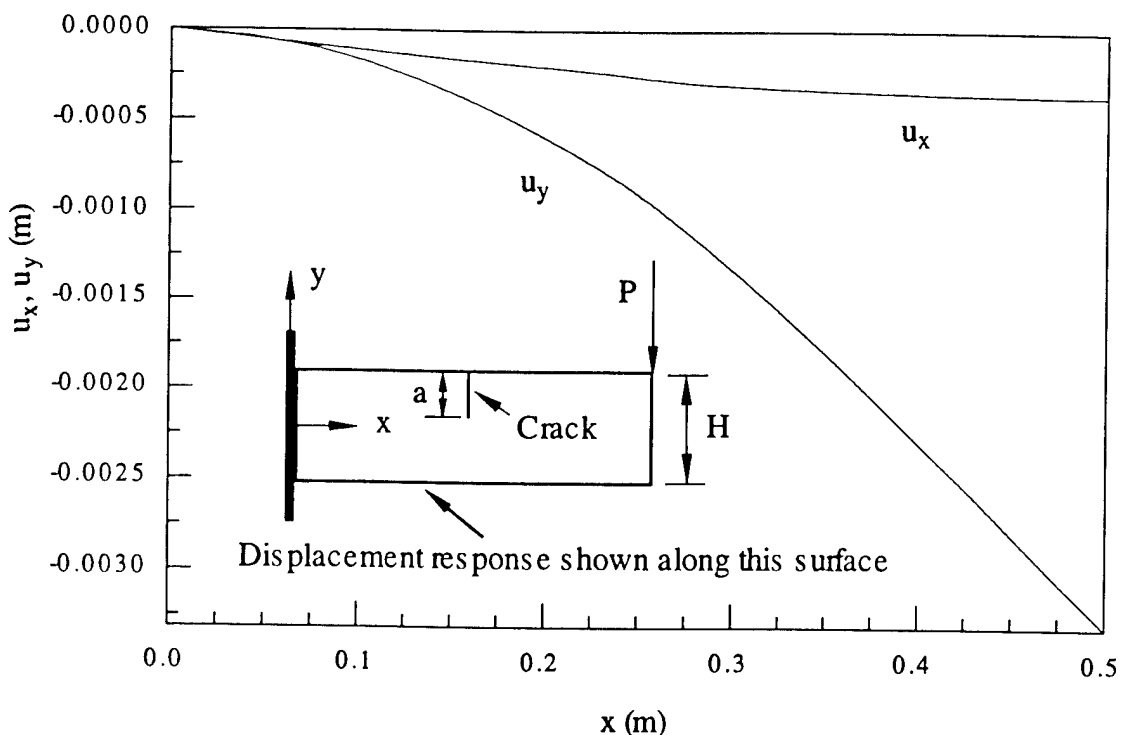


Fig. 6 Wavelet transforms of (a)  $u_x$  and (b)  $u_y$  in Fig. 5 at scales 9 and 10.

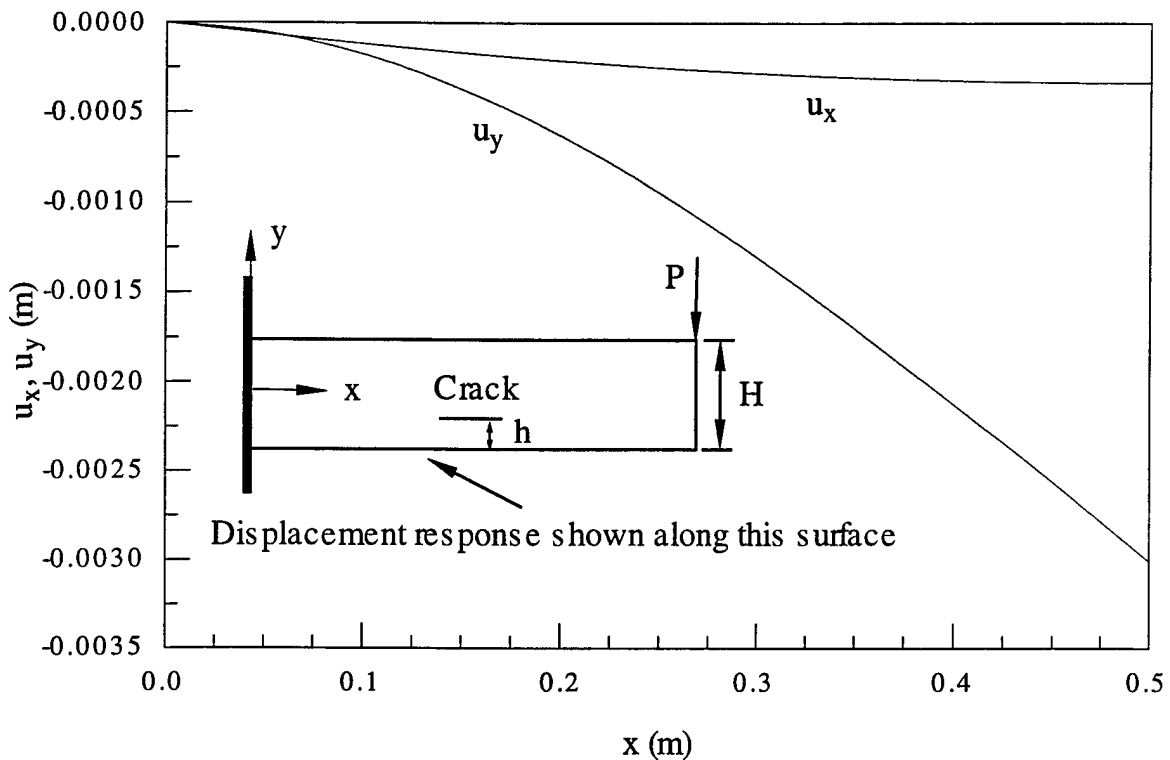


Fig. 7 Elastic displacement response of a cantilever beam with a longitudinal sub-surface crack at mid-span and under a static load at the free end, where beam length=0.5 m, width=75 mm, crack length=50 mm,  $h/H=1/4$ ,  $H=75$  mm, and  $P=878$  kN, with conventional steel properties.

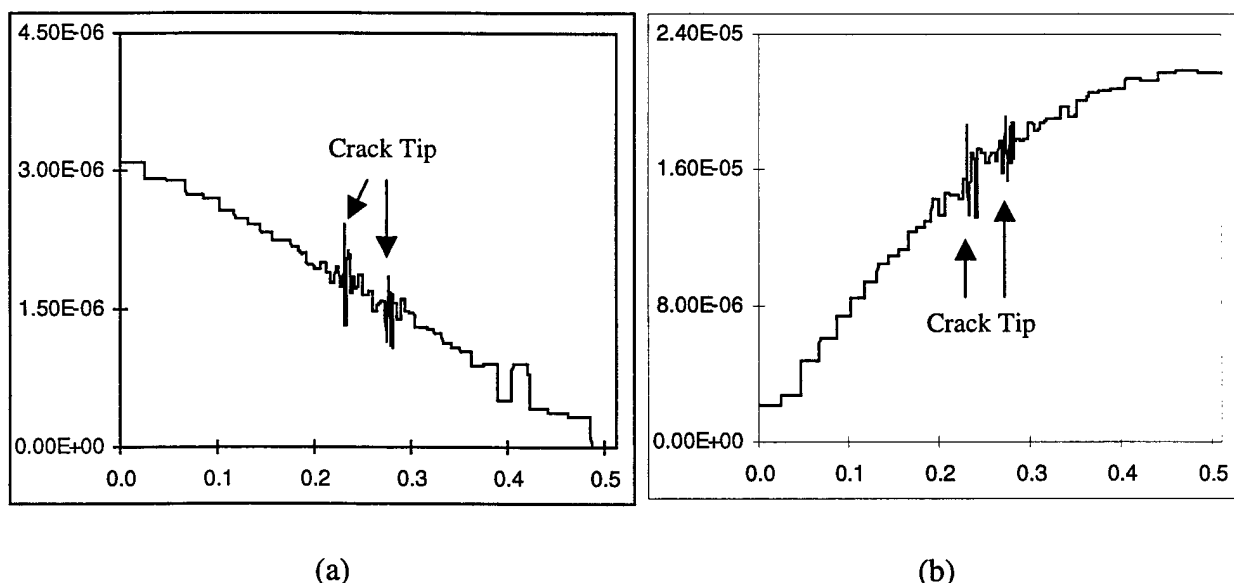


Fig. 8 Wavelet transforms of (a)  $u_x$  and (b)  $u_y$  in Fig. 7 at scale 10.

# Fault Detection in Main Rotor Blades

Jason Kiddy

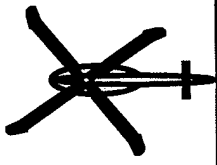
Graduate Research Assistant, Department of Aerospace Engineering  
University of Maryland, College Park, MD 20742-3015

Darryll Pines

Assistant Professor, Department of Aerospace Engineering  
University of Maryland, College Park, MD 20742-3015

## ABSTRACT

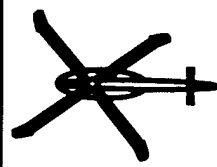
In this work, the detection and identification of damage in a helicopter rotor blade is considered. An eigenstructure assignment technique is developed using measured modal test data and a finite element model of the blade to detect and classify the extent of damage in the system. Previous eigenstructure assignment techniques have not attempted to consider the centrifugal and gyroscopic effects found in rotating systems. Additional elemental stiffness matrix terms are created on the inboard elements due to the centrifugal forces pulling on the mass of the outboard elements. These forces create an enhanced sensitivity of the eigenstructure to mass changes thereby leading to an improved damage detection capability. Feasibility of the methodology is first demonstrated analytically which leads to several important insights.



# Objectives of Research

UM

- Develop an algorithm to detect and characterize damage in main rotor blades.
- Emphasis is placed on detecting damage that affects the global properties of the rotor blade, i.e. modal dynamics.
- Determine effect of damage on hub vibratory loads.
- The goal is to potentially develop a real-time health monitoring scheme for detecting damage.



## Eigenstructure Assignment - cont

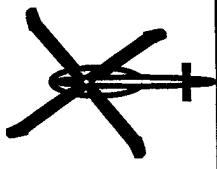
UM

- Advantages

- Eigenstructure Assignment has previously been used to accurately detect and characterize damage in non-rotating structures.
- The strain formulation allows for the use of strain sensors in place of accelerometers.
- No optimization routine is required thereby greatly decreasing computational costs.

- Disadvantages

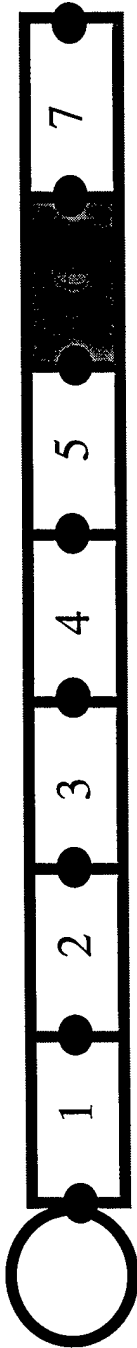
- A distributed array of sensors on the blade is required.
- Structural stiffness changes become harder to detect at higher rotation rates.



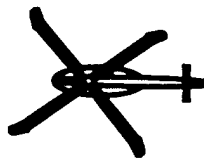
# Simulated Ballistic Damage Results

UM

## 10% Damage in Mass and Stiffness



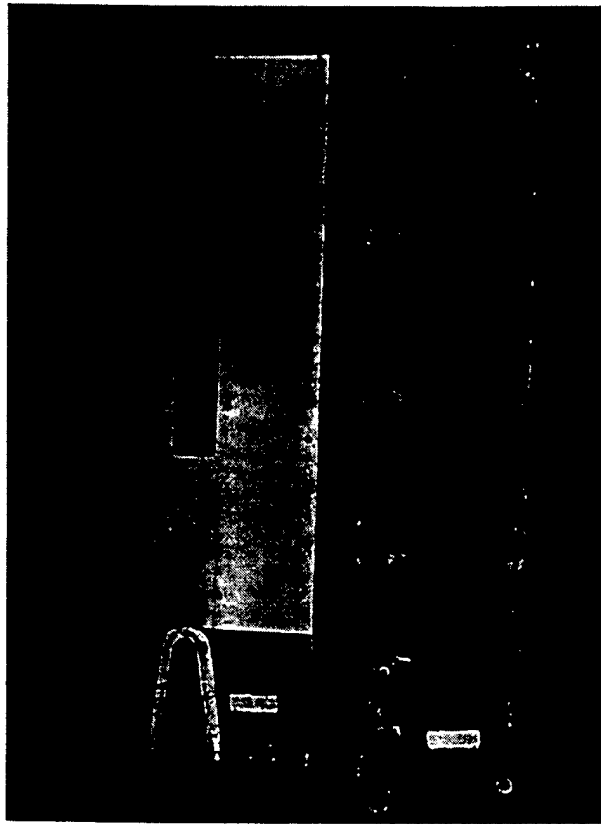
		Element #						
		1	2	3	4	5	6	7
Mass	Stnd Deviation	31.857	3.928	3.659	0.968	0.656	0.003	0.406
	Average	-36.189	-1.787	-2.720	-1.532	-1.262	-0.100	-0.078
Stiffness	Stnd Deviation	0.073	0.702	1.267	0.280	0.114	0.001	0.177
	Average	0.003	1.418	-0.630	-0.299	-0.313	-0.101	-0.360



## Experimental Validation

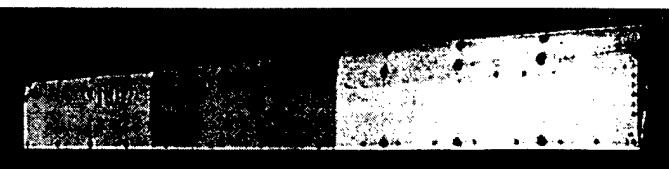
UM

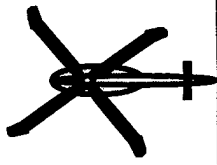
- 2-TH-55A Main Rotor Blades



- One blade undamaged, one blade with partial cut-out of inboard spar to simulate ballistic damage

- Stationary vibration testing performed at Aberdeen Proving Grounds





# Summary and Conclusions

UM

- An eigenstructure assignment based damage detection approach is developed for rotor blades under centrifugal loading in vacuum for flap-lag dynamics.
- The approach is then converted into a strain formulation
- Analytical results confirm that damage can be detected under rotation for losses of mass and stiffness.
- A large decrease in computational effort is achieved in comparison to a sensitivity-based approach.
- An experimental model has been developed for experimental validation.

# Three-Dimensional Boundary Elements for Flawed Piezoelectric Materials

Lisa R. Hill              Thomas N. Farris  
School of Aeronautics and Astronautics  
Purdue University  
1282 Grissom Hall  
West Lafayette, IN 47907-1282  
(765) 494-5156              (765) 494-5134  
[hill@ecn.purdue.edu](mailto:hill@ecn.purdue.edu)   [farris@ecn.purdue.edu](mailto:farris@ecn.purdue.edu)

## Abstract: 1997 ARO Workshop on Smart Structures

Piezoelectricity is a phenomenon in materials where a coupling occurs between the electrical and mechanical fields. These materials are widely used as sensors and actuators and are an integral part of smart structures. Their applications involve dynamic loading conditions under which fatigue failure can occur. In order to understand this dynamic behavior, the effect of flaws, such as voids, inclusions and cracks, on the piezoelectrics must first be determined in a static environment. These flaws can be induced in the manufacture of the material or arise during the sensor/actuator's standard service. The effect of these flaws on the piezoelectric is both mechanical and electrical in nature. The concentrations of stress and electric field at the flaw itself can lead to material yielding or localized depoling, which in turn can affect the sensor/actuator performance or cause failure. Understanding these effects will aid the design and manufacture of the piezoelectric materials for long sensor/actuator life, which is critical to the success of these smart structures. A three-dimensional boundary element method program is developed to evaluate the effect of flaws on these piezoelectric materials. The program is based on the linear governing equations of piezoelectricity and relies on a numerically evaluated Green's function for solution. The boundary element method was selected as the evaluation tool due to its ability to model the interior domain exactly. Thus, for piezoelectric materials the coupling between mechanical and electrical fields is not approximated inside the body.

Holes in infinite and finite piezoceramics are investigated, with the localized stresses and electric fields clearly developed. A discussion of the effect of bound surface charge on the hole boundary is given. Three-dimensional mode I fracture is also examined, combining the boundary element solution with the modified crack closure integral to determine strain energy release rates. Experimental research has shown that the strain, rather than the total, energy release rate accurately predicts crack growth in piezoelectric materials. Only boundary data is needed to determine the strain energy release rate, so discretization of the interior domain is not necessary. The boundary element method is better suited to this problem type than finite element methods for this reason, and its efficiency is more apparent for three-dimensional cases. Applications to penny-shaped, elliptical, and surface breaking cracks are included. Results of this investigation lead to a discussion of the effect of static load conditions on piezoelectric fracture behavior.



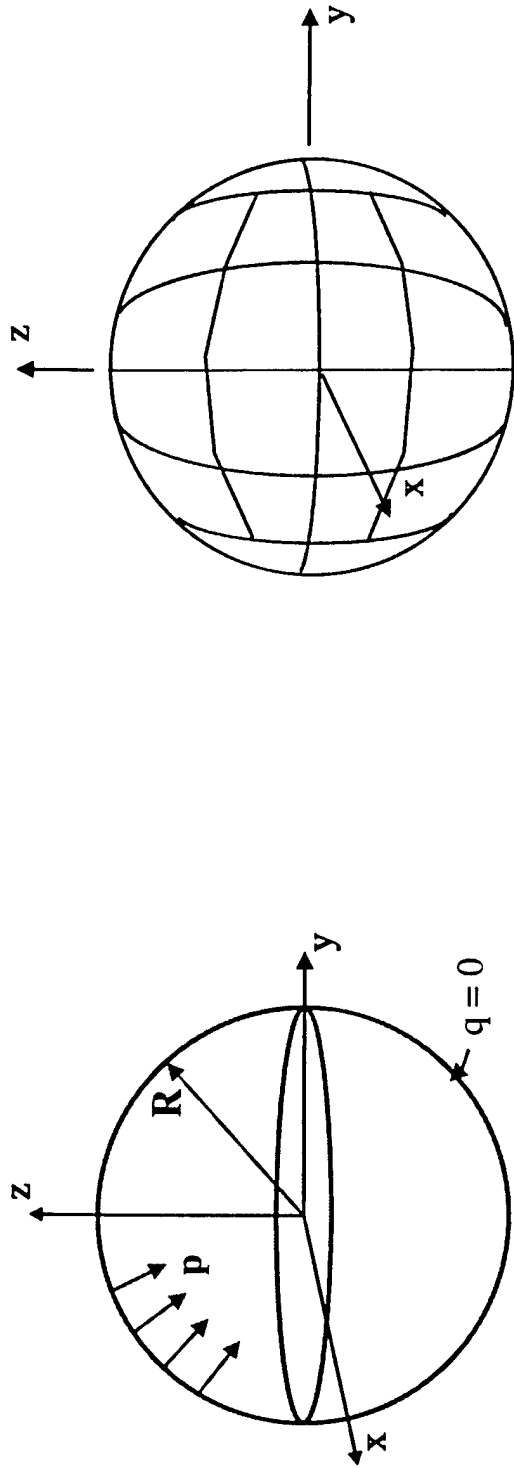
# Research Objectives

- Develop and implement a 3D higher-order piezoelectric boundary element program
- Investigate effects of voids on both the mechanical and electrical fields
- Apply boundary element-modified crack closure integration to 2D and 3D piezoelectric fracture
- Investigate effect of crack face boundary conditions on strain energy release rate



# Spherical Hole BEM Modeling

- Geometry and Spherical Mesh

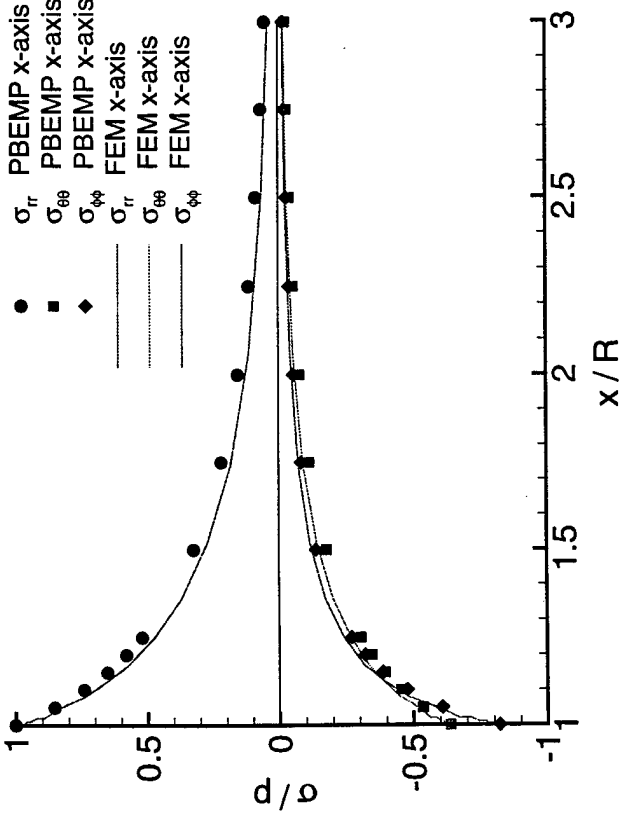


- Mesh validated with isotropic case, errors less than 1.1% for radial displacement
- Piezolectric solution for PZT-6B

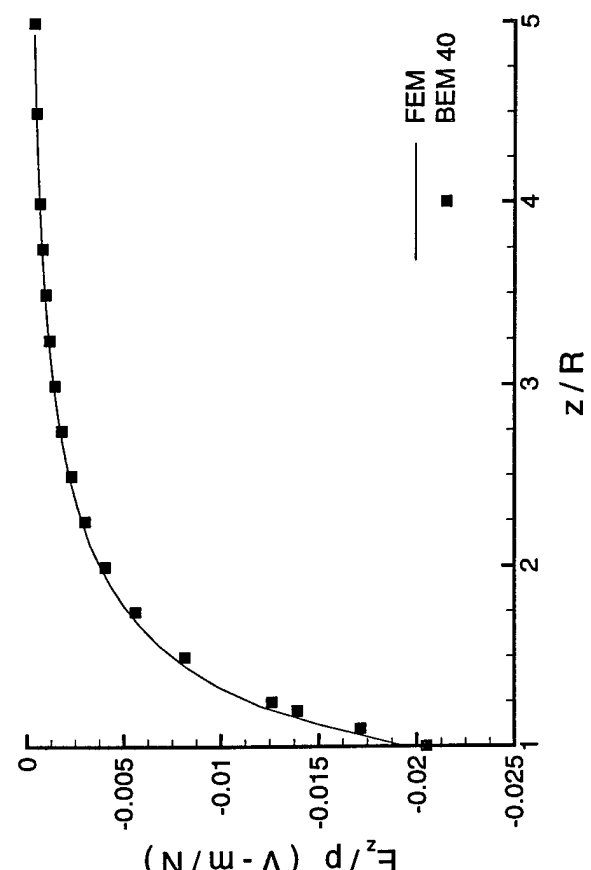


# BEM/FEM Comparison

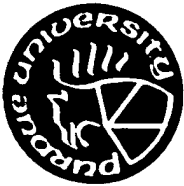
- Comparisons of mechanical and electrical fields



Stress

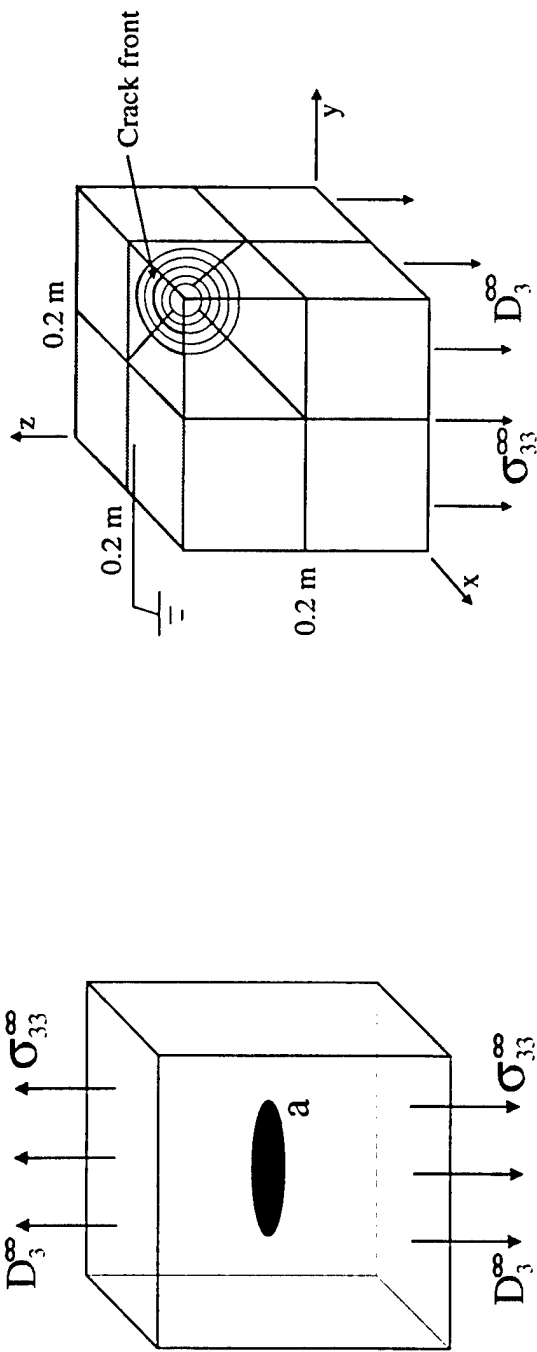


Electric field



# Mode I Penny Crack

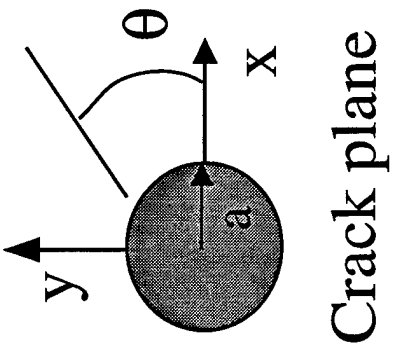
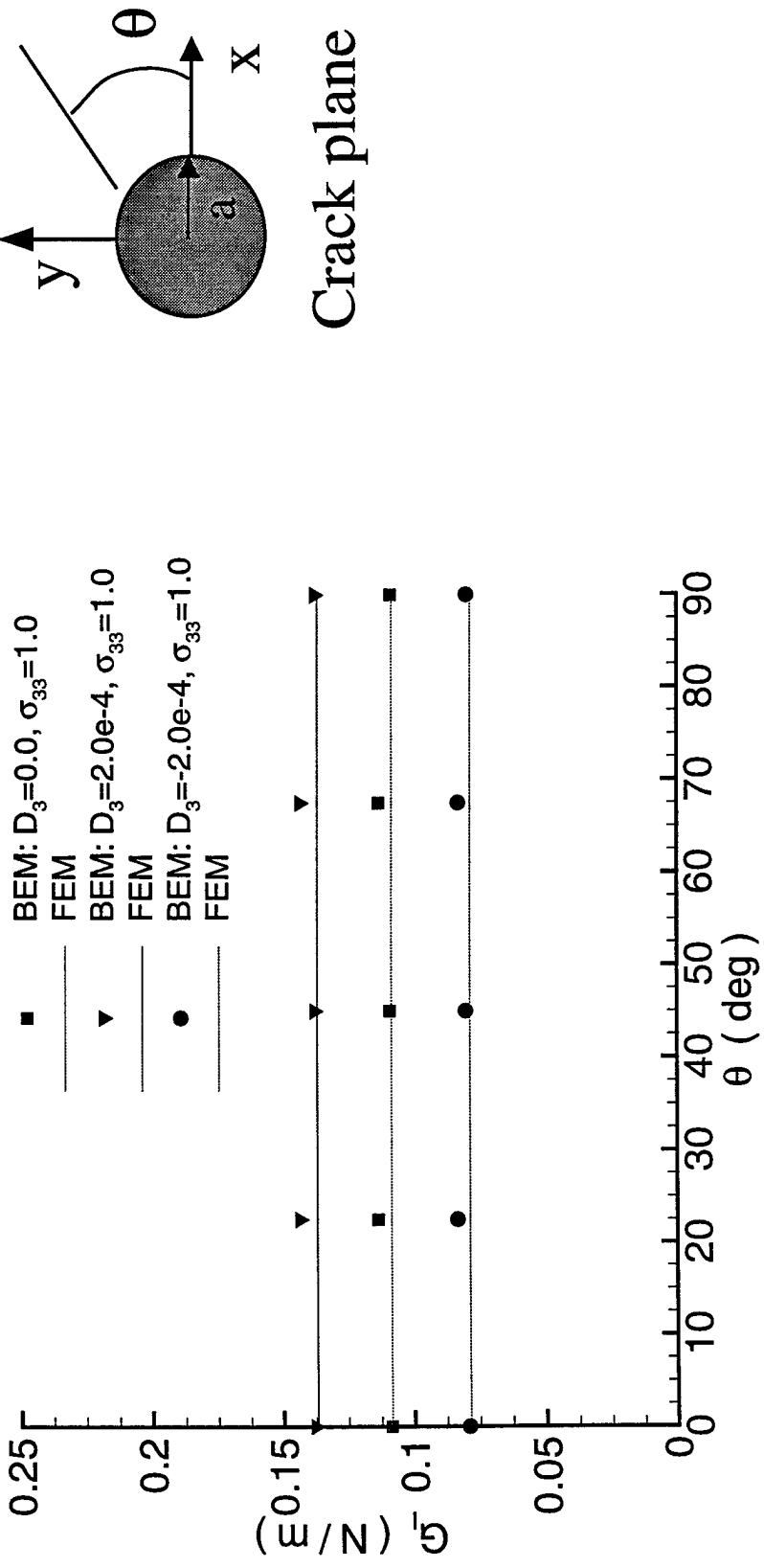
- Modified crack closure used to determine strain energy release rate
- Far-field mechanical and electrical loads
  - 54 elements 164 nodes  $\Delta a/a = 0.1$





# PZT-4 Penny Crack

- Strain energy release rate comparison,  $G_I^M$



# **Finite Dynamic Deformations of Laminated Structures Containing PZT Laminas**

R. C. Batra and X. Q. Liang

Department of Engineering Science and Mechanics  
Virginia Polytechnic Institute and State University  
Blacksburg, VA 24061-0219

## **Abstract**

We study three-dimensional transient finite deformations of a neoHookean beam or plate with piezoelectric (PZT) patches bonded to its upper and lower surfaces. The constitutive relation for the PZT is taken to be linear in the Green-Lagrange strain tensor but quadratic in the driving voltage. The problem formulation accounts for the bending and stretching deformations of the PZTs and the substrate, and also for geometric nonlinearities. A finite element code using 8-noded brick elements, the  $2 \times 2 \times 2$  quadrature rule, a lumped mass matrix, and the central-difference method to integrate with respect to time the coupled ordinary differential equations has been developed and validated by comparing computed results with either analytical solutions or experimental observations. Both Crawley and Anderson's experiments on an unconstrained PZT plate and Moetakef et al.'s experiments on flexural waves in an aluminum beam generated by PZT patches bonded near the free end are simulated. Computed results are found to be in general agreement with test observations. The transverse velocity of a point on the surface of a neoHookean beam is not affected much by the presence of a narrow defect at the mid-span and near its centroidal axis. With PZT patches bonded to the top surface of the beam used as sensors and those affixed to the bottom surface as actuators, a simple feedback algorithm is shown to control well the vibrations of a composite cantilever plate.

# Artificial Robotic Fingers Driven by Piezoelectric Actuators

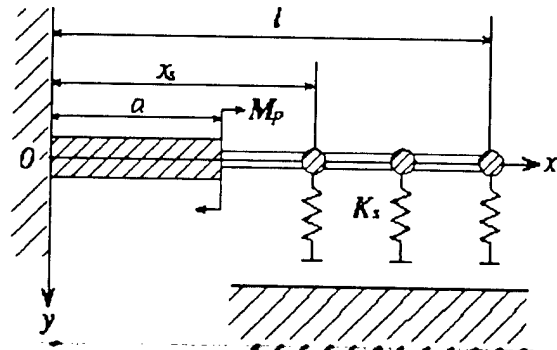
Mami Tanaka, Zhongwei Jiang and Seiji Chonan

Tohoku University, Sendai, Japan

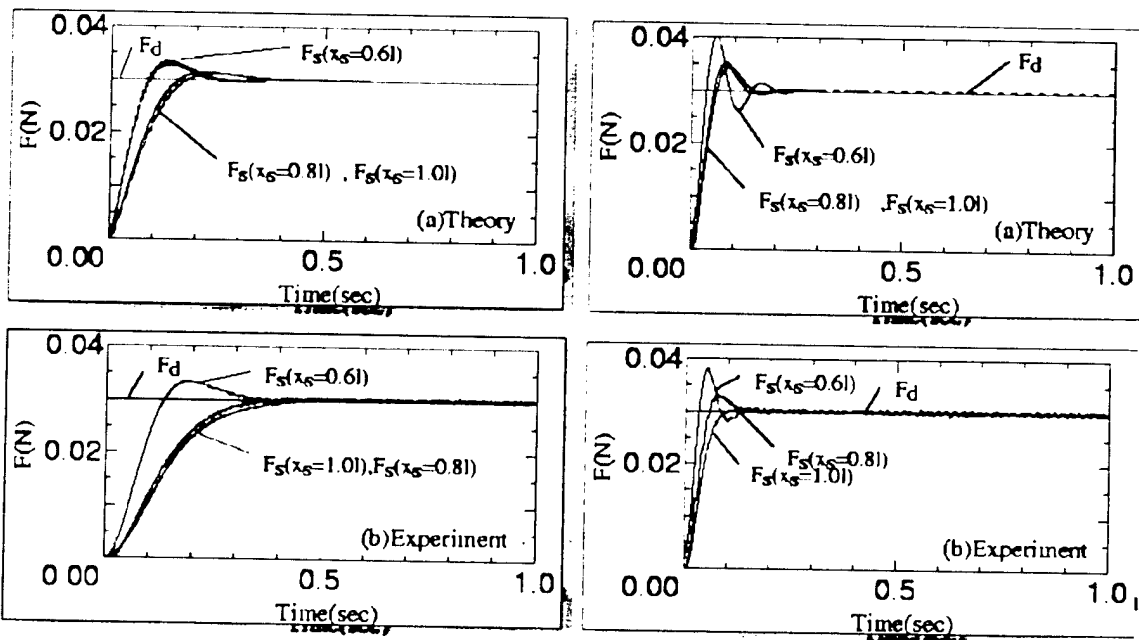
Advances in technology have accelerated the development of robotic hands that are operated in bio-engineering field. Under some circumstances, the end-effector is commanded to execute a sophisticated work such as holding a tiny fragile object without damaging it. In the grasping function of human upper extremities, the objects are mostly captured at the fingertip. However, this is not always the case. In some situations such as capturing a running insect, the target is searched and then seized at other portions of the finger. Artificial hands and fingers capable of grasping a variety of objects has been studied by several researchers.

This study presents a two problems of the flexible finger driven by piezoelectric actuators. First we concerned with the theoretical and experimental study on the force control of a miniature robotic finger that grasps an object at portions other than the fingertip. The artificial finger is a uniform flexible cantilever equipped with a distributed set of compact grasping force sensors. Control action is applied by a piezoceramic bimorph strip placed at the base of the finger. Both the PID and H infinity regulators are tested and their control behaviours are compared with each other both theoretically and experimentally. Next is a study on the hybrid position/force control of a two-fingered miniature gripper driven by piezoelectric bimorph cells. The system is composed of two flexible cantilevers and a compact force sensor attached to the tip of one finger.

## Grasping with a constant force regardless of the contact points of finger with the object



[jiang@rose.mech.tohoku.ac.jp](mailto:jiang@rose.mech.tohoku.ac.jp)



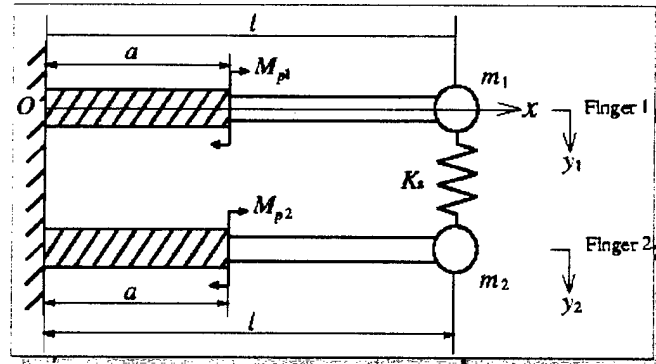
$O_s = 5\%, t_s = 0.3 \text{ sec.}$

$O_s = 10\%, t_s = 0.1 \text{ sec.}$

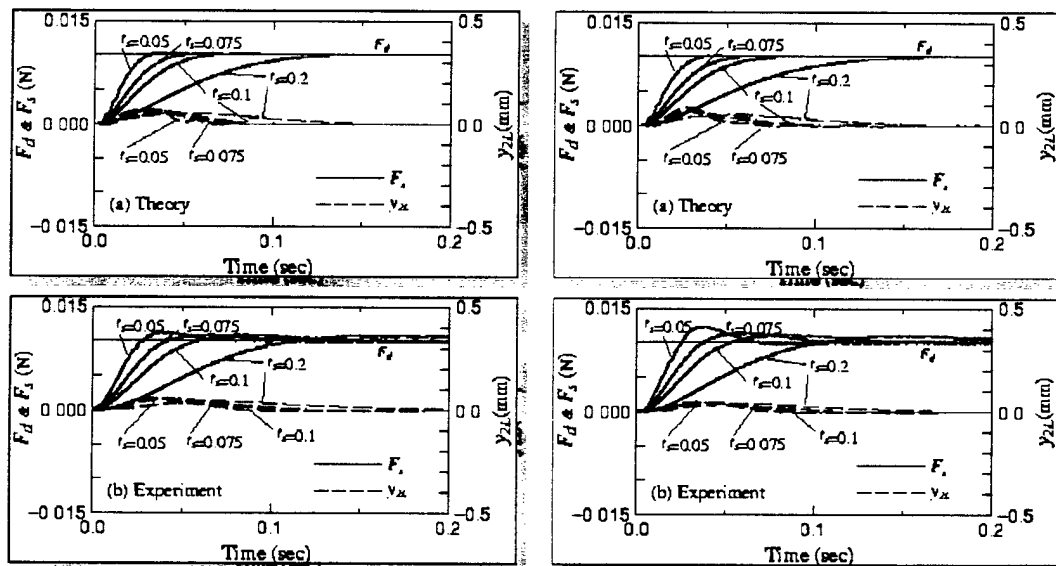
Constant grasping force control with  $H_\infty$  controller.

[jiang@rose.mech.tohoku.ac.jp](mailto:jiang@rose.mech.tohoku.ac.jp)

## Design a controller for two-finger system with object's uncertainties



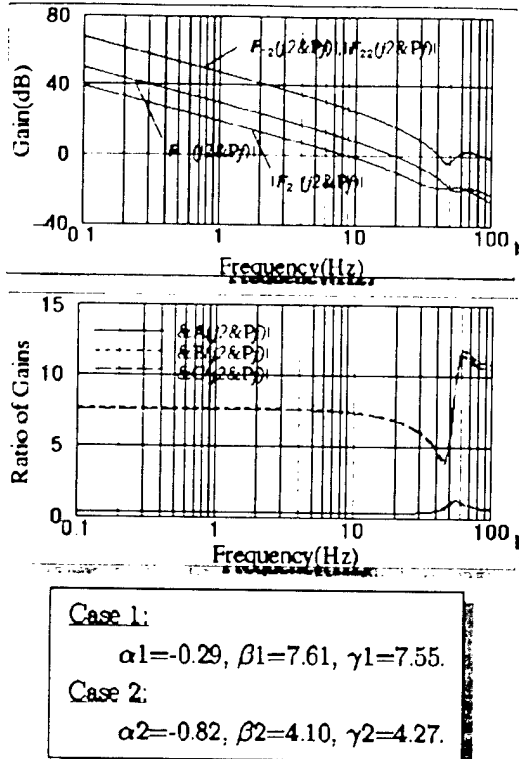
[jiang@rose.mech.tohoku.ac.jp](mailto:jiang@rose.mech.tohoku.ac.jp)



Fingertip force  $F_s$  and displacement  $y_{2L}$  with  $H_\infty$  controller.

Specifications  $O_s = 1\%$ ,  $t_s = 0.1$  sec.,  
(Tip mass in right figures is 2.5 times more than that in left)

[jiang@rose.mech.tohoku.ac.jp](mailto:jiang@rose.mech.tohoku.ac.jp)



$$M_{p1}(k) = G_p[F_d - F_s(k)]$$

$$- G_v[F_s(k) - F_s(k-1)]/T$$

$$+ \frac{1}{2}G_I \sum_{i=0}^k [2F_d - F_s(i) - F_s(i-1)]$$

$$+ \beta G_p[y_{2d} - y_{2L}(k)]$$

$$- \beta G_v[y_{2L}(k) - y_{2L}(k-1)]/T$$

$$+ \frac{1}{2}\beta G_I \sum_{i=0}^k [2y_{2d} - y_{2L}(i) - y_{2L}(i-1)]$$

$$M_{p2}(k) = \alpha G_p[F_d - F_s(k)]$$

$$- \alpha G_v[F_s(k) - F_s(k-1)]/T$$

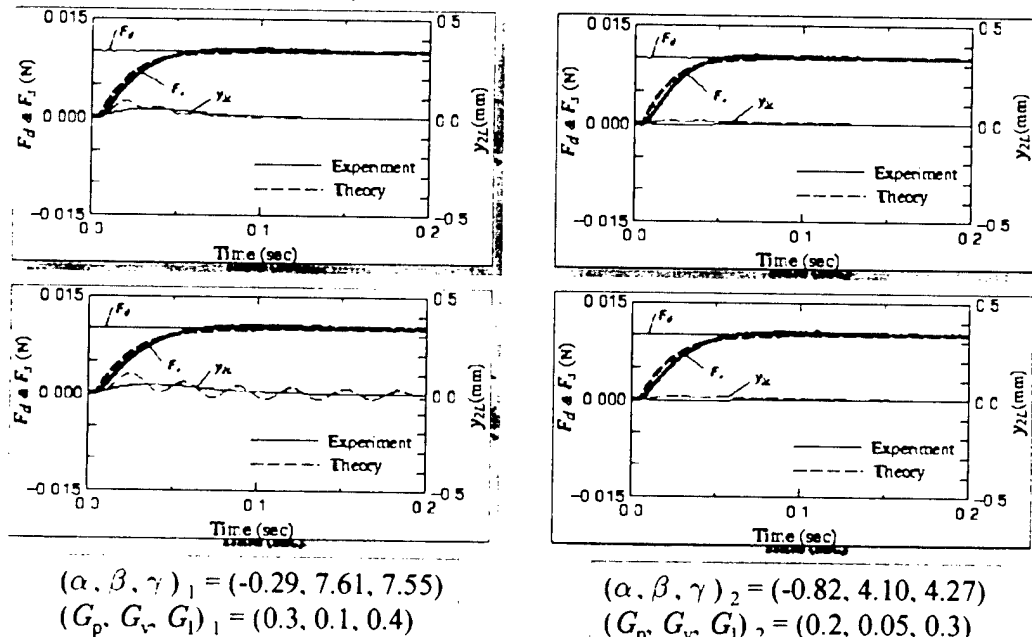
$$+ \frac{1}{2}\alpha G_I \sum_{i=0}^k [2F_d - F_s(i) - F_s(i-1)]$$

$$+ \gamma G_p[y_{2d} - y_{2L}(k)]$$

$$- \gamma G_v[y_{2L}(k) - y_{2L}(k-1)]/T$$

$$+ \frac{1}{2}\gamma G_I \sum_{i=0}^k [2y_{2d} - y_{2L}(i) - y_{2L}(i-1)]$$

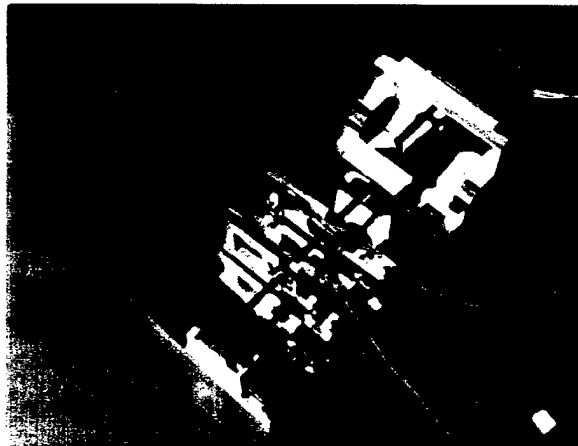
[jiang@rose.mech.tohoku.ac.jp](mailto:jiang@rose.mech.tohoku.ac.jp)



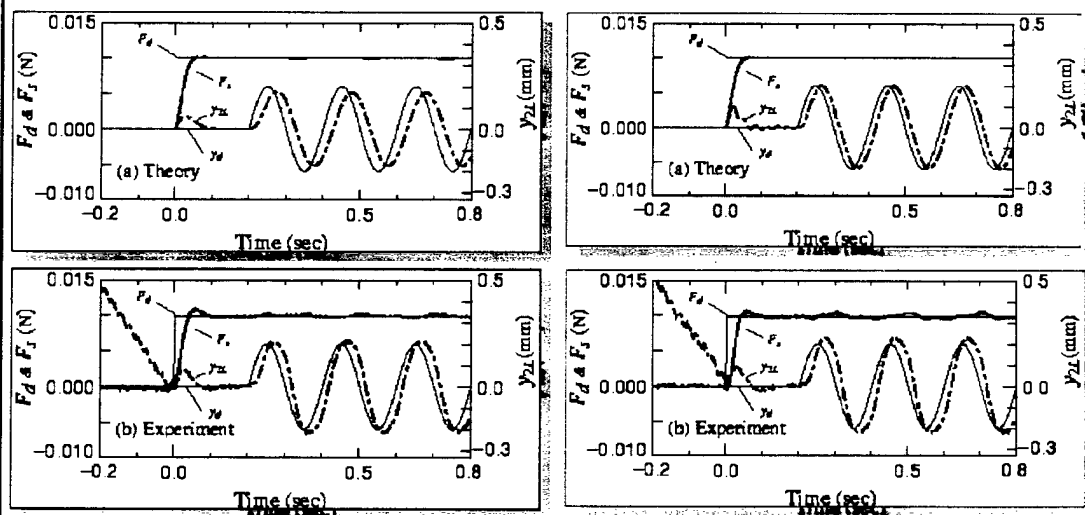
Tip force  $F_s$  and displacement  $y_{2L}$  with modified PID controller.  
(Tip mass in lower figures is 2.5 times more than that in upper.)

[jiang@rose.mech.tohoku.ac.jp](mailto:jiang@rose.mech.tohoku.ac.jp)

## Constant force Grasping during moving and positioning objects.



[jiang@rose.mech.tohoku.ac.jp](mailto:jiang@rose.mech.tohoku.ac.jp)



Keeping grasping force  $F_s$  constant while moving an object  
in a step positioning with  $H_\infty$  controller.

$O_s = 1\%$ ,  $t_s = 0.1\text{ sec.}$ ,  $y_d = 0.3\text{ mm}$ ,  $t_d = 0.2\text{ sec.}$   
(Tip mass in right figures is 2.5 times more than that in left)

[jiang@rose.mech.tohoku.ac.jp](mailto:jiang@rose.mech.tohoku.ac.jp)

## Conclusions and Future Works

- ♥ Theoretical and experimental study has been presented for the miniature gripper. It shows that Piezoelectric actuator works well to drive the gripper grasping objects at demanded condition.
- ♥ In our future works, we need develop new type soft tactile sensors, the active sensing technique, efficient signal analysis method and adaptable control algorithm

# Feedback Control with Shape Memory Alloy Actuators \*

Carrie A. Dickinson and John T. Wen

Center for Advanced Technology in Automation, Robotics & Manufacturing

Department of Electrical, Computer, and Systems Engineering

Rensselaer Polytechnic Institute

110 8th St., Troy, NY 12180

518-276-8744 (o), 518-276-4897 (fax), carrie@cat.rpi.edu, wen@cat.rpi.edu

## Abstract

*Shape memory alloy (SMA) has been considered as an actuator for applications that require large force and displacement. Two factors have hampered the usefulness of such actuators, hysteresis and bandwidth limitation. This paper considers the hysteresis phenomenon from a control perspective. Instead of using a traditional type of open loop hysteresis compensator (e.g., Preisach model), we use a closed loop approach which considers the feedback control of the force exerted by the SMA wire. By using a phase-plane type of argument and a simple lumped temperature model, we argue that proportional feedback with a suitable range of gains would render the closed loop stable. This is verified experimentally in a simple experimental setup consisting of a flexible aluminum beam with a Nitinol shape memory alloy wire load that applies a bending force to the end of the beam. When the gain is chosen too high, clear instability has been observed despite the low bandwidth of this system (about 1 Hz). We also show that stable closed loop control laws can be constructed by suitably choosing the feedback variable.*

## 1 Introduction

Shape memory alloys are those materials which have the ability to "remember" their shape even after large deformations. Once deformed at a low temperature (in a martensitic phase), SMA will remain deformed until heated. Then they return to their original shape (the austenitic phase). SMA can be used as an actuator by coupling applied thermal energy to its internal phase transformation (between austenitic and martensitic phases) which in turn generates a mechanical strain. Although large force and displacement can be realized, the effectiveness of SMA actuators is typically hampered by two factors:

1. Hysteresis: The phase transformation is a hysteretic phenomenon (similar to that of ferromagnetic materials) resulting in the output strain dependent on the history of past heat input.
2. Bandwidth Limitation: Due to the typically large heat transfer time constant, the dynamic response of an SMA actuator is very slow.

This paper addresses the hysteresis of SMA from a control perspective. Generally speaking, there are two types of approaches to deal with hysteretic nonlinearity:

1. Open Loop Compensation: Find a first-principle or phenomenological model, identify the parameters, then invert the model to remove the nonlinearity.
2. Closed Loop Feedback: Form the output error (measured output subtracting the desired output), and use the error to correct the heat input. The output may be the force applied by the SMA wire, or the position, or the strain of the structure to which the SMA wire is connected.

\*This work was supported by the Army Research Office under grant DAALO3-92-G-012. The first author is supported by a National Science Foundation Graduate Research Fellowship.

We will describe our recent work on closed loop feedback compensation of SMA hysteresis.

Because of their light weight and ability to produce large force and displacement, SMA have been used in a wide range of applications including large space structures, robotic arms, medical instruments, and surgical implants. However, systematic study of the closed loop control involving SMA has been scarce since it is assumed to be essentially a static device. Recently, a passivity based method has been used to analyze closed loop stability involving SMA [2], and a variable structure type of controller has also been successfully applied [1]. In our work, we analyze the closed loop stability using a phase-plane type of argument and also show that, in a sample-data implementation, sampling plays an important role in system performance. We have performed preliminary experiments for the feedback control using SMA. If only the load is controlled, we show stability if the wire is clamped at both ends, and instability if the wire is coupled to a flexible beam. If the beam position is used as the feedback variable, closed loop stability is again obtained.

## 2 Feedback Control of SMA

We explore the feedback control approach under several different scenarios in this section. A common approach to "linearize" an actuator that contains nonlinear dynamics is to use a tight feedback loop. In the SMA case, we feed back the difference between the measured SMA force and the desired SMA force to the current input to the SMA wire. We analyze this case both through a highly simplified model and experimentation. There are two subcases: the beam end point is fixed (i.e., the SMA alone), versus the beam end point is free (i.e., the SMA and the flexible beam). We will show that this intuitive idea of direct SMA force feedback works well for the SMA alone, but can become highly oscillatory if the SMA is coupled to the beam. Lastly, we consider the feedback from the beam strain (the beam end point measurement is not currently available).

To analyze the closed loop behavior at least qualitatively, we consider the following lumped temperature model (for the average wire temperature with convective cooling):

$$\dot{T} = -\alpha(T - T_r) + \beta u^2 \quad (1)$$

where  $\alpha$  and  $\beta$  are positive constants,  $T_r$  is the ambient temperature, and  $u$  is the commanded current through the SMA wire. The resistive heating of the wire causes the phase transformation in the SMA wire. When the wire is connected to an external mass, spring, and damper system (a one-mode approximation of the flexible beam), the phase transformation is modeled as an internal lumped displacement,  $z$ , as shown in Figure 1 (left).

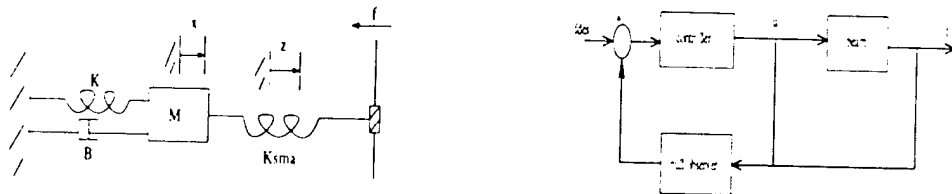


Figure 1: (left) One-mode Approximation of Flex Beam and SMA, (right) Feedback Block Diagram

The dynamical equation of the beam is

$$M\ddot{x} + B\dot{x} + Kx + K_{sma}(x - z) = 0 \quad (2)$$

with  $x$  denoting the displacement of the flexible mode and  $K_{sma}$  the stiffness of the SMA wire. The measured force is then

$$f = K_{sma}(z - x). \quad (3)$$

The internal displacement  $z$  is related to the temperature through a general hysteresis function:

$$z = \begin{cases} g_u(T), & \text{if } \dot{T} > 0 \\ g_d(T), & \text{if } \dot{T} < 0 \end{cases} \quad (4)$$

where  $g_u$  and  $g_d$  are two scalar monotonically increasing functions with  $g_u$  lying strictly below  $g_d$  for the same range of  $T$ .

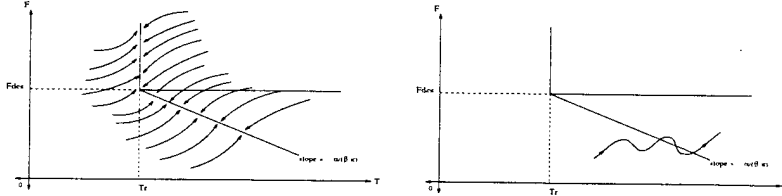


Figure 2: Qualitative Phase Plane Trajectory: (left) Beam Tip Fixed, (right) Beam Tip Free

We first consider the tip of the beam held fixed. In this case,  $x = 0$  and  $f = K_{sma}z$ . Now consider a simple proportional measured force feedback (see Figure 1 (right)):

$$u^2 = \begin{cases} 0, & \text{if } f > f_{des} \\ k|f - f_{des}|, & \text{if } f < f_{des} \end{cases} \quad (5)$$

where  $f_{des}$  is the desired force in the wire.

To analyze the closed loop behavior, we divide the problem into the following cases:

- Case 1:  $(f > f_{des}) \Rightarrow u = 0 \Rightarrow T \rightarrow T_r: T(t) = e^{-\alpha t}[T(0) - T_r] + T_r \Rightarrow$

$$f = \begin{cases} K_{sma}g_d(T), & \text{if } T(0) > T_r \\ K_{sma}g_u(T), & \text{if } T(0) < T_r \end{cases} \quad (6)$$

- Case 2:  $(f < f_{des}) \Rightarrow$

$$\dot{T} = -\alpha(T - T_r) + \beta k |f - f_{des}|. \quad (7)$$

Subcase 1:  $T > T_r$  and  $|f - f_{des}| > \frac{\alpha}{\beta k}(T - T_r) \Rightarrow \dot{T} > 0 \Rightarrow f = K_{sma}g_u(T)$ .

Subcase 2:  $T > T_r$  and  $|f - f_{des}| < \frac{\alpha}{\beta k}(T - T_r) \Rightarrow \dot{T} < 0 \Rightarrow f = K_{sma}g_d(T)$ .

Subcase 3:  $T < T_r \Rightarrow \dot{T} > 0 \Rightarrow f = K_{sma}g_u(T)$ .

Figure 2 (left) summarizes the above cases qualitatively in the  $T$ - $f$  plane. The following conclusions can be drawn from this figure:

1. Under the usual operating condition,  $T > T_r$ . In this case,  $f$  tends to the line  $|f - f_{des}| = \frac{\alpha}{\beta k}(T - T_r)$  asymptotically. This implies that, ideally, the closed loop system is stable with the steady state error varying monotonically with  $\frac{\alpha}{\beta k}$ .
2. If sampling is not considered, then the entire subspace,  $|f - f_{des}| = \frac{\alpha}{\beta k}(T - T_r)$ , consists of equilibria. With sampling, one would expect limit cycle type of behavior around the line segment with the amplitude of the oscillation increasing with increasing feedback gain,  $k$ .

When the same proportional force feedback controller is applied to the moving beam case, a very different behavior is observed. In this case, our model consists of the complete set of equations (1) through (5). For  $f > f_{des}$ , the same situation as before exists (decreasing temperature and force) since the controller is turned off. For  $f < f_{des}$  and  $|f - f_{des}| < \frac{\alpha}{\beta k}(T - T_r)$ , the temperature (and therefore force) continues to decrease. For  $|f - f_{des}| > \frac{\alpha}{\beta k}(T - T_r)$ , the temperature increases, causing  $z$  and then  $x$  to increase. However, increasing  $x$  would cause  $f$  to decrease, increasing the force error feedback. This would then result in a trajectory as shown in Figure 2 (right). Depending on the gain, an unstable behavior could result.

For the case of SMA coupling to a beam, we modify the feedback to servo on the beam deflection. The control law can then be changed to

$$u^2 = \begin{cases} 0, & \text{if } x > x_{des} \\ k|x - x_{des}|, & \text{if } x < x_{des} \end{cases} \quad (8)$$

where  $x_{des}$  is the desired deflection of the beam. In the experiments, a strain feedback is used instead of the deflection feedback (since the beam end point measurement is not available). The closed loop behavior can now be analyzed in a manner similar to the first case by considering trajectories in the  $T$ - $x$  plane. If  $x > x_{des}$ , there is no control, the temperature would decrease causing  $z$  and then  $x$  to decrease. If  $|x - x_{des}| < \frac{\alpha}{\beta k}(T - T_r)$ , temperature still decreases, so  $x$  would decrease toward the  $|x - x_{des}| = \frac{\alpha}{\beta k}(T - T_r)$  subspace. If  $|x - x_{des}| > \frac{\alpha}{\beta k}(T - T_r)$ , temperature would increase, causing  $z$  to increase. This in turn would cause  $x$  to increase toward  $x_{des}$ . Depending on the gain selected, this increase may be monotonic or oscillatory. Therefore, we expect closed loop behavior similar to the first case with large steady state error in the low gain case, reduced steady state error with increased gain, and oscillations about the  $|x - x_{des}| = \frac{\alpha}{\beta k}(T - T_r)$  subspace for very large gains.

### 3 Experimental Results

Figure 3 is an outline of the physical single flexible link testbed. The central component is a flexible beam which is chosen to provide readily measurable flexibility in the horizontal plane that is independent of gravity (ideally). This beam is driven by three types of actuators: a DC motor at the hub, two sets of piezoceramic patches approximately colocated with the outer two strain gauges, and a Nitinol SMA wire muscle attached between the hub and the free end of the beam. The real-time computer is a networked set of four Inmos Transputer micro-processors which are connected to a PC host for software development and user interface. These Transputers also connect to a VME bus on which resides the digital to analog (D/A) and analog to digital (A/D) boards providing the actuator and sensor interfaces. The SMA wires consist of 0.008" thick Nitinol wires, approximately 1.09m long. These are Flexinol wires made by Dynalloy with a characteristic transition temperature given as 90°C and a maximum pull force of 590g approximately. The ambient room temperature for the SMA experiments was 20°C approximately.

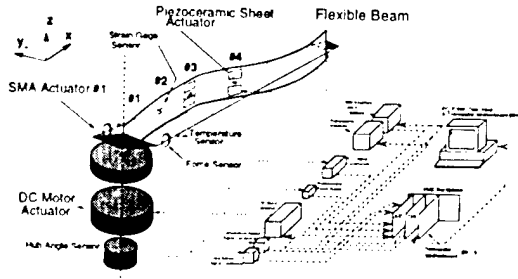


Figure 3: Experimental Testbed Schematic

The qualitative analysis developed in Section 2 has been implemented on the one-link flexible beam testbed. For these experiments, the hub motor and piezoelectric patches were not used (i.e., they were turned off). The SMA wire was connected between the hub end and the free end of the flexible beam. A load cell was attached to the SMA wire to measure the wire force. The strain gauges on the beam were used to measure the strain. The SMA temperature was measured with a thermocouple attached to the wire.

For the first set of experiments, the free end of the flexible beam was held fixed. The controller described by equation (5) was used with  $f_{des} = 50mg$ . Various values of the control gain,  $k$ , were chosen. In Figure 4, the experimental plots of the measured force versus time are shown for feedback gains of  $k = 25, 100$ , and  $300$ . The closed loop sampling rate was 4 Hz. In the low gain case, there was a large steady state error in the force-time plot. When the gain was increased, the steady state error reduced considerably. In the very high gain case, oscillation (about 1Hz) about the desired force occurred. Also, the force-temperature plots behaved as expected. However, the plots were omitted from this paper due to space limitations.

The sampling rate plays an important role to the closed loop response. For example, in the  $k = 300$  case (see Figure 5), when the sampling frequency was increased to 8Hz, 16Hz, and 24Hz, respectively, the overshoot of the measured force was reduced and the steady state oscillations were reduced in amplitude in each case.

Next, the experiments were run with the beam tip free. Again, the desired force was 50mg, and the same feedback control law was used. The behavior described for this case has indeed been observed experimentally as

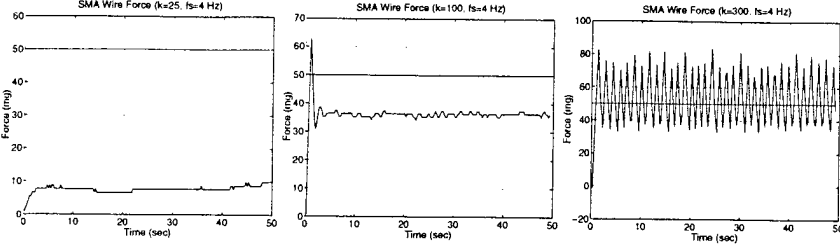


Figure 4: Force Responses: Beam Tip Fixed ( $k = 25, 100, 300$ )

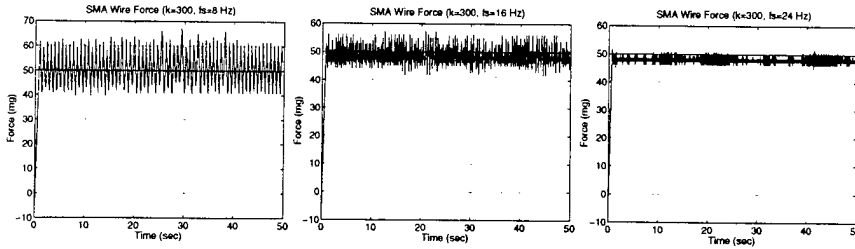


Figure 5: Effect of Higher Sampling on Force Responses ( $f_s = 8 \text{ Hz}, 16 \text{ Hz}, 24 \text{ Hz}$ )

shown in Figure 6 (left). For  $k = 75$ , which would give a stable response in the fixed end point case, now exhibits an unstable behavior.

Finally, the experiments were run for the case of the beam tip free with strain as the feedback variable. The desired beam strain was chosen to be  $25\mu\text{strain}$  with the strain gauges providing the strain measurements. Figure 7 shows the strain responses for  $k = 100, 200$ , and  $500$ . As expected, the closed loop behavior was similar to the force feedback case with beam tip fixed. There was a large steady-state error in the low gain case, reduced steady-state error with increased gain, and oscillations for very high gain.

The sampling rate again plays an important role in the closed loop response. As can be seen in Figure 8, when the sampling frequency was  $8\text{Hz}$ ,  $16\text{Hz}$ , and  $24\text{Hz}$  with  $k = 500$ , the amplitude of the steady state oscillation and the overshoot were reduced.

Some additional controllers have also been implemented experimentally. One such controller was a variation of the beam strain feedback controller given by:

$$u^2 = \begin{cases} 0, & \text{if } x > x_{des} - \epsilon \\ k, & \text{if } x < x_{des} - \epsilon \end{cases} \quad (9)$$

where  $\epsilon$  is a small number and  $k$  is sufficiently large (both chosen by the designer). Figure 6 (right) was produced using this controller with  $\epsilon = 0.01$ ,  $k = 4000$ , and a sampling frequency of  $60 \text{ Hz}$ .

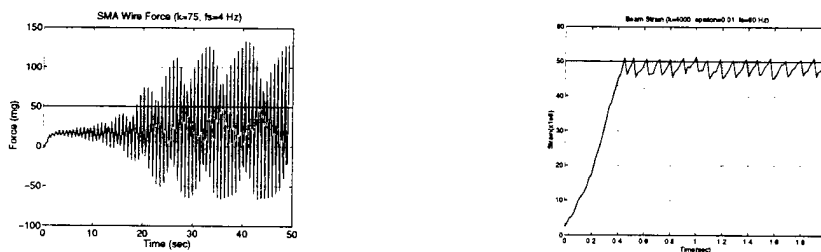


Figure 6: (left) Force Response: Beam Tip Free, (right) Strain Response: Constant Step Controller

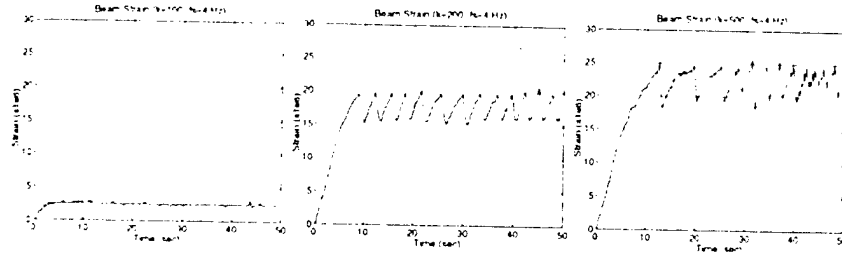


Figure 7: Strain Responses: Proportional Beam Strain Feedback ( $k = 100, 200, 500$ )

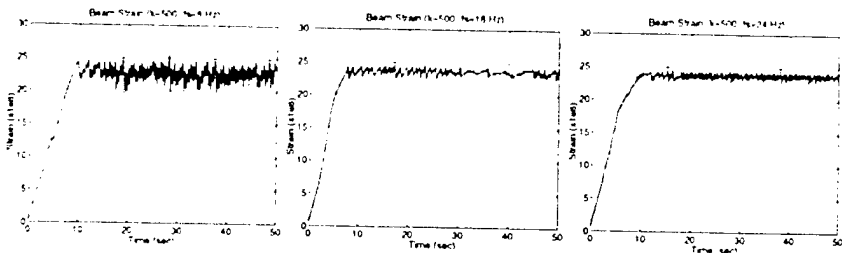


Figure 8: Effect of Higher Sampling on Strain Responses ( $f_s = 8 \text{ Hz}, 16 \text{ Hz}, 24 \text{ Hz}$ )

## 4 Conclusion and Future Work

SMA is an important material for smart structures because of its ability to operate at high temperatures, its light weight, and its ability to produce relatively large force and displacement. This paper addresses the closed loop feedback control approach for SMA.

We used a simple lumped temperature, 1-D constitutive model to qualitatively analyze the closed loop stability of SMA. In the case of SMA force feedback, the closed loop system is stable if the SMA is connected to fixed ends but unstable if connected to a flexible beam. For the case of SMA coupling to an elastic beam, a stable closed loop control law can be constructed by using the beam strain feedback instead of the SMA force feedback. We have performed preliminary experiments that verify this qualitative analysis.

We are currently working on a more detailed model to describe the SMA hysteresis and the stability analysis. One such model that may be appropriate has been developed by Lagoudas, et. al., [3] which takes both temperature and strain into account for the SMA hysteresis. We will also be implementing different controllers to see if we can produce a better response. Also, a second SMA wire will be added to the flexible beam system to act as an opposing force for the first SMA wire (instead of the flexible beam).

## References

- [1] Danny Grant and Vincent Hayward. Controller for a high strain shape memory alloy actuator: Quenching of limit cycles. In *Robotics and Automation Conference*, pages 254–259, 1997.
- [2] Daniel R. Madill and David Wang. The modelling and  $L_2$ -stability of a shape memory alloy position control system. In *Robotics and Automation Conference*, pages 293–299, 1994.
- [3] Gongming Xu, Dimitris C. Lagoudas, John T. Wen, and Declan Hughes. Thermo-electro-mechanical modeling and structural response of a flexible beam with external sma actuators. In *Proceedings of the 1995 Mathematics and Control in Smart Structures Conference*, pages 503–515, San Diego, CA, February 1995.

## MEMS and MOME Sensors and Actuators - Design, Fabrication and Networking

Michael B. Miller  
F&S, Inc.  
2801 Commerce Street  
Blacksburg, VA 24060  
mmiller@f-s.com

MEMS technology offers the ability to implement local and independent sensing and actuation functions through the coordinated response of discrete micro-electro-mechanical "basis function" elements. Substantial research efforts during the past ten years have focused on the implementation of MEMS devices capable of linear and rotational displacements, and the incorporation of such devices into early commercial products, notably diaphragm-based micro-accelerometers for automotive air-bag deployment systems. The realization of other MEMS-based systems now depends largely on the development of alternative materials fabrication methods, the interconnection of discrete MEMS "basis function" elements into more complex functional systems, and the investigation of potential dual-use military and commercial applications that such fabrication and interconnection methods may allow. Multiplexed sensor and actuator arrays have immediate applications in industrial control systems and process monitoring in electrical power generation facilities, chemical plants, petroleum processing plants, and food preparation plants. A schematic of a MEMS sensor network is shown in Figure 1.

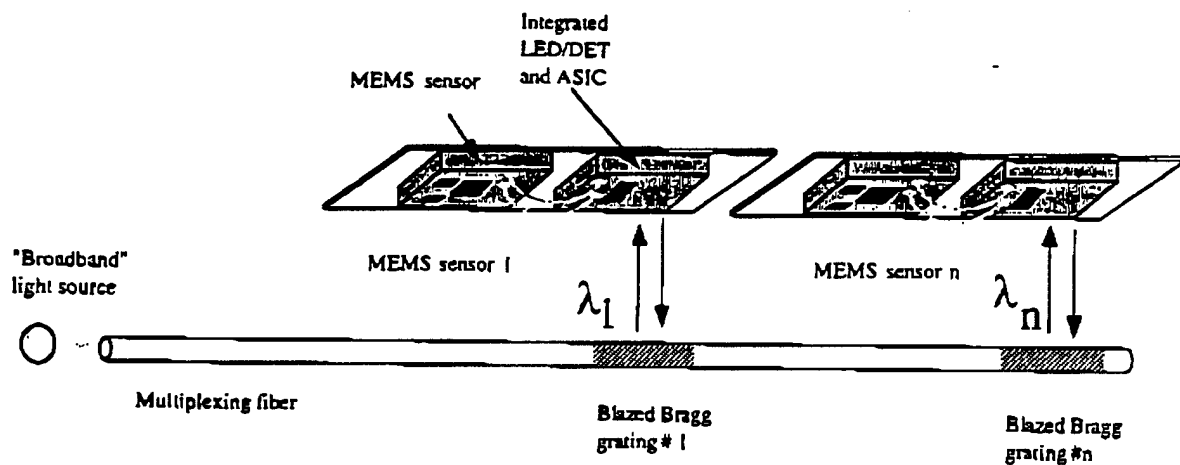


Figure 1. MEMS Sensors Interconnected Using Blazed Bragg Grating Couplers

A summary of recent work accomplished through cooperative efforts between F&S, Inc., FEORC, and others is presented.

## Soft Lithography and Smart Materials

George M. Whitesides  
Department of Chemistry and Chemical Biology  
Harvard University  
12 Oxford Street  
Cambridge MA 02138  
Tel: 617 495 9430  
Fax: 617 495 9857  
E-mail gwhitesides@gmwgroup.harvard.edu

### Abstract

This program is developing unconventional methods and materials applicable to the formation of smart structures:

Soft lithography: One component is concerned with unconventional approaches to the formation of microstructures involving non-photolithography pattern formation. This work includes a range of techniques involving contact pattern transfer methods: microcontact printing, micromolding, and conformal phase-shift lithography. Some of these techniques can be used to form structures that can be used for actuation and sensing from previous difficult-to-access materials such as glassy carbon.

New materials: The second component develops new materials, especially elastomers and materials derived from organic polymers, for potential use in smart structures.

The project is a science-based project, and has an exploratory focus; its output is integrated with other efforts in engineering to produce components for smart structures.

## SMART TRIM PANEL USING MEMS SENSORS IN THE TIME DOMAIN

V. K. Varadan, X. L. Bao and V. V. Varadan

Research Center for the Engineering of Electronic and Acoustic Materials and Devices  
The Pennsylvania State University  
University Park, PA 16802  
Tel: (814) 863-4210  
Fax: (814) 863-7967 or (814) 865-3052  
E-mail: vjvesm@engr.psu.edu

### ABSTRACT

Active control of noise inside an enclosure from exterior noise sources is accomplished by the use of piezoelectric actuators and either piezoelectric or MEMS sensors placed on the enclosure wall. It is generally known that this approach provides very good results at the resonant frequencies of the cabin walls and if the excitation noise is at a single frequency. In the present study, we look at broadband excitation from the exterior, in the time domain. A MEMS sensor mounted on the cabin wall provides the reference signal for the excitation, the error sensor can either be a MEMS sensor on the wall or a sound level meter placed at an appropriate position inside the cabin. Different types of closed loop control are attempted using both analog and digital strategies. The study examines the number and placement of actuators on the wall relative to bandwidth of the external source as well as control of wall vibration as a means of controlling the radiated noise. The results on a cylindrical scale model (smart trim panel) will be presented.

# **Smart Trim Panels using MEMS Sensors for Interior Noise Suppression**

**V.V. Varadan V.K. Varadan and X.L. Bao**

**Research Center for the Engineering of Electronic and  
Acoustic Materials  
Department of Engineering Science & Mechanics  
Penn State University**

**PENNSTATE**



*Research Center for the Engineering of Electronic and Acoustic Materials*



## People

**Xiao Ling Bao ( Research Associate)**

**Young Hun Lim (Graduate Student)**

**Jianna Wang (Graduate Student)**

**Pietro Porco (Undergraduate Student)**

**Aric Levinthal (Undergraduate Student)**  
KARTIK RAMANATHAN (GRADUATE STUDENT)

# Active Trim Panel Vibration Control for Interior Noise Suppression

1. Piezoceramic chips are employed as actuators bonded on trim panel for interior noise suppression. Experimental results show it is effective for suppressing interior noise related to the primary and symmetrical resonance modes of trim panel.
2. MEMS or Accelerometer is colocated on actuator to provide error signal for control systems. These results are compared to those obtained using interior microphone as error signal sensor.
3. Adaptive digital noise control system is setup for single frequency or band noise suppression. The results are compared with the results from analog control system.

## Scope of Research

- Interior Cabin Noise Control using a Discrete Number of Piezolectric Actuators and Co-Located MEMS sensors
- Optimal design of Control System by Numerical Simulation and Experimentation
- Development and Applications of ElectroPolymer Large Displacement Actuators
- Multichannel DSP with MIMO
- Transition Noise Control Experiments to more realistic cabin



## Active Cabin Noise Control

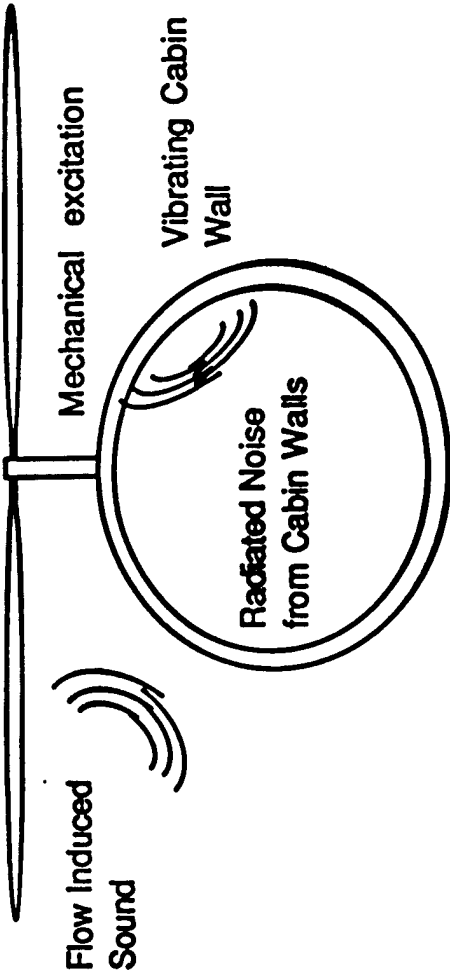
- Purpose
  - Actively Reduce Noise inside a Rotorcraft Cabin.

- Approach

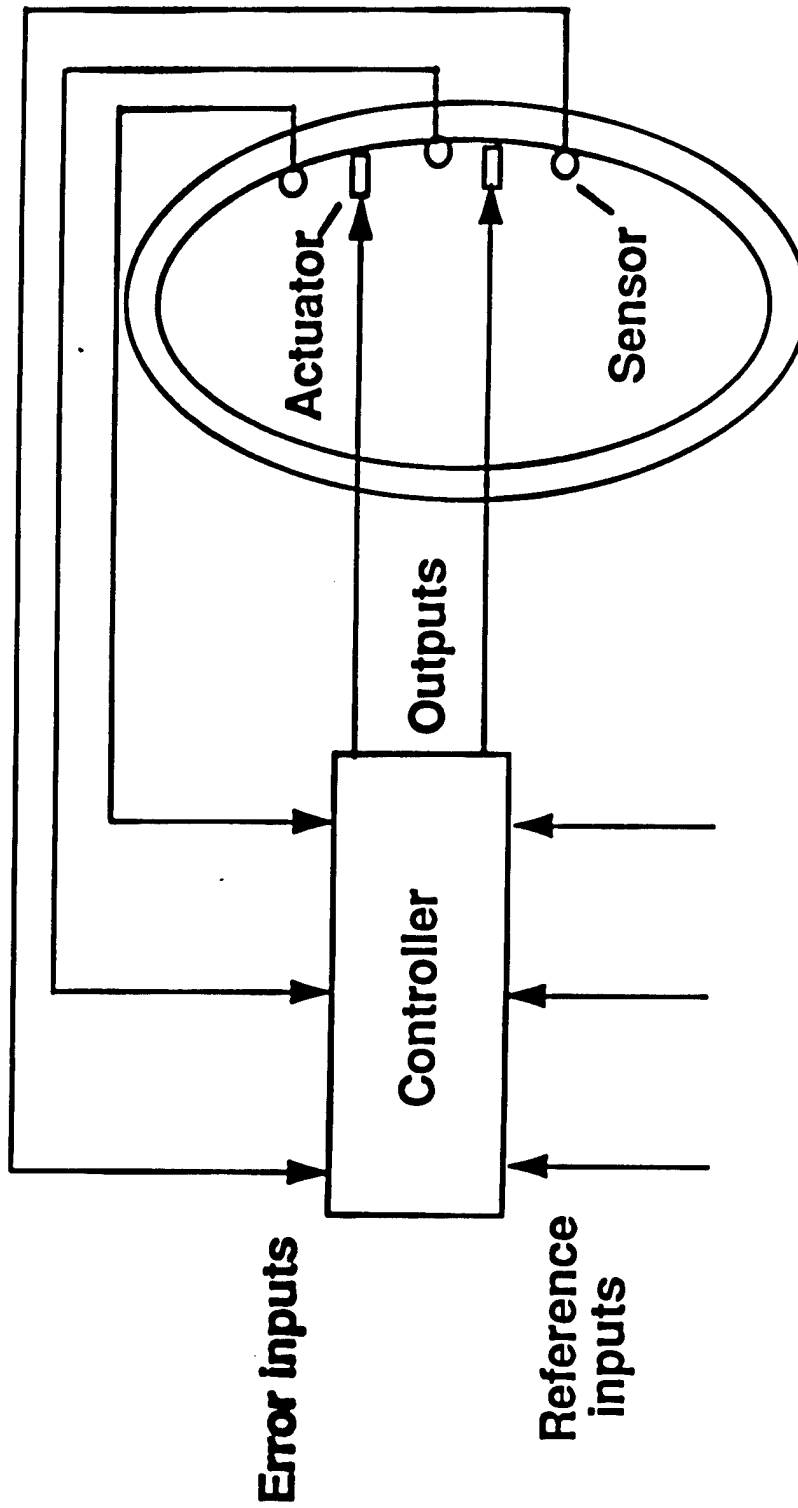
Control the vibration of the walls of the cabin.

Most of the noise interior to the cabin is created by the vibrating walls of the cabin, which may be excited by

- a. the mechanical devices connected to the cabin and
- b. the flow induced noise from rotating blades



## Active Vibration Control



Structure

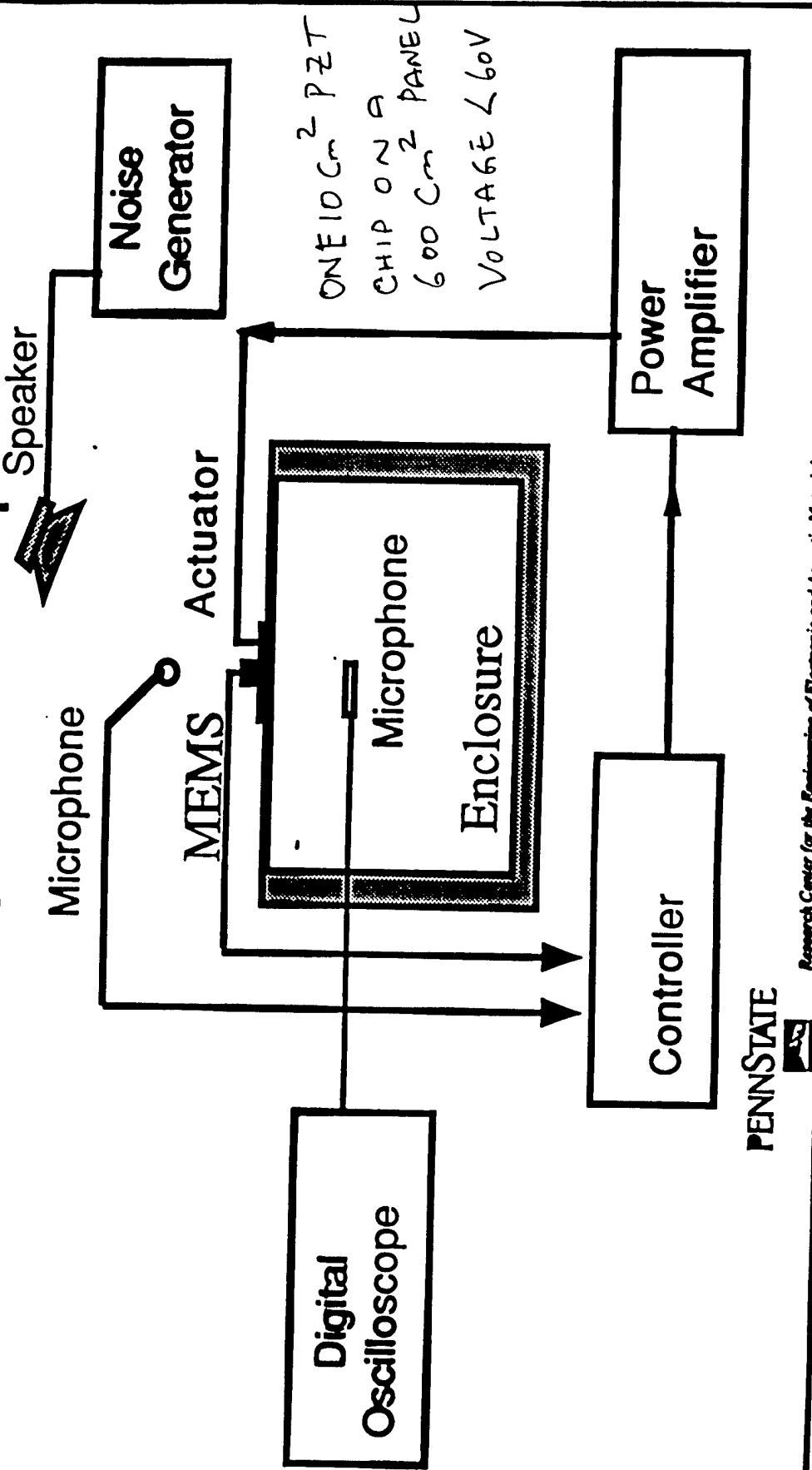
Schematic diagram of feed-forward active vibration control

# Experiments for Interior Noise Suppression

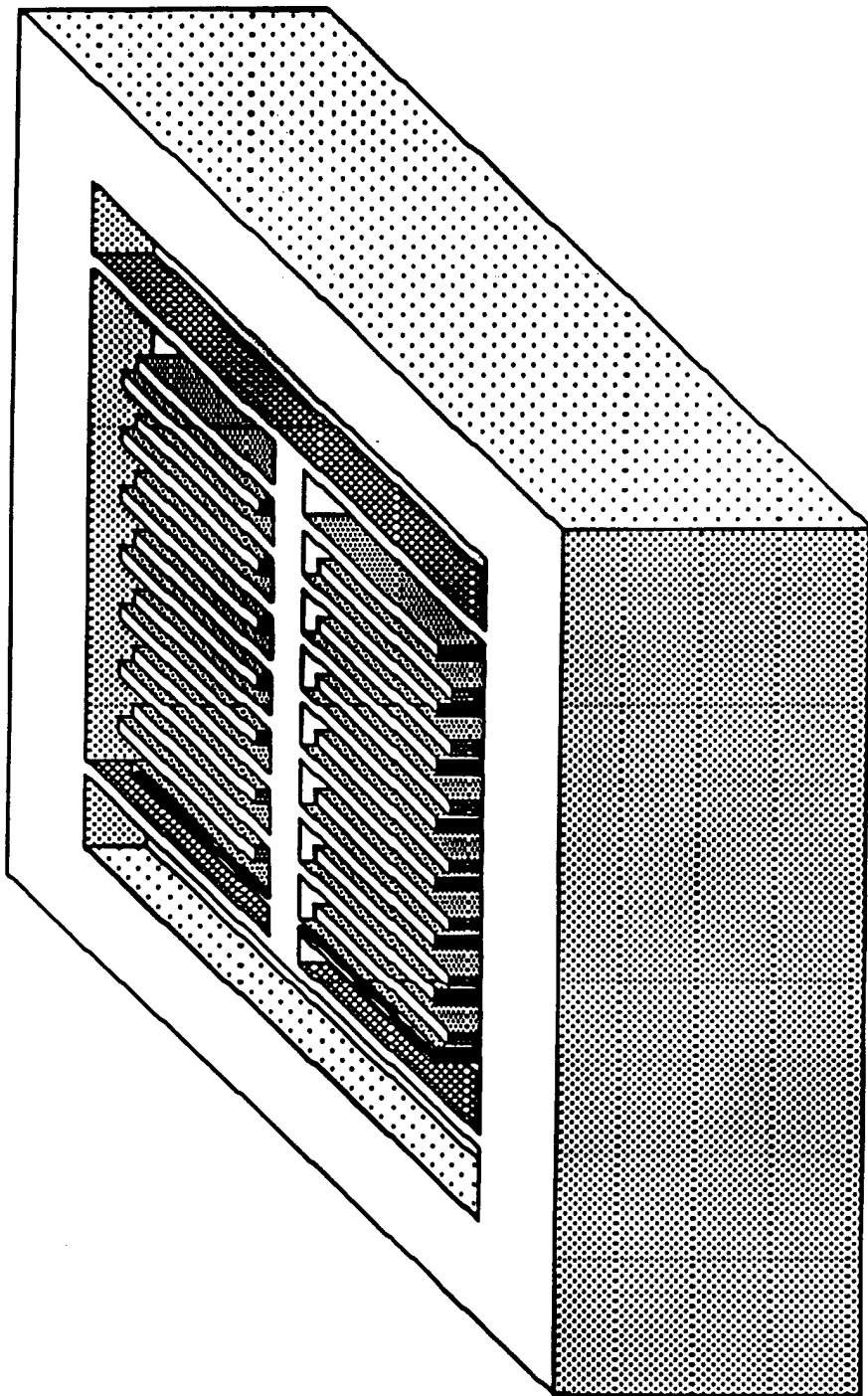
1. One channel & two channel analog active noise control systems are setup for experimentation.
2. Piezoceramic chips are employed as the actuators to suppress the primary resonance modes of the plate.
3. MEMS sensor is colocated on actuator to provide error signal for control systems.

# Single Channel Noise Control System:

## Experiment Setup



**MEMS**

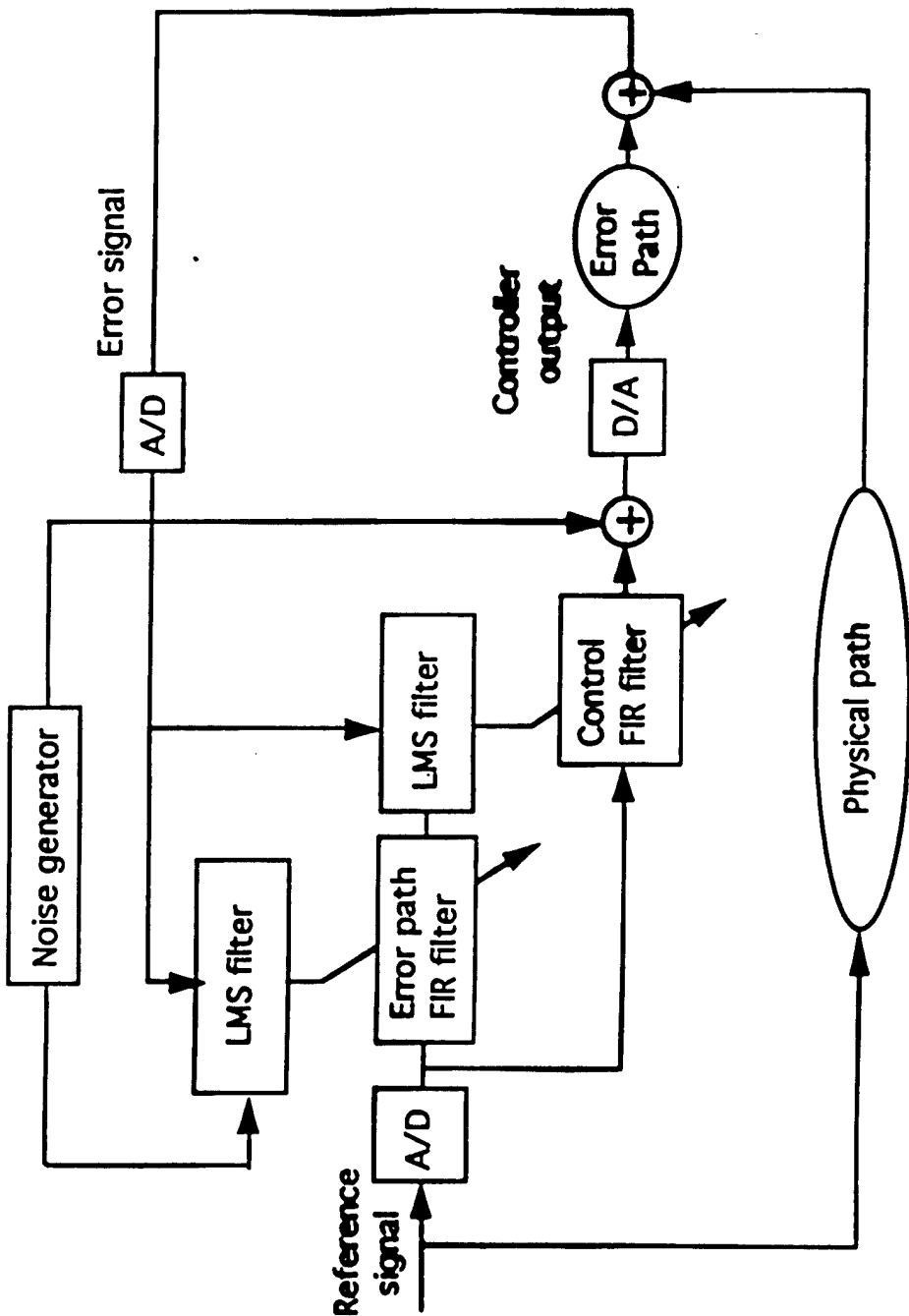


**PENNSTATE**



Research Center for the Engineering of Electronic and  
Acoustic Materials

# Single Channel DSP Control System with Filtered-X LMS Algorithm



## DSP System Adjustment and Test

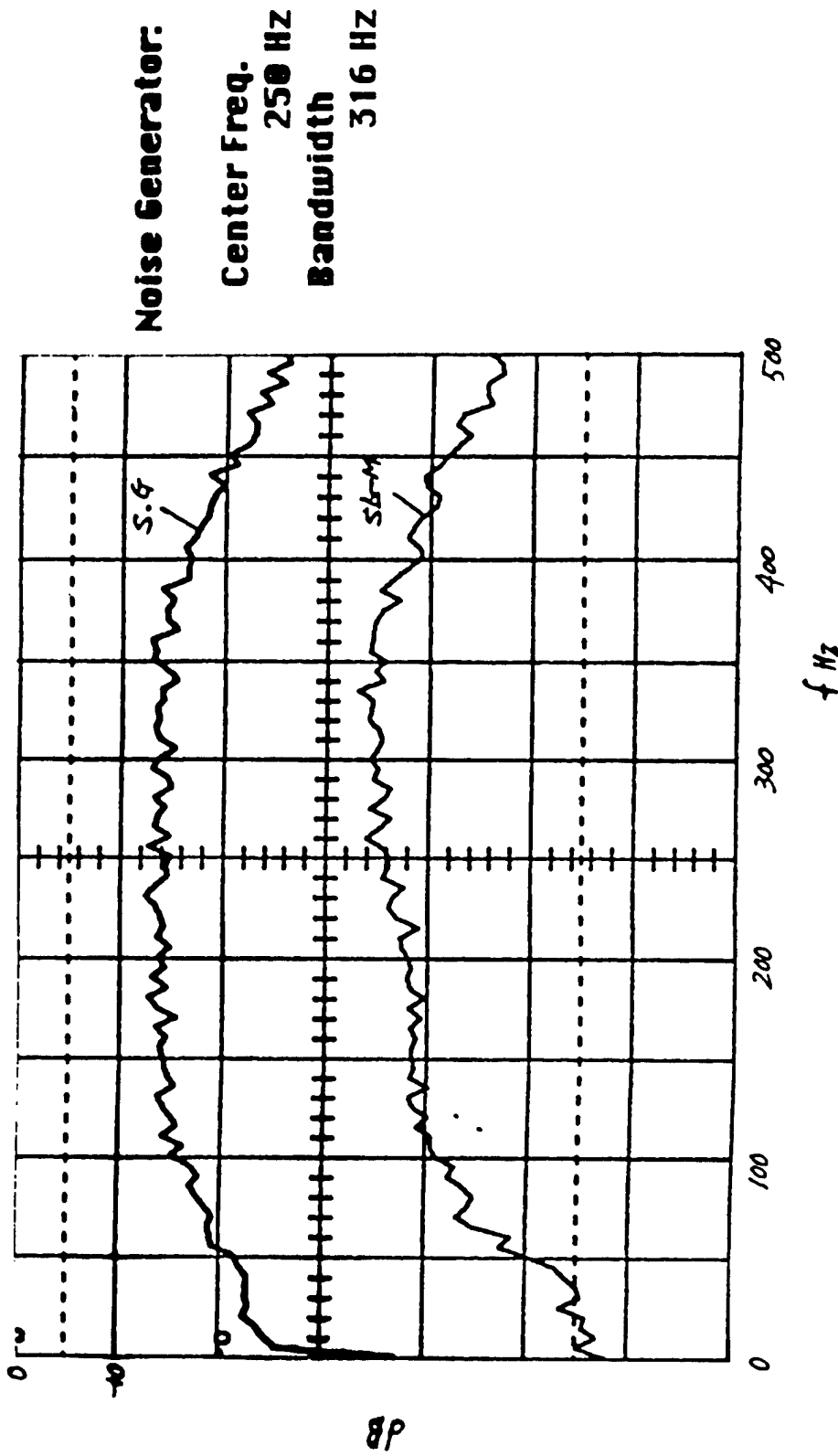
1. Parameter adjustment include:  
Number of filter coefficient; convergence factors;  
sampling rate.
2. Method for error path estimation:  
On-line and off-line estimation methods are set and tested
3. Signal generator or SL-meter employed as reference signal source.
4. MEMS or accelerometer bonded on trim panel employed as error signal sensor
5. Microphone inside the enclosure employed as error signal sensor

PENNSTATE

Research Center for the Engineering of Electronic and Acoustic Materials

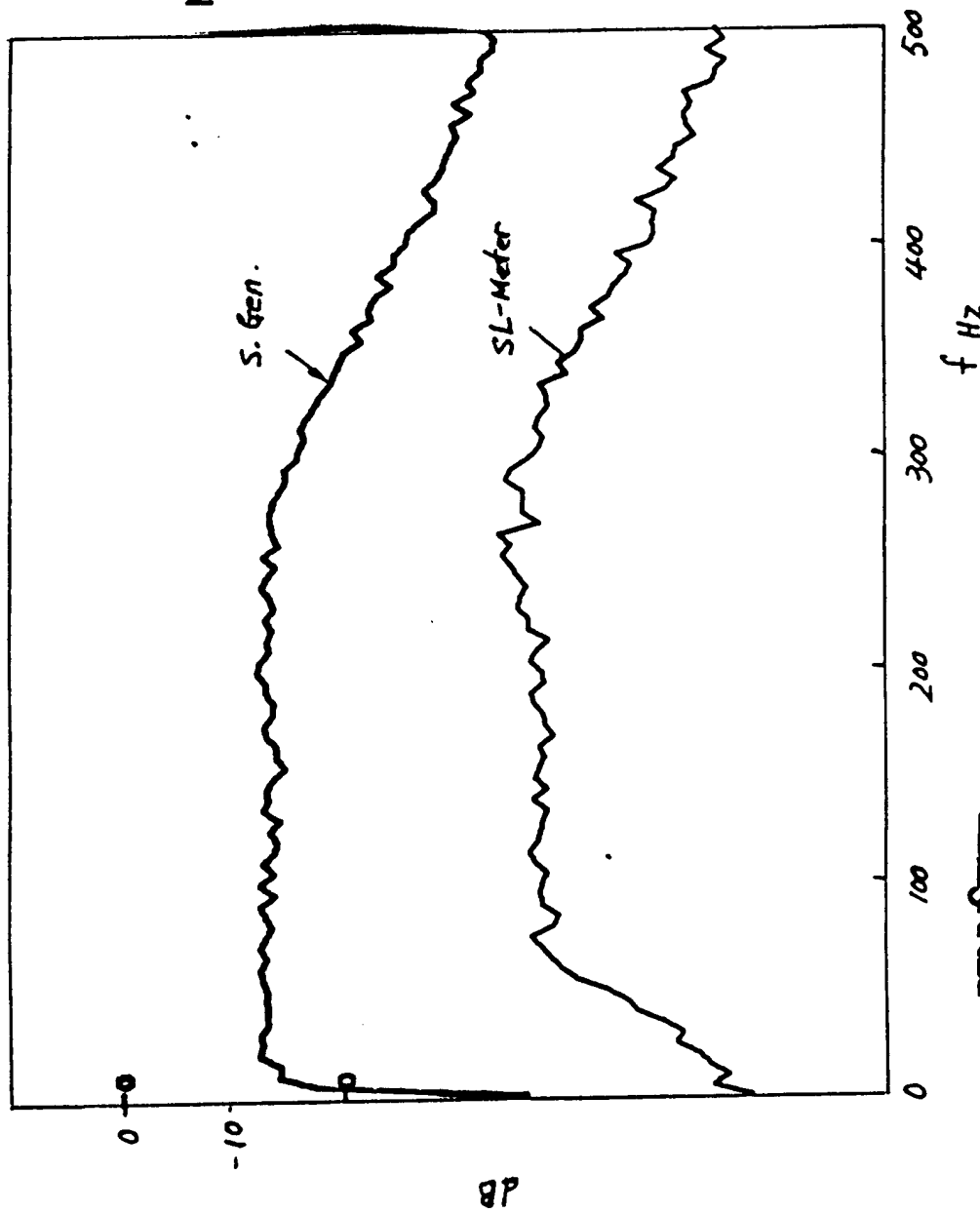
# Experimental Results

## Noise Spectrum From Signal Generator & SL-Meter



# Experimental Results

## Noise Spectrum From Signal Generator & SL-Meter



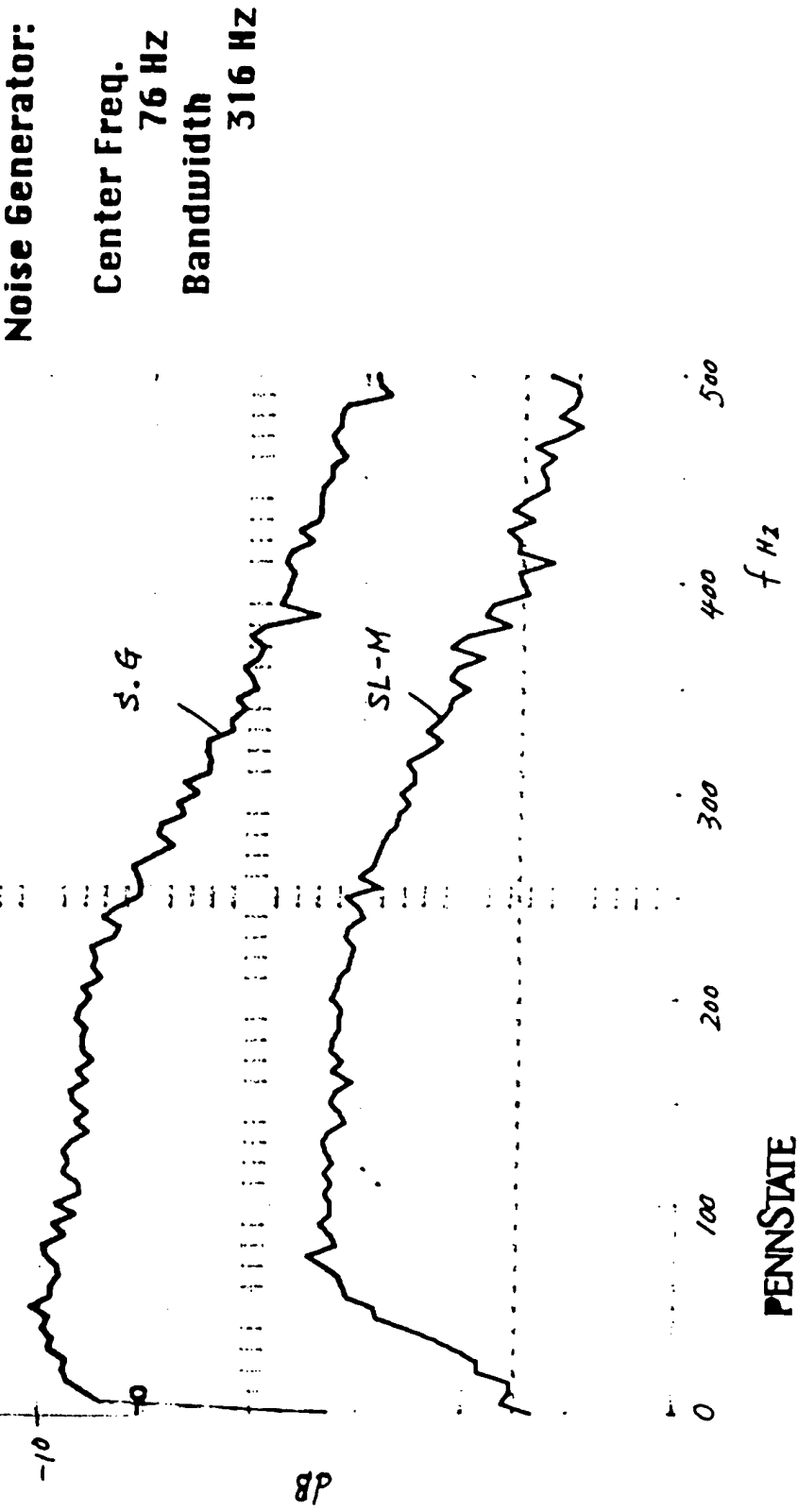
PENNSTATE



Research Center for the Engineering of Electronic and Acoustic Materials

# Experimental Results

## Noise Spectrum From Signal Generator & SL-Meter



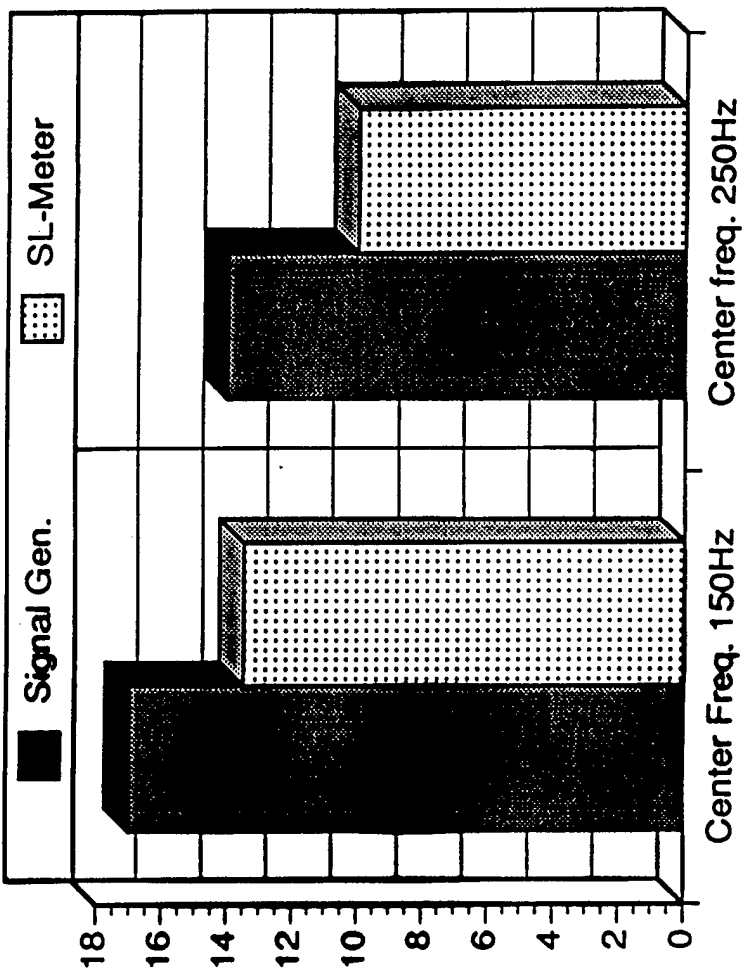
PENNSTATE



Research Center for the Engineering of Electronic and Acoustic Materials

# Experimental Results

## DSP – Interior Noise Reduction (Test A: Ref. Signal from SL-Meter or from Signal Generator)



### Error Sensor:

Interior  
Microphone

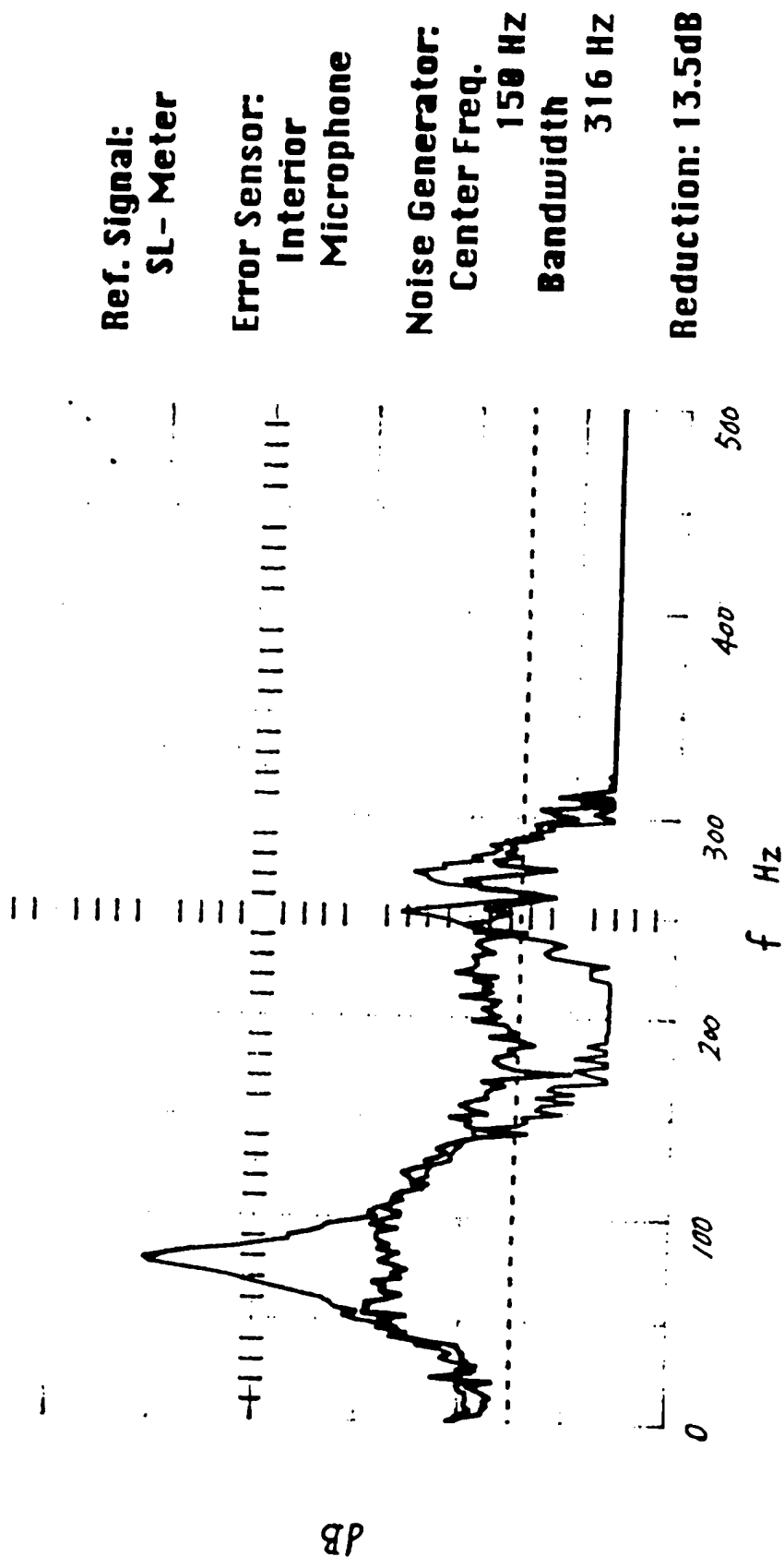
**Noise Generator:**  
Center Freq.  
150 or 250 Hz  
Bandwidth  
316 Hz

### Reduction:

**SL-Meter:**  
13.5 – 10.0 dB  
**Signal Gen.:**  
17.0 – 14.0 dB

# Experimental Results

## DSP - Interior Noise Reduction (Test A: Ref. Signal from SL-Meter or from Signal Generator)



PENNSTATE

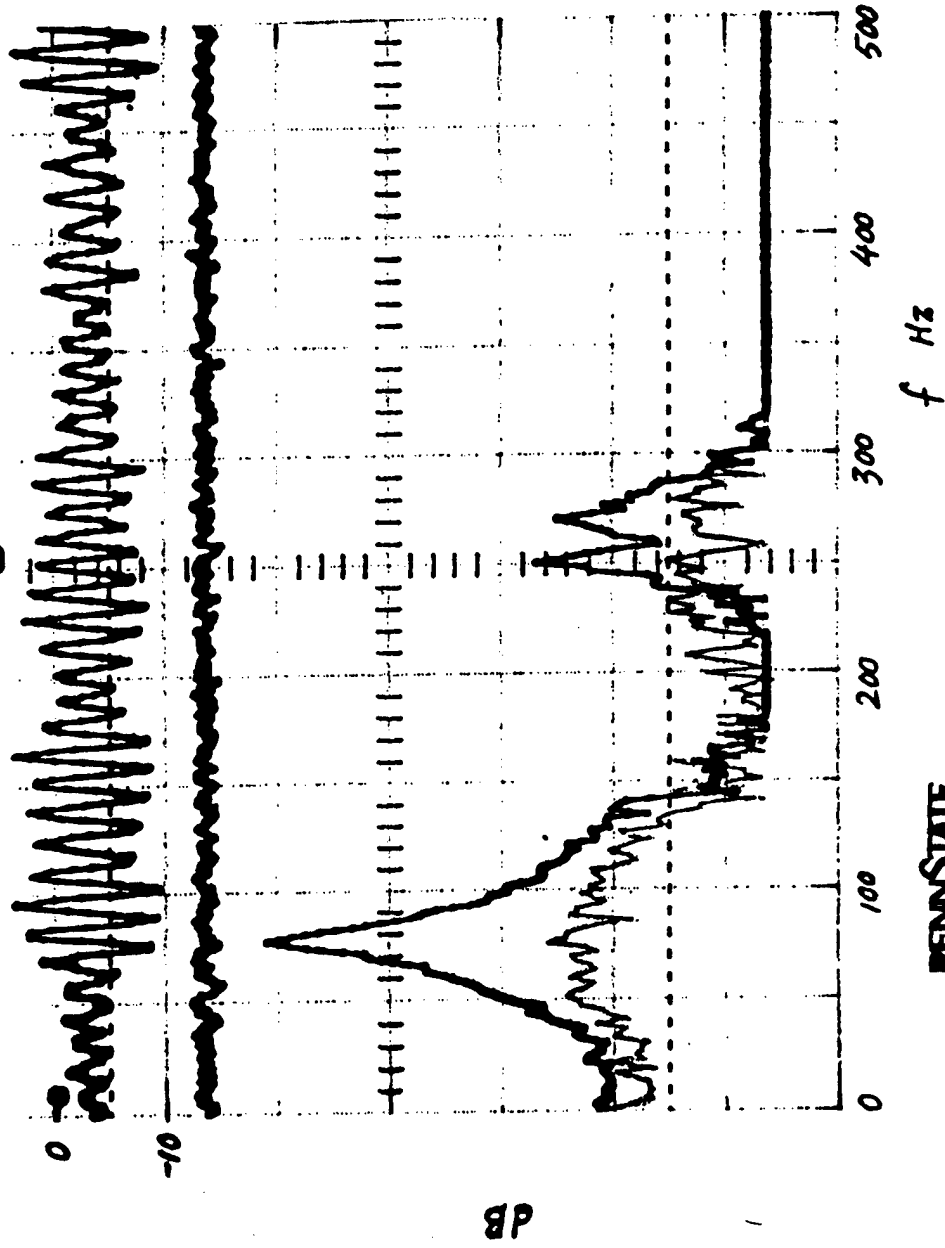


Research Center for the Engineering of Electronic and Acoustic Materials

# Experimental Results

DSP - Interior Noise Reduction

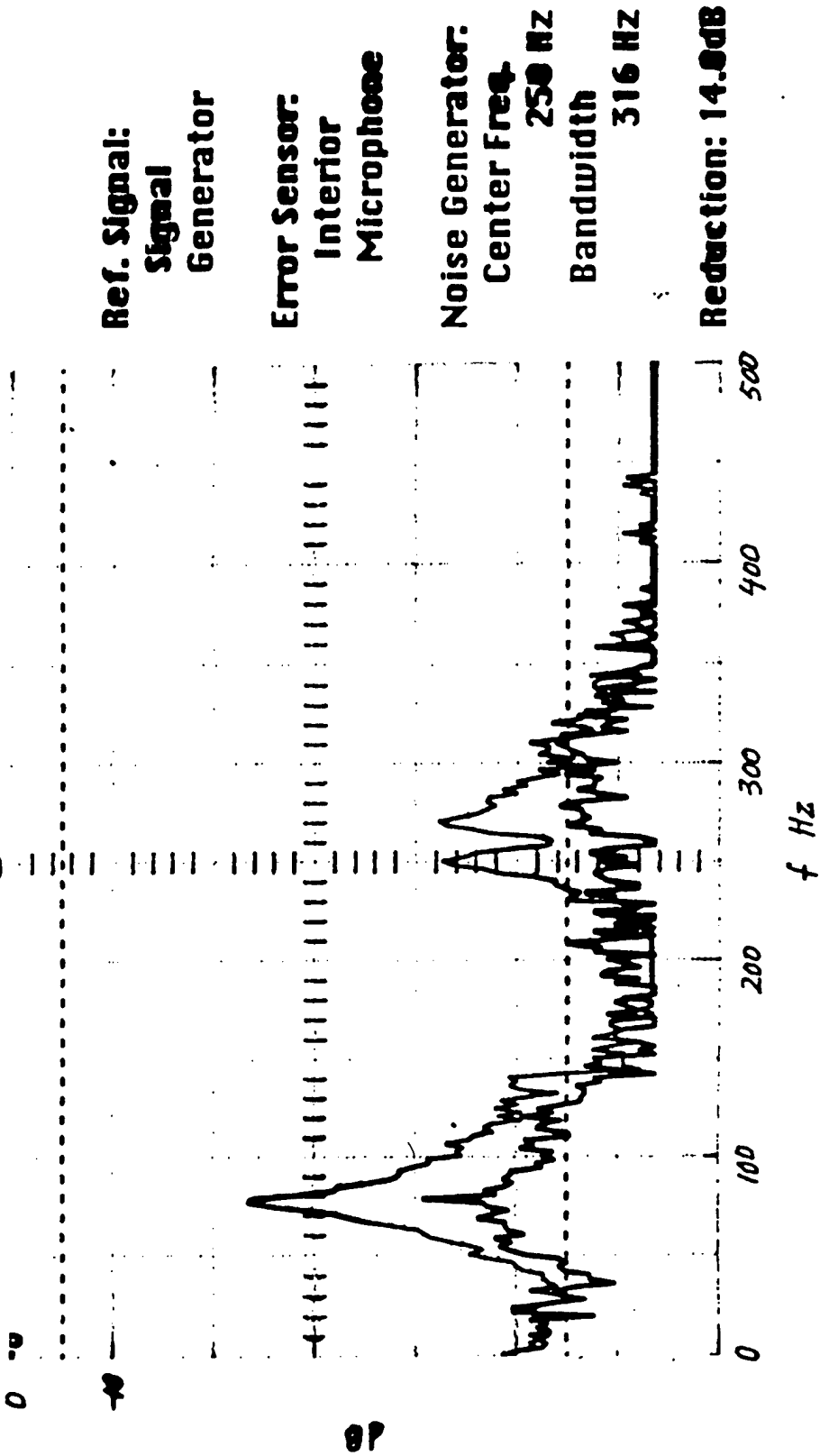
(Test A: Ref. Signal from SL-Meter  
or from Signal Generator)



## Experimental Results

### DSP - Interior Noise Reduction (Test A: Ref. Signal from SL-Meter

or from Signal Generator)

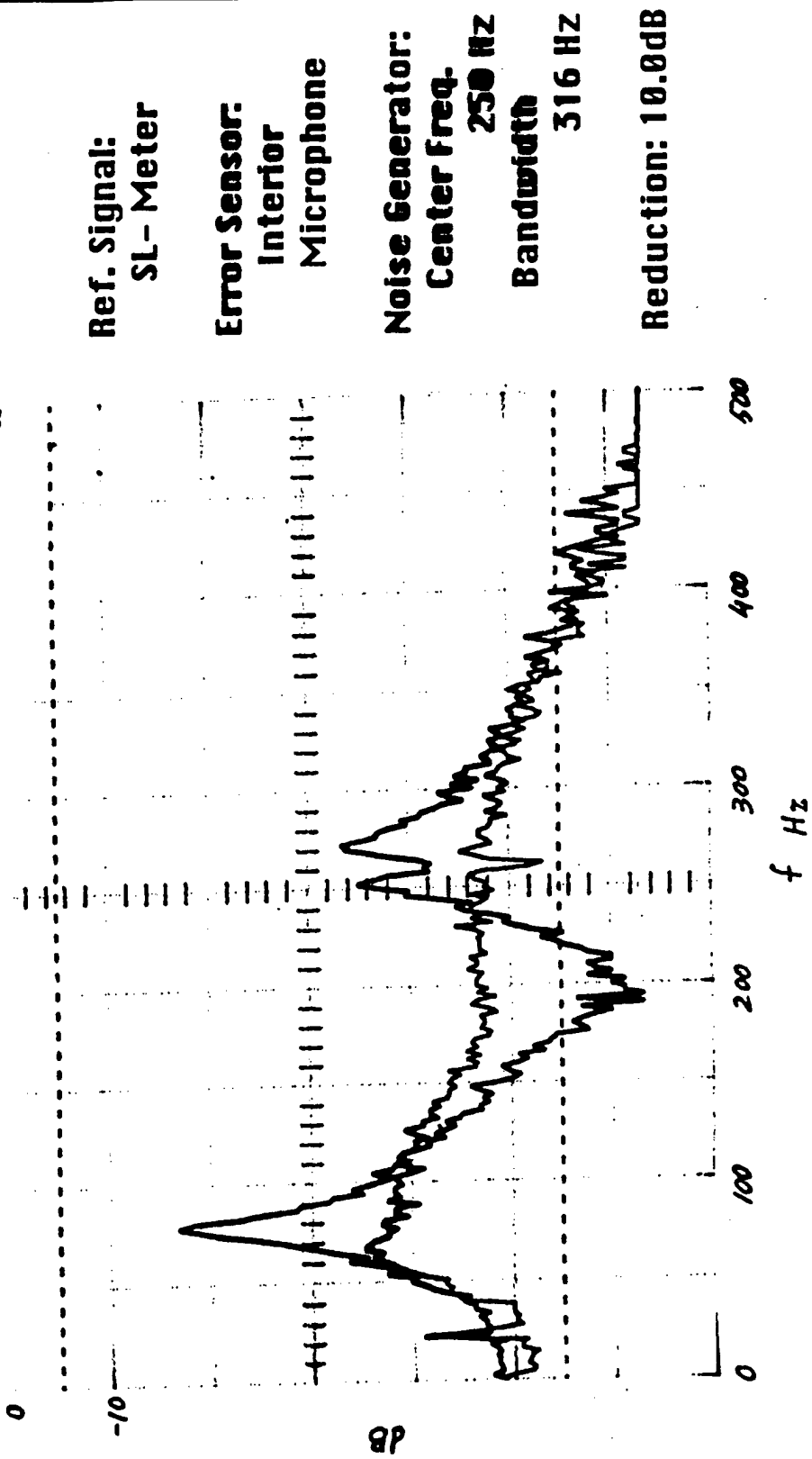


PENNSTATE

Research Center for the Engineering of Electronic and Acoustic Materials

## Experimental Results

### DSP - Interior Noise Reduction (Test A: Ref. Signal from SL-Meter or from Signal Generator)

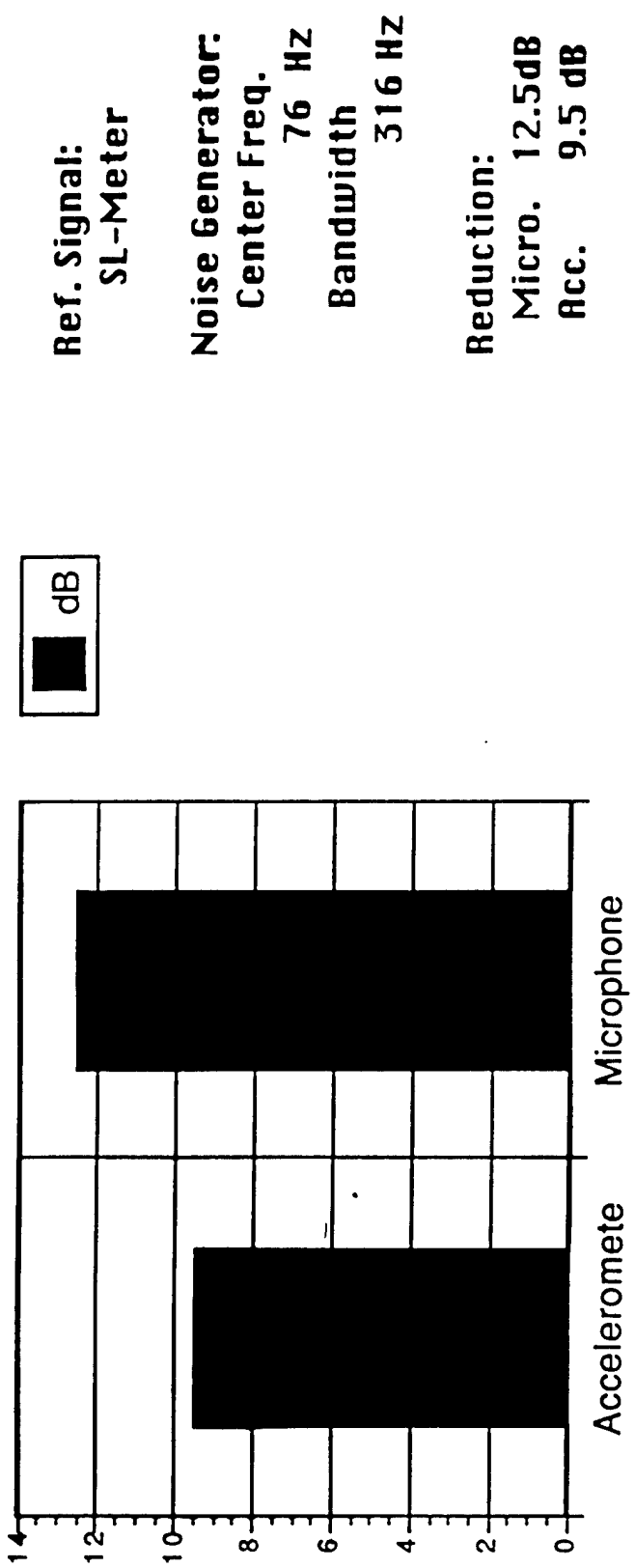


PENNSTATE

Research Center for the Engineering of Electronic and Acoustic Materials

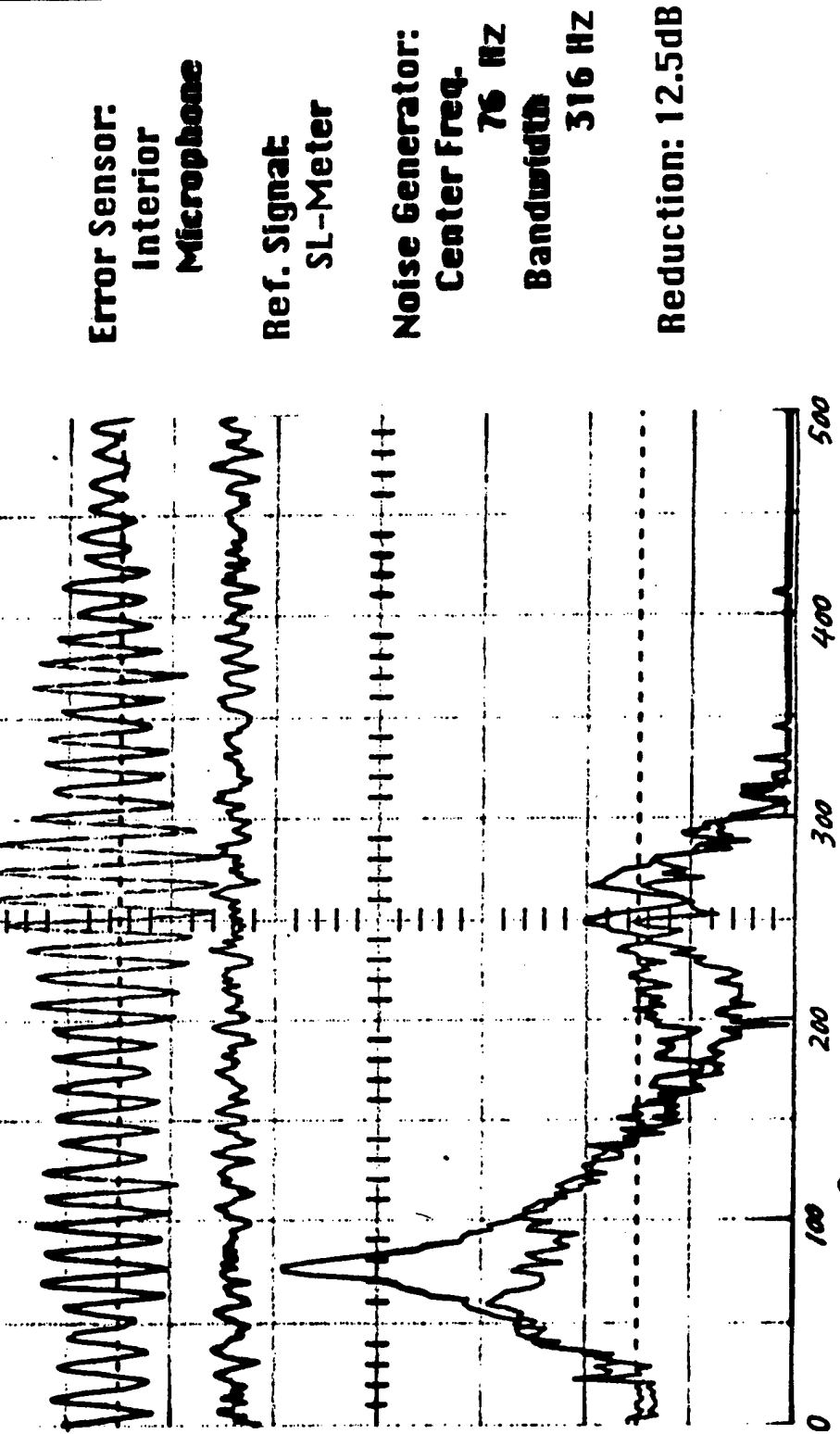
# Experimental Results

## DSP – Interior Noise Reduction (*Test B: Error Signal from Accelerometer or from Interior Microphone*)



## Experimental Results

### DSP - Interior Noise Reduction (Test B: Error Signal from Accelerometer or from Interior Microphone)



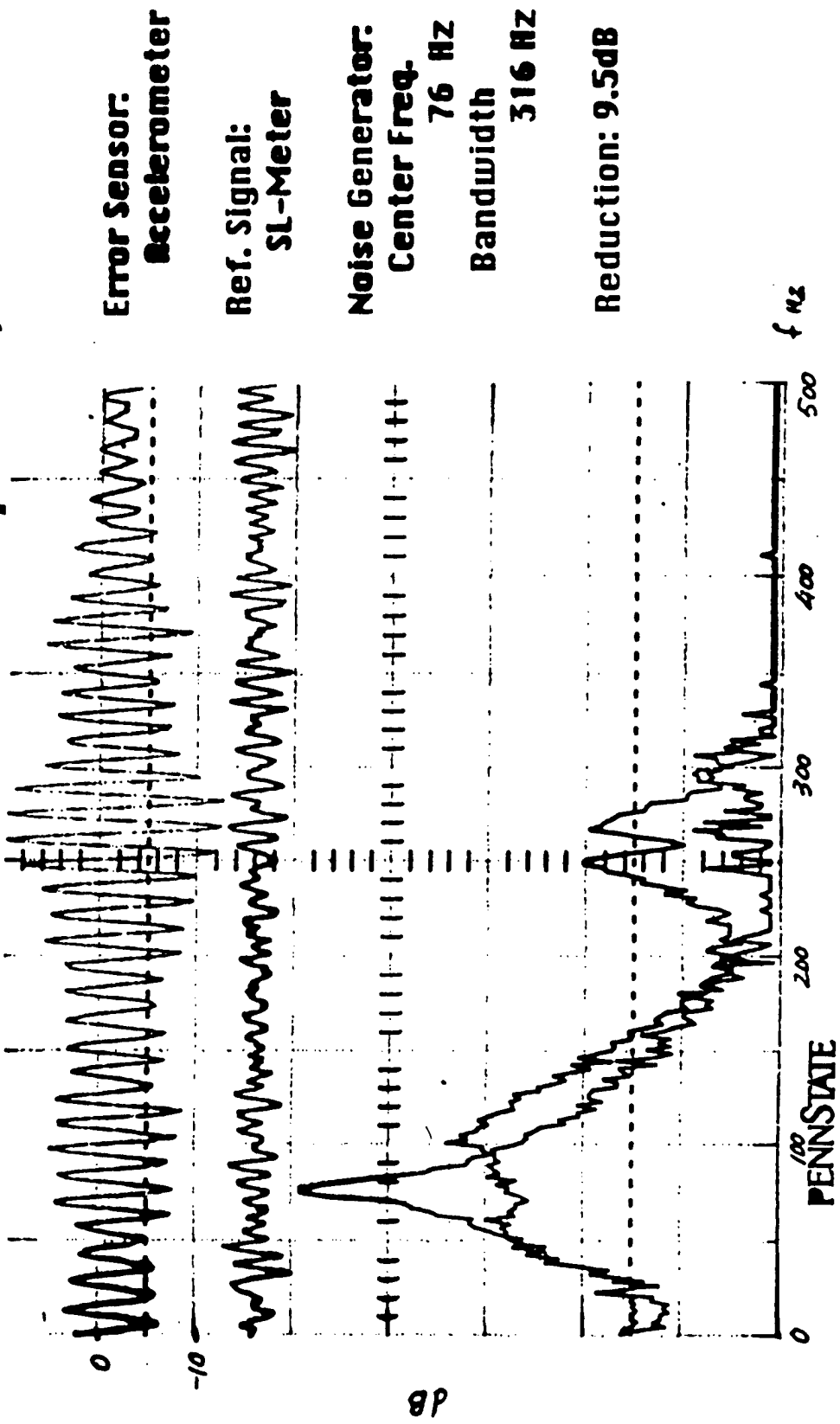
PENNSTATE

Research Center for the Engineering of Electronic and Acoustic Materials

## Experimental Results

### DSP – Interior Noise Reduction

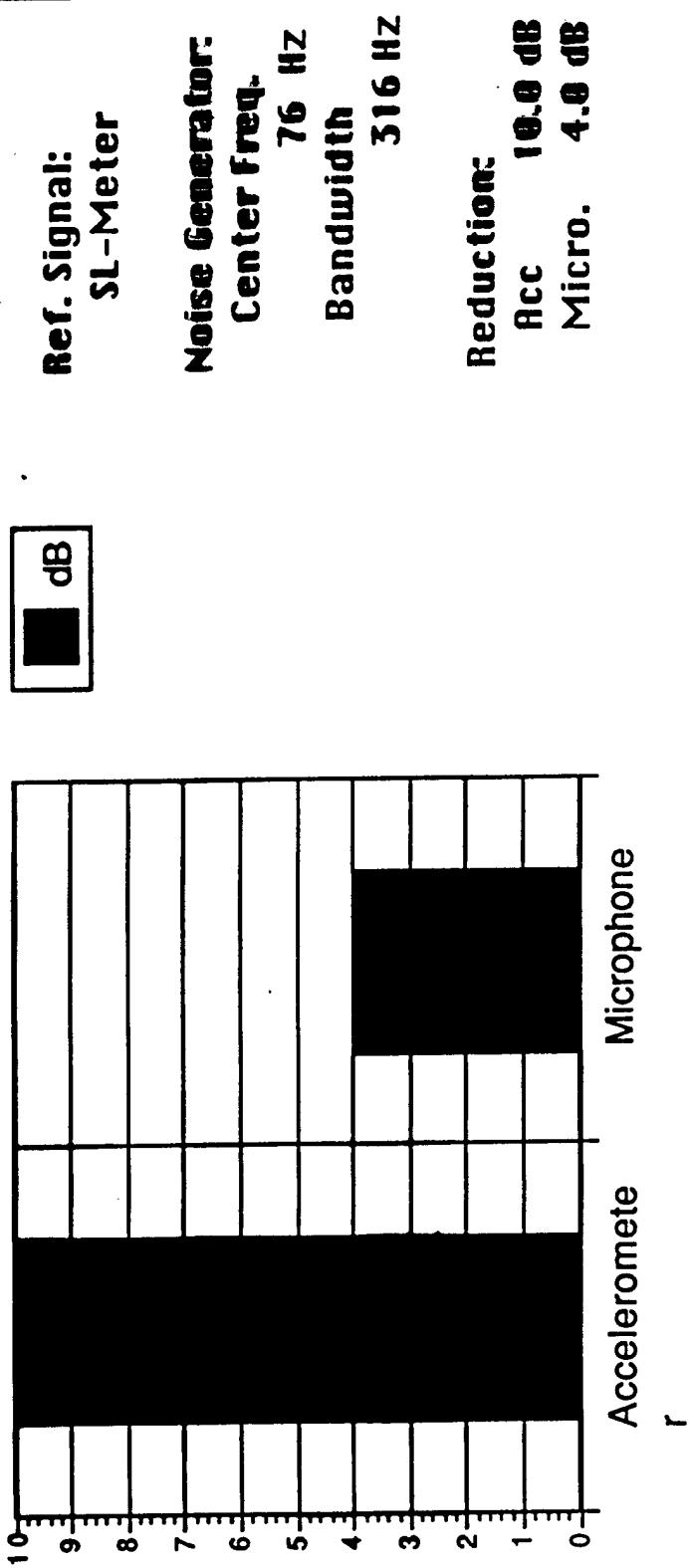
(*Test B: Error Signal from Accelerometer  
or from Interior Microphone*)



## Experimental Results

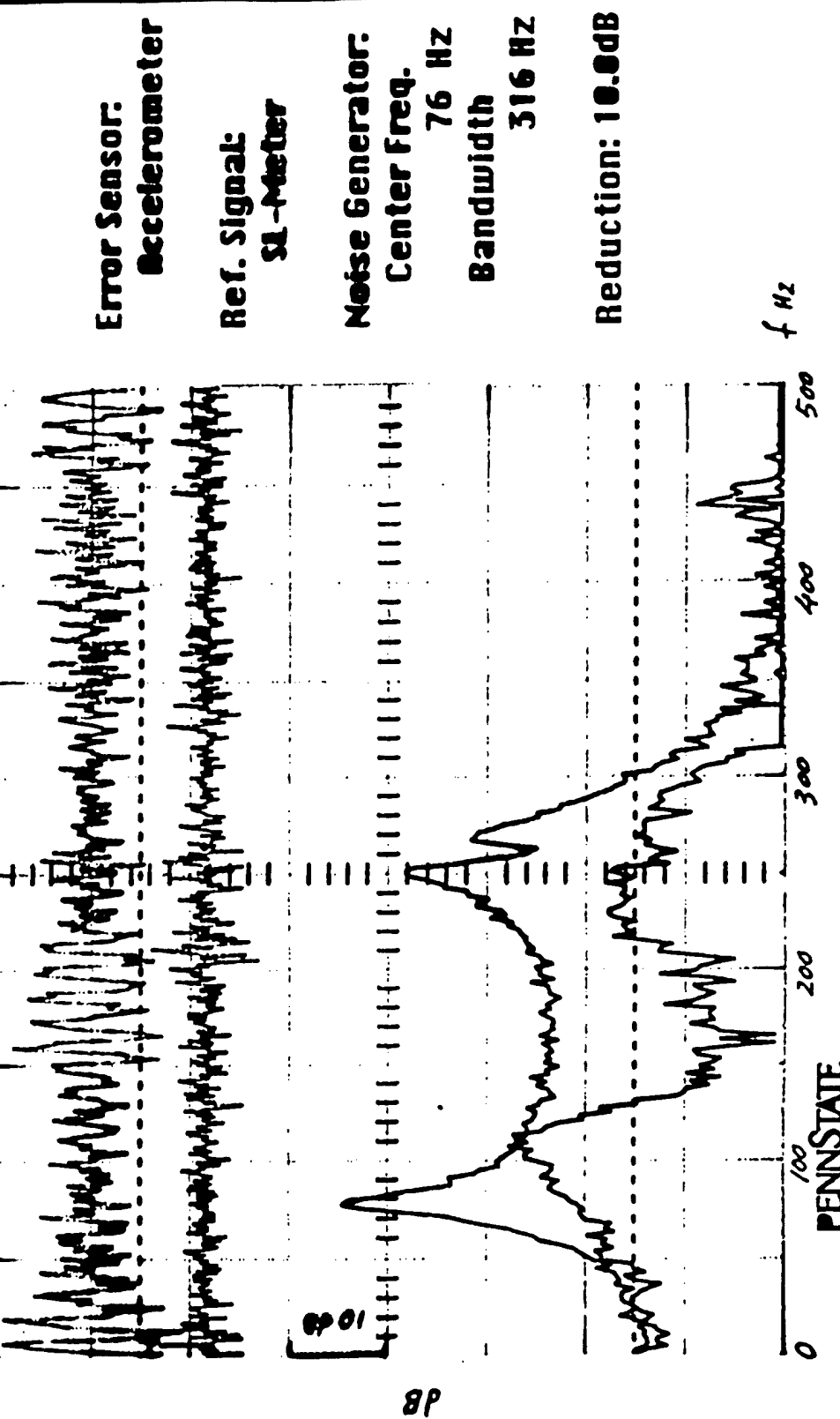
### DSP – Panel Vibration Reduction

#### (Test D: Error Signal from Accelerometer or from Interior Microphone)



## Experimental Results

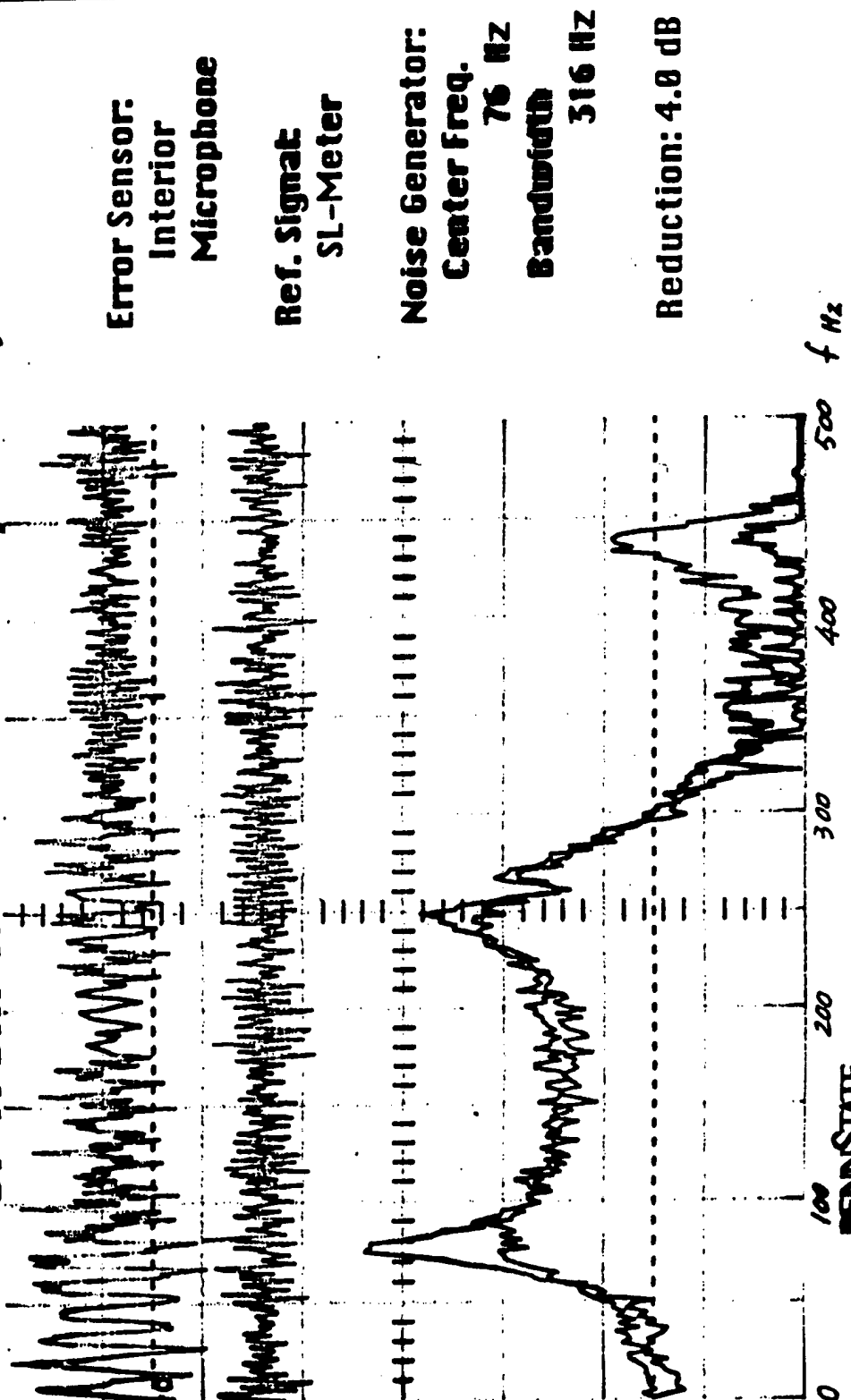
### DSP – Panel Vibration Reduction (Test D: Error Signal from Accelerometer or from Interior Microphone)



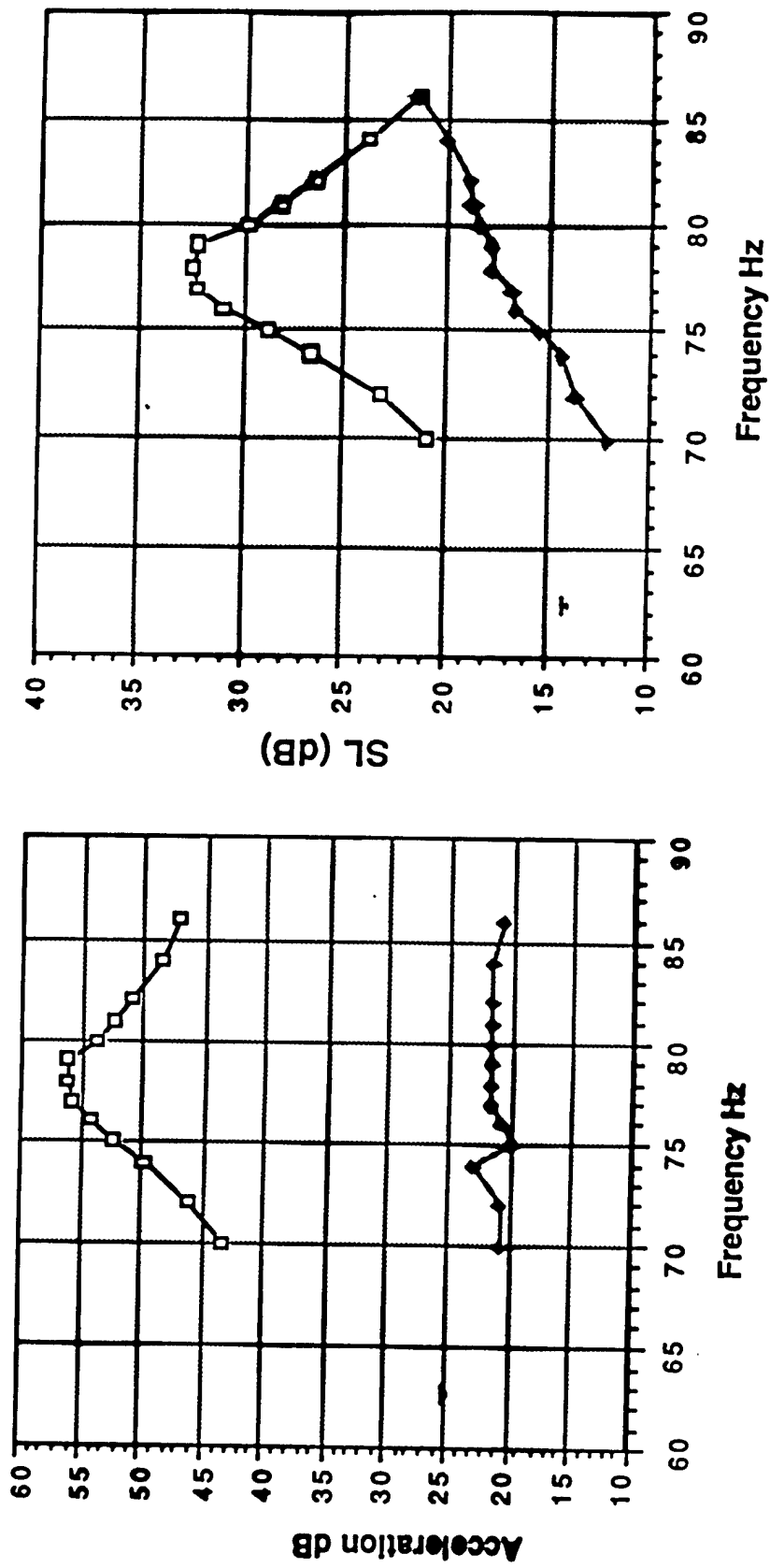
## Experimental Results

DSP - Panel Vibration Reduction

(Test B: Error Signal from Accelerometer  
or from Interior Microphone)



# Interior SL reduction by control of acceleration at the center of plate

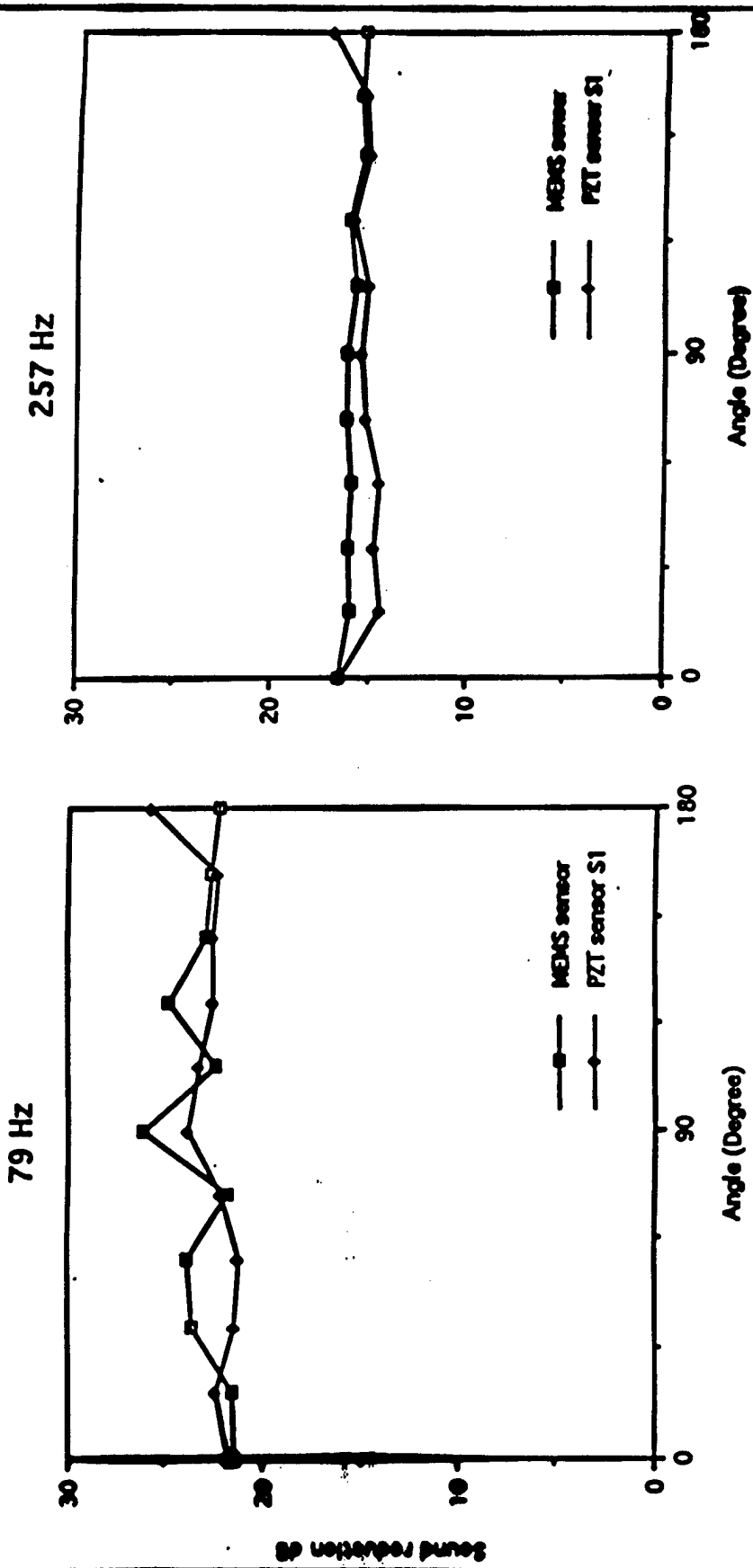


PENNSTATE

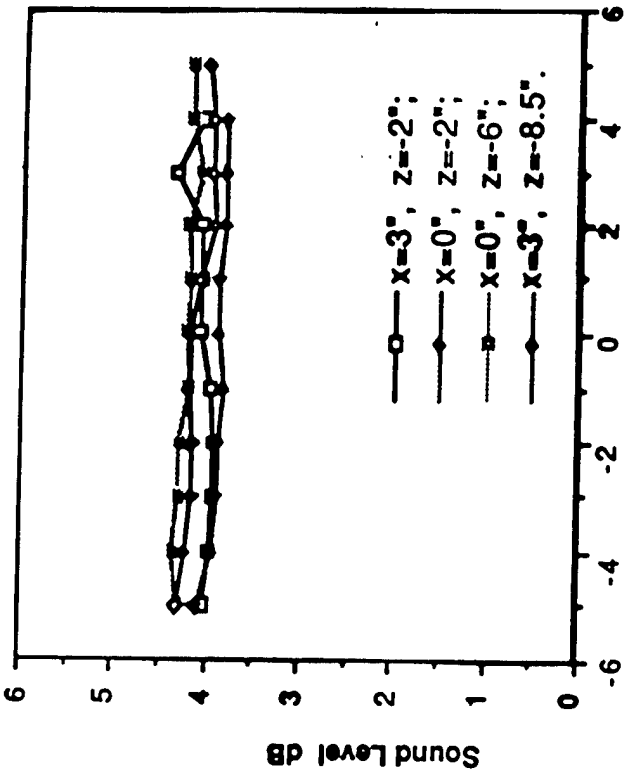
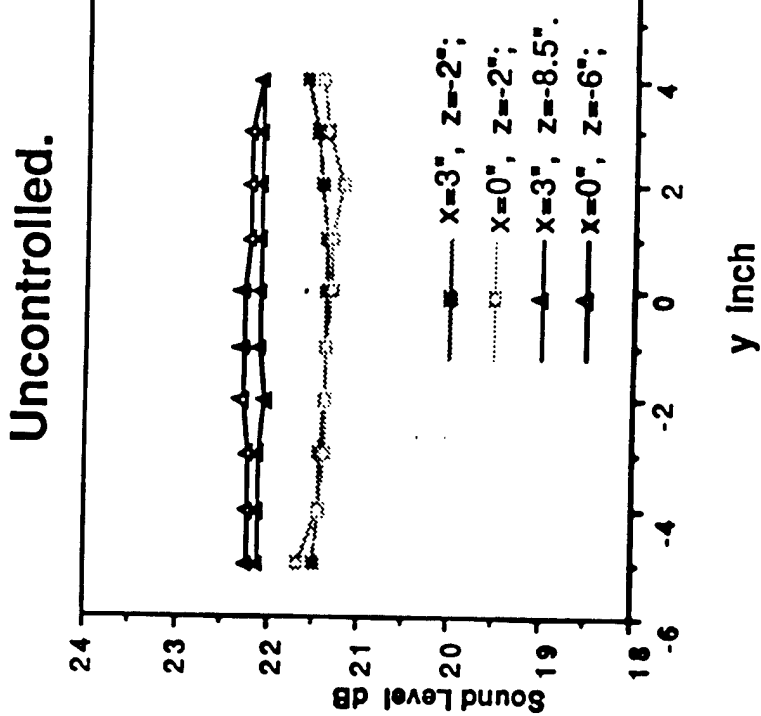


Research Center for the Engineering of Electronic and Acoustic Materials

# Comparison of MEMS and PZT Sensors

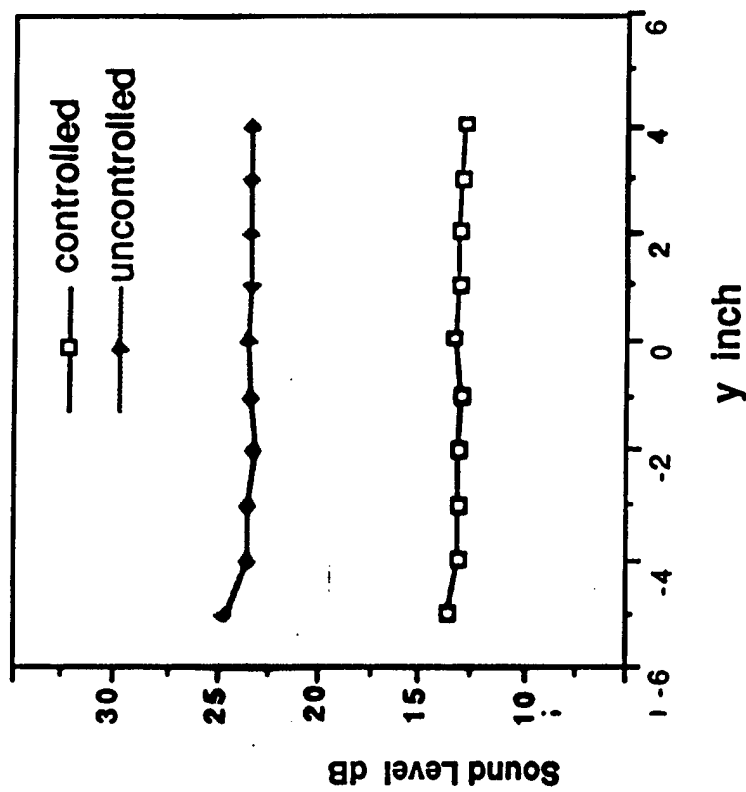


Sound level in enclosure.  
( f = 78Hz)



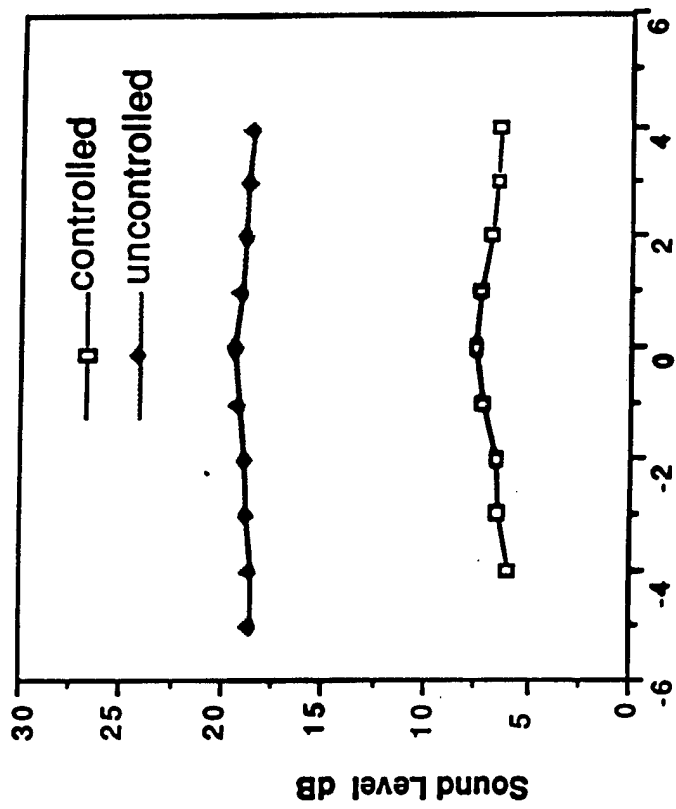
The variation of sound levels is less than 1dB at the first resonance frequency of the plate, as shown at 40 points inside enclosure.

# Sound Level in Enclosure ( $f = 254\text{Hz}$ )



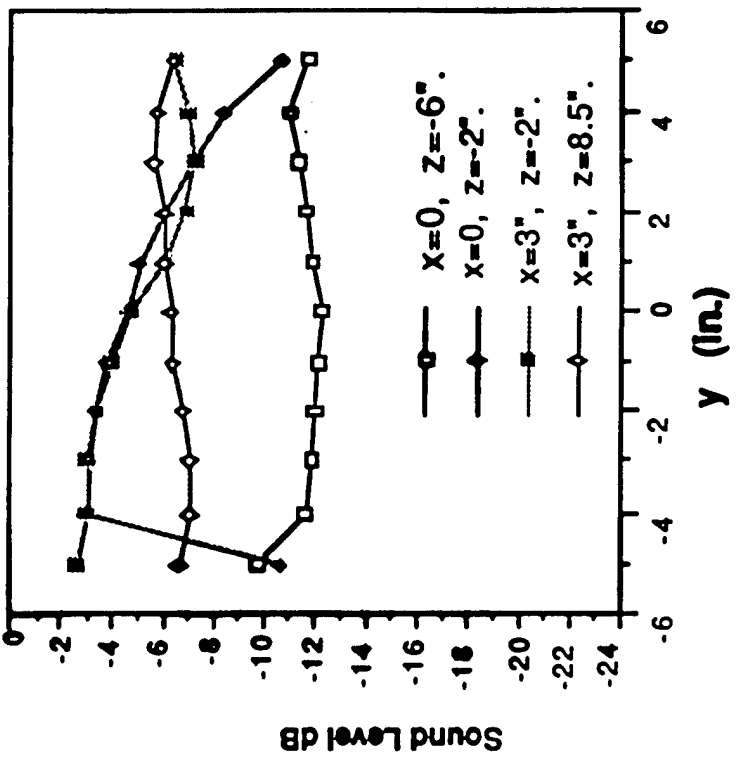
On center line under plate 6"  
( $x=0, z=-6"$ )

Center line under plate 2"  
( $x=0, z=-2"$ )



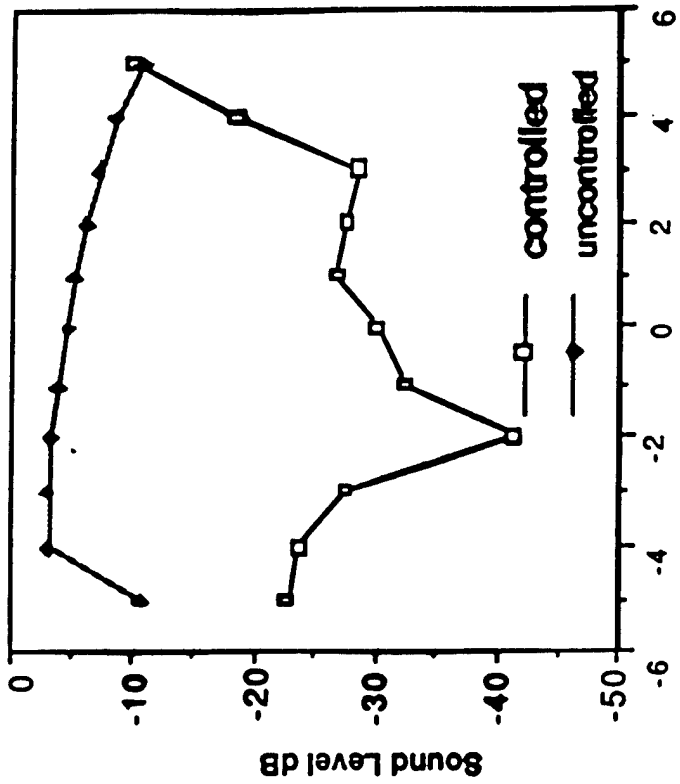
PENNSTATE Research Center for the Engineering of Electronic  
and Acoustic Materials

# Sound level in enclosure ( f = 625Hz)



Uncontrolled

On line under plate 2"  
(x=0, z=-2")



# Conclusions

1. PZT chips are used as actuators to suppress interior cabin noise. The noise reduction levels are around 10- 18dB by using a DSP single channel system for 0 - 500Hz band noise excitation.
2. The reference signal and the error sensor selection are important for the DSP system. The control reduction can change by 3 -4 dB for each choice.
3. DSP control system is better than the analog control system by 5-8 dB for the cases tested.
4. The sound level distribution in the enclosure has been measured for several single frequencies. The reduction achieved is uniform throughout the enclosure at 78 Hz and 254Hz, but at 625Hz, the variation can exceed 20dB. ( Enclosure size/ wave length > 0.5 )
5. To reduce the interior noise by controlling the vibration of the panel, the best controlled regions of frequency are around the resonance modes of the panel. This is true for both DSP and analog control systems.
6. A finite element study of the optimal modes to be controlled for radiated noise reduction is underway.



# Active Controls / Smart Structures S&T Programs for Aviation within ATCOM & ARL

Danny R. Hoad, ARL Vehicle Structures Technology Center  
&  
Dr. Robert Ormiston, ATCOM AeroFlightDynamics Directorate

Presented at the 3rd ARO Workshop on  
Smart Structures, Blacksburg VA

# Outline

- Why smart structures in Army Aviation
- Army Aviation S&T Planning
- Rotorcraft applications at ARL - Vehicle Structures Center & NASA Langley
- SBIR programs at AATD
- Rotorcraft applications at ATCOM -
  - Aeroflightdynamics Directorate & NASA Ames
- Summary

# Smart Structures in Army Aviation (Why & How)?

- Potential to meet RWW Aeromechanics Tech Effort Objectives for max blade loading, aerodynamic efficiency, vibratory loads, and acoustic radiation
  - Vibration Reduction:
    - Trailing edge 'Elevons'; 'Active Twist'
  - Noise Reduction:
    - BVI Noise Control- trailing edge flaps / blade twist
  - Performance Enhancement:
    - Surface 'oscillatory blowing' ; Leading edge deformation / multi-element airfoils
- Power and flexibility provides unique potential to tailor forces and control laws
  - Technical Barriers include:
    - Mechanisms for altering blade shape: materials, mechanisms, & actuators
    - Smart materials with increased force and strain capability
    - Reduce undesirable vibratory blade response - Not affect desireable responses
    - Optimize structural design to include controller strategy at transient flight conditions with highly nonlinear phenomena:
      - Dynamic stall at boundaries of flight envelope
      - Rotor/Wake interaction - BVI acoustic interaction
- Posture technology to be able to support a 6.3 demonstrator (3rdGARD) and/or transfer directly to industry by 2001

# Army Aviation Technology Strategy

## System Capabilities

96	97	98	99	00	01	02	03	04	05	06-20
----	----	----	----	----	----	----	----	----	----	-------

Prototype

EMD RAH-66 EOC Prod

AH-64D Longbow Apache

## Versatility & Flexibility

Rotorcraft Pilots Associate  
Multi-Sensor Aided Targeting-Air  
Radar Deception & Jamming  
Combined Arms C2

## Equipment Weaponization & Integration

Covert Nap of the Earth Flight  
AirLand Enhanced Recon & Targeting  
3rd Gen Sensor Integration  
Low Cost Precision Kill  
Non-Lethal Weapons Full-Spectrum Threat Protection

## Upgrades

OH-58D UH-60 AH-64 CH-47 RAH-66

## Versatility

Adv Rotorcraft Transmission  
Rotary Wing Structures  
Technology

## Advanced Platform Technologies

3rd Gen Advanced  
Rotor Design

## Deployability

Helicopter Active Control Tech  
Adv Rotorcraft Aeromech Tech  
Covert NOE Flight

JTR ATD

Integrated High Performance Turbine Engine Technology /  
Joint Turbine Advanced Gas Generator

On-Board Integrated Diagnostics System  
Subsystem Tech for  
Afford/Support/Survivability Navy Diagnostics Program

Covert NOE Flight

## Sustainability

Joint Transport  
Rotorcraft

CH-47 / Improved Cargo Helicopter

# ARCAT

## Advanced Rotorcraft Aeromechanics Technologies

- High Performance Rotor Aerodynamics
  - Optimized geometry
  - High-lift airfoils
- Multi-element & oscillatory blowing
- Low Noise Concepts
  - Active blade aero-control
  - Reduced blade-vortex interaction
- Low Vibration Rotor
  - Optimized structural dynamics
  - Active blade aero-control
- Increased Inherent Rotor Lag Damping
- Reduced Adverse Aero Forces
  - Rotor-fuselage interaction
  - Download
  - Yaw forces

Increase Efficiency, Reduce Drag  
*expand range/payload envelope*

Reduce Vibration  
*reduce maintenance*

Increase Inherent Rotor Lag Damping  
*reduction in flight safety parts*

125 nmi

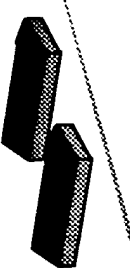
170 nmi

UH-60  
with ARCAT  
Technologies

Current UH-60

Rotary Wing TDA 2000  
TDA  
ARCAT  
Contribution  
+36%

Payoff  
Range  
+55%  
-or-  
Payload  
Cruise Speed  
Maneuverability /  
Agility  
+23%  
+5%  
+6%

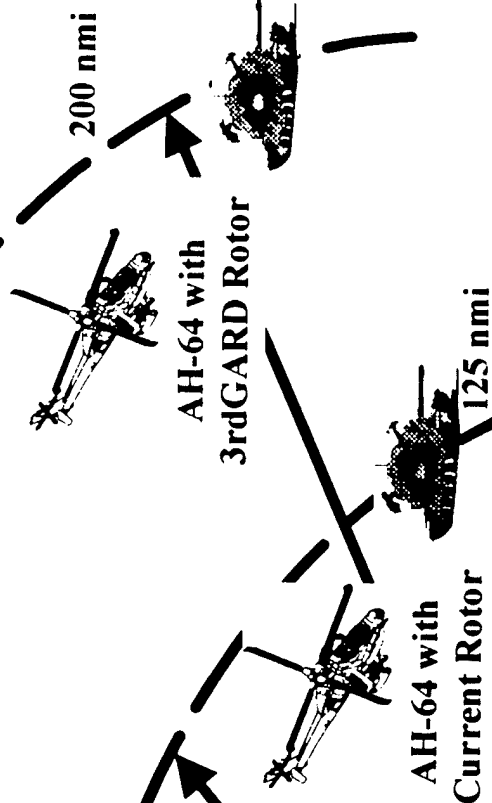


## 3rd GARD

### 3rd Generation Advanced Rotor Demonstration Program

#### AH-64 Mission Profile @ TOGW=15,200 lbs

- 8 Hellfire missiles
- 325 Rounds
- 20 min HOGE Target
- 30 min Fuel Reserve
- Cruise Velocity @ Best Range, 4000 ft, 95° F

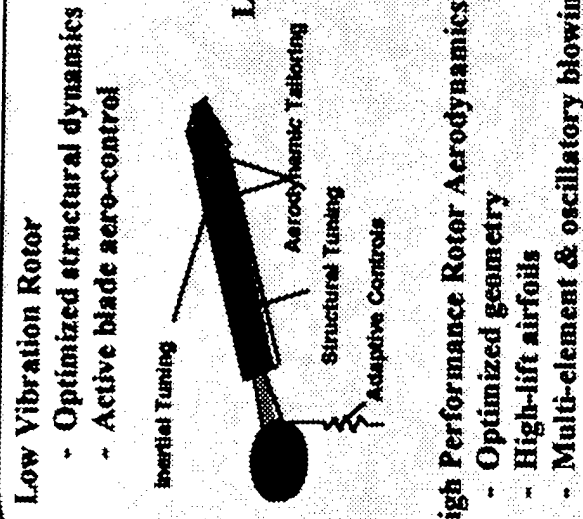


#### Rotary Wing TDA 2005

##### Payoff TDA

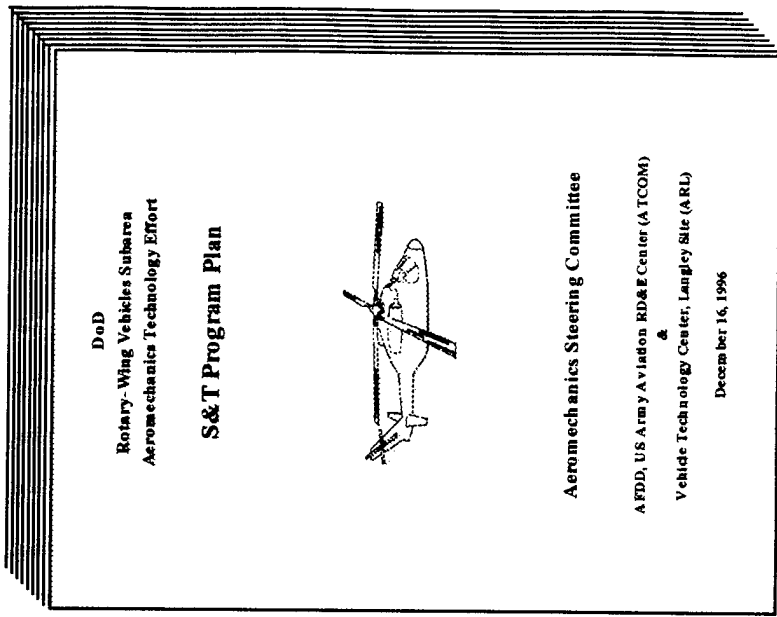
##### 3rdGARD Contribution

Range	+136%	+61%
Cruise Speed	+15%	+6%
Maneuverability /	+50%	+10%
Agility		
Acoustic Footprint		-50%



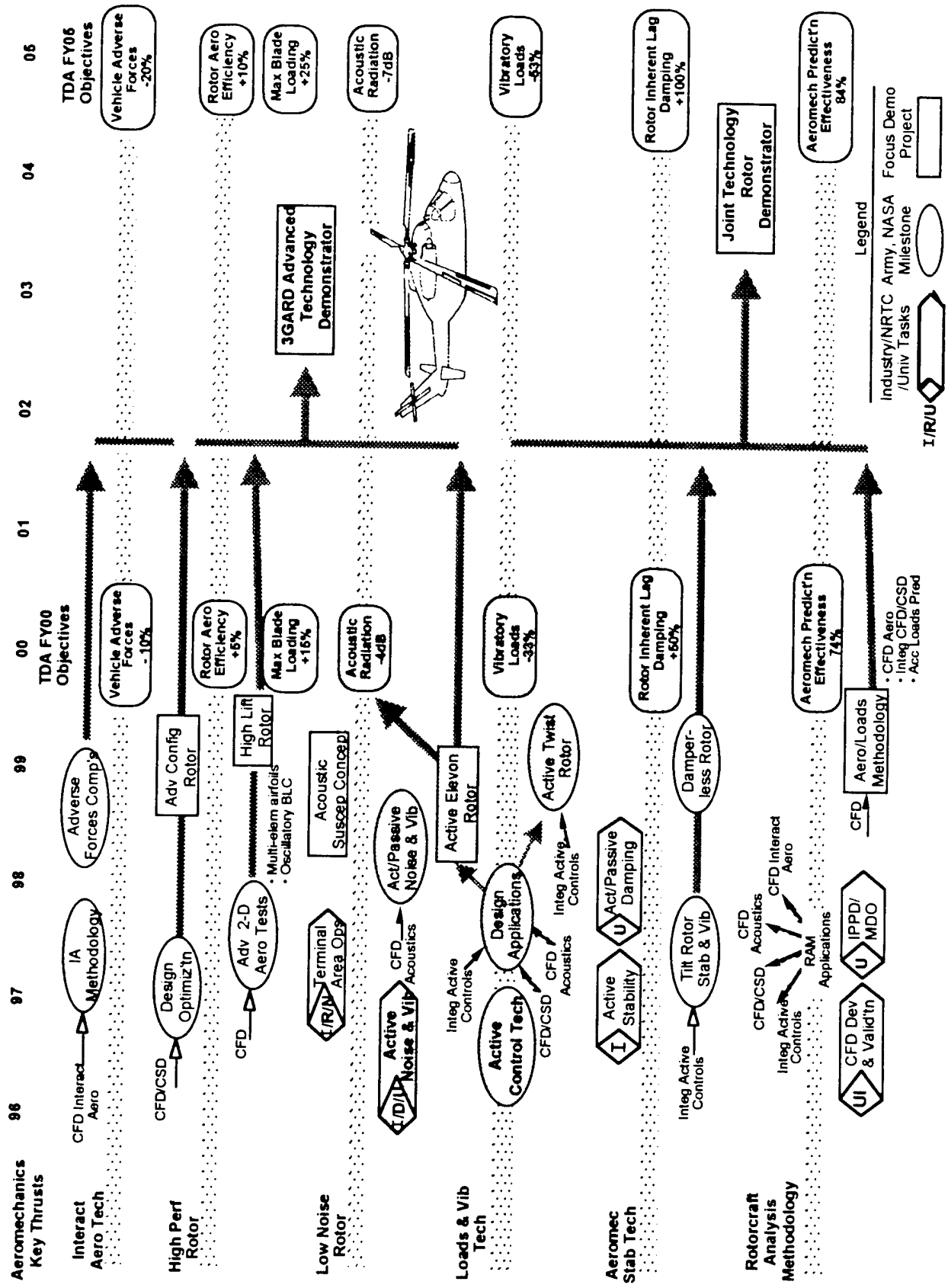
# Rotorcraft Aeromechanics Program Strategy

- Aeromechanics Steering Committee (AVRDEC/NTC) planning - -
- Plan developed to focus on DTAP Aeromechanics technical objectives
- DOD RWV Aeromechanics S&T Program Plan completed - 16 Dec 1996



- Aeromechanics Key Thrust Focus
- Major Milestone Roadmaps
  - Demos leading to 3rdGARD
- Major Milestone Narrative Descriptions
- Integrated Army, NASA, University (ARO/COE), Industry (NRTC/RITA, IR&D) Programs

# **Rotary Wing Vehicles Aeromechanics Tech Effort Roadmap**



# **Langley (Army/NASA) Smart Structures Applications for Rotorcraft**

- Multi-Element Airfoil Technology
- Active Twist Rotor (ATR) Concept

# Multi-Element Airfoil Technology

## Rationale

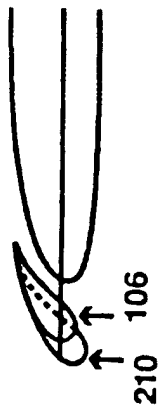
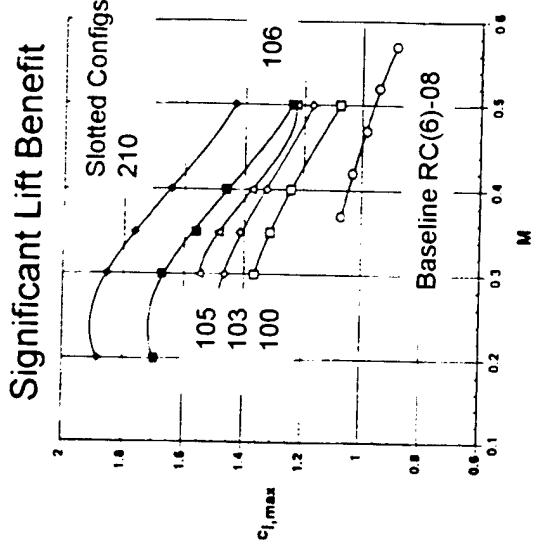
- Forward-slotted airfoils demonstrated major improvements in max lift
- Potential to substantially improve helicopter perf and maneuverability
- MSES and MCARFA codes accurate for attached flow
- Rotor performance test showed mixed results

## Payoffs

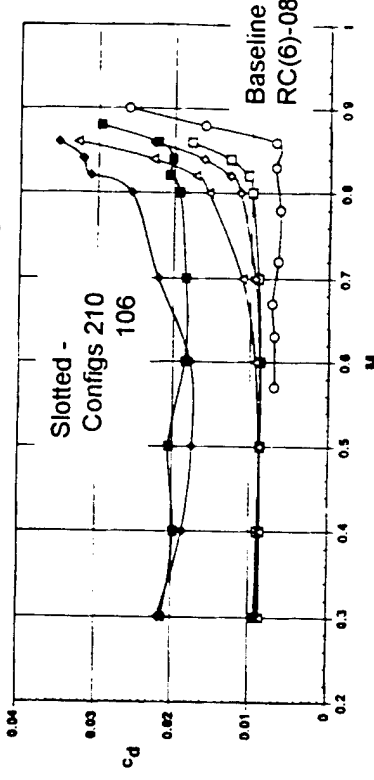
- Increase  $C_l/\sigma_{\max}$ , delay retreating blade stall
- Candidate for HLR Demo

## Plans

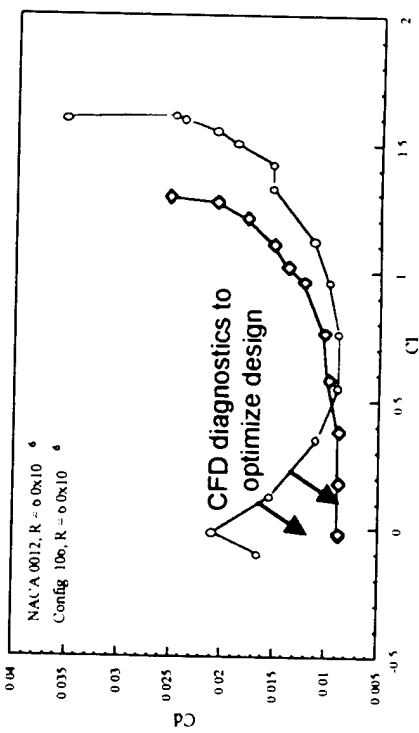
- CFD application to address low  $C_l$ , drag rise
- Baseline Airfoil Analysis
- Rotorcraft Performance Payoff Analysis
- Slotted Airfoil Design and Analysis, Airfoil geometry
- Wind tunnel test confirmation



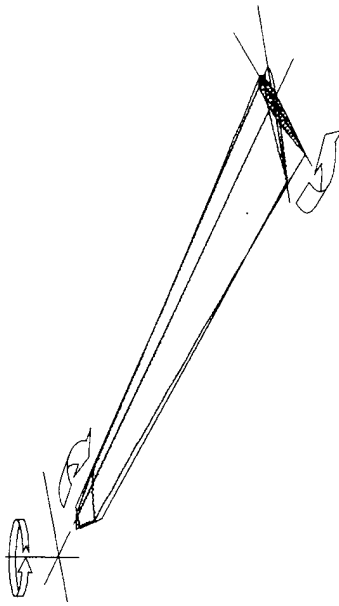
## Favorable Drag Divergence



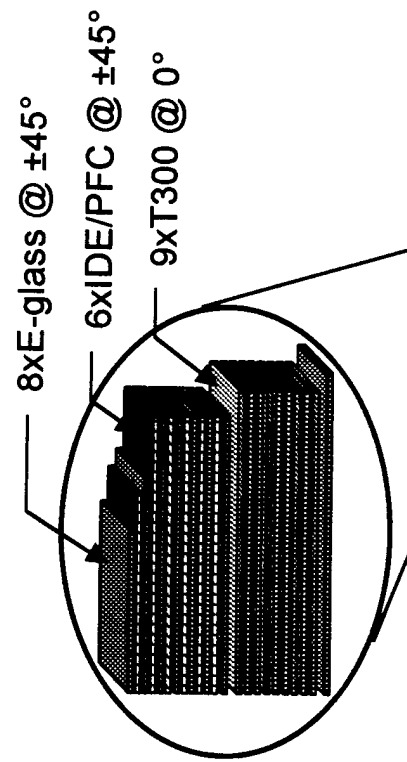
## Drag Rise at Low $C_l$



# Active Twist Rotor (ATR) Concept

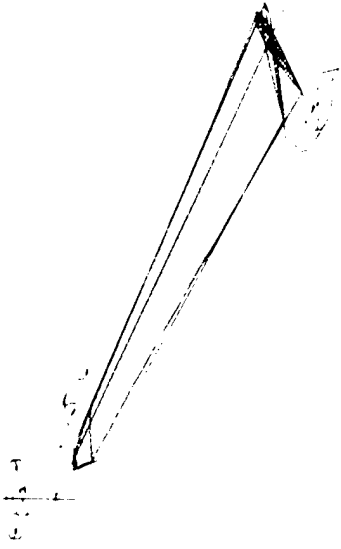


**Conceptual ATR structure with embedded IDE/PFC laminae**



- Piezoelectric control of blade twisting for:
  - reducing vibrations; noise
  - improving performance
  - suppressing stall
  - enhancing stability
- High blade twist possible using *piezoelectric fiber composites* (PFC); *interdigitated poling* (IDP)

# Active Twist Rotor Research



## Analysis of ATR frequency response for 1-g hovering flight; 0P-16P sinusoidal electric field

Title: atr\_frl6.eps  
Creator: MATLAB, The Mathworks, Inc  
CreationDate: 02/13/97 12:06:00

- Analytical efforts:
  - in-house aeroelasticity code for preliminary design; control studies (ARL-Langley Research Center)
  - modified version of CAMRAD II (can apply periodic twisting couples)
- Experimental efforts:
  - 1/5 scale ATR model blade under joint development with MIT

# Aviation Applied Technology Directorate SBIR Programs

- Smart, Compact Packages for Vibration Control
- On-Blade Synthetic Active Control for Vibration and Acoustics Reduction
- High Power Density Magetostrictive Reaction Mass Actuator
- High Bandwidth Rotating to Non-rotating Data Transfer and Power Transmission

# SMART, COMPACT PACKAGES FOR VIBRATION CONTROL

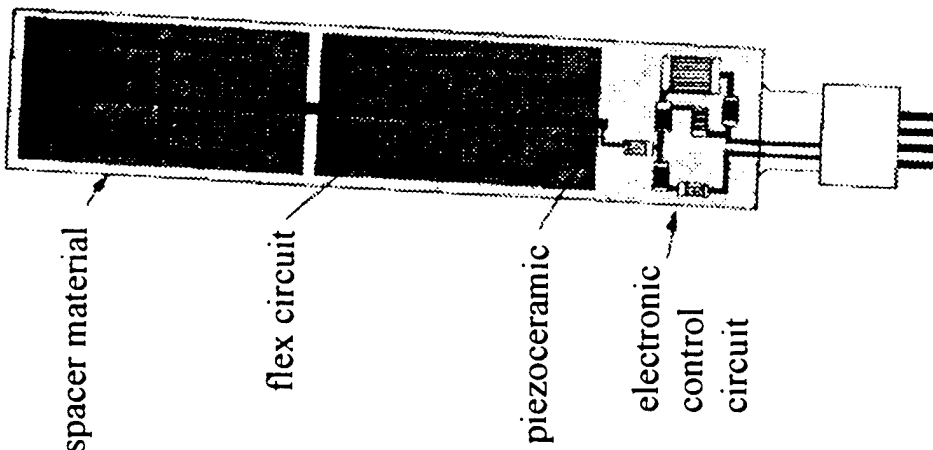
**OBJECTIVE:** Package piezo actuators and sensors, drive electronics, active control electronics into turnkey device for active structural damping.

**APPROACH:** ACX Proprietary packaging technology combined with advances in surface mount electronics.

**RESULTS:** Compact (2x6x1/8"), light weight (1.5 oz) SmartPack™, which has achieved 20x increase in modal damping and 15dB decrease in radiated noise on flat plate.

**CONTRACTOR:** Active Control eXperts, Inc.

**AATD POC:** Eric Robeson (757) 878-2975



# On-Blade Synthetic Active Control for Vibration and Acoustics Reduction

**OBJECTIVE:** Develop a practical method of implementing active arrays of piezoelectric actuators in the rotating frame of the helicopter main rotor to implement active blade control.

**APPROACH:** Design an electronics drive system which will be practically implemented through the use of innovative concepts (synthetic impedance, microcompact CMOS high-speed switching and network controllers) to overcome technology barriers of bulky electronics, large energy consumption and high system losses.

**RESULTS:** An implementation of multimodal structural control using totally decoupled synthetic networks was demonstrated, which proved the feasibility of a self governing, semi-autonomous, active adaptive system capable of addressing multiple mission needs. This concept is under going further development for implementation in the wind tunnel.

**CONTRACTOR:** EMF Industries, Inc.

**AATD POC:** Donald Merkley (757) 878-0139

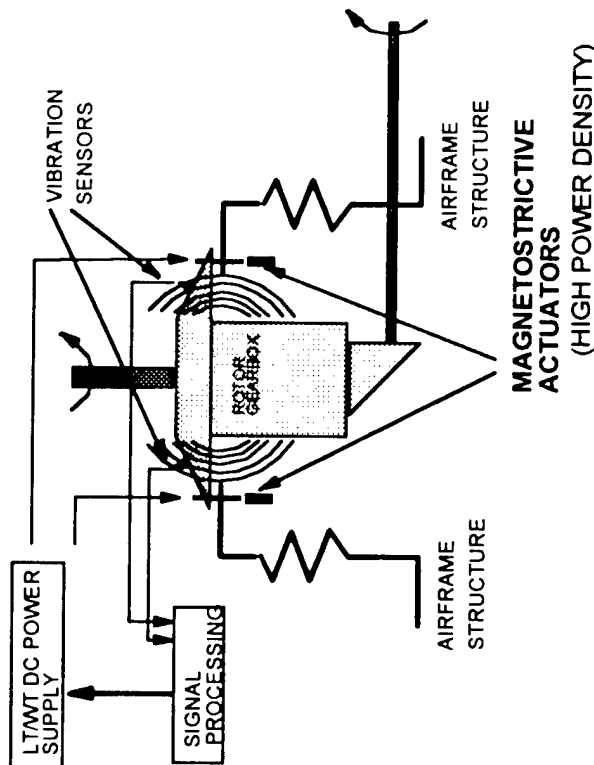
# High Power Density Magnetostriuctive Reaction Mass Actuator

(Active Noise Cancellation for Helicopter Main Transmissions)

## Problem Statement:

- Gearbox Vibrations primary driver of rotorcraft internal noise
- Weight of current active noise cancellation actuators excessive

## Active Noise Cancellation System



## Approach:

- Develop a very high power density actuator for use in active noise cancellation systems
- Utilize TERFENOL-D material to drive reaction mass
- Design actuator to produce 30 lbs force at 800 Hz with weight less than 0.8 lbs

## Results:

- Actuator tested that exceeded requirements
  - 10-15 dB reduction in cabin noise

**Contractor:** SatCon Technology Corp

**AATD POC: Clay Ames**  
**(757) 878-0040**

# High Bandwidth Rotating to Non-rotating Data Transfer and Power Transmission

**OBJECTIVE:** Develop an affordable system for reliably transmitting data and power to/from the rotating main rotor and the fixed fuselage of a helicopter.

## Tetra Corporation

**APPROACH:** Magnetically Coupled Rotating Interface (MCRI) couples a high frequency carrier which contains coded analog and digital signals with no physical contact.

## Saddleback Aerospace

**APPROACH:** Rotor Optical Data Interface (RODI) utilizes optical emitters and detectors for data transfer and separate a device for power transmission.

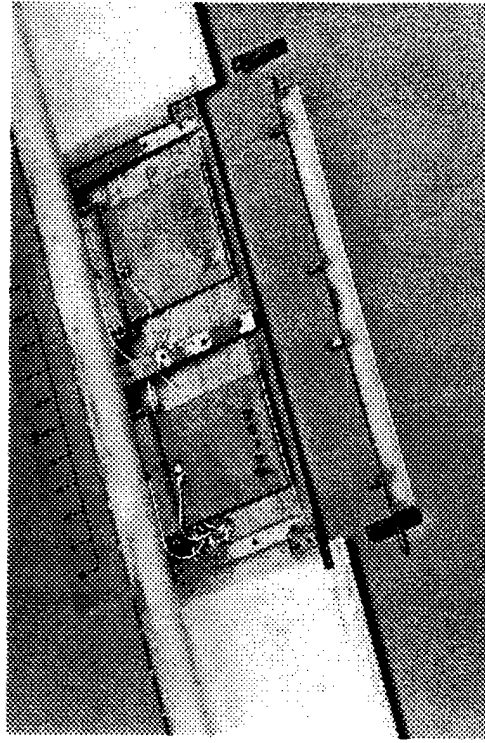
**RESULTS:** Prototype bench testing completed. On going effort to optimize, fabricate and whirl test both concepts.

**AATD POC:** Eric Robeson (757) 878-2975

**Ames (Army/NASA) Smart Structures Applications for  
Rotorcraft**

# Smart Structures Active Elevon Rotor

## Elevon and Piezoceramic Actuator

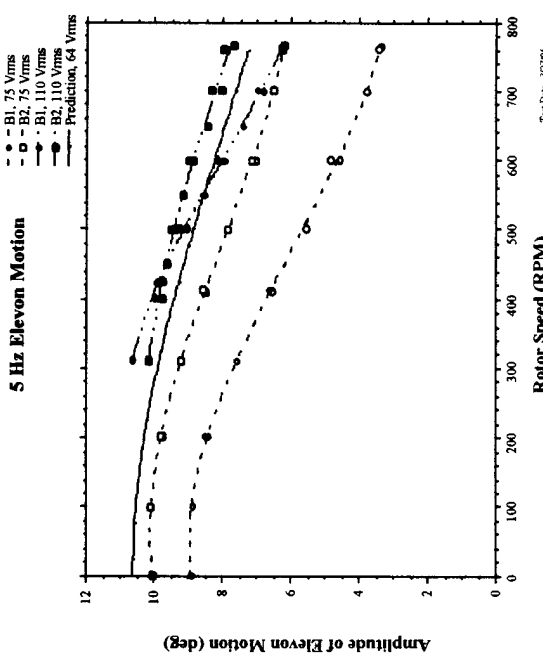


### Rationale

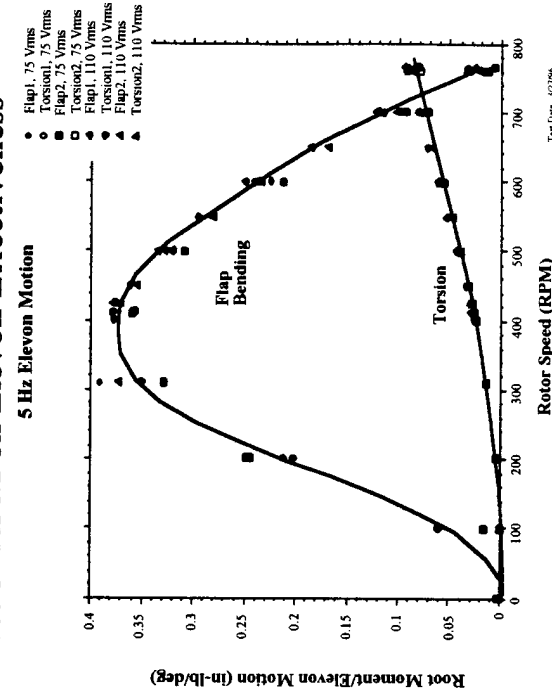
- Reduce loads & vib - provide practical, effective IBC at source; integrate IBC & flight control.
- Reduced BVI noise
- Performance - Improve load distribution, reduce stall
- Enhanced Maneuverability - Reduce load limits; increase thrust capability

## 7.5' Dia ADM Rotor, Hover Testing, Open Loop

### Effect of RPM on Elevon Motion



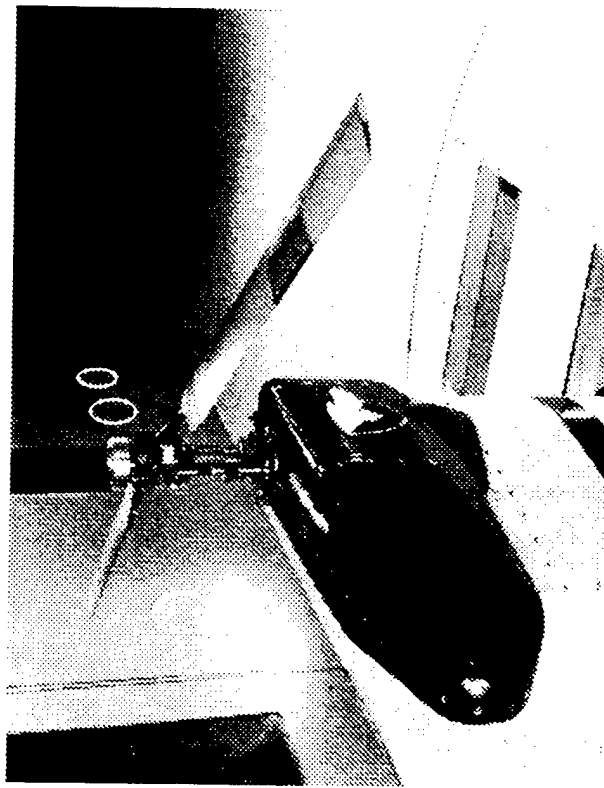
### Effect of RPM on Elevon Effectiveness



# Smart Structures Active Elevon Rotor

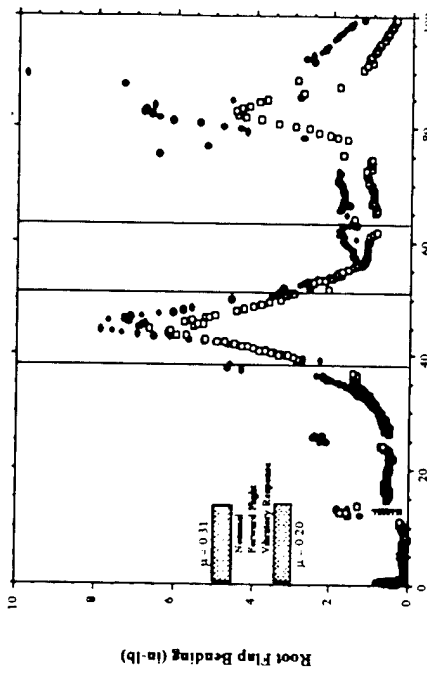
## Status

- Hover testing successful
  - Forward flight testing underway
- Plans
- Closed loop ADM testing
  - Initiate 12-Ft AER Demo for loads, vib, noise objectives

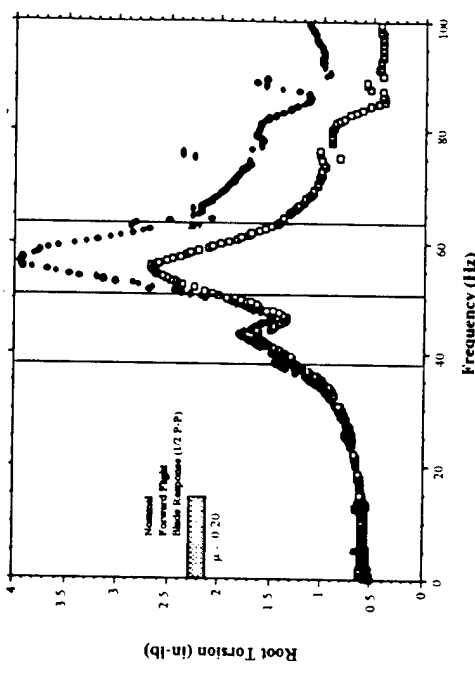


## Hover Test Data

### **Flap Bending Dynamic Response**



### **Blade Torsion Dynamic Response**



**7.5' Dia ADM Rotor, Forward Flight Testing,  
Open Loop Control**

# Summary

# **Innovative Smart Technologies for Actively Controlled Jet-Smooth Quiet Rotorcraft**

**Inderjit Chopra  
Director Alfred Gessow Rotorcraft Center  
University of Maryland, College Park, MD 20742**

Arguably, more than any other system, the closely coupled interdisciplinary structural, mechanical, and aerodynamic complexity of rotorcraft offers many potential opportunities to apply smart structures technology to achieve substantial pay-off in rotorcraft effectiveness. With this in mind, an integrated, innovative, interdisciplinary basic research program is in progress to advance the technology of smart structures, and to explore the means to make major improvements in the vibration and aeroacoustics of rotorcraft through the application of this technology. Taking advantage of the expertise and unique research facilities and equipment available in the Alfred Gessow Rotorcraft Center at Maryland, this program will expand the technology base of smart structures, examine new and innovative actuators, sensors and control strategies, and pursue high-payoff applications to rotorcraft to suppress external/internal/transmission noise and vibration.

The research program is an intensive, coordinated and broad-based effort that interactively considers the rotor, airframe and power train in the active control of noise and vibration. It consists of six interactive tasks with twenty two sub-tasks that directly address the DOD Rotary Wing Vehicle S&T goals for the years 2000 and 2005. The research is evenly balanced between experiment and theory. The various minimization concepts and promising active control elements that show potential will be evaluated for various flight conditions by means of extensive tests on Mach-scaled rotor models on our hover stand, in the Glenn L. Martin wind tunnel, in the David Taylor Research Center (DTRC) acoustics wind tunnel and a proposed anechoic chamber. This program is expected to identify key issues and remove barriers to the application of smart structures technology to minimize vibration and aeroacoustics in full-scale rotorcraft systems.

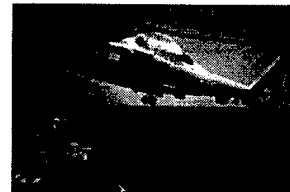
It should be recognized that the proposed complex studies can be carried out within the allocated funds only because of the extensive analytical and experimental capabilities developed by the Rotorcraft Center during the past fifteen years. Personnel from other parts of the College of Engineering and the Department of Psychology at Maryland, from the Rotorcraft Center of Excellence at Pennsylvania State University, from Cornell University and from the University of the District of Columbia (Historically Black College and University), are contributing their expertise to the basic supporting studies. Pennsylvania State University has a long-standing expertise in the areas of smart structures including MEMS technology, and rotorcraft dynamics and acoustics. Cornell University has been a leader in the field of rotorcraft aeroacoustics. The researchers are mutually interactive and work as a team, not as a collection of individuals.

The output of the program will be a direct contribution towards producing more efficient, reliable, cost-effective, jet-smooth quiet rotorcraft.

## Innovative Smart Technologies for Actively Controlled Jet-Smooth Quiet Rotorcraft

### MURI Research Objectives

- Develop a base technology to build a smart rotorcraft to actively control
  - external noise
  - internal noise
  - rotor-induced vibration
  - transmission-induced noise & vibra.
- Refine key technology elements of smart structures for rotorcraft environment
  - actuators, sensors (MEMS, fiber optics), controllers and noise signal analyses



## Innovative Smart Technologies for Actively Controlled Jet-Smooth Quiet Rotorcraft

### Overall Approach

- Build dynamically scaled (Mach) models and test these in vacuum chamber, on hover stand and Glenn L. Martin wind tunnel, in anechoic chamber, and in DTRC anechoic tunnel
- Develop analytical formulations for coupled blades with induced actuation and incorporate these in comprehensive rotorcraft codes, validate analyses with experimental data
- Refine key elements of smart structures technology for simulated rotorcraft environment
  - actuators, sensors, nonlinear controllers and noise analyses; incorporate in scaled models and comprehensive analyses

# MURI

## Innovative Smart Technologies for an Actively Controlled Jet-Smooth Quiet Rotorcraft

### **Task 1 : Active Noise Control**

- 1.1 Active Noise Control Using Smart Trailing-Edge Flaps -- Baeder/Leishman
- 1.2 Active Leading-Edge Droop for High Speed Noise Control -- Baeder/Dooling
- 1.3 Coupled Aeroacoustic/Aeroelastic Comprehensive Analysis -- Long/Gandhi
- 1.4 Parameter Delineation, Directionality and Discretization - George/Sims/Adebayo
- 1.5 Active Attitude Modification for BVI Noise Abatement -- George/Sims

### **Task 2 : Active Interior Noise Control**

- 2.1 Interior Noise Control Using Smart Materials -- Balachandran
- 2.2 Hybrid Active/Passive Trim Panel Damping Control -- Wereley
- 2.3 Interior Noise Control Using Smart Wall Paper -- Varadan/Varadan

### **Task 3 : Active Vibration Control**

- 3.1 Active Vib. Control Using Smart Rotor Tips with Bend-Torsion Coupl. - Chopra
- 3.2 Active Control of Structural Response Using Smart Actuators -- Chopra
- 3.3 Active Stabilator for Tiltrotor Vibration Suppression -- Wereley

### **Task 4 : Active Transmission Noise / Vibration Control**

- 4.1 Active Control of Coupled Rotor-Drivetrain-Airframe Dynamics -- Smith/Wang
- 4.2 Active Gearbox Struts for Control of Noise/Vibration Trans. -- Balachandran
- 4.3 Adaptive Multi-Functional Sensors of Transmission Noise Suppr. -- Pines

### **Active Noise and Vibration Suppression**

- 5.1 Use of Dissimilar Rotors for Vibration and Noise Suppression -- Gandhi
- 5.2 Aeroelastic/Aeroacoustics Analysis of Double Swept Rotor - Ganguli/Baeder
- 5.3 Mach-Scaled Rotor Model with Smart Trailing-Edge Flaps -- Chopra

### **Task 6 : Key Technology Elements**

- 6.1 Smart Conformal MEMS Based Sensors -- Varadan/Varadan
- 6.2 Multiplexed, High Bandwidth Bragg Sensors for Cabin Noise Control -- Sirkis
- 6.3 Nonlinear Adaptive Control Strategies for BVI -- Krstic
- 6.4 Time-Frequency Analysis of Helicopter Noise -- Celi

## MURI Research Team



### UM: Rotorcraft Center:

Inderjit Chopra (301-405-1122) -- Smart Rotor/Piezo, SMA  
Norman Wereley (5-1927) ER-MR Fluids/Active Damping Control  
James Baeder (5-1107) - - External Acoustics  
Darryl Pines (5-0263) - - Sensors and Health Monitoring  
Roberto Celi (5-1132) - - Acoustics Analysis  
Gordon Leishman (5-1126) -- Aerodynamics/Acoustics  
Ben Sims (5-1143) -- External Acoustics

### UM: Mechanical Engineering:

James Sirkis ( 5-5265) -- Fiber Optics  
Amr Baz (5-5206) - - Controls  
B. Balachandran (5- 5309) - - Internal Acoustics Control

### UM: Psychology:

Robert Dooling (5-6843) -- Psycho Acoustics

### Penn State:

Vijay Varadan -- Smart Electronics and MEMS  
Vasu Varadan -- Smart Electronics and MEMS  
Ed Smith- - Dynamics  
Farhan Gandhi -- Dynamics  
Kon-Well Wang -- Damping Control  
Lyle Long -- Computational Acoustics

### Cornell:

Al George -- External Acoustics

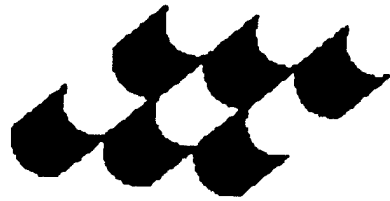
### UDC:

A. Adebayo -- Acoustics Analysis

## Smart Rotor Development; Summary Conclusions



- **Trailing-Edge Flap Concept:**  
Achieved flap deflection 2 - 4 deg., target value 8 deg.  
Concept appears feasible even for a full-scale vehicle
- **Controllable Twist Concept:**  
Achieved flap deflection .4 deg., target value 2 deg.  
Concept appears promising for partial reduction
- **Shape Memory Alloy Actuators:**  
Potential for tab adjustment for tracking
- **Analytical Modeling:**  
Torsional modeling needs refinements, Integration of  
smart actuators in comprehensive rotor analyses needed



ACTIVE  
MATERIALS &  
STRUCTURES  
LABORATORY

<http://web.mit.edu/amsl/>

# Overview of Research in the Active Materials and Structures Lab

Prof. Nesbitt W. Hagood

3rd ARO Workshop on Smart Structures  
August 28, 1997  
Virginia Polytechnic and State University  
Blacksburg, Virginia

# Laboratory Overview

## Active Materials & Structures Laboratory

### Mission

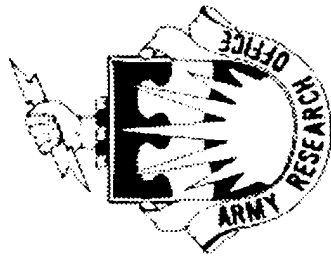
- To develop advanced technologies for control of electro-mechanical systems
- Focusing on solid state actuator and sensor technologies as well as control for critical aerospace applications

### Personnel

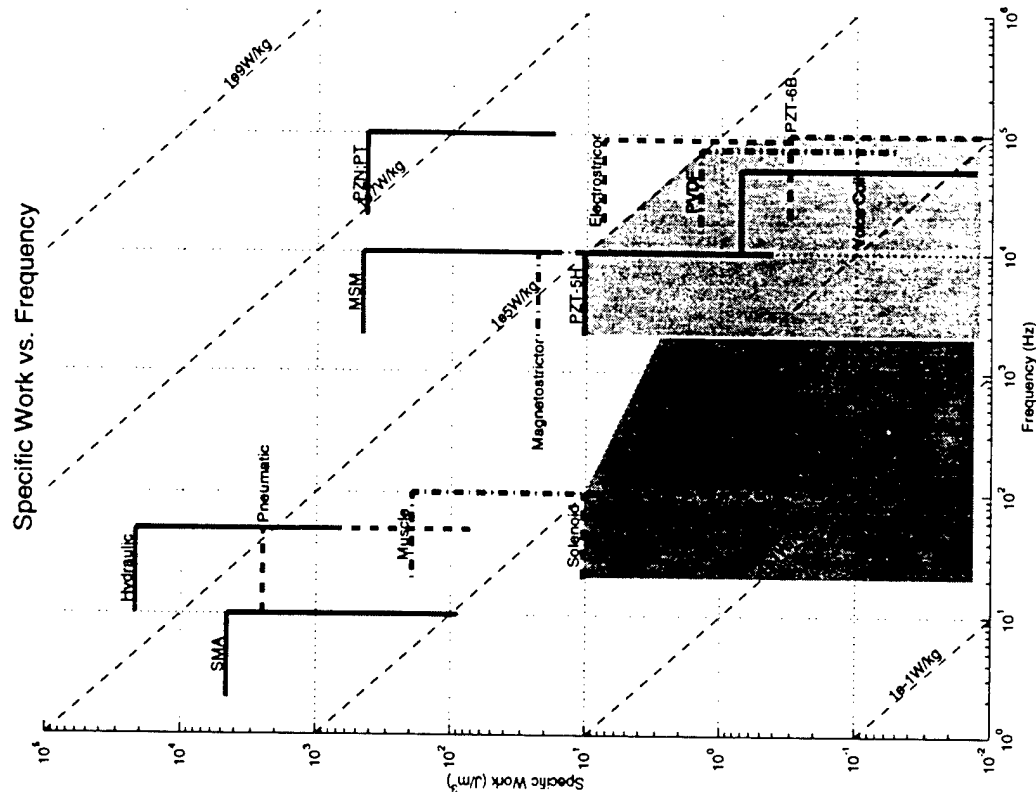
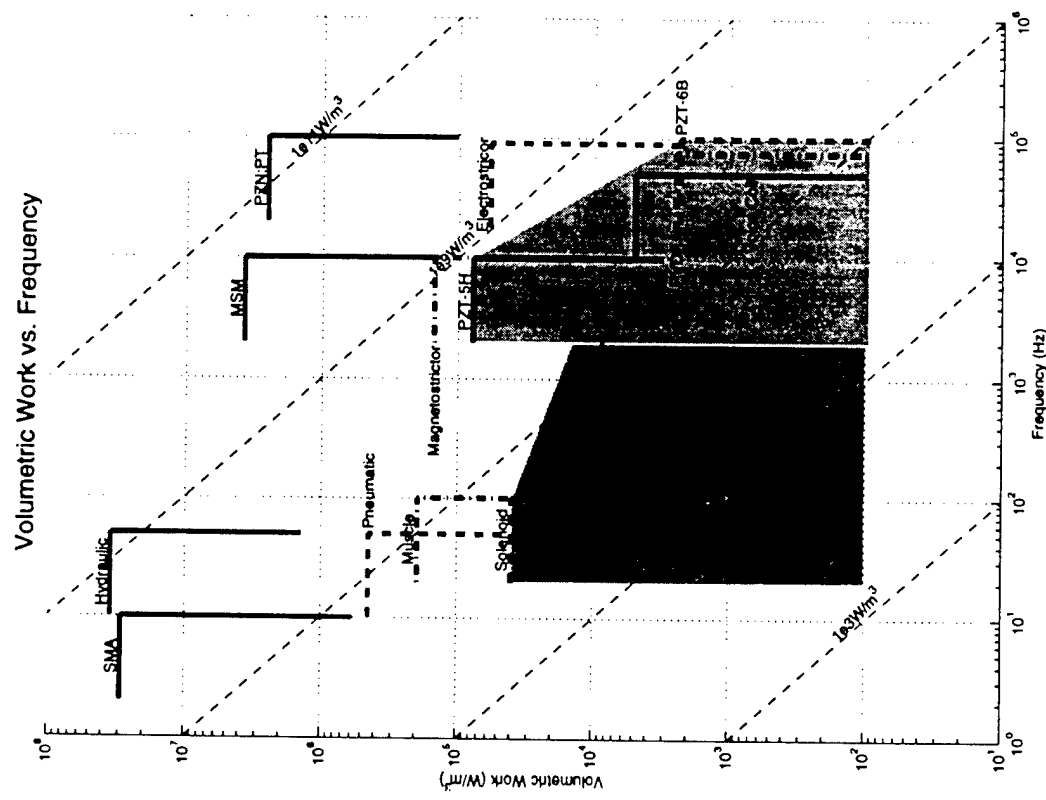
- 8 Faculty (Aero/Astro, Materials)
- 1 Research Associate, 2 Post-docs, 1 Visiting Scientist
- 22 Graduate Students, 13 Undergraduate Researchers

### Funding

- FY 1997, funding at \$2.3 Million
- ARO, DARPA, AFOSR, Boeing, JPL, ONR



# Actuator Comparison Volumetric and Specific Work vs. Frequency



# The Research Vertical Technology Integration

## Applications

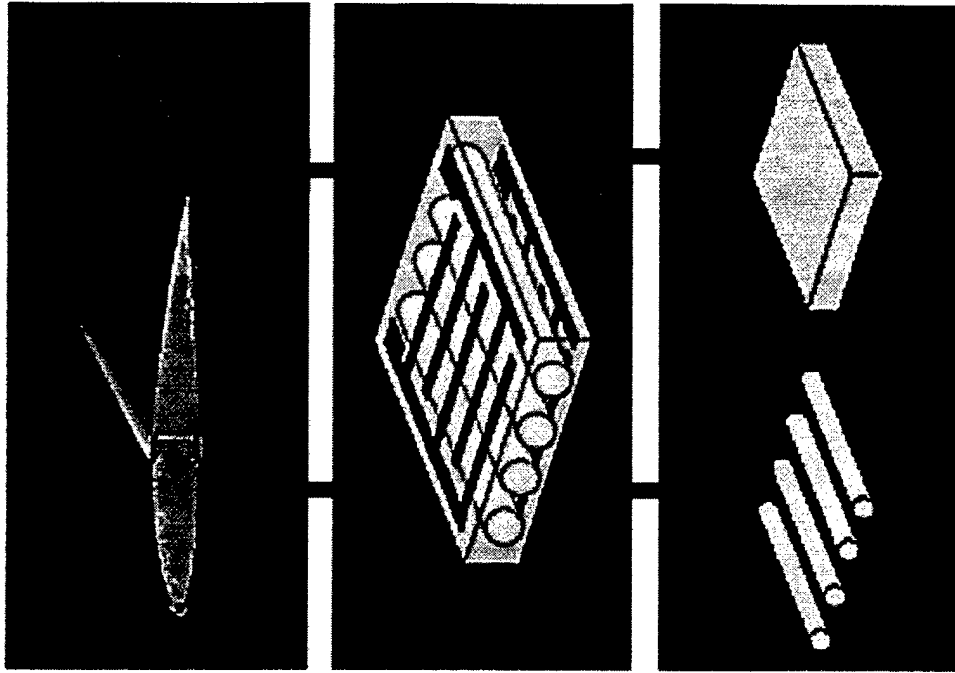
- Acoustics Control
- Aeroelastic Control
- Robotics

## Devices

- Solid State Motors
- Discrete Actuators
- Distributed Actuators
- Servo-Hydraulic Systems

## Materials

- New Compositions and Processing
- Modeling and Characterization



# Active Fiber Synthesis

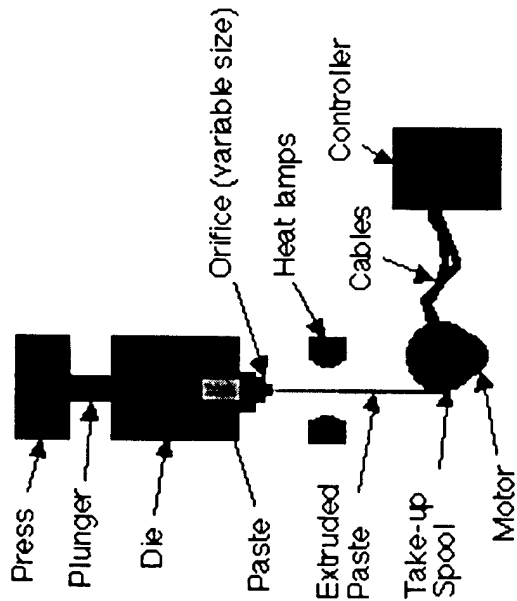
**Objective:** Fabricate low cost, high-quality fibers

## Extrusion Processing

- Continuous fiber forming
- Extrude piezo paste
- Fire fiber and then spool

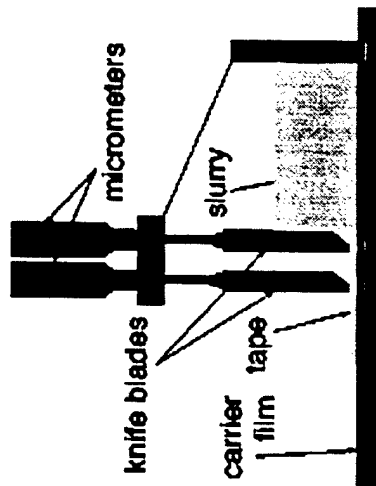


100 $\mu\text{m}$  diameter fiber



## Tape Cast Processing

- Piezo slurry is thinned to form tape
- Tape can be cut to form fibers
- Piezo slurry can be formed in grooves to remove cutting step
- Fibers are later fired
- New technique: etched-mold casting



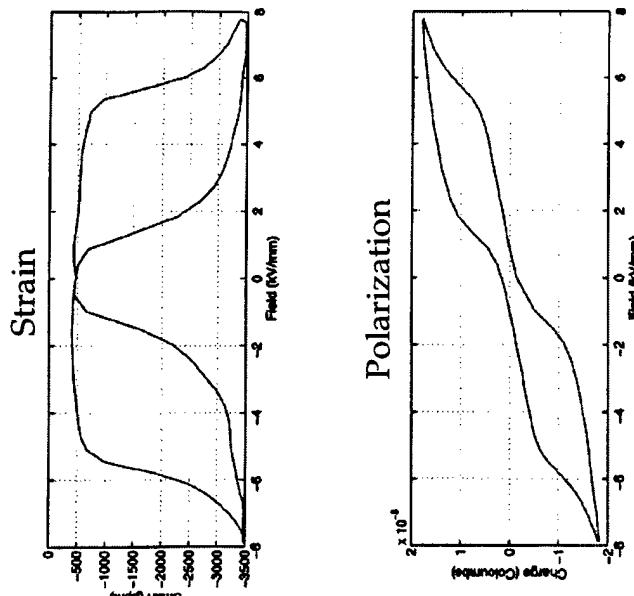
150 $\mu\text{m}$  wide and 70 $\mu\text{m}$  thick

Cima.....ARO MURI

# New Compositions Shape Memory Ceramics

**Shape Memory Objective:** Temperature stable lead-hafnate, lead-titanate ferroelectric-antiferroelectric phase switching materials.

- Composition near the ferroelectric anti-ferroelectric phase boundary.
- Electric field induces phase transition between ferroelectric and anti-ferroelectric phase.
- Large strains accompany phase transitions.
- Material exhibits shape memory and requires electric field or stress to return to original state.
- Experiments on a range of compositions at different temperatures have isolated the phase boundary. The materials are temperature independent and exhibit 3000 ppm strain.



Chiang, Tuller.....ARO/MURI

# New Compositions Single Crystal

**Background:** Work has been done by Shroud at Penn State on PZN-PT single crystals that achieved 1.7% strain.

**Single Crystal Objective:** Develop nonlead-containing single crystal composition for easier manufacturing and high strain.

**Advantages:**

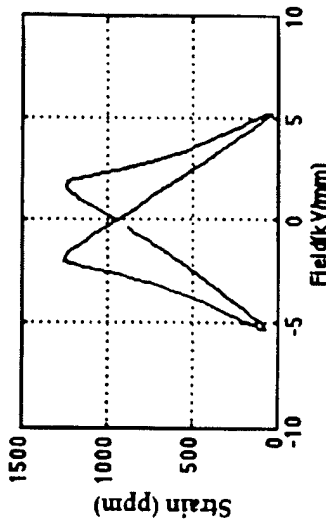
- Low hysteresis and very high strain

**Growth**

- Grown using self flux method. Annealing reduces cracking.

**Current Work**

- Crystals several mm thick with 3000 ppm strain have been grown.
- Some compositional variations occur within each batch but each crystal is uniform.
- New compositions are being tested.
- New manufacturing techniques and refinements are being implemented.



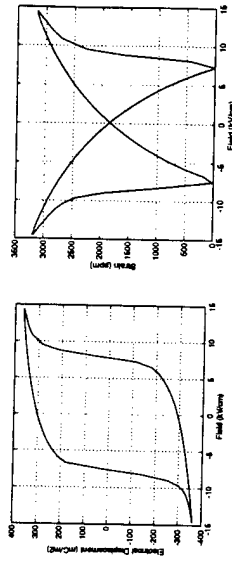
Chiang.....ONR

CLAYE MATERIALS AND STRUCTURES LABORATORY (AMSL)

# Material and Device Modeling

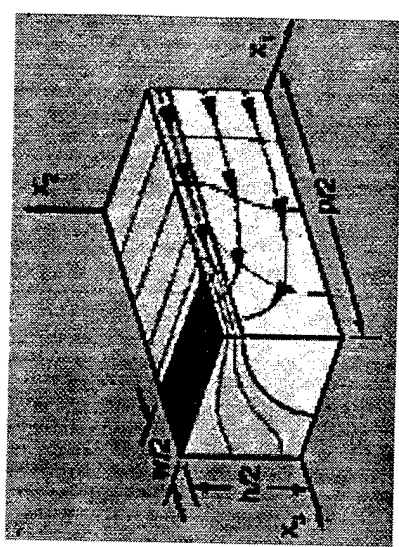
## Nonlinear Material Models

- Energy based nonlinear response
- Partial and non-uniform polarization
- Hysteresis and stress depoling



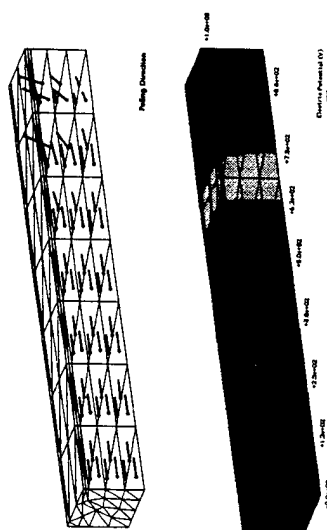
## Effective Medium Models

- Mesoscale model of composite/ceramic behavior
- Model ceramics as composites of crystallites in random orientation
- Calculate effective material properties from the aggregate of inclusion/grain behavior



## Nonlinear Electroelastic Finite Elements

- Active structures with complex geometry
- Nonuniform fields/polarization
- Stress concentrations
- Macroscopic response

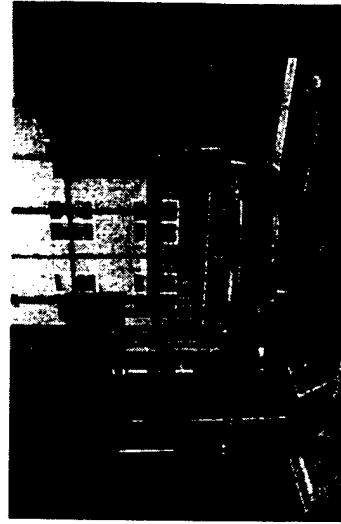


# Characterization

## Nonlinear Material Characterization

- Measure high field material response
- Characterize electrically and mechanically induced repolarization
- For use in nonlinear material models

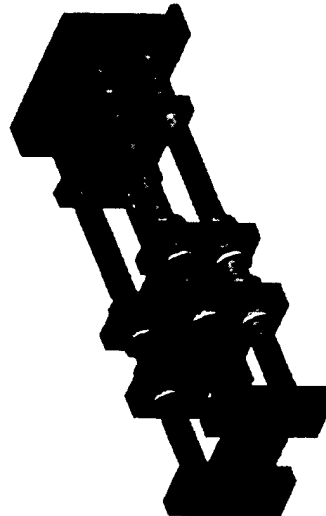
Hagood.....ARO MURI



## Device Characterization/Operation Under Load

- Determine material properties in realistic operating environments
- Dependence on applied load, frequency, and temperature
- Stiffness, permittivity, and electromechanical coupling in nonlinear range

Hagood, Hall.....ONR YI



## Facilities

- Instron Loading Facility
- Component Stiffness Tester

Future Component Tester



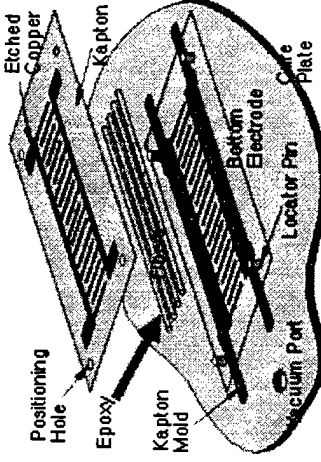
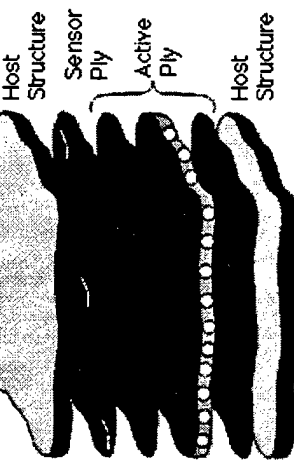
# Active Fiber Composites

## Introduction

### Concept

- Small diameter electro-ceramic fibers in soft polymer
- Configured as an active ply for planar actuation
- Electrode pattern directs field along fibers

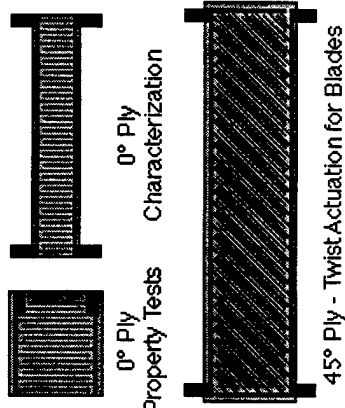
### Components & Manufacture



### Advantages

- High strength
- Tailored directional actuation
- Conformable/large area
- High energy density

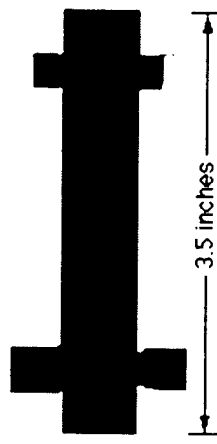
Hagood.....ONR, ARO MURI, DARPA



# Active Fiber Composites Characteristics

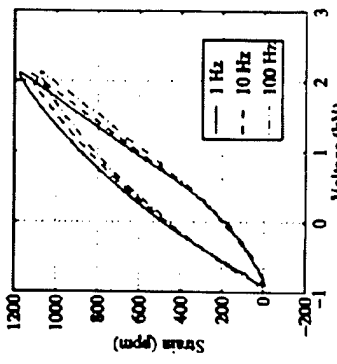
## Test Article:

- Actuator size: 3.5" by 0.5"
- Reinforced configurations use E-glass lamination or S-glass reinforcement



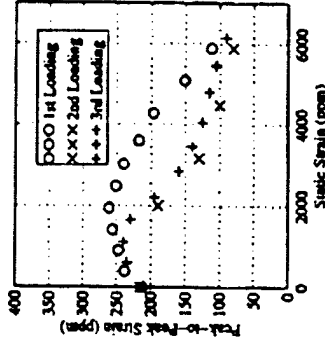
## Tests:

- Electromechanical properties and limits
- Mechanical and electrical fatigue
- Actuation under static tensile load



## Performance:

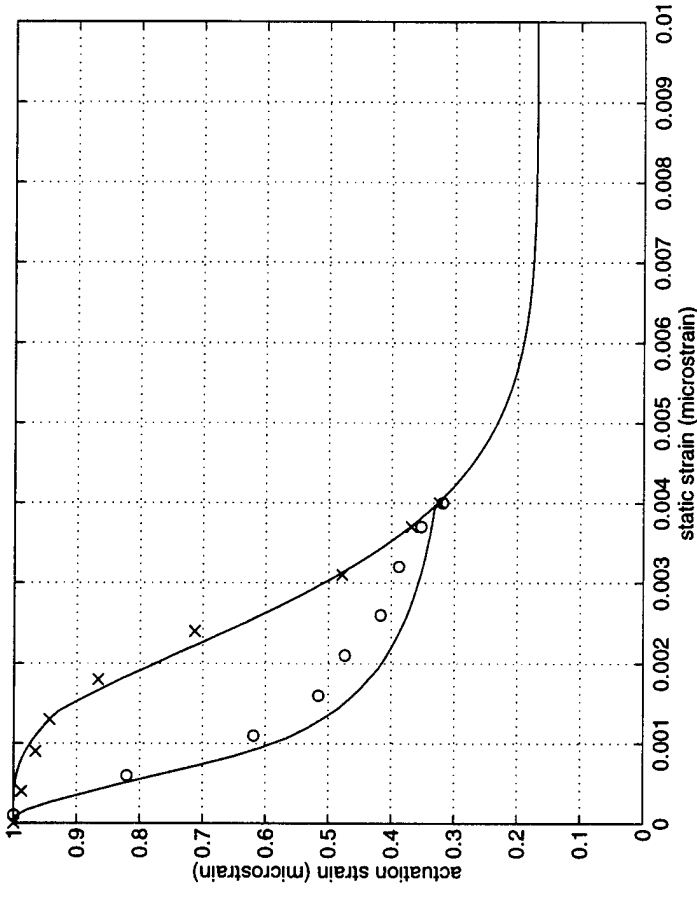
- Passively reinforced AFC's significantly outperform conventional piezos
- Survivability beyond 3000 microstrain without degradation
- Compositing technologies enable distributed actuation within harsh operating environments



# Actuation Under Load Results

- First and second load cycle of a specimen tested under tensile load shown compared to model

Curves shown normalized by maximum actuation



- Model captures trend in reduced actuation capability of composite

# Solid-State Motors

**Concept:** microscopic deflections driven by solid-state active materials are rectified into usable continuous motion

## Objectives

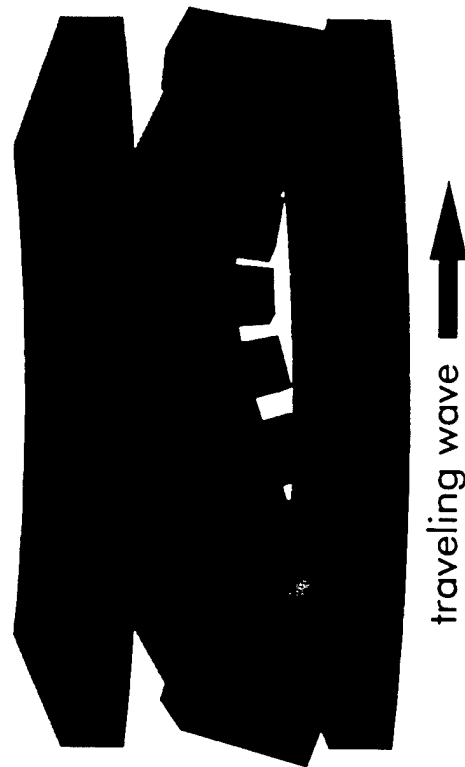
- High torque and power in a compact motor
- Utilize modeling for efficient design and performance prediction

## Motivation

- High torque density, quick response, direct drive, self-braking
- Maximum efficiency at high torque
- Simple structure promotes miniaturization

## Operation — Traveling-Wave Motor

- Orthogonal piezo arrays force traveling wave
- Microscopic displacements are rectified into rotary motion



Hagood.....JPL, ARO MURI

traveling wave

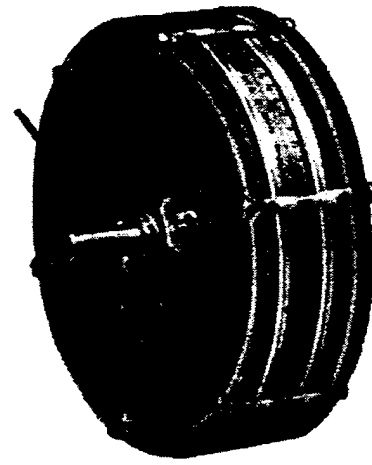
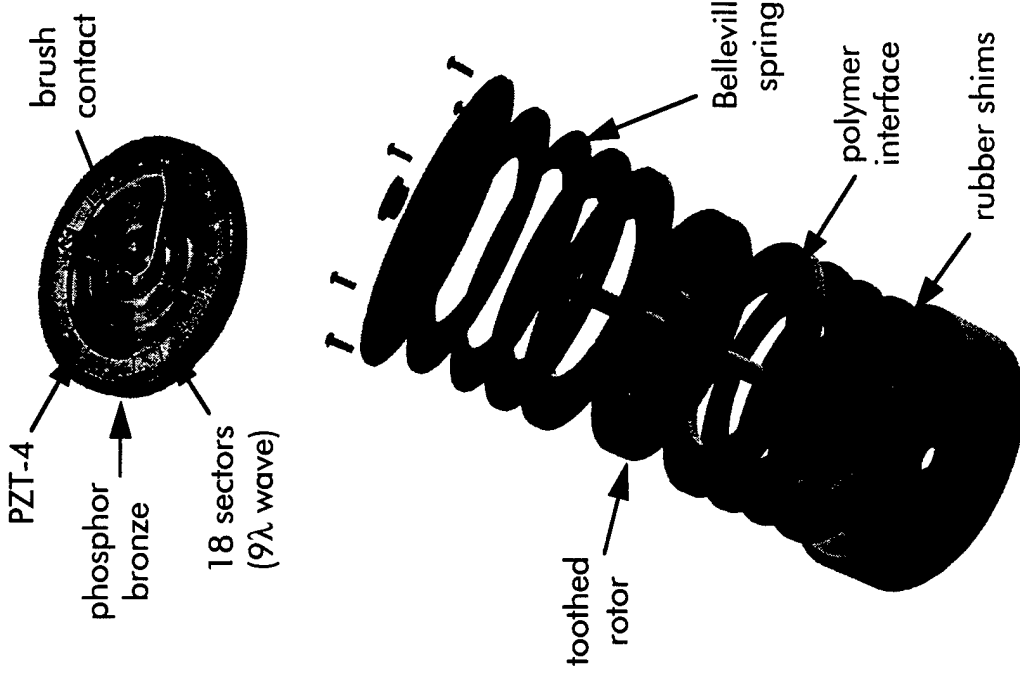
# Two-Sided Ultrasonic Motor Experimental Prototype

## Design

- Novel two-sided operation
  - Increased torque and efficiency
  - Thermal stability
- Nonlinear state-space model
- *A priori* performance prediction

## Characteristics

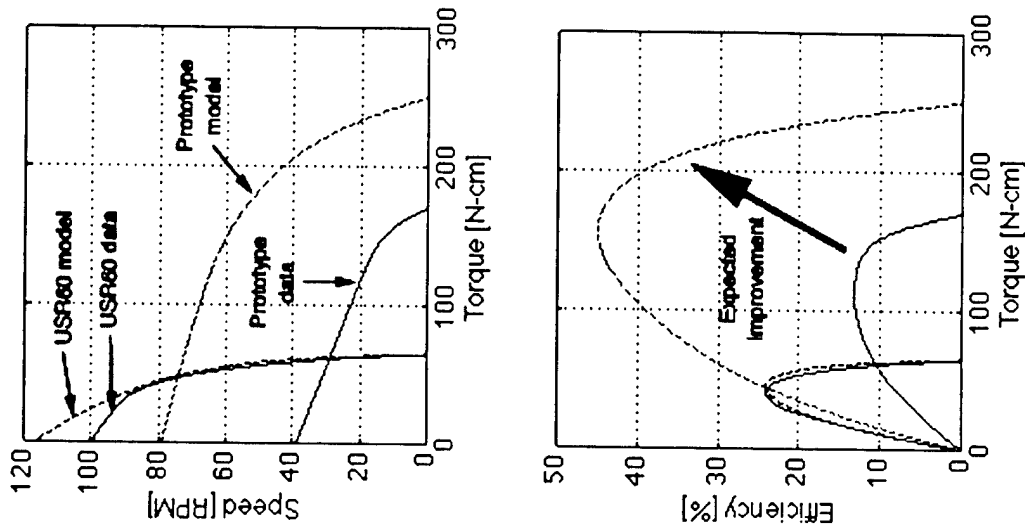
- Vibrating disk constitutes the rotor
- 8-cm diameter, <0.5 kg
- 150 V<sub>p</sub>, 40 lbs, 32 kHz



# Two-Sided Ultrasonic Motor Performance

## Preliminary Results

- Comparison to commercial Shinsei USR60
  - about 3 times the stall torque
  - twice the torque density
- Model comparison
  - correlation with USR60 demonstrates validity
  - prototype performance lower than expected



## Conclusions

- Characteristics and quality of interface surfaces govern performance
- Considerable improvements are expected
- Novel contact mechanisms may improve efficiency

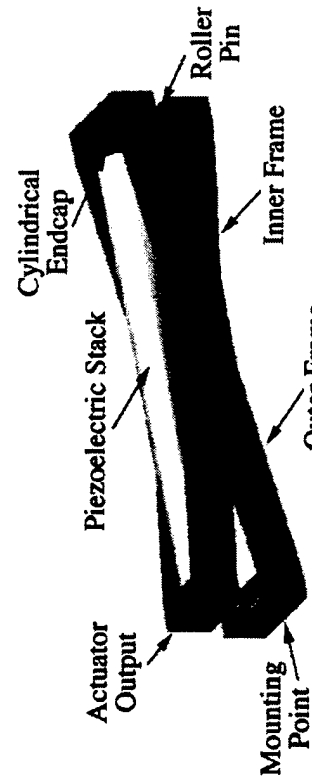
## Potential Applications

- Automobile industry
- Consumer goods
- Space missions
- MEMS
- MRI
- Robotics

# Discrete Actuators

**Goal - Transform active material energy for large stroke applications in a mass efficiency sense.**

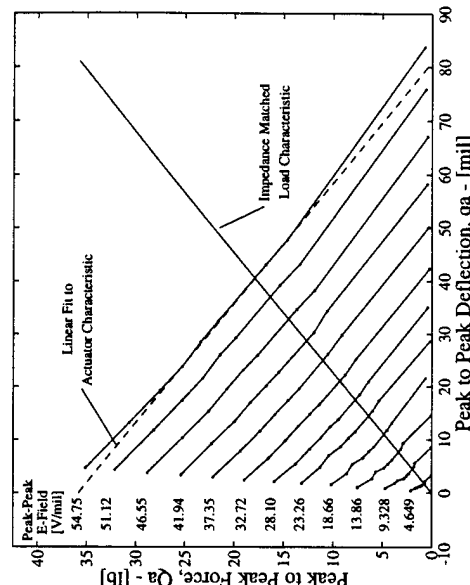
## Application - The X-Frame Actuator



- Two EC-98 stacks reacting against criss-crossed frames. Shallow frame to stack angle results in 15:1 stroke amplification

- Simple design. Pre-loads also easily applied.
- Performance measured upon driving loads of varying impedance.
- Shows mass efficiency approaching 31% (theoretical maximum is 44%).

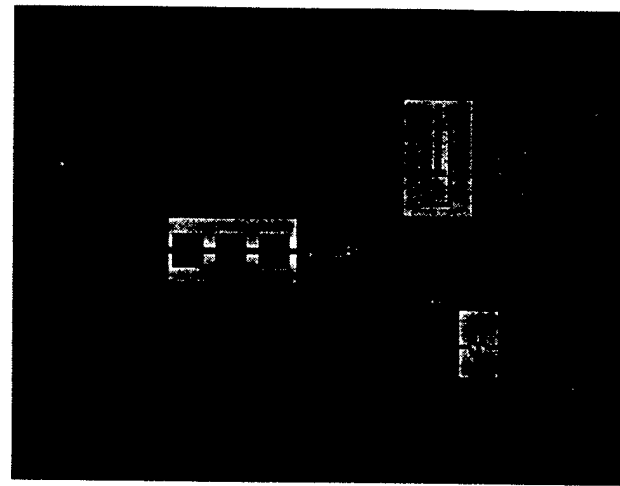
Hall.....DARPA



# Solid-State Servo-Hydraulic Systems

## Concept

- Piezoelectric micropumps
- Energy storage in elastic pressure reservoirs



## Motivation

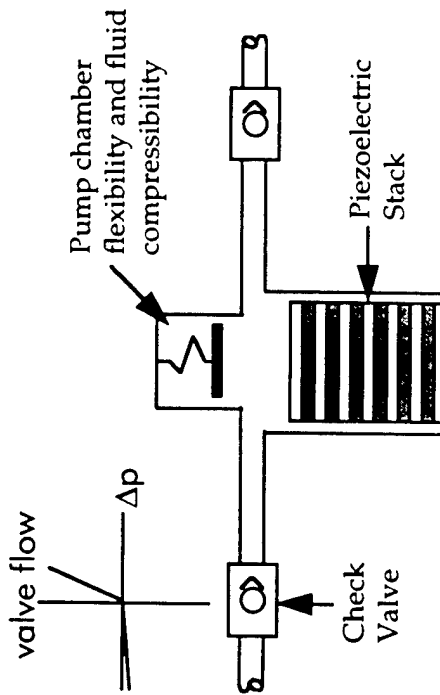
- High power densities of piezos converted to large single-stroke actuator energy densities
- Reduced system scale provides higher effective energy densities

## Approach

- Modeling and numerical simulation of servo-hydraulic systems
- Investigation of scaling effects on performance
- Fabrication of meso- and microscale fluidic components

Hagood.....

ONR



# Active Acoustics

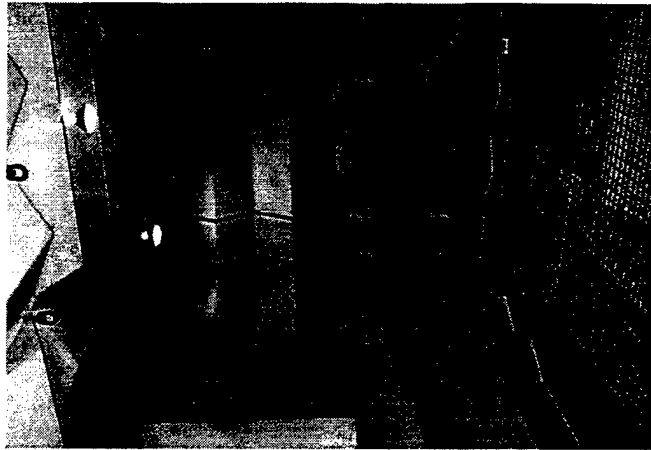
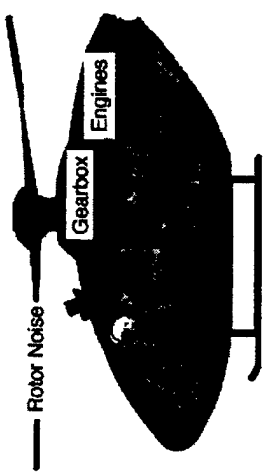
## Structural acoustic control

### Concept

- Minimize acoustic environment utilizing structural actuation
- Innovative control architectures to cope with structural-acoustic coupling

### Applications

- Interior acoustic control
  - Helicopters, airplanes, autos, elevators
- Exterior acoustic control
  - Submarines, torpedos, power transformers



### Anechoic Facility

- Frequency range: 120 Hz - 12,500 Hz
- Internal size: 14' x 10' x 8.5'
- Perforated metal wedges increases anechoic volume

# Fuselage noise control

## Approach

- Representative structural-acoustic testbed
- Apply distributed actuation and control

## Actuation and Control

- Distributed actuation using local control algorithms
- Hierarchic global/local control for reduced computational requirements

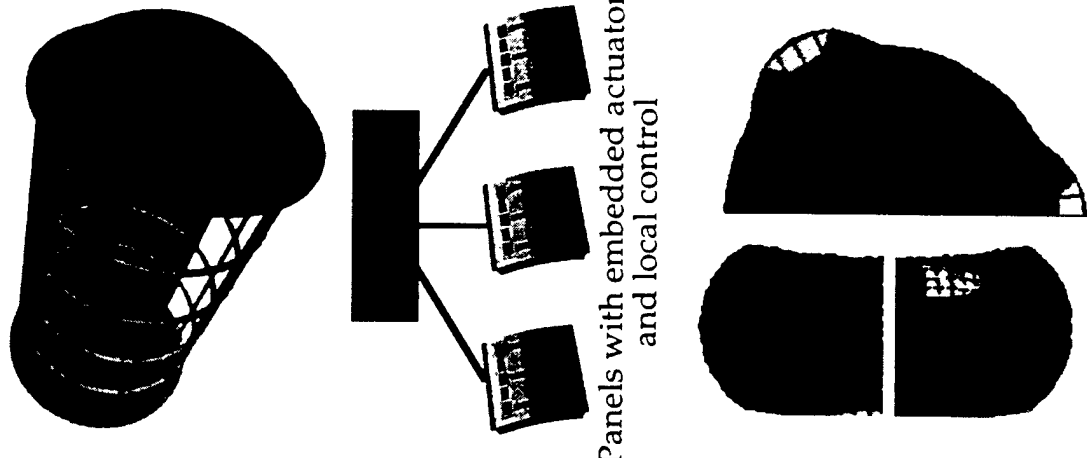
## Coupled Modeling — 2 Methods for Verification

- Finite element modeling in ANSYS, 1/4 cylinder
- Rayleigh-Ritz assumed modes method, 3-D

## Fuselage Testbed Status

Structural-acoustic tesbed has been ordered,  
scheduled to arrive November 1997

Hagood, Hall, Crawley.....  
.....ARO MURI



# Panel Acoustic Radiation Active Noise and Vibration Control

## Approach

- Structural-acoustic coupling in air
- Leverage active fiber composite technology for acoustic control
- Apply model-based feedback control

## Actuation and Control

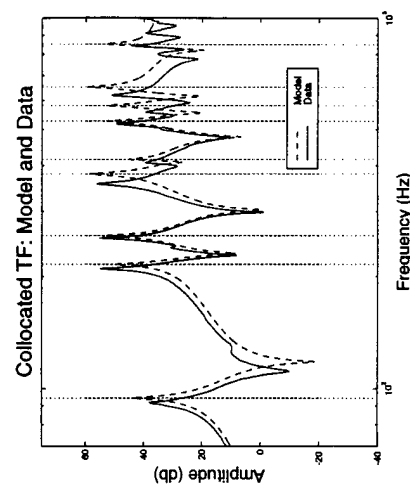
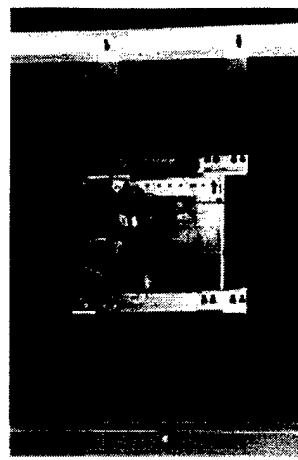
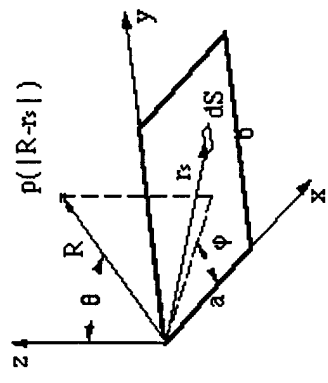
- Piezoelectric fiber composite panels
  - Anisotropic actuation allows specific radiation mode control
- AVAC methodology
  - Acoustic modal restructuring
  - Vibration modal cancellation

## Experiments

- Baffled panel in AMSL anechoic chamber
- Real-time control development using dSPACE DSP/RISC system

Hagood.....

ONR



# Active Rotor Blade Control

## Introduction

**Concept:** Integrate active materials within rotor blades to control vibrations

### Motivation

- Helicopter rotors suffer from vibration and noise due to blade vortex interactions (BVI)
- Feedback control is used to reject aerodynamic disturbances with blade mounted actuators

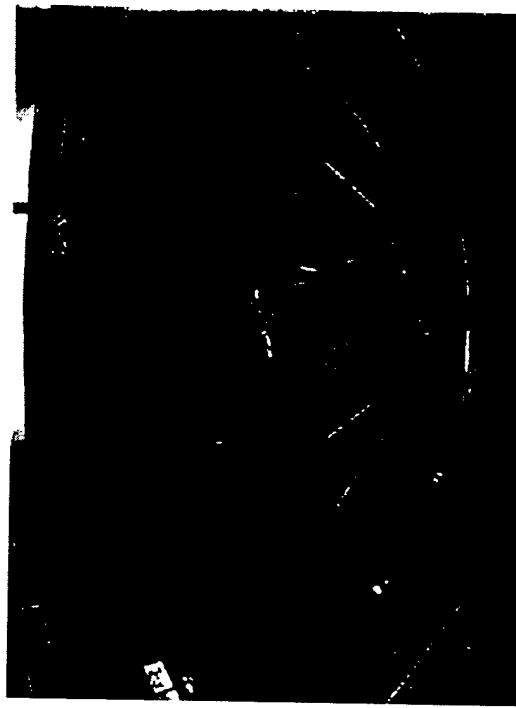
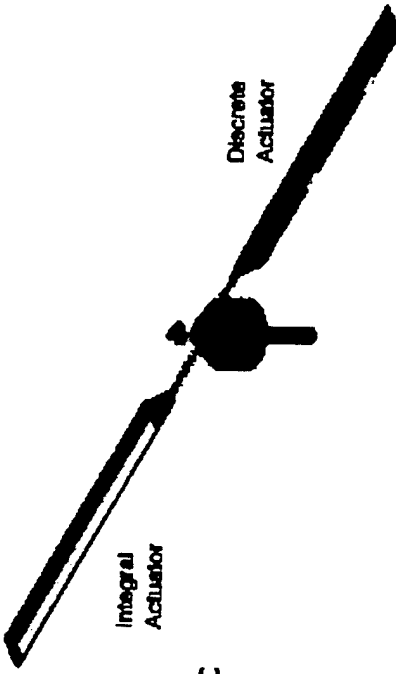
### Approach

- Developing discrete and integral blade mounted actuators.

### MIT Hover Test Stand Facility

- 1/6 Mach scale CH-47D testing facility
- Capable of supplying  $\pm 4000\text{V}$  AC signal to rotating frame.
- 48 Channel data acquisition system.
- 6 axis hub force measurements.
- Statically adjustable blade pitch within  $0.1^\circ$ .

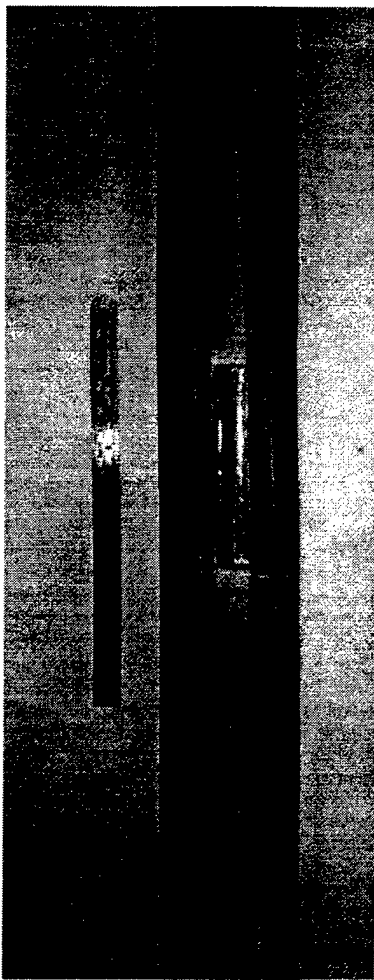
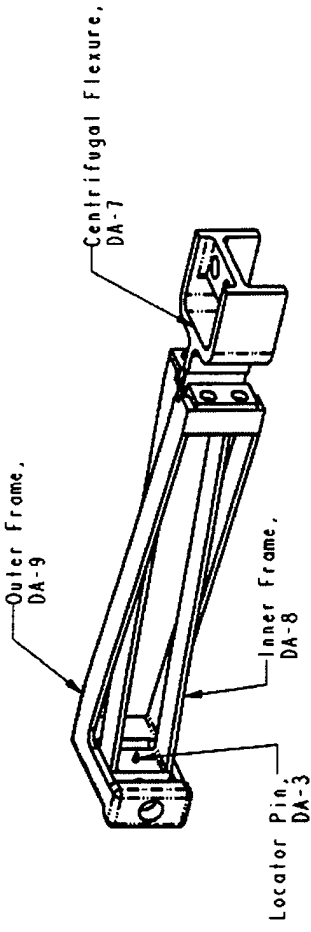
Hagood, Hall .....DARPA, ARO MURI



# Active Rotor Blade Control

## Discrete Rotorblade Actuator Design & Manufacturing

- One outer frame endplate extended with guides for inner frame to slide against.
- Centrifugal flexure restrains actuator spanwise, equilibrating loads on two stacks.
- Actuator attached to blade spar by centrifugal flexure at outboard side and sliding fitting at inboard side.
- Two active blades being manufactured.
- Actuator access facilitated by diverting composite unit's in manufacturing process.

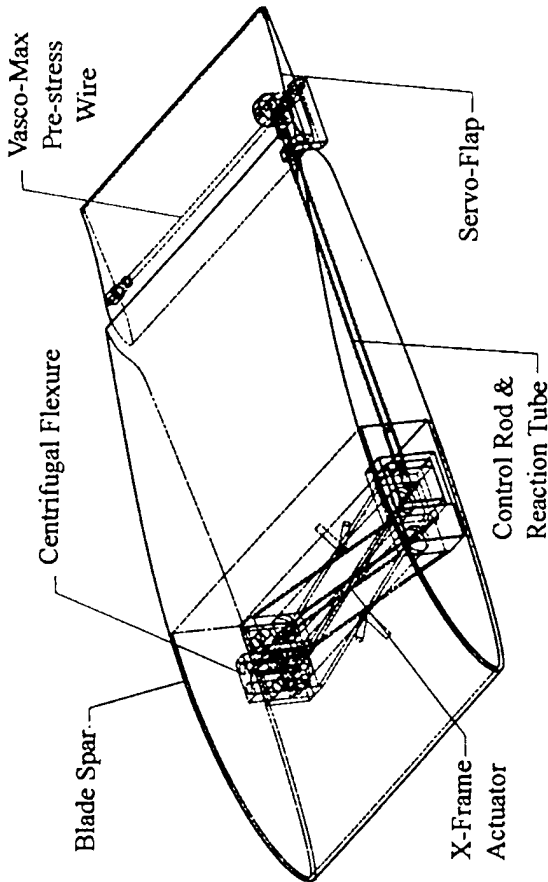


- Separate flap molds being machined for servo-flap.

# Active Rotor Blade Control Discrete Servo-Flap Actuation

## Concept

- Embed X-Frame Actuator in rotor spar, connect to trailing edge servo-flap by 2 push rods.

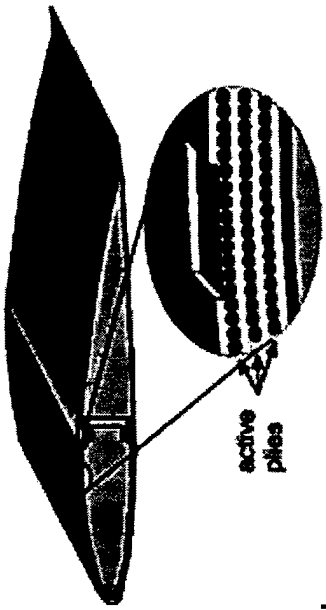


## Design Objectives/Constraints

- Actuator sized to power 20% of chord, 11.5% of span trailing edge servo-flap on 1/6 Mach scaled CH-47D blades.
- Goal:  $\pm 5$  deg flap deflection with 10% mass increase.

# Active Rotor Blade Control Integral Twist Actuation

## Concept



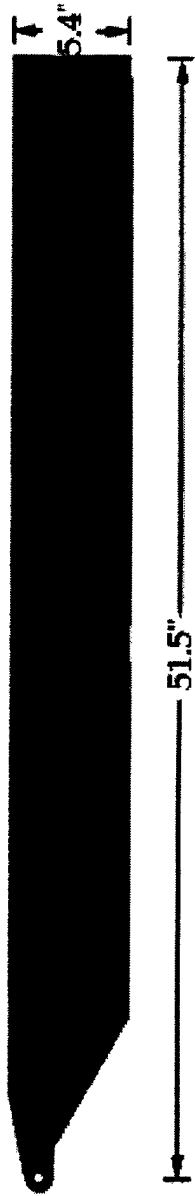
- Active fiber composite plies incorporated in composite spar lay-up
- Actuators induce shear stresses to twist spar

## Design Objectives/Constraints

- 1/6th Mach scale CH-47D composite baseline blade for hover testing
- $\pm 2^\circ$  of tip twist with less than 20% added mass to model blade
- Maintain stiffness and mass distribution except torsional stiffness reduced by up to 50% acceptable
- Maintain fatigue and ultimate strength

## Design details

- 42 packs in 3 active plies from 0.27 to 0.95R
- Electrical connections to packs along web
- Flex circuit designed to interface with electrode flaps



MIT ACTIVE MATERIALS AND STRUCTURES LABORATORY (AMSL)

## Active Rotor Blade Control Section Testing

### Section of spar from root to 0.54R

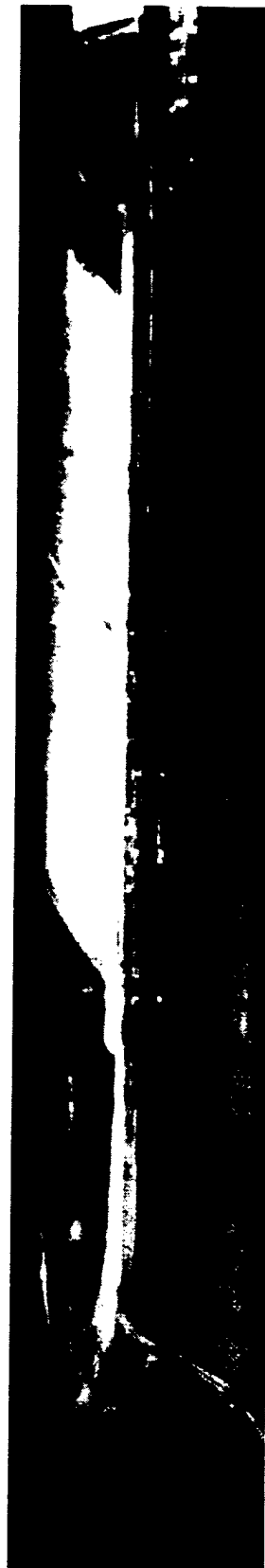
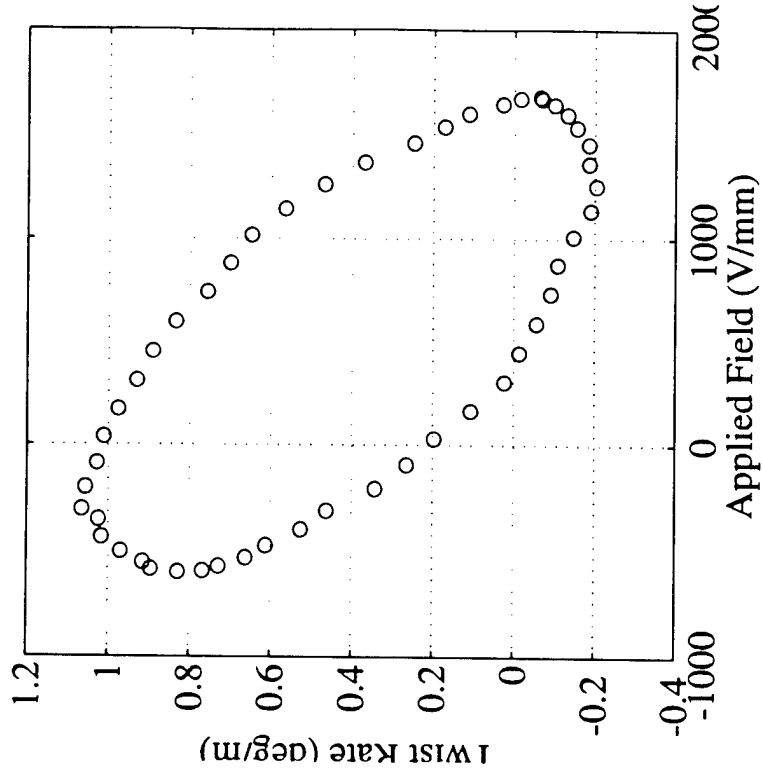
- Incorporates 12 AFC packs
- Interfaces with flex circuit
- 6 full strain gage bridges on foam core

### • Tip fixture for tensile testing

Preliminary twist data at 20 Hz and  
 $600 \text{ V}_{\text{dc}} + 2550 \text{ V}_{\text{pp}}$  cycle

- $1.26^\circ/\text{m}$  peak-to-peak twist rate
- model predicts  $1.69^\circ/\text{m}$  at estimated 450 microstrain cycle

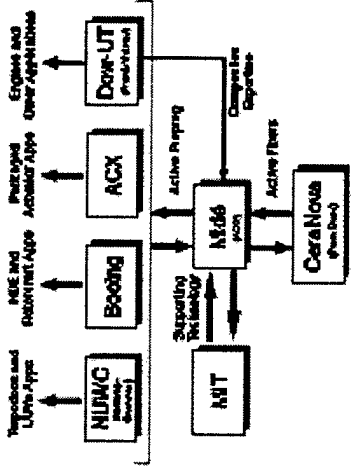
Dielectric breakdown between poorly  
insulated packs limited data



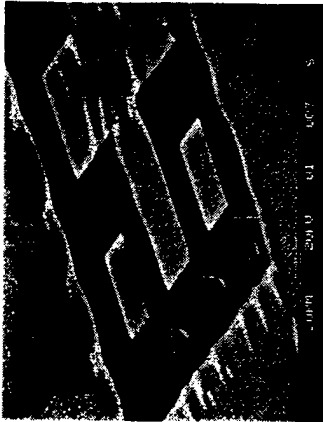
# The Future

## New Programs

- Smart Structures for Rotorcraft Consortium Phase II
  - Downselect between discrete and integral concepts scheduled for December 1997
  - 3 year testing program culminating in flight test



- Langley Integral Blade being developed for ARES rotor in TDT testing



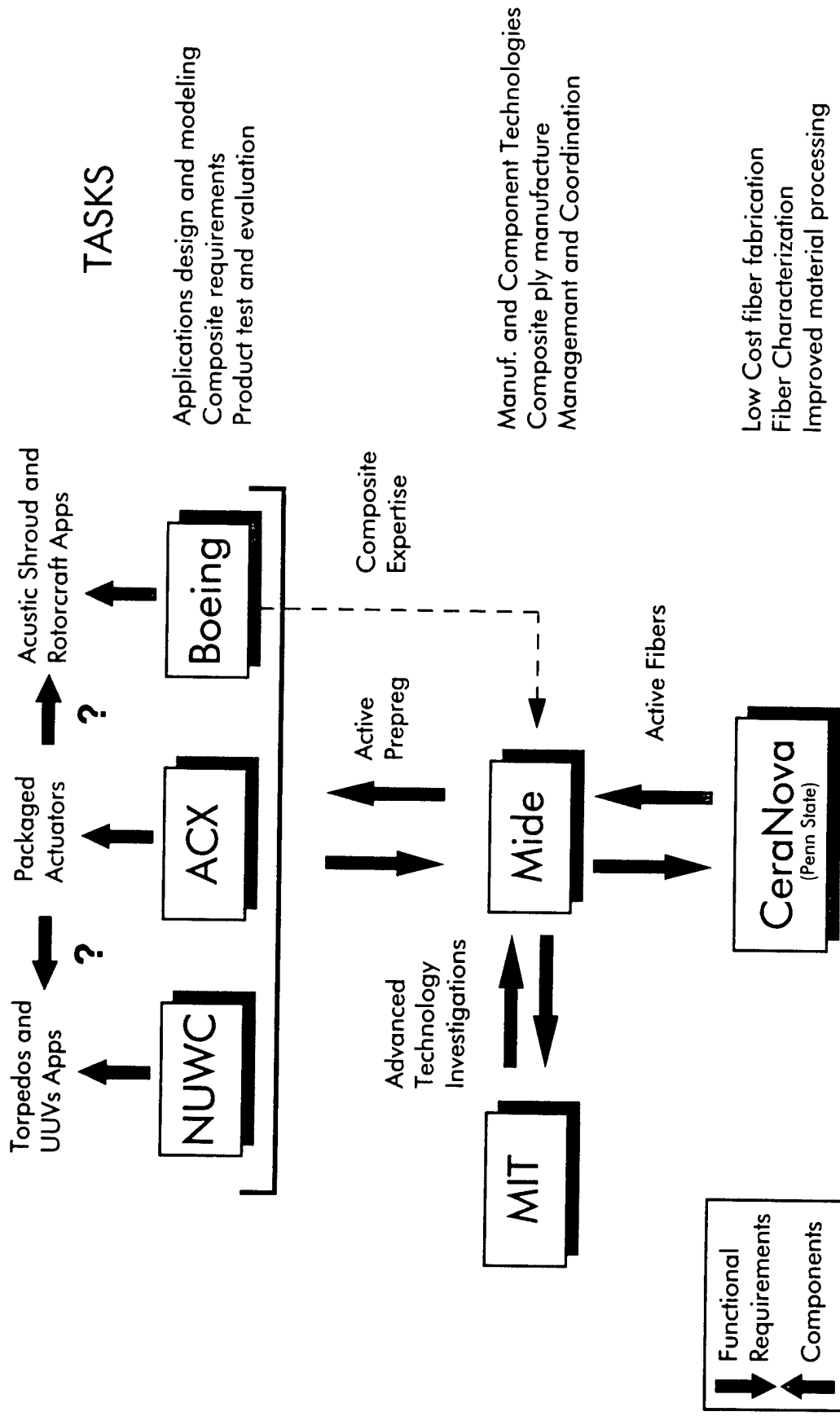
- Active Fiber Composites Consortium
  - ARPA Consortium founded to commercialize active fiber composite technology

## New Directions

- Solid-state micro actuators
- Hydraulic actuation systems
- Instrumented panels for conformal antenna

# Active Fiber Composite Consortium

## AFCC



# Summary

**Solid state actuation materials provide the foundation for control in a broad range of applications**

- Active acoustics
- Active aeroelastic control
- Actuation devices / robotics

**The technology is rapidly growing and evolving**

- New materials
- New applications

**Core future challenges**

- Material improvements
- Incorporating material in useful devices
- Commercialization / coordination with sponsors and industry

## Smart Materials Systems through Mesoscale Patterning

Ilhan A. Aksay,<sup>§</sup> Sol M. Gruner,<sup>†</sup> Peter C. Y. Lee,<sup>‡</sup>

Robert K. Prud'homme,<sup>§</sup> and Salvatore Torquato,<sup>‡</sup>

Departments of <sup>§</sup>Chemical Engineering, <sup>†</sup>Civil Engineering and Operations Research, and

<sup>‡</sup>Physics, and Princeton Materials Institute, Princeton University

Wei-H. Shih,

Materials Engineering Department, Drexel University

George M. Whitesides

Department of Chemistry, Harvard University

This project emphasizes the production of smart material systems using advanced 3-dimensional processing techniques. The specific aim is the fabrication and characterization of smart organic/inorganic composites at the mesoscale ( $\sim 1 \text{ nm} - 1 \text{ mm}$  length scale) to achieve improved performance. Two approaches are used: (i) synthesizing and processing organic/inorganic composites and (ii) developing two novel materials systems. Synthesis and processing studies emphasize three methods: (i) laser stereolithography, (ii) self-assembled monolayers, and (iii) 3-dimensional co-assembly. The two novel systems under investigation are piezoelectric shell transducers and 1-3 piezocomposite hydrophones.

### Novel Smart Material Systems

For the production of novel materials, two systems are under investigation: (i) "Moonies" and "Rainbows" comprising piezoelectric shell transducers (Fig. 2), and (ii) piezocomposite hydrophones and negative Poisson's ratio materials. Piezoelectric shell transducers are of interest because these can achieve large displacement to thickness ratios at relatively high stress levels, amplifying signal intensities and improving the resolution and detection limits of a sensor. The large displacements achievable by these systems would be of use in actuators, promising a new class of sensor/actuator devices. The materials referred to as "moonies" convert piezoelectric radial displacements into large axial displacements through bending stresses (Fig. 1). "Rainbows" convert meridional strain gradients into bending stresses which in turn induce large axial displacements (Fig. 1).

Our guiding concept is the idea that the rainbow shell structure can be used as a unit cell within a larger-scale cellular material (Fig. 2), fabricated using stereolithography. By combining several rainbow structures into a layered structure, the system response is magnified with a concomitant increase in the overall length of displacement. The goal in the case of multilayer shell transducers is to maximize the obtainable work per unit area in micro-actuator.

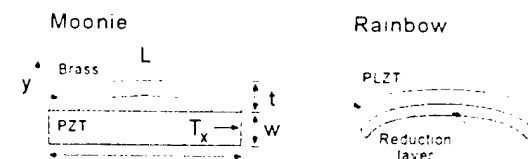


Figure 1: Structure of Moonies and Rainbows.

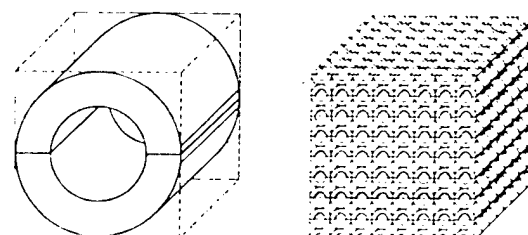


Figure 2: Rainbow unit cell and layered structure being fabricated using stereolithography

To achieve this, we fabricate cellular materials composed of stacks of rainbow actuators (Fig. 2) to enhance the displacement distances through the combination of many small devices. As a first step, we have produced 5 nm PZT powders through modified hydrothermal processing. Tapes made from these materials using standard tape-casting procedures have demonstrated that controlled delamination can be done within a multilayer body to form a cellular body. Our current efforts seek to improve the fabrication of multilayer laminates to provide higher uniformity throughout the unit cells and to develop procedures for attaching the control and sensing electrodes throughout the cellular construct.

The generated displacement of each actuator is dependent on the physical dimensions, electric field, and poling effects. To develop meaningful comparisons between different actuator we compare based on a normalized value. Our samples typically produce  $3.4 \times 10^{-5}$   $\mu\text{m}/\text{V}$ , compared to  $16 \times 10^{-5}$   $\mu\text{m}/\text{V}$  for Haertling's rainbow. If we assume both actuators are cylindrically shaped, 0.8 mm high, 2.54 cm in diameter, and under 1000 V potential, our samples produce 34 microns of displacement. Functioning as a sensor, as in the measurement of the force of impact from a falling rubber ball, our samples were equivalent to the Haertling rainbow in terms of the generated voltage.

### Scaling Analysis of Flexextensional Transducers

In this area, the objective is to analyze the scaling behavior of displacement and stress in transducers with nonuniform  $d_{31}$ . We have found that for piezoelectric shell transducers we can measure the displacements in rainbow ceramics (Fig. 3). Based on preliminary measurements, the effect of the thickness ratio has been modeled: force balance and scaling analyses show that axial displacement  $D \sim d_{31}L \cdot E/t$ , and relative displacement,  $D/t \sim d_{31}L^2 \cdot E/t^2$ , or  $D/t \sim d_{31}L^2 \cdot V/t^2$ , where  $t$  is the rainbow thickness or the brass thickness in the case of moonies (Fig. 3). Further, we have determined that the underlying principles for both moonies and rainbows are very similar (Fig. 3). That is, when a piezoelectric strip is joined with a non-piezoelectric strip, the piezoelectric strip will respond to an axial electric field and the non-piezoelectric strip will not, causing the device to arch. Results of the scaling analysis shows that the maximum pressure a rainbow can withstand is  $P_{\max} \sim t^2/L^2$ , agreeing with data on rainbows and moonies (Fig. 3).

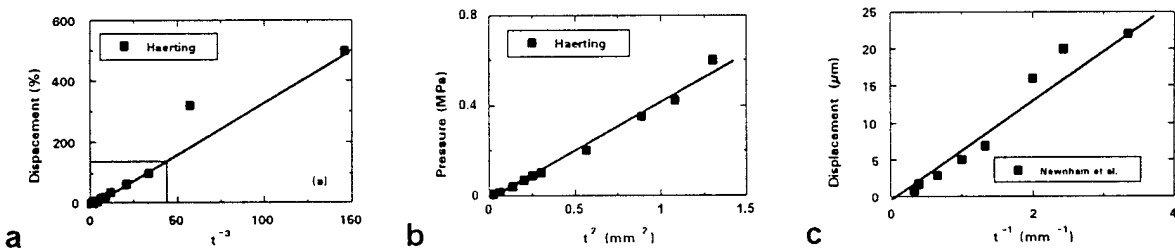


Figure 3: (a) Relative displacement at a constant voltage shows a  $t^{-3}$  dependence as the scaling analysis predicts (■ from Haertling). (b) Pressure on a rainbow shown a  $t^2$  dependence as the scaling analysis predicts (■ from Haertling). (c) Displacement versus brass thickness at a constant electric field.

## Optimal Thermoelastic and Piezoelectric Composites

Given the material properties of a polymer and PZT ceramic composite, the problem is to properly design a composite to achieve the highest possible sensitivity  $d_h$ , hydrostatic coupling factor  $d_h g_h$ , and/or electromechanical coupling factor  $k^2_h$ .

Piezoceramic rods in a polymeric matrix are used to test the fabrication of 1-3 composite hydrophones (Fig. 4). Design parameters for this system include: (i) shape and arrangement of the PZT rods, (ii) volume fraction of the rods, and (iii) the structure of the matrix material. Using the figure of merit for 1-3 PZT/polymer composites as determined by Newnham and

Ruschau, our results indicate: (i) The best structures are space-filling arrays of coated cylinders, approximated well by hexagonal arrays of rods. (ii) Optimal volume fraction for the rods lies between 0.05 and 0.15. (iii) The best matrix material is highly anisotropic and has a *negative Poisson's ratio* (-v). And, (iv) Optimal composites perform 30-500 times better than pure PZT (Table 1).

Table 1: Comparison of the values for the hydrostatic charge  $d_h$ , hydrophone figure of merit  $d_h g_h$ , and the electromechanical coupling factor  $k^2_h$  for pure PZT and PZT/polymer composites.

Material	$d_h$	$d_h g_h$	$k^2_h$
Pure PZT	32.0	0.068	0.006
PZT + isotropic polymer matrix	71.0	2.20	0.02
PZT + best anisotropic polymer matrix	1137	1945	0.36

Negative Poisson's ratio materials *shrink* in one direction in response to orthogonal compression. Few materials have been made having -v, especially at the submicron scale. Such materials, as shown in Fig. 5, have been made using stereolithography. The unit cell is derived theoretically using topology optimization. Beginning with a porous cubic unit cell, the effective piezoelectric properties are determined as a function of the element densities. This is then varied as elements within the unit cell are rearranged, and the structure continues to evolve until an optimal property is reached. Once the optimal geometry has been determined, the model is transferred to a 3-dimensional modeling program which translates the structure into a control program for the stereolithography unit. Finally, we build the structure using 3-dimensional patterning (Fig. 5). As shown we have succeeded in constructing the unit cell and the unit cell can then be replicated throughout a cellular object.

## Materials Processing

We have demonstrated the feasibility for using laser stereolithography effective micrometer scale processing. However, using current rapid prototyping techniques with ceramics results in poor quality materials, due to the formation of low density green bodies. The low solids density in cured layers can be addressed using high

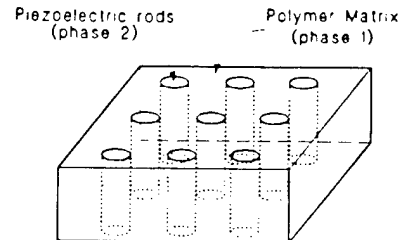


Figure 4: Schematic of a 1-3 piezocomposite

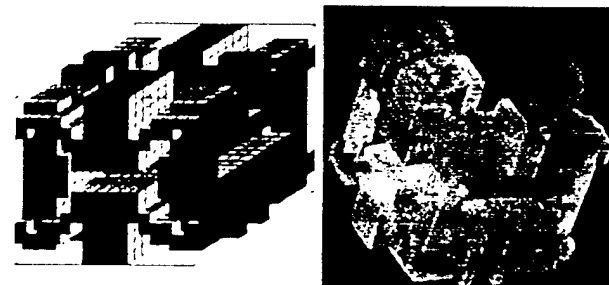


Figure 5: Optimal microstructure (one unit cell) for maximization of the hydrophone figure of merit  $d_h * g_h *$ .

solids content (>55% by volume) suspensions and tapes made using modified photopolymers; these UV curable suspensions can then be fashioned into complex materials by patterning on the surface of a UV-curable resin containing ceramic particles (Fig. 6).

An initial attempt to prove the concept produced a pattern cured from a 50 vol% alumina dispersion containing Zwitcoat as photomonomer. Although the suspension suffers from line broadening due to particle scattering, fine pattern resolution (~25  $\mu\text{m}$ ) can be developed using off-the-shelf materials. An example of the type of part that can be fabricated using this technique is shown in Fig. 7, a small (1 cm diameter) turbine blade assembly constructed from photocuring a 50 vol% alumina suspension. Thus, we have demonstrated that photocuring chemistry based on the Zwitterion monomer and hydrophobically modified polymers is certainly feasible and can be used to fabricate useful parts.

Further, we have determined that photon propagation in dense alumina suspensions exhibits a penetration depth of 200  $\mu\text{m}$  with 25  $\mu\text{m}$  features. The penetration depth is increased by multiple scattering (diffusion) and particle correlation effects. Future work will focus on developing improved photomonomers for specific use with ceramic suspensions in order to increase the solids loadings of the suspensions and to determine the optimal operating parameters to more finely control the pattern resolution.

### 3-Dimensional Self-Assembly and Coassembly

3-D processing via self-assembly involves the coassembly of organic and inorganic species into ordered mesoporous monoliths. Past work within our groups have demonstrated the controlled production of different organic/inorganic morphologies based on solution chemistry and processing parameters. We seek to build upon this knowledge and determining the optimal structure for the fabrication of composites based upon coassembled structures. We have successfully fashioned monoliths of mesoporous silicate with disordered mesophase morphology. In some of these materials, metals have been precipitated into the mesopores to form highly colored ceramic/metal composites in which the metal particles are less than 100 nm in diameter, forming highly scattering color centers.

Previous methods for synthesis of inorganic/organic composites rely on the cooperative assembly between surfactant and inorganic precursor. Under appropriate conditions, an inorganic precursor will coassemble with an organic surfactant to form a mineralized mesoporous structure. Upon the removal of the surfactant, an inorganic mesoporous material

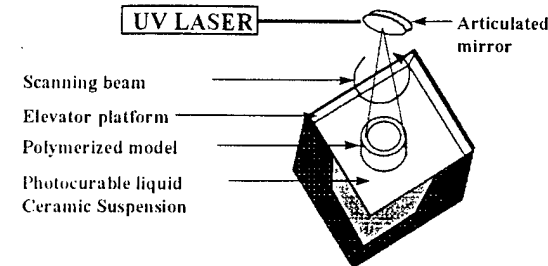


Figure 6: Schematic of stereolithography.

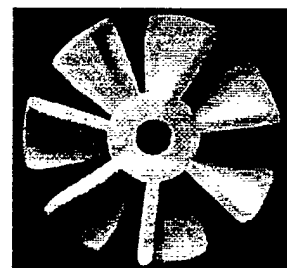


Figure 7: Alumina turbine blade fashioned by photocuring an alumina suspension in the SLA250 stereolithography unit.

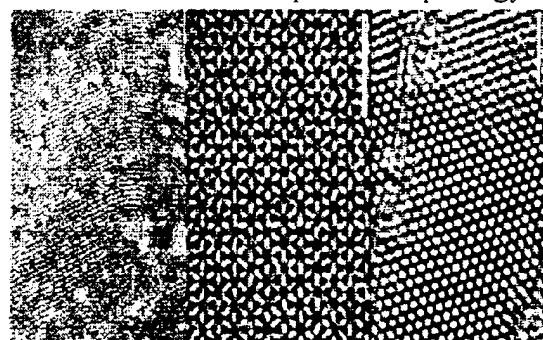


Figure 8: Transmission electron micrograph images of (top) the lamellar morphology, (middle) the cubic phase with Ia3d symmetry, and (bottom) the hexagonal phase (bars = 30 nm)

with well-defined dimensions is formed. However, several problems limit the application of this method: (i) during the course of the reaction, there is little or no control over the shape of the material; (ii) the resulting material is an opaque powder of micron sized grains, with many grain boundaries; (iii) the topology of the final material is unpredictable, and choosing the appropriate parameters is empirical; (iv) the potential use of the material is limited by the synthetic difficulties; and (v) pore dimensions are controlled primarily by the length of the amphiphile.

Our system results in the formation of a "sponge" or random ( $L_3$ ) phase (Fig. 8). In our procedure, we find that we can achieve 3-dimensional packing of a continuous membrane which equally sub-divides 2 continuous sub-volumes. This structure defines well-characterized channels leading to cavities of specific dimension.

Pore dimensions may be varied from 4 Å to over 100 nm. Rather than relying on co-assembly, we template a liquid crystal structure with the inorganic precursor: Siloxane is solubilized into the aqueous region of the liquid crystal and through weak interactions is arranged over the head groups of the amphiphiles. The original topology of the liquid crystal phase is not disturbed.

The sponge phase has variable but well defined pore dimensions which can be easily adjusted during synthesis by changing the solvent volume fraction. The resultant material is an optically isotropic, transparent monolith with a nonperiodic nanoporous network which permeates the material. X-ray scattering indicates that, in contrast to aerogels, there is little variation in the pore widths. Characteristic pores sizes of 3 to > 35 nm have been obtained and larger sizes appear feasible. TEM micrographs confirm the random pore network and BET measurements indicate surface areas between 375 and 535 m<sup>2</sup>/g in the uncalcined silicate. Advantages of the silicate sponge include (i) monodisperse pore dimensions, (ii) defined channel systems, (iii) transparent monoliths devoid of grain boundaries, and (iv) controlled pore dimensions varied from a few nanometers to several hundred.

### Microfabrication

This work utilizes self-assembled monolayers to form patterns on substrate materials, building microdevices through microcontact printing. Currently, resolutions of 0.1 to 10 μm are achieved by stamping patterns of an alkanethiol onto the surface to form the self-assembled monolayer, then reacting this layer with a variety of precursors, including precursors to ceramics, metals, and organic polymers. An extension of microcontact printing to the formation of patterned surfaces has been developed. A photolithographic mask is used to prepare a mold that is then infiltrated with a precursor material. To date, we have used this process to form simple structures on silicon substrates (Fig. 10).

The process of microinfiltration has more recently been extended to the formation of oriented surfactant-silicate nanotubule structures, prepared on solid substrates by infiltrating a reaction fluid into the capillaries of an elastomeric stamp with patterned, micron-scaled relief features in contact with the substrate. Applying an electric field (0.1-1 kV mm<sup>-1</sup>) directed tangentially to the surface within these capillaries causes electro-osmotic fluid motion and enhanced rates of mineralization by localized Joule heating. After conversion is complete and the mold is removed,

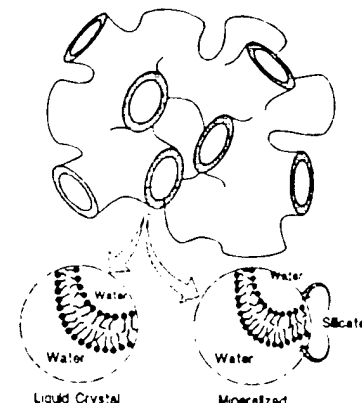


Figure 9: Schematic of  $L_3$  phase, first formed as a liquid crystal, then mineralized by siloxane.

patterned bundles of oriented nanotubules remain on the surface (Fig. 11). The cross-sectional view of each line reveals an identical hexagonally packed pattern of tubules, suggesting global alignment of tubules parallel to the substrate and capillary walls. Similar images have also been obtained for “confined” films grown on silica substrates. The insert displays the corresponding electron diffraction pattern obtained from (b), as well as a fourier transform filtered image. The diffraction pattern reveals a slightly distorted hexagonal lattice with 4% strain, which appears to arise from the rapid mineralization of the inorganic phase due to localized heating. This technique provides a new method for fabricating nanostructured materials with designed microscopic patterns.

*Literature on the above research is available upon request.*

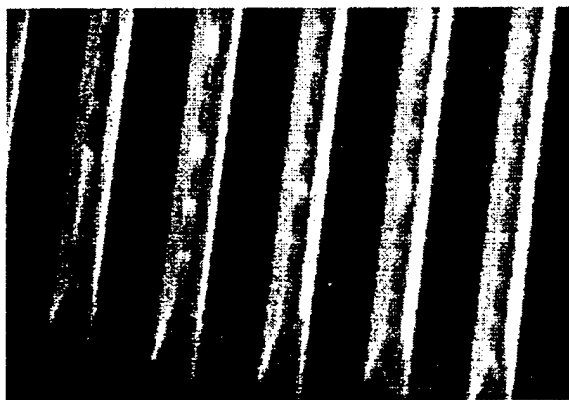


Figure 10: Electron micrograph of silica filaments deposited on a silicon substrate using microcontact printing. Lines are  $\sim 1 \mu\text{m}$  thick.

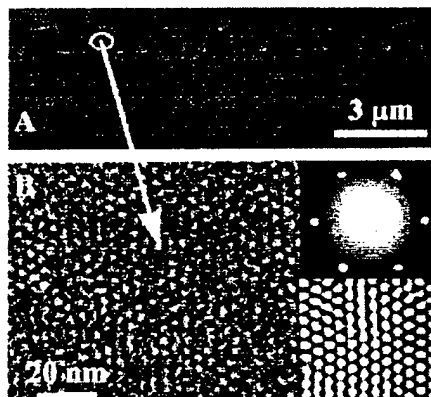


Figure 11: TEM images of a patterned mesoscopic silica. These display a hexagonally packed surfactant tubule structure within the micron-sized lines.

# Active Control for 2-D Dynamic Smart Beam

Duxing Cai & David Yang Gao

*Department of Mathematics, Virginia Polytechnic Institute & State University  
Blacksburg, VA 24061*

## Abstract

The complete analytic solutions for the boundary control of 2-D dynamic smart beam model are discussed. By using the Fourier Series method, the explicit formulations between the state of the beam and the applied controls are obtained. With these results, the method of accurate active control of this beam is proposed. Since this beam model can handle arbitrary forces, we can put actuators on the top and on the bottom of this beam to control its vibration or its shape. Through further study of the analytic solution of this dynamic smart beam, the optimal control of this beam, such as the locations of actuators on the beam, is achieved.

## 1. Dynamic Extended Timoshenko Beam Model and Its Solution

In order to study the active control of smart structures, the dynamic system of the extended Timoshenko beam model proposed by Gao and Russell (1994) is established. Unlike the classical beam models, this new model allows shear forces on the top and on the bottom of the beam. The shear deformation of this model is allowed to vary in lateral direction.

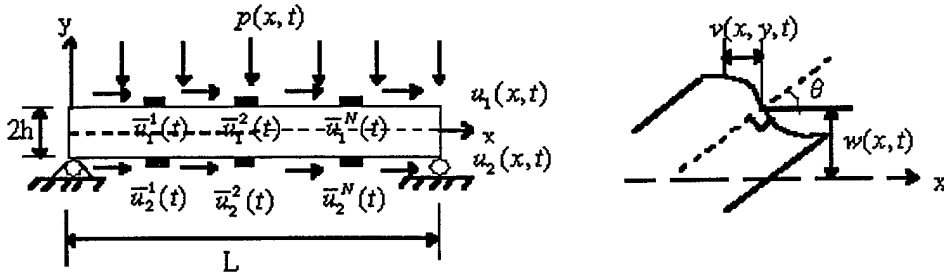


Figure 2. Extended Timoshenko Beam Model.

As shown in Figure 1, the cross section of the elastic beam in the  $x - y$  plane is a rectangle :  $\Omega = \{(x, y) | 0 \leq x \leq L, -h \leq y \leq h\}$ . The beam is subjected vertical load  $p(x, t)$  and horizontal loads  $u_1(x, t)$  on the top and  $u_2(x, t)$  on the bottom of the beam. The horizontal and lateral displacements of the beam are described by means of two functions  $v(x, y, t)$  and  $w(x, t)$  respectively. Then the kinetic energy and the potential energy of the beam are given by  $T(w, v, t)$  and  $P(w, v, t)$ :

$$\begin{aligned} T(w, v) &= \frac{1}{2} \int_{\Omega} \rho(x, y) w_t^2(x, t) d\Omega + \frac{1}{2} \int_{\Omega} \rho(x, y) v_t^2(x, y, t) d\Omega, \\ P(w, v) &= \frac{1}{2} \int_{\Omega} [E v_x^2(x, y, t) + G(v_y(x, y, t) + w_x(x, t))^2] d\Omega \\ &\quad - \int_0^L [p(x, t) w(x, t) + u_1(x, t) v(x, h, t) + u_2(x, t) v(x, -h, t)] dx. \end{aligned}$$

The Hamiltonian of this system is :

$$H(w, v) = \int_0^T [T(w, v) - P(w, v)] dt.$$

We assume that both ends of the beam are simply supported, so the stationary condition  $\delta H(w, v) = 0 \quad \forall \delta v, \delta w$ , gives the governing equations :

$$Ev_{xx} + Gv_{yy} = \rho v_{tt}, \quad (1)$$

$$2hGw_{xx} + G[v_x(x, h, t) - v_x(x, -h, t)] + p = \bar{\rho}w_{tt}, \quad (2)$$

where,  $\bar{\rho}(x) = \int_0^L \rho(x, y) dy$ , and the natural boundary conditions:

$$G[v_y(x, -h, t) + w_x(x, t)] + u_2(x, t) = 0, \quad (3)$$

$$G[v_y(x, h, t) + w_x(x, t)] - u_1(x, t) = 0, \quad (4)$$

$$v_x(0, y, t) = 0, \quad (5)$$

$$v_x(L, y, t) = 0. \quad (6)$$

The given boundary conditions and initial conditions should be:

$$w(0, t) = w(L, t) = 0, \quad (7)$$

$$w(x, 0) = w_t(x, 0) = v(x, y, 0) = v_t(x, y, 0) = 0. \quad (8)$$

This is a second order, coupled partial differential equation system. We are going to solve this system by separating variables. Neglecting the high order small term  $v_{tt}(x, y, t)$ , then eqn (1) becomes:

$$Ev_{xx} + Gv_{yy} = 0. \quad (9)$$

Let  $v(x, y) = X(x)Y(y)$ , from eqns (9), (5), (6) we can get :

$$v(x, y, t) = \sum_{n=0}^{\infty} (C_n e^{\beta_n y} + D_n e^{-\beta_n y}) \cos(\lambda_n x), \quad (10)$$

with  $\beta_n^2 = \frac{E}{G} \lambda_n^2$ ,  $\lambda_n = \frac{n\pi}{L}$ . From eqn (2), we have :

$$w_{tt} - \alpha^2 w_{xx} = F(x, t), \quad \alpha^2 = \frac{2hG}{\bar{\rho}} \quad (11)$$

where,  $F(x, t)$  is a nonhomogeneous term depending on  $v(x, y, t)$  and  $p(x, t)$  :

$$F(x, t) := \frac{G}{\bar{\rho}} [v_x(x, h, t) - v_x(x, -h, t)] + \frac{1}{\bar{\rho}} p(x, t) \quad (12)$$

The nonhomogeneous wave equation (11) with conditions (7) and (8) forms a linear initial value problem of  $w(x, t)$ . Let :

$$w(x, t) = \sum_{n=0}^{\infty} w_n(t) \sin(\lambda_n x), \quad F(x, t) = \sum_{n=0}^{\infty} F_n(t) \sin(\lambda_n x), \quad (13)$$

in which  $w_n(t)$  and  $F_n(t)$  are controled by :

$$w_n''(t) - \omega_n^2 w_n(t) = F_n(t), \quad (14)$$

where,  $\omega_n = \alpha \lambda_n$ . We choose :

$$\bar{u}_1(x, t) = \frac{u_1(x, t)}{G} = \sum_{n=0}^{\infty} \bar{u}_{1n}(t) \cos(\lambda_n x), \quad (15)$$

$$\bar{u}_2(x, t) = -\frac{u_2(x, t)}{G} = \sum_{n=0}^{\infty} \bar{u}_{2n}(t) \cos(\lambda_n x), \quad (16)$$

$$\bar{p}(x, t) = \frac{1}{\bar{\rho}} p(x, t) = \sum_{n=0}^{\infty} \bar{p}_n(t) \sin(\lambda_n x). \quad (17)$$

Pluging eqns (10),(13),(15)–(17) into natural conditions (3),(4) and (12) respectively, we get:

$$\beta_n C_n e^{\beta_n h} - \beta_n D_n e^{-\beta_n h} + \lambda_n w_n(t) = \bar{u}_{1n}(t), \quad (18)$$

$$\beta_n C_n e^{-\beta_n h} - \beta_n D_n e^{\beta_n h} + \lambda_n w_n(t) = \bar{u}_{2n}(t), \quad (19)$$

$$F_n(t) = \bar{p}_n(t) - 2a\lambda_n(C_n - D_n) \sinh(\beta_n h). \quad (20)$$

here,  $a = \frac{G}{\bar{\rho}}$ . Then eqn (14) becomes:

$$w_n''(t) + \omega_n^2 w_n(t) + 2a\lambda_n(C_n - D_n) \sinh(\beta_n h) = \bar{p}_n(t). \quad (21)$$

From (18),(19), (21), we can determine  $C_n, D_n$  and  $w_n$ .

$$w_n(t) = \frac{1}{k_n} \int_0^t [\bar{p}_n(\tau) - \frac{a\lambda_n}{\beta_n} \tanh(\beta_n h)(\bar{u}_{1n}(\tau) + \bar{u}_{2n}(\tau))] \sin(k_n(t - \tau)) d\tau, \quad (22)$$

$$C_n(t) = E_{1n}\bar{u}_{1n}(t) - E_{2n}\bar{u}_{2n}(t) - E_{3n}w_n(t), \quad (23)$$

$$D_n(t) = E_{2n}\bar{u}_{1n}(t) - E_{1n}\bar{u}_{2n}(t) + E_{3n}w_n(t). \quad (24)$$

Where,  $k_n^2 = \omega_n^2 - \frac{2a\lambda_n^2}{\beta_n^2} \tanh(\beta_n h)$ ,  $E_{1n} = \frac{e^{\beta_n h}}{2\beta_n \sinh(2\beta_n h)}$ ,  $E_{2n} = \frac{e^{-\beta_n h}}{2\beta_n \sinh(2\beta_n h)}$ ,  $E_{3n} = \frac{\lambda_n \sinh(\beta_n h)}{\beta_n \sinh(2\beta_n h)}$  are constants. The final solution of the problem is:

$$w(x, t) = \sum_{n=0}^{\infty} w_n(t) \sin(\lambda_n x), \quad (25)$$

$$v(x, y, t) = \sum_{n=0}^{\infty} [C_n(t)e^{\beta_n y} + D_n(t)e^{-\beta_n y}] \cos(\lambda_n x). \quad (26)$$

For any given external load  $p(x, t)$  and controls  $u_1(x, t)$  and  $u_2(x, t)$ , the coefficients  $w_n, C_n$  and  $D_n$  are well defined by (22), (23) and (24) respectively.

## 2. Application to the Control of Smart Beam

We consider the following three cases :

### (i) Vibration Control of Smart Beam.

To control the vibration of smart beam subjected to arbitrary external loads has been

studied by many engineers. With the results obtained in previous section, we can get the exact solution for the input control to dampen the vibration of beam. To do so, we let  $w_n(t) \equiv 0$ , which yields :

$$\bar{p}_n - \frac{a\lambda_n}{\beta_n} \tanh(\beta_n h)(\bar{u}_{1n} + \bar{u}_{2n}) \equiv 0 \Rightarrow \bar{u}_{1n} + \bar{u}_{2n} = \frac{\beta_n}{a\lambda_n} \coth(\beta_n h) \bar{p}_n.$$

If  $\bar{u}_{1n} = \bar{u}_{2n}$ , i.e.  $u_1(x, t) = -u_2(x, t)$ , then the applied controls should be :

$$\bar{u}_{1n} = \bar{u}_{2n} = \frac{\beta_n}{2a\lambda_n} \coth(\beta_n h) \bar{p}_n, \quad (27)$$

$$u_1(x, t) = -u_2(x, t) = \sum_{n=0}^{\infty} \frac{G\beta_n}{2a\lambda_n} \coth(\beta_n h) \bar{p}_n(t) \cos(\lambda_n x) \quad \forall x \in [0, L]. \quad (28)$$

From (28), we see that, to make  $w(x, t) \equiv 0$ , the accurate applied controls must be continuous functions in domain  $[0, L]$ . For practical purpose, we can put some actuators on the top and on the bottom of the beam respectively to get the approximate controls. Suppose  $2N$  pieces of actuators are applied on the top and the bottom of the beam at  $x_1, x_2, \dots, x_N$  respectively, and the corresponding control for the  $i^{th}$  actuator is a  $\delta$ -function:  $u_1^i(x, t) = \delta(x - x_i) \bar{u}_1^i(t)$ . Then,

$$u_1(x, t) = \sum_{i=1}^N u_1^i(x, t) = \sum_{i=1}^N \delta(x - x_i) \bar{u}_1^i(t). \quad (29)$$

Let  $u_1(x, t) = \sum_{n=0}^{\infty} G u_{1n}(t) \cos(\lambda_n x)$ , then

$$u_{1n}(t) = \frac{2}{GL} \int_0^L u_1(x, t) \cos(\lambda_n x) dx = \sum_{i=1}^N \frac{2}{GL} \bar{u}_1^i(t) \cos(\lambda_n x_i) \doteq \sum_{i=1}^N a_{ni} \bar{u}_1^i(t),$$

where,  $a_{ni} \doteq \frac{2}{GL} \cos(\lambda_n x_i)$ . If let  $u_{1n}(t) = \bar{u}_{1n}(t)$ , where  $\bar{u}_{1n}(t)$  depending on  $\bar{p}_n(t)$ ,  $n = 0, \dots, N-1$  are given by (27). i.e.

$$A(\vec{x}) \mathbf{u}_1 = \bar{\mathbf{p}}, \quad (30)$$

where,  $\vec{x} = (x_1, x_2, \dots, x_N)$ , and

$$A(\vec{x}) = \begin{pmatrix} a_{0,1} & a_{0,2} & \dots & a_{0,N} \\ a_{1,1} & a_{1,2} & \dots & a_{1,N} \\ \vdots & \vdots & \ddots & \vdots \\ a_{N-1,1} & a_{N-1,2} & \dots & a_{N-1,N} \end{pmatrix}, \quad \mathbf{u}_1 = \begin{pmatrix} \bar{u}_1^1 \\ \bar{u}_1^2 \\ \vdots \\ \bar{u}_1^N \end{pmatrix}, \quad \bar{\mathbf{p}} = \begin{pmatrix} \bar{u}_{1,0} \\ \bar{u}_{1,1} \\ \vdots \\ \bar{u}_{1,N-1} \end{pmatrix}.$$

So system (30) will determine the  $N$  controls  $u_1^i$ , ( $i = 1, 2, \dots, N$ ). Then with such  $N$  controls  $u_1^i(x, t)$ , ( $i = 1, 2, \dots, N$ ), the first  $N$  terms of the desired accurate controls given by (28) are satisfied. The more accurate control of the smart beam is desired, the more actuators are required. And the controls must satisfy system (30).

### (ii) Optimal Location of Actuators.

To obtain the optimal control of the beam, i.e. with the least cost to get the same result, we must choose the optimal positions  $\vec{x}$  of the applied controls. By quadratic cost function :

$$C(\mathbf{u}_1) = \sum_{i=1}^N (\bar{u}_1^i)^2, \quad (31)$$

the optimal control problem can be described as following :

$$\begin{cases} \min C(\mathbf{u}_1(\vec{x})) \\ s.t. \quad A(\vec{x}) \mathbf{u}_1 = \bar{\mathbf{p}} \end{cases} \quad (32)$$

Where,  $A = [a_{ij}]_{N \times N}$ ,  $a_{ij} = \frac{2}{GL} \cos(\lambda_{i-1} x_j)$  and  $\vec{x} = (x_1, x_2, \dots, x_N)$ . It's easy to prove that matrix  $A$  is full rank. And since  $C(\mathbf{u}_1(\vec{x}))$  is convex, problem (32) is well proposed.

### (iii) Shape control of Dynamic Smart Beam.

Suppose the target shape of the beam is  $\bar{w}(x, t)$ , we have :

$$\bar{w}_n(t) = \frac{2}{L} \int_0^L \bar{w}(x, t) \sin(\lambda_n x) dx. \quad (33)$$

From (22), if we let  $\bar{u}_{1n} = \bar{u}_{2n} = \bar{u}_n$ , the shape control problem is to find control  $u_1(x, t)$ , such that  $w_n(t) = \bar{w}_n(t)$ , i.e.

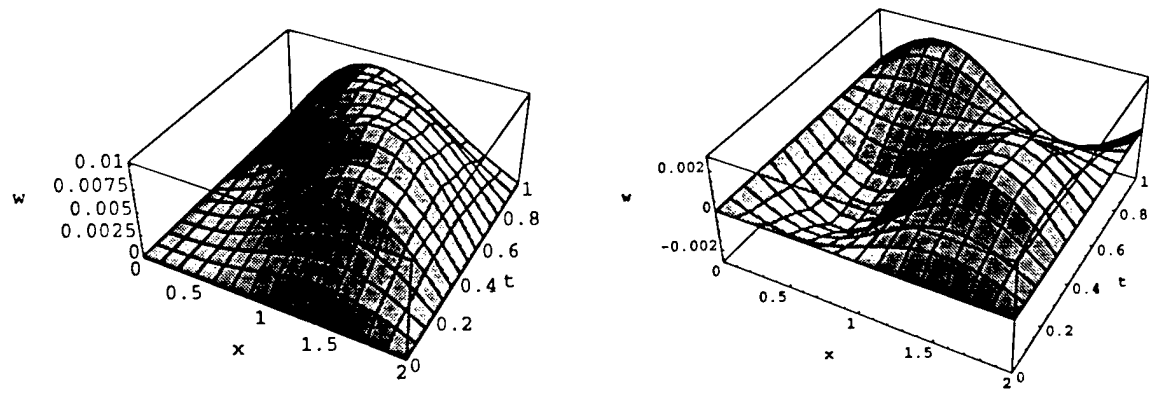
$$\frac{1}{k_n} \int_0^t [\bar{p}_n - \frac{2a\lambda_n}{\beta_n} \tanh(\beta_n h)(\bar{u}_n)] \sin(k_n(t-\tau)) d\tau = \bar{w}_n(t), \quad n = 0, 1, \dots \quad (34)$$

This is an affine system with  $n$  unknown  $\bar{\mathbf{u}} = (\bar{u}_1, \bar{u}_2, \dots, \bar{u}_n)$ . For given target function  $\bar{w}(x, t)$ , eqn (34) has a unique solution.

**Example** Suppose a smart beam is subjected to vertical load  $p(x, t) = x \sin(10\pi t)$  as Figure 1. At  $x = \frac{L}{4}$  and  $x = \frac{3L}{4}$ , four PZTs are applied on the top and the bottom of the beam respectively to control its vibration. If choose  $u_1(x, t) = -u_2(x, t)$ , and  $\bar{u}_1^1(t), \bar{u}_1^2(t)$  satisfy (30), then the results are shown as Figure 2-4. We see that, after applying the controls, the maximum vertical displacement of  $w(x, t)$  reduces about 80%, and the maximum horizontal displacement of  $v(x, y, t)$  reduces about 60%.

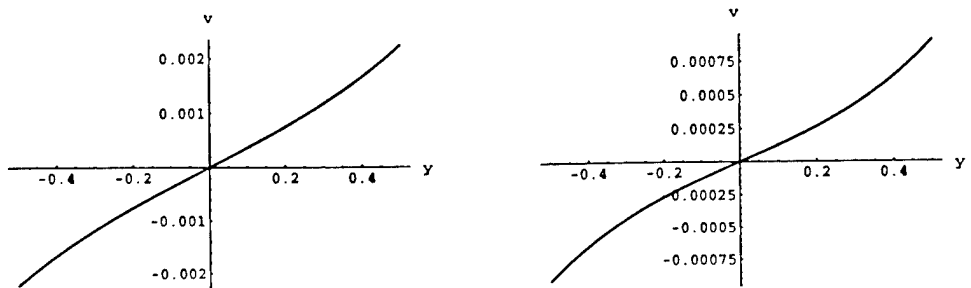
### Conclusion Remark.

Since the Extended Timoshenko Beam model can handle shear forces applied on the top and the bottom of the beam, it can be used to study the active control of smart structures. We can see from Figure 3(a) that, the horizontal displacement  $v(x, y, t)$  varies in  $y$  even without external shear loads applied on the beam. From the example, we see that if given the positions of the applied PZTs, eqn (30) will determine the best controls' signals to dampen the vibration of the beam. On the other hand, if given the number of controls, system (32) will give the optimal positions and controls' signals to the optimal control problem. And furthermore, the shape control problem of the smart beam is given by eqn (34), which has unique solution.



(a) without controls

(b) with controls

Figure 2. Vertical displacements  $w(x,t)$ .

(a) without controls

(b) with controls

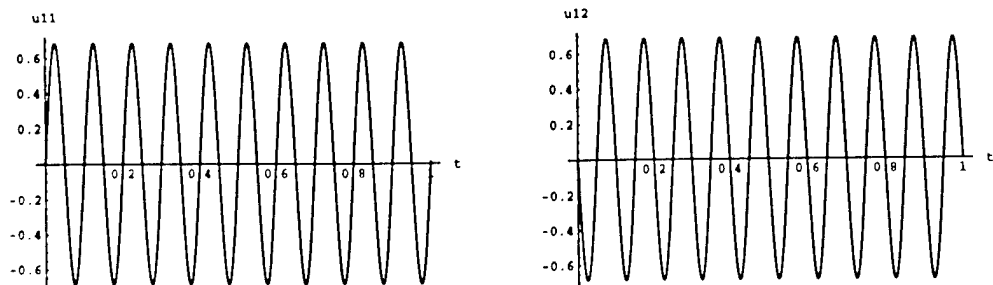
Figure 3. Horizontal displacements  $v(x,y,t)$  (at  $x=L$ ,  $t=0.1$ ).(a)  $\bar{u}_1^1(t)$  at  $x = \frac{L}{4}$ (b)  $\bar{u}_1^2(t)$  at  $x = \frac{3L}{4}$ 

Figure 4. Controls' signals.

## References

- [1] Gao, David Y. and Russell, David L.(1994), A finite element approach to optimal control of a "smart" beam, *Proc. of Int. Conf. Comput. Meth. Struct.*, Ed. by PKK Lee, Y.K.Cheung, The University of Hong Kong, Dec 12-14, Vol.1, pp. 135-140.
- [2] Gao,DY(1996), Contact problem of 2-D elastoplastic beam theory and dual variational inequality, *Appl. Math. Mech.*, **17**, 3, pp. 953-968.
- [3] Gao, DY and Russell, DL(1996), An extended beam theory for smart materials applications, Part I. Extended beam theory, duality theory and finite element simulations, *Appl. Math. Optimization*, Vol. 34(3), pp. 279-298.

The Third ARO Workshop on Smart Structures  
August 27-29, 1997, Virginia Tech, Blacksburg, Virginia.

**Progressive Failure Analysis of Shape Memory Alloy Hybrid Composite  
Beams Under Low-Velocity Impact**

Hongyu Jia<sup>†</sup>, Frederic Lalande<sup>‡</sup>

Center for Intelligent Material Systems and Structures  
Virginia Polytechnic Institute and State University  
Blacksburg, VA 24061-0261

Craig A. Rogers<sup>§</sup>

University of South Carolina  
Columbia, SC 29208

**ABSTRACT**

One of graphite/epoxy's main weaknesses is its poor resistance to impact damage due to the lack of plastic deformation mechanisms for absorbing impact energy. In order to keep the high load-carrying properties while improving the toughness of composite structures, many approaches have been proposed: fiber and matrix toughening, interface toughening, through-the-thickness reinforcements, and hybridizing.

It has been demonstrated that the addition of small amounts of superelastic SMA fibers to graphite composites can improve its low-velocity impact damage resistance. It was found that a 25% reduction in impact-induced delamination could be obtained with only a 2.8% volume fraction of embedded SMA. An increase in absorbed energy of 41% was found with a 6% volume fraction of embedded SMA.

In order to further understand the impact mechanisms in the SMA hybrid composite and the energy transfer between the projectile and the composite, analytical models are needed. To this end, a model has been developed for evaluating the energy absorption capability of superelastic SMA in related work. This model can be used to calculate the impact force and the energy absorption of an SMA/graphite/epoxy composite beam under a low-velocity impact before the damage occurs.

In this paper, the energy absorption model is extended to include the effect of initial damage mechanics, such as matrix cracking, delamination, and fiber breakage, on the energy absorption of the SMA hybrid composite beam (Figure 1). The extended model is

---

<sup>†</sup> E-mail: hjia@vt.edu; Telephone: (540) 231-2900; Fax: (540) 231-2903

<sup>‡</sup> E-mail: lalande@vt.edu; Telephone: (540) 231-2900; Fax: (540) 231-2903

<sup>§</sup> E-mail: rogers@sc.edu; Telephone (803) 777-4259

developed based on the failure criteria of laminated composite beam. Critical matrix cracking criterion proposed by Choi et al will be used:

$$\left(\frac{\sigma_{yy}}{Y}\right)^2 + \left(\frac{\sigma_{xy}}{S_i}\right)^2 = c_M^2 \quad \begin{cases} c_M \geq 1 & \text{Failure} \\ c_M < 1 & \text{No failure} \\ Y = Y_t \text{ if } \bar{\sigma}_{yy} \geq 0 \\ Y = Y_c \text{ if } \bar{\sigma}_{yy} < 0 \end{cases}$$

where the subscripts of x and y are the local coordinates of the nth layer parallel and normal to the fiber directions, respectively, and z is the out-of plane direction.  $S_i$  is the insitu interlaminar shear strength within the laminate under consideration, and  $Y_t$  and  $Y_c$  are the in situ ply transverse tensile and compressive strengths, respectively.

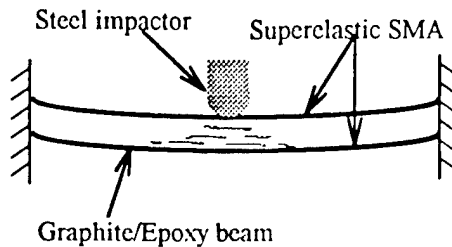


**Figure 1: Schematic of the SMA hybrid composite beam subjected to low-velocity impact.**

The new model is developed based on the failure criteria of laminated composite beam. It will accounts for the contact deformation, the global bending deformation, the transverse shear deformation, the martensitic phase transformation of the superelastic SMA fibers, matrix cracking, delamination and fiber breakage. Displacement and stress fields are solved by performing a progressive failure analysis. The velocity and energy of impactor for initiating the matrix cracking and fiber failure will be determined. The effect of martensite transformation on the damage initiation and energy absorption of SMA hybrid composite beam will be analyzed.

The governing equations of the SMA hybrid composite beam will be briefly derived. The Timoshenko beam theory will be used to include the first-order shear deformation, i.e., the interlaminar shear strains are not neglected.

Based on the conservation of the total energy, the kinetic energy of the projectile is completely absorbed by the beam, and becomes the strain energy and contact energy of the beam:

$$\frac{1}{2} M_p V_p^2 = U(\xi) + U_c(\xi) \quad (1)$$

where  $M_p$  and  $V_p$  are the mass and velocity of the projectile, respectively, and  $U(\xi)$  and  $U_c(\xi)$  are the beam's strain energy and contact energy, respectively.

The energy absorbed by the SMA hybrid composite was calculated for each of the absorption mechanisms: contact deformation, global bending deformation, and transverse shear deformation. The extended model also accounts for the energy that causes the matrix cracking, delamination, and fiber breakage. The relationship between the total energy absorption in the beam and the extent of martensitic phase transformation will be given. The numerical results will give us a useful guideline for design SMA hybrid composite for low-velocity damage resistance.

## BORING BAR CHATTER CONTROL

Jon Pratt

Department of Engineering Science and Mechanics  
Virginia Polytechnic Institute and State University  
Blacksburg, Virginia 24061-0219  
Phone:(540) 231-3247  
Fax:(540) 231-4574  
email: prattj@vt.edu

Ali H. Nayfeh

Department of Engineering Science and Mechanics  
Virginia Polytechnic Institute and State University  
Blacksburg, Virginia 24061-0219  
Phone:(540) 231-5453  
Fax:(540) 231-4574  
email: anayfeh@vt.edu

**Abstract:** Boring bars for single-point turning on a lathe are particularly susceptible to chatter and have been the focus of numerous studies. Chatter is, in general, a problem of stability. Clearly, the cutting process can be limited to regions of known stable operation. However, this severely constrains the machine-tool operation and causes a loss of productivity. The more aggressive approach is to attack the stability problem directly through application of vibration control. A variety of vibration-control solutions have been proposed in the literature using both active- and passive-design strategies. The proposed active-control schemes have been uniaxial, controlling the vibrations only in the direction normal to the cut surface. The control has been achieved using either reaction-mass actuators located within the boring bar or piezoelectric benders incorporated in the tool shank. We will point out some of the shortcomings of these design practices and demonstrate a new biaxial approach, which uses Terfenol-D actuators that apply control forces in both the horizontal and vertical directions. In this new approach, "virtual" absorbers are achieved by using tuned electronic circuits coupled to the bar through the grounded Terfenol-D actuators. We locate the actuators near the base of the boring bar to exploit their high-force/low-displacement character, thereby eliminating the need for strain amplification that is inherent in the reaction-mass approach and overcoming the tool restrictions of the bender approach. The design allows for static compensation, an option that may be desirable in precision machining applications where tolerances to nanometers are not uncommon. Finally, the resulting smart tool has been designed to apply control forces in two directions, a feature that has great importance for robustness.

# NATURAL FREQUENCIES OF MULTI-LAYER COMPOSITE PLATE WITH SHAPE MEMORY ALLOY

W. Ostachowicz, M. Krawczuk, A. Zak  
Polish Academy of Sciences, Institute of Fluid Flow Machinery  
ul. Gen. J. Fiszera 14, 80-952 Gdańsk, Poland

## INTRODUCTION

This paper illustrates stress-strain relationships for a single composite lamina with SMA wires and shows their influence upon changes in natural frequencies of a composite multi-layered plate. Governing equations based on the finite element method are presented in the paper. The plate is modeled by plate finite elements with eight nodes and five degrees of freedom at each node (i.e., three axial displacements and two rotations). For both axial displacements and rotations biquadratic shape functions are used.

Recent years focus the attention of many investigators on the special class of materials which are the shape memory materials. Many publications about the use of the shape materials in the field of modern engineering can be found but few of them are devoted to the vibration analysis of composite structures with SMA components. Zhong, Chen, and Mei [5] used the finite element method for the thermal buckling and postbuckling analysis of composite plates with embedded SMA wires. Ro and Baz [3] introduced fundamental equations ruling the behavior of the fiber-reinforced plates with Nitinol wires and using the same technique they described dynamic characteristics of such structures [7].

In the present work a more general description of this problem is introduced. Results obtained from the finite element analysis are compared with analytical continuum solutions.

## MECHANICAL AND PHYSICAL PROPERTIES OF SHAPE MEMORY ALLOYS

Mechanical and physical properties of shape memory alloys (SMA) strongly depend on the temperature and initial stress [2]. Variations in the temperature and initial stress involve changes in the volume fraction of the martensite phase in the alloy. During the martensite transformation the martensite fraction  $\xi$  in the alloy can be described by the following formulas [2]:

– for the cooling process:

$$\begin{cases} T \geq \tilde{T}_{sm} & \xi = 0 \\ T < \tilde{T}_{sm} & \xi = 1 - \exp[b_m(T_{sm} - T) + c_m \sigma(\xi, T)] \end{cases} \quad \begin{cases} T \leq \tilde{T}_{sa} & \xi = 1 \\ T > \tilde{T}_{sa} & \xi = \exp[b_a(T_{sa} - T) + c_a \sigma(\xi, T)] \end{cases} \quad (1)$$

– for the heating process:

where  $T$  is the current temperature of the shape memory alloy,  $T_{sa}$  and  $T_{sm}$  are the austenite and the martensite phase start temperatures under stress free conditions, respectively, while  $b_m$ ,  $c_m$ ,  $b_a$  and  $c_a$  are coefficients depending on the temperature and materials properties and  $\sigma$  denotes the stress in the alloy. The coefficients  $b_m$ ,  $c_m$ ,  $b_a$  and  $c_a$  are given as:

$$b_m = \frac{\ln(0.01)}{T_{sm} - T_{fm}} \quad b_a = \frac{\ln(0.01)}{T_{sa} - T_{fa}} \quad c_m = \frac{b_m}{d_m} \quad c_a = \frac{b_a}{d_a} \quad (2)$$

while  $T_{fm}$  and  $T_{fa}$  are the martensite and austenite finish temperatures while  $d_m$  and  $d_a$  are constants defining the slopes of martensitic and reverse transformation lines, respectively.

The characteristic temperatures depend also on the stress [2]:

$$\begin{cases} \tilde{T}_{sm} = T_{sm}|_{\sigma=0} + \sigma(\xi, T)/d_m & \tilde{T}_{fm} = T_{fm}|_{\sigma=0} + \sigma(\xi, T)/d_m \\ \tilde{T}_{sa} = T_{sa}|_{\sigma=0} + \sigma(\xi, T)/d_a & \tilde{T}_{fa} = T_{fa}|_{\sigma=0} + \sigma(\xi, T)/d_a \end{cases} \quad (3)$$

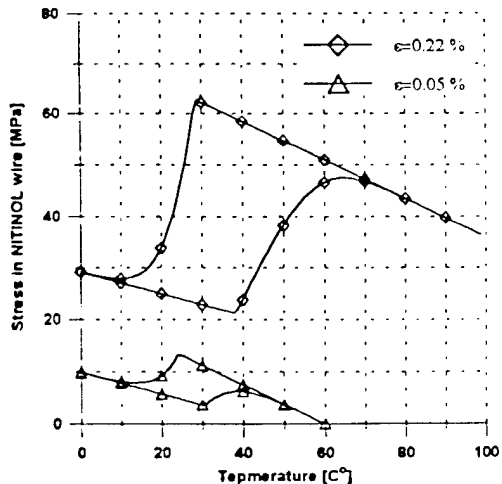


Fig. 1. Stress in Nitinol (Ni-44.8 %) wires as a function of the temperature and initial strains.

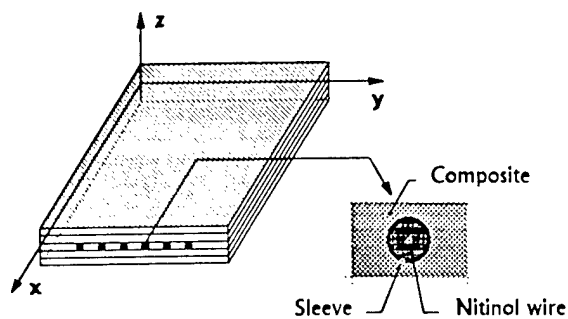


Fig. 2. A plate finite element with Nitinol wires.

In this paper the following material properties for SMA Nitinol Ni-44.8 % wires were used:

Table 1. Material properties of Nitinol Ni-44.8 %.

$E_s$	[GPa]	30.0
$E_m$	[GPa]	13.0
$\alpha_a (\cdot 10^{-6})$	[1/°C]	12.5
$\alpha_m (\cdot 10^{-6})$	[1/°C]	18.5
$T_{sm}$	[°C]	23.0
$T_{fm}$	[°C]	5.0
$T_{sa}$	[°C]	29.0
$T_{fa}$	[°C]	51.0
$d_m$	[MPa/°C]	11.3
$d_a$	[MPa/°C]	4.5

Assuming that both the martensitic and austenitic phases are isotropic, mechanical and physical properties of the SMA wires can be the linear functions of the martensite fraction [2]:

$$M = \xi M_m + (1 - \xi) M_a \quad (4)$$

where subscripts m and a identify the martensite and austenite phases, respectively.

In Fig. 1 changes in the stress in Nitinol (Ni-44.8 %) wires for two different values of initial strains ( $\epsilon = 0.05\%$  and  $\epsilon = 0.22\%$ ) and both the heating and cooling processes are presented. It can be noticed that the increase in the initial strains involves the higher stress in the Nitinol wires. Simultaneously this effects on changes in the temperatures of the phase transformation and the martensite fraction as well.

## STATE OF THE PROBLEM

An multi-layer composite plate with SMA wires is considered, as shown in Fig. 2. Each single composite lamina has an arbitrary orientation of graphite fibers. The SMA wires are embedded in the mid-plane of the plate.

The displacements field within the single layer of the plate can be described as follows:

$$\begin{cases} u(x, y, z) = u_0(x, y) + z \bar{\alpha}(x, y) \\ v(x, y, z) = v_0(x, y) + z \bar{\beta}(x, y) \\ w(x, y, z) = w_0(x, y) \end{cases} \quad (5)$$

where  $u_0$ ,  $v_0$  and  $w_0$  are the mid-plane displacements while the second terms in the first two equations are related to rotations. Using the finite element notation we can write:

$$\begin{Bmatrix} u \\ v \\ w \end{Bmatrix} = \begin{bmatrix} L & N & 0 & 0 & zN & 0 & | & L \\ L & 0 & N & 0 & 0 & zN & | & L \\ L & 0 & 0 & N & 0 & 0 & | & L \end{bmatrix} \begin{Bmatrix} q_{1,e} \\ M \\ q_{40,e} \end{Bmatrix} \quad (6)$$

where  $N_i$  denotes shape functions and  $\{q_e\}$  is a column matrix containing generalized coordinates of the plate finite element. In this analysis we use a plate-bending quadrilateral finite element called PBQ8 [6]. The element has eight nodes and five degrees of freedom at each node. The shape functions of the element have the following form:

– for the mid-side nodes :                    – for the corner nodes :

$$N_i = (1 + \xi_i)(1 + \eta_i)(\xi_i + \eta_i - 1)/4 \quad \begin{cases} \xi_1 = 0 & N_1 = (1 - \xi^2)(1 + \eta_o)/2 \\ \eta_1 = 0 & N_1 = (1 + \xi_o)(1 - \eta^2)/2 \end{cases} \quad (7)$$

where  $\xi_0 = \xi_1$  and  $\eta_0 = \eta_1$ .

Considering the plate composed of  $M$  laminae constitutive relations for the  $k$ -th lamina takes the following form:

$$\begin{Bmatrix} \sigma_x \\ \sigma_y \\ \sigma_{yz} \\ \sigma_{xz} \\ \sigma_{xy} \end{Bmatrix} = Q_k \begin{Bmatrix} \varepsilon_x^0 + z \kappa_x - \alpha_x \Delta T \\ \varepsilon_y^0 + z \kappa_y - \alpha_y \Delta T \\ \varepsilon_{yz} \\ \varepsilon_{xz} \\ \varepsilon_{xy}^0 + z \kappa_{xy} - \alpha_{xy} \Delta T/2 \end{Bmatrix} \quad (8)$$

where  $\alpha_x$ ,  $\alpha_y$ ,  $\alpha_{xy}$  are coefficients of thermal expansions and:

$$\begin{cases} \varepsilon_x^0 = \partial_x u_0 & \varepsilon_y^0 = \partial_y v_0 & \varepsilon_{xy}^0 = (\partial_y u_0 + \partial_x v_0)/2 \\ \kappa_x = \partial_x \bar{\alpha} & \kappa_y = \partial_y \bar{\beta} & \kappa_{xy} = (\partial_y \bar{\alpha} + \partial_x \bar{\beta})/2 \\ \varepsilon_{xz} = (\bar{\alpha} + \partial_x w_0)/2 & \varepsilon_{yz} = (\bar{\beta} + \partial_y w_0)/2 \end{cases} \quad (9)$$

The matrix  $\mathbf{Q}_e$  has a well known structure [4]. The equation of motion can be derived from the principle of virtual work:

$$\delta U_e = \delta V_e = \delta (V'_e + V''_e) \quad (10)$$

where  $\delta U_e$  is the virtual strain energy of the internal stress and  $\delta V_e$  is the virtual work of the external load on the element. For the plate with the mid-plane symmetry and no coupling effects, the strain energy stored in the plate finite element is given by:

$$U_e = \iint_{(A)} \left\{ A_{11} (\partial_x u_o)^2 / 2 + D_{11} (\partial_x \bar{\alpha})^2 / 2 + A_{12} (\partial_x u_o)(\partial_x v_o) + D_{12} (\partial_x \bar{\beta})(\partial_x \bar{\alpha}) + A_{22} (\partial_y v_o)^2 / 2 + A_{45} [\bar{\alpha} \bar{\beta} + \bar{\alpha}(\partial_y w_o) + \bar{\beta}(\partial_x w_o) + (\partial_x w_o)(\partial_y w_o)] + A_{55} [\bar{\alpha}^2 / 2 + \bar{\alpha}(\partial_x w_o) + (\partial_x w_o)^2 / 2] + A_{44} [\bar{\beta}^2 / 2 + \bar{\beta}(\partial_y w_o) + (\partial_y w_o)^2 / 2] + A_{66} [(\partial_y u_o)^2 / 2 + (\partial_y u_o)(\partial_x v_o) + (\partial_x v_o)^2 / 2] + D_{66} [(\partial_y \bar{\alpha})^2 / 2 + (\partial_y \bar{\alpha})(\partial_x \bar{\beta}) + (\partial_x \bar{\beta})^2 / 2] \right\} dA \quad (11)$$

where  $A_i = \sum_{k=1}^M (Q_i)_k (h_k - h_{k-1})$  and  $D_i = \sum_{k=1}^M (Q_i)_k (h_k^3 - h_{k-1}^3) / 3$  for  $i, j = 1, 2, 6$ .

$$A_i = 5 \sum_{k=1}^M (Q_i)_k [(h_k - h_{k-1}) / 4 - (h_k^3 - h_{k-1}^3) / 3h^2] \text{ for } i, j = 4, 5.$$

The work of in-plane forces which include the recovery forces of the Nitinol fibers, the thermal load induced by heating the Nitinol fibers and the external in-plane loads are formulated as follows [3]:

$$\delta V'_e = h / 2 \iint_{(A)} \{ N_x (\partial_x w_o)^2 + N_y (\partial_y w_o)^2 + 2N_{xy} (\partial_x w_o)(\partial_y w_o) \} \delta w dA \quad (12)$$

$$\text{where } N_x = P_{m,x} + P_{t,x} - F_{w,x} \quad N_y = P_{m,y} + P_{t,y} \quad N_{xy} = P_{m,xy} + P_{t,xy} .$$

Quantities  $P_{m,x,y,xy}$  and  $P_{t,x,y,xy}$  denoting the compressive in-plane mechanical and thermal loads in x, y and xy directions while  $F_{w,x}$  denotes the total tension in the Nitinol fibers:

$$F_{w,x} = \iint_{(A_w)} E_w (\xi) [\varepsilon_0 + \alpha_w (\xi) (T - T_0)] dA_w \quad \text{where } \alpha_w (\xi) = \xi \alpha_m + (1 - \xi) \alpha_s \quad (13)$$

In the Eqn. 13  $\alpha_w$ ,  $E_w$  and  $A_w$  denote the thermal expansion coefficient of the SMA wires, their modulus of elasticity, and their cross-sectional area, respectively.

The thermal load  $P_t$  is given by:

$$\{P_{t,x}, P_{t,y}, P_{t,xy}\}^T = \sum_{k=1}^M \int_{h_{k-1}}^{h_k} \mathbf{Q}_k \{\alpha_x, \alpha_y, \alpha_{xy}\}^T \Delta T dz \quad (14)$$

$$\text{while } \alpha_x = m^2 \alpha_1 + n^2 \alpha_2 \quad \alpha_y = m^2 \alpha_2 + n^2 \alpha_1 \quad \alpha_{xy} = mn (\alpha_1 - \alpha_2)$$

The principal material axes are labeled 1 and 2 and the direction 1 is parallel to the fibers while the direction 2 is normal to them. Symbols  $m$  and  $n$  denote  $\cos(\theta)$  and  $\sin(\theta)$ , respectively and  $\theta$  is defined as the angle of the fibers locations.

The thermal load is generated by changes in the temperature  $\Delta T$  of the element and is caused by the activation and de-activation of the Nitinol fibers. If dynamic effects are included, then this relationship, supplemented with  $p_z = -\rho \frac{\partial w}{\partial t}$ , becoming:

$$\delta V_e = -\iint_{(A)} h \rho \frac{\partial w}{\partial t} dA \quad (15)$$

Using standard finite element formulae the inertia and stiffness matrices of the plate can be determined.

## NUMERICAL CALCULATIONS

Numerical calculations for a simply supported plate have been carried out for the following plate dimensions: length 400 mm, width 400 mm and thickness 5 mm. The plate consisted of 4 layers of materials with the angle of fibers ( $+20^\circ, -20^\circ, +20^\circ, -20^\circ$ ). Each layer of the plate was made of a graphite-epoxy composite for which mechanical properties of the components are presented in Table 2. It was assumed that all mechanical properties except the angle of the fibers are the same in the each layer.

Table. 2. Mechanical properties of composite components.

$E_f$	[GPa]	275.6
$G_f$	[GPa]	114.8
$v_f$		0.20
$\rho_f$	[kg/m <sup>3</sup> ]	1900
$\alpha_f (\cdot 10^{-6})$	[1/°C]	24.4
$E_m$	[GPa]	3.43
$G_m$	[GPa]	1.27
$v_m$		0.35
$\rho_m$	[kg/m <sup>3</sup> ]	1250
$\alpha_m (\cdot 10^{-6})$	[1/°C]	64.8

Assumed volume fraction of the fibers in the composite was 0.2. In the present study, Nitinol wires cover 5% of the cross sectional area of the plate. They are embedded in the mid-plane of the plate. It was also assumed that all material properties (except density and coefficients of thermal expansions) are a function of the temperature  $T$ , as presented in the Fig. 4 (see also [1]). In this study only a uniform temperature distribution within the plate is considered, Fig. 3.

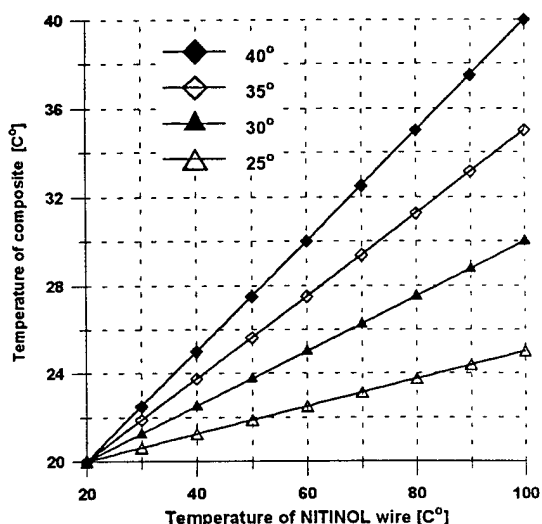


Fig. 3. Temperature of the plate as a function of the temperature of NITINOL wire.

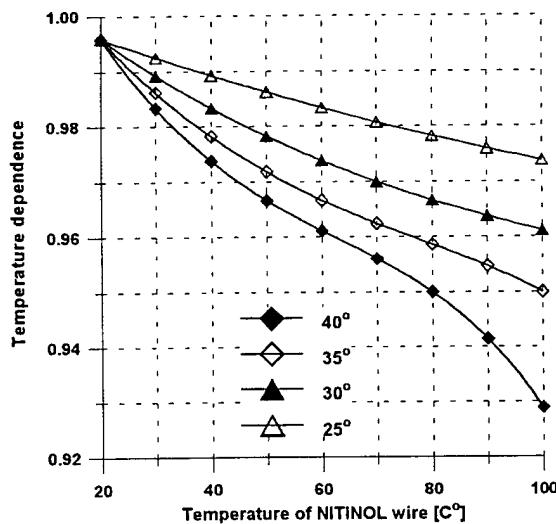


Fig. 4. Temperature dependence of the composite material properties.

Results of numerical investigations illustrate the influence of the ambient temperature upon the drop in the first natural frequency of the analyzed plate. These changes are presented in Figs. 5, 6. The results of these calculations are related to those obtained for the same plate with the non-activated SMA wires. It is clearly seen that the activation process of the SMA wires generally involves changes in natural frequencies. This effect grows if both the temperature and initial strain are higher.

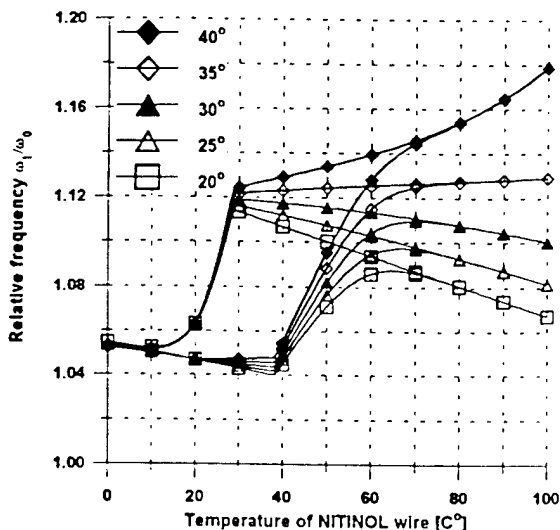


Fig. 5. The influence of the ambient temperature at initial strains  $\varepsilon = 0.22\%$  upon the relative change of the first frequency.

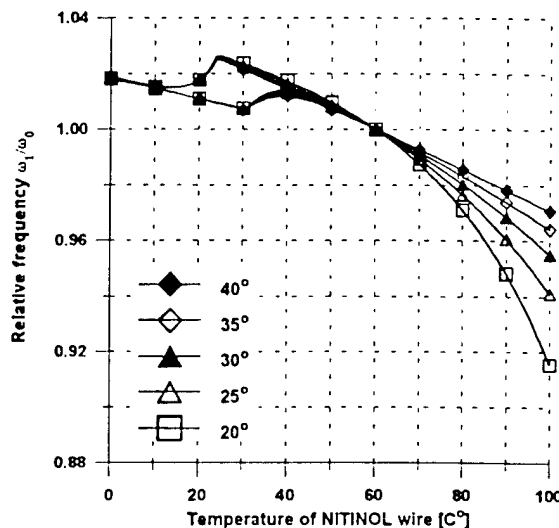


Fig. 6 The influence of the ambient temperature at the initial strain  $\varepsilon = 0.05\%$  upon the relative change of the first frequency.

The obtained results demonstrate the potential effectiveness of the use of Nitinol wires in the vibration control. The effect of the activation of the Nitinol wires on natural frequencies, normalized with respect to the natural frequencies of the uncontrolled plate, is shown.

## CONCLUSIONS

Applications of the SMA wires in the natural frequency analysis of the multi-layer plate have been successfully demonstrated. The fundamental equations ruling the behavior of the multi-layer composite plate as well as the stress-strain relationships for a single composite lamina with embedded SMA wires have been presented in the paper. The finite element formulations and the results of calculation for the natural frequencies and modes of vibrations were also presented.

## BIBLIOGRAPHY

- [1] A. Baz, S. Poh, J. Ro, J. Gilheany: Control of the natural frequencies of Nitinol – reinforced composite beams. *Journal of Sound and Vibration*, Vol. 185, No. 1, pp. 171–185, 1995.
- [2] V. Birman, D. A. Saravanos, D. A. Hopkins: Micromechanics of composites with shape memory alloy fibers in uniform thermal fields. *AIAA Journal*, Vol. 34, No. 9, pp. 1905–1912, 1996.
- [3] J. Ro, A. Baz: Nitinol-reinforced plates, Part I–III. *Composites Engineering*, Vol. 5, No. 1, pp. 61–106, 1995.
- [4] J. R. Vinson, R. L. Slerakowski: *Behaviour of Structures Composed of Composite Materials*. Martinus Nijhoff, London 1981.

- [5] Z. W. Zhong, R.R. Chen, C. Mei: Buckling and postbuckling of shape memory alloy fiber reinforced composite plates. AD-Vol. 41/PVP-Vol. 233, Buckling and Postbuckling of Composite Structures, ASME 1994.
- [6] W. Weaver, P. R. Johnston: Finite Element for Structural Analysis. Prentice Hall Inc., Englewood Cliffs, New Jersey 1984.
- [7] C. A. Rogers, C. Liang, D. K. Barker: Dynamic Control Concepts Using Shape Memory Alloy Reinforced Plates. Smart Materials, Structures, and Mathematical Issues, Technomic Publishing Company, Inc. ,1989.

# Temperature Effects in PZT Based Control Design

Michael I. Friswell

Department of Mechanical Engineering  
University of Wales Swansea  
Swansea SA2 8PP, UK.  
E-Mail: m.i.friswell@swansea.ac.uk

Daniel J. Inman

Engineering Science and Mechanics  
Virginia Tech.  
Blacksburg, Virginia 24061-0219, USA.  
E-Mail: dinman@vt.edu

## ABSTRACT

The prospect of using active damping in a smart structure to suppress thermally induced vibration is investigated. A simply supported aluminium beam is used to illustrate the nature of thermally induced vibrations caused by a suddenly applied heat flux. A distributed piezoelectric self-sensing sensor/actuator pair is used to actively suppress the motion caused by thermal disturbances. The effect of large temperature changes on the structure and actuator are taken into account in the control system design. A Proportional-Derivative controller, a Linear Quadratic Regulator and a Positive Position Feedback filter are considered. Simulation results show that thermally induced vibrations can be damped using currently available smart structure technology, provided temperature effects are properly accounted for in the control law.

## INTRODUCTION

The problems associated with thermally induced vibrations in space structures and other application areas are well documented. Since the advent of space exploration, thermal disturbances have been linked to serious reductions in performance for certain spacecraft as well as the loss of spacecraft due to uncontrolled thermally induced oscillations. Unmodeled thermal effects are also believed to be the primary cause of many unexplained spacecraft failures. Thus there is sufficient motivation to study the active control of thermally induced vibrations.

Yaralugala *et al.* (1995) documented the sensitivity of piezoceramic materials to thermal influence and highlighted the need to include thermal properties. The motivation for considering the use of the smart structures approach to controlling thermally induced vibrations lies in the unobtrusive nature of embedded and/or surface mounted piezoceramic elements. Compared to other choices of actuators, piezoceramic devices are relatively light weight, have reasonable power requirements (Dosch *et al.*, 1992) and are spatially much smaller than traditional actuators used in vibration suppression, such as proof mass or reaction mass actuators. Here we examine control in the presence of thermal excitation.

Several authors have approached closed loop control of structures using piezoceramics to counter thermal effects or to reject thermal disturbances. Bruch *et al.* (1993) also examined a thermoelastic beam controlled by piezoceramic actuators. However, they did not account for thermal effects in the piezoceramic actuator or sensor and treated the piezoceramic only as a source of actuation. Inman *et al.* (1996) improved on their result by accounting for these effects, although their treatment was limited to velocity feedback. Others, for example Tzou *et al.* (1996), included thermal effects in the piezoceramic material, but treated the structure as being in thermal equilibrium subject to velocity feedback only. Coupling to the heat conduction equation was ignored. Here, the thermal effects are included by using uncoupled heat conduction analysis to determine the moment induced by the temperature changes which is then suppressed by the control system. The present work examines a variety of standard control methods.

## SYSTEM MODELING

The thermoelastic effects considered here are limited to a linear theory. This requires the direct thermal-mechanical coupling to be negligible, the strains to be small and the structure to possess constant (temperature-independent) properties. The first of these assumptions implies that the temperature distribution in the body can be determined independently from the structural vibration and that the temperature of the structure does not change as a result of its deformation. Small strains are assumed, and shear effects are assumed to be negligible so that an Euler-Bernoulli beam approximation may be used.

As an example, the closed loop control of a simply supported beam, which is initially at rest will be considered. A constant uniform heat flux is suddenly applied to the top surface of the beam, and the bottom surface is assumed to be insulated. This scenario is motivated by satellites moving from dark to direct sunlight.

**The Heat Conduction Model.** The heat conduction model used here is fairly simple and straightforward. Let  $T(x, y, t)$  indicate the temperature as a function of elapsed time  $t$ , the displacement through the thickness of the beam,  $y$ , and the displacement along the length of the beam,  $x$ . If the top surface of the beam exposed to a heat flux  $q_0$ , the bottom surface insulated, and a zero initial temperature is assumed, then the governing relationship is

$$\frac{k}{\rho c} \left( \frac{\partial^2 T}{\partial y^2} \right) = \frac{\partial T}{\partial t} \quad (1)$$

with boundary and initial conditions

$$T(x, y, 0) = T_0, \quad \left. \frac{\partial T}{\partial y} \right|_{y=-t_b/2} = 0, \quad \left. k \frac{\partial T}{\partial y} \right|_{y=t_b/2} = q_0 - h_0(T - T_0)$$

Here, the top of the beam is at  $y=t_b/2$ , and the bottom at  $y=-t_b/2$  where  $t_b$  is the beam thickness,  $k$  is the thermal conductivity of the structure,  $q_0$  is a constant magnitude (uniform) heat flux,  $\rho$  is the mass density, and  $c$  is the specific heat of the beam. The coefficient  $\kappa=k/\rho c$  is the thermal diffusivity. The beam is assumed to be at the ambient temperature,  $T_0$ , initially and the coefficient  $h_0$  determines the rate of heat loss from the beam by conduction. Without the heat loss from the beam the temperature will rise without bound. If the applied heat flux and the heat loss are constant over the surface of a rectangular section beam then the temperature distribution may be obtained by solving Equation (1) using the separation of variables method (Rietz *et al.*, 1997).

Following Boley and Weiner (1960), the temperature distribution  $T(x, y, t)$  gives rise to a moment applied to the beam. This thermal moment is distributed along the length of the beam, and is

$$M_T(x, t) = \iint_A E\alpha(T - T_0) y dA \quad (2)$$

where  $A$  is the cross sectional area,  $dA=dydz$ ,  $E$  is the beam's modulus of elasticity and  $\alpha$  is the coefficient of thermal expansion for the beam. Because of the initial assumptions, the thermal moment will only provide forcing in the standard Euler-Bernoulli beam equation.

**Self-Sensing Actuators.** The “smart” structure aspect of the system proposed here refers simply to the use of a piezoceramic sensor actuator system and corresponding active control system. The piezoceramic system is described in this section and the control laws are described later. The piezoelectric actuator system is assumed to apply a bending moment,  $M_a(t)$ , over the length of the actuator (Dosch *et al.*, 1992), given by

$$M_a(t) = K_a v_a(t) \quad (3)$$

where  $v_a(t)$  is the voltage (command) applied to the piezoceramic self-sensing actuator and  $K_a$  is the actuator constant. Crawley and Anderson (1990) give more detail.

The sensor equation associated with the self-sensing actuator system can be characterized by the voltage  $v_s(t)$  developed across the piezoceramic and is

$$v_s(t) = K_s \left[ \frac{\partial w}{\partial x}(L_2, t) - \frac{\partial w}{\partial x}(L_1, t) \right] \quad (4)$$

where  $w(x, t)$  is the displacement of the beam in the  $y$  direction,  $L_1$  and  $L_2$  denote the extent of the sensor, and  $K_s$  is the sensor constant. The self-sensing actuation circuit allows the same piezoceramic patch to provide both sensing and actuation (Dosch *et al.*, 1992) which forms a perfectly collocated input and output pair.

**Structural Model.** The beam will be modeled using Euler-Bernoulli theory. In the example the assumed modes method will be used to generate approximate equations of motion. Notice that the thermal moment may be calculated independently and is given by Equation (2). Internal damping in the beam is approximated by adding 1% viscous damping to each mode, which is consistent with the damping ratios for aluminium. Although this a gross approximation, the internal damping is very low and most of the damping arises from the controller.

## THERMAL EFFECTS ON THE SENSOR

One difficulty in using a smart structure approach to control thermally induced structural vibration is the effect of changes in temperature on the piezoceramic. Piezoceramics exhibit a pyroelectric effect, so that a temperature change produces an electric displacement. In lead zirconate titanates (used in the simulation to follow), the charge generated by a temperature change is approximately  $2 \times 10^4$  coulombs/m<sup>2</sup>K and is linear in our range of interest (-50°C < θ < 200°C, typically experienced by orbiting satellites). If the temperature is measured independently, the thermally induced electric displacement can be compensated for in any control scheme. The other effect possible is the change of the piezoelectric constant,  $d_{31}$ , with temperature. This is known to change ±4% in the temperature range of interest, (Rietz, 1995). This variation does not affect the controller design or the closed loop behaviour. However, the pyroelectric effect must be accounted for, since otherwise the control system will see the temperature induced change in voltage as structural motion and attempt to compensate for it.

## CONTROLLER DESIGN

A number of controller designs will now be considered for the simply supported beam with the parameters given in Table 1. The response of the beam to the thermal effects is mainly due to the first mode and the response due to the higher modes is at least an order of magnitude lower than this. Thus the controllers will be designed based on a single mode approximation to the beam

system. The thermal load produces a non-zero steady state response, that is then larger in the closed loop system. This is unsatisfactory and the Proportional term ensures that the steady state stiffness is the same in the open and closed loop systems. An added advantage is that the voltage applied to the actuator in steady state is zero. In the standard PPF filter, the second order nature of the filter causes the response to roll off quickly at high frequency, thus eliminating the usual spill over problems often associated with modal control laws. Unfortunately the addition of the Proportional term removes this advantage.

Figure 2 shows the closed loop response of the beam centre using a PPF controller designed for the first mode only. The filter damping ratio and natural frequency were set as 0.25 and  $1.2\omega_n$ , where  $\omega_n$  is the first natural frequency. The gain was then adjusted to ensure the actuator voltage remained below 100V. These parameters were chosen to ensure that energy was transferred from the structure to the filter degree of freedom, and that this energy was then dissipated in the filter. The compensator damping cannot be set too high as this would hinder the energy transfer. It is apparent from Figure 2 that the PPF compensator has reduced the settling time of the beam more than the LQR controller.

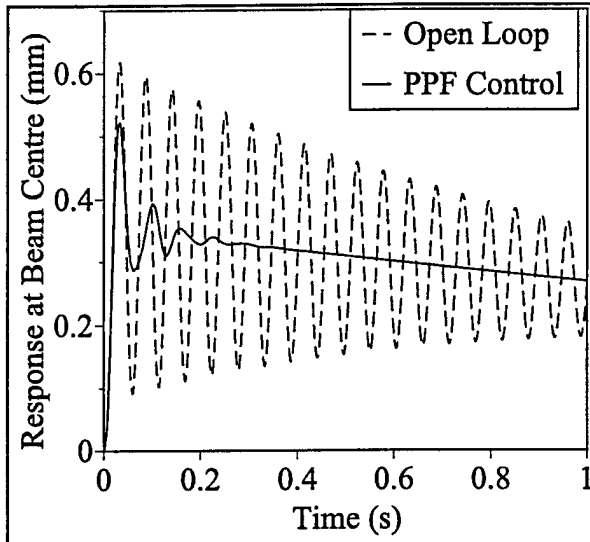


Figure 2. Time response of a simply supported beam due to a thermal load, for open loop and with a PPF controller.

**The Pyroelectrical Effect.** The pyroelectrical temperature effect can produce large responses in the closed loop system. The voltage in the sensors caused by the pyroelectrical may be estimated from the measured temperature and removed from the sensor output voltage. Figure 3 shows the result of compensating for the temperature effects on the piezoceramics. The plot indicates clearly that without compensation for the pyroelectrical effect in the piezoceramic sensor circuit, the closed loop response would seek the different steady state value. Effectively, the uncompensated closed loop system produces an unnecessary static deflection.

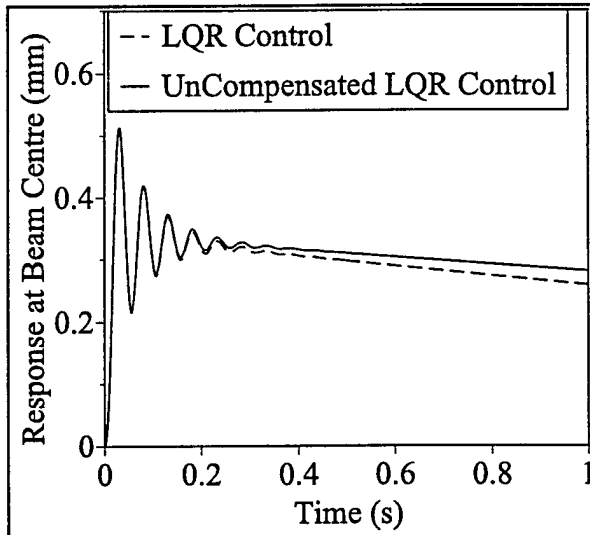


Figure 3. Time response to a thermal disturbance for PD/LQR closed loop control with and without temperature compensation.

## CONCLUSIONS

The analysis and simulation of the response of a simple “smart structure”, consisting of a simply supported beam with a piezoceramic sensing and actuator system, subject to a thermal disturbance has been presented. A linear model is assumed with only a partially coupled thermal elastic mechanical model. The heat flux is assumed to affect the structural model through a forcing term, and the temperature may be calculated independently of the structural response. It

dynamics. The response of the closed loop control of the beam will be simulated using a 5 mode approximation. Three controller designs will be considered, namely a Proportional-Derivative (PD) controller, a Linear Quadratic Regulator (LQR) and a Positive Position Feedback (PPF) filter. In the single mode approximation the state feedback required in the LQR controller is equivalent to PD control. Thus the LQR approach will be used to generate the state gains which will be implemented as a PD controller.

Heat Flux, $q_0$	$0.3 \times 10^6 \text{ W m}^{-2}$
Ambient Temperature, $T_0$	$0^\circ\text{C}$
Steady State Temperature	$200^\circ\text{C}$
Beam Parameters	Piezoceramic Parameters
Breadth	0.02m
Thickness	$0.254 \times 10^{-3} \text{ m}$
Length	0.5m
Modulus of Elasticity, $E$	$69 \times 10^9 \text{ N m}^{-2}$
Mass Density, $\rho$	$2700 \text{ kg m}^{-3}$
Thermal Conductivity, $k$	$170 \text{ W m}^{-1} \text{ K}^{-1}$
Thermal Diffusivity, $\kappa$	$64 \times 10^{-6} \text{ m}^2 \text{ s}^{-1}$
Coefficient of Thermal Expansion	$24 \times 10^{-6} \text{ K}^{-1}$
	Piezoelectric Constant, $d_{31}$ $\text{mV}^{-1}$
	Modulus of Elasticity $63 \times 10^9 \text{ N m}^{-2}$
	Capacitance $0.275 \times 10^{-6} \text{ F}$

Table 1. Physical parameters of the system used in the simulation

In order to compare the controller designs constraints are placed on the actuator voltage. For illustration, in this example, the controller gains will be chosen so that this voltage is less than 100V, that is  $v_a < 100\text{V}$ . Energy constraints could also be imposed on the actuator.

**LQR Control.** Figure 1 shows the response of the beam centre using an LQR controller, and demonstrates a significant reduction in settling time over the open loop response. A similar controller could be implemented based on a multi mode approximation of the beam dynamics, requiring state feedback. This is equivalent to the feedback of all the modal displacements and velocities of interest.

**PPF Compensator.** Another effective and practical control scheme for vibration suppression in smart structures is Positive Position Feedback control (PPF) described by Fanson and Caughey (1987). The system works well in experiments because its inherent stability depends only on knowledge of the open loop natural frequencies. The PPF control law couples the energy dissipation term in the compensator to a particular structural mode.

The standard PPF regulator design is modified by adding a Proportional controller term (Rietz *et al.*, 1997). Without this term the resulting closed loop system is more flexible than the open loop

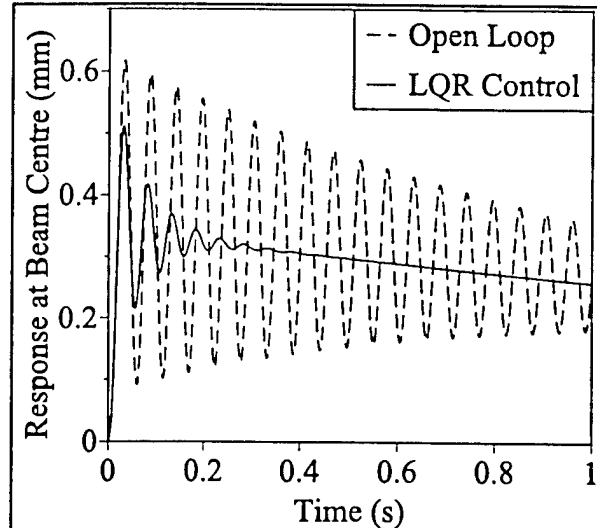


Figure 1. Time response of a simply supported beam due to a thermal load, for open loop and with a PD/LQR controller.

has been demonstrated that the pyroelectric effect is significant and the closed loop control system should compensate for it. An effective method for controlling temperature induced structural vibrations has been formulated which compares well with, but is more practical than, those previously published.

## REFERENCES

- Boley, B. and Weiner, J.H., 1960. *Theory of Thermal Stresses*. John Wiley and Sons.
- Bruch, J.C., Adalis, S., Sadek, I.S. and Sloss, J.M., 1993. "Structural Control of Thermoelastic Beams for Vibration Suppression", *Journal of Thermal Stresses*, **16**(3), 249-263.
- Crawley, E.F. and Anderson, E.H., 1990. "Details and Models of Piezoceramic Actuator of Beams", *Journal of Intelligent Material Systems and Structures*, **1**(1), 4-25, (also AIAA paper no. 89-1388).
- Dosch, J.J., Inman, D.J. and Garcia, E., 1992. "A Self Sensing Piezoelectric Actuator for Collocated Control", *Journal of Intelligent Material Systems and Structures*, **3**, 166-185.
- Fansen, J.L. and Caughey, T.K., 1987, "Positive Position Feedback Control for Large Space Structures", *Proceedings of the 28th AIAA Structures, Structural Dynamics and Materials Conference*, 588-598.
- Inman, D.J., Rietz, R.W. and Wetherhold, R.C., 1996. "Control of Thermally Induced Vibrations Using Smart Structures", *Dynamics and Control of Structures in Space*, ed. C. K. Kirk and D. J. Inman, Computational Mechanics Publications, Southampton, UK, 3-16.
- Rietz, R., 1995. "Dynamics and Control of Thermally Induced Vibration", PhD Dissertation, State University of New York at Buffalo.
- Rietz, R., Friswell, M.I. and Inman, D.J., 1997. "Active Damping of Thermally Induced Vibration", submitted to *Journal of Intelligent Material Systems and Structures*.
- Tzou, H.S., Ye, R. and Venkayya, V.B., 1996. "Active Control of Mechanical and Thermal Shock Induced Vibrations", *Proceedings of the AIAA/ASME/AHS Adaptive Structures Forum*, AIAA Paper No. 96-1270-CP, 39-45.
- Yarlagadda, S., Chan, M.H., Lee, H., Lesiuetre, G.A., Jensen, D.W. and Messer, R.S., 1995. "Low Temperature Thermal Conductivity, Heat Capacity, and Heat Generation of PZT", *Journal of Intelligent Material Systems and Structures*, **6**, 757-764.

# Active Control of Vibration Transmission Through Struts

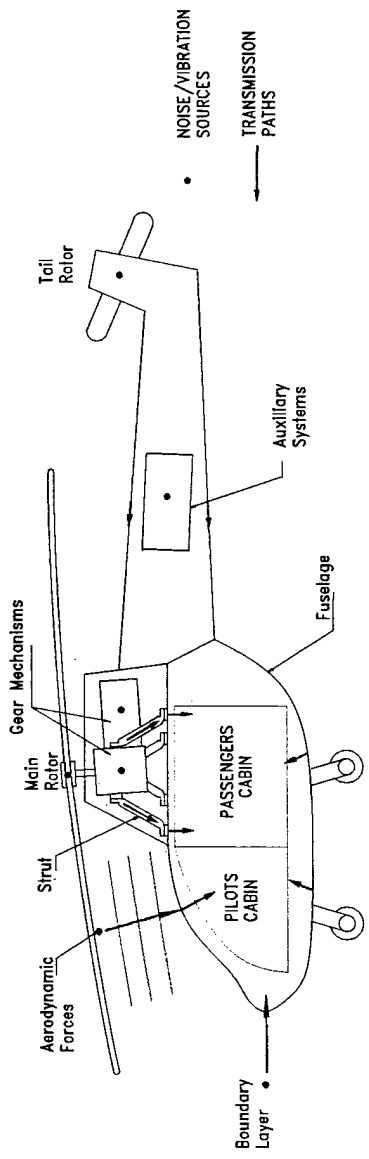
I. Pelinescu and B. Balachandran

Department of Mechanical Engineering  
University of Maryland at College Park  
MD 20742-3035  
Phone: (301) 405-5309  
Fax: (301) 314-9477  
Email: psorin@eng.umd.edu

As shown in Illustration 1, the noise and vibration problems in a helicopter have many complex characteristics. Here, the focus is on reducing the vibrations transmitted at the gearbox/fuselage interface. In this work, analytical investigations into active control of longitudinal vibrations transmitted through a cylindrical strut are conducted. This strut is representative of a helicopter gearbox strut. Piezoelectric actuator(s) fitted to the strut are used to minimize the displacements transmitted through the strut. A mechanics-based model for the strut incorporating the piezoelectric actuator is developed (Illustration 2). In this model, a linear dynamic formulation describing the motion of the actuator (Illustration 3) is integrated with the formulation describing longitudinal wave transmission through the strut, and the solution of the resulting boundary value problem is studied. For tonal disturbances the system is studied in the frequency domain. Parametric studies are conducted for the open-loop system, and the effectiveness of the actuator in controlling the vibration transmission is highlighted (e.g., Illustrations 4 and 5). In the current scheme, high current inputs into the actuator are required. The results of the current study point to the potential of actively controlling vibration transmission through struts.

Acknowledgements: ARO/MURI program  
Drs. Gary Anderson and Tom Doligalski

## Illustration 1: Problem Depiction



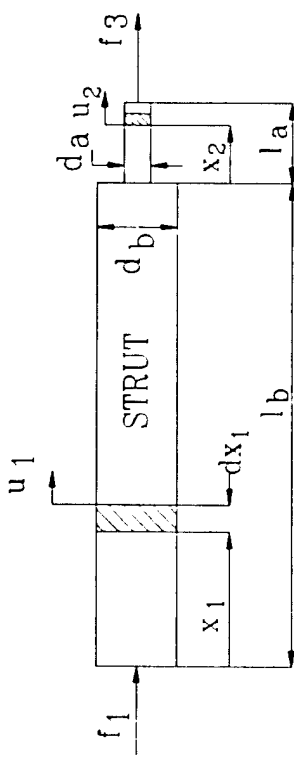
- Sources of noise and vibrations:

1. Air-Borne
    - (a) Propeller
    - (b) Boundary Layer
  2. Structure-Borne
    - (a) Main/Tail Rotor
    - (b) Turbines
    - (c) Gear mechanisms
    - (d) Auxiliary Systems
- Transmission paths:
    1. Gearbox/fuselage interface
    2. Fuselage
    3. Cabin windows and panels
  - Receiving space:
    1. Pilots cabin
    2. Passengers cabin



## Illustration 2: Mechanics Model

Attachment to  
the gearbox



$(\rho_a, A_a)$

- Equation of motion of the strut:

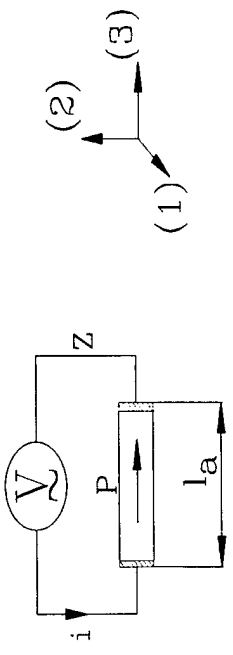
$$\frac{\partial^2 u_1}{\partial x_1^2} - \frac{1}{c^2} \frac{\partial^2 u_1}{\partial t^2} = 0 \quad (1)$$

- Equation of motion of the actuator:

$$\frac{\partial^2 u_2}{\partial x_2^2} - \frac{1}{(v_3^D)^2} \frac{\partial^2 u_2}{\partial t^2} = 0 \quad (2)$$



### Illustration 3: Piezoelectric Actuator Model



Thin rod shaped polarized along  $(3)^{rd}$  axis with the electric field  $E_3$  applied on the polarization direction.

- Linear constitutive equations of the actuator:

$$S_3 = s_{33}^D \cdot T_3 + g_{33} \cdot D_3 \quad (3)$$

$$E_3 = g_{33} \cdot T_3 + \beta_{33}^T \cdot D_3 \quad (4)$$

- Electrical boundary conditions:

$$i = \frac{2V}{Z} \cdot e^{j(\omega t + \theta)} \quad (5)$$

$$D_3 = \frac{2V}{j\omega A_a Z} \cdot e^{j(\omega t + \theta)} \quad (6)$$

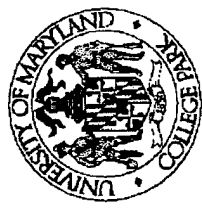


## Illustration 4: Analysis - Solutions

- Frequency domain solution:

$$\{U\} = \{U\}_0 + \{U\}_c = [\alpha] \cdot \{F\} + [\beta] \cdot \{F_c\} \quad (7)$$

- $[\alpha]$  is the receptance matrix and  $[\beta]$  is a matrix dependent on characteristics and locations of actuator
- $\{U\}$ ,  $\{F\}$ , and  $\{F_c\}$  are amplitudes of displacement, force and secondary control force vectors respectively

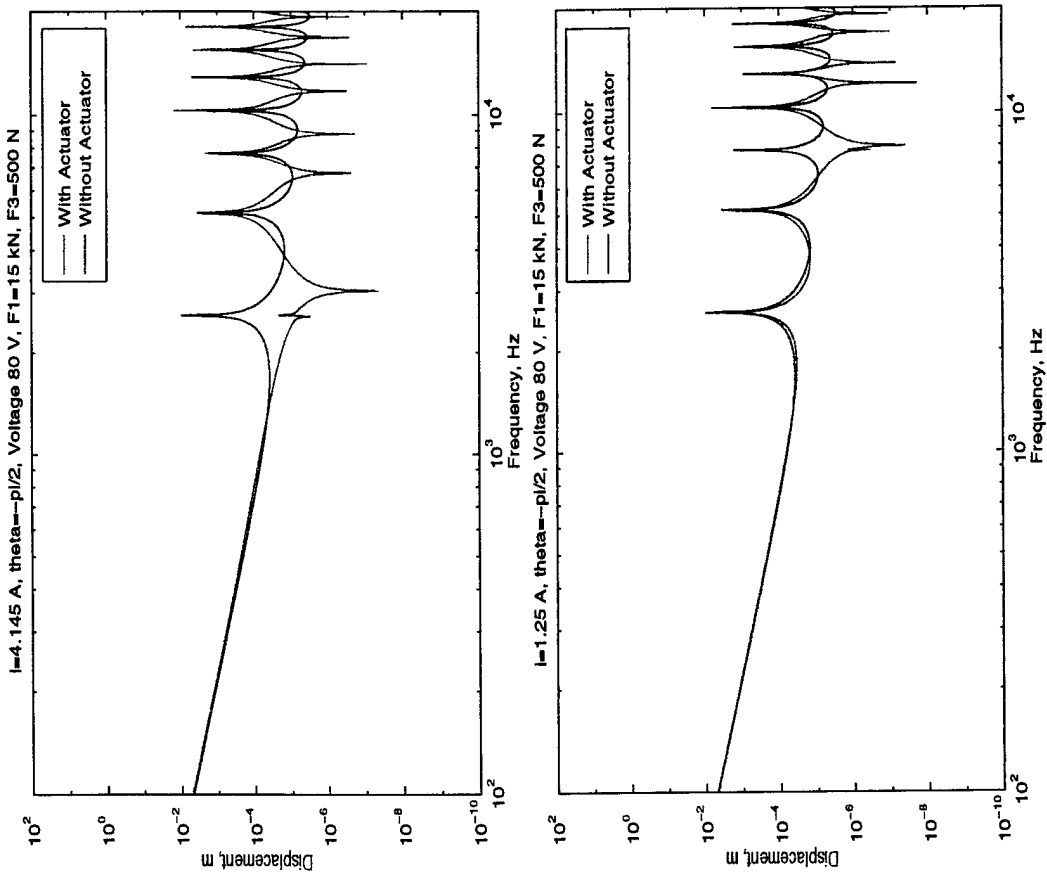
- Control force amplitude:

$$F_c = \frac{g_{33}}{s_{33}^D} \cdot \frac{2V}{\omega Z(\omega)} \cdot e^{j\theta} \quad (8)$$



## Illustration 5: Numerical Results

### Displacement at the Fuselage Attachment



# MICROFABRICATED CONFORMAL WALL SHEAR STRESS SENSOR FOR AIRCRAFT

V. K. Varadan and V. V. Varadan

Research Center for the Engineering of Electronic and Acoustic Materials and Devices  
The Pennsylvania State University  
University Park, PA 16802  
Tel: (814) 863-4210  
Fax: (814) 863-7967 or (814) 865-3052  
E-mail: vjvesm@engr.psu.edu

## ABSTRACT

A critical variable describing flow conditions on an aircraft is the wall shear stress. Microsensors capable of accurate wall shear measurement with adequate spatial and temporal resolution are not available. Moreover, in real aerodynamic environments, the sensors are hampered by their sensitivity to airborne contaminants, such as dust, rain, ice, insects, dirt, etc. Recently, wall shear stress sensors have been fabricated using MEMS and IDT technology which overcome these problems and provide superior spatial and temporal resolution.

In this paper such microsensors with remote telemetry capability will be presented.

## Self-Assembled Nanoparticle-Based Multi-Layer Thin-Films and Devices

Y. Liu<sup>a</sup>, J. R. Heflin<sup>b</sup>, W. Zhou<sup>a</sup> and R. O. Claus<sup>a</sup>

<sup>a</sup>Bradley Department of Electrical Engineering

<sup>b</sup>Department of Physics

Virginia Tech, Blacksburg, VA 24061

540-231-7203, fax 540-231-4561, email <yliu@vt.edu>

We have developed and demonstrated a technique for the self-assembly of inorganic nanoparticles with high-performance polymers into multi-layer thin-films and two- and three-dimensionally-patterned passive and active devices. We report new results in the demonstration of quantum size effects in chemically synthesized nanoparticles, the formation of nonlinear optical thin-film materials by self-assembly, and the patterning of self-assembled materials into early prototype optical and optoelectronic devices.

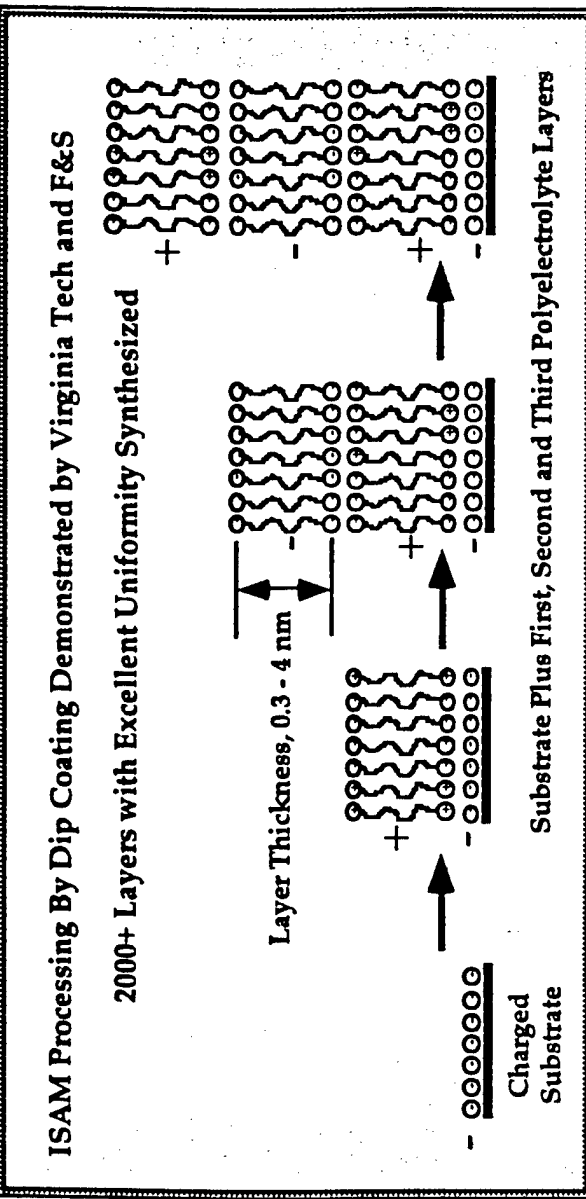
Our fabrication technique is based on three separate developments. The first is the chemical synthesis of nanoparticles of desired inorganic molecules having desired optical, electronic, electromagnetic, mechanical and other properties. We review our recent published work in this area, and describe results in the synthesis of iron oxide, TiO<sub>2</sub>, and other small particles with dimensions on the order of several nanometers. We briefly describe efforts to analytically model both the electronic state properties of such nanoparticles and the corresponding properties of larger material systems fabricated from arrays of such nanoparticles, and relate these models to our recent observations of quantum size effects in TiO<sub>2</sub> nanoparticle colloids.

The second development is the synthesis of the nanoparticles, and water soluble high-performance polymers, into larger physical structures. We have used the ionic self-assembled monolayer (ISAM) technique in which successive layers of polyelectrolytes are adsorbed onto an initially charged substrate. Judicious selection of the molecular species of each layer, and the controlled geometric arrangement of the molecules within the layer, may lead to important optical, magnetic and mechanical material properties. In particular, we report exciting recent results in the ISAM formation of thin-films with nonlinear optical (NLO) properties important to optoelectronic devices. This work demonstrates the ability to control the internal thin-film geometrical structure, here using noncentrosymmetric dye and other molecules, which is key to the larger structuring of multi-layer systems.

Third, we describe methods to pattern extremely small scale features into the resulting thin-films in two-dimensions, and our recent progress in registering multi-layer patterns into larger structures having long-range, three-dimensional order, and extending the process to a wider range of substrate materials.

This work has been supported in part by the Army Research Office through grant DAAG55-97-1-0101, and by the Virginia Center for Innovative Technology. The authors appreciate the help of Dr. R. Davis and his group in the Department of Chemical Engineering.

# Modified Ionic Self-Assembly of Organic/Inorganic Thin-Films

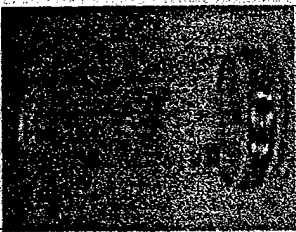
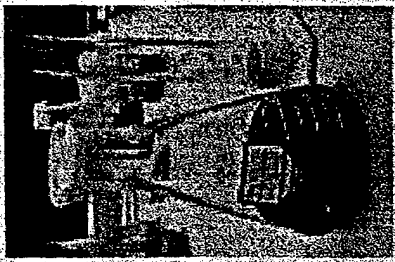
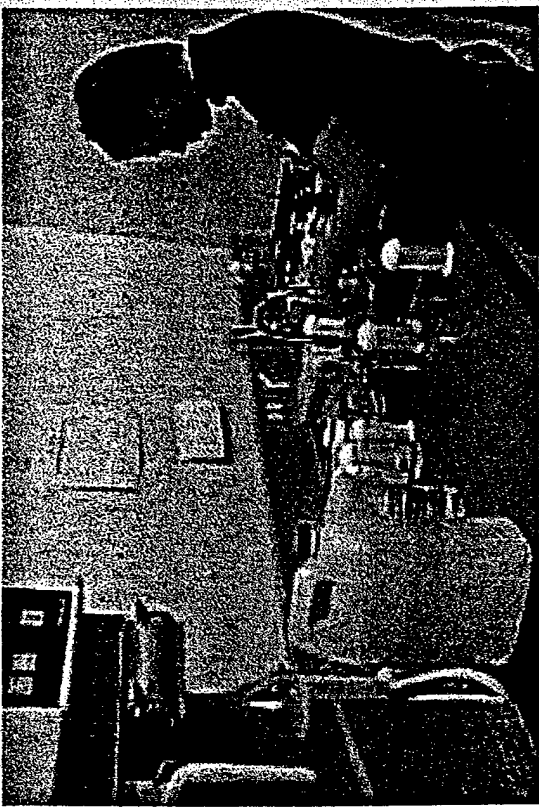
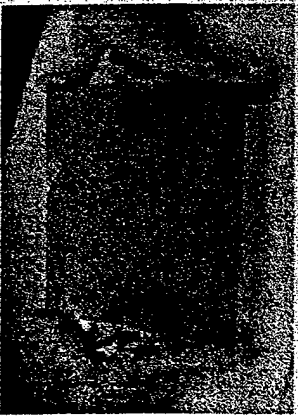
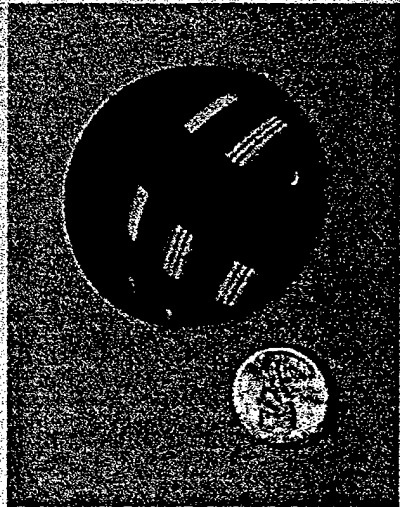


## Process

- first reported by Iler, 1966
- alternate adsorption of anion, cation complexes onto substrate
- properties dependent upon chemical precursor synthesis and physical ordering/structure
- excellent nanoscale molecular level uniformity
- coatings on surfaces with complex shapes
- synthesis at room temperature and pressure
- low-cost, rapid synthesis
- self-healing assembly allows multi-micron thickness
- no VOCs
- broad range of layer functionality

## Advantages

# Thin-Film Self-Assembly Process



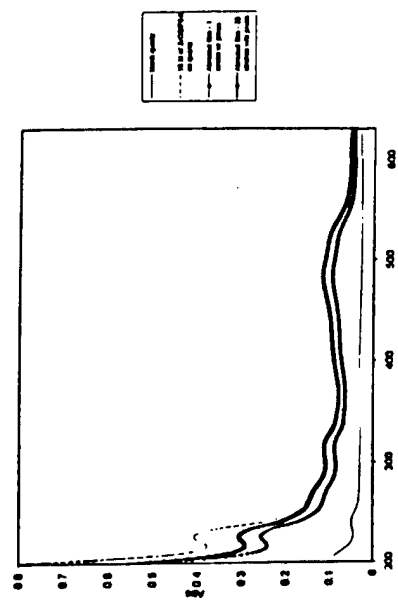
FEORC, Virginia Tech

# Protective Thin-Film Characterization

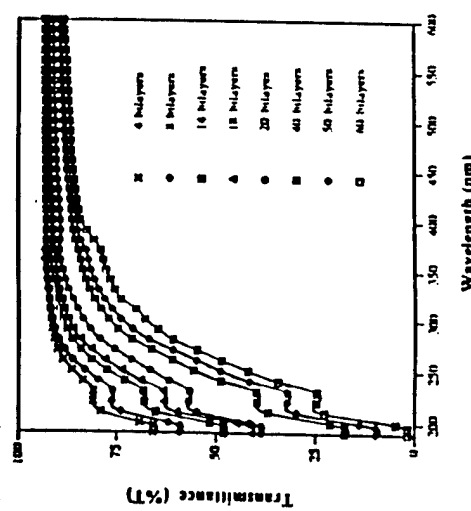
## Goal

Design and synthesis of coatings with  
desired multi-functional properties

- strong UV absorption
- EMI shielding ( $\rho$ ,  $\mu$ )
- abrasion protection



UV Absorption of Multi-Layer TiO<sub>2</sub> Coating



Before/After UV-Vis Absorption of ZrO<sub>2</sub> Coating

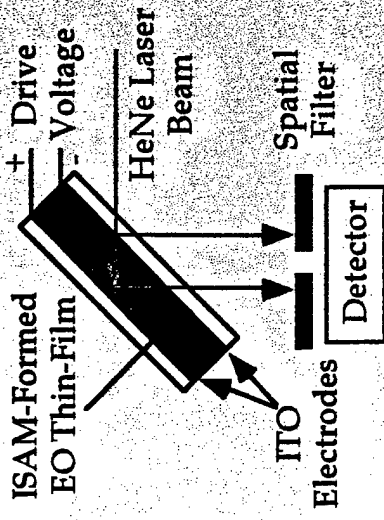
# Electro-Optic Thin-Film Synthesis

## Goal

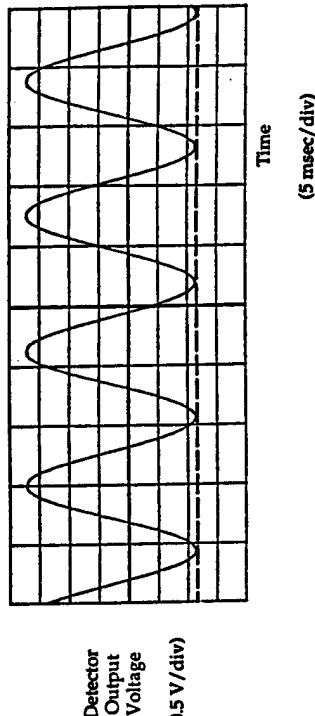
Demonstrate precursor synthesis and molecular self-assemble of electro-optic thin-films and prototype devices.

## Result

General ferroelectric behavior demonstrated.



Modulation Detection Experimental Set-Up



Prototype Self-Assembled EO Modulator

Output Phase Modulation Signal

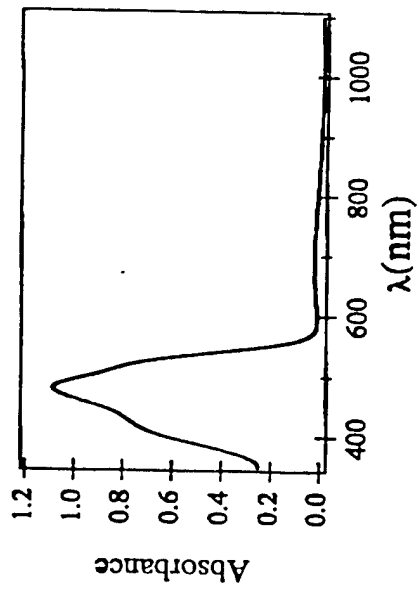
FEORC, Virginia Tech

# NLO Thin-Film Synthesis and Demonstration

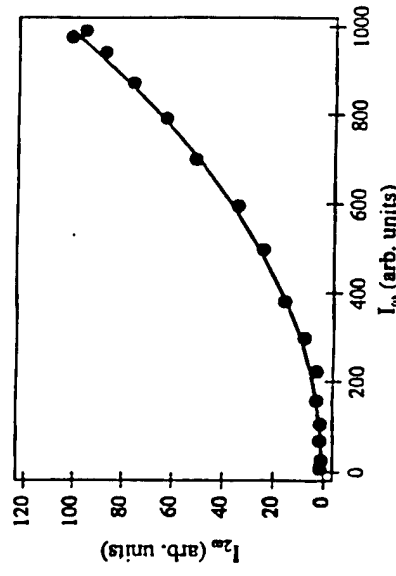
## Results

First demonstration of self-assembly of noncentrosymmetric thin-films with large  $\chi^{(2)}$  values greater than quartz.

Characterization through SHG.



Absorbance Spectrum of 68 Layer  $\chi^{(2)}$  Thin-Film



Quadratic Dependence of SHG at 600 nm on Fundamental Intensity at 1200 nm



Multiple NLO Thin-Films Synthesized

# Effects of Implementation of Smart Materials Technology and Optimal Control on Dynamic Response of Cantilevers Exposed to Blast Loadings

S. S. Na and L. Librescu  
Engineering Science and Mechanics Department  
Virginia Polytechnic Institute & State University  
Blacksburg, VA 24061-0219, USA

A study of the vibration control of cantilevered beams exposed to blast pressure signatures is presented. Whereas the structure used in this analysis is in the form of a thin-walled beam of closed cross-section contour, the control is based upon the simultaneous implementation of the adaptive materials technology and the optimal feedback control.

Issues related with the influence upon eigenfrequencies and dynamic response of size and location along the wing span of piezoactuator patches are investigated and the efficiency of this combined control methodology is outlined. Other issues resulting in the minimization of the input power required in the control process, maximization of the sensing voltage output and implications of the limitation of control input voltage on dynamic response are also addressed and pertinent conclusions are outlined.

The results of this study constitute a continuation and extension of those obtained previously in Refs. 1 and 2. The attached figure depicts the dimensionless transverse deflection time-history of the beam when subjected to a sonic-boom pressure pulse (indicated in the inset), when there are no voltage limitations, limited voltage ( $\equiv 250$  volts) and for the un-controlled structure as well. The results reveal the capability of this dual control methodology to suppress the vibration, especially in the free-motion regime (i.e. when  $t > rt_p$ .)

## References

1. Librescu, L. and Na, S.S., "Dynamic Response of Cantilevered Thin-Walled Beams to Blast and Sonic Boom Loadings," *The Journal of Shock and Vibration* (in press).
2. Librescu, L. and Na, S.S., "Bending Vibration Control of Cantilevers Via Boundary Moment Control and Combined Feedback Control Laws," *Journal of Vibration and Control* (in press).

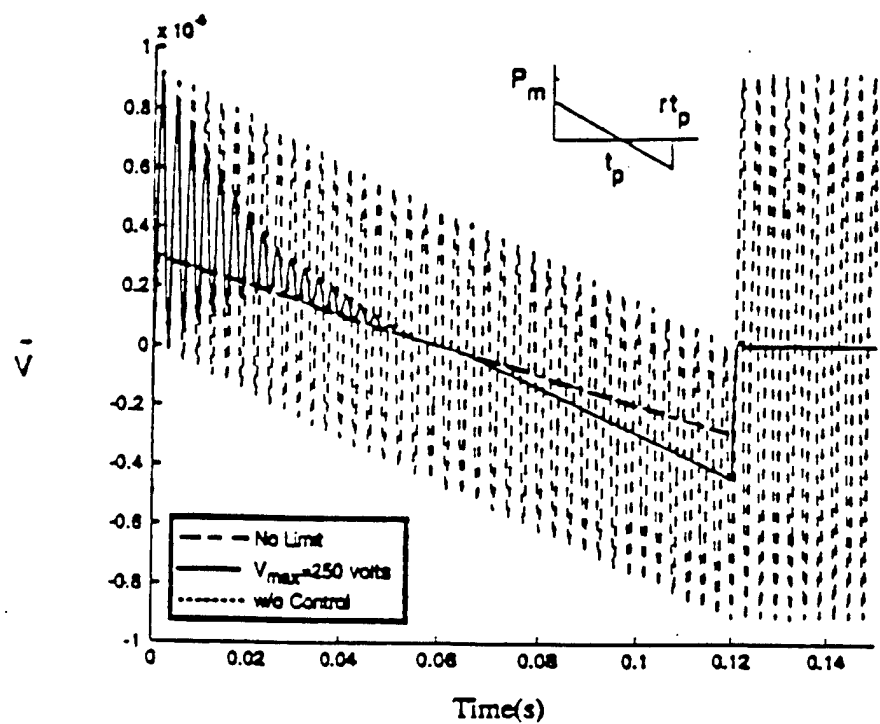


**Figure Caption**

Fig. 1 Influence of limitation of the control input voltage upon the dimensionless transversal deflection time-history at the beam tip. Piezoactuator patch located at  $z^a(0.2 - 0.1)L$ , where  $L$  is the beam span. Sonic-boom pressure-pulse characterized by  $P_m = 0.4437$  lb/in;  $t_p = 0.06$  sec;  $r = 2$ .

# ADAPTIVE TUNING OF PIEZO-ACTUATED DELAYED RESONATOR ABSORBERS

MARK RENZULLI

RAJIV GHOSH-ROY

NEJAT OLGAC\*

Department of Mechanical Engineering

University of Connecticut U-139

Storrs, CT 06269-3139

A recent vibration absorption methodology, the **Delayed Resonator (DR)**, is the topic of this study. This method uses delayed acceleration feedback on a passive absorber in order to introduce ideal resonance features to it. When such a resonator is installed on an oscillating body (primary structure), it becomes a 'notch filter' at its resonance frequency, acting against excitations on the primary structure. The DR absorber is shown to be real-time tunable to the time varying disturbance frequencies and capable of effective suppression within a frequency range. Additional properties of the method are decoupled nature of the control loop from the primary dynamics, and simplicity of implementation.

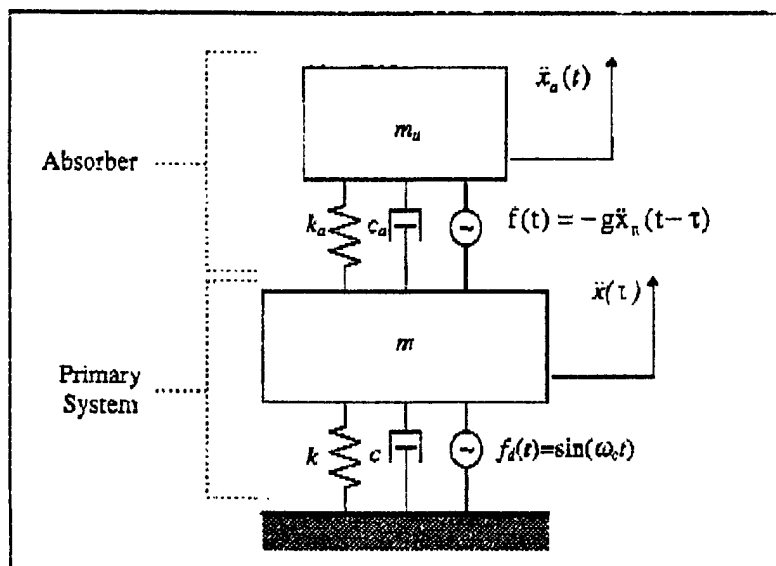


Figure 1: Delayed Resonator Absorber

\* Author for correspondence; email: olgac@eng2.uconn.edu

In this article, a number of new issues are considered. First, the basic control algorithm is advanced to add adaptive tuning capability to grapple with **variations of structural parameters**. Second, an experimental demonstration of this adaptive tuning routine is performed. In what follows, we summarize these achievements.

Consider the DR absorber in Fig. 1 shown with the primary structure. As is indicated on the figure, the feedback is  $g\ddot{x}(t-\tau)$ . Pursuing the governing dynamics and their respective characteristic equations it is proven that the absorber can perform perfect suppression at  $\omega_c$  if the feedback parameters are selected as

$$g = \frac{1}{\omega_c^2} \sqrt{(k - m\omega_c^2)^2 + (\omega_c c)^2}$$

$$\tau = \frac{-1}{\omega_c} \arctan 2 \left( \frac{\omega_c c}{m\omega_c^2 - k} \right)$$

It is clear that, these control gain and delay parameters are sensitive to the variations in the properties of the absorber (i.e.  $m_a$ ,  $k_a$ ,  $c_a$ ). Considering  $m_a$  to be a fixed quantity, the fluctuations in  $k_a$  and  $c_a$  will effect the tuning of the DR and its absorption performance. It is common in practice that, the absorber 'de-tunes' itself due to these fluctuations. In this study, a gradient based technique is used for this purpose. The DR is adaptively tuned to resonate at the desired frequency, by updating the parameters  $g$  and  $\tau$  periodically.

The algorithm may be summarized as follows:

- the excitation frequency is measured from the absorber acceleration signal.
- the complex transfer function between the absorber and primary displacements *at the frequency of excitation* is determined as

$$G(\omega_c i) = \frac{x(\omega_c i)}{x_a(\omega_c i)} = \rho e^{i\phi}$$

This is achieved by monitoring the time traces of  $x$  and  $x_a$ .

- In order to achieve perfect suppression,  $g + \Delta g$  and  $\tau + \Delta \tau$  are selected such that  $G + \Delta G = 0$  is assured, indicating  $x \rightarrow 0$ .

- d) Using the analytical expressions for the complex function  $\nabla G$  (gradient), the adaptive increments  $\Delta g$  and  $\Delta \tau$  are evaluated, and the values of  $g$  and  $\tau$  updated.

The sequence (a)—(d) is executed periodically, and the new values of  $g'$  and  $\tau'$  are delivered to the controller. This period is selected to be larger than the system settling time, in order to avoid crosstalk between the control loop and the parameter update loop.

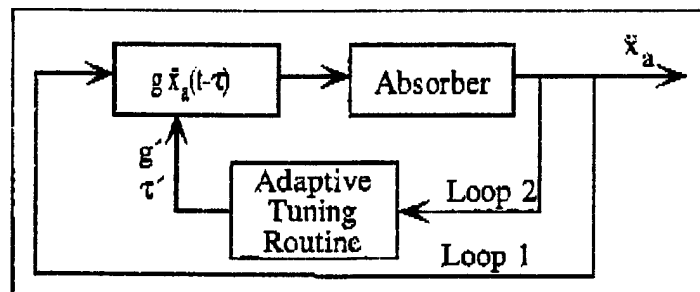


Figure 2: Adaptive tuning routine

The block diagram of the delayed control using the adaptive tuning is shown in Figure 2. Loop 1 depicts the absorber actuation loop, while Loop 2 depicts the adaptive parameter update loop.

Experimental verification of the proposed scheme is achieved on an oscillating plate. The experiments show superlative improvement over the non-adaptive implementation of the method.

# **Analysis and Testing of an Electrorheological Bypass Damper**

*Jason E. Lindler*  
Research Assistant

*Norman M. Wereley*  
Assistant Professor

Alfred Gessow Rotorcraft Center  
Department of Aerospace Engineering  
University of Maryland  
College Park, MD 20742

Modern helicopter design focuses on replacing traditional complex rotor systems with mechanically less complex hingeless and bearingless rotors. Although rotors have been simplified by the elimination of hinges and bearings, these advanced rotors are very susceptible to aerodynamic instabilities, such as air and ground resonance [1]. Resonance, which can cause fatigue and wear in moving parts, is responsible for greatly increasing life-cycle cost in a rotorcraft. Therefore, if modern rotor systems are to be cost effective, progress needs to be made in reducing resonance in mechanical system. While a simple passive damper can reduce resonance, most mechanical systems operate at a range of frequencies too large for passive damping to fully remove all of the vibrations. Active dampers can eliminate many of the shortcomings of passive dampers, but their complexity is contrary to the idea of simplifying rotorcraft systems. This need to produce damping which can adjust to a system's changing needs yet still have few moving parts has led to the development of semi-active damping systems. Dampers utilizing electrorheological (ER) and magnetorheological (MR) fluids can adjust to the changing needs of rotor blades while still incorporating the main goal of reducing the number of moving parts. However, before design engineering can take advantage of ER and MR dampers there needs to be an excellent understanding between the physical attributes of a damper and its performance. This is the motivation to develop, not just another ER damper, but a test bed where multiple damper variations can be tested and then fully modeled.

An ER damper test platform has been constructed to allow for development of quasi steady and dynamic models of ER dampers. The damper works by a piston head pushing electrorheological fluid through a narrow gap between two concentric aluminum

cylinders (Figure 1). Most importantly, the damper is designed to support a number of configuration, all of which can be analyzed and tested in a reasonable amount of time. This flexibility is achieved by using commercially available parts. Commercially available parts allows the main piston to be bought and shipped in one week, as opposed to being design and manufactured over a 6 week period. Furthermore, the plastic caps which insulated the concentric cylinders are outfitted with a standard 11/16 - 16 threads. This allows the damper to be connected to the hydraulic cylinder with standard industrial pipe fittings (Figure 2). The use of off the shelf pipe fittings allows for multiple configurations, even a parallel variation (Figure 3), to be constructed with no redesign of the hydraulic cylinder. Finally, by using in stock pieces for the aluminum cylinders, dampers of varying lengths and gaps between cylinders can be quickly built with no major redesign of the hydraulic cylinder's bypass.

Testing of these dampers will allow for the building of experimental data set to be used for validation of non-dimensional equations for ER dampers [2]. Furthermore, the quasi steady analysis will go to support current works by Kamath and Wereley on the modeling of ER dampers [3]. The goal of the damper platform is to relate a damper's physical characteristics and damping performance to already establish parameters such as the Bingham number and the non-dimensional plug thickness.

Already, preliminary testing of the ER damper platform has been completed (Figure 4 and 5). With its large dynamic range, the bypass design has proved to be an effective ER fluid damper. Furthermore the damper has demonstrated that commercial off the self parts can be used to accelerate the development process. The ER damper is preparing to undergo further test with different variations to its design dimensions. From testing the design with different dimensions it will be possible to develop a model that shows not only how electrorheological dampers behave, but how their physical attributes affect behavior. It is from this understanding, of how the physical dimensions effect the performance, that will allow ER dampers to be employed in today's mechanical designs.

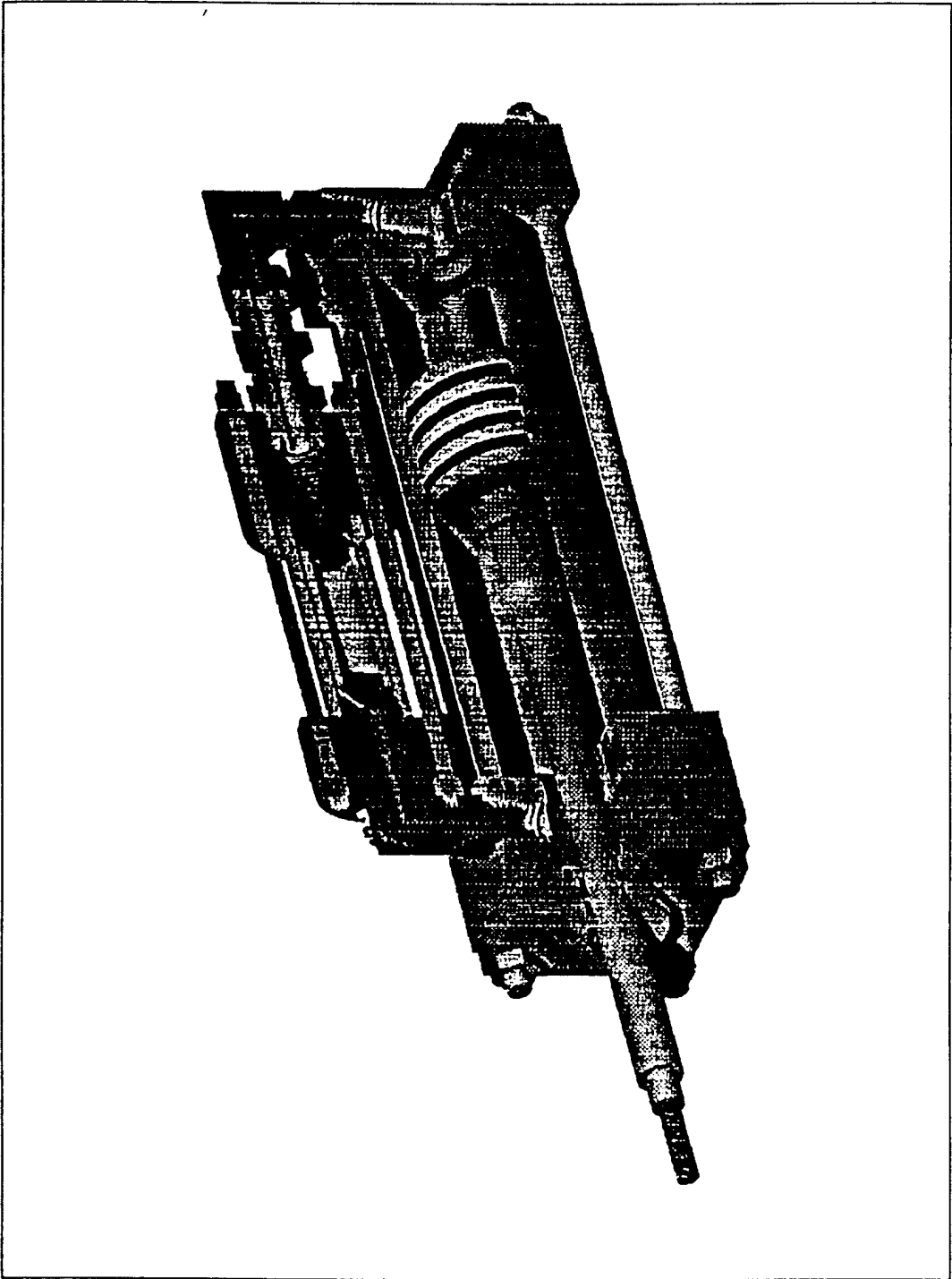
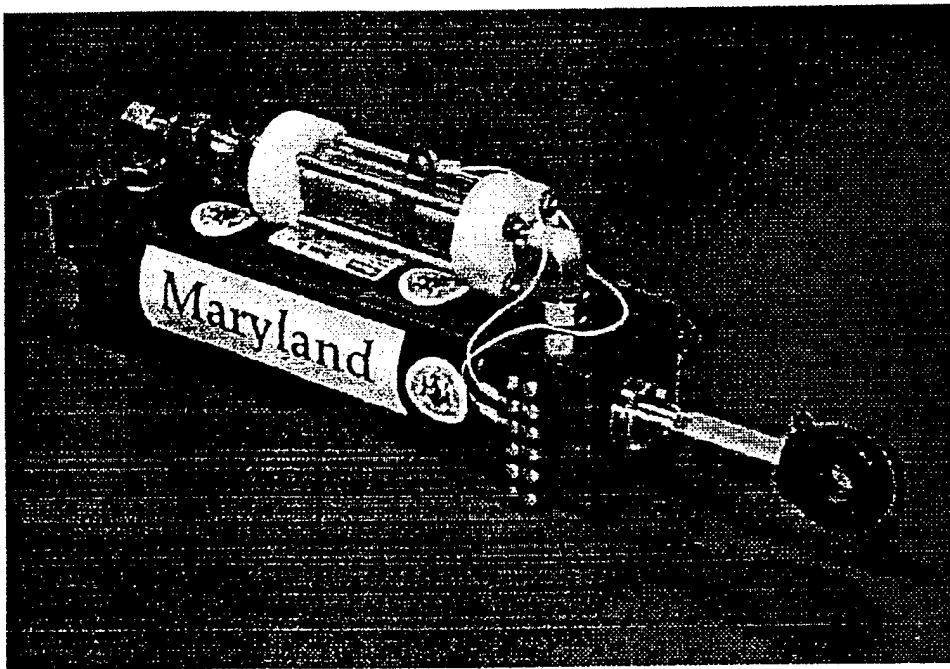
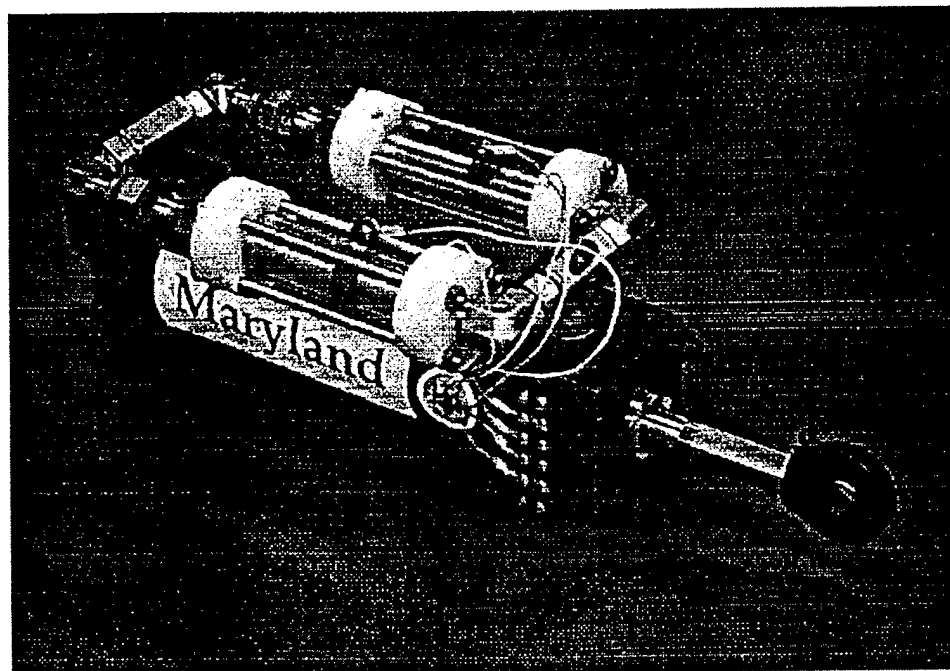


Figure 1 : Section View of ER Damper



**Figure 2 : Single Bypass Damper Design**



**Figure 3 : Double Bypass Damper Design**

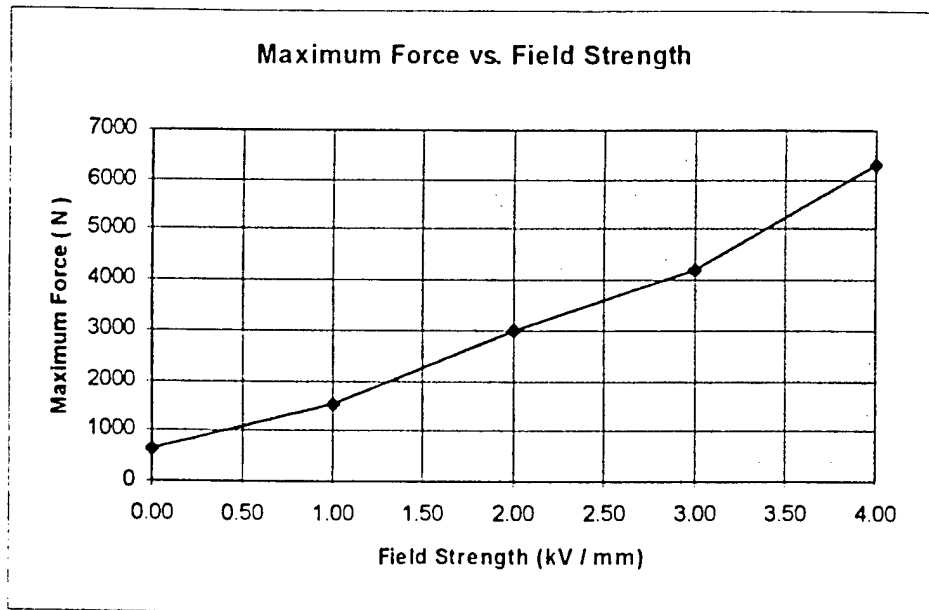


**Figure 4 : Results at 0.5 Hz with a 1.5 in. Stroke**

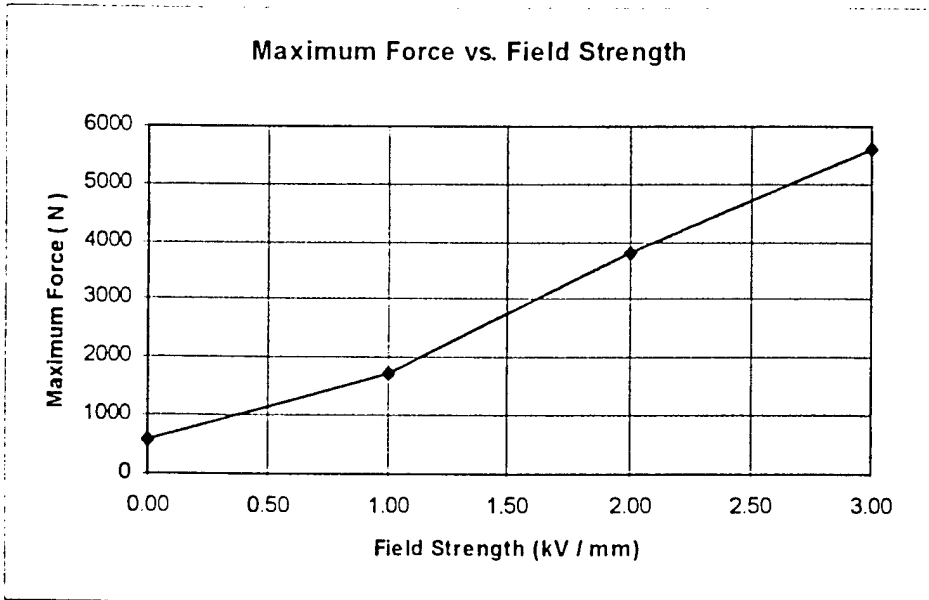


**Figure 5 : Results at .75 Hz with a 1 in. Stoke**

## References

- [1] Chopra, I., "Perspectives in Aeromechanics Stability of Helicopter Rotors," *Vertica*, Vol. 14, No. 4, pp. 457-508.
- [2] Pang, L., "Non-dimensional Analysis of Semi-Active Electrorheological Dampers Using Approximate Parallel Plate Models,"
- [3] Kamath, G., "A Nonlinear Viscoelastic-plastic Model for Electrorheological Fluids," *Smart Materials and Structures*, Vol. 6, pp. 351 - 359

# Dynamic Response of Sandwich Beam With Viscoelastic Layer

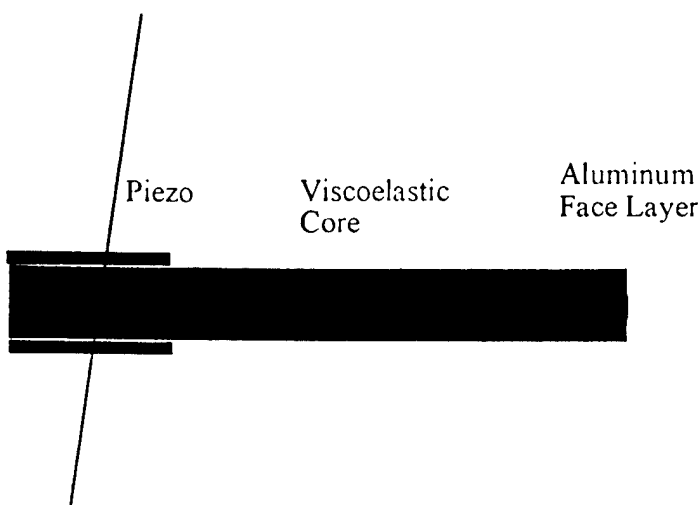
Gang Wang  
*Research Assistant*

Norman M. Wereley  
*Assistant Professor*

Alfred Gessow Rotorcraft Center, Department of Aerospace Engineering  
University of Maryland at College Park, College Park, MD 20742

A hybrid damping scheme using passive dissipative layer, and smart actuators has been proposed for the control of interior acoustics. In order to better understand the behavior of this kind of structures. We start from the 1-dimensional case: cantilever beam. The 3-layered sandwich consists of aluminum face layer with surface bonded piezoelastic actuator and a viscoelastic core. The analysis includes the extension and transverse energies in the faces and shear in the core. Complex shear modulus has been used in the viscoelastic core. The equation<sup>[1]</sup> of motion is established in term of the transverse displacement w and solved by the wave progressive method<sup>[2,3]</sup>. Also a simple finite element formulation<sup>[4]</sup> is employed to model the response of the beam. The assumed mode method is discussed as well. All the analytical works have been validated by the experimental results. Also for all the beams, the analytical results are compared to the experimental results. Some agreements have been achieved. We need modify our models further to predict the response accurately. Also we will use the laser sensor to measure the tip displacement of the beam. This will give us better experimental results.

From the results which we have gotten, we know that using the analytical models to predict the behavior of the sandwich structures with dissipative core is feasible. And this is very helpful for the study of the sandwich plate and acoustic control panel in future.



## **Reference**

1. Mead, D J and Markus, S. 'The Forced Vibration of a Three-Layer , Damped Sandwich Beam with Arbitrary Boundary Condition, ' J. Sound and Vibration, Vol. 10, NO2, 1969.
2. Subhobroto Nath and Norman M Wereley 'Active coonstrained Layer Damping For Rotorcraft Flex Beams', AIAA Adapative structures Forum, 13-14 April 1995.
3. D. J. Pines and A.H. von Flotow, ' Active Control of Bendig Wave Propogation at Acoustic Frequency', J. Sound and Vibration, 1990 142(3).
4. William C. Van Nostrand, Gareth J. Knowles and Daniel J. Inman, 'Finite Element Model For Active Constrained Layer Damping', SPIE, Vol. 2193

# Damping Identification in Helicopter Rotor Systems

Clifford B. Smith<sup>†</sup>  
Graduate Research Assistant

Julieta Perez<sup>‡</sup>  
Undergraduate Research Assistant

Norman M. Wereley<sup>§</sup>  
Assistant Professor

Alfred Gessow Rotorcraft Center  
Department of Aerospace Engineering  
University of Maryland  
College Park, Maryland 20742

## ABSTRACT

### Introduction

Advanced helicopter rotor systems, including hingeless and bearingless rotors, are mechanically less complex than traditional rotor systems, due to the elimination of various hinges and bearings. These components were replaced with a flexure, or flexbeam, which is subject to all of the vibratory loads from the rotor. These advanced rotor systems tend to be soft in-plane, implying that the first lag mode frequency,  $\sim 0.7\Omega$ , is less than the rotational frequency,  $\Omega$ . Since the rotor is soft-in-plane, the lag mode can couple with either the fuselage modes in forward flight, or the landing gear modes on the ground, leading to air and ground resonance instabilities. Damping is a major stabilizing influence of both air and ground resonance, and methods of introducing damping into the rotor are currently under investigation. In order to study damping in a helicopter rotor system, it is necessary to first determine an appropriate method for identifying the damping level achieved based on the vibratory response of the system. A helicopter rotor system is typically a spectrally dense environment, which often leads to difficulties in assessing the damping performance of a given rotor system. The most common method in recent years for identifying damping is the moving block analysis. More recently, a damping identification method based on Hilbert transform analysis was suggested by Smith and Wereley, and in this work, a modified version of the Hilbert transform analysis is also introduced, which accounts for possibility of two closely spaced modes.

### Performance Analysis of Damping Identification Techniques

Damping identification techniques for rotorcraft applications are needed for data collected in a variety of situations. Transients may be obtained from tests as simple as a laboratory benchtop experiment or as complex as real flight test data. In the case of the more complex situations, the task of estimating the modal frequencies and damping ratios can be complicated by the presence of persistent periodic steady state vibrations that typically occur at harmonics of the rotor rotational frequency, poor signal to noise ratios, closely spaced modes, and the difficulty of exciting these modes in the rotating frame. The helicopter rotor testing environment is especially prone to experimental difficulties in the characterization of damping due to high noise levels.

---

<sup>†</sup> Student Member, AIAA, AHS, SAMPE.

<sup>‡</sup> Student Member, AIAA

<sup>§</sup> Member, AIAA, AHS. Tel: (301) 405-1927, Fax: (301) 314-9001. Email: [wereley@eng.umd.edu](mailto:wereley@eng.umd.edu).

Thus, high levels of sinusoidal excitation at modal frequencies are required to guarantee sufficiently high signal-to-noise ratios in transient decay signatures, so as to calculate reliable damping estimates. In order to study the performance of the damping identification algorithms considered here, data sets collected from three different types of tests (benchtop, vacuum spin chamber, and hover stand) were analyzed and the results compared. The benchtop testing was performed on a set of flat, 8 ply Gr/Ep beams with post bonded constrained viscoelastic layers, providing the ability to study a highly damped(5%-7%), single mode system. The vacuum chamber tests were conducted on a set of flat, 24 ply Gr/Ep beams with cocured viscoelastic layers. The maximum damping level was lower than the benchtop tests, but this configuration allowed for the study of centrifugal effects and minor noise effects. Finally, the hover stand tests were performed for a 1/8<sup>th</sup> Froude scaled rotor with a set of composite coupled Gr/Ep flexbeams in an I-beam configuration. This is the most complex testing environment used in this study, and includes many problems found in real world testing.

## Results and Conclusions

The first situation investigated was the single mode benchtop test. This test was performed on a set of four Gr/Ep beams with varying viscoelastic layer thicknesses (0, 5, 10, and 15 mil). The overall damping level varied from approximately 1% in the beam with no viscoelastic to 6%-7% in the beam with the 15 mil layer of viscoelastic material. Figure 1. shows the results obtained from both the single mode Hilbert technique and the moving block technique. Particularly interesting are the effects of varying the block length used for the moving block calculations. The adaptive block length is calculated on a transient by transient basis to use the same data as the Hilbert transform algorithm, while the other cases are run using the fixed length block indicated. It is easily seen that although a longer block length may increase frequency resolution, if the transient is too long, and if there is any noise present, the calculated damping level can be significantly underpredicted.

In the case of the vacuum spin chamber testing, testing was performed on another set of passively damped Gr/Ep beams. These specimens consisted of 24 plies of Gr/Ep with two cocured damping layers. One damping layer was located two plies in on each side of the beam. Again the thickness of the layers was varied from 0 to 15 mils. Testing was performed in vaccum at rotational speeds from 0 RPM to 900 RPM in increments of 150 RPM. The results of this testing are shown in Figure 2. It can be seen from the Hilbert transform results in figure 2a that there is an increase in damping as the viscoelastic thickness is increased, and as the rotational speed is increased, centrifugal loading stiffens the beam, reducing the effectiveness of the damping layers. The moving block results in figure 2b, agree with this, but the trends are not nearly as smooth. This is possibly due to the fact that a fixed block length (2 sec) was used in the analysis of the data.

The final data set considered here was obtained from a hover stand test of a 1/8<sup>th</sup> Froude scaled rotor with a set of composite coupled Gr/Ep flexbeams. This data set is both spectrally dense and has significant amounts of noise; problems which would be encountered in many real world applications. Figure 3 shows the results of both the single and dual mode Hilbert algorithms, as well as the moving block algorithm with a 4 second block length. It is evident that all three techniques have reasonable agreement, with the single mode Hilbert transform method tending to slightly underpredict the other two methods. Figure 4 shows the effects of varying

block length on the moving block predictions for this data set. It can be seen that if the block length chosen is too short, the moving block technique tends to have problems, while the longer block lengths produce better results. This is primarily due to the low damping level and correspondingly longer transient length of this data as compared to the benchtop case. It is also important to note that the Hilbert transform techniques do a good job of identifying damping without requiring the computational expense of multiple FFT calculations, making the Hilbert transform techniques a viable option for faster damping identification in situations such as this.

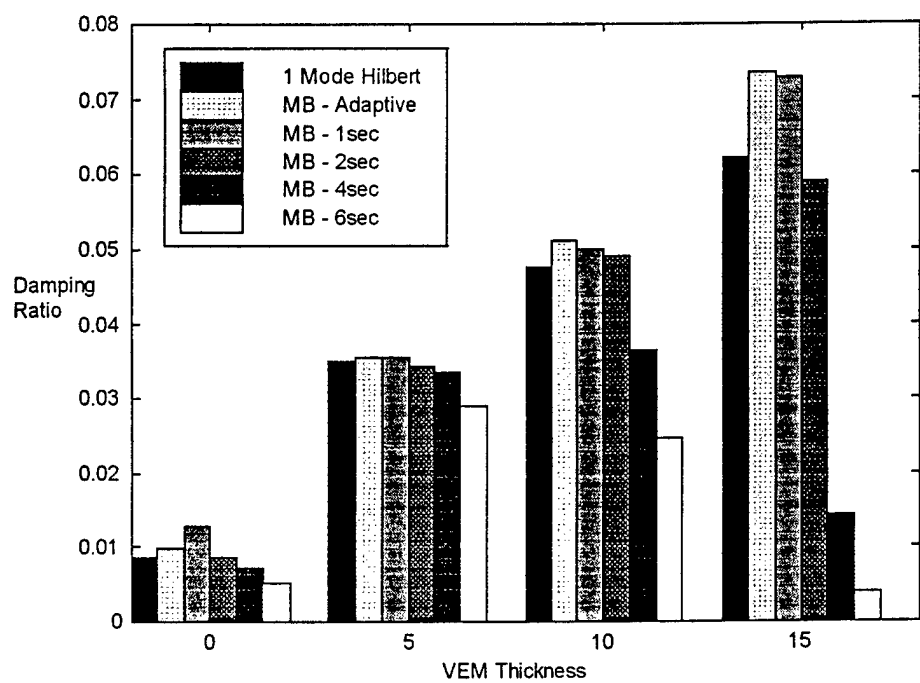
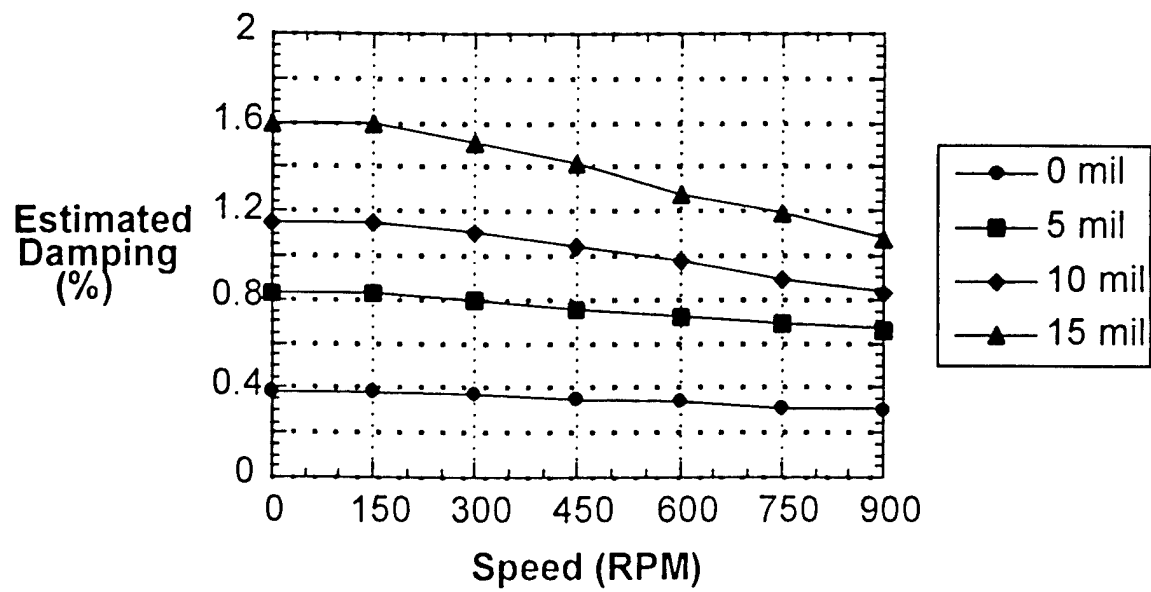
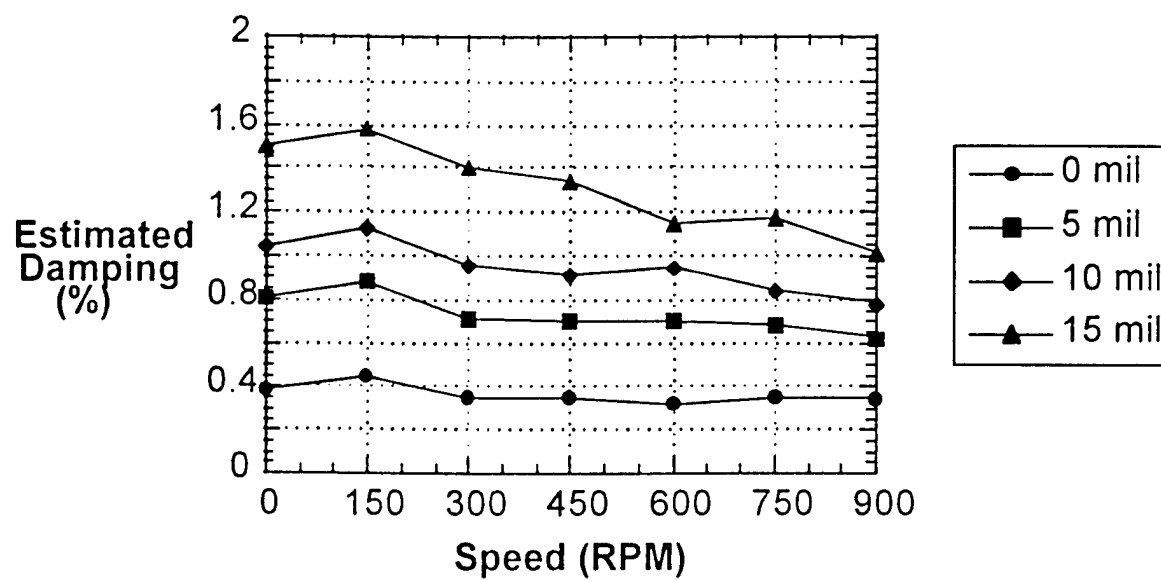


Figure 1. Hilbert transform and moving block results for benchtop tests

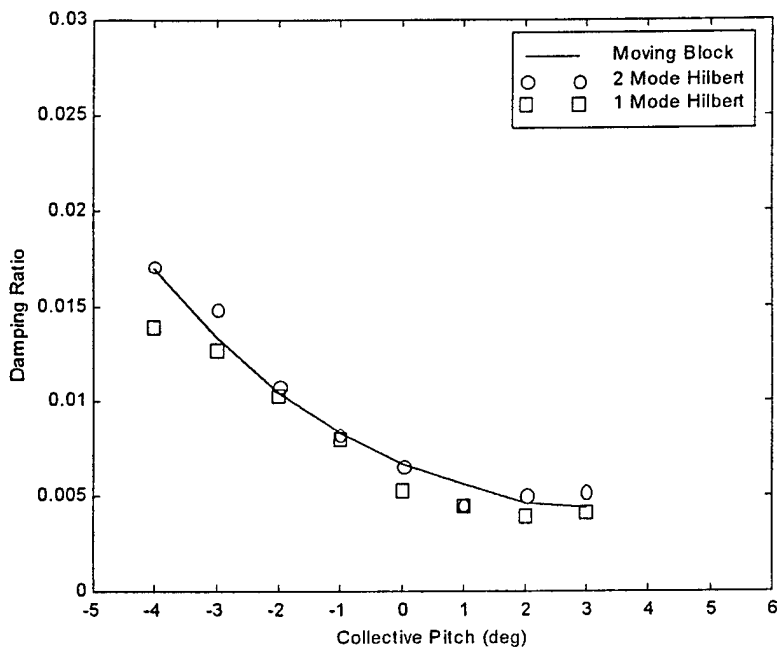


(a) Hilbert transform results for vacuum chamber tests

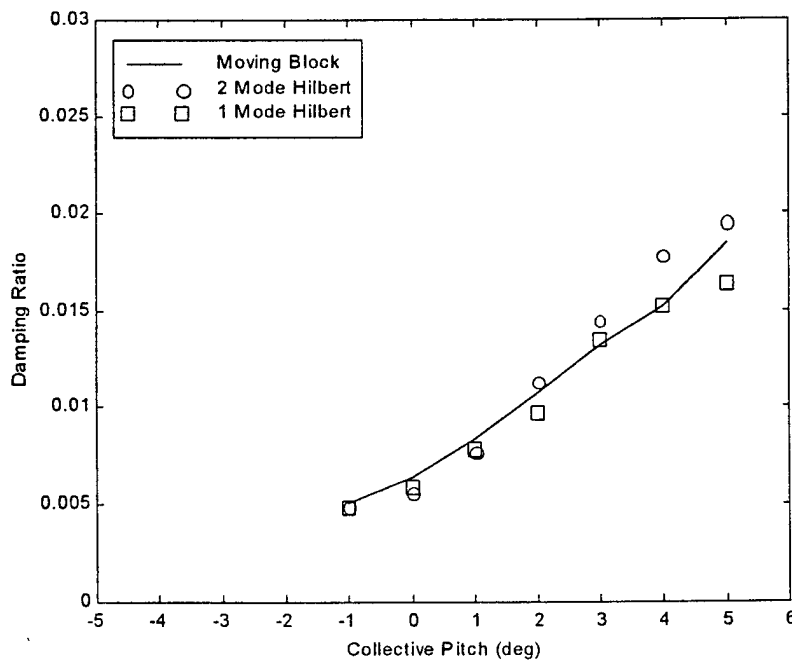


(b) Moving block results for vacuum chamber tests

Figure 2. Vacuum chamber test results

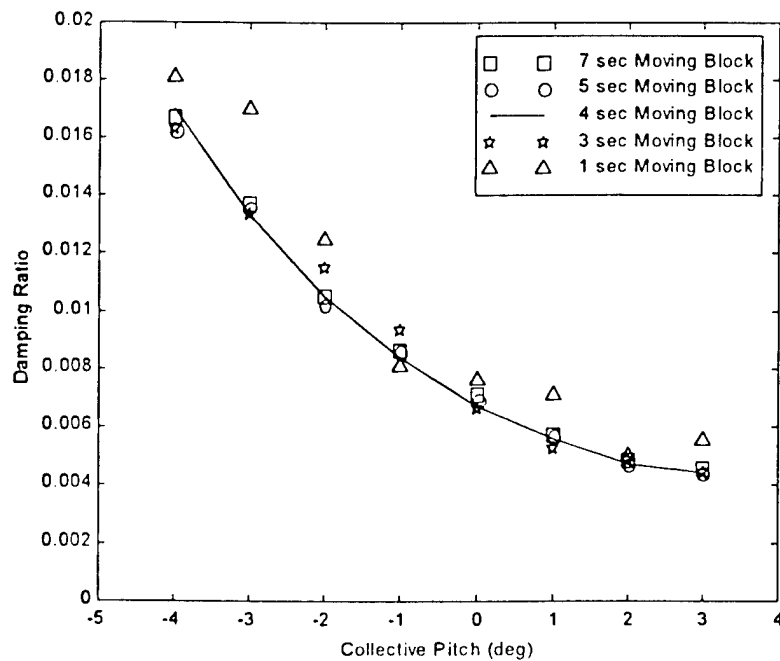


(a) Results for positively coupled flexbeam on hover stand at 600 RPM

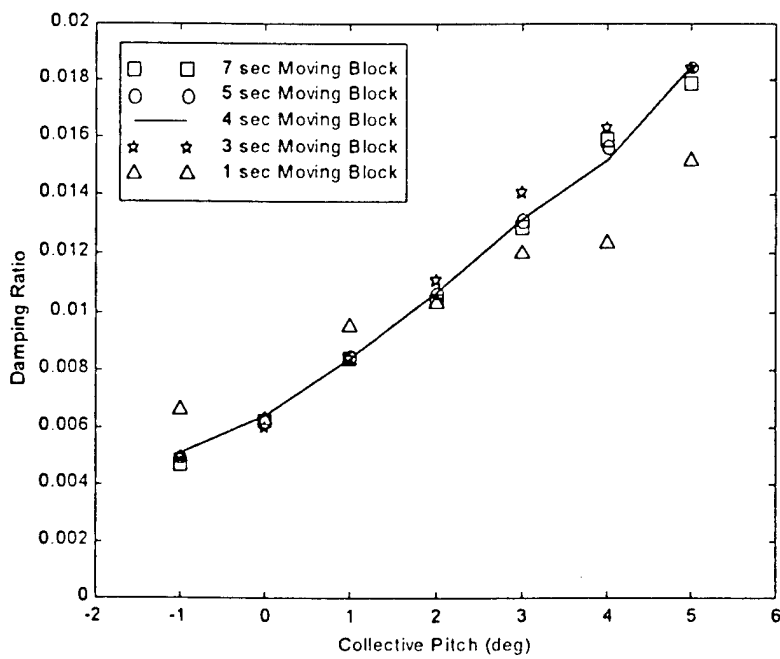


(b) Results for negatively coupled flexbeam on hover stand at 600 RPM

(c) Figure 3. Hover stand test results



(a) Effects of block length on identified damping level for positive coupling



(b) Effects of block length on identified damping level for negative coupling

Figure 4. Hover stand results for multiple block lengths

## Switchmode Amplifiers for Smart Materials

by

Troy Schelling,  
Virginia Power Technologies, Inc.  
Blacksburg, VA

Douglas K. Lindner and Gregory A. Zvonar  
Bradley Department of Electrical Engineering  
Virginia Polytechnic Institute and State University  
Blacksburg, VA 24061-0111

As smart materials become a part of integrated systems, more attention is being paid to the electronics that operate them. The power amplifiers required in these systems convert the signal from the control system into the voltage or current waveform required by the actuators. This often involves the conversion of a very low voltage waveform from a computer into a waveform of several hundred volts for the actuators. The amplifiers used in research have traditionally been bulky linear amplifiers, only suitable for laboratory use. One option that is available is the switchmode amplifier, which does not have the same inherent power dissipation requirements as a linear amplifier. Since the switchmode amplifier generates less heat, it can be made several times smaller than a linear amplifier. Virginia Power Technologies, Inc., working with Virginia Tech, has developed switchmode amplifiers for both PMN and PZT material. These amplifiers have shown remarkable reductions in size, while still offering the performance required by the smart material systems.

Since PMN material has a nonlinear relationship between its electrical and mechanical properties, a nonsinusoidal electrical signal is required to develop a sinusoidal mechanical output. A nonlinear control system has been developed and integrated into a PMN amplifier that compensates for the material characteristics, providing a velocity output that matches the input control signal.